

REPORT DOCUMENTATION PAGE			Form Approved OMB NO. 0704-0188		
<p>The public reporting burden for this collection of information is estimated to average 1 hour per response, including the time for reviewing instructions, searching existing data sources, gathering and maintaining the data needed, and completing and reviewing the collection of information. Send comments regarding this burden estimate or any other aspect of this collection of information, including suggestions for reducing this burden, to Washington Headquarters Services, Directorate for Information Operations and Reports, 1215 Jefferson Davis Highway, Suite 1204, Arlington VA, 22202-4302. Respondents should be aware that notwithstanding any other provision of law, no person shall be subject to any penalty for failing to comply with a collection of information if it does not display a currently valid OMB control number. PLEASE DO NOT RETURN YOUR FORM TO THE ABOVE ADDRESS.</p>					
1. REPORT DATE (DD-MM-YYYY) 12-05-2018		2. REPORT TYPE Final Report		3. DATES COVERED (From - To) 15-Sep-2013 - 1-Mar-2018	
4. TITLE AND SUBTITLE Final Report: Influence of Grain Boundary Structure on Nanocrystalline Thin Film Stress States			5a. CONTRACT NUMBER W911NF-13-1-0436		
			5b. GRANT NUMBER		
			5c. PROGRAM ELEMENT NUMBER 611102		
6. AUTHORS			5d. PROJECT NUMBER		
			5e. TASK NUMBER		
			5f. WORK UNIT NUMBER		
7. PERFORMING ORGANIZATION NAMES AND ADDRESSES University of Alabama - Tuscaloosa Box 870104 Tuscaloosa, AL 35487 -0104			8. PERFORMING ORGANIZATION REPORT NUMBER		
9. SPONSORING/MONITORING AGENCY NAME(S) AND ADDRESS (ES) U.S. Army Research Office P.O. Box 12211 Research Triangle Park, NC 27709-2211			10. SPONSOR/MONITOR'S ACRONYM(S) ARO		
			11. SPONSOR/MONITOR'S REPORT NUMBER(S) 64472-MS.25		
12. DISTRIBUTION AVAILABILITY STATEMENT Approved for public release; distribution is unlimited.					
13. SUPPLEMENTARY NOTES The views, opinions and/or findings contained in this report are those of the author(s) and should not be construed as an official Department of the Army position, policy or decision, unless so designated by other documentation.					
14. ABSTRACT					
15. SUBJECT TERMS					
16. SECURITY CLASSIFICATION OF:			17. LIMITATION OF ABSTRACT UU	15. NUMBER OF PAGES	19a. NAME OF RESPONSIBLE PERSON Gregory Thompson
a. REPORT UU	b. ABSTRACT UU	c. THIS PAGE UU			19b. TELEPHONE NUMBER 205-348-1589

RPPR Final Report

as of 13-Jun-2018

Agency Code:

Proposal Number: 64472MS

Agreement Number: W911NF-13-1-0436

INVESTIGATOR(S):

Name: Gregory Thompson
Email: gthompson@eng.ua.edu
Phone Number: 2053481589
Principal: Y

Organization: **University of Alabama - Tuscaloosa**

Address: Box 870104, Tuscaloosa, AL 354870104

Country: USA

DUNS Number: 045632635

EIN: 636001138

Report Date: 01-Jun-2018

Date Received: 12-May-2018

Final Report for Period Beginning 15-Sep-2013 and Ending 01-Mar-2018

Title: Influence of Grain Boundary Structure on Nanocrystalline Thin Film Stress States

Begin Performance Period: 15-Sep-2013

End Performance Period: 01-Mar-2018

Report Term: 0-Other

Submitted By: Gregory Thompson

Email: gthompson@eng.ua.edu

Phone: (205) 348-1589

Distribution Statement: 1-Approved for public release; distribution is unlimited.

STEM Degrees: 2

STEM Participants: 7

Major Goals: This research program aims to elucidate the underlying effects of alloy composition on thin film growth. When a thin film grows, it will intrinsically develop either tensile or compressive residual stresses that lead to delamination, cracking, or buckling failures of the film on the substrate. Historically, this film stress has been controlled by processing changes that include deposition rate variation, substrate temperature, and/or pressure variations. Here, this program aims to utilize intrinsic chemical partitioning in alloys to control the resulting structure of the film and thereby the stress. In particular, the program is centered on how solutes are able to control the mix mobility of adatoms during growth, manipulate the film's grain size and texture, and alter the chemical structure of the film.

A series of case study alloys have been selected based upon their thermodynamic tendencies to phase separate and regulate either a compressive or tensile stress condition. Using both experimental in situ measurements with post deposition characterization via TEM and atom probe, the links between structure and properties have and are being made. Computational studies have also been undertaken to better understand the experimental findings as well as lead experimental direction.

Accomplishments: A summary of each topical area is given below with details developed in the uploaded technical document.

(1) Modeling of thin film growth: This research involved molecular dynamic simulations of sputter deposition where a variety of microstructures were simulated with experimental parameters (such as deposition rate and energy) to study their effect on film stress evolution.

(2) Experimental study of high mobility Cu growth: This research provided a self-contained data set of Cu films grown over extensive range of deposition processing parameters (pressures between 0.266 Pa to 2.66 Pa and rates between 0.012 nm/s to 2.4 nm/s). As a result, this work is distinct in that it has the data set necessary to compare to kinetic models to understand thin film growth. In order to remove microstructural effects to stress, we devised a means to control the grain size to be consistent between each of these conditions.

(3) Alloying effects in Cu based films: By alloying Cu with Ag and V, the intrinsic effects of a solute with different mobility's on Cu's stress state was evaluated.

(4) Influence of solid solution mixing on Cu film growth: This research discusses how Ni (unlike Ag or V, which are immiscible) influences the stress state of a growing Cu film when the solute is retained in solution. It was found that the film became compressive with the Ni solute, but once the grain boundary was thermodynamically saturated, the compressive stress was reduced.

(5) Growth stresses in Fe(Cr) films: This research investigated the effect of low Cr solute segregation on the growth

RPPR Final Report as of 13-Jun-2018

stresses in Fe. Unlike the Cu (which is a high mobility adatom), Fe is a low mobility adatom providing a comparative example to Cu. Though Fe and Cr are both low mobility adatoms, which grow with a tensile stress, at low concentrations, the mixing of the species reduces the tensile stress.

(6) Correlated precession electron diffraction and atom probe tomography: Based on the findings of the stress changes with Cr solute additions to Fe, the use of precession electron diffraction and atom probe was used to determine the specificity of Cr segregation to particular Fe grain boundaries, which were then compared to a hybrid molecular dynamics and kinetic Monte Carlo simulation.

(7) Annealing effects on the stress evolution in Fe-Cr films: Expanding on the study of Fe(Cr) investigations, the influence of in situ annealing during deposition on film stress was investigated. The results revealed both partitioning to the grain boundaries, spinodal decomposition in the grains themselves, and composition dependent abnormal grain growth

(8) Stability and ordering behavior in FeCr films: This work revealed, even at ambient temperature deposition, near equatomic FeCr films will chemical order into the high temperature sigma phase, even though the substrate is not annealed. Furthermore, using advanced atom probe clustering techniques, we have revealed chemical ordering of Cr when in solution with Fe, which had been postulated in the literature.

(9) Early oxidation effects in nanocrystalline Fe(Cr): Using a DURIP award to study in situ grain growth via heating in the TEM, the early oxidation of Cr₂O₃ was found to occur from the residual gas pressure in the TEM.

(10) Alloying and stress effects in other systems: Though the majority of the research focused on the alloying effects on a high mobility adatom (Cu) and a low mobility adatom (Fe), the research also explored alloying effects in other systems to set forth the ground work for future studies. These are as follows:

(10a) Influence of phase stability on film stress: Here the "beta-to-alpha" W film stress evolution was studied and modified by the use of Ti, which was shown to remove the influence of oxygen in stabilizing the metastable "beta" W phase in the early stages of film growth

(10b) Influence of mix alloying on the intrinsic partitioning and stress evolution: In the original paper by Fu and Thompson (Journal of Applied Physics 2010) which showed how the solute segregation regulated stress, this follow on work examined if indeed zero stress states are achieved with the matrix and grain boundary compositions being uniform.

(10c) Stress evolution in highly reflective coatings: In this investigation, the effect of mixing of Al and Ag was studied to determine how the stress changed surface roughness, which impacts diffuse scattering from reflective coatings.

(11) Connections of solute stabilization and film stress: In this invited review article, the paper outlines the connections of solute segregation with the ideas of solute partitioning in nanocrystalline thin films to control residual stress.

Training Opportunities: Xuyang (Rhett) Zhou - graduate student
Tyler Kaub - graduate student

Bhargava Samanthula – New Albany High School, New Albany, Ohio - HSAP 2015

Mason McKechnie – University of Alabama - URAP 2015

Ryan Anthony – Northridge High School, Tuscaloosa AL - HSAP 2016

Jaeden Joyner – Northridge High School, Tuscaloosa AL - HSAP 2017

Morgan Ross - University of Alabama - URAP 2017

RPPR Final Report as of 13-Jun-2018

Results Dissemination: Publications:

In print -

- (1) Xuyang Zhou and Gregory B. Thompson "Influence of solute partitioning on the microstructure and growth stresses in nanocrystalline Fe(Cr) thin films" *Thin Solid Films* 648 (2018) 83-93: 10.1016/j.tsf.2018.01.007
 - (2) Grégory Abadias, Eric Chason, Jozef Keckes, Marco Sebastiani, Gregory B. Thompson, Etienne Barthel, Gary L. Doll, Conal E. Murray, Chris H. Stoessel, and Ludvik Martinu "Review Article: Stress in thin films and coatings: Current status, challenges, and prospects" *Journal of Vacuum Science & Technology A: Vacuum, Surfaces, and Films* 36, 020801 (2018); doi:10.1116/1.5011790 *From the leading work on alloy design of stress evolution, Prof. Thompson was asked to join other leading researchers in film stress evolution to participate in a review article on the status of the field. Through the support of this grant, Prof. Thompson was able to particulate and references the grant in the acknowledgement section.
 - (3) Olivia K. Donaldson, Khalid Hattar, Tyler Kaub, Gregory B. Thompson, and Jason R. Trelewicz "Solute stabilization of nanocrystalline tungsten against abnormal grain growth" *Journal of Materials Research* 33(1) (2017) 68-80: 10.1557/jmr.2017.296 *From the stress evolution work in W(Ti), the team was asked to collaborate with Prof. J. Trelewicz in the growth of a series of similar films at U of Alabama, as well as providing characterization of them, for a series of studies on thermal stability. This paper references this grant for the support to do this collaborative research.
 - (3) Tyler Kaub and Gregory B. Thompson "Ti segregation in regulating the stress and microstructure evolution in W-Ti nanocrystalline films" *Journal of Applied Physics* 122(8) (2017) 085301: 10.1063/1.4991880
 - (4) Tyler M. Kaub, Ryan Anthony, and Gregory B. Thompson "Intrinsic stress response of low and high mobility solute additions to Cu thin films" *Journal of Applied Physics* 122 (2017) 225302: 10.1063/1.5008269
 - (5) M. Kapoor, T. Kaub, K. A. Darling, B.L. Boyce, and G.B. Thompson "An atom probe study on Nb solute partitioning and nanocrystalline grain stabilization in mechanically alloyed Cu-Nb" *Acta Materialia* 126 (2017) 564-575: 10.1016/j.actamat.2016.12.057 (specifically sites this award, via synergy with ARL scientists)
 - (6) Xuyang Zhou and Gregory B. Thompson "Linking experimental solute segregation specificity in nanocrystalline alloys to computational predictions" *Microsc. Microanal.* 23 (suppl. 1) 2017, 704-705: 10.1017/S1431927617004184
 - (7) C. Sterwerf, T. Kaub, C. Deng, G.B. Thompson, L. Li "Deformation mode transitions in amorphous-Cu₄₅Zr₅₅/crystalline-Cu multilayers" *Thin Solid Films* 626 (2017) 184-189: 10.1016/j.tsf.2017.02.035 *Based on Dr. Kaub and Prof. Thompson's work on stress evolution in Cu thin films, they were asked to fabricate and characterize a series of Cu and glassy CuZr films by Prof. Lin Li. Through the support of this grant, which is acknowledge, this synergistic work to the proposed studies were done in this collaboration.
 - (8) X. Zhou, Xuyang Zhou, Xiao-xiang Yu, Tyler Kaub, Richard L. Martens, and Gregory B. Thompson "Grain Boundary Specific Segregation in Nanocrystalline Fe(Cr)" *Scientific Reports* 6 (2016) 34642: 10.1038/srep34642
 - (9) T.M. Kaub, P. Felfer, J.M. Cairney, and G.B. Thompson "Influence of Ni solute segregation on the intrinsic growth stresses in Cu(Ni) thin films" *Scripta Materialia* 113 (2016) 131-134: 10.1016/j.scriptamat.2015.10.010
 - (10) X. Zhou, T. Kaub, R.L. Martens, and G.B. Thompson "Influence of Fe(Cr) miscibility on thin film grain size and stress" *Thin Solid Films* 612 (2016) 29-35: 10.1016/j.tsf.2016.05.024
 - (11) M. Kapoor and G.B. Thompson "Role of atomic migration in nanocrystalline stability: Grain size and thin film stress states" *Current Opinion in Solid State and Materials Science* 19 (2015) 138-146: 10.1016/j.cossms.2014.11.001
 - (12) G.B. Thompson, M. Kapoor, T. Kaub, B. Boyce, B. Clarke, K. Darling, P. Felfer, and J. Cairney "Investigations into solute stabilizing effects in nanocrystalline materials: an atom probe characterization study" *Microsc. Microanal.* 21 (suppl. 3) 2015, 357-358: 10.1017/S1431927615002585
- Under-review/preparation:
- (1) Xuyang Zhou and Gregory B. Thompson "The influence of alloy atoms interactions on thin films stress" submitted to *Applied Surface Science* (2018)
 - (2) Xuyang Zhou, Xiaoxiang Yu, David Jacobson, and Gregory B. Thompson "Molecular dynamic study of the stress generation during thin film growth" submitted to *Physical Review B* (2018)
 - (3) Xuyang Zhou and Gregory B. Thompson "In situ TEM observations of initial oxidation behavior in Fe-rich Fe-Cr alloys" submitted to *Journal of Materials Science* (2018).
 - (4) Xuyang Zhou and Gregory B. Thompson "Phase and Microstructural evolution in sputtered Fe-Cr films" submitted to *Materialia* (2018)
 - (5) Tyler Kaub, Zhaoxia Rao, Eric Chason, and Gregory B. Thompson "The Influence of Deposition Parameters on the Stress Evolution of Sputter Deposited Copper" submitted to *Surface Coatings and Technology* (2018)
 - (6) Tyler Kaub, Bhargava Samanthula, and Gregory Thompson "Stress Evolution and Microstructure in Ag-Al Thin Films" to be submitted to *J. Vac. Sci. Techn. A* (2018)

RPPR Final Report as of 13-Jun-2018

Presentations:

2017

- (1) Xuyang Zhou and Gregory B. Thompson "Linking Experimental Solute Segregation Specificity in Nanocrystalline Alloys to Computational Predictions" Microscopy & Microanalysis August 6-10, 2017, St. Louis MO
- (2) T.M. Kaub, D. Jacobson, and GB Thompson "Influence of Chemical Interface Structure on Thin Film Stress Evolution" Materials Science & Technology 2017, Pittsburg, PA
- (3) Xuyang Zhou, Tyler Kaub, Florian Vogel, Ryan Anthony, and Gregory B. Thompson "Correlative Precession Electron Diffraction and Atom Probe Tomography Characterization of Cluster Formations in Nanocrystalline Cu(V)" Southeastern Microscopy Conference Athens, GA May 24-26, 2017
- (4) Xuyang Zhou, Tyler Kaub, Florian Vogel, Ryan Anthony, and Gregory B. Thompson "Correlative Precession Electron Diffraction and Atom Probe Tomography Characterization of Cluster Formations in Nanocrystalline Cu(V)" Southeast Microscopy (SEM) Conference, Athens, Georgia, May 24-26, 2017 (Oral presentation – finalist for the Ruska Award Competition)

2016

- (5) Tyler Kaub, David Jacobson, and Gregory B. Thompson "Use of Solute Segregation to Tune Intrinsic Stress States in Metallic Thin Films" Joint ICMCTC-SVC Workshop on Stress Evolution in Thin Films and Coatings: from Fundamental Understanding to Control, Rosemont, IL October 2-5, 2016 (Poster presentation)
- (6) Xuyang Zhou, Tyler Kaub, and Gregory B. Thompson "Influence of Phase Separation on the Microstructure and Growth Stresses in Nanocrystalline Fe(Cr) Thin Films" Joint ICMCTC-SVC Workshop on Stress Evolution in Thin Films and Coatings: from Fundamental Understanding to Control, Rosemont, IL October 2-5, 2016 (Oral presentation)
- (7) X. Zhou, XX Yu, T Kaub, RL Martens, and GB Thompson "Revealing Specific Grain Boundary Segregation Behavior in Nanocrystalline Fe(Cr)" Atom Probe Tomography & Microscopy 2016, Gyeongju, South Korea, June 12-17, 2016 (Poster presentation)
- (8) X. Zhou, XX Yu, T Kaub, RL Martens, and GB Thompson "Specific Grain Boundary Character Segregation in Nanocrystalline Fe(Cr) Thin Films" EBSD 2016, The University of Alabama, Tuscaloosa, AL (Poster presentation)

2015

- (9) Gregory B. Thompson "Nanoscale Stability: An investigation of how intermixing and segregation stabilizes nanocrystalline phases" Department of Chemical Engineering Invited Seminar, University of Melbourne, Australia, April 21st, 2015
- (10) Gregory B. Thompson, Monica Kapoor, Tyler Kaub, Brad Boyce, Blythe Clark, Kris Darling, Peter Felfer and Julie Cairney "Investigation into the solute stabilizing effects in nanocrystalline materials: An atom probe characterization study" Microscopy & Microanalysis, Portland, OR August 2-6, 2015

REMAINING PRESENTATIONS FOUND IN TECHNICAL REPORT (out of characters)

Honors and Awards: 2017 – Professor Gregory B. Thompson was recognized at The Minerals Metals and Materials Society Brimacombe Medalist, with the citation reading " For notable contributions in linking analytical microscopy with phase and property studies across materials and length scales, commitment to STEM education, and service to TMS."

2017 – Graduate student Xuyang (Rhett) Zhou was the Microscopy Society of America Student Award winner for his work "Linking Experimental Solute Segregation Specificity in Nanocrystalline Alloys to Computational Predictions"

2014 – Professor Gregory B. Thompson was awarded the Blackmon-Moody Outstanding Professor of the Year – The Frederick Moody Blackmon and Sarah McCorkle Moody Outstanding Professor Award is presented annually to a UA faculty member judged to have made extraordinary research contributions that reflect credit on the individual, his or her field of study and on the University. It was created by Frederick Moody Blackmon of Montgomery to honor the memory of his grandmother, Sarah McCorkle Moody of Tuscaloosa

Protocol Activity Status:

RPPR Final Report

as of 13-Jun-2018

Technology Transfer: Synergy with ARL labs:

Through the support of this award, Professor Thompson has been able to engage with Drs. Kris Darling and B. Chad Hornbuckle at the Army Research Laboratory in the areas of nanocrystalline stability and characterization. Specifically, Professor Thompson's group has been able to provide detailed characterization of nano-scale oxide dispersive alloys being prepared by the Army Research Lab as well as a Cu-based nanogranular stabilized microstructures. The results of which have generated the following papers and new areas of research investigation.

(1) Dallin J. Barton, Chaitanya Kaleb, B. Chad Hornbuckle, Kristopher A. Darling, Kiran N. Solanki, Gregory B. Thompson "Microstructure and dynamic strain aging behavior in oxide dispersion strengthened 91Fe-8Ni-1Zr (at%) alloy" Materials Science & Engineering A 725 (2018) 503–509 10.1016/j.msea.2018.04.016

(2) K.A. Darling, M. Kapoor, H. Kotan, B.C. Barton, S.D. Walck, G.B. Thompson, M.A. Tschopp, and L.J. Kecskes "Structure and mechanical properties of Fe-Ni-Zr oxide dispersion strengthened (ODS) alloys" Journal of Nuclear Materials 467 (2015) 205-213: 10.1016/j.jnucmat.2015.09.011

(3) M. Kapoor, T. Kaub, K. A. Darling, B.L. Boyce, and G.B. Thompson "An atom probe study on Nb solute partitioning and nanocrystalline grain stabilization in mechanically alloyed Cu-Nb" Acta Materialia 126 (2017) 564-575: 10.1016/j.actamat.2016.12.057 (specifically sites this award)

PARTICIPANTS:

Participant Type: PD/PI

Participant: Gregory Bruce Thompson

Person Months Worked: 1.00

Funding Support:

Project Contribution:

International Collaboration:

International Travel:

National Academy Member: N

Other Collaborators:

Participant Type: Graduate Student (research assistant)

Participant: Tyler Micheal Kaub

Person Months Worked: 12.00

Funding Support:

Project Contribution:

International Collaboration:

International Travel:

National Academy Member: N

Other Collaborators:

Participant Type: Graduate Student (research assistant)

Participant: Xuyang Zhou

Person Months Worked: 12.00

Funding Support:

Project Contribution:

International Collaboration:

International Travel:

National Academy Member: N

Other Collaborators:

Participant Type: Undergraduate Student

Participant: Mason McKechnie

Person Months Worked: 3.00

Funding Support:

Project Contribution:

International Collaboration:

International Travel:

National Academy Member: N

RPPR Final Report
as of 13-Jun-2018

Other Collaborators:

Participant Type: Undergraduate Student

Participant: Morgan Ross

Person Months Worked: 3.00

Funding Support:

Project Contribution:

International Collaboration:

International Travel:

National Academy Member: N

Other Collaborators:

Participant Type: High School Student

Participant: Ryan Anthony

Person Months Worked: 3.00

Funding Support:

Project Contribution:

International Collaboration:

International Travel:

National Academy Member: N

Other Collaborators:

Participant Type: High School Student

Participant: Bhargava Samanthula

Person Months Worked: 3.00

Funding Support:

Project Contribution:

International Collaboration:

International Travel:

National Academy Member: N

Other Collaborators:

Participant Type: High School Student

Participant: Jaeden Joyner

Person Months Worked: 3.00

Funding Support:

Project Contribution:

International Collaboration:

International Travel:

National Academy Member: N

Other Collaborators:

Participant Type: Faculty

Participant: Eric Chason

Person Months Worked: 1.00

Funding Support:

Project Contribution:

International Collaboration:

International Travel:

National Academy Member: N

Other Collaborators:

Participant Type: Undergraduate Student

Participant: David Jacobson

Person Months Worked: 4.00

Funding Support:

Project Contribution:

International Collaboration:

International Travel:

RPPR Final Report
as of 13-Jun-2018

FINAL REPORT

Influence of Grain Boundary Structure on Nanocrystalline Thin Film Stress States

W911NF1310436

Table of Contents:

Executive Summary	2
Chapter 1: Molecular dynamic study of the stress generation during thin film growth	4
Chapter 2: The Influence of Deposition Parameters on the Stress Evolution of Sputter Deposited Copper	49
Chapter 3: Intrinsic Stress Response of Low and High Mobility Solute Additions to Cu Thin Films.....	65
Chapter 4: Influence of Solute Segregation on Thin Film Growth Stresses: The Cu(Ni) System.....	79
Chapter 5: Influence of Fe(Cr) Miscibility on Thin Film Grain Size and Stress.....	87
Chapter 6: Grain Boundary Specific Segregation in Nanocrystalline Fe(Cr).....	102
Chapter 7: Influence of Solute Partitioning on the Microstructure and Growth Stresses in Nanocrystalline Fe(Cr) Thin Films.....	143
Chapter 8: Phase and Microstructural evolution in sputtered Fe-Cr films.....	167
Chapter 9: <i>In situ</i> TEM observations of initial oxidation behavior in Fe-rich Fe-Cr alloys.....	186
Chapter 10: Ti Segregation in Regulating the Stress and Microstructure Evolution in W-Ti Nanocrystalline Films.....	220
Chapter 11: The influence of alloy atoms interactions on thin films stress.....	240
Chapter 12: Stress Evolution and Microstructure in Ag-Al Thin Films.....	261
Chapter 13: Role of Atomic Migration in Nanocrystalline Stability: Grain Size and Thin Film Stress States.....	270
Listing of publications	291
Graduations	293
Outreach	293
Awards	294
Synergy with ARL	295
Presentations:	296
<i>Dissertation slides of Drs. Kaub and Zhou</i>	298

Executive Summary:

Thin films are a vital subset of material structures that are relevant in several technologically important applications, including information storage, optical devices, and tribological coatings. It has been well documented that the intrinsic stress associated with thin films plays a fundamental role in tuning its physical and mechanical properties. In these material systems, the stresses are often generated from the crystallographic interfaces and their evolutionary response to minimize this energy. To date, most experimental research has focused on the *in situ* stress evolution of a thin film consisting of a single element. This research explored some of these elemental systems, both computationally and experimentally as well as alloy films. Unlike single element films, these multi-species systems have the added complexity of interactions between different atom types, which can lead to chemical partitioning at various interfaces. Although this can be complex, it does offer several tantalizing opportunities to engineer the growth and subsequent stress conditions of thin films.

Work conducted in the grant has shown how the stress state in an alloy film is regulated by the segregation of particular species to the grain boundaries, even when that species is the lower concentration component, and how the solute controls the grain size of the film. The role of grain boundary character evolution, including its structure and chemistry, in response to these changes was quantified using precession enhanced electron diffraction and atom probe tomography. The novelty of this research resided in coupling *in situ* stress measurements with high fidelity structural characterization to elucidate how chemical segregation at nanocrystalline interfaces alters stress behavior.

The report is provided in an article style from manuscripts already in print to papers that are still under review. A brief summary of each topical area investigated below.

- *Modeling of thin film growth:* This research involved molecular dynamic simulations of sputter deposition where a variety of microstructural controls and experimental parameters were studied to determine their effect on film stress evolution.
- *Experimental study of high mobility Cu growth:* A self-contained data set of Cu films was grown over extensive range of deposition processing parameters (pressures between 0.266 Pa to 2.66 Pa and rates between 0.012 nm/s to 2.4 nm/s). As a result, this work is distinct in that it has the data sets necessary to compare to kinetic models to understand thin film growth. In order to remove microstructural effects to stress, we devised a means to control the grain size to be consistent between each of these conditions.
- *Alloying effects in Cu based films:* By alloying Cu with Ag and V, the intrinsic effects of a solute with different mobility's on Cu's stress state was evaluated.
- *Influence of solid solution mixing on Cu film growth:* This section of the report discusses how Ni (unlike Ag or V, which are immiscible) influences the stress state of a growing Cu film. It was found that the film became compressive with the Ni solute, but once the grain boundary was thermodynamically saturated, the compressive stress was reduced.

- *Growth stresses in Fe(Cr) films:* This research investigated the effect of low Cr solute segregation on the growth stresses in Fe. Unlike the Cu (which is a high mobility adatom), Fe is a low mobility adatom providing a comparative example to Cu. Though Fe and Cr are both low mobility adatoms, which grow with a tensile stress, at low concentrations, the mixing of the species reduces the tensile stress.
- *Correlated precession electron diffraction and atom probe tomography:* Based on the findings of the stress changes with Cr solute additions to Fe, the use of precession electron diffraction and atom probe was used to determine the specificity of Cr segregation to particular Fe grain boundaries, which were then compared to a hybrid molecular dynamics and kinetic Monte Carlo simulation.
- *Annealing effects on the stress evolution in Fe-Cr films:* Expanding on the study of Fe(Cr) investigations, the influence of in situ annealing during deposition on film stress was investigated. The results revealed both partitioning to the grain boundaries, spinodal decomposition in the grains themselves, and composition dependent abnormal grain growth
- *Stability and ordering behavior in FeCr films:* This work revealed, even at ambient temperature deposition, near equatomic FeCr films will chemical order into the high temperature sigma phase, even though the substrate is not annealed. Furthermore, using advanced atom probe clustering techniques, we have revealed chemical ordering of Cr when in solution with Fe, which had been postulated in the literature.
- *Early oxidation effects in nanocrystalline Fe(Cr):* Using a DURIP award to study in situ grain growth via heating in the TEM, the early oxidation of Cr₂O₃ was found to occur from the residual gas pressure in the TEM.
- *Alloying and stress effects in other systems:* Though the majority of the research focused on the alloying effects on a high mobility adatom (Cu) and a low mobility adatom (Fe), the research also explored alloying effects in other systems to set forth the ground work for future studies. These are as follows:
 - *Influence of phase stability on film stress:* Here the “beta-to-alpha” W film stress evolution was studied and modified by the use of Ti, which was shown to remove the influence of oxygen in stabilizing the metastable “beta” W phase in the early stages of film growth. These transitions were observed by the stress response measured.
 - *Influence of mix alloying on the intrinsic partition and stress evolution:* In the original paper by Fu and Thompson (Journal of Applied Physics 2010) which showed how the solute segregation regulated stress, this work examined if indeed zero stress states are achieved with the matrix and grain boundary compositions are uniform.
 - *Stress evolution in highly reflective coatings:* In this investigation, the effect of mixing of Al and Ag was studied to determine how the stress changed surface roughness, which impacts diffuse scattering from reflective coatings.
 - *Connections of solute stabilization and film stress:* In this invited review article, the paper outlines the connections of solute segregation with the ideas of solute partitioning in nanocrystalline thin films to control residual stress.

CHAPTER 1

Molecular dynamic study of the stress generation during thin film growth

Xuyang Zhou¹, Xiaoxiang Yu¹, David Jacobson¹, and Gregory B. Thompson¹

1. The University of Alabama, Department of Metallurgical & Materials Engineering,
Tuscaloosa, AL USA

ABSTRACT

Molecular Dynamics (MD) simulations have been employed to model the growth of tungsten thin films as well as determine the relation between stress evolution and island texture, grain size, grain morphology, deposition rate, and deposition energy. Depending on the shape and size of the deposited islands, the tensile stress varied and was a function of the available contact area. If the adatoms were sufficiently confined to the surface, the tops of these islands initiated the elastic strain for coalescence. This was particularly relevant to island morphologies that had varied curvature gradients near the contact points. Depending on the texture of the film, the deposited roughness changed, with the $\langle 111 \rangle$ orientation being the roughest and $\langle 001 \rangle$ orientation being the smoothest. These topologies are explained by differences in surface diffusivities. The injection energy of adatoms was found to have a dramatic effect on film stress. Species with injection energies in excess of 50 eV resulted in a notable increase in the structural disorder at the grain boundary-free surface intersection which corresponded to a reduction of the tensile stress. Upon ceasing deposition, these disordered regions experienced a recovery to a body centered cubic (bcc) structure with an increase in the tensile stress. Upon resuming deposition, at the same energies, the disordered structure re-developed and the stress became less tensile and matched the prior deposited stress evolution. Finally, reducing the grain size resulted in an increase in tensile stress up to a critical size, whereupon it decreased. This reversion is explained in terms of grain growth and grain boundary structure during deposition. Through these series of systemically controlled MD simulations, the paper addresses the significance of different microstructures on the evolution of thin film stress development.

Key words: Molecular dynamic, stress, thin film

1. Introduction

Thin films are a vital architecture in several technologically important applications including information storage [1], optical devices [2, 3], semiconductor transistor design [4, 5], energy harvesting [6, 7], and tribological coatings [8]. During the deposition of thin films, the residual stresses can be quite large and in some cases exceed the bulk elastic properties of the material being deposited. These intrinsic stresses can be responsible for the failure of thin film devices with tensile stresses leading to cracking [9, 10] and compressive stresses facilitating delamination, buckling, and/or blistering [10-12]. Furthermore, stresses coupled with electromigration in electrical based films can facilitate diffusional reactions that assist in the creation of whiskers and hillocks that cause short circuit failures in integrated circuit devices [13, 14]. Thus, intrinsic stresses contribute to a fundamental role in the tuning of physical and mechanical properties of thin films [15-21].

This stress state develops as adatoms from the deposition vapor nucleate and grow on the substrate. During the deposition process, adatoms are not able to achieve their fully relaxed positions. Dependent on the stage of growth, different stress states develop. Three growth modes have been identified: (1) Volmer-Weber (VW) also known as island growth [22, 23] (2) Frank-van der Merwe (FM) also known as layer-by-layer growth and (3) the Stranski-Karastanov (SK) which is a combination of VW and FM with a layer evolving into islands. Though each type of growth behavior is important to a particular type of film deposition technology or an application, this paper will focus on the VW mode, which is common in many sputter deposited films. The reader is referred to reference [24] for more details for the other two modes.

In the early stages of VW growth, an initial compressive stress is normally observed. Abermann *et al.* proposed that the origin of this pre-coalescence compressive stress is a result of the Laplace pressure associated with the surface stress of the islands [25]. Friesen and Thompson suggested an alternative explanation that

regarded this pre-coalescence stress as being associated with adatom-surface interactions [26]. They suspected this interaction because of a reversible stress relaxation that occurred in the pre-coalescence regimes where changes in the adatom population during and after deposition could be used to explain this behavior [26].

In the second stage of VW growth, a tensile stress is generated from the islands impinging with each other. Hoffman [27] first suggested that such an impingement would create a tensile stress from the elastic strains induced by each island closing the gaps between themselves to eliminate the free surface energy created by the isolated islands. Such a stress can be then be calculated using equation 1

$$\sigma = \frac{E \Delta}{1-\nu L} \quad (1)$$

where E is Young's modulus, ν is Poisson's ratio, L is crystalline diameter, and Δ is the distortion at the boundary. In general, this equation has been found to overestimate the magnitude of the tensile stress. Nix and Clemens developed this Hoffman model as a crack-closure process [28], which has an inverse progression of the Griffith's crack elongation concepts. Here the energy reduction to close the gap between adjacent islands must be more than the increase in the strain energy. Freund and Chason then furthered these ideas by demonstrating it for realistic deposition island geometries [29]. Most recently, finite element method (FEM) analysis calculations [30-32] and molecular dynamics (MD) [33] methods have been used to quantify the stress generated by the formation of grain boundaries by this crack closure mechanism. Reported studies have shown good agreement between calculated stresses and stresses observed experimentally [30]. For example, in Seel *et al.*'s MD simulation work, they noted that the prior over estimation of the tensile stress by the Hoffman's model [27] could be corrected by using a modestly lower energetic barrier for a thermally activated coalescence process [33].

From these collective works, there is general agreement that the tensile stress is likely associated with the elastic strains that occur as islands impinge. Several subtle factors can further refine this impinging process such as interfacial energy differences,

grain size variations, grain shape differences, surface roughness, and contact angle variations [27-29, 32, 34]. In this work, we apply various forms of these factors in a MD model to determine how the tensile stress would vary under different impinging conditions.

In the third stage of VW growth, elemental films with low adatom mobility like Fe [35, 36] and Cr [36] usually tend to retain the tensile condition with continued growth. Thin films with high adatom mobility, such as Cu and Ag [37, 38], can experience a return to a compressive stress state. The generation of this post coalescence compressive stress is still under debate [28, 35, 39-51]. Nix and Clemens initially suggested that the tensile stress was relaxed by the addition of atoms into grain boundaries [28]. In the work of Shull and Spaepen [49], they noted a relaxation of this compressive stress when the deposition ceased, but upon returning to the equivalent deposition conditions, the former compressive stress response returned. They termed this behavior as a 'reversible' stress relaxation phenomenon. In a later paper, they attributed the generation of this compressive stress relaxation and returning behavior to a surface effect which adatoms were trapped between coalescing ledges [52]. Thus, near-surface trapped adatoms were released during growth and the interruption of growth allowed for a recovery. Upon redepositing the film, the adatoms were then trapped again and the stress state returned [52]. Friesen and Thompson [39] reported similar observations of a reversible stress during intermittent growth and demonstrated a connection of that effect to variations in surface defects concentrations.

Chason *et al.* has also suggested that a compressive stress generation is due to the insertion of adatoms into the grain boundaries during grain growth [40, 45]. But, different from the Nix and Clemens model [28], Chason suggested that this is a consequence of the non-equilibrium nature of the surface during deposition [45] which created an impinging growth flux that raises the surface chemical potential and drives excess adatoms into the boundaries. In the Chason model, the reversible growth stress interruptions occur as a change in the surface chemical potential from the

supersaturation effect created by the deposition flux on the surface that drives adatoms into or out of the boundaries [45]. Pao *et al.* [53, 54] and Buehler *et al.* [55] have recently used MD simulation to demonstrate this injection of adatoms into the grain boundaries.

Other post-coalescence stress generation ideas include those posed by Koch *et al.* [35] who proposed a recrystallization process to explain the growth interruptions. However, as Friesen and Thompson [47] pointed out, a recrystallization process is non-reversible and cannot be used to explain the reversible stress changes. Koch *et al.* [42] insisted that the reverse process may appear to be symmetric but is not reversible. In more recent years, Leib *et al.* [46] and Magnfält *et al.* [51] experimentally demonstrated a clear role of grain size in this reversible stress change for gold films [46] and refractory polycrystalline metal films [51]. Saedi and Rost [56] used thermodynamic arguments to validate the grain boundary insertion model by considering a ‘funneling effect,’ which is a fast mass transfer channel for terraces which can decrease the stress level. In our forthcoming MD model, we will also consider this third stage of growth and its associated ‘reversible’ stress relaxation in context to these models.

Recently Chason *et al.* [57] summarized a comprehensive model to sort out different effects on thin film stress. This ‘summary model’ contains three components - the growth stress σ_{growth} , the ballistic impacts of energetic ions at grain boundaries $\sigma_{gb}^{energetic}$, and the defects created in the film $\sigma_{bulk}^{energetic}$ with the summation as

$$\sigma^{sputt} = \sigma_{growth} + \sigma_{gb}^{energetic} + \sigma_{bulk}^{energetic} \quad (2)$$

Each of these generic stresses were then explicitly written as

$$\sigma^{sputt} = \left[\sigma_C + (\sigma_T - \sigma_C) e^{\frac{-\beta D}{RL}} \right] + \left(\frac{l}{L} \right) A_0 + \left(1 - \frac{l}{L} \right) \frac{B_0}{\left(1 + \frac{l}{R\tau_s} \right)} \quad (3)$$

where σ_T is the tensile stress that generated from the impingement of grain boundaries and σ_C is the compressive stress. The exponential term captures the effects of the growth rate, R , grain size L , the effective diffusivity of atoms from the surface into the

grain boundaries, D , and a parameter β that describes the concentration of mobile defects and the mechanical properties of the layer [57]. In the second term, l is the densification width near a grain boundary that can lead to compressive stress through the incorporation of atoms into a more favorable sites or the formation of interstitial defects as a result of the ballistic impacts of depositing adatoms. This value is proportional to the depth from the surface and will depend on the energy of incoming particles. A_0 and B_0 are numerical fitting parameters. τ_s is a characteristic time associated with the diffusion of generated defects to the surface. If the growth rate is too high, those defects are not able to diffuse to the surface resulting in a compressive stress being retained in the film. Through our MD simulation below, we will use this model's identification of key features, such as surface diffusivity, the kinetic effects for the migration of defects to the surface, injection energies of the deposition species, and grain sizes to understand how the stress evolves.

One of the challenges to understanding the residual stress generation is the limitations of *in-situ*, real time imaging of the surface (and in particular individual adatom behavior) during growth. There are very limited experimental studies with respect to this level of atomic imaging [58]. It is clear from equation (2) and (3), that several atomistic-scale features will contribute to the stress. Thus, post-deposition characterization of the experimental film is most often done to infer how adatom migration contributed to stress developments. Efforts to change processing conditions such as pressure, deposition rate, substrate material and orientation, film material type, and deposition temperature have all lead to new information to help develop a comprehensive model and/or mechanism(s) for stress generation [59-63]. Nevertheless, many microstructural factors within the film change simultaneously when one of these experimental variables is adjusted, making it difficult to ascertain one effect from another. For example, heating can facilitate grain growth but can also change the prevalence of different grain boundary types, surface morphology, and film texture. All of these phenomena contribute to changes in the film stress, making it difficult to decipher how much each microstructural feature contributes to the change

in the stress state of the film. In contrast to experiments, simulations allow one to fix multiple variables and vary a single factor, such as grain size, to see its contribution to the residual stress generation. Though this may not be what occurs experimentally (i.e., specific variables working independent of each other), it does give one the ability to gain insights into the significance each variable has towards the overall stress generation. The use of such atomistic models can also capture how atoms themselves are contributing to the intrinsic stress under defined conditions, whether that be by grain size formations, grain morphologies, or how the grain adopts a fiber texture.

In this paper, MD simulations are discussed to provide an understanding to this complex deposition process and the associated stress generation. MD simulations operate by iteratively solving Newton's equations of motion to obtain the positions for all of the atoms as a function of time. The energy and by extension force exerted on each atom can be calculated using a user specified interatomic potential. In this work an embedded atom method potential was used that could accurately simulate elastic constants, vacancy, surface energies, stacking-fault energies, and other primary physical properties of metals and alloys [64, 65]. This paper will employ MD to provide a series of studies that investigates how topology, morphology, and grain size for a simple bcc metal system contribute to stress formation during thin film growth. In particular, we will investigate sputter deposition behavior, where the depositing species includes energetic particles which are absent in evaporation or electrodeposition processes. These energetic particles create additional contributions in terms of defect creations in the bulk of the film [57].

However, just like experimental limitations, simulations also have constraints. In MD simulations deposition rates are significantly faster (orders of magnitude larger) than those in experimental deposition rates. This is because the timestep of MD solves for atomic vibrations and these vibrations must be less than the shortest lattice vibration, which is typically a Debye frequency ($\sim 10^{-15}$ sec.). Thus, when an adatom arrives on a surface, the atomic vibrations allow the atom to jump from one site to another, for example, by thermal activation until it reaches an equilibrium state. By

repeating the deposition process of adatoms landing on the surface, the adatoms will then accumulate and the growth behavior is mimicked. In order to yield an appreciable film, the deposition rate must be accelerated in a reasonably available computational time to reveal the film structure. Though these time scales between the model and experiments are different, MD simulations have been shown to agree well with thin film stress development [53, 66-69] and microstructural evolution [70, 71]. This agreement with experiments gives confidence that these MD simulations are a viable tool for understanding film growth. During the simulation, several monolayers of atoms on the free surface are also fixed to prevent the simulated crystal from shifting because of the momentum transfer created by the adatom impact. Thus, a periodic boundary condition will be used for the two in-plane coordinate directions (growth surface) with a free boundary condition used for the third coordinate direction to simulate the growth.

2. Simulation method

2.1 Model generation

The MD simulations were performed using the Large-scale Atomic/Molecular Massively Parallel Simulator (LAMMPS) [72] and embedded atom method interatomic potentials found in references [73, 74]. As shown in Figure 1(a), a four region model has been created to mimic the deposition process. These specific regions include: (1) *Fixed region*: a 1nm thick substrate at the bottom of the simulation box where the atom positions are held constant. (2) *Temperature region*: In this region the incoming atoms interact with the growth surface with this region subdivided into three individual parts labeled substrate, island, and vacuum. (3) *Insertion region*: this is the region where individual atoms are introduced to the simulation with kinetic energy, E_k , are injected normal to the layers growing in the temperature region. It is worth mentioning that the velocity of the adatoms are only assigned in the Z direction with the energy being altered by changing the velocity of adatoms. And (4) *Virtual wall*: This region improves the efficiency of the deposition simulation where any re-sputtered atoms reflected from the growth surface are sent back to the surface with the initial kinetic energy E_k . In each

cycle the system was relaxed after depositing a new atom. The microcanonical NVE (number, volume, energy) ensemble was used to insert more atoms into the system. After which the canonical NVT (number, volume, temperature) ensemble was introduced to solve the equations of motion for the atoms such that system temperature was maintained at a pre-defined temperature. The deposition rate is related to the ratio of microcanonical NVE time period and the canonical NVT time period. Depending on relaxation steps in the NVT ensemble, our simulation could also study the kinetic effect of thin film growth. Temperature and pressure were maintained using a Nose-Hoover thermostat and barostat. The Open Visualization Tool (OVITO) software was used to visualize the final, deposited structure [75].

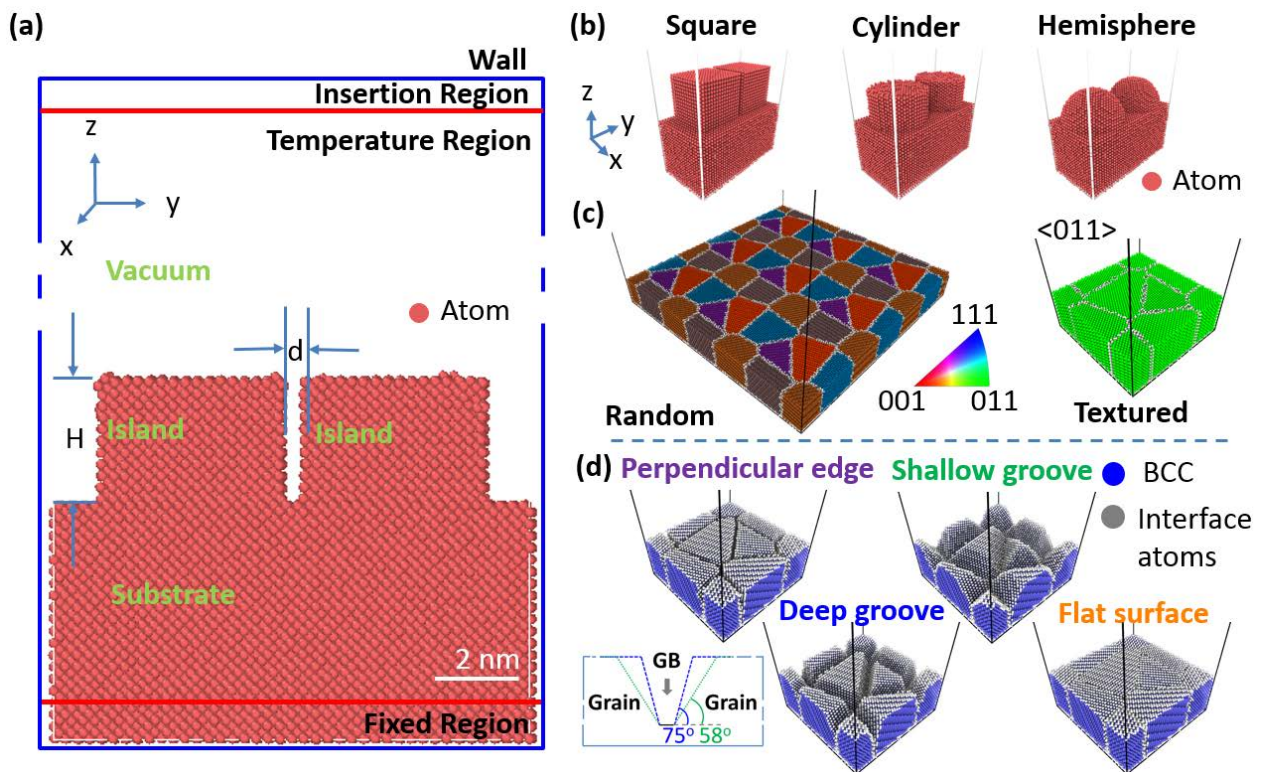


Figure 1 (a) A sketch of the MD model (b) single crystalline islands model (c) Polycrystalline islands model with random and <001> texture (d) Polycrystalline islands with different surface morphologies. The insert sketch helps the reader find the slope of island grains for the *deep groove* model and the *shallow groove* model. The slope angles

for the deep and the *shallow groove* models are 75° and 58° , respectively. Color available on-line.

2.2 Building structure

The primary focus of the current work is to understand stress generation in coalescence and post coalescence stages. The nucleation process was assumed to have been completed before the deposition simulation started. Matlab® codes have been written to create predefined islands with the texture and morphology related to the interactions between the adatoms and substrate. In this method, we were able to see the effect of different island morphologies on the microstructural evolution as well as stress generation. Single crystalline and polycrystalline island models were also compared, and will be discussed below to further understand how these differences contribute to the stress generation mechanisms.

2.2.1 Single crystalline islands

In the single crystalline island mode, a bcc $\langle 001 \rangle$ substrate orientation was used, with the specific element discussed in Section 3.1. The different morphologies, shown in Figure 1(b), were two square islands, two cylindrical islands, and two hemispherical islands. An intentional gap of ~ 0.4 nm was left between each island pair in the designated Y-axis coordinate to capture the impingement process. In this way, the impingement of islands will be confined to the Y-direction with the impinging tensile stress only expected along this axis. But, the other two orthogonal axes will be solved for as well to check this assumption. To ensure that the island pairs were isolated in the periodic boundary conditions, a much larger spacing of ~ 2 nm surrounded the islands.

2.2.2 Polycrystalline islands

According to the Thornton zone model of growth, a polycrystalline columnar grain structure will reside in the designated regions called zone 1, zone T and zone 2 [76]. Thus it is reasonable that a thin film will adopt a columnar grain structure over a range of different processing temperatures and pressures. To simulate this columnar

structure, the Voronoi method [77] was implanted to mimic the poly-granular structure. Here, we constructed randomly orientated and multiple fiber textures that were $\langle 001 \rangle$, $\langle 011 \rangle$, and $\langle 111 \rangle$. Figure 1(c) shows an example of the random and $\langle 011 \rangle$ structures with the colors seen in the inverse pole figure representing the orientation of each grain and the gray atoms defining the boundaries [78]. Finally, we constructed different growth morphologies in the polycrystalline simulation, designated as *perpendicular edge*, *shallow groove*, *deep groove* and *flat surface*, with each illustrated in Figure 1(d). The shortest width for the gap between each morphology (excluding the *flat surface*) was set to be 3 times the atomic radius for the perfect crystal. For the deep and *shallow grooves*, the gap obviously increased with the Z-direction, but at different rates. The slope angles for the deep and the *shallow groove* models were 75° and 58° , respectively.

2.3 Calculation of thin film stress

With the different surface morphologies and textures constructed, the LAMMPS code was then implemented to simulate the growth of each system and measure any stresses generated during growth. The stress in MD simulations can be calculated by two different methods – the overall stress or the stress for each atom [79]. The former stress calculation is based on the Virial theorem from statistical mechanics and has been shown to be consistent with macroscopic stresses [79, 80]. Though stress is associated with area, the Virial theorem provides a connection between stress and volume volume which is what is commonly in MD simulations to compute stress [80]. There are two shortcomings of this method to study film deposition. First, since space is not necessarily filled with all the atoms, the volume term used for the stress calculation overestimates its value. Second, this method does not provide stress information for any one particular region. In the latter method, the stress for each atom is found which can then summarize the stress state in one particular region [79]. For this work, we have used the latter method because of the inherent errors that would be propagated by the former method considering the absence of atoms in several of the morphologies shown in Figure 1.

Specific details of our calculation then involved computing from LAMMPS six stress state values, xx , yy , zz , xy , xz , yz , for each atom [80]. This stress tensor for atom i is then calculated, atom-by-atom, from decomposing the Virial theorem by removing the summation operator in the stress calculation formula given in equation

$$S_{IJ} = -mv_i v_j + \frac{1}{2} \sum_{n=1}^{N_p} (r_{1I} F_{1J} + r_{2I} F_{2J}) + \frac{1}{2} \sum_{n=1}^{N_b} (r_{1I} F_{1J} + r_{2I} F_{2J}) + \sum_{n=1}^{N_f} r_{1I} F_{1J} \quad (4)$$

where I and J taken on values, x , y , z . The first term in this equation is a kinetic energy contribution for atom i , with m represents mass of atoms i , v_i and v_j are the component of the velocity of atom i . The second term is a pairwise energy contribution from neighboring atoms from 1 to N_p , r_1 and r_2 are the positions of those two atoms in pair, and F_1 and F_2 are the forces on those two atoms in pair. The third term is the bond contribution that relates to atom i . The last term N_f , is from the internal constraint forces to atom i . The volume of the system is then simply that of the single atom. Since the calculation of an atomic volume can be complicated, for the purpose of convenience, the volume term has been omitted in LAMMPS. As a result, if the stress of a given region needs to be found, the stress value is simply obtained by dividing the summation value of each atom's stress by the volume of that region. Thus the volume of the island region is estimated by multiplying the average atomic volume with the number of atoms in that region.

Finally, when the simulations yielded a sufficient film thickness through the accelerated deposition, the stress behavior was represented as a stress thickness product vs. thickness. The thickness of the film was calculated from the ratio of the volume of the film to the X-Y dimensional area in one periodical cell. Since the stress state is a function of film thickness, the product of it with the instantaneous film thickness being generated can then allow one to better infer how the stress behaves independent of its particular growth thickness.

3. Results and discussion

3.1 Stress generation in single crystal island templates

We will first discuss the stress generation associated with the impingement of two isolated square islands. The square islands model is similar to the Hoffman model [27]. In our simulations the system was designated as iron, with the injection energy of adatoms set to 1eV. In each deposition cycle, the system was relaxed for 99 time steps after depositing a new atom. This deposition rate is low and was regarded as a quasi-static process, in which adatoms have enough time to diffuse to a low energy saddle point. As the deposition continued, the gap between the islands began to fill. Interestingly, the adatoms did not necessarily fill the gap from the bottom up. Rather the majority of adatoms were found to adhere near the top surfaces. As a result, the top of the islands grew slightly horizontally and then elastically strained to impinge each other. This can be seen in the simulated inset image #1 shown in Figure 2(a). Since the interisland separation was small and the island walls were flat and parallel, few trajectories existed that would allow adatoms arriving the base of the two islands. Adatoms that collected near the tops of the islands could move more freely whereas atoms at the bottom portions of the islands were restricted by the substrate interaction. This can be seen in the stress map in Figure 2(b), where the atoms on the substrate exhibit a compressive stress (black) whereas the atoms above this region and in the prior gap are tensile (white). The nearest neighboring distance for these 'gap atoms' is larger than the equilibrium distance of the perfect lattice generating the attractive force that generated the tensile stress. If the interisland gap was made much smaller, this zipping behavior occurred without the need for deposition, which is in agreement with a study by Seel *et al.* [33]. If the gap was increased, the adatoms filled the gap and the resultant tensile stress decreased as the area to elastically strain towards each other was reduced. With this particular arrangement in Figure 2(a), the tensile stress increased dramatically upon impingement as shown in the stress vs. time plot.

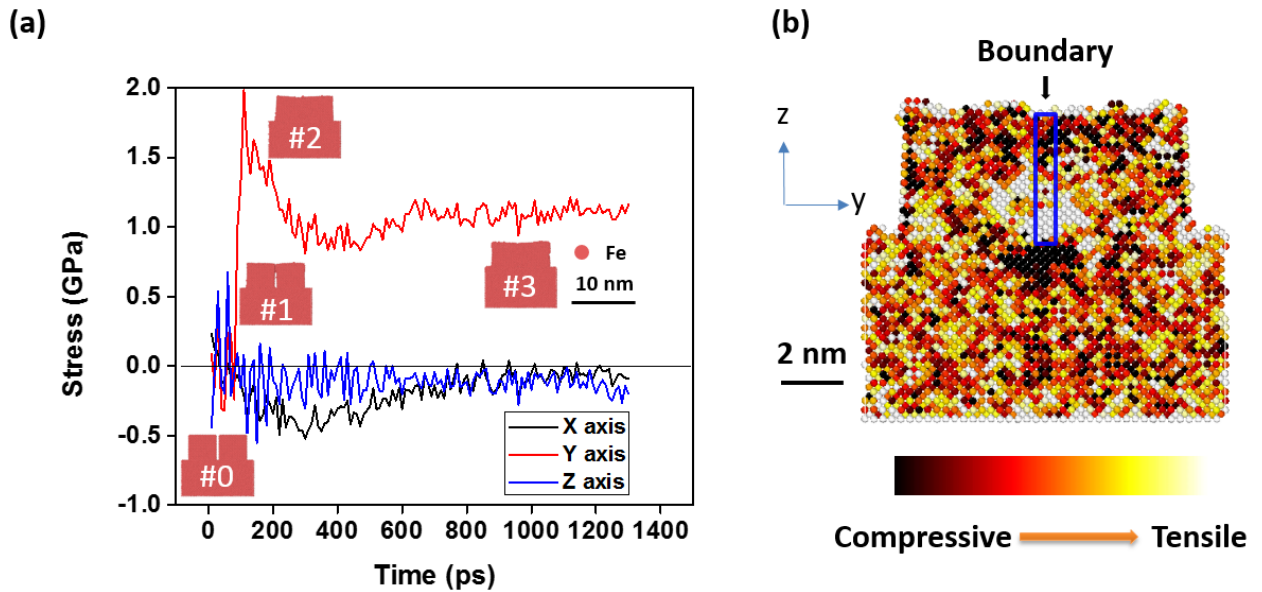


Figure 2(a) Stress varying with deposition time for different axes during the deposition of iron at 1eV/atom onto the surface of square islands surface **(b)** atomic stress map of the coalescent square-islands model. Color available on-line.

Once all of the surfaces were in contact, inset image #2 in Figure 2(a), the tensile stress was at a maximum value. What is particularly interesting to note, is that when the maximum tensile stress is achieved, the atoms at the highest tensile stress state are under the surface and close to the substrate, Figure 2(b). The impingement of the initial top surface stresses is qualitatively less than those atoms that must elastically strained in the final stages of impingement. This is a situation analogous to the uniaxial loading of a bar with a fixed end that results in the greatest stress response at the fixed end of the bar. Since impingement was along the Y-axis, the stress in the islands in the other two orthogonal directions were slightly compressive or zero, Figure 2(a), which one could expect based on the designated arrangement of the two islands.

We now consider the stress evolution associated with two additional island geometries: cylinders and hemispheres. For comparison, the stress resulting from the impingement of the two square islands are also plotted in Figure 3. The stress generation resulting from the cylindrical and hemispherical islands were drastically

different from the square island case. In order to understand why different island geometries result in different stress responses, we must define the concept of contact area. Inter-island gaps can be resolved by two mechanisms: filling or zipping. Filling involves the gap being filled by incoming adatoms. Zipping involves the gap being bridged by the elastic straining of each island. Whether a gap is resolved by filling, zipping, or some combination of the two is dependent on the geometry of the islands (morphology), and the interisland separation. Zipping will occur spontaneously as long as the reduction in surface energy of the two islands exceeds the increase in energy associated with the lattice strain. Thus, small gaps between islands are more likely to be resolved by zipping and large gaps in islands are more likely to be resolved by filling. The idea of contact area describes the separation distance between faces of two impinging islands. Higher contact areas correspond to lower inter-island separation distances, and results in higher degrees of zipping. Lower contact areas correspond to larger inter-island separation distances, and results in less zipping and more filling. This concept can be applied to the three island geometries presented in Figure 1. The square islands have the highest contact area because the separation distance remains at a constant distance (~ 0.4 nm). The cylinders have a lower contact area because the inter-island separation distance increases with lateral movement along the face of the cylinder. The hemispheres have the lowest contact area because the inter-island separation distance (~ 0.4 nm) exists only at the base of the hemispheres centered in the gap between hemispheres. The inter-island distance increases both with vertical and lateral movement from this point on the hemisphere. Because zipping involves an increase in the tensile stress and filling does not, one would expect that island geometries with higher contact areas that are more likely to zip will produce a greater tensile response.

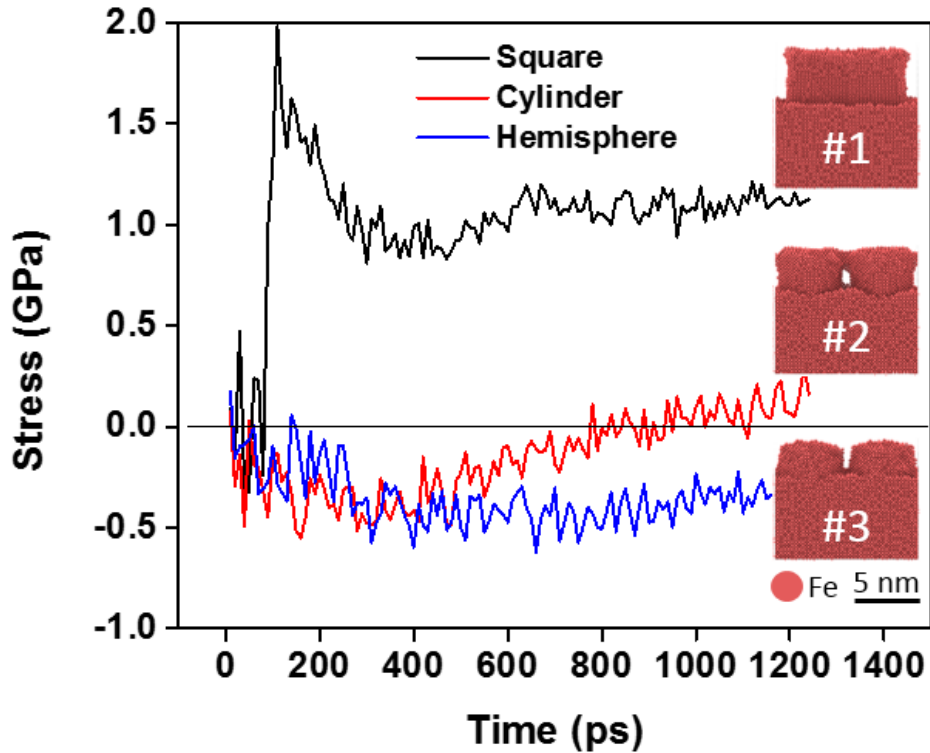


Figure 3 Stress as a function of deposition time when iron atoms are deposited with 1eV of energy onto the surface of square islands, cylindrical islands, or hemispherical islands. Color available on-line.

3.2 Stress generation in polycrystalline, columnar grains templates

Though the single crystal islands model was informative, it is not necessarily realistic given that islands usually undergo impingement in all directions. Here, we have developed a columnar polycrystalline structure using tungsten as our case material. Furthermore, we have increased the rate of deposition to a ‘high-rate’ where 9 relaxation steps are now used before the insertion of the next adatom. Doing so enabled us to simulate larger more realistic systems. Figure 4(a) shows the in-plane stress thickness product (x - and y - axis values) vs. thin film thickness for the tungsten film. This polycrystalline structural template is composed of five periodic grains with an average grain diameter of approximately 6 nm. The gap in between the adjacent faces of islands prior to deposition filled the space with is 3 times the atomic radius of the

perfect crystal, ~ 0.42 nm for tungsten. Adatoms with 5 eV injection energy were deposited onto this surface and a tensile stress was generated by the attractive forces from the adjacent faces of the islands. The mechanism of tensile generation is similar to that of the single crystal island model but now we have elastic straining across multiple faces making the deformation more homogenous. Three cross-sectional views of each film from a height of 2nm at different stages of growth are shown in Figure 4(c)-(e). These images capture the evolution of the impingement process. In Figure 4(c), the initial state of islands can be observed with clear gaps. As the adatoms deposit onto the surface, the majority of them appear to adhere on the surface and/or edges of the existing islands rather than in the gap, as noted previously in the single crystalline island simulation. As the gap sizes decreased, the tensile stress gradually increased. The maximum tensile stress, Figure 4(e), occurred when the gaps filled. As the film thickened, the ratio of atoms in the impinging region to all atoms was reduced resulting in a decrease in overall tensile stress. Figure 4(f) shows a cross-sectional view to reveal the grain structure evolution as the film thickened. Two grain boundaries merged into one grain boundary indicating grain growth and a non-steady state stress condition. This grain growth will also contribute to the change in the tensile stress [10].

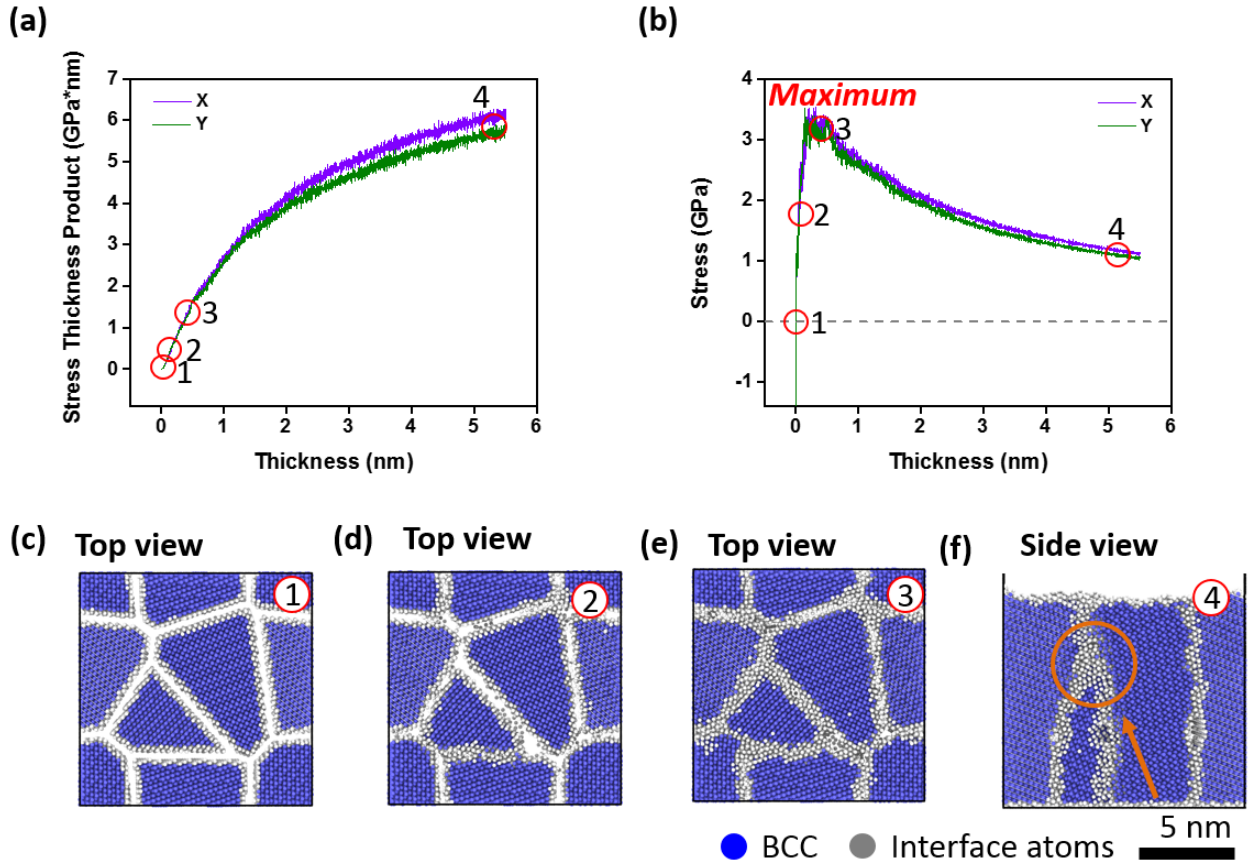


Figure 4 (a) Stress and thickness products (b) Stress varying with film thickness when 5 eV tungsten atoms deposited onto the surface of a *perpendicular edge* islands (c)-(e) Three 2 nm top view slices, which is near the surface of the substrate, were chosen to show the coalescence process. (f) One 2 nm side view slice to illustrate grain growth during deposition. The number represents the position where the slices have been selected to show. Color available on-line.

3.3 Stress generation as a function of surface morphology

To this point, we have studied the growth stress behavior as a function of shape in single crystalline islands, and the growth stress behavior of a polycrystalline structure. We now merge those studies together to understand how the stress evolves as a function of the surface morphology in a columnar polycrystalline system. As shown in the previous section, the coalescence of the adjacent islands will generate a tensile stress, which was as high as ~ 3 GPa in the case of the islands having *perpendicular edges*

to each other, Figure 4, which represents the extreme case for contact area impingement. In reality the islands will more likely form more complex island morphologies where the vertical island wall has some convex shape from the outer edge to the center. In Figure 5 we have simulated these various convex shapes having a ‘*deep groove*’ or rapid slope gradient near the edge to a more gradual gradient change referred to as a ‘*shallow groove*.’ The details of these morphologies have been provided in the Figure 1(d). For an extreme case to the perpendicular island impingement, we have also simulated a ‘flat’ surface, where there is no gap between the islands.

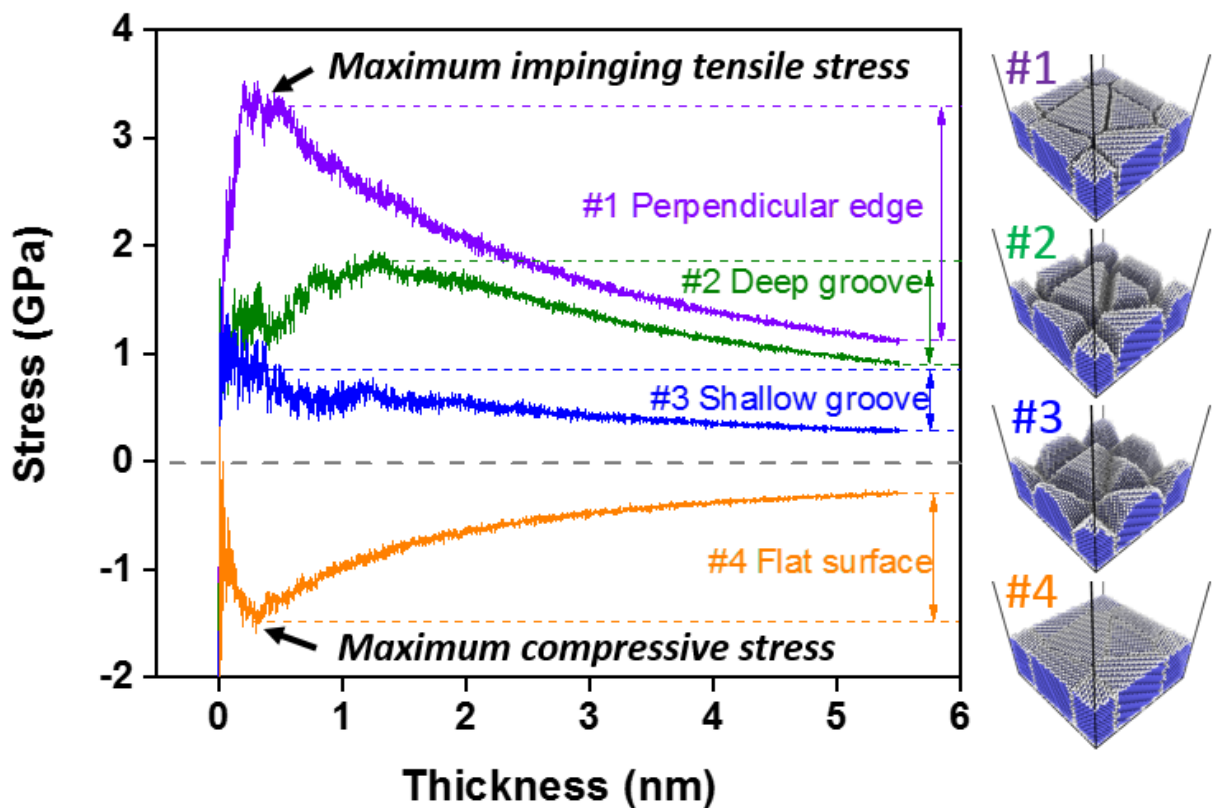


Figure 5 Stress varying with film thickness when 5 eV tungsten atoms deposited onto the surface of *perpendicular edge* islands, deep slope islands, shallow slop islands, or flat surface. The slope angles for the deep and the *shallow groove* models are 75° and 58°. Color available on-line.

In the case of the “*deep groove*” template, the maximum tensile stress was ~2 GPa. The reduced contact area from this morphology trended with the reduced tensile

stress response noted for a reduction in the contact area between the islands. As the slope gradient lessened, the '*shallow groove*' still revealed the tensile stress response, but the stress value was less and the thickness for the maximum stress was at a larger layer thickness of growth. Thus, these polycrystalline simulations trend with a reduction of tensile stress and a corresponding reduced impingement area. For the extreme case, where film deposits as a *flat surface*, only a compressive stress appeared on the stress curve in Figure 5. Thus, Figure 5 illustrates that maximum tensile stress increases with increasing contact area.

3.4 Stress recovery behavior

Simulations were run where adatom deposition was stopped and restarted to observe the effects of growth interrupts on the film stress and microstructure. Figure 6(a) shows the stress evolution of W film, which has a *perpendicular edge* islands surface morphology and an injection energy of 50 eV of adatoms, with the associated atom images at different sequences of the growth (labeled as #1-#4) in Figure 6(c). The grey atoms are not fully BCC coordinated and are most often associated with atoms at surfaces and grain boundaries. The blue atoms represent BCC coordinated W atoms. At point #1, a varied grain boundary width in the growing direction is observed, where the largest width occurs at the intersection of the grain boundary with the free surface. At point #2 the deposition is ceased. An increase in tensile stress is observed in Figure 6(a) #1, and a reduction in the width of the grain boundary near the film surface can be observed in Figure 6(c) #2. When the deposition was resumed at point #3, the width of grain boundaries near the surface return to dimensions similar to those that existed before the growth interrupt, Figure 6(c) #1. The growth interrupt process was repeated beginning at step 4 with similar results. The relation between grain boundary width and stress relaxation during growth interrupts would suggest that deposited adatoms are reducing the tensile stress of the film, resulting in the disorganization of atoms near the grain boundaries. When deposition ceases, these disorganized atoms are capable of relaxing back into equilibrium states. There are two theories as to the mechanism

responsible for this reduction in tensile stress. The first, as described by Chason, involves a change in the chemical potential of the film surface with deposition that results in the inclusion of excess atoms in the grain boundary. The second involves a peening effect where momentum transfer during deposition is responsible for the decrease in tensile stress; whenever deposition is interrupted, the boundary is able to heal and tensile stress increases.

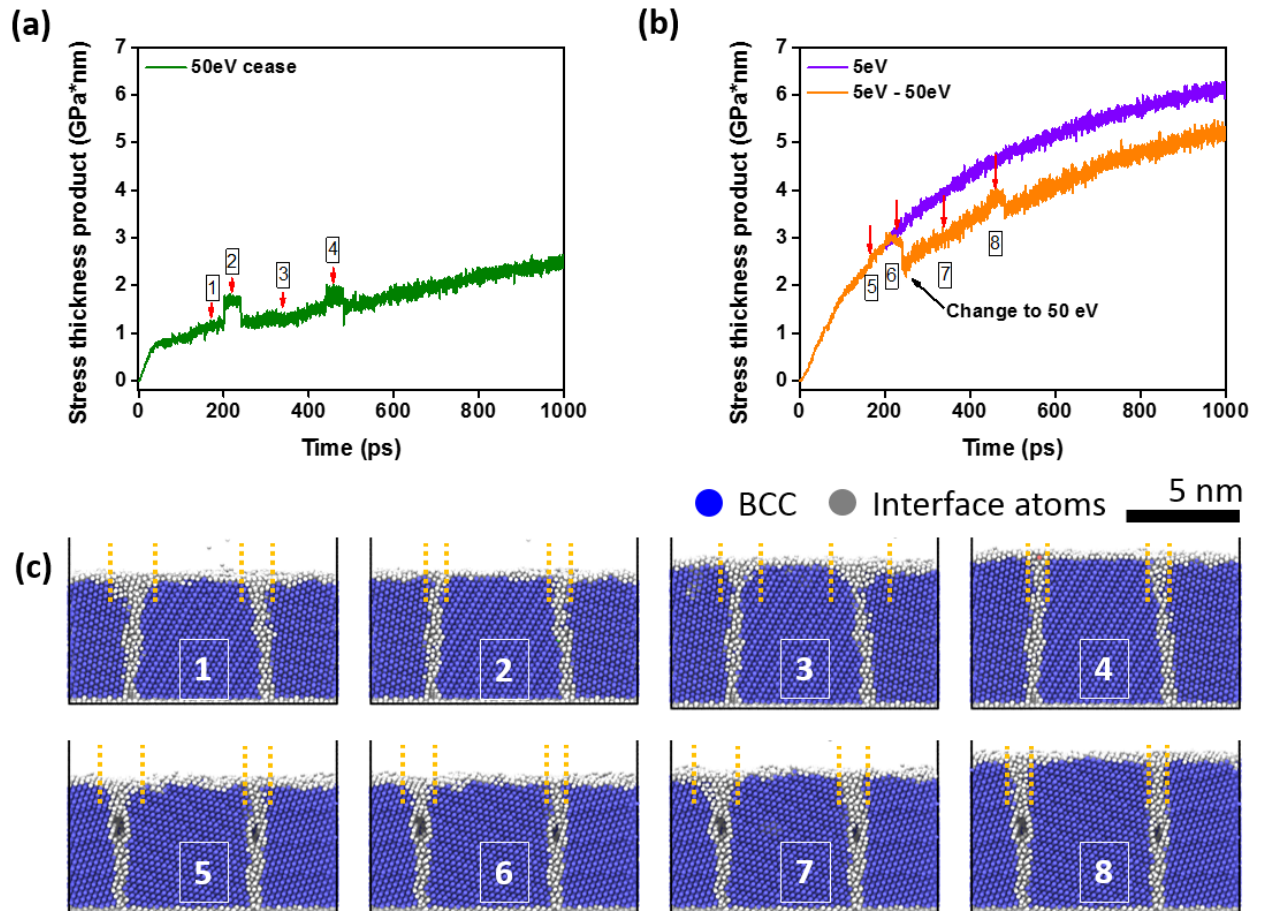


Figure 6 Stress thickness product stress varying with time when there is a growth interruption for films deposited with **(a)** 50 eV injection energy and **(b)** 5 eV-50 eV injection energy. **(c)** Cross-sectional slices were chosen to show the change of grain boundary width. The number represents the position where the slices were selected to show. Color available on-line.

In the model developed by Chason *et al.* [45], the compressive stress associated with post coalescence film growth is attributed to an increase in surface chemical potential that drives adatoms into the grain boundaries. We decided to check and see if the grain boundary widening near film surfaces during deposition might be a result of the inclusion of excess adatoms into the boundary [45]. Pao *et al.* [53, 54] has performed similar MD simulations for a few deposited layers for Ni and did note adatom diffusion into the grain boundaries. They employed an average displacement field of atoms to reveal the insertion of adatoms into grain boundaries. Similar to Pao's method, we used atom trajectory mapping to capture atomic motion during the growth interrupts in the simulation. Figure 7(a) and (b) show the atom maps of the deposited atoms at the interface, including surface and grain boundaries, before and after ceasing deposition. Figure 7(c) contains the atom trajectories during a relaxation process and the final position of inspected atoms. Areas of highest atomic mobility included grain boundaries and defects with one of each being highlight by an arrow in Figure 7. After an interruption in deposition, the defects on the dynamic surface, Figure 7(a), have been healed resulting in an ordered lattice structure shown in Figure 7(b). Also, the thickness of the grain boundary structures has been narrowed, the phenomenon of which is similar to that shown in Figure 6(c). Despite this fact, the directional migration of adatoms out from grain boundary is not observed from Figure 7(c). This would suggest that the healing of the boundary peripheral during growth interrupts is the main source of the reduced stress in these simulations. This is not to say that Chason's model is incorrect, but rather that adatom migration to boundaries was not observed during these simulations and that the compressive stress associated with adatom deposition is at least partially a result of the boundary healing phenomena described here.

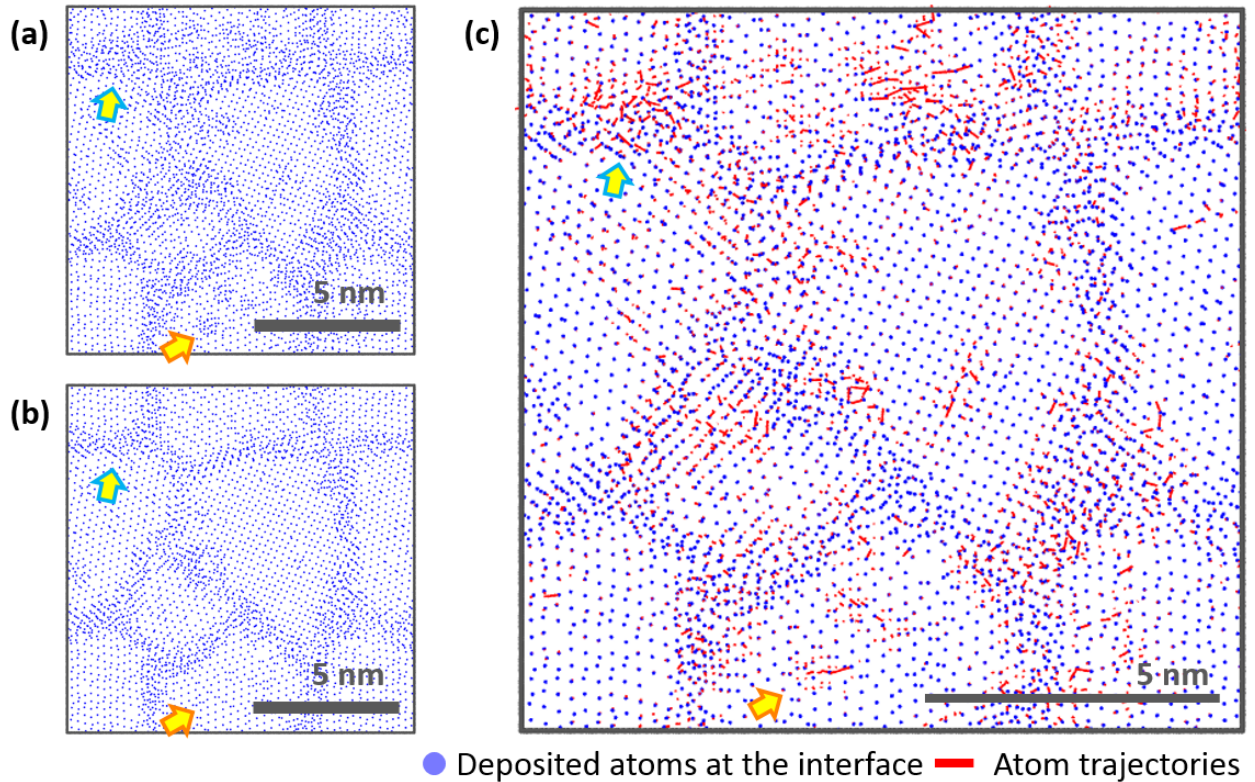


Figure 7 Top view images (Z-direction) of atom maps of the deposited atoms at the interface **(a)** before and **(b)** after ceasing deposition when 50 eV tungsten atoms deposited onto the surface of a *perpendicular edge* islands. Those two images are linked to the cross-sectional images showing in Figure 6 (c)#1 and Figure 6 (c)#2, respectively. **(c)** The atom trajectories between Figure 7 (a) and Figure 7 (b). The atom map after ceasing deposition is also included in Figure 7 (c). Color available on-line.

Unlike Pao *et al.*'s [53] work, where only one energy (which was not specified) was studied, we now explore how the stress evolves with a change in the deposition energy. In our prior simulation, Figure 6(a), the deposition rate was returned to the previous value, #3 in Figure 6(a), after the momentary ceasing of the deposition at #2 in Figure 6(a). The stress state exhibited a reversible stress trend, i.e. returned to the same trend in deposition stress noted in #1 for Figure 6(a). This type of reversal stress behavior is what is observed experimentally [45, 52]. However, if the deposition flux

conditions change, such as different injection energies, the stress relaxation and associated recovery should also change. If the grain boundary-free surface intersection region contributes to this stress, it too should change. To explore these ideas, our simulated deposition energy was altered between 5 eV to 50 eV, Figure 6(b), with the corresponding atom images collected at different points on the stress curve, #5-#8 in Figure 6(c).

In Figure 6(b), the orange curve is the stress-thickness evolution for a film initially deposited with 5 eV injection energy, #5 on the curve, but then changed to 50 eV after growth resumption, #7 on the same curve. The pure 5 eV deposition curve, which appeared in Figure 4(a), is also included for comparison in Figure 6(b). At this lower 5 eV adatom deposition energy, Figure 6(b) #6's curve, a very modest reduction in a stress recovery upon ceasing deposition occurred. In contrast, a notable change is observed for the 50 eV injection energy, Figure 6(a) #2 or #4. As shown in Figure 6(c) #5, which is the 5 eV injection energy condition, the grain boundary-free surface intersection structure was observed to be narrower than the prior 50 eV deposition condition, Figure 6(c) #1. This lower deposition energy also yielded a void defect within it, Figure 6(c)#5, which is believed to be a result of the lower adatom energies and will be further elaborated upon in Section 3.5. Regardless of this defect, the extent of the boundary-surface intersection region's width is clearly a function of the arrival adatom energies. Looking at the atom maps from when the deposition at 5 eV was ceased, Figure 6(c)#6, there is a very limited difference in the visual shape and width of this boundary-surface intersection as compared to the same region during deposition, Figure 6(c)#5. In contrast, a clear change is observed for the 50 eV state during, Figure 6(c)#1, and ceasing, Figure 6(c)#2. Thus, we can conclude that the adatom deposition energy plays a key role in controlling the stress response and growth interruption behavior by creating a significant change in the film's microstructure at the grain boundary-free surface intersection region.

To further confirm this idea, the deposition in Figure 6(b) that was at 5 eV was returned to a higher injection energy of 50 eV. A clear demarcation of the boundary

curve is seen in the indicated region in Figure 6(b). At this higher energy, the grain boundary-free surface intersection width increased, Figure 6(c) #7. Upon ceasing deposition, this boundary region once again narrowed, Figure 6(c)#8. Thus, we are able to toggle back and forth the stress, and corresponding disordered region width at the grain boundary-free surface intersection, based on the arrival energy. Collectively, these results provide direct atomic scale evolution of how the near surface boundaries are evolving and recovering under various deposition conditions, which would be linked to the $\sigma_{gb}^{energetic}$ term in equation (2). The widening of the boundary-surface intersection during deposition does appear to directly translate to a lower stress state for the film. And, upon ceasing deposition, this boundary region narrows and the stress state recovers. To better understand this behavior, a larger range of arrival energies was investigated.

3.5 Injection energy

Changing the injection energy directly affects the $\sigma_{gb}^{energetic}$ and $\sigma_{bulk}^{energetic}$ stress terms in equation (2). The injected adatoms will create a peening effect within the film [57, 81-84], with such effects being a contributing mechanism for stress generation besides proposed adatom migration into the boundaries [45]. The effect of injection energy was determined by simulating the deposition of tungsten films, which have a *perpendicular edge* islands surface morphology, at injection energies ranging from 1eV to 110eV. Figure 8 shows (a) the stress-thickness product and (b) stress as a function of films thicknesses for each of these simulations. With increasing injection energy, the stress-thickness product changes from a positive value to a negative value indicating an overall change from tensile to compressive stress. Figure 8(b) shows that the maximum tensile stress generated by island impingement will also change with injection energy. Maximum tensile stress increased with injection energy up to 50eV after which the maximum tensile stress began to decrease with increasing injection energy.

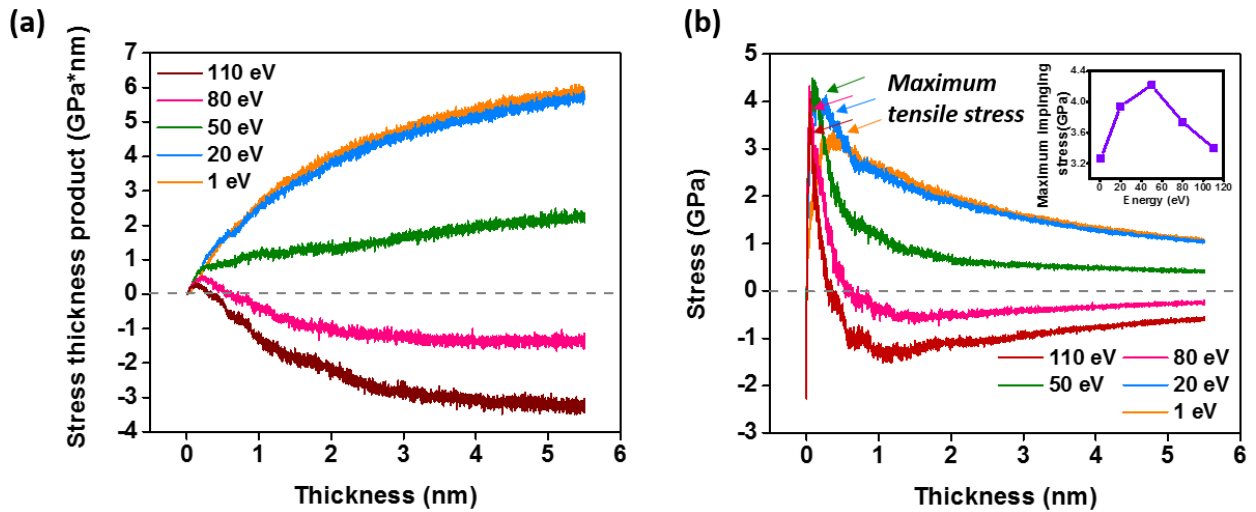


Figure 8 (a) Stress and thickness products **(b)** Stress varying with film thickness when 1 eV, 20 eV, 50 eV, 80 eV, and 110 eV tungsten atoms deposited onto the surface of a *perpendicular edge* islands. The maximum impinging tensile stress for different injection energies were embedded in Figure 8(b). Color available on-line.

The change in film stress from tensile to compressive is believed to be related to the microstructural evolution, as previously discussed in Section 3.4 and seen in Figure 6. Figure 9 is the atom maps for various representations of the film at the various injection energies in Figure 8. As shown in Figure 9(a), at low injection energies, the two prior islands were quickly sealed by the arrival of the new adatoms with the further arrival of the low energy adatoms unable to penetrate into this gap. This left a void within the film's boundary (see arrow at 1 and 20 eV) and would explain the formation of the similar defect noted in the 5 eV deposited tungsten film in Figure 6(c) #5-#8. Since the islands are not fully coalesced, a relatively low maximum impingement stress was generated, Figure 8(b).

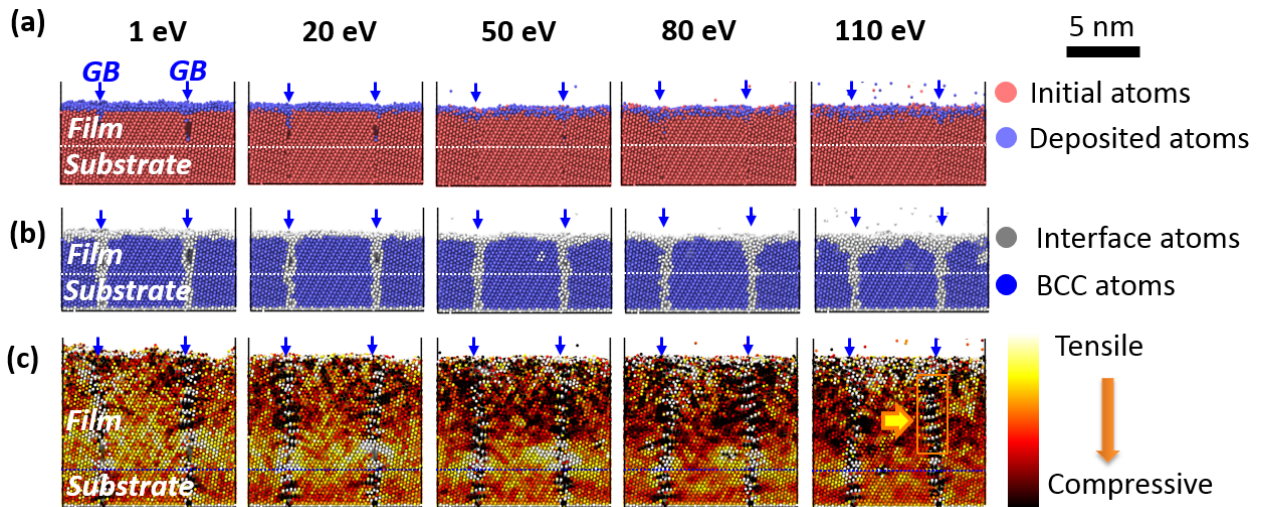


Figure 9 Cross-sectional maps when tungsten atoms with different energy deposited onto the surface of *perpendicular edge* islands. In **(a)**, the colors distinguish the initial substrate and island atoms vs. the deposited atoms. In **(b)**, the colors distinguish interface atoms and atoms in BCC lattice. **(c)** is the atomic stress maps. In (a)-(b), the images show the films when the maximum tensile stress is reached, as illustrated in Figure 8(b). In (c), the images show the films where film deposition completes. Color available on-line.

With an increase in injection energy, the width of the aforementioned grain boundary-surface intersection increased. This indicates that increasing injection energies of the impacting adatoms results in increasingly large losses of structural symmetry for atoms near this region. Such damage effects have been proposed to occur by sputter deposition [57]. When deposition was halted, these regions did heal and recover the bcc symmetry evident by the narrowing of the boundary. This suggests that the impact energy has a profound effect on defect creation, with such disordering more susceptible at interface junctions between the free-surface and the grain boundary.

The grain boundaries beneath the film surface exhibited a unique stress pattern where horizontal groups of atoms alternated between highly compressive and highly tensile stress states, as indicated by the bold arrow in Figure 9(c). A possible explanation for this alternating stress state pattern is that the alternating stresses would cancel out

each other's strain fields resulting in a minimized stress state within the boundary.. The mechanism of this behavior could also be linked to dislocation climb in the grain boundary region, as suggested in references [55, 85]. The frequency and clarity of this stress alteration become more predominate in the boundaries with increasing injection energy.

One can note a qualitative increase in the presence of darker (more compressive) atoms within the grain of the film with increasing injection energy (compare Figure 9(c) at 1 eV and 110 eV). If the grain boundaries themselves are self-organizing in a way to minimize or 'zero-out' the stress as noted above by the altering stress responses, then the compressive stress retained in the film could be from the deformation created by the higher injection energies. The arriving atoms transfer energy into the film upon impact, resulting in a state of strain. The high deposition rate prevents the film from being able to fully relax, causing the retention of such a strain state within the subsurface of the film as it grows [57]. Consequently, the strain accumulated in the film as a compressive stress would also contribute to the increasing stress change with increasing injection energy in Figure 8(a).

By comparing the surface atoms at 50 eV to 110 eV in Figure 9(c), as the injection energy increased, the atoms that remained on the surface were in a tensile stress state (white). This would suggest that any peening effect, if active, creates a compressive effect that is retained by the sub-surface atoms, by virtue of those being shaded darker. The tensile stress state of these atoms are contributed to the free surface effects as well as a higher density of defects on the surface.

The effect of injection energy on the post-coalescence stress as a function of the polycrystalline morphology were also investigated. Using the previous morphologies in Section 3.3, Figure 10 plots the stress range for these different grain morphologies. Here the stress range represents the maximum and minimum reported stress values from a simulation. The stress vs thickness plots associated with each range are provided in the appendix. In all cases, the stress generated from films with different surface morphologies was sensitive to the injection energy. It can be seen that the stress range

tends to increase with increasing deposition energy, and that morphologies with the shallower gradient resulting in less tensile stress generation.

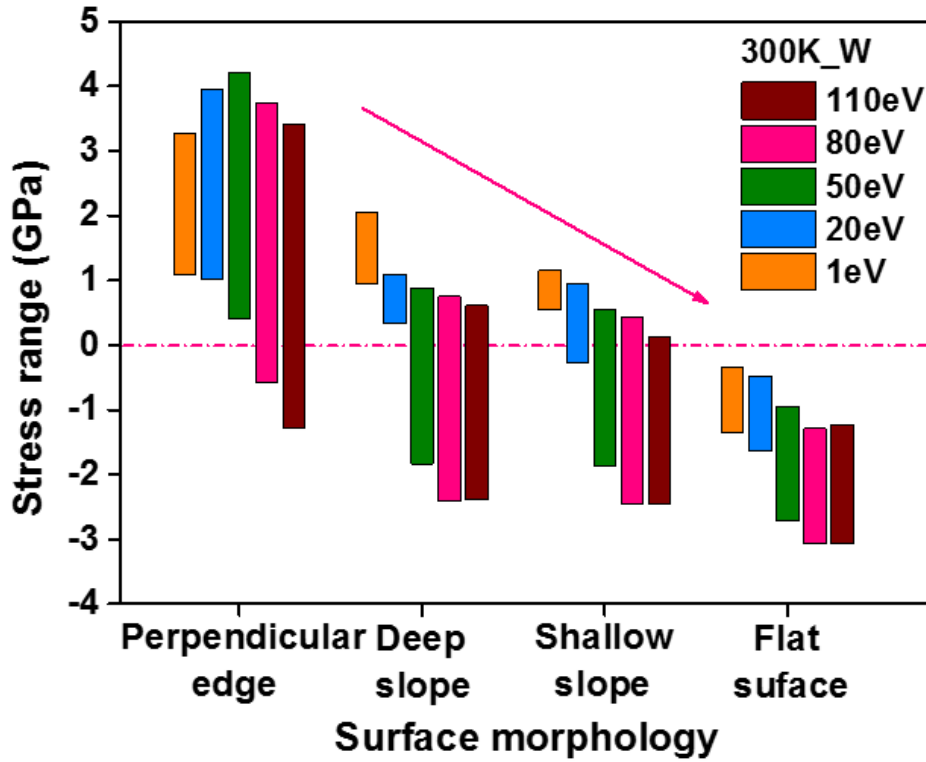


Figure 10 Stress range varying with surface morphology and injection energy when tungsten atoms were deposited to form a film. Color available on-line.

3.6 Growth rate and grain size

Equation (2) reveals that grain size, L , and growth rate, R , will also have an impact on the film stress. The stress of tungsten film has been reported to be either compressive or tensile with its grain size and phase (crystalline or amorphous) being sensitive to the growth rate. We now consider how variations in the deposition rate and grain size effect the stress evolution. The low rate of deposition was set to 19 time steps in between adatom insertions (the high rate was 9 time steps in between adatom insertions). The injection energy was set to 5 eV.

The variation in stress-thickness vs film thickness for high and low deposition rates on a *perpendicular edge* islands template with 6nm grains are shown in Figure 11(a)-(c). The two curves are close in value, but the low deposition rate is slightly lower in its stress response. To determine if this difference is indeed due to grain size and if such effects can be changed with an ever increasing grain size, analogous simulations were ran with 3 nm and 9 nm grains, the results of which are presented in Figure 11(a) and (c). For the smaller grain size simulation, Figure 11(a), an appreciable difference in the stress response was noted between the low and high deposition rates. With increasing grain size the difference in stress response between high and low deposition rates diminished Figure 11(b)(d). Thus the influence of deposition rate on film stress is inversely proportional to grain size.

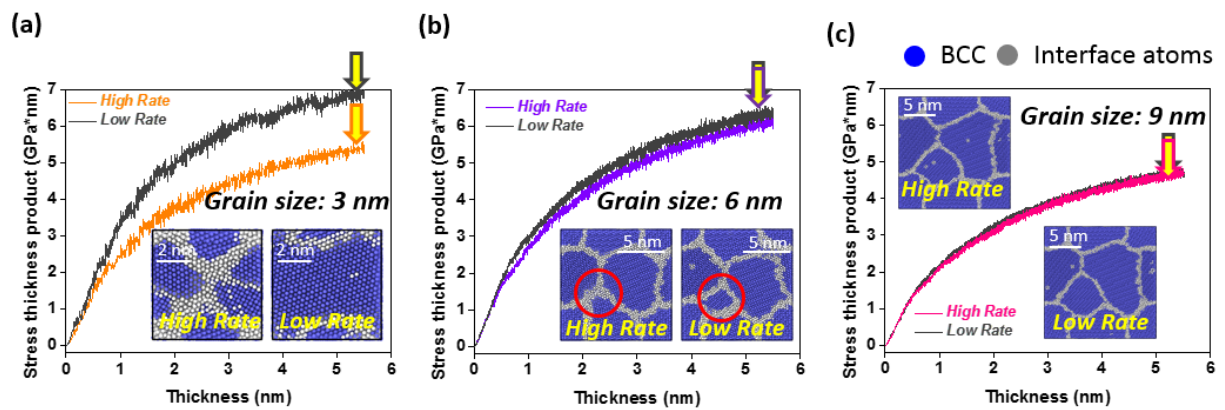


Figure 11 (a) Stress-thickness product varies with deposition time for films at a low and a high deposition rate when 5 eV tungsten atoms deposited onto the surface of a perpendicular edge islands. The average grain size is ~ 6 nm. Stress-thickness product varies with film thickness for films with average grain sizes of **(b)** ~ 6 nm, **(c)** ~ 3 nm, and **(d)** ~ 9 nm at a low and a high deposition rate. A few atom maps are embedded in each figure to help illustrate structural evolution with their locations pointed by arrows in the stress-thickness product plots. Color available on-line.

Reviewing equation (3), the rate based term is captured in the energetic bulk stress contribution. Here, the rate, R , and the time for a defect in the bulk to migrate to the surface, τ_s , are inversely related. It has been suggested that if the film growth rate exceeds the time it takes for the defect to reach the surface and be annihilated, it is retained in the film and can contribute to the compressive stress generating mechanisms [57]. However, upon reviewing the stress relaxation simulations where the grain boundary-free surface region healed upon the ceasing of the deposition, the second term in equation (2), $\sigma_{gb}^{energetic}$, should also depend on a growth rate, R , and a relaxation time for the grain boundary, τ_s' . This will have a similar form as $\sigma_{bulk}^{energetic}$, which is now given as

$$\sigma_{gb}^{energetic} = \left(\frac{l}{L}\right) \frac{A_0}{\left(1 + \frac{l}{R\tau_s'}\right)} \quad (5)$$

It was observed that grain growth occurred during deposition in the small grain size simulation, Figure 11 (a). The initial average grain size was $\sim 3\text{nm}$. The final average grain size for the high rate of deposition was $\sim 3.9\text{nm}$, and for the low rate of deposition was $\sim 4.8\text{nm}$. The reason for the discrepancy in final average grain size is that the lower deposition rate provided extra time for grains to grow and be eliminated. This process of eliminating a grain boundary results in the free volume of the grain boundary being transferred to the lattice of the grain. For large grains this produces a negligible strain per atom. For small grains, the additional strain per atom could be large enough to produce an appreciable tensile stress believed to be the cause of the large jump in tensile stress associated with the low rate of deposition, Figure 11 (a). The reason that this deposition rate dependent discrepancy in stress diminishes with increasing grain size, Figure 11 (b) and (c), is that the driving force for grain growth is inversely proportional to grain size. An additional phenomena that is believed to be partly responsible for the variation in stress with deposition rate is the peening effect mentioned in section 3.5. Higher deposition rates will provide less time for the boundary to heal, resulting in a lower tensile stress. This is the motivation for the modification of

the $\sigma_{bulk}^{energetic}$ term in equation 2 to include a dependency on growth rate and boundary relaxation or “healing” time.

Additional simulations were run at the high-rate with larger grain sizes. The stresses associated with each simulation are present in Figure 12(a). The adatom injection energy was set to 5 eV to eliminate potential peening effects observed in section 3.5 at the higher injection energies. When comparing the stress-thickness curves for simulations with grain sizes between 3 nm to 12 nm, Figure 12(b), a grain size dependence of the stress-thickness can be seen, which would be consistent with reports of a grain size dependence on film stress [27, 29]. As the grain size was reduced, a larger impinging tensile stress was generated. Such responses would scale with the prior behavior noted in sections 3.1, for the isolated island impingement, and section 3.2, the polycrystalline coalescence, where a larger contact area will result in an increase tensile stress response with impingement. A reduction in grain size will increase the surface area to volume ratio, resulting in increased intergranular strain and higher levels of stress. For example, as the mean grain size decreased from ~15 nm to ~6 nm, the maximum impinging tensile stress increased from ~2 GPa to ~3 GPa, Figure 12(c).

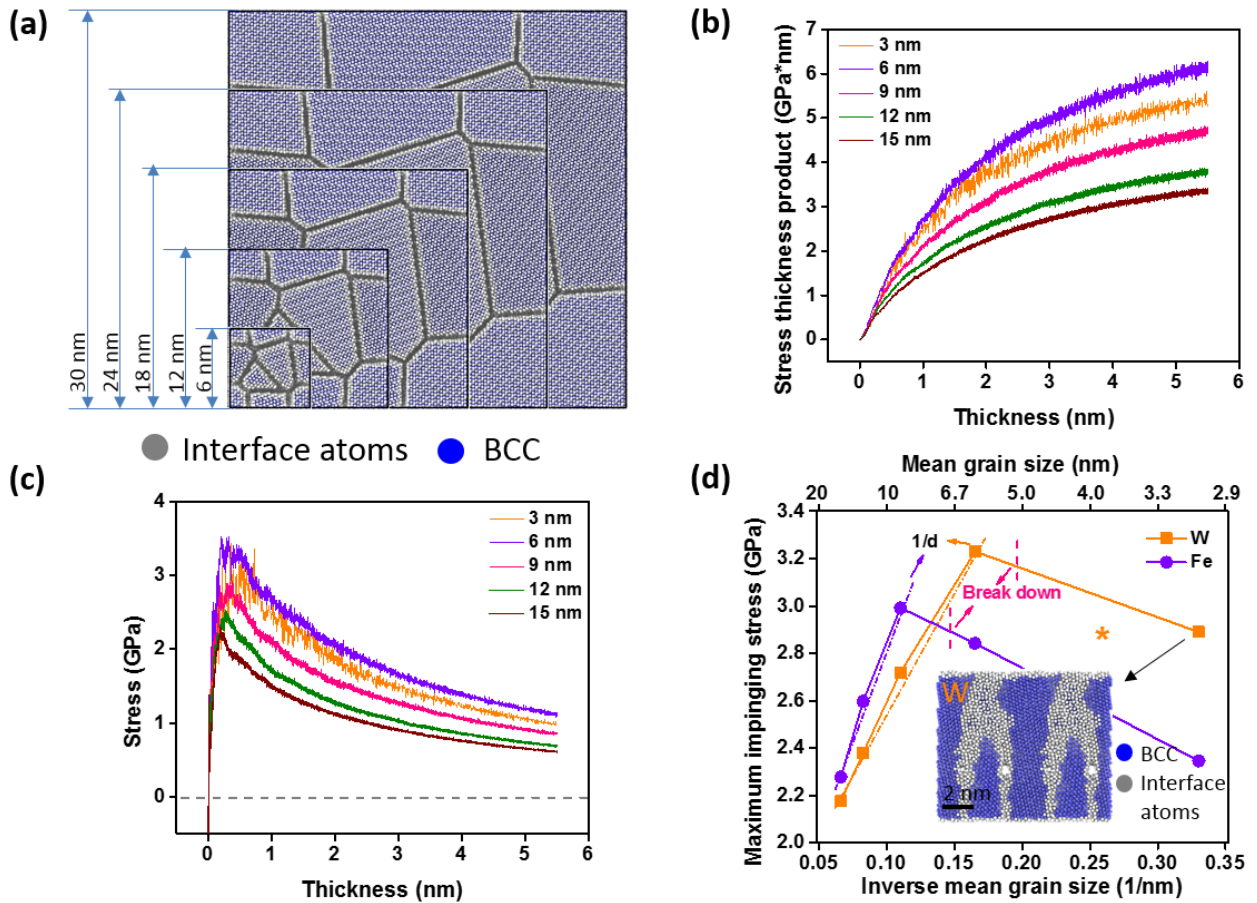


Figure 12 (a) Plan-view atom maps from the *perpendicular edge* islands model with different grain sizes (b) Stress and thickness products (c) Stress varying with film thickness when 5 eV tungsten atoms deposited onto the surface of a *perpendicular edge* islands with different grain sizes. (d) Maximum impinging tensile stress varying with inverse mean grain size for W films and Fe films. The embedded cross-sectional image shows the grain growth of W film when the initial grain size is ~ 3 nm. Color available on-line.

In Figure 12(d), the maximum impinging tensile stress scales with inverse mean grain size, as predicted by Eq. (1) for sizes as small as 6 nm. However, at an initial grain size of ~ 3 nm, this inverse relationship appears to break down and the tensile stress no longer increases. As we mentioned above, this initial grain size is highly unstable because a large fraction ($>50\%$) of the atoms now reside at the boundaries creating a disordered, unstable structure. It was observed in the 3 nm grain simulation that the

grains grew from the initial ~ 3 nm size to a final grain size ~ 3.9 nm. This final grain size, denoted by the asterisk in Figure 12(d) does not reside on the inverse grain size trend. Such behavior suggests a limitation to studying grain size stress dependencies with equation (1). If the grains are too small, they may inherently grow during deposition to mitigate the instabilities associated with the increased energies of small structures.

Because the film stress response is dependent on the kinetics associated with grain growth and relaxation we hypothesize that the film stress response is a function of material type. Grain boundary mobilities vary with material type and it can be inferred that grain boundary relaxation times do as well. Thus the stress response of a particular film might deviate in trend and magnitude if the material type was changed and all other variables were held constant. To test and verify this hypothesis, a set of simulations identical to those presented in figure 12 (a)-(c) were completed using iron as the deposition species. Figure 12(d) shows the relationship between the maximum impinging stress and the inverse mean grain size for iron and Tungsten. For the iron simulation, the breakdown in the relationship between inverse grain size and stress occurs for an average grain size above ~ 6 nm, which is 2X larger than that observed for tungsten. We would note that the binding energy of Tungsten is approximately ~ 8.8 eV [59], which is nearly twice that of iron's (~ 4.32 eV) [59]. We hypothesize that this increased binding energy enabled tungsten to retain stability at a smaller grain size than iron.

3.7 Stress generation as a function of texture

Finally, we address how film texture can influence the stress evolution. Using the '*deep groove*' polycrystalline morphology from section 3.3, the film islands were studied in the $\langle 001 \rangle$, $\langle 011 \rangle$, and $\langle 111 \rangle$ fiber orientations. Tungsten was deposited with an injection energy of 5 eV for an initial grain size of ~ 6 nm. Based on the prior studies, the effects of grain size and injection energy can be differentiated from that of texture. These different orientations will affect the adatom mobility and in doing so how the morphology of the islands evolve with their corresponding stress responses. For

example, when adatoms have a higher mobility, they should easily fill the grooves in the surface and create a smooth film which will change the morphology and the corresponding stress evolution, where such changes have already been noted as a function of morphologies in Figure 5.

We first address the morphological evolution. Of all the films, the $\langle 111 \rangle$ fiber texture exhibited the roughest surface with a root mean square (RMS) of 0.54 nm, Figure 13(a). This would indicate that the adatoms have a lower mobility on this particular surface. Of all the other surfaces, the $\langle 001 \rangle$ fiber surface was found to be the smoothest with a RMS of 0.19 nm, Figure 13(a).

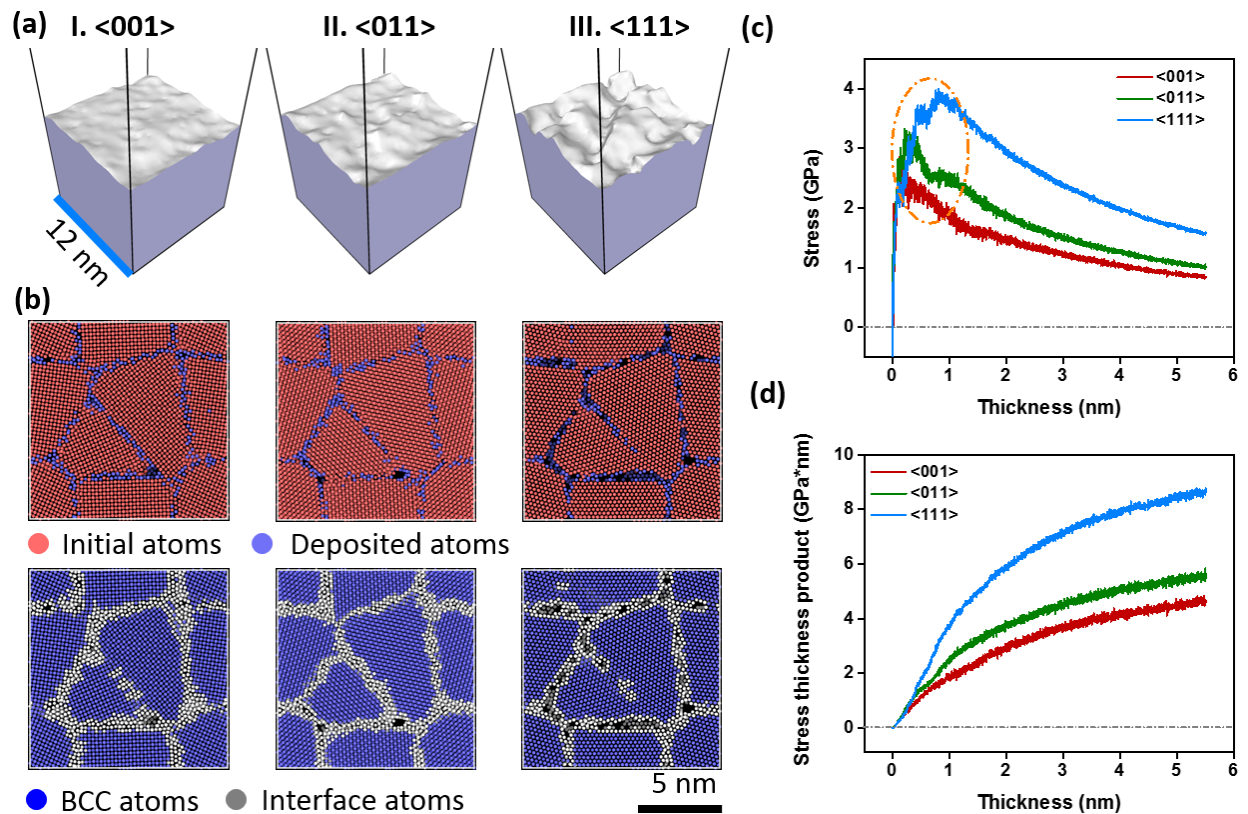


Figure 13 (a) Surface mesh of *deep groove* islands with I $\langle 001 \rangle$ texture, II $\langle 011 \rangle$ texture, and III $\langle 111 \rangle$ texture after 5 eV tungsten atoms deposition. (b) Plan-view images of islands coalescence for $\langle 001 \rangle$ textured, $\langle 011 \rangle$ textured, and $\langle 111 \rangle$ textured films when 5 eV tungsten atoms deposited onto the surface of *perpendicular edge* islands. The colors in the up images distinguish initial atoms and deposited atoms, and in the low

images distinguish interface atoms and atoms in bcc lattice **(c)** Stress and **(d)** Stress-thickness product varying with film thickness for films in (b).

Using these orientations, the stress evolution for each textured islands was then computed for the various morphologies listed in section 3.3. For convenience, we have explicitly listed the impingement stress evolution for the perpendicular contact surfaces, Figure 13(b), as they yield the most pronounced changes, Figure 13(c)&(d). The other morphologies are plotted in the appendix section of this manuscript.

The films with a $\langle 111 \rangle$ fiber texture exhibited the highest impinging tensile stress. This behavior is likely a result of the low mobility of adatoms on the $\langle 111 \rangle$ surface which hindered diffusion into the grain boundary regions. Figure 14 III shows the atom trajectories of the surface atoms on the $\langle 111 \rangle$ fiber surface by the red lines. A large number of red dots rather than lines indicate that the surface adatoms are immobile. This low adatom mobility and the corresponding topology created a larger tensile stress response. In Figure 13(b) III, the $\langle 111 \rangle$ fiber islands exhibited less diffusion into the gaps between the initial islands (represented as red atoms). In contrast, the other fiber textures showed a significantly higher fraction of deposited adatoms in these boundaries (Figure 13(b) I-II).

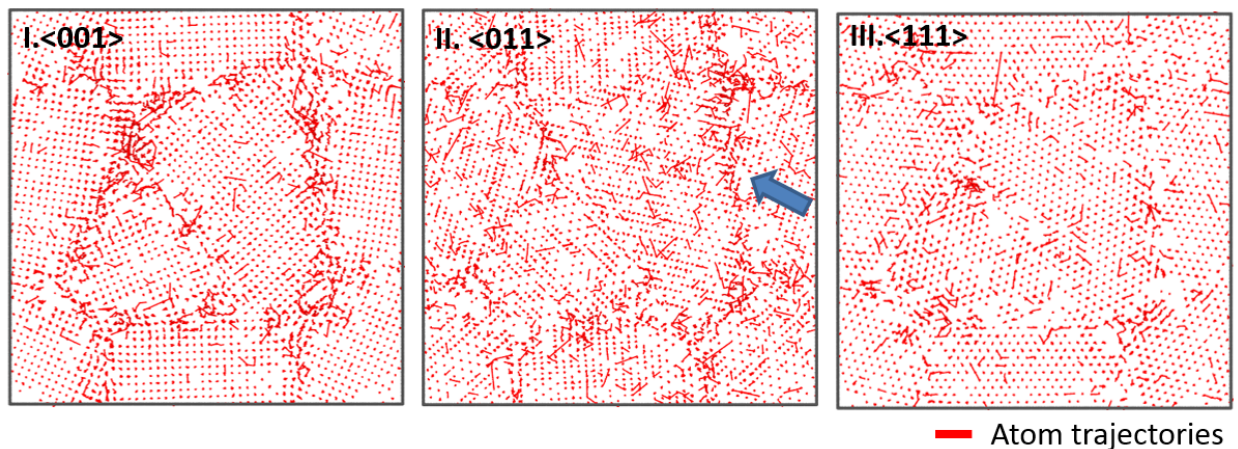


Figure 14 The atom trajectories of deposited interface atoms when 5 eV tungsten atoms deposited onto the surface of a perpendicular edge islands with **(a)** $\langle 001 \rangle$ texture, **(b)** $\langle 011 \rangle$ texture, or **(c)** $\langle 111 \rangle$ texture. Those images are from the top view (Z direction)

Freund and Chason [29] have proposed that the impinging tensile stress is inversely related to interfacial energies of the surface, γ_s , and grain boundaries, γ_{gb} , which is given as:

$$\langle \sigma \rangle = \frac{4(2\gamma_s - \gamma_{gb})}{d} \quad (6)$$

Since the surface energy, γ_s , of the <111> orientation is 3.98 eV*atom⁻¹, as calculated in LAMMPS, and is higher than that of the <011> surface, 3.3 eV*atom⁻¹, and <001> surface, 3.55 eV*atom⁻¹, this too could provide an additional effect to increasing the tensile stress response.

Upon closer inspection of Figure 13(c)&(d), the tensile stress generated on the <011> surface was found to be larger than that created on the <001> surface, even the <011> surface energy, 3.3 eV*atom⁻¹, is lower than that of <001> surface, 3.55 eV*atom⁻¹. To explain this potential discrepancy, the difference between adatom mobilities must be considered. As discussed above, the <001> textured surface generated the smoothest surface, which would suggest that that this surface has the highest adatom mobility. Thus, it is easier for the adatoms to diffuse into the grain boundary regions for these <001> fiber surfaces. By plotting the atom trajectories maps, Figure 14 I, we found that adatoms have a low mobility in the grain surface region but have a long diffusion path near the grain boundary region for the <001> fiber surface. Therefore, these adatoms are more likely to target grain boundary regions on the <001> fiber surface. Even the overall jumping frequency is higher on the <011> surface, as shown in Figure 14 II; the difference in jumping frequency between grain surface region and grain boundary is not large. Only one grain boundary, indicated by an arrow symbol in Figure 14 II, shows preferentially faster diffusion within the boundary indicated by the increased path lengths. Therefore, most adatoms on the <011> fiber surface do not have a strong preference to diffuse into the grain boundary region. This idea is confirmed by Figure 13(b) I and II where the number of deposited atoms in the grain boundary regions is higher for the <001> simulation (412 atoms) than for the <011> simulation (346 atoms). With these extra atoms in the grain boundaries, the extent of elastic straining and available contact surface area is reduced translating to a reduction

of the tensile stress. Furthermore, it has been shown that $\langle 011 \rangle$ surfaces are more likely to yield special character boundaries such as low twin boundaries. Since Eq. (6) is dependent on the difference in the surface energy and grain boundary energy, lower average grain boundary energies associated with the $\langle 011 \rangle$ fiber texture could also result in higher tensile stress. Though no special character boundaries, which are generally associated with lower energies, were produced in our simulated MD impingement model, the experimental confirmation of these types of boundaries in this particular texture [86, 87] does provide some potential future work guidance for these simulations.

4. Conclusions

MD simulations have been used to study the mechanism of the stress generation during thin film growth via the LAMMPS software platform. Single crystalline and polycrystalline grains were created to mimic the initial nucleated islands. The stress evolution was then studied after additional adatoms arrived on the surface of these pre-created islands. Using the simulation's ability to change one variable at a time, the following conclusions were found:

1. The generation of tensile stress results from the coalescence of adjacent islands. A larger tensile stress can be created if there is a larger contact area between adjacent islands with square island contact > cylindrical (line) contact > hemispherical (point) contact. (Section 3.1)

2. Polycrystalline, columnar grains created a more realistic simulation at larger length scales. The elastic straining across multiple faces makes the deformation more homogeneous and generates identical in-plane tensile stress in x-axis and y-axis. (Section 3.2)

3. Surface morphology was observed to influence the stress generation and magnitude. From a *perpendicular edges* morphology to a *flat surface*, the slope gradient lessens, resulting in a reduction of contact area and a decrease of the maximum tensile stress response. (Section 3.3)

4. Upon ceasing deposition, the disordered region width at the grain boundary-free surface intersection narrowed and a post-deposition recovery of the tensile stress was observed. This behavior is linked to the injection energy of incoming atoms depositing on the surface of the islands. As the injection energy increased, the amount of atomic disorder at the grain boundary-free surface region increased resulting in a stronger stress recovery behavior after ceasing deposition. (Section 3.4)

5. Higher injection energy results in incoming atoms transferring momentum into the film, known as an atomic peening effect, which causes the reduction of tensile stress or the generation of compressive stress. Alternating atomic stress responses at the grain boundary region revealed that the grain boundary self-organized in a way to minimize or 'zero-out' the stress. (Section 3.5)

6. In general, the larger grain size, the higher the impinging tensile stress that can be generated. However, if the grain size was reduced to a certain critical value, this relationship was no longer valid and a less tensile stress would be obtained than the linear prediction, resulting from grain growth during deposition caused by the inherently unstable grain structure. Such a critical grain size was linked to the binding energy of the deposited atom. (Section 3.6)

7. Depending on the texture of the film, the deposited roughness changed. The $\langle 111 \rangle$ texture was found to be the roughest and $\langle 001 \rangle$ texture was found to be the smoothest. The lowest tensile stress was generated on the roughest $\langle 111 \rangle$ textured surface. This is caused by large non-coalesced gaps found in between adjacent grains on the $\langle 111 \rangle$ textured surface that generated due to a low adatom mobility. (Section 3.7)

Acknowledge

The authors gratefully recognize support from the Army Research Office, grant W911NF1310436, as well as the High-performance computing (HPC) facility in Alabama supercomputer center and Center for Materials for Information Technology (MINT) at the University of Alabama.

Appendix:

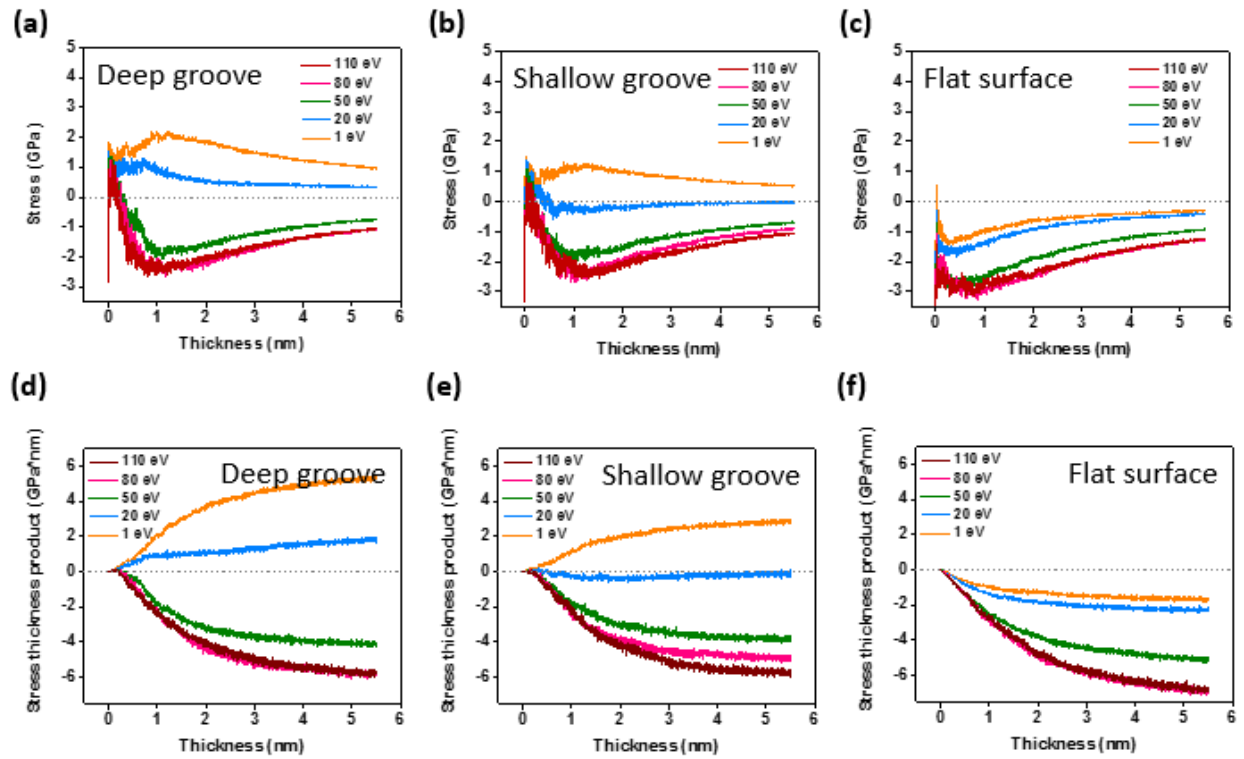


Figure A1 Stress varying with film thickness when tungsten atoms with different energies deposited onto the randomly textured islands with (a) deep groove, (b) shallow groove, and (c) a flat surface. Stress-thickness product varying with film thickness when tungsten atoms with different energies deposited onto the randomly textured islands with (d) deep groove, (e) shallow groove, and (f) a flat surface. The stress ranges of all curves have been represented in Figure 10. Color available on-line.

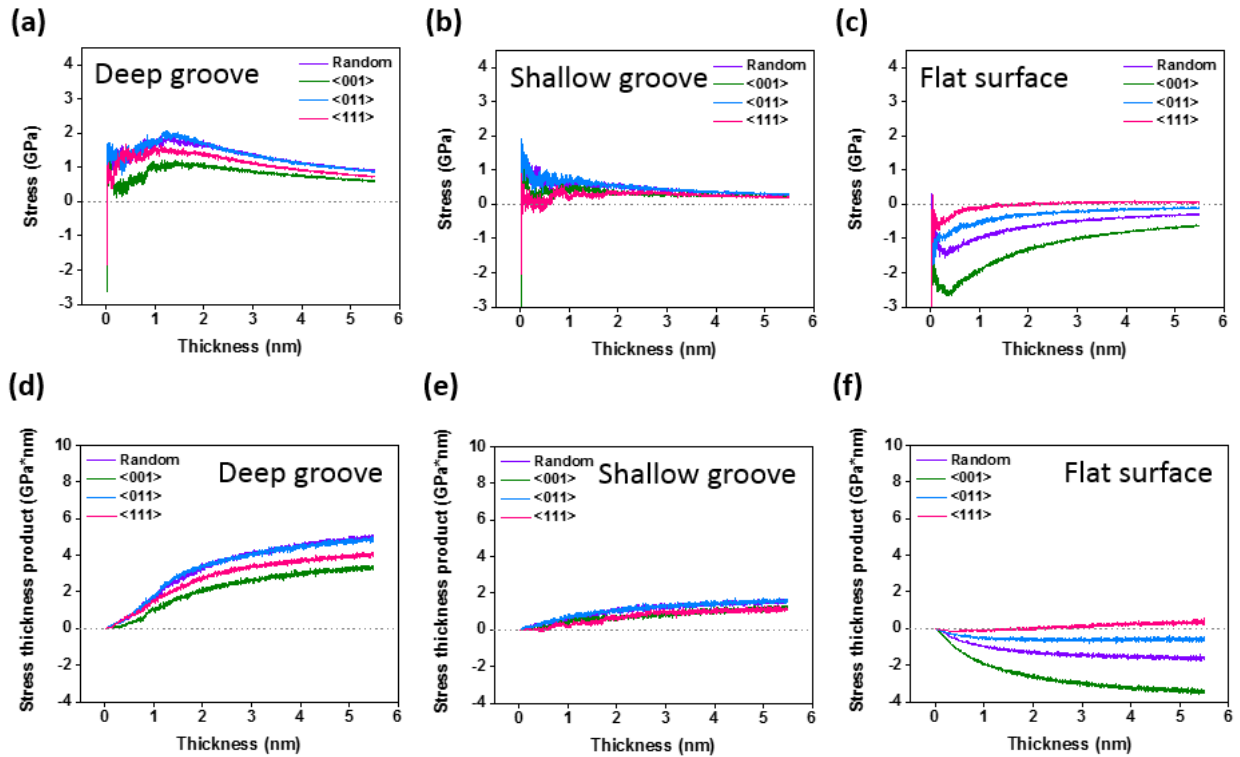


Figure A2 Stress varying with film thickness when 5 eV tungsten atoms with different textures deposited onto the islands with **(a)** deep groove, **(b)** shallow groove, and **(c)** a flat surface. Stress thickness product varying with film thickness when 5 eV tungsten atoms with different textures deposited onto the islands with **(d)** deep groove, **(e)** shallow groove, and **(f)** a flat surface. Color available on-line.

Reference

- [1] F.J. Himpsel, J.E. Ortega, G.J. Mankey, R.F. Willis. Magnetic nanostructures, *Advances in Physics* 47 (1998) 511-597.
- [2] P.K. Tien. Light Waves in Thin Films and Integrated Optics, *Appl. Opt.* 10 (1971) 2395-2413.
- [3] K. Nomura, H. Ohta, A. Takagi, T. Kamiya, M. Hirano, H. Hosono. Room-temperature fabrication of transparent flexible thin-film transistors using amorphous oxide semiconductors, *Nature* 432 (2004) 488-492.
- [4] S. Kovesnikov, W. Tsai, I. Ok, J.C. Lee, V. Torkanov, M. Yakimov, S. Oktyabrsky. Metal-oxide-semiconductor capacitors on GaAs with high-k gate oxide and amorphous silicon interface passivation layer, *Applied Physics Letters* 88 (2006) 022106.
- [5] B. Radisavljevic, A. Radenovic, J. Brivio, V. Giacometti, A. Kis. Single-layer MoS₂ transistors, *Nature nanotechnology* 6 (2011) 147-150.

- [6] X. Chen, S.S. Mao. Titanium dioxide nanomaterials: synthesis, properties, modifications, and applications, *Chemical reviews* 107 (2007) 2891-2959.
- [7] I. Repins, M.A. Contreras, B. Egaas, C. DeHart, J. Scharf, C.L. Perkins, B. To, R. Noufi. 19.9%-efficient ZnO/CdS/CuInGaSe² solar cell with 81.2% fill factor, *Progress in Photovoltaics: Research and Applications* 16 (2008) 235-239.
- [8] P.H. Mayrhofer, C. Mitterer, L. Hultman, H. Clemens. Microstructural design of hard coatings, *Progress in Materials Science* 51 (2006) 1032-1114.
- [9] I. Mizushima, P. Tang, H. Hansen, M. Somers. Residual stress in Ni-W electrodeposits, *Electrochimica Acta* 51 (2006) 6128-6134.
- [10] E. Chason, P. Guduru. Tutorial: Understanding residual stress in polycrystalline thin films through real-time measurements and physical models, *Journal of Applied Physics* 119 (2016) 191101.
- [11] M. Moon, J. Chung, K. Lee, K. Oh, R. Wang, A. Evans. An experimental study of the influence of imperfections on the buckling of compressed thin films, *Acta Materialia* 50 (2002) 1219-1227.
- [12] J. Wang, A. Evans. Effects of strain cycling on buckling, cracking and spalling of a thermally grown alumina on a nickel-based bond coat, *Acta Materialia* 47 (1999) 699-710.
- [13] I. Blech. Electromigration in thin aluminum films on titanium nitride, *Journal of Applied Physics* 47 (1976) 1203-1208.
- [14] E. Chason, N. Jadhav, F. Pei, E. Buchovecky, A. Bower. Growth of whiskers from Sn surfaces: Driving forces and growth mechanisms, *Progress in Surface Science* 88 (2013) 103-131.
- [15] M.A. Steiner, R.B. Comes, J.A. Floro, W.A. Soffa, J.M. Fitz-Gerald. L1' ordering: Evidence of L₁₀-L₁₂ hybridization in strained Fe_{38.5}Pd_{61.5} epitaxial films, *Acta Materialia* 85 (2015) 261-269.
- [16] M. Seita, C.M. Pecnik, S. Frank, R. Spolenak. Direct evidence for stress-induced texture evolution and grain growth of silver thin films upon thermal treatment and self-ion bombardment, *Acta Materialia* 58 (2010) 6513-6525.
- [17] K. Yalamanchili, I.C. Schramm, E. Jiménez-Piqué, L. Rogström, F. Mücklich, M. Odén, N. Ghafoor. Tuning hardness and fracture resistance of ZrN/Zr_{0.63}Al_{0.37}N nanoscale multilayers by stress-induced transformation toughening, *Acta Materialia* 89 (2015) 22-31.
- [18] K.S. Park, J.K. Park. Effect of thin film stress on the elastic strain energy of Cr thin film on substrate, *Acta Materialia* 47 (1999) 2177-2184.
- [19] D. Sander. The correlation between mechanical stress and magnetic anisotropy in ultrathin films, *Reports on Progress in Physics* 62 (1999) 809-858.
- [20] T. Shibata, H. Irie, D.A. Tryk, K. Hashimoto. Effect of Residual Stress on the Photochemical Properties of TiO₂ Thin Films, *The Journal of Physical Chemistry C* 113 (2009) 12811-12817.
- [21] R.C. Cammarata. Surface and interface stress effects in thin films, *Progress in Surface Science* 46 (1994) 1-38.
- [22] J.A. Floro, E. Chason, R.C. Cammarata, D.J. Srolovitz. Physical origin of intrinsic stresses in Volmer-Weber Thin films, *MRS Bulletin* (2002) 19-25.
- [23] E. Bauer. Phänomenologische Theorie der Kristallabscheidung an Oberflächen. I, *Zeitschrift für Kristallographie* 110 (1958) 372-394.
- [24] R.W. Vook. Structure and growth of thin films, *International Metals Reviews* 27 (1982) 209-245.
- [25] R. Abermann, R. Kramer, J. Mäser. Structure and internal stress in ultra-thin silver films deposited on MgF₂ and SiO substrates, *Thin Solid Films* 52 (1978) 215-229.
- [26] C. Friesen, C.V. Thompson. Reversible stress relaxation during precoalescence interruptions of Volmer-Weber thin film growth, *Physical Review Letters* 89 (2002) 126103.

- [27] R.W. Hoffman. Stresses in thin films: The relevance of grain boundaries and impurities, *Thin Solid Films* 34 (1976) 185-190.
- [28] W.D. Nix, B.M. Clemens. Crystallite coalescence: A mechanism for intrinsic tensile stresses in thin films, *Journal of Materials Research* 14 (1999) 3467-3473.
- [29] L.B. Freund, E. Chason. Model for stress generated upon contact of neighboring islands on the surface of a substrate, *Journal of Applied Physics* 89 (2001) 4866-4872.
- [30] S.C. Seel, C.V. Thompson, S.J. Hearne, J.A. Floro. Tensile stress evolution during deposition of Volmer–Weber thin films, *Journal of Applied Physics* 88 (2000) 7079.
- [31] A. Rajamani, B.W. Sheldon, E. Chason, A.F. Bower. Intrinsic tensile stress and grain boundary formation during Volmer-Weber film growth, *Applied Physics Letters* 81 (2002) 1204-1206.
- [32] S.C. Seel, C.V. Thompson. Tensile stress generation during island coalescence for variable island-substrate contact angle, *Journal of Applied Physics* 93 (2003) 9038-9042.
- [33] S.C. Seel, J.J. Hoyt, E.B. Webb, J.A. Zimmerman. Modeling metallic island coalescence stress via adhesive contact between surfaces, *Physical Review B* 73 (2006) 245402.
- [34] A. Bhandari, B.W. Sheldon, S.J. Hearne. Competition between tensile and compressive stress creation during constrained thin film island coalescence, *Journal of Applied Physics* 101 (2007) 033528.
- [35] R. Koch, D. Hu, A. Das. Compressive Stress in Polycrystalline Volmer-Weber Films, *Physical Review Letters* 94 (2005) 146101.
- [36] G. Thurner, R. Abermann. Internal stress and structure of ultrahigh vacuum evaporated chromium and iron films and their dependence on substrate temperature and oxygen partial pressure during deposition, *Thin Solid Films* 192 (1990) 277-285.
- [37] D. Winau, R. Koch, A. Führmann, K.H. Rieder. Film growth studies with intrinsic stress measurement: Polycrystalline and epitaxial Ag, Cu, and Au films on mica(001), *Journal of Applied Physics* 70 (1991) 3081.
- [38] R. Abermann. Measurements of the intrinsic stress in thin metal films, *Vacuum* 41 (1990) 1279-1282.
- [39] C. Friesen, C.V. Thompson. Correlation of stress and atomic-scale surface roughness evolution during intermittent homoepitaxial growth of (111)-oriented Ag and Cu, *Physical Review Letters* 93 (2004) 056104.
- [40] J.W. Shin, E. Chason. Compressive stress generation in Sn thin films and the role of grain boundary diffusion, *Physical Review Letters* 103 (2009) 056102.
- [41] H.Z. Yu, J.S. Leib, S.T. Boles, C.V. Thompson. Fast and slow stress evolution mechanisms during interruptions of Volmer-Weber growth, *Journal of Applied Physics* 115 (2014) 043521.
- [42] R. Koch, D.Z. Hu, A.K. Das. Comment on "Compressive stress in polycrystalline Volmer-Weber films" - Reply, *Physical Review Letters* 95 (2005) 229602.
- [43] H.Z. Yu, C.V. Thompson. Correlation of shape changes of grain surfaces and reversible stress evolution during interruptions of polycrystalline film growth, *Applied Physics Letters* 104 (2014) 141913.
- [44] D. Flötotto, Z.M. Wang, L.P.H. Jeurgens, E.J. Mittemeijer. Kinetics and magnitude of the reversible stress evolution during polycrystalline film growth interruptions, *Journal of Applied Physics* 118 (2015) 055305.
- [45] E. Chason, B. Sheldon, L. Freund, J. Floro, S. Hearne. Origin of Compressive Residual Stress in Polycrystalline Thin Films, *Physical Review Letters* 88 (2002) 156103.
- [46] J. Leib, R. Mönig, C. Thompson. Direct Evidence for Effects of Grain Structure on Reversible Compressive Deposition Stresses in Polycrystalline Gold Films, *Physical Review Letters* 102 (2009) 256101.

- [47] C. Friesen, C.V. Thompson. Comment on "Compressive stress in polycrystalline Volmer-Weber films", *Physical Review Letters* 95 (2005) 229601.
- [48] C. Friesen, S. Seel, C. Thompson. Reversible stress changes at all stages of Volmer-Weber film growth, *Journal of Applied Physics* 95 (2004) 1011-1020.
- [49] A.L. Shull, F. Spaepen. Measurements of stress during vapor deposition of copper and silver thin films and multilayers, *Journal of Applied Physics* 80 (1996) 6243-6256.
- [50] E. Chason, M. Karlson, J. Colin, D. Magnfält, K. Sarakinos, G. Abadias. A kinetic model for stress generation in thin films grown from energetic vapor fluxes, *Journal of Applied Physics* 119 (2016) 145307.
- [51] D. Magnfält, A. Fillon, R.D. Boyd, U. Helmersson, K. Sarakinos, G. Abadias. Compressive intrinsic stress originates in the grain boundaries of dense refractory polycrystalline thin films, *Journal of Applied Physics* 119 (2016) 055305.
- [52] F. Spaepen. Interfaces and stresses in thin films, *Acta Materialia* 48 (2000) 31-42.
- [53] C.-W. Pao, S.M. Foiles, E.B. Webb, D.J. Srolovitz, J.A. Floro. Thin Film Compressive Stresses due to Adatom Insertion into Grain Boundaries, *Physical Review Letters* 99 (2007) 036102.
- [54] C.-W. Pao, S.M. Foiles, E.B. Webb, D.J. Srolovitz, J.A. Floro. Atomistic simulations of stress and microstructure evolution during polycrystalline Ni film growth, *Physical Review B* 79 (2009) 224113.
- [55] M.J. Buehler, A. Hartmaier, H.J. Gao. Atomistic and continuum studies of crack-like diffusion wedges and associated dislocation mechanisms in thin films on substrates, *Journal of the Mechanics and Physics of Solids* 51 (2003) 2105-2125.
- [56] A. Saedi, M.J. Rost. Thermodynamics of deposition flux-dependent intrinsic film stress, *Nature Communications* 7 (2016) 10733.
- [57] E. Chason, M. Karlson, J.J. Colin, D. Magnfalt, K. Sarakinos, G. Abadias. A kinetic model for stress generation in thin films grown from energetic vapor fluxes, *Journal of Applied Physics* 119 (2016) 145307.
- [58] M.J. Rost, D.A. Quist, J.W.M. Frenken. Grains, growth, and grooving, *Physical Review Letters* 91 (2003) 026101.
- [59] G.M. Turner, I.S. Falconer, B.W. James, D.R. McKenzie. Monte Carlo calculations of the properties of sputtered atoms at a substrate surface in a magnetron discharge, *Journal of Vacuum Science & Technology A: Vacuum, Surfaces, and Films* 10 (1992) 455-461.
- [60] H.Z. Yu, C.V. Thompson. Grain growth and complex stress evolution during Volmer-Weber growth of polycrystalline thin films, *Acta Materialia* 67 (2014) 189-198.
- [61] A.J. Detor, A.M. Hodge, E. Chason, Y. Wang, H. Xu, M. Conyers, A. Nikroo, A. Hamza. Stress and microstructure evolution in thick sputtered films, *Acta Materialia* 57 (2009) 2055-2065.
- [62] J. Musil. Low-pressure magnetron sputtering, *Vacuum* 50 (1998) 363-372.
- [63] M. Itoh, M. Hori, S. Nadahara. The Origin of Stress in Sputter-Deposited Tungsten Films for X-Ray Masks, *Journal of Vacuum Science & Technology B* 9 (1991) 149-153.
- [64] S. Foiles, M. Baskes, M. Daw. Embedded-atom-method functions for the fcc metals Cu, Ag, Au, Ni, Pd, Pt, and their alloys, *Physical Review B* 33 (1986) 7983-7991.
- [65] M. Daw, M. Baskes. Embedded-atom method: Derivation and application to impurities, surfaces, and other defects in metals, *Physical Review B* 29 (1984) 6443-6453.
- [66] C.-W. Pao, D.J. Srolovitz. Stress and Morphology Evolution during Island Growth, *Physical Review Letters* 96 (2006) 186103.
- [67] C.-W. Pao, D.J. Srolovitz. Atomistic simulation of stress evolution during island growth, *Journal of the Mechanics and Physics of Solids* 54 (2006) 2527-2543.

- [68] L. Wan, X.-x. Yu, G. Thompson. Influence of the Nb growth surface on the allotropic Ti phase transformation in Nb/Ti/Nb nanolaminates, *Applied Physics Letters* 109 (2016) 111602.
- [69] L. Wan, X. Yu, G. Thompson. Phase stability and in situ growth stresses in Ti/Nb thin films, *Acta Materialia* 80 (2014) 490-497.
- [70] E. Holm, S. Foiles. How Grain Growth Stops: A Mechanism for Grain-Growth Stagnation in Pure Materials, *Science* 328 (2010) 1138-1141.
- [71] C. Deng, C.A. Schuh. Atomistic simulation of slow grain boundary motion, *Physical Review Letters* 106 (2011) 045503.
- [72] S. Plimpton. Fast Parallel Algorithms for Short-Range Molecular Dynamics, *Journal of Computational Physics* 117 (1995) 1-19.
- [73] A. Stukowski, B. Sadigh, P. Erhart, A. Caro. Efficient implementation of the concentration-dependent embedded atom method for molecular-dynamics and Monte-Carlo simulations, *Modelling and Simulation in Materials Science and Engineering* 17 (2009) 075005.
- [74] X.W. Zhou, R.A. Johnson, H.N.G. Wadley. Misfit-energy-increasing dislocations in vapor-deposited CoFe/NiFe multilayers, *Physical Review B* 69 (2004) 144113.
- [75] S. Alexander. Visualization and analysis of atomistic simulation data with OVITO—the Open Visualization Tool, *Modelling and Simulation in Materials Science and Engineering* 18 (2010) 015012.
- [76] J.A. Thornton. High rate thick film growth, *Annual Review of Materials Research* 60 (1977) 239-260.
- [77] S. Traiviratana. A Molecular Dynamics Study of Void Initiation and Growth in Monocrystalline and Nanocrystalline Copper. *Engineering Sciences (Mechanical Engineering)*, vol. Doctor of Philosophy: University of California, San Diego, 2008.
- [78] J.F. Panzarino, T.J. Rupert. Tracking Microstructure of Crystalline Materials: A Post-Processing Algorithm for Atomistic Simulations, *Jom* 66 (2014) 417-428.
- [79] A.P. Thompson, S.J. Plimpton, W. Mattson. General formulation of pressure and stress tensor for arbitrary many-body interaction potentials under periodic boundary conditions, *Journal of Chemical Physics* 131 (2009) 154107.
- [80] M.P. Allen, D.J. Tildesley. *Computer Simulations of Liquids*, Clarendon Press, Oxford, 1991.
- [81] F.M. Dheurle, J.M.E. Harper. Note on the Origin of Intrinsic Stresses in Films Deposited Via Evaporation and Sputtering, *Thin Solid Films* 171 (1989) 81-92.
- [82] Y.G. Shen, Y.W. Mai, Q.C. Zhang, D.R. McKenzie, W.D. McFall, W.E. McBride. Residual stress, microstructure, and structure of tungsten thin films deposited by magnetron sputtering, *Journal of Applied Physics* 87 (2000) 177-187.
- [83] D. Magnfält, G. Abadias, K. Sarakinos. Atom insertion into grain boundaries and stress generation in physically vapor deposited films, *Applied Physics Letters* 103 (2013) 051910.
- [84] R. Koch. Stress in Evaporated and Sputtered Thin Films – A Comparison, *Surface and Coatings Technology* 204 (2010) 1973-1982.
- [85] A. Hartmaier, M.J. Buehler, H. Gao. Multiscale Modeling of Deformation in Polycrystalline Thin Metal Films on Substrates, *Advanced Engineering Materials* 7 (2005) 165-169.
- [86] S. Kobayashi, H. Takagi, T. Watanabe. Grain boundary character distribution and texture evolution during surface energy-driven grain growth in nanocrystalline gold thin films, *Philosophical Magazine* 93 (2013) 1425-1442.
- [87] K.T. Lee, J.A. Szpunar, D.B. Knorr. The Influence of Texture and Grain Boundary Character Distribution on the Reliability of Aluminium Thin Films, *Materials Science Forum* 204-206 (1996) 423-430.

CHAPTER 2:

The Influence of Deposition Parameters on the Stress Evolution of Sputter Deposited Copper

Tyler Kaub¹, Zhaoxia Rao², Eric Chason², and Gregory B. Thompson¹

¹University of Alabama
Department of Metallurgical & Materials Engineering
Tuscaloosa, AL 35401
²Brown University
School of Engineering
Providence, RI 02912

Abstract

The growth rate and pressure dependence on the intrinsic stress in sputter deposited Cu thin films has been investigated and compared to a kinetic growth model, which contains both growth and energetic contributions to stress in its description. Since microstructure also has a strong effect on intrinsic growth stress, we have been able to systematically control a fixed grain size over multiple growth conditions spanning 0.012 nm/s to 2.4 nm/s deposition rates and 0.267 Pa to 2.667 Pa pressures using a seed layer prior to film deposition. At high deposition pressures, the stress became more tensile as the growth rate increased. In the low deposition pressure regime, the stress became more tensile with increases in deposition rate until a critical cross-over point where upon further increases in deposition rate resulted in the stress becoming more compressive. This cross-over has been explained in terms of the energetic contributions to the stress and the intrinsic high mobility of Cu to reveal this behavior. The fitting parameters and corresponding stress contributions from the kinetic model were extracted and compared to other films and deposition techniques. Though caution should be used in comparing absolute values, the kinetic model revealed the correct trends in predicting energetic trapping of defects between low and high mobility films as well as similar growth stress values, which are independent of energetic contributions, between sputtering and electrodeposition. These results suggest that the kinetic model shows promise in fitting different materials and deposition techniques intrinsic stress behavior.

Introduction

Thin film deposition often results in large intrinsic stresses arising from the growth process across all deposition techniques[1]. These stresses can have a significant impact on thin film performance and reliability and in some cases even alter physical properties[2]. The presence of either tensile or compressive stress can result in film failures or reduced performance through delamination, cracking and/or buckling of the film[3,4]. While research in this area has been active for well over 100 years[5], the advent of *in-situ* stress measurement techniques coupled with post-deposition microstructural characterization has led to the development of a fundamental understanding of the mechanisms behind intrinsic stress evolution. These studies have found a

strong correlation between stress and microstructure[6–8] with tensile stresses generally associated with columnar, fine grained microstructures that are commonly observed in low atomic mobility films (denoted as Type 1 by Abermann[9]), while compressive stresses are associated with denser, high atomic mobility (Type 2) films[9].

When metallic thin films are deposited, they typically demonstrate a Volmer-Weber growth mechanism[10] with an accompanying multi-stage stress evolution. If the deposited film consists of high mobility adatoms, a compressive-tensile-compressive stress evolution is observed. In contrast, low mobility adatom films exhibit a compressive-tensile stress evolution behavior. The initial compressive stress in both cases is believed to originate from island nucleation on the substrate surface which is attributed to Laplace pressures that lead to smaller than equilibrium lattice spacing values, which generate the initial compressive stress[11]. As the film thickens, a tensile stress will then arise from the islands on the substrate surface elastically straining to coalesce into a continuous film by forming grain boundaries with neighboring islands to reduce their surface area[12,13]. Low mobility metals will continue to exhibit this tensile stress as the film thickens through continued grain boundary formation and the associated tensile straining mechanism. For high mobility metals, a secondary post-coalescence compressive stress will occur after tensile growth whose origins has several proposed mechanisms. These include pre-coalescence compressive stress inheritance [11], capillary effects[14], excess adatoms generating stress on the surface[15], and insertion of excess adatoms onto film ledges[16] or into grain boundaries[17]. The understanding of this stress evolution is further compounded by the wide number of deposition techniques used to produce thin films. Techniques with high-energy particles such as sputtering, ion-beam assisted deposition and pulsed laser deposition can result in stress modification from energetic bombardments contributions (referred to as ion peening) during film growth. This can promote atomic rearrangements, dislocation generation, and/or grain boundary densification[18,19]. Such mechanisms often result in low mobility films exhibiting compressive stresses under high-energy deposition conditions. Low energy techniques, such as electrodeposition and evaporation, do not have these energetic contributions and the stress is primarily linked to growth and intrinsic material properties such as diffusivity.

To alter the intrinsic stress behavior, the deposition parameters of temperature[20], rate[21], and pressure[22] are typically adjusted. From these variations, several general trends have emerged. As the deposition temperature is increased, the mobility of the deposited atoms also increases. For low mobility films, this can result in a transition from tensile to compressive growth[20]. In higher mobility films, increases in temperature, which trigger grain growth during deposition, lead to transitions from compressive to tensile stresses[6]. With changes in growth rates, a higher deposition rate for a low mobility film will increase the tensile stress whereas a lower deposition rate for a high mobility film will lead to even larger compressive stresses[21]. As one increases the deposition pressure, the mean free path of the deposition species is decreased. For energetic based deposition techniques, reducing the arrival energy and the associated contribution of the energetic stress generating mechanisms to the film's stress state. This results in the film shifting towards a tensile stress with increasing pressure.

Clearly, a range of different stress states can form as a function of materials type and how it is deposited. This explains the variations in stresses that have been report. For example, sputtered Mo can be highly compressive, ≈ -2.4 GPa, to highly tensile, $\approx +3.5$ GPa[23]. Similarly, electrodeposited Ni has a reported range of stresses from ≈ -60 MPa to $\approx +400$ MPa[24]. In order to relate this type of film stress variation as a function of processing conditions, a kinetic model

has been proposed [25,26]. The model bases its stress generation by the events occurring at the grain boundaries as the film grows. To date, there has only been one self-contained study of different process variables (for energetic deposition) that has yielded a sufficient database that can be collectively compared to this model. This was done for a low mobility Mo film[26]. Here, this approach is expanded to a higher mobility film, Cu, over a much wider parametric range of experimental data points to test the kinetic model.

The equations of the model, which will be described in further detail below, are divided into two parts - a term for the stress from the film growth and two terms associated with stress effects from energetic growth mechanisms, which are additive. The model equations depend upon the kinetic parameters of growth including the effective diffusivity (D), growth rate (R), and grain size (L) with the deposition pressure (P) effects associated with the energetic contributions.

We will first consider the tensile contributing mechanism in the kinetic model. This mechanism, originally proposed by Hoffman[12], is based on the concept that the surface energy of two adjacent islands will be lowered through the creation of a grain boundary. If this event occurs, this new grain boundary reduces the free surface area of each individual island at the expense of the elastic strain necessary to close the spatial gap between the two islands. As long as the reduction in interfacial energy is larger than the strain energy, coalescence will occur. Thus, tensile stress generation will have a $1/L^{1/2}$ dependence, where L is the grain size. This relationship then predicts larger tensile stresses with smaller grain sizes because of the increased interfacial area, which has been noted experimentally[13,27]. Building upon this idea, the kinetic model by Chason[25,26] suggested that the gap closing between these islands would occur through a layer-by-layer coalescence process rather than a simultaneous closing of the gap as proposed by Hoffman.

In order to account for the compressive stress generation during growth, Chason suggested that excess adatoms could be inserting themselves into the grain boundaries[17]. This insertion is driven by a supersaturation of adatoms on the surface created by the deposition flux. This flux would increase the chemical potential on the surface that would then drive the adatoms into the grain boundaries creating a compressive stress mechanisms. Upon ceasing deposition, the adatoms would then migrate out from the boundaries resulting in a stress relaxation, which is what is experimentally observed[28].

Using these two mechanisms, the total stress in the film (during non-energetic growth) can be accounted for as the balance between each mechanism, if the films are fully coalesced. This is described as

$$\sigma_{growth} = \sigma_C + (\sigma_T - \sigma_C)e^{-\frac{\beta D}{RL}} \quad (1)$$

where σ_T and σ_C are the tensile and compressive stresses respectively. The exponent term captures the growth rate, R , the grain size, L , the effective diffusivity of atoms, D , from the surface into the grain boundary, and a parameter, β , depending on the concentration of mobile defects and mechanical properties of the layer. Thus, changing R , L , and D can result in a shift in the observed stress state of the film. For example, when $\frac{\beta D}{RL} \ll 1$ the incremental stress is tensile because there is little time for excess adatoms to diffuse into the grain boundaries whereas for the opposite conditions, $\frac{\beta D}{RL} \gg 1$, a compressive incremental stress results because the adatoms have sufficient time to diffuse into the grain boundaries.

This equation has been shown to be successful in describing non-energetic growth such as evaporation and electrodeposition[7,29]. However, for energetic deposition, like sputtering, this equation requires modification to account for collision-induced densification, or peening, of the film near the grain boundaries and the incorporation of microstructural defects into the bulk of the film. For collision-induced densification at the grain boundaries, which creates a compressive stress, the kinetic model assumes a relative range, l , for this effect. When an energetic particle hits within this range, it will introduce a compressive stress in the top most layer of the film which will be relative to the particle's energy[26]. This compressive stress originates when the atoms are incorporated into favorable sites through ballistically induced defects[30]. The stress then depends on the number of defects created per deposited atom given as

$$\sigma_{gb}^{energetic} = A_0 \times \left(\frac{l}{L}\right) \quad (2)$$

where A_0 is, an adjustable parameter used to compare the model to experimental data and will depend on the energy (pressure), growth rate, and flux of the energetic species. In this work the ratio of the flux, f , to rate, R , is assumed to be constant so that the energetic flux scales with the R allowing for one A_0 to be used in fitting the data. The $\frac{l}{L}$ term will be used to approximate the fraction of energetic particles that induce a stress in the grain boundary region and is only expected to hold true when $L > l$, which will be the case for this work.

The second energetic stress generation mechanism is linked to bulk defect incorporation where the stress from point defects is assumed to be proportional to the number of defects that are trapped in the bulk during energetic deposition. This is described as

$$\sigma_{bulk}^{energetic} = \left(1 - \frac{l}{L}\right)\sigma_0 C_{ss} \quad (3)$$

where σ_0 is the stress due to a single defect, $\left(1 - \frac{l}{L}\right)$ accounts for just the bulk of the film (subtracting out the prior the grain boundary effected region discussed above), and C_{ss} defines the steady-state concentration of defects in a layer during deposition. C_{ss} is specifically given as

$$C_{ss} = \frac{c_{of}}{R} \frac{1}{\left(1 + \frac{l}{R\tau_s}\right)} \quad (4)$$

with $\frac{c_{of}}{R}$ being the steady state concentration of defects, R is still defined as the growth rate, and τ_s the characteristic time for a defect to diffuse to the surface and be annihilated. To generate a steady state stress value for energetic deposition, equations 1-3 are combined ($\sigma_{steadystate}^{sputtering} = \sigma_{growth} + \sigma_{gb}^{energetic} + \sigma_{bulk}^{energetic}$) to generate a total stress description below

$$\sigma_{steadystate}^{sputtering} = \left[\sigma_c + (\sigma_T - \sigma_c)e^{-\frac{\beta D}{RL}}\right] + A_0 \left(\frac{l}{L}\right) + \left(1 - \frac{l}{L}\right) \frac{B_0}{\left(1 + \frac{l}{R\tau_s}\right)} \quad (5)$$

Note that $\sigma_0 C_{ss}$ is now replaced with a constant B_0 for ease of fitting to the experimental data. In this simplified form, the stress in the film is related to grain size, L , growth rate, R , and pressure (via the A_0 and B_0 terms).

While the individual effects of changing either the non-energetic or the energetic processing parameters are well documented in the literature, the combined effects and interplay between these two processes are not fully linked. Thus, the kinetic model here has the capability to potentially shed light on these processes by how the experimental data fit to behavior predicted by the balance of all the terms in equation (5). Nevertheless, the validity of the kinetic model needs to be confirmed through comparisons with experimental data to check for its consistency in fitting the correct stress-deposition trends.

Prior comparisons for electrodeposited Cu[24,31] and Ni[7,24] have shown good agreement using the non-energetic growth portions of the model, i.e. equation (1). As already mentioned above, for low mobility energetic growth, good agreement has also been shown in sputtered Mo[26], but was rather limited in parametric space. In particular, low deposition rates were not explored in this work, we expand the experimental parametric experimental space and use Cu, a high mobility adatom, under energetic deposition. To date, there has not been any holistic processing conditions for these types of films to be compared to the kinetic model. In addition, Cu is an excellent case study because it is technically important to several thin film technologies as electrical connectors and has a database from electrodeposition from which we can compare to in the framework of the kinetic model above.

Experimental

The Cu films for the stress measurements were deposited using balanced magnetron sputtering in an AJA ATC-1500 stainless-steel chamber. To achieve the desired deposition rate for the specific conditions used in this study, the films were deposited from either a single Cu target or co-sputtered using two to four Cu targets all having a purity of > 99.95%. All of the films were deposited at ambient temperature onto a Si [100] substrate that had a thermally grown 100 nm surface oxide. The base pressure prior to deposition was < 1.33×10^{-5} Pa, where ultrahigh purity Ar was flowed at 15 standard cubic centimeters per minute to 0.267 Pa for the sputtering working gas. An initial 50 nm Cu “seed” layer was deposited at a rate of 0.12 nm/sec to establish a uniform starting grain morphology and size distribution for every subsequent different deposition condition. Upon completion of the seed layer from those growth conditions, the deposition rate and pressure was immediately changed to one of the following conditions: 0.267 Pa and 0.012 nm/s, 0.12 nm/s, 1.2 nm/s and 2.4 nm/s deposition rates; 1.333 Pa and 0.012 nm/s, 0.12 nm/s and 1.2 nm/s deposition rates; and 2.667 Pa with deposition rates of 0.012 nm/s, 0.12nm/sec and 1 nm/s. This latter growth will be referred to as the “film” layer. The specific thicknesses of the film layer was varied between each of the aforementioned deposition conditions depending on the observed changes in the films’ microstructure with increased layer thickness. Attention to this particular grain size was done to mitigate significant microstructural changes from occurring under the new deposition conditions, where grain growth or voiding can become more prevalent and contribute a microstructural variation effect to the stress response. Under such conditions, deciphering processing dependent and microstructural dependent contributions to the stress would be difficult. The growth rates at each pressure condition were determined using a quartz crystal microbalance calibrated by comparing measurements with small angle x-ray reflectivity[32] using an X’Pert Philips x-ray diffractometer (XRD) operated with a Cu K_{α} source at 45 kV and 40 mA.

All the intrinsic stress measurements were collected *in-situ* during film growth using a K-Space Associates® multibeam optical sensor system (MOS). This unit measures the change in the radius of curvature of the substrate using a reflected laser beam that is passed through an etalon creating an array of spots that reflect off of the substrate and are collected on a charge coupled

device camera[33]. The relative displacement between the laser spots in the array is measured and then used to calculate the average stress in the film via the Stoney equation,

$$\sigma t_f = \frac{M_s t_s^2 \cos \alpha}{12L} \frac{\delta d}{d} \quad (1)$$

where M_s is the biaxial modulus of the substrate, t_s and t_f are the thickness of the substrate (250 μm) and thin film respectively, α is the angle of incidence of the laser beam (2°), L is the substrate detector optic length (88 cm) and $\frac{\delta d}{d}$ is the differential laser spot spacing on the detector[34]. The product σt_s , which is proportional to the measured curvature is referred to as the stress-thickness. The use of relative displacement in the array of laser spots makes the measurement insensitive to the vibration generated by the vacuum pumping system. An average error in the stress measurements for each of the specific deposition conditions was determined by looking at the variation in the seed layer measurements, which offered a reasonable estimate considering multiple, identical deposition condition stress measurements were made through the course of the entire study.

Samples for microstructural characterization were prepared by a lift-out technique described elsewhere[35] using a FEI Quanta 200 Dual-Beam SEM-FIB. The transmission electron microscopy (TEM) samples were prepared in cross section and analyzed using a FEI Tecnai G² Supertwin TEM. In addition, orientation mapping of the samples was performed with the Nanomegas ASTAR system in the TEM using a precession angle of 2° and a step size of 3 nm to give grain size measurements[36]. Chemical analysis to measure oxygen content in the films was also performed using atom probe tomography (APT) with these samples also prepared using a lift-out technique[37]. Oxygen has been reported to effect the stress responses in Cu film[38]. The APT specimens were field evaporated in a Cameca LEAP 5000 XS using a laser mode with a pulse energy of 50pJ, a set-point temperature of 40K, a detection rate of 0.5% and a pulse frequency of 333 kHz. Analysis of the atom probe data was performed in IVAS 3.8.

Results & Discussion

The *in-situ* stress measurements for all the deposition conditions are displayed in Figure 1. The first 50 nm of growth corresponds to the seed layer to control the subsequent grain size which will be further elaborated upon below. Each of these ‘seed’ stress thickness product vs thickness curves are consistent with each other demonstrating good reproducibility. After the seed deposition, the growth conditions were then changed to explore the effects of process on stress evolution. During this changeover, a small ($\sim 1\text{-}3$ nm) transient region developed at the start of the film growth, which could be expected considering the extreme variations in process variables (for some cases) the film underwent from the seed growth conditions. The curves after this transient were observed to be relatively linear for the length of the subsequent deposition for many of the conditions studied. This linear slope infers that the film experienced little to no grain growth or microstructural change. This was confirmed by cross-sectional TEM images in Figure 2. However, we do note, that at the higher-pressures, particularly in the thicker thicknesses, some curvature in the stress thickness plots do appear. This is believed to be associated to density changes within the film created by voiding in the microstructure. This phenomenon is commonly observed in high-pressure deposition conditions[39] and/or a dependence of the growth stress on the grain size[6]. We believe it is likely a voiding issue, evident by the onset of pores within the columnar grain boundaries near the surface of these films. This is shown by the white arrows for the 20 mTorr 1.2 nm/s film’s cross section in Figure 2. For this reason, we analyzed the stress over film thicknesses of 25 to 50 nm depending

on the magnitude of this effect. Within this thickness range, a linear growth response, after the initial transient behavior, was observed and provided the consistent data between the process variables for comparison to the kinetic model.

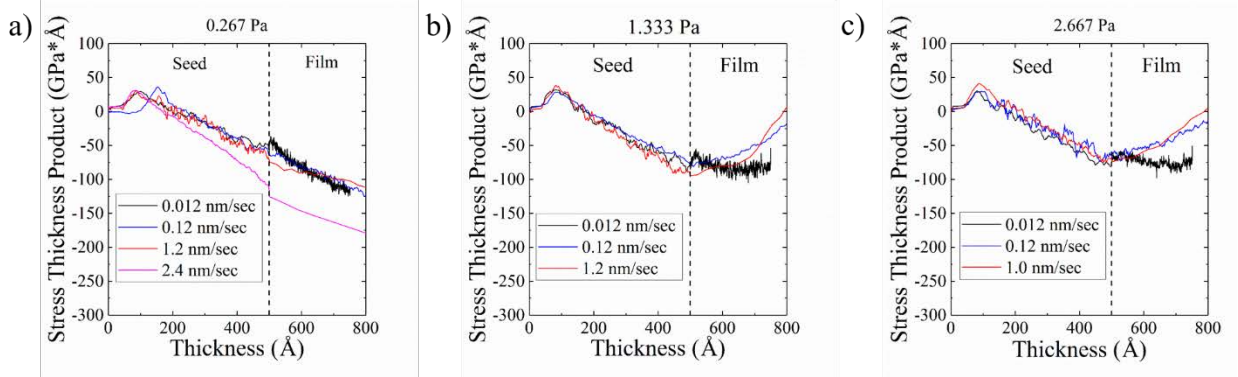


Figure 1. Stress thickness plots for films deposited at (a) 0.266 Pa (b) 1.33 Pa and (c) 2.66 Pa. Color online.

Besides identification of potential defects in the microstructure, Figure 2 also confirmed the continuous microstructure between the seed and film layers. In these images, it is difficult, if not impossible, to distinguish the seed layer from the film suggesting that the corresponding film did indeed grow epitaxially on the grains of the seed layer thereby maintaining the initial microstructural control we required. To generate a more quantitative picture of the microstructure, orientation maps were collected using PED with the grain sizes displayed in Table 1. The average grain size across all the samples was 22.5 ± 4 nm with a range that spanned 16.7 – 29.3 nm. In our initial efforts, if we did not use this seed layer, we observed grain size variations over two orders of magnitude between the processing conditions. Besides the normal experimental distributions in grain sizes, the limited cross sectional sampling area used (typically 150 nm x 2 μm) would also contribute to the small size variations noted. For example, if the sampling area had a single, large grain in it, this would have a disproportional effect on the final size distribution. Regardless of these issues – expected experiential variation and sampling size - the data does demonstrate a reasonably good control of the film microstructure. As will be shown in the latter fitting to the kinetic model, a lack of any clear trend with grain size associated with deposition rate and/or pressure was found furthering supporting that any grain size variation was not a significant factor on the stress response.

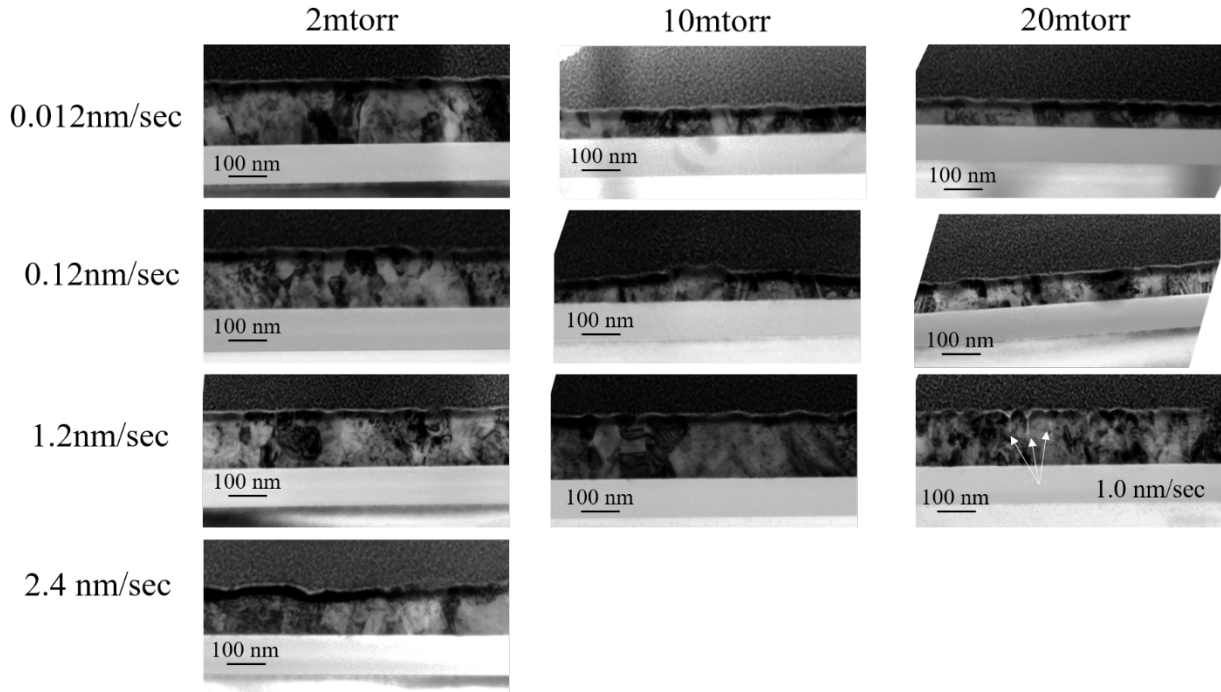


Figure 2. Bright field cross sectional TEM images of the films grown on the seed layer

Table 1. Average grain size measurements (in cross-section) obtained from PED

Deposition Pressure (Pa)	Grain Size (nm)				
	Deposition Rate (nm/sec)				
	0.012	0.12	1.0	1.2	2.4
0.267	18.45 ± 20.2	23.19 ± 16.1	x	24.39 ± 17.6	29.35 ± 29.7
1.333	16.71 ± 14.0	20.64 ± 12.9	x	25.31 ± 22.1	x
2.667	24.02 ± 17.6	24.89 ± 17.8	18.00 ± 9.8	x	x

Besides grain size, and noted in the experimental section, oxygen can also influence Cu film stress[38]. To ensure that the films did not have this potential effect, we performed APT at the highest deposition pressure where the potential for oxygen contamination would be the maximum since the highest deposition pressure would be from the reduced pumping speed in the deposition chamber as the gate valve was nearly closed off. Figure 3 is the time-of-flight mass spectrum from the field evaporation as well as the concentration profile as a function of film depth, which would quantify potential oxygen migration through the film as it grew. The results revealed that the oxygen content was ~ 0.3 at. % with minimal oxygen variation through the film depth. This low oxygen content is contributed either from the target itself, the background gas in the chamber, and/or during the sample transfer between the deposition to the LEAP chamber (< 24 hours). Its

low value provides confidence that oxygen-based effects are negligible in the forthcoming stress results discussion.

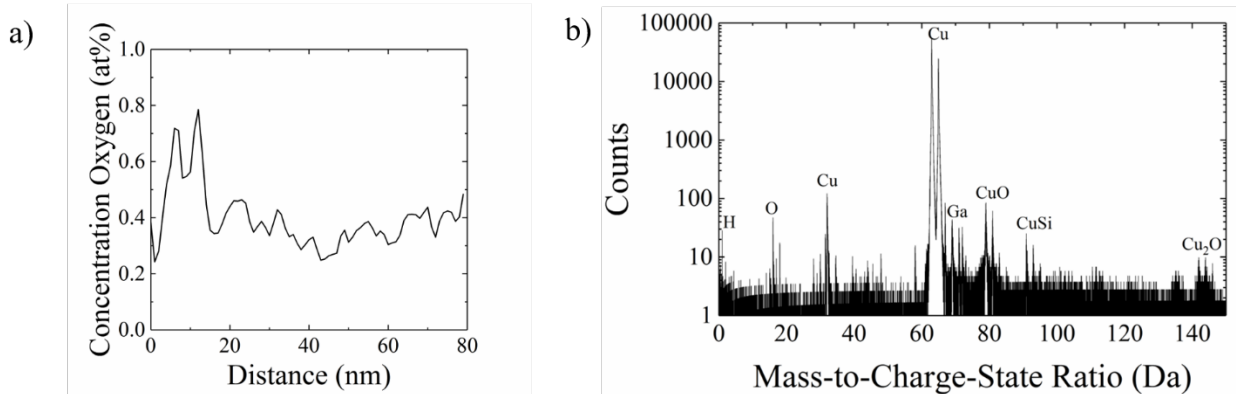


Figure 3. (a) Concentration profile showing little to no variation in oxygen content through film thickness (b) Mass spectrum from APT, note the low level of oxygen.

Returning to Figure 1(a), the stress-thickness evolution at the different deposition rates for the pressure of 0.267 Pa are plotted. As the deposition rate increased from 0.012 nm/s to 1.2 nm/s, the steady state stress (which is the slope of the curve) was observed to decrease (or become less compressive). With a further increase in the rate up to 2.4 nm/s, the steady-state compressive stress then increased (or became more compressive). This initial decrease in the steady state stress is consistent with prior work for energetic depositions, where lower deposition rates are associated with larger compressive stresses[21,40]. The change in the compressive stress at the higher deposition rates is believed to be associated with the trapping of defects in the bulk of the film [41–43]. Through our comprehensive span of deposition rates, within one study, both effects are captured. Upon looking at the higher deposition pressures of 1.333 Pa and 2.667 Pa, Figure 1(b) and Figure 1(c) respectively, the slope of the stress response is observed to become more tensile as the deposition rate is increased and we no longer see this transition in slope seen in the lower pressure conditions.

The steady-state stress data obtained from the slope of the stress-thickness, Figure 1, are plotted against the growth rate at the different measured pressures in Figure 4. Several trends can be noted in this data representation. For each growth rate, the stress is more compressive when the pressure is lower. For the lowest growth rates, the stress is more compressive than at high growth rates for all pressures. However, there is a different behavior for the stress at high growth rates depending on the pressure. At high pressure, the stress appears to retain the same tensile value when the growth rate is increased, while at the low pressure regime, the stress appears to become more compressive at the highest growth rates.

The dependence of the steady-state stress in Figure 4 can now be fitted to the kinetic model given in equation 5, shown as solid lines. The optimum values for the parameters were obtained by using a non-linear least-squares fitting routine that minimized the residual between the model and the measurements. Because of the large number of potential fitting parameters, we constrained A_0 , B_0 and l to have a linear dependence on the pressure below a threshold value of P_0 with further details of this fitting discussed in reference[26]. This constraint makes the magnitude of these parameters increase with particle energy. Enforcing a linear dependence on pressure reduces the number of free parameters from thirteen to eight. The constrained parameters were then optimized

over the entire data set to produce physically reasonable values that can then be used to compare the calculations between the different data sets. The resulting fitting parameters are tabulated in Table 2.

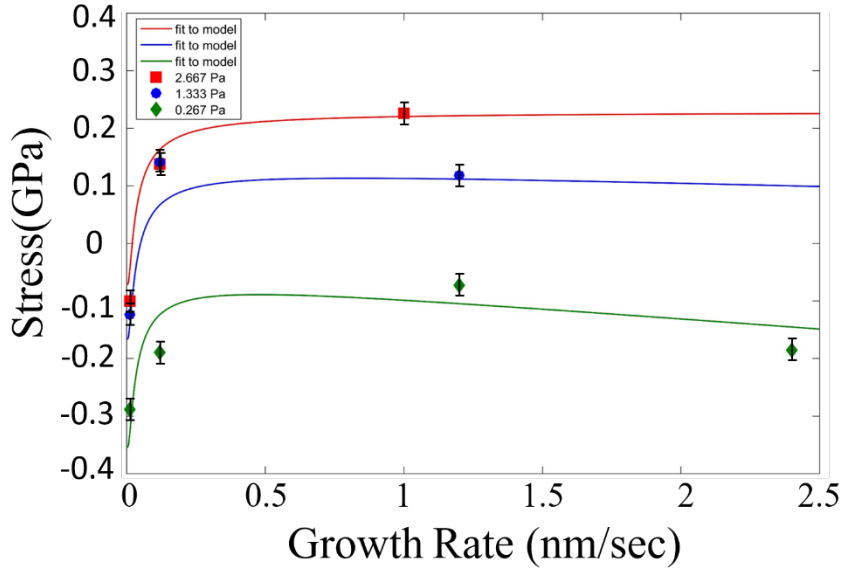


Figure 4. Kinetic model fitting curves (solid lines) overlaid on stress versus growth rate measurements of Cu. Color online.

Table 2. Values obtained when applying the non-linear least squares fitting of the stress data to the kinetic model.

Pressure (Pa)	σ_C (GPa)	σ_T (GPa) at $L=22.5\text{nm}$	βD (nm^2/s)	D_i (nm^2/s)	P_0 (Pa)	A_0 (GPa)	B_0 (GPa)	l (nm)
0.267	-0.0707	0.23	0.67	5503.14	2.81	-3.82	-131.19	1.67
1.333	-0.0707	0.23	0.67	5503.14	2.81	-2.22	-76.24	0.97
2.667	-0.0707	0.23	0.67	5503.14	2.81	-0.22	-7.475	0.10

Comparing the experimental data and fitting results from the kinetic model, Figure 4, the model is capturing the growth rate and pressure dependence trends on the stress evolution in the energetically deposited, high mobility system. To understand these fitting parameters produced by the model, comparisons between these values and different elemental systems and deposition techniques were undertaken. Nonetheless, one should exhibit measured caution on strict comparisons between the absolute fitting parameter values. Since they are fitted from experimental data, there will be some uncertainty from those measurements. If the uncertainty were only from experimental error, then statistical analysis would be sufficient to determine the fitting parameter uncertainty. However, simplifying assumptions were required in the model and these assumptions would also contribute to differences from the data. Such systematic errors would then indicate that differences between the fit and the experimental data are not strictly related to statistical

experimental error. Thus, the fitting parameters are ‘best values’ but do not have their own errors reported, as they would be convoluted between the experimental and modeling assumptions’ uncertainties. Rather these fitting parameters provide semi-quantitative information that aid in the exploration of trends and help provide insights into the stress generating contributions from different physical mechanisms that may otherwise be unavailable to assess.

To begin this comparison, we will relate the experimental data reported for the low mobility Mo films [26] to our high mobility Cu films. While the Mo data was obtained over a much narrower pressure range (0.11 – 0.43 Pa) and growth rates (0.05 – 0.3 nm/s) than the Cu films studied here, it does contain some overlap in processing conditions. In the highest deposition pressure regime for Mo (0.43 Pa), the steady-state stress was tensile and exhibited little to no dependence on growth rate. In contrast, for Cu at the highest deposition pressure (2.66 Pa), the film exhibited a much stronger rate dependence, becoming more tensile with increasing deposition rate. At the lowest deposition rate for the high pressure Cu, a compressive stress was observed which was not experimentally reported in the Mo study. Considering that the Cu was deposited at a much higher pressure than Mo, this difference in behavior is striking because one might assume at higher pressures, with the reduction of energetic contributions, the stress would remain tensile over the entirety of growth conditions. The difference in the behavior for Cu can be attributed to the effect of the non-energetic growth stresses in equation 5. For the higher atomic mobility Cu, the growth stress is predicted to become compressive at low growth rates. For the low mobility Mo, the reported growth stress remains tensile over the range of growth rates measured. In terms of the kinetic model, this behavior is predicted by the dependence on the kinetic parameter βD . For large values of $\beta D/R$ (as in Cu), the stress is predicted to become compressive while for low values (as in Mo), it remains tensile.

At low pressures, the energetic effects of the incoming species become greater than at high pressures. For this reason, at each growth rate, the stress becomes more compressive as the pressure is lowered. Furthermore, for the experimental data in the Mo study at low pressure, the compressive stress becomes even more compressive as the deposition rate increases. This same dependence is observed in the Cu system in the higher deposition rate regimes of 1.2 nm/s and 2.4 nm/s. In these cases, the energetic particle stress effects become larger when the flux of energetic particles is larger. The fact that the stress becomes more compressive at higher growth rates suggests that the energetic effects are larger than the growth effects. Conversely, at the lowest Cu deposition rate, a stress turnaround is observed and the compressive stress becomes more compressive at low growth rates. This again can be attributed to the effect of the growth stress being larger than that of the energetic particle stress at the low growth rates. This turnaround behavior fits well to the kinetic model for the Cu system, Figure 4’s 0.267 Pa fit. In the case of Mo, similar behavior is predicted for the lower growth rates, but it was not observed because the experimental data was not acquired at a sufficiently low growth rate. By going to a higher mobility material, like Cu, we have been able to observe this crossover between the energetic and growth stress behavior as predicted by the model.

At high growth rates and low deposition pressures, the arrival energy of the sputtered atoms would be high. In this condition, the stress would be predicted to become ever more compressive. This too is predicted by the model and was observed in both this work and the Mo study, with the slope of the stress verses growth rate (in the high growth rate regime) being greater for Mo. This would indicate that more defects are being incorporated into the Mo film because Mo has lower diffusivity than Cu which would enable it to trap these defects. In the kinetic model, this defect

incorporation is reflected in the B_0 term. Considering the cases where the Mo and Cu pressures are similar (0.24 Pa versus 0.267 Pa, respectively), we have used the same fitting routine to both datasets, with the Mo data fits provided as a supplement to this paper. The B_0 for Mo was approximately -501 GPa and for Cu it was -131 GPa. Though there can be some uncertainty in the absolute values used, the nearly 3.5X difference does demonstrate a significant effect where one can reasonably infer that indeed the defect incorporation is higher in Mo than that of Cu or that a defect in Cu contributes a small contribution to the stress than that in Mo. The ability to use the kinetic model to begin to semi-quantitatively ascertain such contributions provides potential toolset to compare stress behavior mechanisms and contributions across systems.

While there are many differences that can exist between sputter-deposition and electrodeposition, comparing the growth stresses, which are believed to be independent of the energetic contributions of sputtering, allows for another opportunity to compare the stress influences between the two techniques. When looking at the growth contributions of σ_c and σ_T in equation (1), the sputter-deposited Cu was approximately -70 MPa and 230 MPa respectively whereas electrodeposited Cu is approximately -19.9 MPa[24] and 380 MPa[24] respectively. We once again recognize that care should be taken in any comparison of the absolute parameters, but the values are relatively comparable (and within the same order of magnitude) between the two techniques which adds confidence in the kinetic model's ability to extract individual contributions to the stress in the sputtered deposition conditions. While further studies in more materials systems are needed to further elucidate a more thorough understanding of these observations, it does suggest that the intrinsic elemental, atomic mobility behavior does indeed influence stress effects. The good agreement of the kinetic model with this data, along with a prior study[26], indicates that the kinetic model has potential for understanding the contributions of different non-energetic and energetic growth processes to the stress evolution of thin films.

Summary

This work has examined the growth rate and pressure dependence on the intrinsic stress for sputter deposited Cu, a high mobility metal film. To mitigate the effect of microstructure, i.e. grain growth and size, to the stress evolution, a 50 nm Cu seed layer was deposited for all films under identical deposition conditions. It was found that it was sufficient in keeping the subsequent Cu film, from rates of 0.012 nm/s to 2.4 nm/s and pressures between 0.267Pa to 2.667 Pa, relatively similar up to 50 nm. The linear steady-state growth enabled the effect of processing changes to be ascertained. It was found that the intrinsic stress exhibited a rate dependent behavior with different trends emerging for high and low deposition pressures, which were fitted to a kinetic model that contains contributions from growth and energetic stress generation mechanisms. At high deposition pressures, the stress became more tensile as the growth rate increased. In the low deposition pressure regime, the stress became more tensile with increases in deposition rate until a critical cross-over point where further increases in deposition rate resulted in the stress becoming more compressive. This cross-over has been explained in terms of the energetic contributions to the stress. The ability to observe the crossover by Cu is contributed to its high intrinsic; in previous work in Mo, a low mobility film, this crossover behavior was not observed. Through the use of the kinetic model, the fitting parameters and corresponding stress contributions were extracted and compared to other films and deposition techniques. Though caution should be used in comparing absolute values between these findings and prior reported values, as various uncertainties exist, the kinetic model revealed the correct trends in predicting energetic trapping of defects between low and high mobility films as well as similar growth stress values, which are independent of energetic

contributions, between sputtering and electrodeposition. The kinetic model, with the experimental data here, appears to be a promising description in revealing and understanding the different contributions of intrinsic thin film stress.

Acknowledgments

The authors TK and GBT gratefully acknowledge the Army Research Office, Grant No. W911NF1310436, Dr. Michael Bakas, program manager. The work of EC and ZR was supported by the NSF under contract DMR-1602491. The UA Central Analytical Facility is recognized for additional assistance and access to the microscopes used in this research.

References

- [1] R. Koch, The intrinsic stress of polycrystalline and epitaxial thin metal films, *Journal of Physics: Condensed Matter*. 6 (1994) 9519–9550. doi:10.1088/0953-8984/6/45/005.
- [2] T.M. Shaw, Z. Suo, M. Huang, E. Liniger, R.B. Laibowitz, J.D. Baniecki, The effect of stress on the dielectric properties of barium strontium titanate thin films, *Appl. Phys. Lett.* 75 (1999) 2129–2131. doi:10.1063/1.124939.
- [3] M.-W. Moon, J.-W. Chung, K.-R. Lee, K.H. Oh, R. Wang, A.G. Evans, An experimental study of the influence of imperfections on the buckling of compressed thin films, *Acta Materialia*. 50 (2002) 1219–1227. doi:10.1016/S1359-6454(01)00423-2.
- [4] V.B. Shenoy, A.F. Schwartzman, L.B. Freund, Crack patterns in brittle thin films, *International Journal of Fracture*. 103 (2000) 1–17. doi:10.1023/A:1007673320058.
- [5] G. Gore, On the Properties of Electro-Deposited Antimony, *Philosophical Transactions of the Royal Society of London*. 148 (1858) 185–197.
- [6] H.Z. Yu, C.V. Thompson, Grain growth and complex stress evolution during Volmer–Weber growth of polycrystalline thin films, *Acta Materialia*. 67 (2014) 189–198. doi:10.1016/j.actamat.2013.12.031.
- [7] E. Chason, A.M. Engwall, Relating residual stress to thin film growth processes via a kinetic model and real-time experiments, *Thin Solid Films*. 596 (2015) 2–7. doi:10.1016/j.tsf.2015.06.061.
- [8] A. Bhandari, B.W. Sheldon, S.J. Hearne, Competition between tensile and compressive stress creation during constrained thin film island coalescence, *Journal of Applied Physics*. 101 (2007) 033528. doi:10.1063/1.2432376.
- [9] R. Abermann, Measurements of the intrinsic stress in thin metal films, *Vacuum*. 41 (1990) 1279–1282. doi:10.1016/0042-207X(90)93933-A.
- [10] E. Bauer, Phänomenologische Theorie der Kristallabscheidung an Oberflächen. I, *Zeitschrift Für Kristallographie*. 110 (1958) 372–394. doi:10.1524/zkri.1958.110.1-6.372.
- [11] R.C. Cammarata, T.M. Trimble, D.J. Srolovitz, Surface stress model for intrinsic stresses in thin films, *Journal of Materials Research*. 15 (2000) 2468–2474. doi:10.1557/JMR.2000.0354.
- [12] R.W. Hoffman, Stresses in thin films: The relevance of grain boundaries and impurities, *Thin Solid Films*. 34 (1976) 185–190. doi:10.1016/0040-6090(76)90453-3.

- [13] W.D. Nix, B.M. Clemens, Crystallite coalescence: A mechanism for intrinsic tensile stresses in thin films, *Journal of Materials Research*. 14 (1999) 3467–3473. doi:10.1557/JMR.1999.0468.
- [14] R. Koch, D. Hu, A.K. Das, Compressive Stress in Polycrystalline Volmer-Weber Films, *Phys. Rev. Lett.* 94 (2005) 146101. doi:10.1103/PhysRevLett.94.146101.
- [15] C. Friesen, S.C. Seel, C.V. Thompson, Reversible stress changes at all stages of Volmer–Weber film growth, *Journal of Applied Physics*. 95 (2004) 1011–1020. doi:10.1063/1.1637728.
- [16] F. Spaepen, Interfaces and stresses in thin films, *Acta Materialia*. 48 (2000) 31–42. doi:10.1016/S1359-6454(99)00286-4.
- [17] E. Chason, B.W. Sheldon, L.B. Freund, J.A. Floro, S.J. Hearne, Origin of Compressive Residual Stress in Polycrystalline Thin Films, *Phys. Rev. Lett.* 88 (2002) 156103. doi:10.1103/PhysRevLett.88.156103.
- [18] D. Magnfält, A. Fillon, R.D. Boyd, U. Helmersson, K. Sarakinos, G. Abadias, Compressive intrinsic stress originates in the grain boundaries of dense refractory polycrystalline thin films, *Journal of Applied Physics*. 119 (2016) 055305. doi:10.1063/1.4941271.
- [19] G. Carter, Peening in ion-assisted thin-film deposition: a generalized model, *J. Phys. D: Appl. Phys.* 27 (1994) 1046. doi:10.1088/0022-3727/27/5/024.
- [20] G. Thurner, R. Abermann, Internal stress and structure of ultrahigh vacuum evaporated chromium and iron films and their dependence on substrate temperature and oxygen partial pressure during deposition, *Thin Solid Films*. 192 (1990) 277–285. doi:10.1016/0040-6090(90)90072-L.
- [21] A.L.D. Vecchio, F. Spaepen, The effect of deposition rate on the intrinsic stress in copper and silver thin films, *Journal of Applied Physics*. 101 (2007) 063518. doi:10.1063/1.2712150.
- [22] M. Pletea, W. Brückner, H. Wendrock, R. Kaltoven, Stress evolution during and after sputter deposition of Cu thin films onto Si (100) substrates under various sputtering pressures, *Journal of Applied Physics*. 97 (2005) 054908. doi:10.1063/1.1858062.
- [23] A. Fillon, G. Abadias, A. Michel, C. Jaouen, Stress and microstructure evolution during growth of magnetron-sputtered low-mobility metal films: Influence of the nucleation conditions, *Thin Solid Films*. 519 (2010) 1655–1661. doi:10.1016/j.tsf.2010.07.091.
- [24] A.M. Engwall, Z. Rao, E. Chason, Origins of residual stress in thin films: Interaction between microstructure and growth kinetics, *Materials & Design*. 110 (2016) 616–623. doi:10.1016/j.matdes.2016.07.089.
- [25] E. Chason, J.W. Shin, S.J. Hearne, L.B. Freund, Kinetic model for dependence of thin film stress on growth rate, temperature, and microstructure, *Journal of Applied Physics*. 111 (2012) 083520. doi:10.1063/1.4704683.
- [26] E. Chason, M. Karlson, J.J. Colin, D. Magnfält, K. Sarakinos, G. Abadias, A kinetic model for stress generation in thin films grown from energetic vapor fluxes, *Journal of Applied Physics*. 119 (2016) 145307. doi:10.1063/1.4946039.
- [27] L.B. Freund, E. Chason, Model for stress generated upon contact of neighboring islands on the surface of a substrate, *Journal of Applied Physics*. 89 (2001) 4866–4873. doi:10.1063/1.1359437.

- [28] C. Friesen, C.V. Thompson, Reversible Stress Relaxation during Precoalescence Interruptions of Volmer-Weber Thin Film Growth, *Phys. Rev. Lett.* 89 (2002) 126103. doi:10.1103/PhysRevLett.89.126103.
- [29] A.M. Engwall, Z. Rao, E. Chason, Residual Stress in Electrodeposited Cu Thin Films: Understanding the Combined Effects of Growth Rate and Grain Size, *J. Electrochem. Soc.* 164 (2017) D828–D834. doi:10.1149/2.0921713jes.
- [30] D. Magnfalt, G. Abadias, K. Sarakinos, Atom insertion into grain boundaries and stress generation in physically vapor deposited films: *Applied Physics Letters: Vol 103, No 5*, (n.d.). <http://aip.scitation.org/doi/full/10.1063/1.4817669> (accessed June 6, 2017).
- [31] E. Chason, A. Engwall, F. Pei, M. Lafouresse, U. Bertocci, G. Stafford, J.A. Murphy, C. Lenihan, D.N. Buckley, Understanding Residual Stress in Electrodeposited Cu Thin Films, *J. Electrochem. Soc.* 160 (2013) D3285–D3289. doi:10.1149/2.048312jes.
- [32] Y. Sasanuma, M. Uchida, K. Okada, K. Yamamoto, Y. Kitano, A. Ishitani, Characterization of long-periodic layered structures by X-ray diffraction IV: Small angle X-ray diffraction from a superlattice with non-ideal interfaces, *Thin Solid Films.* 203 (1991) 113–120. doi:10.1016/0040-6090(91)90522-Y.
- [33] Taylor, C., Bartlett, D., Chason, E., Floro, J., *The Industrial Physicists.* 4 (1998) 25.
- [34] G.G. Stoney, The Tension of Metallic Films Deposited by Electrolysis, *Proceedings of the Royal Society A: Mathematical, Physical and Engineering Sciences.* 82 (1909) 172–175. doi:10.1098/rspa.1909.0021.
- [35] L.A. Giannuzzi, F.A. Stevie, A review of focused ion beam milling techniques for TEM specimen preparation, *Micron.* 30 (1999) 197–204. doi:10.1016/S0968-4328(99)00005-0.
- [36] E.F. Rauch, M. Véron, J. Portillo, D. Bultreys, Y. Maniette, S. Nicolopoulos, Automatic crystal orientation and phase mapping in TEM by precession diffraction, *Microscopy and Analysis-UK.* 128 (2008) S5–S8.
- [37] K. Thompson, D. Lawrence, D.J. Larson, J.D. Olson, T.F. Kelly, B. Gorman, In situ site-specific specimen preparation for atom probe tomography, *Ultramicroscopy.* 107 (2007) 131–139. doi:10.1016/j.ultramicro.2006.06.008.
- [38] R. Abermann, R. Koch, In situ study of thin film growth by internal stress measurement under ultrahigh vacuum conditions: Silver and copper under the influence of oxygen, *Thin Solid Films.* 142 (1986) 65–76. doi:10.1016/0040-6090(86)90303-2.
- [39] J.A. Thornton, High Rate Thick Film Growth, *Annual Review of Materials Science.* 7 (1977) 239–260. doi:10.1146/annurev.ms.07.080177.001323.
- [40] A.L. Shull, F. Spaepen, Measurements of stress during vapor deposition of copper and silver thin films and multilayers, *Journal of Applied Physics.* 80 (1996) 6243–6256. doi:10.1063/1.363701.
- [41] C.A. Davis, A simple model for the formation of compressive stress in thin films by ion bombardment, *Thin Solid Films.* 226 (1993) 30–34. doi:10.1016/0040-6090(93)90201-Y.
- [42] H. Windischmann, An intrinsic stress scaling law for polycrystalline thin films prepared by ion beam sputtering, *Journal of Applied Physics.* 62 (1987) 1800.

- [43] F.M. D'Heurle, J.M.E. Harper, Note on the origin of intrinsic stresses in films deposited via evaporation and sputtering, *Thin Solid Films*. 171 (1989) 81–92. doi:10.1016/0040-6090(89)90035-7.

CHAPTER 3

Intrinsic Stress Response of Low and High Mobility Solute

Additions to Cu Thin Films

Tyler Kaub¹, Ryan Anthony², and Gregory B. Thompson¹

¹University of Alabama
Department of Metallurgical & Materials Engineering
Tuscaloosa, AL 35401

²Northridge High School
Northport, AL 35406

Abstract

Thin film stress is frequently controlled through adjustments applied to the processing parameters used during film deposition. In this work, we explore how the use of solutes with different intrinsic growth properties influence the residual growth stress development for a common solvent Cu film. The findings demonstrated that the addition of a high atomic mobility solute, Ag, or a low atomic mobility solute, V, result in both alloy films undergoing grain refinement that scaled with increases in solute content. This grain refinement was associated to solute segregation and was more pronounced in the Cu(Ag) system. The grain size reduction was also associated with an increase in the tensile stresses observed in both alloy sets. These findings indicate that solutes can be used to control the grain size under the same deposition conditions as well as alter the stress evolution of a growing thin film.

Introduction

Metallic thin films deposited through physical vapor deposition (PVD) often develop large intrinsic stresses. These stresses contribute to the occurrence of thin film failure modes: such as buckling and delamination when compressive stresses are present¹ and cracking in the case of tensile stresses². In addition to influencing film failures, intrinsic stress levels have been associated with influencing film properties such as electromigration³, capacitance⁴ and optical performance⁵. Thus, the control of stress is of vital importance to producing high quality films and coatings. Typically, the intrinsic stress in a film is controlled through altering the processing parameters of working gas pressure⁶, deposition rate⁷, and the substrate temperature⁸. This in turn alters the resulting microstructure of the film and the corresponding intrinsic stress that is associated with such a microstructure. For example, as the grain size decreases in a film, it creates a higher density of interfaces, which correspondingly increases the tensile stress⁹. Developing a further understanding of the origins and mechanisms behind intrinsic stress formation, and its connections to microstructural evolution of film growth, will assist in systematic improvements in film and coating reliability. This work explores the influence of alloying using intrinsically low and high mobility species as a means to manipulate the microstructure and corresponding stress behavior. Such research would enable composition, similar to the types of processing parameters listed above, to be viable means for thin film stress and microstructural control.

The stress evolution observed during thin film growth is strongly related to the atomistic growth mode of the film and in the case of metallic thin films this is typically Volmer-Weber

growth¹⁰. This growth mode can result in two different characteristic stress evolutions, which are dependent on the atomic mobility of the arriving adatoms from the vapor flux. For systems with an intrinsically high mobility species, the films display a compressive-to-tensile-to-compressive stress evolution. In contrast, lower mobility species exhibit a compressive-to-tensile stress evolution as the film thickens and never develop the post-coalescence secondary compressive stress. The initial compressive stress observed in both types of films originates from surface stresses from the nucleating islands. Here Laplace pressures lead to smaller than equilibrium lattice spacing values in the island resulting in a compressive stress¹¹. As the film thickens, the islands come in near contact with each other and elastically strain in order to coalesce into a continuous film, which creates a tensile stress state¹²⁻¹⁴. Films with low atomic mobilities continue to exhibit this tensile stress, which is generated by grain boundary formations as the film thickens¹⁵. For high atomic mobility films, the physical origins of the secondary (post-coalescence) compressive stress is an area of active research and debate. Several potential mechanisms proposed to explain this stress evolution include inheriting the compressive stress from the pre-coalescence regime¹¹, capillary effects¹⁶, generation of stress from excess adatoms on the surface¹⁷, or insertion of excess adatoms on the film at ledges¹⁸ or grain boundaries¹⁹.

A number of recent studies described below have supported the validity of the grain boundary insertion mechanism proposed by Chason *et al.*¹⁹, which suggests the compressive stress is the result of the insertion of excess adatoms into the grain boundaries. This insertion is driven by differences in the chemical potential on the film surface and in the grain boundaries during deposition. Upon ceasing deposition, the surface chemical potential is lowered and the excess adatoms then migrate out of the grain boundaries resulting in a compressive stress relaxation, which has been experimentally observed²⁰. Friesen and Thompson²⁰ have shown compressive stress reversal data for Cu that seems to support the excess adatom ideas of the Chason model²¹. Saedi and Rost have proposed a thermodynamic driving force for this insertion process because of an induced entropic effect on the surface driving the excess adatoms into the grain boundaries²². Molecular dynamics modeling of film growth^{23,24} additionally supports this excess adatom insertion concept. Recent work by Magnfalt *et al.*^{25,26} found a correlation between film density and compressive stress magnitude by energetic bombardment of ions, which increased film density and suggested to them that adatom incorporation into the grain boundaries was also likely.

Since the stress state will be a function of the thickness of the film as discussed above, the product of the stress multiplied by the instantaneous film thickness, where that stress is being generated provides for a means to remove this thickness dependence. This is commonly referred to as the 'stress thickness product.' Thus, if the stress thickness product vs. thickness is linear, the stress state within the film is in steady-state. In this manner, one can now better infer how the stress behaves independent of its particular growth thickness. For example, changes in the slope of the stress thickness product now allow other effects, such as grain growth during film deposition, to be deconvoluted from the stress dependent thickness. In this paper, we will use this means of data representation to better understand the effect of the growth stress with respect to composition.

In an alloy, segregation tendencies of a solute species would contribute to partitioning behavior at the interfaces and free surfaces. Such effects would then influence the coalescence behavior of the film and the resulting stresses derived from those interactions that would not be present in a single species elemental film. There has some limited work in investigating solutes control on thin film. In the work by Fu and Thompson²⁷, it was found that the stress state could be tuned to 'zero' by the preferential segregation of Pt to the grain boundaries in FePt. In other work,

the addition of Cr in Fe(Cr) where seen to refine the grain size and change the corresponding tensile stress²⁸. Work by the authors here has shown that the stress state in Cu(Ni) was governed by the equilibrium concentration of the Ni solute in the grain boundaries²⁹.

To further investigate these potential alloying effects, a series of solvent Cu films, which is an intrinsically high mobility species, was sputter deposited and mixed with different concentrations of Ag, another high mobility species, and V, a low mobility species. Unlike the former studies, which were rather limited in scope and alloy concentrations, this work aims to provide a more comprehensive understanding by comparing mobility effects within the same solvent species. Cu films are an ideal case system in that it is a simple crystal structure and there has been extensive work on its growth behavior^{7,30,31} because of its technically important use as electrical interconnects in integrated circuit designs. Furthermore, the use of Ag and V both are immiscible solutes with Cu providing compatible thermodynamic behavior but different individual (intrinsic) growth stresses when deposited as an elemental species.

Experimental

Cu(Ag) and Cu(V) alloy films along with elemental Cu, Ag and V thin films for comparison to the alloys were deposited in an AJA ATC-1500 stainless-steel chamber through co-sputtering >99.95% pure elemental targets to a thickness of 300 nm for Cu(Ag) and 200 nm for Cu(V) onto a Si [100] substrate with a 100 nm surface oxide. The different film thickness between the alloys was to ensure a steady-state stress was achieved in each system. The base pressure prior to deposition was $< 1.33 \times 10^{-5}$ Pa, where ultrahigh purity Ar was flowed at 10 standard cubic centimeters per minute to 0.266 Pa for the sputtering working gas. All films were deposited at ambient temperature. The deposition rates for the Cu(Ag) alloys ranged from 0.42 to 0.071 nm/sec with the Ag rate being held constant at 0.021 nm/sec and the Cu rate varied to achieve the desired composition. The Cu(V) alloys range from 0.7 nm/sec to 0.034 nm/sec with the V sputtering rate held constant at 0.006 nm/sec and the Cu rate varied to achieve the desired composition. In addition, elemental films of V and Ag were deposited at 10W and 3W, respectively, to determine how the elemental films' power dependent growth rates compared to the alloy films. In the case of Cu, where power (rate) was varied to regulate the composition of each alloy, the lowest and highest power dependent growth rates, which spanned the power settings between 9W to 261W, were deposited as elemental films to ensure that deposition power did not have a dominate contribution to the stress evolution. The growth rates were determined using a quartz crystal microbalance and verified by small angle x-ray reflectivity³² using an X'Pert Philips x-ray diffractometer (XRD) operated with a Cu K_{α} source at 45 kV and 40 mA.

A K-Space Associates® multibeam optical sensor system (MOS) was used to measure the *in situ* stress evolution during deposition. The MOS measures the change in the radius of curvature of the substrate using a reflected laser beam passed through an etalon to form an array of spots collected on a charge coupled device camera³³. The displacement of the reflected laser spots is then used to calculate the average stress using the Stoney equation,

$$\sigma t_f = \frac{\delta d M_s t_s^2 \cos \alpha}{a 12L} \quad (1)$$

where M_s is the biaxial modulus of the substrate, t_s and t_f are the thickness of the substrate (250 μm) and thin film respectively, α is the angle of incidence of the laser beam (2°), L is the substrate detector optic length (88 cm) and $\frac{\delta d}{a}$ is the differential laser spot spacing on the detector³⁴.

Phase identification of the films was conducted through XRD along with grain size determination using x-ray line broadening and the Scherrer equation³⁵ with a shape factor of 0.9. Transmission electron microscopy (TEM) was performed using an FEI Tecnai G² Supertwin TEM to verify the grain size measurements obtained from XRD. Selected area electron diffraction was done to compliment the phase identification from XRD. Atomic level chemical analysis was performed using atom probe tomography. Samples were prepared using a focused ion beam lift out technique³⁶ using a FEI Quanta 200 and subsequently run on a Cameca LEAP 5000 XS in laser mode at 40 K and 100 pJ. The atom probe data sets were analyzed using IVAS 3.8. The surface roughness measurements were obtained using a Digital Instruments Dimension 3100 AFM in tapping mode.

Results

The growth stress curves along with the steady state stress values for the elemental films along with the mixed high mobility solute Cu(Ag) films, Figure 1(a), and the corresponding mixed low mobility solute Cu(V) films, Figure 1(b), revealed a range of stress responses dependent on solute species and concentrations. The intrinsic stress measurements of the Cu(Ag) system shows both elemental Cu and Ag species exhibited a compressive stress behavior. In comparison, the Cu(V) revealed Cu as being compressive but V as being tensile. In the alloy compositions, for either system, a varied response was observed that spanned both the compressive and tensile stress regimes. Since one could assume that changing the Cu rate (which was the variable used to control composition), could influence the stress response in the alloys, the extremes of the Cu deposition rates used in the two system studied are also plotted in Figure 1. For Cu(Ag), the Cu power settings were Cu (18W) (0.05 nm/sec) and Cu (150W) (0.401 nm/sec) and each exhibited a near equivalent compressive growth stress response, Figure 1(a). The same invariant effect for Cu (9W) (0.028 nm/sec) and Cu (261W) (0.69 nm/sec) was seen in the Cu(V) system, Figure 1(b). Thus, the change in the solvent Cu species deposition rate was not suspected to significantly influence the growth stresses in these alloys.

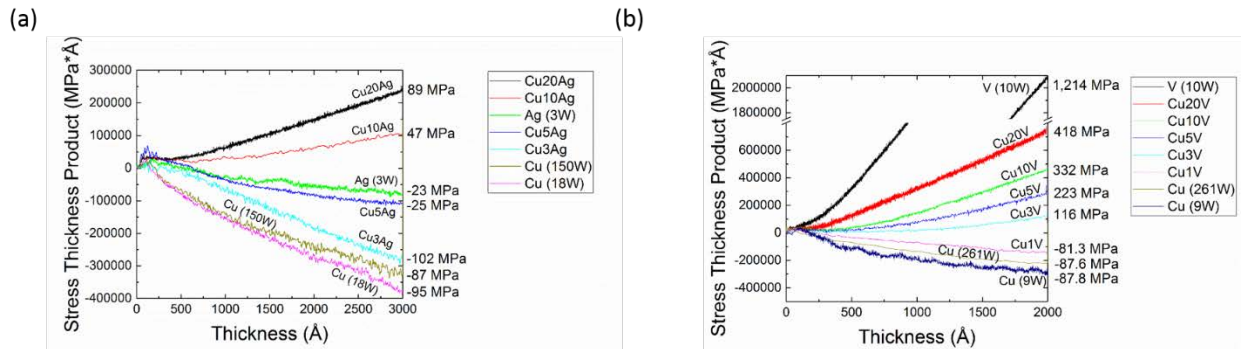


Figure 1. *in-situ* growth stress curves and steady state stress values presented right of the respective curve for (a) Cu(Ag) system and (b) Cu(V) system. (Note the y-axis break in the graph at 800 GPa*Å; since the V film exhibited a much higher stress thickness product than the alloy films, this was done to provide the ability to view both the alloys and this particular element film on the same plot)

When comparing the Cu(Ag) and Cu(V) alloys, some interesting observations can be drawn. For Cu(Ag), only the Cu3Ag (at%) and Cu5Ag (at%) exhibited a post-coalescence secondary compressive stress state. The Cu10Ag and Cu20Ag both maintained the tensile behavior in the post-coalescence regime, which is not a behavior seen in either of the elemental species that compose the alloy. Furthermore, these two higher solute concentrations are no longer bound between the Cu and Ag growth stress curves in Figure 1(a). As the Ag content increased in Cu(Ag), the Cu films became less compressive. For the Cu(V) system, the Cu1V exhibited a secondary compressive stress state whereas all other compositions retained a tensile stress upon coalescence. Unlike the Cu(Ag) alloys, the Cu(V) alloys were bounded between the two elemental stress states that composed the alloy.

The post-deposition stress behavior for the alloys and elemental films are plotted in Figure 2. Unlike the near equivalent growth stresses of Cu for both rates, the post-deposition stress relaxation revealed a much more pronounced and larger extent of compressive stress relaxation with increasing deposition rate or power. This was observed in both systems. This is attributed to the higher deposition rate resulting in a greater difference in the surface chemical potential from the increased deposition flux, which ceases upon stopping deposition thereby creating a larger compressive stress reversal. Upon reviewing the elemental behavior of the alloying elements, Ag was observed to undergo a much smaller stress relaxation than Cu, which would be consistent with its much lower deposition rate. The elemental V, being an intrinsically low mobility species with a tensile stress response in the post-coalescence regime, did not show any changes in its post-deposition stress behavior, which would be expected as it is not under compressive stress. Upon alloying Cu with V a rule of mixtures response would be expected for the post deposition stress behavior, which is observed with V appearing to have a stronger influence. For the Cu(Ag) alloy films, as the Ag content increased, the post-deposition stress reveals smaller tensile stress increases upon ceasing deposition.

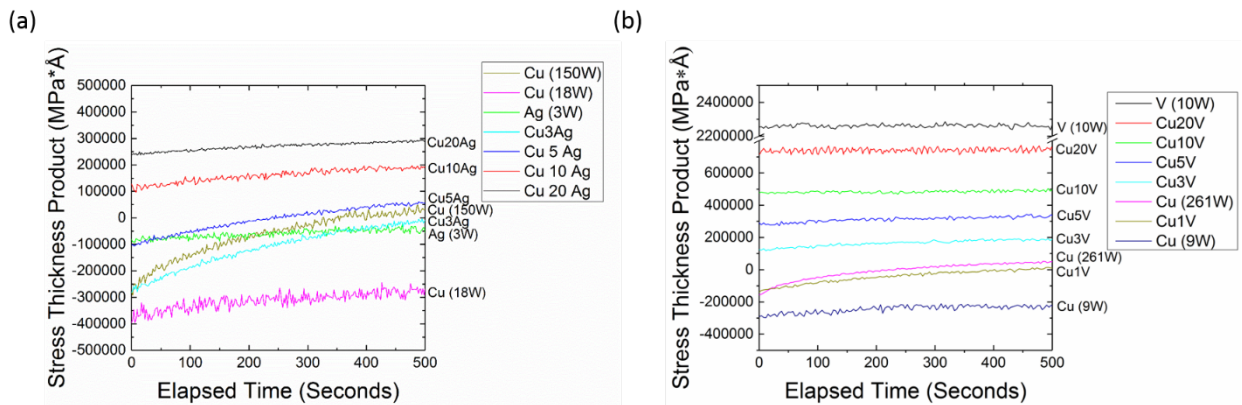


Figure 1. Post Deposition stress behavior of (a) Cu(Ag) system and (b) Cu(V) system

If we compare the elemental Cu (150W) grown film to the Cu-3Ag alloy film, which had the same Cu deposition rate, we observed a reduced stress relaxation response with the alloy. At 500 sec. the difference in the stress thickness product is $\sim 50 \text{ GPa}\cdot\text{\AA}$. This would suggest that the adatom mobility in the alloy has been altered by the presence of the solute. Upon examining the

low mobility Cu(V) alloys, the same effect is also observed. The elemental Cu (261W) grown film and the Cu1V alloy film, which again had the same Cu deposition rate, resulted in a reduced stress relaxation for the alloy. At 500 sec., this difference is $\sim 140 \text{ GPa}\cdot\text{\AA}$. Considering that each of these alloys contained either 3 at.% Ag or 1 at.% V, one can conclude that compositional variations can have a dramatic effect. Upon increasing the V content, which drove the Cu(V) system to a tensile stress state, the post-deposition stress behavior displayed little to no change when the V content exceeded 10 at. %. This is a different response than the tensile Cu10Ag and Cu20Ag films, which exhibited minor changes to becoming more tensile upon ceasing deposition.

The phase identification of these films was determined by indexing the XRD scans in Figure 3. The Cu(Ag) films revealed both solid solutions as well as phase separation dependent on composition. In Figure 3(a), as the Ag content increased, a notable hump to the left of the $\{111\}$ Cu peak is observed in the Cu20Ag film. The selected area diffraction pattern, Figure 3(b), of this film confirmed both Cu and Ag rings with the bright field image revealing separate Ag grains. Interestingly, once the Ag clearly phase separated, as it did in the Cu20Ag film, other textures previously seen in the lower Ag content alloys are now absent. Both a $\{200\}$ and $\{220\}$ are observed in the Cu3Ag, Cu5Ag, and Cu10Ag films. However, the relative heights of these peaks diminishes at Cu10Ag. Besides the $\{111\}$ lower surface texture, the Cu film also diffracted a modest $\{200\}$ peak, which is the elastically softer direction in FCC materials. The observation that this $\{200\}$ peak is relatively pronounced with Ag incorporation, as compared to the elemental Cu film, as well as the observation of a $\{220\}$ reflection indicates that the matrix has been strained by producing a supersaturated Cu(Ag) FCC solution. Once the Ag precipitated from the solution, i.e. Cu20Ag, these $\{200\}$ and $\{220\}$ texture reflections are no longer observed indicating the strain has relaxed in the matrix phase.

The Cu(V) films revealed a FCC solid solution through all alloy compositions, determined both by XRD, Figure 3(c) and TEM (not shown). The XRD revealed a strong $\{111\}$ fiber growth texture whereas V, a bcc element, exhibited a $\{110\}$ fiber texture only when it was deposited as a single species. Both of these surfaces are consistent with being the lowest surface energy for each phase. Unlike Cu(Ag), the Cu(V) alloys did not phase separate nor generate any substantial secondary reflections associated with strain energy consideration. This has been contributed to both species having a similar atomic size³⁷.

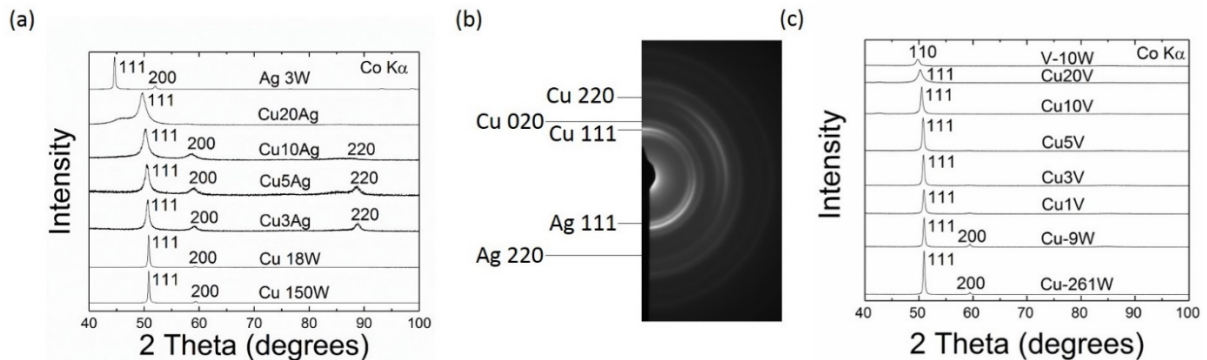


Figure 2. (a) X-ray diffraction of Cu(Ag) system and (b) selected area diffraction of Cu20Ag showing extra diffraction ring corresponding to Ag (c) X-ray diffraction of Cu(V) system

The bright field plan-view micrographs of the films are shown in Figure 4(a). The micrographs revealed an equiaxed grain structure for the films with a grain size that decreased with solute content. This has been quantified in the grain size plot in Figure 4(b). The grain sizes between the Cu films grown at different power (rate) settings is also plotted in Figure 4(b), though the micrographs are not shown. As can be seen, these sizes were fairly consistent with each other suggesting, once again, the solute is having a dramatic impact on regulating the grain size. At the highest solute concentrations, the two alloys exhibited nearly equivalent grain sizes. The grain sizes for the elemental solute films are also plotted in Figure 4(b), with the images not shown. In this case, Ag exhibited a much larger grain size than V, which could be expected because of the mobility differences and that smaller grain sizes are associated with tensile film stresses^{9,14}. Representative cross-sectional images for the Cu(V) system are shown in Figure 5(a) and the Cu(Ag) system in 5(b). The cross sectional images reveal that the grain size appears to be approximately the same throughout the thickness of the film, indicating that the grain size differences observed in the plan-view samples are representative of the film's overall microstructure and not a specific depth.

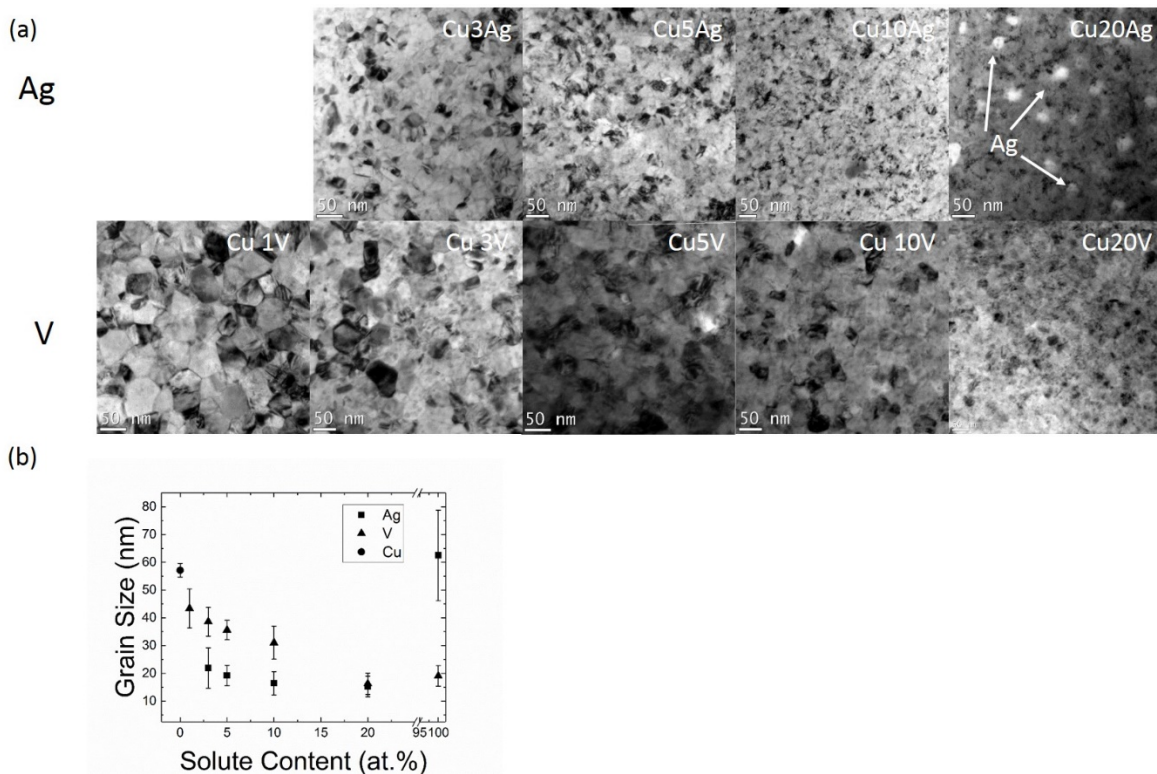


Figure 3. (a) Bright field TEM micrographs of Cu(Ag) and Cu(V) alloy films (b) plot of grain size compared to solute content.

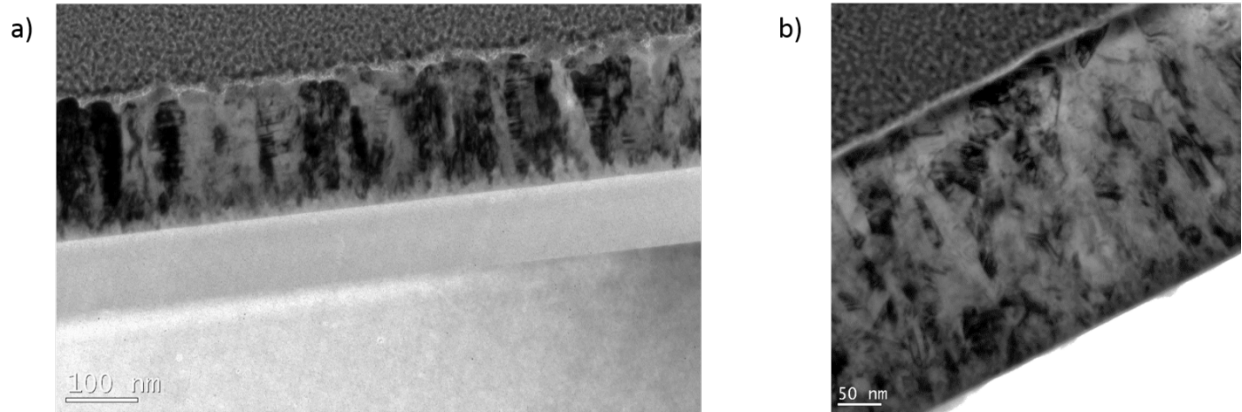


Figure 5. Representative bright field cross sectional images for (a) the Cu(V) system showing Cu₁₀V and (b) the Cu(Ag) system showing Cu₃Ag

Discussion

Grain size is often associated with the film stress state^{14,25,38}. For example, Chason *et al.* produced a series of controlled island sizes and observed that the films became more tensile with ever smaller island sizes³⁹. This response occurs due to tensile stress generation occurring by the creation of new grain boundary length, thus if a film has a greater fraction of grain boundaries more sites are present for the generation of tensile stresses. In Figure 6 the inverse grain size and the corresponding steady-state stress for each film is plotted. As the grain size decreased, the stress became more tensile, which is a consistent finding with these other studies. As grain size can be controlled by deposition rate, we first discuss if this could have had an impact on the stress responses observed. Since Cu was the solvent species, we grew a series of elemental Cu films at the different rates that were used to achieve the alloying conditions. No significant changes in grain size or stress was observed between the highest and lowest deposition powers of Cu used in this study. These elemental Cu films, at their various power settings, have been plotted along with the alloy versions in Figure 1. Thus, any modest changes in rate with alloying is not likely the contributor to the grain refinement and stress response.

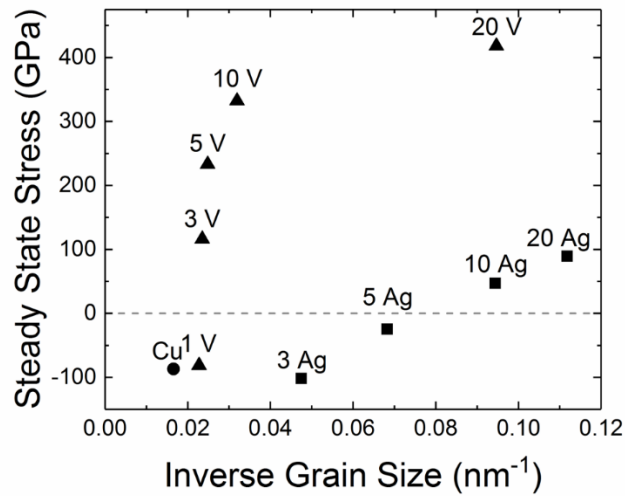


Figure 6. Steady state stress values compared to the inverse grain size illustrating different slopes for the Cu(Ag) and Cu(V) systems

In contrast, a clear change in grain size with solute content is observed for both alloy systems, Figure 4(b). The grain refinement is most likely contributed to the solute segregation between the two species in each alloy. As noted in the introduction, both systems are thermodynamically immiscible⁴⁰. In prior work by Zhou *et al.*, phase separation in immiscible Fe(Cr) was seen even in room deposited films²⁸. In those cases, as the Cr content increased, the grains refined with the refinement contributed to a solute drag effect⁴¹. As evident in this work, if the solute content is sufficiently large, this segregation can even promote clear phase precipitation as observed in Cu20Ag. This Ag precipitation observed is linked to this system having a high enthalpy of segregation of 63 KJ/mol⁴² compared to Cu(V)'s enthalpy of mixing of 5KJ/mol⁴³. In addition Cu(Ag) exhibits well as more strain in the solid solution matrix upon deposition evident by multiple {hkl} reflections^{40,44}. As a consequence of this partitioning, more solute would be expected to be located in the boundaries and can have a greater impact on grain refinement, which is manifested by Cu(Ag) exhibiting grain refinement more readily at lower solute concentrations than the equivalent Cu(V) films, Figure 4(b).

To experimentally confirm the occurrence of the predicted segregation in each alloy system atom probe tomography was performed with results depicted in Figure 7. For the Cu3Ag film the higher density grain boundary regions are clearly present in the dataset Figure 7(a). Upon performing a 1D concentration profile perpendicular to the boundary a small increase in Ag content is measured in the boundary region Figure 7(b). This indicates that solute segregation to the grain boundaries appears to be occurring in the lowest concentration Cu(Ag) alloys. Coupling this finding with the phase separation observed in the Cu20Ag film leads us to infer that upon increasing the Ag content the amount of segregation in the films would be increasing. Upon looking into the Cu(V) system at the lowest solute concentration Cu1V atom probe tomography revealed the presence of small V-rich clusters forming Figure 7(c). While the bulk composition and the matrix of the film was approximately 1 at.% V the small clusters possessed a concentration of 60 at.% V. Observing this clustering at the lowest solute concentration along with Cu(V) having a positive enthalpy of mixing of 5 KJ/mol⁴³ suggests that at higher solute contents more segregation would be observed.

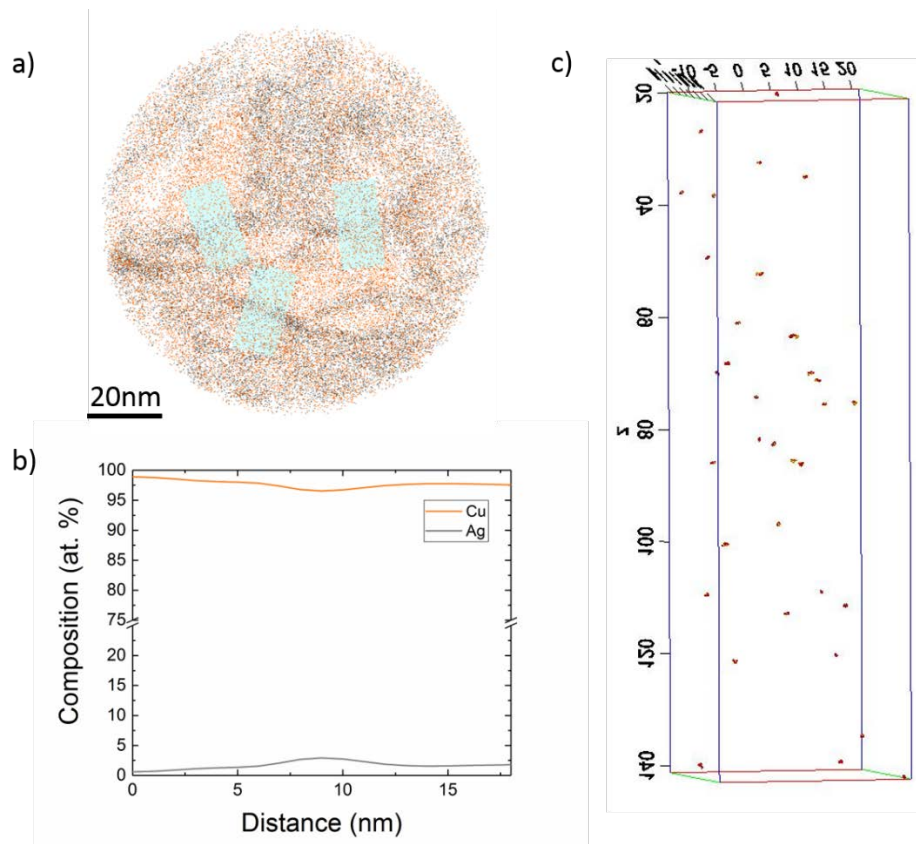


Figure 7. (a) Atom map of Cu₃Ag showing Ag enrichment at the grain boundary (b) 1-D concentration Profile showing Ag enrichment in the grain boundary (c) vanadium clustering in Cu₁V

Furthermore, it is interesting to note that two intrinsically compressive films – Cu and Ag - can yield an alloy that is in a tensile state. This change from compressive-to-tensile under the same deposition conditions is suspected to be associated again with the phase separating tendencies. As the Ag content increased, coupled with its high enthalpy of segregation, Cu-rich and Ag-rich regions formed within the film as evident from the APT and TEM. Such partitioning was confirmed in the Cu₂₀Ag film where it was sufficient that Ag grains (precipitates) themselves were observed in the microstructure and in the diffraction pattern. Since sputtering has produced a highly supersaturated Cu(Ag) solution, the film now competes between coalescence of grains and phase separation at interfaces between its species. As a consequence of this competition, along with the grain size refinement, a tensile stress developed as solute concentration increased.

Each of the solutes used in this study has a very different intrinsic mobility. This is exemplified by their individual stress responses in Figure 1, where Ag readily adopted a compressive steady-state stress and V grew tensile. As a consequence of this difference in mobility, the solute influenced how the solvent Cu grew. Using atomic force microscopy, the surface roughness was measured for the high and low solute content alloys. Table 1 tabulates the RMS surface roughness of these films. The higher mobility Cu(Ag) alloys exhibited lower surface

roughness's than the Cu(V) alloys. Previous studies have revealed that when the surface self-diffusivity for adatoms is sufficiently low, the surface roughness of the film increased⁴⁵. Our results here would support the surface diffusivity of Cu has been lowered by the presence of the solute V even in concentrations as low as 1 at.%. This observation would suggest the following: (1) As the solute content in both films increased, the surface mobility decreased. And (2) that for equivalent solute additions, the surface mobility was lower in the V films as compared to the Ag films because V is a lower mobile species addition to the alloy. In both cases excess adatom incorporation would be reduced and larger tensile stresses would be expected, which is what was observed in this study.

Table 3. Surface Roughness obtained from AFM for Cu(Ag) and Cu(V) alloys

Sample	RMS (nm)
Cu1V	2.1
Cu3V	2.7
Cu20V	8.8
Cu3Ag	0.4
Cu20Ag	2.5

It is also interesting to note that the Cu(Ag) alloys exhibited a near linear relationship between its inverse grain size and stress. The Cu(V) films also exhibit a similar linear relationship, except for its highest solute content film which deviated from this trend, Figure 5. This deviation could be associated to either solute saturation at the grain boundaries⁴⁶ or nonlinear associations in interfacial stresses⁴⁷. If we compare either the linear portions of their relationship or the equivalent grain sizes between the alloys, we noted that the stresses do not match. For example, the Cu(V) alloys, even with larger grain sizes, exhibited higher tensile stresses, which would normally be related to films with smaller grain sizes. If we compare the two alloys where the grain sizes are approximately the same, i.e. Cu20Ag vs. Cu20V, the Cu20V film retained a much higher tensile stress. These differences suggest that the origins of the stress response are related to intrinsic interactions of the solutes with the solvent matrix.

Examining the Lennard-Jones interatomic potentials for Cu, Ag, and V⁴⁸ reveals key differences that may be contributing to the intrinsic differences observed from the different solutes. The potentials show V to possess the deepest potential well followed by Cu than Ag. The equilibrium atomic spacing shows V to possess only a 3% difference from Cu as compared to the 11% difference for Ag⁴⁸. Thus at the grain boundaries a greater tensile stress would be expected to be exerted by V atoms on the surrounding grain boundary atoms because of its deeper potential well than Ag. While the magnitude of this effect would be difficult to quantify, it would be expected to increase with increasing levels of segregation and increasing grain boundary fraction. Thus, one would expect the tensile stress to increase as the solute segregates to the grain boundary, which was observed in the experiments. In addition, the plateauing of stress at the highest V content would then be explained by grain boundary saturation. Any additional solutes above this concentration would migrate into the matrix and in the case of V would have minimal effects on the stress due to the similar equilibrium interatomic spacing⁴⁸. Thus, solutes appear to offer a complex interaction within the film microstructure with its corresponding stress response.

Summary

This paper has explored the differences in film stress and microstructure that evolve from the addition of either a high or low mobility material solutes into Cu. Each of these solutes were immiscible in the matrix material and resulted in a grain refinement with increasing solute content. This reduction in grain size is attributed to a solute drag effect, which has been observed in other alloy systems. The increase in tensile stress observed in both systems is attributed to the reduction in the grain size and the intrinsic properties of the solutes. Particularly interesting findings from this work This transition is understood as a competition between the coalescence of the film and an intrinsic desire to phase separate during growth. Similarly, a tensile stress was created in a high mobility - low mobility mixed system i.e. Cu(V). It was found that very low solute content was required to produce a tensile steady state stress. This rapid change in stress response of the solvent matrix was suspected to be associated again with the intrinsic mixed mobility of the two species. Using AFM the Cu(V) film was found to be significantly rougher for the equivalent Cu(Ag) films. The collective results of this work found that mixed mobilities offers ample control of microstructures and thin film stress states.

Acknowledgments

The authors gratefully acknowledge the Army Research Office, Grant No. W911NF1310436, Dr. Michael Bakas, program manager. The authors would also like to thank David Jacobson for insightful discussion on thin film stress evolution. The UA Central Analytical Facility is recognized for the additional assistance and access to the microscopes used in this research.

References

- ¹ M.-W. Moon, J.-W. Chung, K.-R. Lee, K.H. Oh, R. Wang, and A.G. Evans, *Acta Materialia* **50**, 1219 (2002).
- ² J.S. Wang and A.G. Evans, *Acta Materialia* **47**, 699 (1999).
- ³ K.N. Tu, *Phys. Rev. B* **45**, 1409 (1992).
- ⁴ T.M. Shaw, Z. Suo, M. Huang, E. Liniger, R.B. Laibowitz, and J.D. Baniecki, *Appl. Phys. Lett.* **75**, 2129 (1999).
- ⁵ R. Kumar, N. Khare, V. Kumar, and G.L. Bhalla, *Applied Surface Science* **254**, 6509 (2008).
- ⁶ M. Pletea, W. Brückner, H. Wendrock, and R. Kaltoven, *Journal of Applied Physics* **97**, 054908 (2005).
- ⁷ A.L.D. Vecchio and F. Spaepen, *Journal of Applied Physics* **101**, 063518 (2007).
- ⁸ G. Turner and R. Abermann, *Thin Solid Films* **192**, 277 (1990).
- ⁹ E. Chason, A.M. Engwall, C.M. Miller, C.-H. Chen, A. Bhandari, S.K. Soni, S.J. Hearne, L.B. Freund, and B.W. Sheldon, *Scripta Materialia* **97**, 33 (2015).
- ¹⁰ E. Bauer, *Zeitschrift Für Kristallographie* **110**, 372 (1958).
- ¹¹ R.C. Cammarata, T.M. Trimble, and D.J. Srolovitz, *Journal of Materials Research* **15**, 2468 (2000).
- ¹² W.D. Nix and B.M. Clemens, *Journal of Materials Research* **14**, 3467 (1999).

- ¹³ L.B. Freund and E. Chason, *Journal of Applied Physics* **89**, 4866 (2001).
- ¹⁴ R.W. Hoffman, *Thin Solid Films* **34**, 185 (1976).
- ¹⁵ G.C. a. M. Janssen and J.-D. Kamminga, *Appl. Phys. Lett.* **85**, 3086 (2004).
- ¹⁶ R. Koch, D. Hu, and A.K. Das, *Phys. Rev. Lett.* **94**, 146101 (2005).
- ¹⁷ C. Friesen, S.C. Seel, and C.V. Thompson, *Journal of Applied Physics* **95**, 1011 (2004).
- ¹⁸ F. Spaepen, *Acta Materialia* **48**, 31 (2000).
- ¹⁹ E. Chason, B.W. Sheldon, L.B. Freund, J.A. Floro, and S.J. Hearne, *Phys. Rev. Lett.* **88**, 156103 (2002).
- ²⁰ C. Friesen and C.V. Thompson, *Phys. Rev. Lett.* **89**, 126103 (2002).
- ²¹ E. Chason, *Thin Solid Films* **526**, 1 (2012).
- ²² A. Saedi and M.J. Rost, *Nature Communications* **7**, 10733 (2016).
- ²³ C.-W. Pao, S.M. Foiles, E.B. Webb, D.J. Srolovitz, and J.A. Floro, *Phys. Rev. Lett.* **99**, 036102 (2007).
- ²⁴ C.-W. Pao, S.M. Foiles, E.B. Webb, D.J. Srolovitz, and J.A. Floro, *Phys. Rev. B* **79**, 224113 (2009).
- ²⁵ D. Magnfält, A. Fillon, R.D. Boyd, U. Helmerson, K. Sarakinos, and G. Abadias, *Journal of Applied Physics* **119**, 055305 (2016).
- ²⁶ D. Magnfalt, G. Abadias, and K. Sarakinos, (n.d.).
- ²⁷ B. Fu and G.B. Thompson, *Journal of Applied Physics* **108**, 043506 (2010).
- ²⁸ X. Zhou, T. Kaub, R.L. Martens, and G.B. Thompson, *Thin Solid Films* **612**, 29 (2016).
- ²⁹ T.M. Kaub, P. Felfer, J.M. Cairney, and G.B. Thompson, *Scripta Materialia* **113**, 131 (2016).
- ³⁰ A.L. Shull and F. Spaepen, *Journal of Applied Physics* **80**, 6243 (1996).
- ³¹ R. Abermann and R. Koch, *Thin Solid Films* **142**, 65 (1986).
- ³² Y. Sasanuma, M. Uchida, K. Okada, K. Yamamoto, Y. Kitano, and A. Ishitani, *Thin Solid Films* **203**, 113 (1991).
- ³³ Taylor, C., Bartlett, D., Chason, E., and Floro, J., *The Industrial Physicists* **4**, 25 (1998).
- ³⁴ G.G. Stoney, *Proceedings of the Royal Society A: Mathematical, Physical and Engineering Sciences* **82**, 172 (1909).
- ³⁵ P. Scherrer, *Nachrichten von der Gesellschaft der Wissenschaften zu Göttingen, Mathematisch-Physikalische Klasse* **1918**, 98 (1918).
- ³⁶ K. Thompson, D. Lawrence, D.J. Larson, J.D. Olson, T.F. Kelly, and B. Gorman, *Ultramicroscopy* **107**, 131 (2007).
- ³⁷ J.C. Slater, *The Journal of Chemical Physics* **41**, 3199 (1964).
- ³⁸ J. Leib, R. Mönig, and C.V. Thompson, *Phys. Rev. Lett.* **102**, 256101 (2009).
- ³⁹ A. Bhandari, B.W. Sheldon, and S.J. Hearne, *Journal of Applied Physics* **101**, 033528 (2007).
- ⁴⁰ H.A. Murdoch and C.A. Schuh, *Journal of Materials Research* **28**, 2154 (2013).
- ⁴¹ R.W. Cahn and R.G. Davies, *Acta Metallurgical* **10**, 170 (1962).
- ⁴² M. Menyhard, M. Yan, and V. Vitek, *Acta Metallurgica et Materialia* **42**, 2783 (1994).
- ⁴³ M.A. Atwater and K.A. Darling, (2012).
- ⁴⁴ J.A. Floro, C.V. Thompson, R. Carel, and P.D. Bristowe, *Journal of Materials Research* **9**, 2411 (1994).

- ⁴⁵ C.V. Thompson, Annual Review of Materials Science **30**, 159 (2000).
⁴⁶ F. Liu and R. Kirchheim, Scripta Materialia **51**, 521 (2004).
⁴⁷ C.H. Turner, J. Phys. Chem. B **109**, 23588 (2005).
⁴⁸ S. Zhen and G.J. Davies, Phys. Stat. Sol. (a) **78**, 595 (1983).

CHAPTER 4

Influence of Solute Segregation on Thin Film Growth Stresses: The Cu(Ni) System

T.M. Kaub¹, P. Felfer², J.M. Cairney² and G.B. Thompson¹

¹*Department of Metallurgical and Materials Engineering, The University of Alabama, Tuscaloosa, Alabama 35487-0202, USA*

²*Australian Centre for Microscopy and Microanalysis, The University of Sydney, Madsen Building F09, NSW 2006, Camperdown, Australia*

Abstract

Using intrinsic solute segregation in alloys, the compressive stress in a series of Cu(Ni) thin films has been studied. The highest compressive stress was noted in the 5 at.% Ni alloy, with increasing Ni concentration resulting in a subsequent reduction of stress. Atom probe tomography quantified Ni's Gibbsian interfacial excess in the grain boundaries and confirmed that once grain boundary saturation is achieved, the compressive stress was reduced. This letter provides experimental support in elucidating how interfacial segregation of excess adatoms contribute to the post-coalescence compressive stress generation mechanism in thin films.

Manuscript

When a thin film is deposited and not subjected to epitaxial growth conditions, a polycrystalline, columnar structure forms¹. Such films develop intrinsic growth stresses that can exceed their bulk elastic values. These intrinsic stresses lead to decreased performance, deformation, and failure in thin film based devices through delamination from the substrate, film cracking, surface roughening, or mass transport². Understanding the stress evolution behavior during thin film growth and being able to control the stress state of a thin film has been an area of active investigation for several years¹⁻⁵.

In the early stages of thin film growth, a compressive stress state develops as adatoms diffuse together to form embryonic islands. The compressive stress is a result of these adatoms maximizing their collective volume by forming an island, which can minimize the number of adatoms on the surface⁶. As these islands grow and come in close proximity to each other, the film develops a tensile stress as each island elastically strains towards the other, with the island surfaces eventually meeting to reduce their interfacial energy⁷. This leads to the eventual coalescence of the film. For low adatom mobility atoms, the film tends to retain a tensile condition. However, for higher mobility adatoms, the stress reverts back to a compressive stress state, which is less understood. There are several competing theories on the origins of this post-coalescence stress evolution^{4,6,8-11}. Chason *et al.*⁴ suggested that the post coalescence compression is created by adatoms reversibly moving into (and out) of grain boundaries. During deposition, the rise in the surface chemical potential provides the driving force for the flow of these adatoms into the coalescence film's grain boundaries, which then creates the compression of these grains. Hence, the stress evolution is closely related to the film's microstructure.

To change the film's microstructure, the majority of research has focused on altering deposition processing through substrate temperature^{8,12}, deposition rate^{4,13} and sputter pressure^{14,15}. These have all been found to alter the fraction of grain boundary-to-grain size, which has been shown to correlate with the stress^{1,16}. Hence, the control of the interfaces during growth can be a means of regulating the stress evolution of the thin film.

To date, the majority of these stress evolution studies have been on elemental films^{3,5,12-15}. In single element films, quantifying this mechanism of compressive stress can be an experimental challenge because there is no chemical distinction to differentiate atoms at the boundaries and atoms within the bulk of the film. Alloy films may provide a means to both tune the stress in a film through control of their intrinsic microstructure as well as provide chemical dissimilarity at the interface that reveals possible mechanisms of post-coalescence compressive stress in post mortem characterization.

Fu et al.¹⁷ reported how compressive stress recovery varied as a function of the chemical order parameter in FePt thin films. The recovery was related to the grain boundary energy, which varied based on the degree of chemical order or disorder within the film. Fu and Thompson¹⁸ further showed that intrinsic solute segregation in a disordered FePt film could even manipulate the retained stress in achieving a 'zero-stress' state when the composition at the grain boundary and the grain matrix were equivalent. Other related work has shown how solutes in grain boundaries can even reduce the grain boundary energy to zero, which stabilizes nanocrystalline grains against elevated temperature growth¹⁹⁻²¹. Collectively, the use of alloys, and in particular their intrinsic solute segregation to grain boundaries, appears to be a promising means of microstructure control.

In this letter, we report how Cu(Ni) alloy films evolve their stress as a function of its intrinsic solute segregation. This alloy readily forms a solid solution face centered cubic (FCC) phase that weakly segregates at interfaces. Hence this system provides a case study of how a subtle compositional changes at the interface can be used to manipulate the thin film's growth stresses. Moreover the chemical distinction at the interface provides an opportunity to experimentally characterize prior concepts of post-coalescence compressive stress mechanisms which have been difficult, if not impossible, to quantify in single species films as discussed above.

The Cu(Ni) alloy thin films were co-sputter deposited in an AJA ATC-1500 stainless-steel chamber from >99.95% pure elemental targets to a thickness of 200 nm onto a Si [100] substrate which had a native surface oxide. All depositions were done at ambient temperature. The base pressure prior to deposition was < 1×10^{-7} Torr, where ultrahigh purity Ar was flowed at 10 standard cubic centimeters per minute to 2 mTorr for the sputtering working gas. The deposition rates for the elemental films were 0.336 nm/sec for Cu and 0.154 nm/sec for Ni and the alloy films (depending on composition) varied from 0.422 nm/sec to 0.376 nm/sec. The growth rates were determined by the final film thickness divided by the growth time and verified by small angle x-ray reflectivity²² using an X'Pert Philips x-ray diffractometer (XRD) operated with a Cu K_{α} source at 45 kV and 40 mA. The phase of each film was characterized by XRD with the average grain size determined by x-ray line broadening using the Scherrer equation²³ with a shape factor of 0.9.

A K-Space Associates multibeam optical sensor system (MOS) was used to measure the *in situ* stress state during deposition. The MOS measures the change in the radius of curvature of the substrate using a reflected laser beam passed through an echelon to form an array of spots collected on a charge coupled device camera²⁴. The displacement of the reflected laser spots is then used to calculate the average stress using the Stoney equation,

$$\sigma = -\frac{1}{12} \frac{E_s}{1-\nu_s} \frac{\cos(\alpha)t_s^2}{Lt_f} \left(\frac{1}{R_1} - \frac{1}{R_0} \right) \quad (1)$$

where $\frac{E_s}{1-\nu_s}$ is the biaxial modulus of the substrate, t_s and t_f are the thickness of the substrate (250 μm) and thin film respectively, α is the angle of incidence of the laser beam (2°), L is the substrate detector optic length (88 cm) and R_0 and R_1 are the radii of curvature of the substrate before and during film deposition²⁵.

The post-deposited films' atom probe tomography (APT) samples were prepared by an *in situ* lift-out from the wedge of the thin film wafer in a similar manner reported by Thompson *et al.*²⁶ using either a FEI Quanta 3D dual-beam focus ion beam (FIB)-scanning electron microscope (SEM) or a Tescan Lyra FIB-FESEM. The annular mill to shape the film into the required atom probe tip geometry used an ion beam current between 0.1-1.0 nA at 30 keV. The Ga implantation was reduced in the final shaping of the tip using a final 5 keV "clean up" step. The atom probe tips were analyzed in a Cameca Scientific Instruments Local Electrode Atom Probe (LEAP) 3000XSi in a voltage mode with a target evaporation of 0.5% at a tip set temperature of 60 K with reconstruction of the data sets using the IVAS 3.6.8 platform.

Figure 1(a) is the growth stress evolution for the deposited films, which includes Cu, Ni, 95Cu5Ni, 90Cu10Ni, 85Cu15Ni, and 80Cu20Ni (at.%). The post growth recovery, Figure 1(b), is approximately the same for each film and all retain a compressive stress condition after deposition suggesting that the atomic mobility to be approximately the same across the studied compositional range. Each of the films experienced a compressive-to-tensile-to-compressive stress transition which is consistent with prior reports for the elemental species^{3,5,10,13,14}. The elemental films showed near equivalent stress evolution, which made the observation of a significant increase in compressive stress with Ni additions to Cu peculiar. The grain sizes are tabulated in Table I, and are approximately equivalent except for Cu, which is larger than all the other films. Considering that Cu and Ni have near equivalent stress behavior, Figure 1, this grain size difference is not thought to be a significant contributor to the stress changes noted in the alloys.

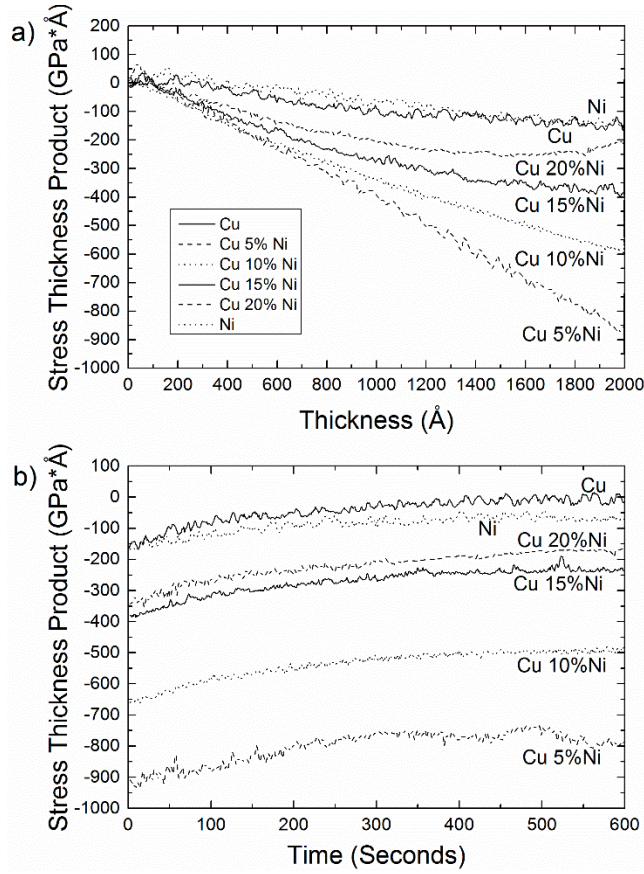


FIG 4. (a) Intrinsic growth stresses of Cu(Ni) thin film systems (b) The evolution of the residual stress after ceasing deposition.

TABLE I: Tabulated grain sizes for the films estimated by the Scherrer equation using the XRD results shown in Figure 2.

Composition (at.%)	Cu	95Cu5Ni	90Cu10Ni	85Cu15Ni	80Cu20Ni	Ni
Average Grain Size (nm)	40.6 ± 0.7	19.6 ± 7.0	19.3 ± 6.9	16.8 ± 4.9	12.2 ± 3.2	18.2 ± 3.5

Of all the Cu(Ni) films, the least alloyed (5 at.% Ni) showed the highest amount of compressive stress. With further solute addition, the alloyed films began to trend toward the elemental species film behavior. Hence, the addition of more solute does not result in an increasing amount of compression in the film. The XRD scan, Figure 2, revealed that all the films were FCC or the A1 solid solution FCC phase with a dominant {111} growth texture. A subtle {002} texture is also observed and is contributed to it being the elastically soft direction for FCC metals, which competes with the lowest surface energy {111} planes. Hence, each film does not reveal any

obvious structural differences that could explain the observed stress differences. To elucidate the effect of the solute on the stress, APT of the grain boundaries and matrix was done.

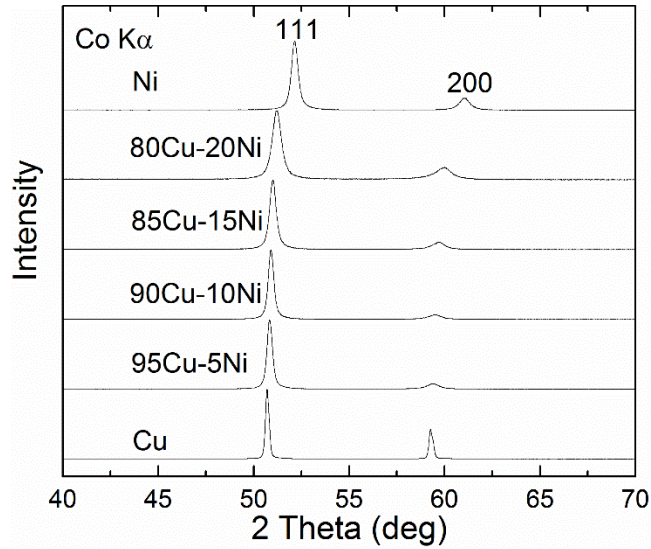


FIG 2. X-ray Diffraction results revealing the FCC phase for Ni and Cu and the solid solution A1 FCC phase for the alloy Cu(Ni) films.

Figure 3 (a-c) is the APT reconstructions from the Cu5Ni film. Each map shows a slight atom density variation within the reconstruction which indicates the grain boundaries. The diameter between the networks of boundaries was consistent with the XRD estimated grain sizes, Table I. Using the method developed by Felfer *et al*²⁷, the Gibbsian interfacial excess for the 95Cu5Ni and 85Cu15Ni films were found to be 0.88 ± 0.43 atoms/nm² and 0.97 ± 0.45 atoms/nm² respectively. A representative ladder diagram is shown in Figure 3(d) from one of the grain boundaries whose position is indicated by the arrow in the reconstructed atom map in the same figure. From the interfacial excess values, a few points can be gleaned. First, excess Ni was found in the grain boundaries. This is consistent with former experimental observations and modeling [28]. Second, the absolute value of Ni's interfacial excess is very low consistent with this being a weakly segregating system which has a reported enthalpy of segregation of ≈ -17 kJ/mol²⁸. Third, the error values for the interfacial excess are large. This is contributed to both the low level of solute segregation present, where small variations will result in larger disparities between boundaries, and that specific segregation could be a function of grain boundary character resulting in a variation in solute concentration between the boundaries. Though we can detect grain boundaries in the APT reconstruction, the reconstruction technique was not sensitive enough to capture the crystallographic rotation between grains where misorientation (grain character) could be readily identified.

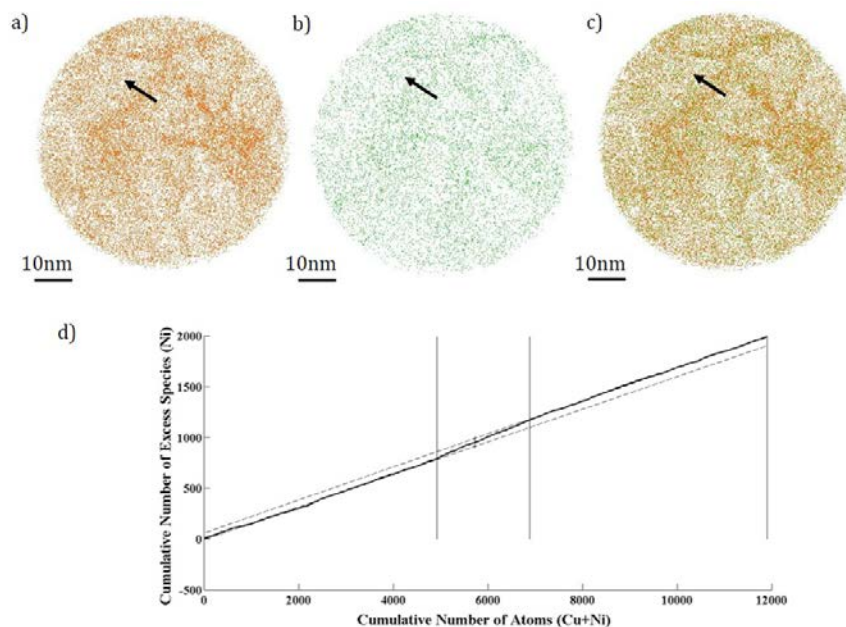


FIG 3. (a) Cu atom map for 95Cu5Ni film (b) Ni atom map for 95Cu5Ni film (c) Atom map of all elements 95Cu5Ni film (d) Representative ladder diagram used to calculate the interfacial excess. Note the change in slope across the boundary is indicative of solute segregation in the boundary.

Regardless of these interfacial excess variations, the presence of Ni in the boundary is revealing in how the stress evolved. With the additional Ni solute being driven into the boundary from its intrinsic thermodynamic behavior, these Ni adatoms in the boundary are suspected to have facilitated the increase in compressive stress that was not present in the pure elemental Cu film, Figure 1(a). One could then infer that the addition of more solute would further increase the compress stress by thermodynamically driving more solute to the boundary. However, if one considers the Gibbsian interfacial excess values between the 5 at.% and 15 at.% Ni films, the values are equivalent within each other's error. This is suggestive that the grain boundary has achieved its solute saturation. Kirchheim and Liu²⁹ have shown that further solute segregation to a grain boundary is not likely once it reaches its equilibrium concentration. Darling *et al.*²⁰ has shown how solute grain boundary equilibrium values change as a function of grain size, and in our case, the films have reasonably similar grain sizes. Thus, it appears after adding 5 at.% Ni, the system reached its grain boundary saturation limit.

Monma *et al.*³⁰ reported that the diffusivity in Cu decreases with increasing Ni content. Considering that adatom mobility into and out of a grain boundary will be a function of not only the enthalpy of segregation (thermodynamics) but also the ability to migrate (kinetics), a higher diffusivity (lower Ni content) film has a more preferred kinetic path for Ni segregation to the grain boundaries. The ability for Ni to be more easily incorporated into the grain boundaries at the lower Ni contents would also support the higher compressive stress forming at these compositions.

If the compressive stress is primarily driven by solutes within the boundary, the inability to add more solute to the boundary would result in the system being unable to further increase its compressive stress, which is what is observed in these films. Thus grain boundary saturation represents the greatest possible relative enrichment of Ni at the boundary in controlling the

compressive stress state for these grain sizes. With increasing the solute concentration, and the grain boundary saturated, the Ni is then forced into solid solution with the Cu matrix. This is noted by the shift in the XRD diffraction peaks in Figure 2. As more Ni is added, the alloy films now trend back to their elemental species stress response.

Finally, as shown by prior literature, the compressive stress can be reduced upon ceasing deposition¹⁰. This has been explained by adatoms being driven out of the grain boundary, hence causing a lowering of the stress, by the change in the surface chemical potential [4]. Figure 1(b) shows the stress relaxation upon ceasing deposition where only a moderate loss of compressive stress is noted. This minimal change is suggestive that the chemical potential between the grain boundary and surface was small and that the excess adatoms in the grain boundary remained relatively similar in providing the post-coalescence compressive stress mechanism.

This letter has shown how solute segregation, even in a weakly segregating system, can have a profound impact on stress evolution in thin films. Through the use of APT, the grain boundary chemistry was quantified and confirmed a solute saturation. With the system unable to place more solutes in the grain boundary, the alloy film's compressive stress was reduced and trended towards its elemental species behavior. The combined use of *in situ* stress measurements coupled with atomic scale characterization using an alloy system has provided experimental insights to help validate and verify prior modeling concepts that address the perplexing questions concerning post-coalescence stress generation. The use of alloys, and their intrinsic interfacial properties, appears to be material variable for the tailoring thin film stresses.

GBT and TMK acknowledge support from the Army Research Office, grant W911NF1310436, Dr. David Stepp, program manager

References

- ¹ R. Koch, *Journal of Physics: Condensed Matter* **6**, 9519 (1994).
- ² J.A. Floro, E. Chason, R.C. Cammarata, and D.J. Srolovitz, *MRS Bulletin* **27**, 19 (2002).
- ³ D. Winau, R. Koch, A. Führmann, and K.H. Rieder, *Journal of Applied Physics* **70**, 3081 (1991).
- ⁴ E. Chason, B.W. Sheldon, L.B. Freund, J.A. Floro, and S.J. Hearne, *Phys. Rev. Lett.* **88**, 156103 (2002).
- ⁵ H.Z. Yu and C.V. Thompson, *Acta Materialia* **67**, 189 (2014).
- ⁶ R.C. Cammarata, T.M. Trimble, and D.J. Srolovitz, *Journal of Materials Research* **15**, 2468 (2000).
- ⁷ W.D. Nix and B.M. Clemens, *Journal of Materials Research* **14**, 3467 (1999).
- ⁸ R. Koch, D. Hu, and A.K. Das, *Phys. Rev. Lett.* **94**, 146101 (2005).
- ⁹ F. Spaepen, *Acta Materialia* **48**, 31 (2000).
- ¹⁰ C. Friesen and C.V. Thompson, *Phys. Rev. Lett.* **89**, 126103 (2002).
- ¹¹ A. González-González, C. Polop, and E. Vasco, *Phys. Rev. Lett.* **110**, 056101 (2013).
- ¹² G. Thurner and R. Abermann, *Thin Solid Films* **192**, 277 (1990).
- ¹³ A.L.D. Vecchio and F. Spaepen, *Journal of Applied Physics* **101**, 063518 (2007).
- ¹⁴ M. Pletea, W. Brückner, H. Wendrock, and R. Kaltofen, *Journal of Applied Physics* **97**, 054908 (2005).
- ¹⁵ M. Pletea, W. Brückner, H. Wendrock, R. Kaltofen, and R. Koch, *Journal of Applied Physics* **99**, 033509 (2006).

- ¹⁶ J. Leib, R. Mönig, and C.V. Thompson, Phys. Rev. Lett. **102**, 256101 (2009).
- ¹⁷ B. Fu, W. An, C.H. Turner, and G.B. Thompson, Phys. Rev. Lett. **105**, 096101 (2010).
- ¹⁸ B. Fu and G.B. Thompson, Journal of Applied Physics **108**, 043506 (2010).
- ¹⁹ C.C. Koch, R.O. Scattergood, K.A. Darling, and J.E. Semones, J Mater Sci **43**, 7264 (2008).
- ²⁰ K.A. Darling, M.A. Tschopp, B.K. VanLeeuwen, M.A. Atwater, and Z.K. Liu, Computational Materials Science **84**, 255 (2014).
- ²¹ T. Chookajorn, H.A. Murdoch, and C.A. Schuh, Science **337**, 951 (2012).
- ²² Y. Sasanuma, M. Uchida, K. Okada, K. Yamamoto, Y. Kitano, and A. Ishitani, Thin Solid Films **203**, 113 (1991).
- ²³ P. Scherrer, Nachrichten von der Gesellschaft der Wissenschaften zu Göttingen, Mathematisch-Physikalische Klasse **1918**, 98 (1918).
- ²⁴ Taylor, C., Bartlett, D., Chason, E., and Floro, J., The Industrial Physicists **4**, 25 (1998).
- ²⁵ G.G. Stoney, Proceedings of the Royal Society A: Mathematical, Physical and Engineering Sciences **82**, 172 (1909).
- ²⁶ K. Thompson, D. Lawrence, D.J. Larson, J.D. Olson, T.F. Kelly, and B. Gorman, Ultramicroscopy **107**, 131 (2007).
- ²⁷ P. Felfer, A. Ceguerra, S. Ringer, and J. Cairney, Ultramicroscopy **132**, 100 (2013).
- ²⁸ S. Divinski, J. Ribbe, G. Schmitz, and C. Herzig, Acta Materialia **55**, 3337 (2007).
- ²⁹ F. Liu and R. Kirchheim, Scripta Materialia **51**, 521 (2004).
- ³⁰ K. Monma, H. Suto, and H. Oikawa, Nippon Kinzoku Gakkaishi **28**, 192 (1964).

CHAPTER 5

Influence of Fe(Cr) Miscibility on Thin Film Grain Size and Stress

Xuyang Zhou¹, Tyler Kaub¹, Richard L. Martens¹, and Gregory B. Thompson¹

1. The University of Alabama, Department of Metallurgical & Materials Engineering,
Tuscaloosa, AL USA

ABSTRACT

During the post coalescence portion of thin film deposition, thin film stress is related to the grain size and adatom mobility of the depositing material. Using a Fe(Cr) alloy thin film, the manipulation of the tensile stress for thick films was studied as a function of Cr solute content up to 8 at.%. Solute concentrations up to 4 at.% resulted in an approximate 50% increase in grain size that resulted in a reduction of the tensile stress to be lower than either elemental film. Upon increasing the Cr content, the grain size refined and the tensile stress of the films increased. Gibbsian interfacial excess quantification of Cr in the grain boundaries was characterized by atom probe tomography. These results suggested that the chemical partitioning of Cr to the boundaries appears to refine the grain size which alters the film stress state. The use of intrinsic segregation, rather than deposition processing variations, appears to be another viable option for regulating film stress.

Key words: *In situ* stress; thin films; Fe-Cr; Precession Electron Diffraction; Atom Probe, segregation

1. Introduction

Thin films are a vital architecture in several technologically important applications including information storage [1], optical devices [2, 3], semiconductor transistor design [4, 5], energy harvesting [6, 7], and tribological coatings [8]. In these applications, the intrinsic thin film stress plays a fundamental role in tuning physical and mechanical properties [9-15]. By understanding stress evolution during thin film growth, and even controlling the stress state in the thin film, one can enhance the reliable performance of such thin film based devices and help improve their functional properties.

In general, researchers have focused on understanding the *in situ* stress evolution of thin films consisting of single element species [16-26]. It is generally accepted that initial compressive stress at the first stage of growth is a result of the atomic-scale migration into embryonic islands that form to minimize surface area-to-volumetric energies. After then a subsequent tensile stress is generated by the elastic strain created from the islands as they begin to coalesce. Once coalescence is complete, thin films with high

adatom mobility, such as Cu, Ag and Co, experience a return to a compressive stress state [21, 27, 28]. However, elemental films with low adatom mobility, like Fe [29], Cr [29], and Al [19], usually tend to retain the tensile condition with continued growth.

The stress state of a thin film is typically controlled by regulating the microstructure of the film. In elemental species films, changes in grain size have been shown to directly correlate with the stress of the film [20]. A change in grain size can be done through altering the substrate temperature, deposition rate, and pressure [30, 31]. Unlike single element films, an alloy film has the added complexity of different adatom interactions. This could alter initial island sizes and coalescence behavior through changes in surface and grain boundary energies. For example, Fu and Thompson reported how the stress state of a FePt thin film changed based on the composition of the grain boundary [32]. In this case, the mixing of Fe, a low adatom mobility species, and Pt, a high adatom mobility species, resulted in a range of tensile to compressive stress dependent on the composition. Unlike this former work, this paper addresses Fe-Cr alloy films, where both individual species have lower adatom mobility which facilitates tensile stress behavior. In such a study we will be able to elucidate how similar mix adatom mobility alters the intrinsic tensile growth stresses. Moreover, Fe-Cr exhibits a miscibility gap which would indicate a strong preference for chemical partitioning at the interfaces which could also influence the segregation of specific species to the grain boundaries and alter the aforementioned interface/grain boundary energies.

2. Experimental

Elemental and alloyed nanocrystalline thin films of Fe, Cr and Fe_{1-x}Cr_x were sputter deposited from 99.95 at.% pure Fe and Cr targets in an AJA ATC-1500 stainless steel magnetron-sputtering system. The films were grown to an approximate thickness of 300 nm on to 300 μm thick Si [001] substrates, with a native surface oxide, at ambient temperature. The sputtering rates were 0.11 nm/sec for Fe, 0.14nm/sec and 0.11-0.14 nm/sec for the alloys dependent on composition. The base pressure prior to sputtering system was < 5 × 10⁻⁸ Torr whereupon ultra-high-purity argon was introduced as the working gas with a flow rate of 10 standard cubic centimeters per minutes to a pressure of 2 mTorr.

The *in situ* stress state was measured through a K-Space Multi-beam Optic Sensor (MOS) equipped onto the sputter chamber [33]. By reflecting a series of laser spots from the substrate to a charge-coupled detector, the relative position of the spots change as the substrate bends in response to the growth stresses. Using the Stoney equation, given below, the stress within the film was measured and calculated.

$$\sigma_f = \frac{E_s}{6(1-\nu_s)} \frac{t_s^2}{t_f} \left(\frac{1}{R} - \frac{1}{R_0} \right) \quad (1)$$

where σ_f is the films stress, ν_s and E_s are the Poisson ratio and the Young's modulus of the substrate respectively, t_f is the film thickness, and $1/R_0$ and $1/R$ are measured curvatures of the films before and during the deposition.

Post deposition, the compositions of the alloy thin films were verified from the co-sputtering calculations using Energy Dispersive X-ray Spectrum (EDX) in TESCAN LYRA dual electron-focus ion beam (FIB) microscopes operated at 20 keV. X-Ray Diffraction (XRD) was performed for phase identification and lattice parameter measurements via a Philips diffractometer with Cu $K\alpha$ radiation as the source operated at 45 kV and 40 mA. Transmission electron microscopy (TEM) was performed in an FEI Tecnai SupertwinF20 microscope. The TEM plan-view foils, prepared by cutting, dimpling and ion-milling a 3 mm disc, were also used to confirm phase as well as grain sizes and grain boundary character using the NanoMEGAS Precession Electron Diffraction (PED) platform. The details of how the NanoMEGAS platform works can be found in reference [34]. The PED scanning was operated with a 0.2° precession angle and a scanning step size of 4 nm, in the same size of region of interest (ROI), which was $1.5 \mu\text{m} \times 1.5 \mu\text{m}$. After scanning, the data was converted for analysis using TSL OIM Analysis 5 software. After grain dilation optimization, the reconstructed grain size and grain boundary characters were calculated based on at least 800 grains.

Selected alloy thin films were also characterized by Atom Probe Tomography (APT) in a Cameca Scientific Instruments Local Electrode Atom Probe (LEAP) 3000XSi. The required needle shaped geometry was prepared in cross-section using a FIB lift out technique and annular milling procedure described in reference [35] in either the TESCAN LYRA FIB-FESEM or a FEI Quanta 3D dual beam FIB-SEM. The specimens were set at a base temperature 37 K where upon they were field evaporated with a laser energy of 0.3 nJ for a 0.5% targeted evaporation rate. The APT data was reconstructed using the IVAS 3.6.0 software platform.

3. Results

The *in situ* stress evolution of the 300 nm thick Fe, Cr and $\text{Fe}_{1-x}\text{Cr}_x$, where x ranged from 0.03 to 0.08, are displayed in Fig. 1. Both Fe and Cr elemental thin films experienced post coalescence tensile stresses as similarly reported in the literature [16, 27], with Cr being more tensile. As Cr was added to the Fe film, the tensile stress was lowered to be less than that of elemental Fe with a minimum stress for the $\text{Fe}_{0.96}\text{Cr}_{0.04}$ thin film.

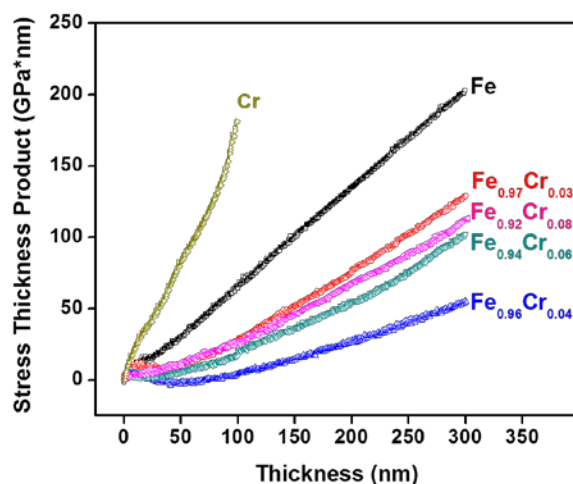


Fig. 1: Plot of stress thickness product versus thickness for films deposited at different Cr contents - $\text{Fe}_{1-x}\text{Cr}_x$, $x=0, 0.03, 0.04, 0.06, 0.08$ and 1.00 . Color available on-line.

All of the films were indexed to either a body centered cubic (BCC) or solid solution A2 BCC phase in the XRD, Fig. 2(a). This phase was also confirmed by subsequent electron diffraction (shown in Fig. 3). Using the $\{110\}$ reflection and a Lorentz fit of the peak, the cubic lattice constant as a function of Cr content is plotted in Fig. 2(b). As the Cr was initially added to the film, the lattice parameter increased where it peaks at 4 at.%. Further alloying resulted in a decrease in the lattice parameter.

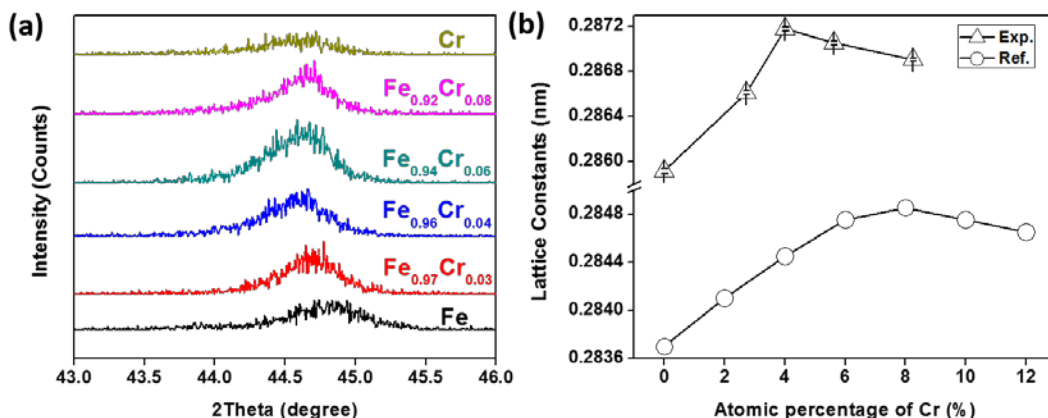


Fig. 2 (a) XRD spectra for the Fe, $\text{Fe}_{0.97}\text{Cr}_{0.03}$, $\text{Fe}_{0.96}\text{Cr}_{0.04}$, $\text{Fe}_{0.94}\text{Cr}_{0.06}$ and $\text{Fe}_{0.92}\text{Cr}_{0.08}$ thin films. **(b)** The lattice constants of bcc Fe(Cr) alloy. The unfilled triangles are the experimental results calculated by the peak value obtained from Lorentz fitting from the reflection in (a). The unfilled circles are the calculated lattice parameters data from reference [48]. Color available on-line.

Fig. 3 shows representative TEM bright field and PED plan view images for each of the films. The inset diffraction pattern was consistently indexed to a single BCC phase. The PED scans from the films provide a clearer image of the grain sizes as well as revealing, in large part, that the grains are equiaxed. The PED scans also reveal a mosaic of colors that represent the different grain orientations. Fig. 4 (a-e) are the histograms of the grain sizes, which was calculated by the area fraction distribution, $F_A(D_i)$, given below

$$f_A(D_i)\delta D_i = \frac{A_i}{A_{total}} \quad (2)$$

where A_i is the area of grain 'i', A_{total} is the total area occupied by the grains which is equal to the surface of the measurement of all the pixels belonging to grains[36], and δD_i is the bin size. Each histogram was fitted to a log normal function, superimposed in Fig. 4 [36, 37], and showed good agreement for each composition, e.g. there was no noted abnormal grain growth. Fig. 4(f) is plot of the mean grain size with the Cr content. The initial addition of Cr resulted in a nearly 50% increase in the grain size peaking at 4 at.% Cr. Further increases in Cr resulted a reduction of grain size toward the initial elemental Fe sizes.

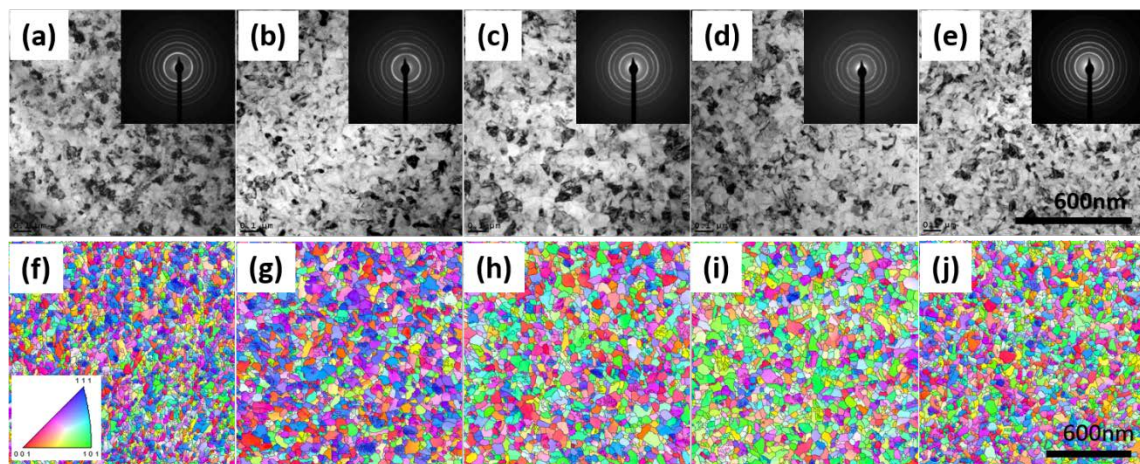


Fig. 3 Plan-view TEM images and corresponding diffraction patterns from **(a)** Fe **(b)** $\text{Fe}_{0.97}\text{Cr}_{0.03}$ **(c)** $\text{Fe}_{0.96}\text{Cr}_{0.04}$ **(d)** $\text{Fe}_{0.94}\text{Cr}_{0.06}$ **(e)** $\text{Fe}_{0.92}\text{Cr}_{0.08}$. All the SAED patterns can be indexed as the BCC structure. Grain boundary traces, extracted from the PED reconstruction results for **(f)** Fe **(g)** $\text{Fe}_{0.97}\text{Cr}_{0.03}$ **(h)** $\text{Fe}_{0.96}\text{Cr}_{0.04}$ **(i)** $\text{Fe}_{0.94}\text{Cr}_{0.06}$ **(j)** $\text{Fe}_{0.92}\text{Cr}_{0.08}$.

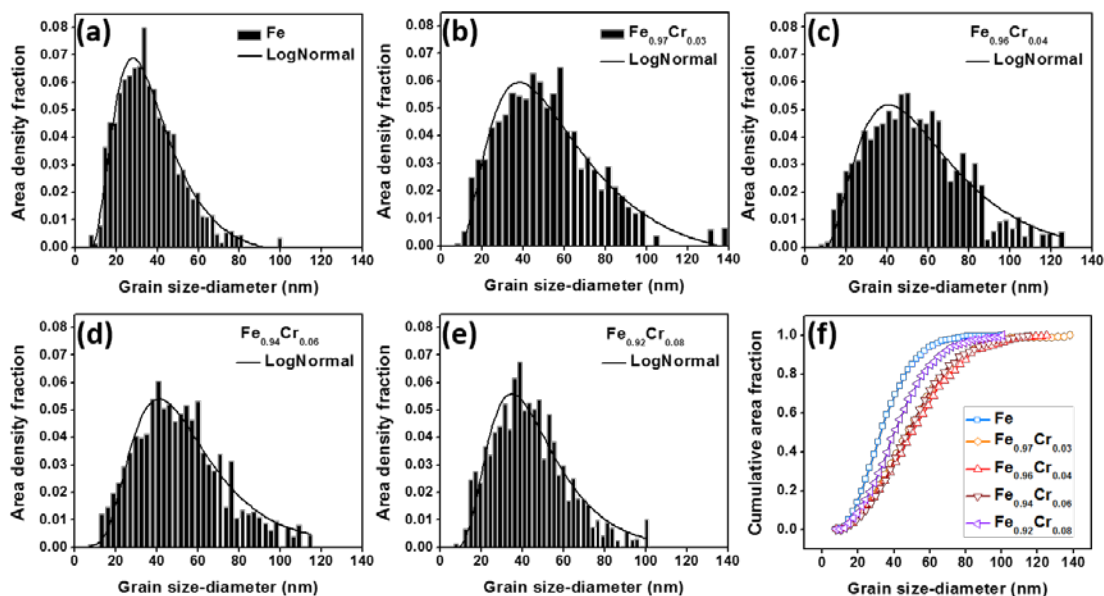


Fig. 4 Grain size distribution for (a) Fe (b) $\text{Fe}_{0.97}\text{Cr}_{0.03}$ (c) $\text{Fe}_{0.96}\text{Cr}_{0.04}$ (d) $\text{Fe}_{0.94}\text{Cr}_{0.06}$ (e) $\text{Fe}_{0.92}\text{Cr}_{0.08}$, Log normal function was used for grain size distribution fitting. (f) Cumulative grain size distribution plot quantifying each of the $\text{Fe}_{1-x}\text{Cr}_x$ ($x = 0 - 0.08$) thin films. Color available on-line.

With the dramatic change in grain size with Cr content, APT was used to quantify the grain boundary chemistries between the 3 at.% and 8 at.% Cr films. Each data set contained over 40 million ions. Fig. 5 is the reconstructed atom probe atom map of each sample with a variety of cylindrical analysis tubes that cross the grain boundaries. The grain boundaries were delineated in the matrix using a variety of isodensity values to create density isosurfaces which were coupled to 2-dimensional density profile maps, Fig. 5(c), and compared to specific atom maps, Fig. 5(d). The Gibbsian interfacial excess, Γ_i , were quantified for each boundary and plotted as a ladder diagram as shown in the representative image in Fig. 5(e) using the method described in reference [24] [38]. A spread in Γ_i values was noted, Fig. 6, between the two films and will be addressed in detail in the proceeding section.

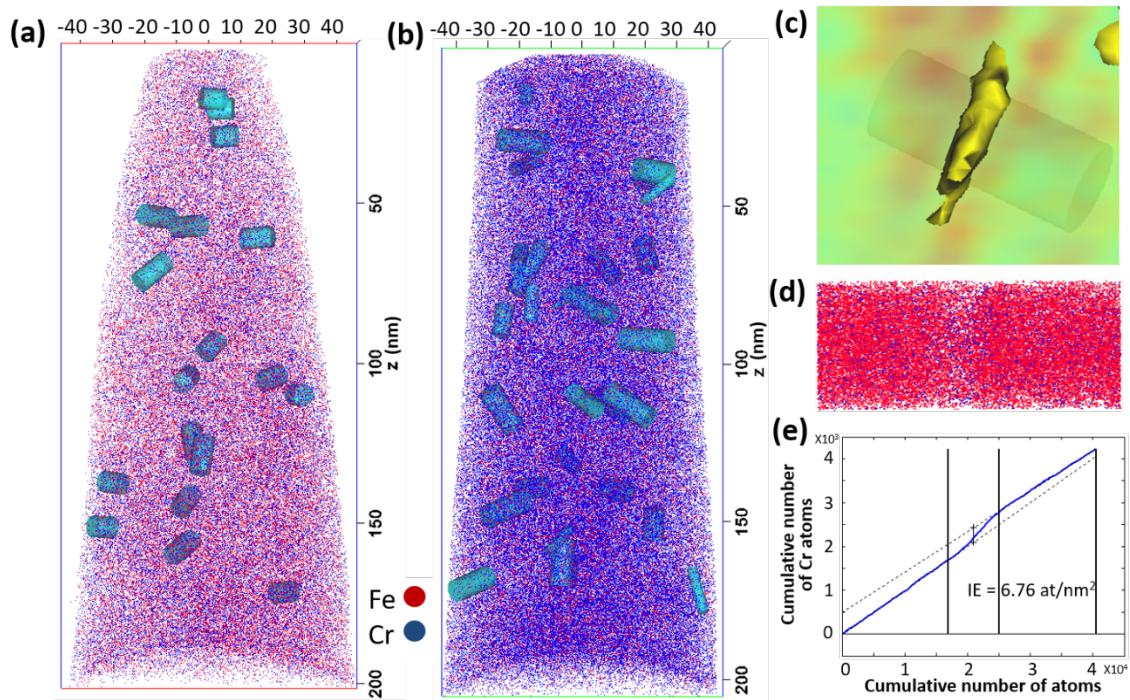


Fig. 5 Reconstructed atom maps from **(a)** $\text{Fe}_{0.97}\text{Cr}_{0.03}$ **(b)** $\text{Fe}_{0.92}\text{Cr}_{0.08}$. Cylinders in the atom maps represent measurement regions of interest across various detected grain boundaries. **(c)** Density isosurface map laid over the 2-dimension density profiles in an identified grain boundary. **(d)** Atoms map from a selected cylinder **(e)** A representative ladder diagram that provides the interfacial excess count determined from the cumulative curve.

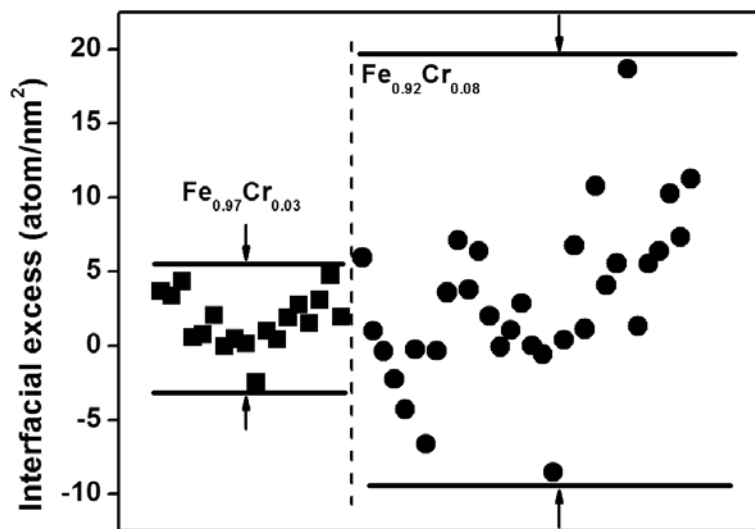


Fig. 6: Interfacial excesses values from the grain boundaries for $\text{Fe}_{0.97}\text{Cr}_{0.03}$ and $\text{Fe}_{0.92}\text{Cr}_{0.08}$

4. Discussion

As observed in these films, the tensile stress in an elemental Fe film can be reduced by small additions of Cr. Interestingly, the addition of Cr, which exhibits a more tensile behavior than Fe is able to yield an alloy film with a lower tensile stress than either of the constituent elemental films. From the phase identification, the as-deposited film is a single, solid solution BCC phase. From the PED scans, Fig. 3, there is no strikingly obvious texture differences. Hence, these two microstructure quantities – phase and grain orientation – do not appear to have a significant effect on regulating the stress. However, upon further review of the PED results, Fig. 4, the grain size does show a marked change, with the initial solute addition increasing the grain size.

Fig. 7 is a plot of mean grain size coupled with the measured stress at 100 nm. The stress and grain size have an inverse relationship, i.e. as the grain size increased, the stress was reduced. Similar grain size and film stress relationships have been noted by others [20]. As addressed in the introduction, tensile stress has been attributed to the formation of grain boundaries as islands that elastically strain during coalescences [17, 39, 40]. This tensile stress can be estimated based on an impinging spherical-cap shaped island model [17, 39, 40]. For a three-dimensional case [17], this stress is described as

$$\langle \sigma \rangle = \frac{2(2\gamma_s - \gamma_{gb})}{r} \quad (3)$$

where γ_s and γ_{gb} are the interfacial energies of the surface and grain boundaries respectively and r is the impinging grain size radius. For this calculation, γ_s and γ_{gb} for Fe were taken from reference [41, 42] to be $\gamma_s = 2.4 \text{ J/m}^2$ and $\gamma_{gb} = 1.4 \text{ J/m}^2$ respectively. For the Fe(Cr) the values slightly varied using estimates from reference [41, 43], which showed an approximate 10% increase in the surface energy with respect to Fe. The experimentally measured grain size was used to estimate r . The calculated stress showed good agreement with the experimental stress as the Cr content increased. However, a large discrepancy between the 3 dimensional calculated and experimental values for the stress existed for the pure Fe and low solute Cr films in Fig. 7.

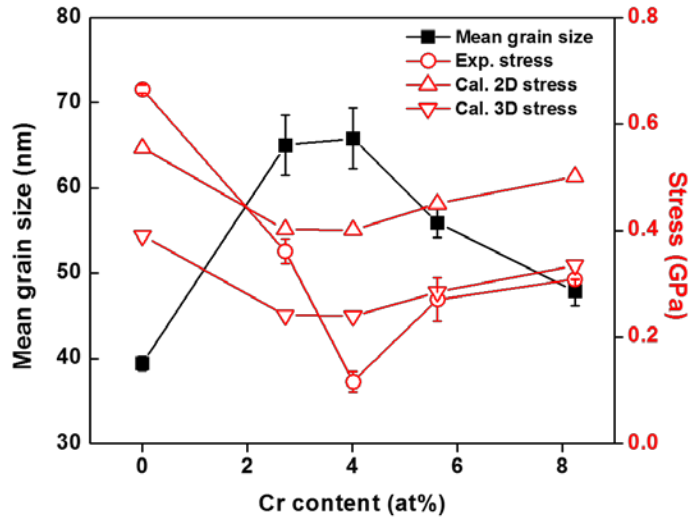


Fig. 7: Mean grain size, experimental and calculated growth stress of $\text{Fe}_{1-x}\text{Cr}_x$ ($x = 0 - 0.08$) thin films with various Cr contents. The filled in markers represent grain size (left y-axis) and the unfilled markers are for the film stress (right y-axis). Color on-line.

As noted above, the tensile stress model is based on the assumption of a spherical-cap shaped island, which is most likely formed in the very early stages of growth as the adatoms move across the substrate. In the case of a coalescence film, the formation of such islands may not necessarily occur in the same 3 dimensional shape as the film grains have already impinged on each other. For island growth to continue, these adatoms would need to form new island features on the top surface of the coalesced granular film. Considering that the surface energy for the atoms on the substrate and those on the surface of the film would be different, it is reasonable to expect the formation of islands, and in particular their morphology, would change dependent on these growth surfaces. Experimental determination of such morphological changes would require some form of *in situ* imaging, such as scanning tunneling microscopy (STM) or atomic force microscopy (AFM), which was not available in these experiments. Attempts were done to perform *ex situ* AFM to verify this morphology change, however the results were inconclusive because of possible oxidation contamination upon removal of the film from the vacuum chamber. Nonetheless, such changes on a growth surface have been noted by others [44, 45]. If one considers the 2-dimensional morphological driven tensile stress condition [17], the stress is now given as

$$\langle \sigma \rangle = 0.44E \left(\frac{\gamma_s - \gamma_{gb}}{Er} \right)^{2/3} \quad (4)$$

where γ_s and γ_{gb} are the interfacial energies of the surface and grain boundaries respectively, E is the elastic modulus, and r is the impinging grain size radius.

Using the 2-dimensional stress calculations, plotted on Fig. 7, a much closer agreement with the pure Fe and low Cr solute films is observed. Using the 2- and 3- dimensional modeled stresses, we infer that the growth morphology between the pure Fe and low Cr solute films as compared to the higher solute Cr films is different. This difference can be rationalized considering the chemical partitioning behavior in this alloy where one needs to consider the influence of Fe-Cr's miscibility gap on the mix-mobility adatom migration in forming the embryonic growth islands.

In the binary Fe-Cr phase diagram, Fe has some solubility for Cr. Malerba [46] noted that the enthalpy of mixing for Fe-Cr was slightly negative for compositions up to ≈ 4 at.% Cr. Hence, Fe and the low solute Fe(Cr) films would behave in a similar manner as they would be a thermodynamically equilibrium solid solution. However, at higher solute concentrations, the Cr would become insoluble with Fe and result in phase separation. The lack of phase separation in these films, Figs. 2 and 3, is contributed to the highly dynamical processing of physical vapor deposition which can cause adatoms to be 'quenched' into a single phase. Though the system is single phase, the Cr adatoms will be thermodynamically driven to migrate from the Fe matrix to the surface or interfaces. The APT results of this paper, Fig. 5 and 6, confirms this Cr enrichment at the interfaces. Mild Cr enrichment at the grain boundaries, as compared to the higher Cr solute film, was even noted for the 3 at.% Cr film where Cr solubility would be expected.

As the Cr content increased from 3 at.% to 8 at.%, the spread in interfacial excess values increased, Fig. 6. This increase is contributed to the higher solute content now being driven to the boundaries beyond the miscibility limit. It is interesting to note that in some rare cases, the interfacial excess was found to be negative. This result, as well as the wider spread in the interfacial excess, is indicative that the migration of Cr to the boundaries could be a function of the grain boundary type [43]. Though the atom probe can provide detailed chemical mapping, exact crystallographic rendering is difficult due to slight reconstruction aberrations in the placement of the atoms as well as detector inefficiencies, i.e. only able to capture $\approx 50\%$ of the atoms from the specimen [47]. This makes determination of the grain boundary character in an atom probe atom map difficult. The field evaporation events in these alloys did not allow such precise lattice rectifications. Regardless of these experimental limitations, the APT data clearly showed continual Cr enrichment to the grain boundaries with increasing Cr solute and is consistent with the thermodynamic behavior of this system.

If one considers the enrichment of Cr to the interfaces, this would provide a thermodynamic surface barrier for the continual migration of new Fe adatoms diffusing into the island. These new Fe adatoms would need to overcome the Cr surface to be incorporated into the interior of the embryonic island. Hence, to achieve coalescence of

the film, a higher density of islands on the surface would develop and lead to a refinement of the final film's grain size with increasing Cr content. As noted in Fig. 4 and Fig. 7, the grain size was reduced upon increasing Cr content above 4 at.%. It is believed that this mix-mobility, and in particular the chemical partitioning of Cr above the thermodynamic solubility limit, controlled the final grain size as it enriched the surface of the embryonic islands.

In the case where the grains grew (very low Cr solute), the Cr is thermodynamically predicted to have some solubility in Fe, which would reduce the amount of Cr at these interfaces. The data spread in interfacial excess values was smaller for the 3 at.% versus 8 at.% Cr films, Fig. 5, suggesting that Cr was being incorporated within the matrix volume of the island. This was confirmed by the linear increase in the lattice values, Fig. 2(b), up to ≈ 4 at.% Cr, which trended well with modeling predictions of mutual solubility [48].

Though solute segregation to specific grain boundaries can occur [43, 49], no conclusive evidence to suggest that Cr controlled the formation of specific boundary types were found. PED analysis of the special grain boundary characters, Fig. 8, were done for each of the films. Though the 3 at.% Cr sample showed a higher fraction of $\Sigma 3$ boundaries than all other compositions, suggesting that Cr could have promoted the increase in grain size by favoring a this type of low energy grain boundary, the 4 at.% Cr film, which had a near equivalent grain size, did not show this increase for this particular special boundary. The growth of the grains appears to be more associated with the solubility behavior of Cr with Fe during the early stages of growth at low concentrations than boundary type. The closer stress agreement of the 2-dimension stress (rather than the 3-dimensional stress) model with the compositions that had a larger grain size also infers possibly better wettability and mobility for these films in promoting the larger grain size.

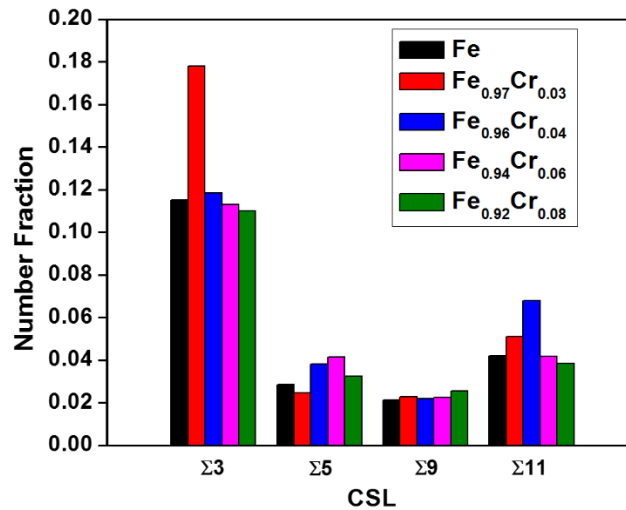


Fig. 8: Number fraction of specific grain boundaries of Fe_{1-x}Cr_x (x = 0 - 0.08) thin films

5. Conclusions

A series of Fe_{1-x}Cr_x, where x = 0 – 8 at.%, films were sputter deposited. Each film grew in a post-coalescence tensile state with the tensile stress reduced with the addition of Cr. Each deposited film formed a single BCC phase. At low Cr solute concentrations, ≤ 4 at.% Cr, the grain size grew which accounted for a reduction in the tensile stress values. Upon increasing the Cr solute concentration, the grain size began to be refined and the tensile stress increased. Using APT, the interfacial excess of Cr in the film’s boundaries were quantified and Cr was found to enrich these interfaces. Once the solubility limit was exceeded for the Fe(Cr) films, the Cr further enriched the surfaces (noted by the increase in interfacial excess values) which is suspected to alter the film growth behavior. With an enrichment of Cr on the surfaces of the embryonic islands, they would provide a thermodynamic barrier against the unrestricted incorporation of Fe adatoms consequently resulting in a reduced grain size as noted in these films. The formation of these types of shaped islands on the surface of the coalesced film was inferred from model calculations of stress that indicated reasonable matching to the experimental values. Unlike prior findings [32], where the grain boundary composition controlled the stress state, the composition of these film appears to have a more dramatic impact on film grain size controlling the stress state. The connection of grain size with growth stresses, as shown here, is in agreement with prior studies using elemental films [20]. Unlike those prior studies, where the grain size was processed controlled, these results reveal the ability to use intrinsic material properties (solute segregation) in the manipulation of grain growth during the growth of the thin film.

Acknowledgement

The authors gratefully recognize support from the Army Research Office, grant W911NF1310436, Dr. David Stepp program manager. The UA Central Analytical Facility is recognized for additional assistance and access to the microscopes used in this research

Reference

- [1] F.J. Himpsel, J.E. Ortega, G.J. Mankey, R.F. Willis. Magnetic nanostructures, *Advances in Physics* 47 (1998) 511-597.
- [2] P.K. Tien. Light Waves in Thin Films and Integrated Optics, *Appl. Opt.* 10 (1971) 2395-2413.
- [3] K. Nomura, H. Ohta, A. Takagi, T. Kamiya, M. Hirano, H. Hosono. Room-temperature fabrication of transparent flexible thin-film transistors using amorphous oxide semiconductors, *Nature* 432 (2004) 488-492.
- [4] S. Kovesnikov, W. Tsai, I. Ok, J.C. Lee, V. Torkanov, M. Yakimov, S. Oktyabrsky. Metal-oxide-semiconductor capacitors on GaAs with high-k gate oxide and amorphous silicon interface passivation layer, *Applied Physics Letters* 88 (2006) 022106.
- [5] B. Radisavljevic, A. Radenovic, J. Brivio, V. Giacometti, A. Kis. Single-layer MoS₂ transistors, *Nature nanotechnology* 6 (2011) 147-150.
- [6] X. Chen, S.S. Mao. Titanium dioxide nanomaterials: synthesis, properties, modifications, and applications, *Chemical reviews* 107 (2007) 2891-2959.
- [7] I. Repins, M.A. Contreras, B. Egaas, C. DeHart, J. Scharf, C.L. Perkins, B. To, R. Noufi. 19.9%-efficient ZnO/CdS/CuInGaSe² solar cell with 81.2% fill factor, *Progress in Photovoltaics: Research and Applications* 16 (2008) 235-239.
- [8] P.H. Mayrhofer, C. Mitterer, L. Hultman, H. Clemens. Microstructural design of hard coatings, *Progress in Materials Science* 51 (2006) 1032-1114.
- [9] M.A. Steiner, R.B. Comes, J.A. Floro, W.A. Soffa, J.M. Fitz-Gerald. L₁' ordering: Evidence of L₁₀-L₁₂ hybridization in strained Fe_{38.5}Pd_{61.5} epitaxial films, *Acta Materialia* 85 (2015) 261-269.
- [10] M. Seita, C.M. Pecnik, S. Frank, R. Spolenak. Direct evidence for stress-induced texture evolution and grain growth of silver thin films upon thermal treatment and self-ion bombardment, *Acta Materialia* 58 (2010) 6513-6525.
- [11] K. Yalamanchili, I.C. Schramm, E. Jiménez-Piqué, L. Rogström, F. Mücklich, M. Odén, N. Ghafoor. Tuning hardness and fracture resistance of ZrN/Zr_{0.63}Al_{0.37}N nanoscale multilayers by stress-induced transformation toughening, *Acta Materialia* 89 (2015) 22-31.
- [12] K.S. Park, J.K. Park. Effect of thin film stress on the elastic strain energy of Cr thin film on substrate, *Acta Materialia* 47 (1999) 2177-2184.
- [13] D. Sander. The correlation between mechanical stress and magnetic anisotropy in ultrathin films, *Reports on Progress in Physics* 62 (1999) 809-858.
- [14] T. Shibata, H. Irie, D.A. Tryk, K. Hashimoto. Effect of Residual Stress on the Photochemical Properties of TiO₂ Thin Films, *The Journal of Physical Chemistry C* 113 (2009) 12811-12817.
- [15] R.C. Cammarata. Surface and interface stress effects in thin films, *Progress in Surface Science* 46 (1994) 1-38.
- [16] R. Koch, D. Hu, A. Das. Compressive Stress in Polycrystalline Volmer-Weber Films, *Physical Review Letters* 94 (2005) 146101.

- [17] L.B. Freund, E. Chason. Model for stress generated upon contact of neighboring islands on the surface of a substrate, *Journal of Applied Physics* 89 (2001) 4866.
- [18] H.Z. Yu, C.V. Thompson. Grain growth and complex stress evolution during Volmer–Weber growth of polycrystalline thin films, *Acta Materialia* 67 (2014) 189-198.
- [19] M. Pletea, R. Koch, H. Wendrock, R. Kaltofen, O.G. Schmidt. In situ stress evolution during and after sputter deposition of Al thin films, *Journal of physics. Condensed matter : an Institute of Physics journal* 21 (2009) 225008.
- [20] J. Leib, R. Mönig, C. Thompson. Direct Evidence for Effects of Grain Structure on Reversible Compressive Deposition Stresses in Polycrystalline Gold Films, *Physical Review Letters* 102 (2009) 256101.
- [21] E. Chason, B. Sheldon, L. Freund, J. Floro, S. Hearne. Origin of Compressive Residual Stress in Polycrystalline Thin Films, *Physical Review Letters* 88 (2002) 156103.
- [22] R.C. Cammarata, T.M. Trimble. Surface stress model for intrinsic stresses in thin films, *Journal of Materials Research* 15 (2000) 2468-2474.
- [23] C.-W. Pao, S.M. Foiles, E.B. Webb, D.J. Srolovitz, J.A. Floro. Atomistic simulations of stress and microstructure evolution during polycrystalline Ni film growth, *Physical Review B* 79 (2009) 224113.
- [24] C.-W. Pao, S.M. Foiles, E.B. Webb, D.J. Srolovitz, J.A. Floro. Thin Film Compressive Stresses due to Adatom Insertion into Grain Boundaries, *Physical Review Letters* 99 (2007) 036102.
- [25] S.C. Seel, J.J. Hoyt, E.B. Webb, J.A. Zimmerman. Modeling metallic island coalescence stress via adhesive contact between surfaces, *Physical Review B* 73 (2006) 245402.
- [26] A.J. Detor, A.M. Hodge, E. Chason, Y. Wang, H. Xu, M. Conyers, A. Nikroo, A. Hamza. Stress and microstructure evolution in thick sputtered films, *Acta Materialia* 57 (2009) 2055-2065.
- [27] F. Spaepen. Interfaces and stresses in thin films, *Acta Materialia* 48 (2000) 31-42.
- [28] T. Zhi Luo, L. Guo, R.C. Cammarata. Real-time intrinsic stress generation during Volmer–Weber growth of Co by electrochemical deposition, *Journal of Crystal Growth* 312 (2010) 1267-1270.
- [29] G. Thurner, R. Abermann. Internal stress and structure of ultrahigh vacuum evaporated chromium and iron films and their dependence on substrate temperature and oxygen partial pressure during deposition, *Thin Solid Films* 192 (1990) 277-285.
- [30] J.A. Thornton. High rate thick film growth, *Annual Review of Materials Research* 60 (1977) 239-260.
- [31] R. Messier. Revised structure zone model for thin film physical structure, *Journal of Vacuum Science & Technology A: Vacuum, Surfaces, and Films* 2 (1984) 500.
- [32] B. Fu, W. An, C.H. Turner, G.B. Thompson. In Situ Thin Film Growth Stresses during Chemical Ordering, *Physical Review Letters* 105 (2010) 096101.
- [33] C. Taylor, D. Barlett, E. Chason, J. Floro. A Laser-Based Thin-Film Growth Monitor, *Industrial Physicist* 4 (1998) 25.
- [34] K. Hattar, J. Gregg, J. Han, T. Saif, I.M. Robertson. In situ TEM Observations of Grain Growth in Nanograined Thin Films, *MRS Online Proceedings Library* 854 (2004).
- [35] K. Thompson, D. Lawrence, D.J. Larson, J.D. Olson, T.F. Kelly, B. Gorman. In situ site-specific specimen preparation for atom probe tomography, *Ultramicroscopy* 107 (2007) 131-139.
- [36] L.S. Toth, S. Biswas, C. Gu, B. Beausir. Notes on representing grain size distributions obtained by electron backscatter diffraction, *Materials Characterization* 84 (2013) 67-71.

- [37] K. Okazaki, H. Conrad. Recrystallization and Grain Growth in Titanium: I. Characterization of the Structure, Metallurgical Transactions 3 (1972) 1972-2411.
- [38] P. Felfer, A. Ceguerra, S. Ringer, J. Cairney. Applying computational geometry techniques for advanced feature analysis in atom probe data, Ultramicroscopy 132 (2013) 100-106.
- [39] R.W. Hoffman. Stresses in thin films: The relevance of grain boundaries and impurities, Thin Solid Films 34 (1976) 185-190.
- [40] W.D. Nix, B.M. Clemens. Crystallite coalescence: A mechanism for intrinsic tensile stresses in thin films, Journal of Materials Research 14 (1999) 3467-3473.
- [41] S. Schonecker, S.K. Kwon, B. Johansson, L. Vitos. Surface parameters of ferritic iron-rich Fe-Cr alloy, Journal of physics. Condensed matter : an Institute of Physics journal 25 (2013) 305002.
- [42] W.R. Tyson, W.A. Miller. Surface free energies of solid metals: Estimation from liquid surface tension measurements, Surface Science 62 (1977) 267-276.
- [43] D. Terentyev, X. He, E. Zhurkin, A. Bakaev. Segregation of Cr at tilt grain boundaries in Fe-Cr alloys: A Metropolis Monte Carlo study, Journal of Nuclear Materials 408 (2011) 161-170.
- [44] C.W. Snyder, B.G. Orr, D. Kessler, L.M. Sander. Effect of strain on surface morphology in highly strained InGaAs films, Physical Review Letters 66 (1991) 3032-3035.
- [45] J.E. Van Nostrand, S.J. Chey, M.A. Hasan, D.G. Cahill, J.E. Greene. Surface Morphology during Multilayer Epitaxial Growth of Ge(001), Physical Review Letters 74 (1995) 1127-1130.
- [46] L. Malerba, A. Caro, J. Wallenius. Multiscale modelling of radiation damage and phase transformations: The challenge of FeCr alloys, Journal of Nuclear Materials 382 (2008) 112-125.
- [47] A. Cerezo, P.H. Clifton, M.J. Galtrey, C.J. Humphreys, T.F. Kelly, D.J. Larson, S. Lozano-Perez, E.A. Marquis, R.A. Oliver, G. Sha, K. Thompson, M. Zandbergen, R.L. Alvis. Atom probe tomography today, Materials Today 10 (2007) 36-42.
- [48] V.I. Razumovskiy, A.V. Ruban, P.A. Korzhavyi. First-principles study of elastic properties of Cr- and Fe-rich Fe-Cr alloys, Physical Review B 84 (2011) 024106.
- [49] Y. Shibuta, S. Takamoto, T. Suzuki. Dependence of the grain boundary energy on the alloy composition in the bcc iron-chromium alloy: A molecular dynamics study, Computational Materials Science 44 (2009) 1025-1029.

CHAPTER 6

Grain Boundary Specific Segregation in Nanocrystalline Fe(Cr)

Xuyang Zhou¹, Xiao-xiang Yu¹, Tyler Kaub¹, Richard L. Martens², and Gregory B. Thompson^{1,*}

1. The University of Alabama, Department of Metallurgical & Materials Engineering, Tuscaloosa, AL USA

2 The University of Alabama, Central Analytical Facility, Tuscaloosa, AL USA

*Correspondence to gthompson@eng.ua.edu

ABSTRACT

A cross-correlative precession electron diffraction – atom probe tomography investigation of Cr segregation in a Fe(Cr) nanocrystalline alloy was undertaken. Solute segregation was found to be dependent on grain boundary type. The results of which were compared to a hybrid Molecular Dynamics and Monte Carlo simulation that predicted the segregation for special character, low angle, and high angle grain boundaries, as well as the angle of inclination of the grain boundary. It was found that the highest segregation concentration was for the high angle grain boundaries and is explained in terms of clustering driven by the onset of phase separation. For special character boundaries, the highest Gibbsian interfacial excess was predicted at the incoherent $\Sigma 3$ followed by $\Sigma 9$ and $\Sigma 11$ boundaries with negligible segregation to the twin and $\Sigma 5$ boundaries. In addition, the low angle grain boundaries predicted negligible segregation. All of these trends matched well with the experiment. This solute-boundary segregation dependency for the special character grain boundaries is explained in terms of excess volume and the energetic distribution of the solute in the boundary.

Key words: Correlative microscopy, atom probe, TEM, precession electron diffraction, Fe-Cr, segregation, interfacial excess

Introduction

Grain boundary energy plays a significant role in controlling grain morphology and growth behavior in polycrystalline materials. This energy is directly linked to the grain boundary character between the polycrystalline grains. Since the relative grain size can be crucial in regulating the strength and electrical management of materials, particularly at small length scales¹⁻⁴, the ability to manage grain boundary energy is essential. In recent years, the use of solute segregation as a means to alter the grain boundary energy to control the grain size and shape has been shown to help stabilize nanocrystalline grains against growth at high homologous temperatures⁵⁻⁸. Though these reports assume that solute segregation is isotropic and equivalent, in reality grain boundaries are diverse in energy, structure, and mobility⁹⁻¹². This would imply that solute segregation would be a function of grain boundary type. However, quantifying the solute segregation to specific boundaries to determine this solute-orientation dependence is an arduous task because one must have both high chemical sensitivity and high spatial resolution to detect the solute in the known grain boundary. Of the available techniques, atom probe tomography (APT) is capable in providing the local grain boundary composition but only rarely is able to provide the necessary atomic spatial resolution to identify grain boundary misorientation¹³. In the vast majority of APT data sets published, the identification of different lattice planes from different grains is either not done or is not possible because of inherent reconstruction issues associated with the APT technique¹⁴. In contrast, electron diffraction and high resolution transmission electron imaging can provide the grain boundary misorientation and even solute identification¹⁵⁻¹⁷, but the two-dimensional projection limits the depth perspective of the solute over the grain boundary and even the determination of the inclination angle of the boundary. In addition, the imaging of the boundary also requires that it is orientated to a specific crystallographic zone axis to meet the imaging requirements. As with APT, electron-based imaging also has experimental limitations in its ability to quantify solute-boundary interactions.

To overcome those issues, in recent years, cross-correlated electron microscopy with atom probe has been used^{18,19}. For example, Li *et al.*¹⁸ used electron backscatter diffraction (EBSD) to identify prior austenite grain boundaries in steel from which site specific focus ion beam (FIB) lift out samples were prepared into the APT required needle-shape geometries. The results revealed B and Mo segregation to these boundaries. More recently, Herbig *et al.*¹⁹ directly FIB lifted out and annular ion milled a ferrite steel APT specimen and directly performed transmission electron diffraction of the APT specimen needle which subsequently mapped out the grain boundary misorientations within the tip. The tip was field evaporated and the atom map was reconstructed with *a priori* knowledge of the grain boundary types revealing C segregation behavior between low and high angle grain boundaries.

In this paper we further those efforts by quantifying the solute segregation to specific nanocrystalline grains using precession electron diffraction (PED)²⁰⁻²² and APT. Unlike these prior experimental studies, we have expanded the work to directly compare the findings to computational predictions for specific types of grain boundaries and their segregation. As these types of cross correlation microscopy experiments are difficult, the development of simulations that predict solute segregation to specific grain boundary types are needed.

A simulated grain boundary will require the full character of the boundary to be known, which can pose a challenge to several of the current experimental diffraction techniques. For instance, two-dimensional EBSD images provide three of the five parameters needed to fully define a grain boundary²³. To achieve the missing parameters, the material must be serial sectioned to reveal the sub-surface grain boundary inclination angle²⁴. Though similar restrictions can also exist in PED scans, recent work by Kiss *et al.*²⁵⁻²⁷ has shown how the inclination angle can be estimated by a weight average from the overlapping transmission diffraction patterns across the boundary. Moreover, one could also conceive using the APT data set volume itself to reveal the grain boundary topology¹³. This information could then be coupled to the prior diffraction of the boundary. However, the identification of the APT

boundary surface necessitates particular reconstruction artifacts, such as a density variations, to be used to identify the boundary. Often these variations will not be uniform over the surface creating inconsistencies in the topology. If solutes are used to identify the boundary surface, then those solutes also need to form a uniform coverage which may not be the case. These examples provide some of the experimental challenges one can encounter in providing the full character identification of an experimental boundary.

In this work, we detail our use of PED with the intrinsic morphology of a thin film columnar grain boundary to overcome those challenges such that the full character of the boundary could be revealed and linked to the simulations. Revealing that full character of the boundary is critical as recent simulation work has shown the importance of the inclination angle on grain boundary energies and motilities. For example, in body centered cubic metals, the $\Sigma 3$ boundary energy was highly sensitive to the inclination angle whereas $\Sigma 5$ were found to be more invariant²⁸⁻³¹. Homer *et al.*³² have reported how the grain boundary inclination angle is sensitive to the mobility of equivalent Σ boundaries even when those boundary energies were similar.

In this paper, using computational methods, we examine specific boundaries and how their grain boundary energies change with Cr solute segregation. Using that information, we compare the interfacial excess of those simulated Σ boundaries to experimentally measured Σ boundaries. By linking the experiment with these models, we are able to better understand the solute-boundary segregation behavior. These models then provide information on segregation over a larger compositional range without the need for the laborious experimental effort.

Our test material is a nanocrystalline Fe-8 at.% Cr thin film prepared by sputter deposition. We have recently reported how minor Cr additions to Fe can be used to change the as-deposited thin film stress state³³. In that report, we described how the tensile stress varied with grain size with the grain

size controlled by Cr segregation. Atom probe results in that work revealed a range of Gibbsian interfacial excess values for the boundaries studied which suggested boundary specific segregation behavior. However this was never confirmed and provided motivation for this new work. Besides thin films, larger scaled Fe-Cr systems are of strong technical interest because of their resistance to radiation effects, *e.g.* damage accumulation and swelling in future nuclear reactors^{34,35}. Atom probe studies in these alloys has been done to address its spinodal decomposition³⁶⁻⁴¹. Marquis's group⁴²⁻⁴⁶ has shown that Cr segregation to specific grain boundaries does occur with respect to phase instability under irradiation conditions. Using EBSD, a specific grain boundary from a coarse grain material was extracted, FIB milled into the APT needle shape, and field evaporated in the atom probe. The results revealed irradiation enhanced Cr segregation to the $\Sigma 3$ boundary with very little effect on low angle grain boundary (LAGBs) which were denoted as $\Sigma 1$ boundaries⁴². Others have reported how Cr can desegregate from the boundaries after irradiation^{47, 48}.

Experimental details

The case study material was deposited as a 300 nm thick Fe-8 at.% Cr film by co-magnetron sputtering from 99.95 at.% pure elemental Fe and Cr targets in an AJA ATC-1500 stainless steel chamber. Prior to deposition, the base pressure was $< 5 \times 10^{-8}$ Torr where upon ultrahigh purity Ar was flowed into the chamber to 2 mTorr and served as the working gas. The film was grown on a Si [001] wafer which had a native surface oxide. After deposition, the film phase was identified to be a solid solution body centered cubic structure by X-ray Diffraction via a Philips diffractometer with Cu K_{α} radiation as the source operated at 45 keV and 40 mA.

The film was prepared into an atom probe tip by extracting the sample in cross section (parallel to the film-substrate interface) using FEI Quanta dual electron beam-FIB microscope. *In situ* Pt, using a Gas Injection System, was deposited over the film's region of interest to serve as a protective coating

during the FIB milling, as shown in Fig. 1 (a). The extracted film wedge was then attached to a silicon half grid, Fig. 1 (b)⁴⁹, whereupon it was annular ion milled at 30 keV using a range of step down ion currents from 137 to 32 pA in a Tescan Lyra dual beam FIB, Fig. 1 (c). When the final tip shape was approached (radius of curvature ~ 100 nm), the milling parameters were reduced to 5 keV 25 pA to reduce Ga⁺ implantation and surface damage. Further details of the sample preparation method can be found in references^{50,51}.

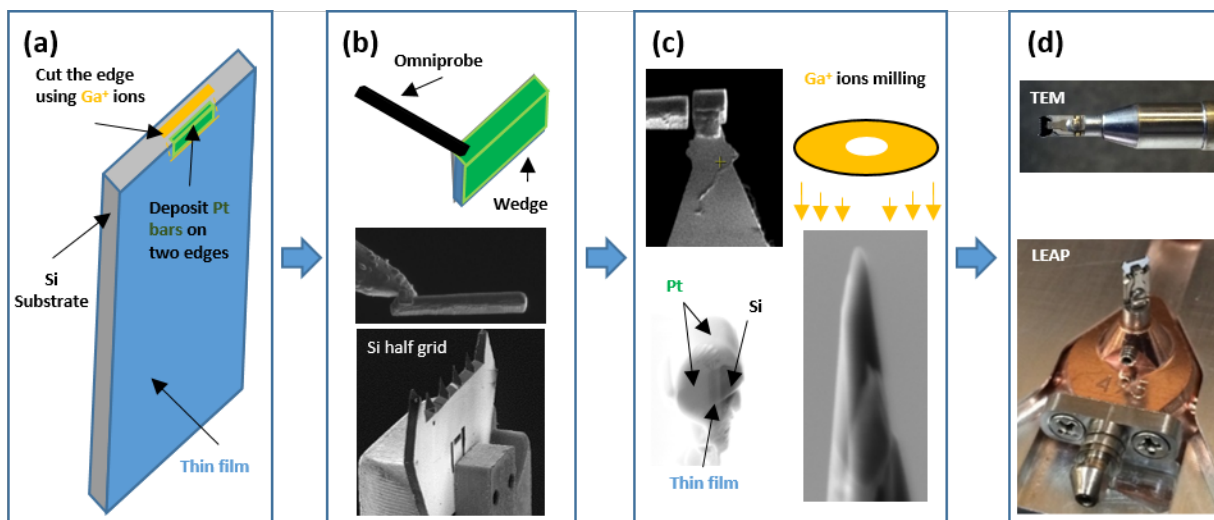


Figure 1: The procedure to prepare sample for correlative TEM and APT: **(a)** the bar with Pt protection on the top and left was cut by Ga⁺ ions; **(b)** the bar was lift out by Omniprobe. Si half grid into a hummingbird hold was also shown; **(c)** pieces of the bar were mounted to the top of Si half grid and milled and cleaned up by Ga⁺ ions using 30 kV and 5kV, respectively; **(d)** the grid holder fitted directly into a hummingbird Tecnai F20 TEM single-tilt holder. Modification of a Cameca puck specimen assembly that allows the insertion of the hummingbird holder into the local electrode atom probe (LEAP) instrument. (Color available on-line)

With the APT tip prepared, the specimen was loaded into a Hummingbird TEM holder, Fig. 1 (d), and placed into a FEI Tecnai F20 S(TEM) operated at 200 keV. The grain-to-grain mapping of the film was conducted using the precession electron diffraction (PED) technique from the Nanomegas ASTAR™ platform²⁰⁻²². By focusing the electron beam, a high spatial resolution for point-to-point diffraction imaging is achieved; coupled with precessing the beam, the dynamical diffraction effects are reduced allowing the diffracted intensities to be more uniform and kinematical in nature²⁰. In addition, the precessed beam intersects more of reciprocal space increasing the number of diffracted reflections which increases the confidence for identifying the diffraction pattern. The collected patterns are indexed and the rotation between diffracted patterns used to quantify the grain boundary character using an off-line TSL OIM Analysis 7 software package. The estimated inclination angle of the grain boundary using the PED was done following the procedure by Kiss *et al.*²⁵ with details specific to this work given in the supplementary material section. For these experiments, the beam was precessed at 0.1° at a scanning step size of 2 nm. After completing the PED scan, the tip was moved to a Cameca puck specimen assembly, Fig. 1 (d), and field evaporated in a Cameca Instruments Local Electrode Atom Probe 3000 XSi operated with a specimen set point of 37 K, laser pulse energy of 0.3 nJ at a pulse repetition rate of 200 kHz for a 0.5% atoms per pulse detection rate. The atom probe data sets were analyzed using the IVAS 3.6 platform with the interfacial excess measurements done in a manner previously reported by the authors in reference³³. Note, between the PED scan and the LEAP analysis, the APT tip was subjected to a brief, 5 keV Ga⁺ ion milling step to remove any surface and hydrocarbon damage created during the PED scan.

A TEM plan-view foil was also prepared by cutting, dimpling, and ion-milling a 3 mm disc. This foil provided a larger field of view of the nanocrystalline film to confirm phase, grain sizes, and grain boundary misorientations using the aforementioned NanoMEGAS PED platform. The TEM foil analysis provided a benchmark comparison to determine the representative nature of the boundaries quantified

in the much smaller field of view provided by the APT tip. A TEM cross-sectional foil was also prepared by a FIB lift out technique with its grain boundaries quantified using PED. These results verified the columnar (linear) nature of the boundaries through the film thickness.

Computational details

The computational simulations for twenty-seven types of Σ boundaries were done to provide insights into solute segregation specificity using the methods in reference⁵². Of these twenty-seven boundaries, six specific type of boundaries were found in the experimental data set and provide the major discussion of the paper. The relevant information concerning the balance of these other boundaries are provided in the supplementary section. Of these six boundaries, several different orientation angles were done for each boundary type to determine the influence of inclination angle on the asymmetric boundary energy. The tilt grain boundary was created by rotating two BCC grains pertaining to a tilt axis, $\langle uvw \rangle$, and joining the two grains by a grain boundary with the Miller index (hkl) ^{52,53} creating a single boundary between the two lattices. The following relationship is required since the tilt axis and grain boundary plane must be parallel (1):

$$\begin{pmatrix} u \\ v \\ w \end{pmatrix} \cdot \begin{pmatrix} h \\ k \\ l \end{pmatrix} = 0 \quad (1)$$

The (hkl) of the grain boundary plane is associated with the tilt angle, θ , with respect to the $\langle uvw \rangle$ tilt axis:

$$\cos \frac{\theta}{2} = \frac{|vh-uk|}{\sqrt{(u^2+v^2)(h^2+k^2+l^2)}} \quad (2)$$

The minimum grain boundary structure was defined as rectangular cells that satisfied this periodic condition. The created CSL grain boundaries are given in Table 1, which have been relaxed using the Molecular Dynamics (MD) conjugate gradient minimization energy procedure. The work only minimizes

a single structure. Though the selected grain boundary does not in of itself indicate the minimum energy structure, the simple structure of the boundary likely is the minimum or is a structure whose energy is closely related to the minimum energy structure as suggested by the work of Olmsted *et al.*⁵⁴.

Fig. 2 is a representation of part of these boundaries where the yellow lines serve as guides to identity the lattice and tilt angle; the black lines on either side of the boundary reveal the repeated atomic structure for that particular special character arrangement. The LAGB was constructed by tilting two grains with a small angle at either 4° or 8° which would technically classify them as a symmetric Σ 1 boundary. This created a periodic edge dislocation spaced along the boundary with most of the lattice structure on either side of the boundary overlapping. This approximation is reasonable because of the low degree of coincidence associated with those CSL values. Since LAGBs have a range of misorientations, it is not reasonable to simulate every possible angle; hence we have averaged the findings between the values found in these specific LAGB simulations and reported the maximum and minimum values on the forthcoming simulated plots. The random high-angle grain boundary (HAGB) network was simulated using a polycrystalline structure based on reference⁵⁵. Table 1 contains the tabulation of these and all Σ - constructed grain boundaries, with the ones bolded in the table highlighting the relevant boundaries that will be discussed in the paper (with the non-bolded boundaries found in the supplementary section).

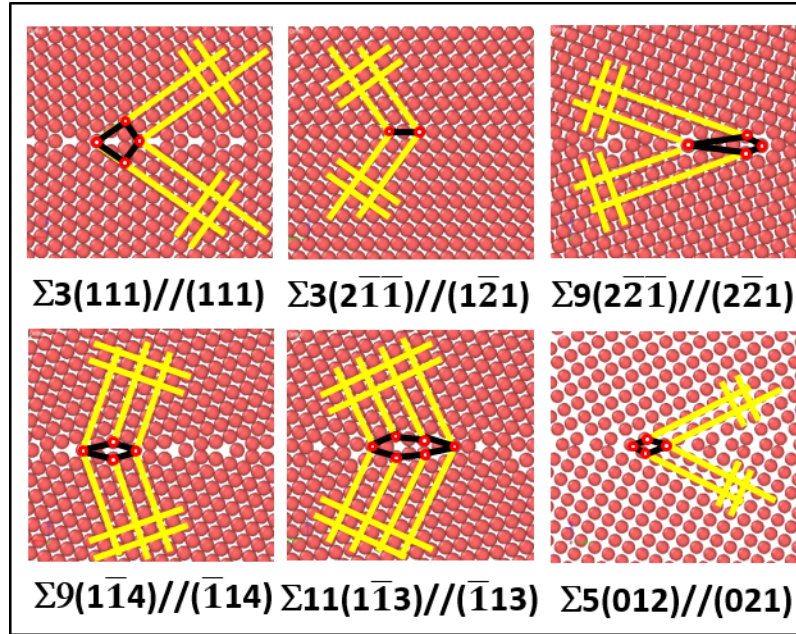


Figure 2: Structural views of CSL grain boundaries. The yellow lines guide the eye for the lattice structure whereas the black lines reveal the repeat structure of the boundary. (Color available on-line)

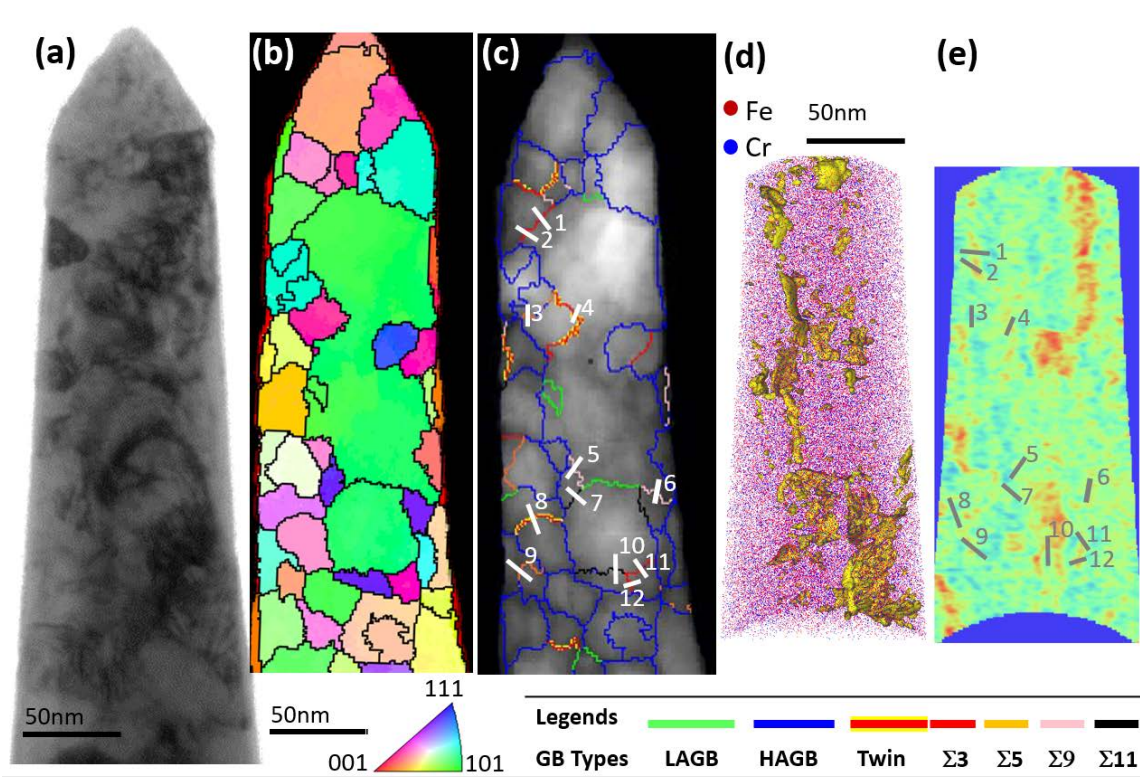
Using these boundaries, we have implemented a progressive computation method that is a hybrid algorithm combining MD and Monte Carlo (MC) to determine the preferential segregation of Cr to these Fe grain boundaries⁵⁶. The code was run using LAMMPS⁵⁷ with the Fe-Cr binary concentration dependent embedded atom model potential found in reference⁵⁸. To change the Cr content, we adjusted the system's chemical potential until the Cr content matched the targeted composition. We performed both a variance-constrained semi-grand-canonical ensemble and a semi-grand-canonical ensemble and noted that the results were similar for both methods over the compositions range from 0 – 14 at.% Cr. One MC cycle was carried out per 10^2 MD steps. The equations of motion were integrated for 10^5 MD steps, which included the 10^2 MC cycles, using a time step of 2 fs. Temperature and pressure were maintained using the Nose-Hoover thermostat and barostat, respectively.

Table 1: Structural information for the various CSL GBs studied. The first group are the symmetric GBs, the second is the LAGBs, the third is the asymmetric tilt Σ GBs, and the last un-bolded designation are the GBs discussed in the supplemental material, as those misorientation were not observed experimentally.

Type	Tilt axis	GB plane	Tilt angle	Inclination Angle	No. of atoms
$\Sigma 3$	$\langle 110 \rangle$	$(111)//(111)$	70.5°	90°	51840
$\Sigma 3$ Twin		$(2\bar{1}\bar{1})//(1\bar{2}1)$	109.5°	0°	55296
$\Sigma 9$		$(2\bar{2}\bar{1})//(2\bar{2}1)$	38.9°	90°	54432
		$(1\bar{1}4)//(\bar{1}14)$	141.1°	0°	51840
$\Sigma 11$		$(1\bar{1}3)//(\bar{1}13)$	129.5°	0°	57024
$\Sigma 5$	$\langle 100 \rangle$	$(012)//(021)$	53.1°	45°	56160
$\Sigma 801$	$\langle 110 \rangle$	$\{1\ 1\ 40\}$	4.0°	0°	57600
$\Sigma 201$		$\{1\ 1\ 20\}$	8.1°	0°	57600
$\Sigma 3$	$\langle 110 \rangle$	$(1\bar{1}1)//(\bar{1}\bar{1}5)$	109.5°	21°	62150
		$(100)//(2\bar{1}2)$		37°	54416
		$(55\bar{1})//(711)$		51°	66066
		$(110)//(411)$		61°	51814
$\Sigma 9$		$(1\bar{1}1)//(1\bar{1}5)$	141.1°	35°	62208
		$(1\bar{1}2)//(5\bar{5}2)$		55°	58320
$\Sigma 11$		$(5\bar{5}4)//(1\bar{1}8)$	129.5°	35°	71280
		$(4\bar{4}1)//(2\bar{2}5)$		55°	76032
		$(3\bar{3}2)//(3\bar{3}2)$		90°	63360
$\Sigma 5$	$\langle 100 \rangle$	$(031)//(03\bar{1})$	36.9°	0°	58240
		$(010)//(04\bar{3})$		18°	52000
		$(110)//(071)$		26°	62400
$\Sigma 7$	$\langle 111 \rangle$	$(3\bar{2}\bar{1})//(2\bar{3}1)$	38.2°	-	50400
$\Sigma 13a$	$\langle 100 \rangle$	$(023)//(032)$	22.6°	-	56784
$\Sigma 15$	$\langle 210 \rangle$	$(1\bar{2}5)//(\bar{1}25)$	48.2°	-	57600
$\Sigma 17a$	$\langle 100 \rangle$	$(041)//(04\bar{1})$	28.1°	-	53040
$\Sigma 17b$	$\langle 221 \rangle$	$(3\bar{2}\bar{2})//(2\bar{3}2)$	61.9°	-	48960
$\Sigma 19a$	$\langle 110 \rangle$	$(3\bar{3}\bar{1})//(3\bar{3}1)$	26.5°	-	54720
$\Sigma 19b$	$\langle 111 \rangle$	$(5\bar{3}\bar{2})//(3\bar{5}2)$	46.8°	-	58368

Results and discussion

Fig. 3 is the correlative bright field TEM image [Fig. 3(a)] with the PED grain orientation map [Fig. 3(b)-(c)] as well as various atom probe map reconstructions [Fig. 3(d)-(e)] from the APT specimen. Electron diffraction confirmed that the alloy was a solid solution, body centered cubic, A2, phase. The reconstructed atom map contained over 47 million ions collected from a 220 nm vertical length. By comparing the isoconcentration reconstruction, Fig. 3(e), to the PED quality index boundary map, Fig. 3(c), we are able to directly correlate the composition to the specific grain boundary character. From the boundary map [Fig. 3(c)], we identified twenty-three grain boundaries with either LAGBs (2 GBs), HAGBs (9 GBs), or one of the five special character boundary types – $\Sigma 3$ (twin) (2 GBs), $\Sigma 3$ (4 GBs), $\Sigma 5$ (2 GBs), $\Sigma 9$ (2 GBs), and $\Sigma 11$ (2 GBs). The positions of special character boundaries were marked in Fig. 3(c) & (e).



1. **Table 2:** List of GB characters and the corresponding interfacial excess data for the experimental CSL GBs investigated. The No. value represents where that boundary is located in reference to Fig. 3. The misorientation, deviation, rotation axis, and the orientation (1) and (2) (for the grains), and the GB planes are extracted directly from the reconstructed PED data using the OIM software. The inclination angle “REF” refers to reference inclination angle as described in the supplementary section and the inclination angle “PED” refers to measured values from the method found in the paper of Kiss *et.al.*²⁵ also detailed in the supplementary section. Finally the interfacial excess, IE, for each to the measured special character boundaries is given.

2.	Sigma	3.	No.	Mis-orientation	Deviation	Rotation axis	Orientation (1)	Orientation (2)	GB planes	Inclination angle (REF)	Inclination angle (PED)	IE (atoms/nm ²)
4.	$\Sigma 3$ (Twin)	5.	08	59.3°	0.7°	$[\bar{1} 1 1]$	$(\bar{4} \bar{3} \bar{8})[1 28 \bar{1}\bar{1}]$	$(2 1 5)[9 7 \bar{5}]$	$[7 25 \bar{1}\bar{2}]/[\bar{1}\bar{4} \bar{1}\bar{9} 10]$	4°	5°	-0.05
6.		7.	04	59.6°	2.2°	$[13 \bar{1}\bar{3} 12]$	$(19 2 20)[8 \bar{6} \bar{7}]$	$(5 4 20)[\bar{4} 15 \bar{2}]$	$[12 \bar{1}\bar{9} \bar{1}\bar{0}]/[\bar{3} \bar{2}\bar{8} 6]$	11°	15°	0.33
8.	$\Sigma 3$	9.	02	59.5°	7.2°	$[\bar{1}\bar{9} 16 14]$	$(\bar{1}\bar{8} \bar{3} \bar{2}\bar{3})[\bar{9} 8 6]$	$(14 1 16)[6 \bar{4} \bar{5}]$	$[\bar{1} 19 \bar{1}]/[\bar{1}\bar{5} \bar{1}\bar{0} 14]$	32°	16°	3.63
10.		11.	01	59.5°	7.2°	$[\bar{1}\bar{9} 16 14]$	$(\bar{1}\bar{8} \bar{3} \bar{2}\bar{3})[\bar{9} 8 6]$	$(14 1 16)[6 \bar{4} \bar{5}]$	$[\bar{4} 13 2]/[\bar{1}\bar{1} \bar{2} 10]$	50°	9°	3.83
12.		13.	11	58.0°	8.4°	$[18 \bar{1}\bar{4} 13]$	$(\bar{5} \bar{1} \bar{5})[\bar{6} \bar{5} 7]$	$(7 6 26)[10 \bar{2}\bar{9} 4]$	$[\bar{1}\bar{6} 1 16]/[\bar{2}\bar{0} 17 1]$	59°	-	7.93
14.		15.	12	59.6°	6.1°	$[4 5 \bar{4}]$	$(1 1 4)[2 \bar{6} 1]$	$(8 8 11)[\bar{1}\bar{9} 41 \bar{1}\bar{6}]$	$[\bar{1}\bar{4} \bar{1}\bar{1} 6]/[\bar{4} \bar{3} 5]$	90°	-	7.34
16.	$\Sigma 5$	17.	09	36.0°	5.4°	$[\bar{3} \bar{2}\bar{0} 0]$	$(15 5 18)[\bar{9} \bar{9} 10]$	$(\bar{8} \bar{3} \bar{2}\bar{4})[15 24 \bar{8}]$	$[\bar{5} \bar{1}\bar{9} 10]/[\bar{1}\bar{6} \bar{9} 6]$	24°	-	0.40
18.		19.	03	34.4°	6.4°	$[0 \bar{6} \bar{1}]$	$(3 1 3)[\bar{4} 9 1]$	$(1 1 5)[\bar{8} 23 \bar{3}]$	$[\bar{4} 9 1]/[7 \bar{2}\bar{2} 3]$	38°	22°	0.45
20.	$\Sigma 9$	21.	06	41.3°	4.6°	$[\bar{2}\bar{3} \bar{1} 19]$	$(\bar{9} \bar{1} \bar{9})[11 9 \bar{1}\bar{2}]$	$(2 2 3)[\bar{3} 6 \bar{2}]$	$[11 18 \bar{1}\bar{3}]/[5 \bar{2}\bar{6} 14]$	24°	-	2.89
22.		23.	05	38.7°	3.2°	$[\bar{1}\bar{7} 0 20]$	$(8 1 8)[11 \bar{8} \bar{1}\bar{0}]$	$(19 17 25)[\bar{1}\bar{6} 37 \bar{1}\bar{3}]$	$[5 \bar{2}\bar{4} \bar{2}]/[\bar{6} \bar{1}\bar{3} 14]$	59°	-	0.45
24.	$\Sigma 11$	25.	10	49.5°	2.4°	$[10 0 \bar{1}\bar{1}]$	$(\bar{9} \bar{1} \bar{9})[\bar{1}\bar{2} \bar{9} 13]$	$(8 8 11)[\bar{1}\bar{9} 41 \bar{1}\bar{6}]$	$[\bar{2}\bar{0} \bar{9} 21]/[6 \bar{9} 2]$	6°	19°	2.03
26.		27.	07	49.1°	1.7°	$[\bar{2}\bar{2} 21 0]$	$(5 5 7)[\bar{1}\bar{3} 27 \bar{1}\bar{0}]$	$(\bar{2}\bar{2} \bar{3} \bar{2}\bar{3})[\bar{1}\bar{6} \bar{1}\bar{3} 17]$	$[\bar{2}\bar{3} 17 5]/[14 \bar{4} \bar{1}\bar{3}]$	51°	-	1.07

Figure 3: (a) TEM image of the Fe 8 at.% Cr atom probe tip (b) PED orientation map of the same atom probe tip (c) CSL boundary line map laid over the image quality map of the tip; (d) Atom map image with grain boundaries delineated by an isodensity surface (e) 2D composition profile map with grain boundary sequences overlaid. (Color available on-line)

To determine if the $\Sigma 3$ was or was not a twin involved two criteria. First, the misorientation across a grain boundary must be very near the twin misorientation, which was readily identified by the OIM reconstruction software from the PED patterns. The second criteria involved the boundary plane coinciding with the twin plane. Though this is more difficult (if not impossible) to identify in two-dimensional projections, one can assess whether the trace of the boundary plane is aligned with the trace of the twinning plane as a partial check. When that occurs, the boundary, approximately 90% of the time, is a twin⁵⁹. This provided a fairly high confidence means in twin identification. Subsequently, the twins were also confirmed by a comparison of their deviation from the symmetric plane position taken from the PED scan itself in our inclination angle determination. This, and all other boundaries, inclination angles are tabulated in Table 2.

The inclination angle was determined by either measuring the PED projected boundary by the method in reference²⁵ and/or assuming that the boundary itself was perpendicular to the plane normal when the PED scan was inconclusive. This latter assumption was confirmed by the TEM cross sectional view, Fig. 4(a), which showed the columnar morphology of the boundary. To validate that the APT tip is representative of the specimen as a whole, a PED scan over a planar TEM foil capturing over 800 grains, Fig. 4(b) and (c), was performed. Though the APT analysis region is smaller, we noted the same grain boundary types with good agreement with respect to their fractional lengths in the material between the two PED scans, Table 3.

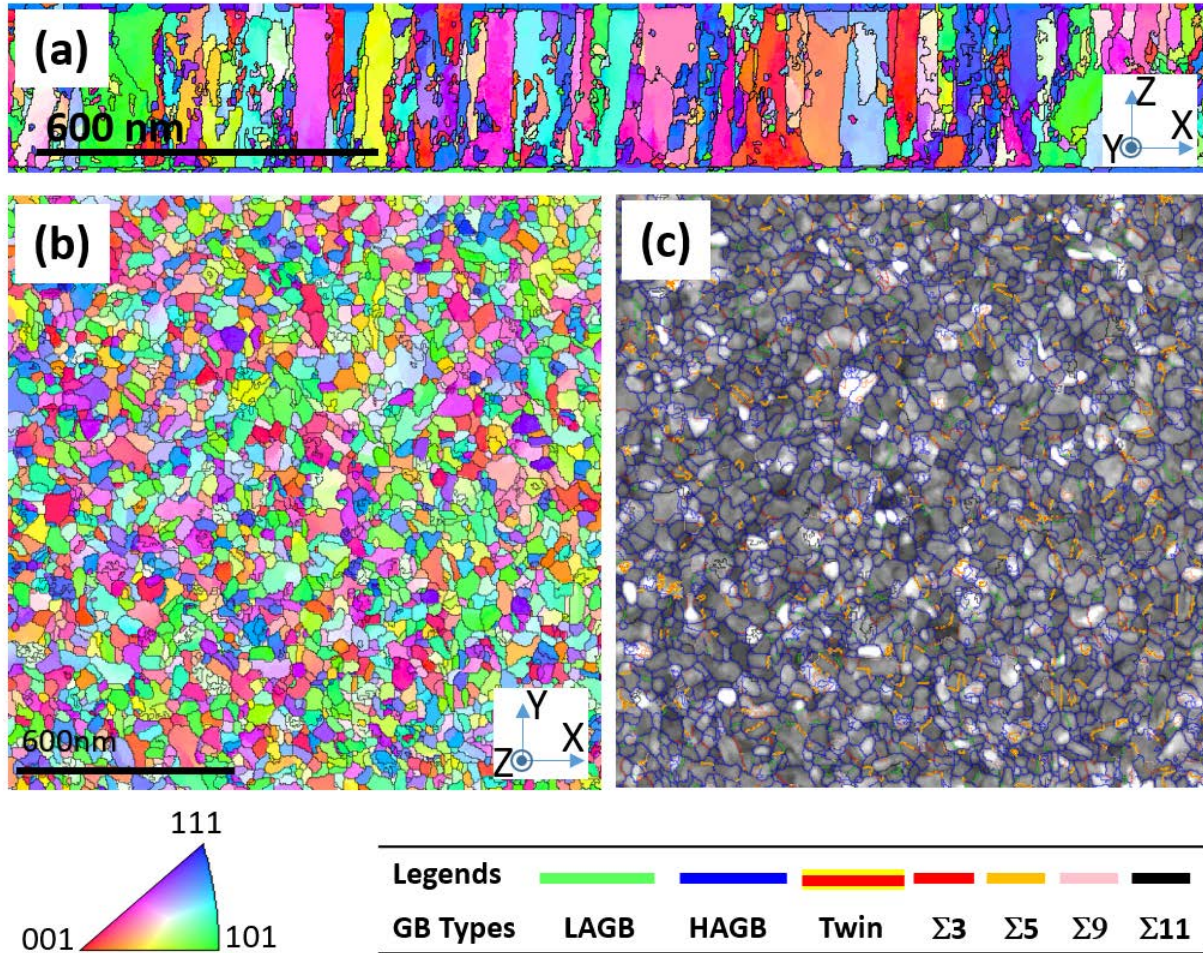


Figure 4: (a) Cross-sectional and (b) Plan-view PED orientation map with (c) Different grain boundary lines laid over the image quality map for the $\text{Fe}_{0.92}\text{Cr}_{0.08}$ film (Color available on-line)

Table 3: Fraction of grain boundaries in the APT tip and planar TEM foil

Type	LAGB	HAGB	$\Sigma 3$ (Twin)	$\Sigma 5$	$\Sigma 9$	$\Sigma 11$
Fraction APT Tip	5.9%	75.3%	9.4%(4.6%)	3.1%	3.5%	2.8%
Planar foil	5.2%	74.1%	11.0%(5.2%)	3.4%	2.9%	3.4%

With the grain boundaries now identified in the atom probe data set, the experimental Gibbsian interfacial excess, Γ_{Cr} , of Cr solute at those boundaries was calculated⁶⁰ and tabulated in Table 2. The HAGBs, followed by $\Sigma 3$, revealed the highest concentration of solute species than any other boundary. Our findings are consistent with prior reports of other solute segregates in Fe-based alloys by Herbig *et al.*⁶¹ and Hu *et al.*⁴², who also noted a solute segregation preference to $\Sigma 3$ boundaries.

From the correlated PED-APT data set, it is clear that preferential partitioning of Cr to specific grain boundaries has occurred. To understand this boundary specific segregation behavior, as well as survey the effect of Cr segregation over a larger compositional range and boundary types, the hybrid MD / MC simulation was performed.

Fig. 5(a) is a series of plots of simulated Cr segregation behavior for the Fe-8%Cr alloy at various inclination angles. The $\Sigma 3$ grain boundary energy appears to be the most sensitive to inclination angle. As the inclination angle increased, so did the grain boundary energy, Fig. 5(a), which is consistent with prior reports³². The other special character boundaries – $\Sigma 5$ and $\Sigma 11$ – also showed some modest increase in energy with inclination angle in contrast to $\Sigma 9$, which was relatively invariant over the inclination angle range.

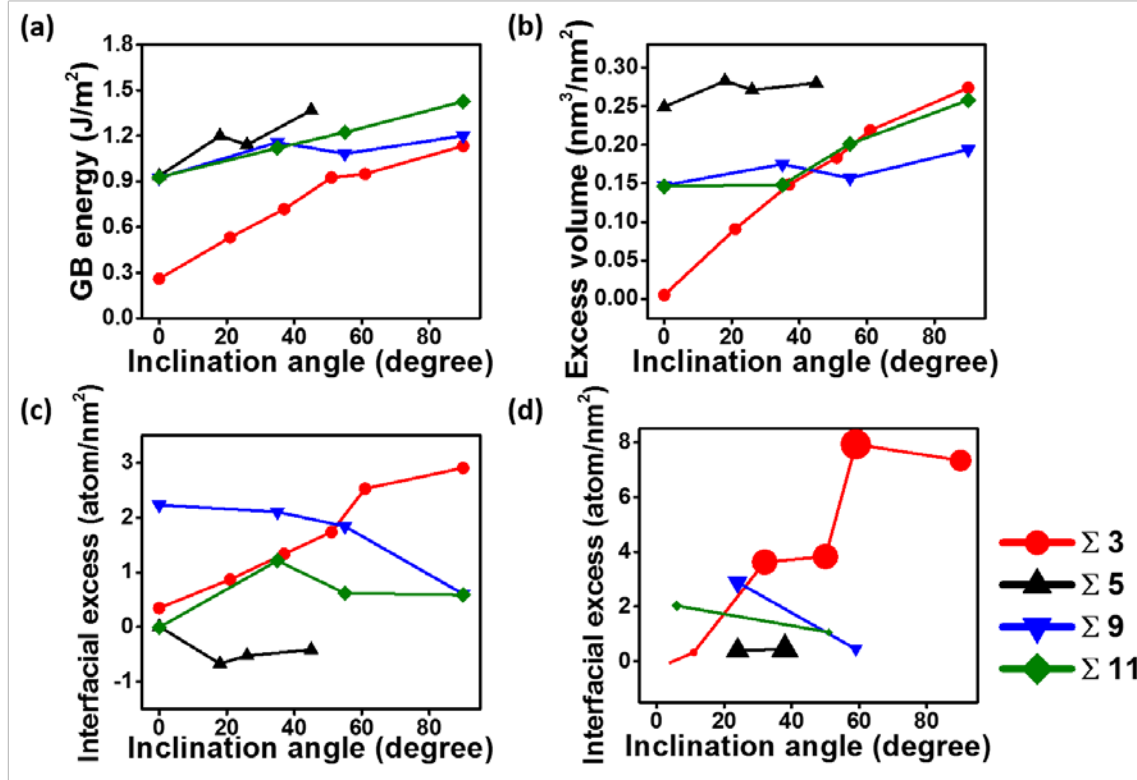


Figure 5: (a) Calculated grain boundary energy (b) Calculated excess volume (c) Calculated and (d) Experimentally measured interfacial excess for $\Sigma 3$, $\Sigma 5$, $\Sigma 9$ and $\Sigma 11$ asymmetric GBs as a function of inclination angle. The symbol size in Fig. 5(d) was in direct proportion to the deviation of the values measured for those particular misorientation angle for those GBs. (Color available on-line)

Since segregation could be influenced by the reduction of excess volume in the boundary by Cr, we have also explored the change in grain boundary excess volume and the solute energetic distribution in those special character boundaries^{53,62}. In the case of the volume excess change, the Cr atom is a slightly larger atom than Fe⁶³ where one can expect that Cr at the grain boundary would reduce the excess grain boundary volume. Hence, the volume excess, V_{excess} , was computed as

$$V_{excess} = \frac{V_{CSL} - N_{CSL}V_{atom}}{A_{GB}} \quad (3)$$

where V_{CSL} is the simulated volume that contains the CSL boundary, N_{CSL} is the number of atoms in total volume, V_{atom} is the average atomic volume for a specified composition but with no CSL boundary, and A_{GB} is the surface area of the CSL grain boundary in the simulated volume. Fig. 5(b) is a plot of how that volume would change with inclination angle for each of the identified boundaries in this study.

Comparing Fig. 5(a) and (b), similar trends can be noted, with the excess volume increasing the most for the $\Sigma 3$ boundary for the Fe-8%Cr alloy. However, of all the boundaries, only the $\Sigma 3$ shows a clear increase in the interfacial excess of Cr with increasing inclination angle, Fig. 5(c). $\Sigma 11$ predicts a modest increase and then decrease in interfacial excess initiating near 30° inclination; $\Sigma 5$ revealed a strong preference for rejecting Cr from its boundary regardless of inclination angle; and $\Sigma 9$ indicated a reduction of Cr concentration in its boundary with increasing inclination angle. Of all Σ boundaries, $\Sigma 3$ provides a consistent trend between boundary energy, increase in excess volume, and increase in solute concentration with increases in the inclination angle. This suggests that as this boundary becomes more asymmetric, changes in Cr segregation will be the most sensitive (noticeable).

Fig. 5(d) is a plot of the experimentally determined excess for each of the boundaries quantified by the cross correlation microscopy. Comparing these findings with the predicted interfacial excess in Fig. 5(c), the trends as a function of inclination angle are in good agreement, with $\Sigma 3$ showing an increase in interfacial excess with inclination angle; $\Sigma 5$ being invariant and very low (near zero); and $\Sigma 9$ and $\Sigma 11$ revealing a decrease in solute concentration with increasing angle. Considering the limited number of boundaries that could be captured within the finite field of view of the APT reconstruction, the good agreement with the predicted trends adds confidence in the more limited experimental findings.

Though the trends were in good agreement, in general, all of the boundaries did reveal slightly higher absolute values in the experimental interfacial excess than predicted values; the exceptions being

the $\Sigma 9$ and $\Sigma 11$ at the higher inclination angles where close agreement with the predicted values was seen. The most dramatic differences in absolute values was noted for the $\Sigma 3$, being nearly 2.5 times larger. Though the exact reasoning for this difference is not fully understood, particularly considering consistent trends between the two studies as well as some limited boundaries having a much closer agreement with each other, one potential source could be the thin film process itself. During deposition, the segregation to those boundaries had not achieved the lowest energy state since they were not annealed. During the dynamic growth of the Fe(Cr) film, as the grain boundaries developed during film coalescence, it is possible that excess Cr was likely incorporated within some of these special character boundaries. Computational modeling the effects of solute segregation during film growth is the subject of ongoing work by the authors and is beyond the scope of the current work. Regardless of the absolute value difference, the experimental values are realistic and within the correct order of magnitude of the predictions and mimic the predicted trends added confidence in linking the two studies. For easier comparison, a histogram of the experimentally measured and computationally predicted Γ is plotted in Fig. 6, with the addition of both the low and high angle grain boundaries, which will be discussed in further detail below.

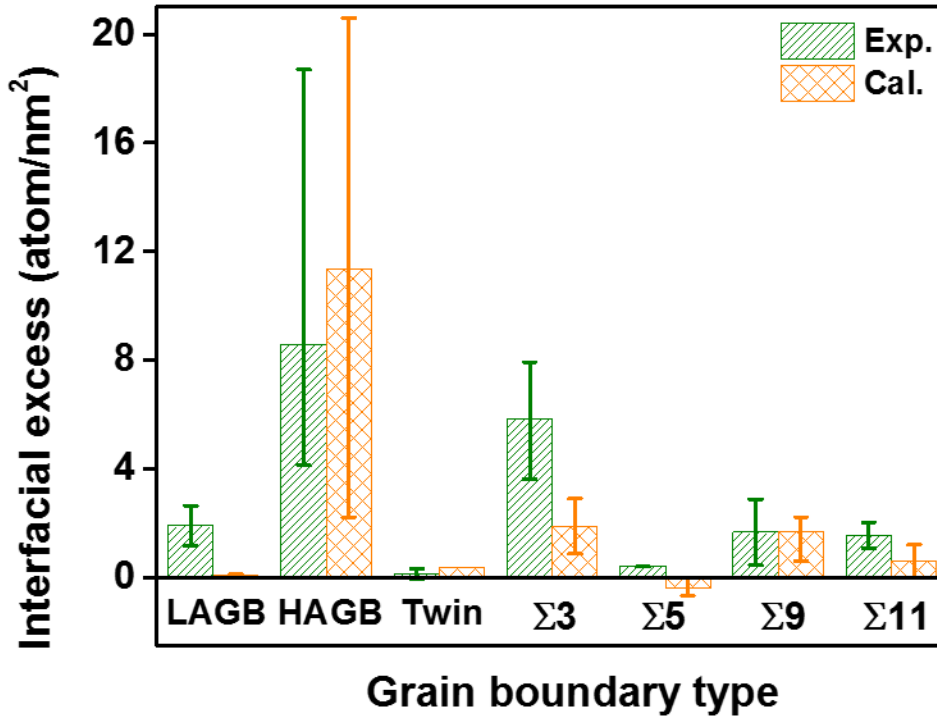


Figure 6: Experimental and simulated interfacial excesses varying with grain boundary types. Error bars represent upper and lower limits. Cal. (calculated) refers to the simulated boundaries. (Color available on-line)

To expand our computational study, we have also looked at the segregation as a function of Cr content for specific boundary constructions, $\Sigma 3(111)//(111)$, $\Sigma 3(2\bar{1}\bar{1})//(1\bar{2}1)$ (twin boundary), $\Sigma 9(2\bar{2}\bar{1})//(2\bar{2}1)$, $\Sigma 9(1\bar{1}4)//(\bar{1}14)$, $\Sigma 11(1\bar{1}3)//(\bar{1}13)$ and $\Sigma 5(012)//(021)$. Fig. 7(a) is a plot of grain boundary energy with increasing Cr content, where the energy values for the majority of these boundaries were reduced⁶⁴; the exceptions being the $\Sigma 3(2\bar{1}\bar{1})//(1\bar{2}1)$ (twin boundary) and $\Sigma 5$ boundaries, Fig. 7(a). The Cr is predicted to have discernable segregation to all of those represented boundaries expect, again, the twin and the $\Sigma 5$, which were nearly invariant, Fig. 7(b). Recall that $\Sigma 5$ was

also relatively invariant in response with inclination angle for Fe-8%Cr composition, Fig. 5. For the boundaries where segregation was predicted, the interfacial excess was the largest at the lower Cr contents. In all of these cases, the amount of grain boundary energy reduction (and segregation tendency) was not found to be equivalent for each boundary type. This was similar to the inclination study previously discussed; where the $\Sigma 5$ and $\Sigma 9$ grain boundary energy increased or was relatively consistent, respectively, with inclination angle but the interfacial excess was invariant or decreased respectively for each of these boundaries. In these new studied boundaries, the $\Sigma 3(111)/(111)$ appeared to have a monotonic reduction in energy with increasing Cr content whereas $\Sigma 9(2\bar{2}\bar{1})/(2\bar{2}1)$ revealed an initial decrease with a ‘leveling-out’ of the energy with Cr content, Fig. 7(a).

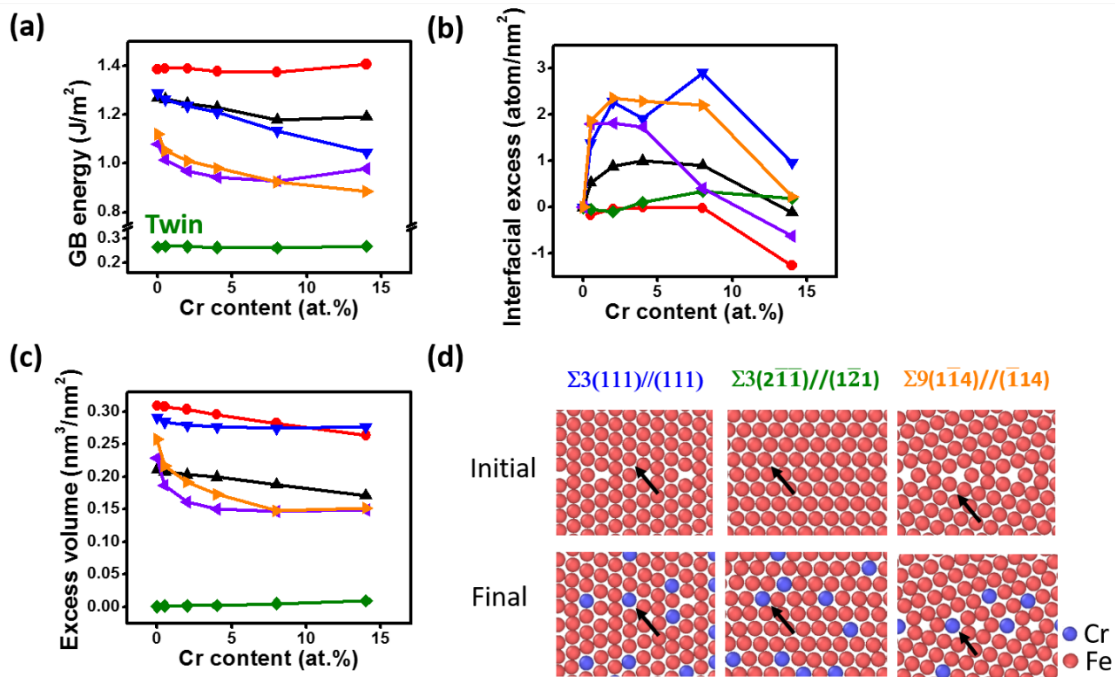


Figure 7: (a) Calculated grain boundary energies (b) Interfacial excess and (c) Excess volume for various Cr contents for specific Σ -GBs. (d) Simulated atomic configuration for Σ -GBs with and without Cr segregation. The arrows direct to local lattice locations where relaxation from the initial to final states can be tracked. (Color available on-line)

As before, we have applied equation (3) to compare how these boundary energies and segregation scale with the change in excess volume created by the segregation of Cr. The excess volume change with Cr content is plotted in Fig. 7(c). The $\Sigma 3(2\bar{1}\bar{1})//(\bar{1}\bar{2}1)$ twin did not show any significant change in excess volume. A very limited free volume change would be expected since this special boundary has a high frequency of coincident lattice sites overlapping each other at the boundary. The near invariant change in excess volume is similar to the equivalent invariant change in grain boundary energy, Fig. 7(a). Hence, no substantial energy gain would occur by the placement of Cr into this boundary. This is schematically shown in Fig. 7(d), where the boundary structure does not change and is in agreement with the predicted and experimentally measured interfacial excess found for the twin boundary in Fig. 5(c) and 5(d), with $\Gamma \sim 0$ atoms/nm². In contrast, the excess volume reduction trends in Fig. 7(c) for $\Sigma 11(1\bar{1}3)//(\bar{1}13)$, $\Sigma 9(1\bar{1}4)//(\bar{1}14)$, and $\Sigma 9(2\bar{2}\bar{1})//(\bar{2}\bar{2}1)$ did show relative agreement with how the grain boundary energy changed with Cr content in Fig. 7(a). This could suggest that a driving force for Cr segregation to these boundaries is linked to the reduction in excess volume. In Fig. 7(d), the Cr segregation to the $\Sigma 9(1\bar{1}4)//(\bar{1}14)$ is shown with the arrow to lead the eye to view where the boundary relaxation occurred.

Interestingly, the $\Sigma 3(111)//(111)$ and $\Sigma 5(012)//(021)$ do not show similar trends between grain boundary energy and excess volume behavior with Cr content. This discrepancy between trends gives insights into the subtle and complex differences that regulate grain boundary segregation as a function of boundary type. In the case of the $\Sigma 3(111)//(111)$, similar to its twin counterpart ($\Sigma 3(2\bar{1}\bar{1})//(\bar{1}\bar{2}1)$), the $\Sigma 3$ CSL boundary has a high frequency of overlapping lattice sites at the boundary, Fig. 7(d). As before, one could infer that a reduction of excess volume would be minimal for this particular type of special boundary. However, the $\Sigma 3(111)//(111)$ has a higher interfacial excess than its $\Sigma 3(2\bar{1}\bar{1})//(\bar{1}\bar{2}1)$ twin.

This difference in segregation between the $\Sigma 3$ boundaries likely resides in one being coherent and the other being incoherent.

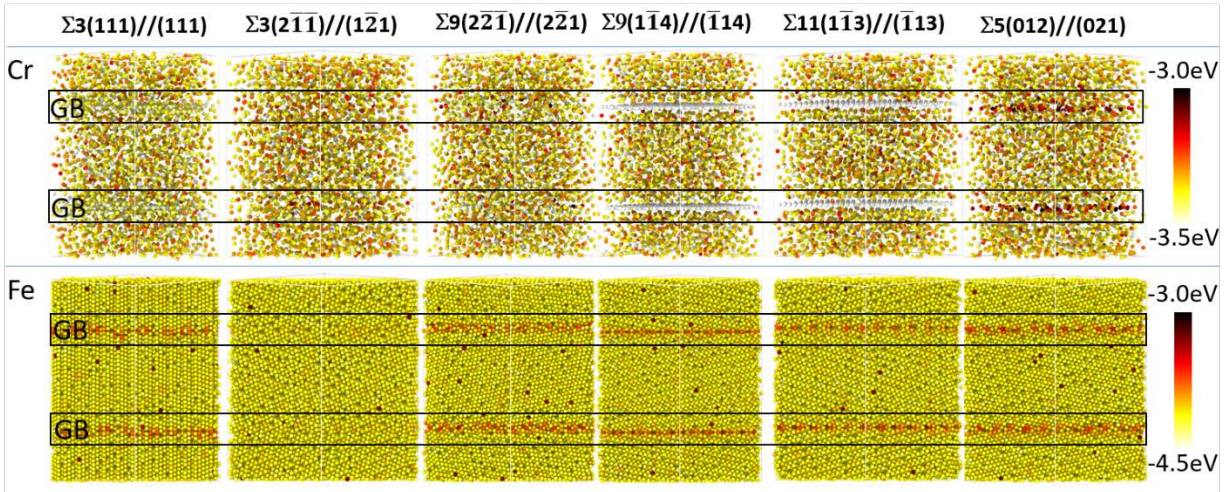


Figure 8: Cr or Fe atomic energetic distribution for different types of Σ -GBs. The GB is highlighted by the rectangular box. (Color available on-line)

To explore this concept further, the energetic distribution for the atoms in and away from these specified boundaries are shown in Fig. 8 for the Fe-8at.%Cr alloy. In this figure, the top and bottom row of images are the Cr and Fe atoms respectively. The color variation within each row corresponds to potential energy of that atom (Cr or Fe) in the matrix or at the boundary. For the $\Sigma 3(111)//(111)$, the Fe atoms in the boundary has a higher energy as compared to those in the matrix, evident by the linear cluster of red spheres in the boundary. In contrast, the Cr atoms in the same boundary appeared to have a lower energy. Comparing this to the twin $\Sigma 3(2\bar{1}\bar{1})//(1\bar{2}1)$, which revealed no discernable energy differences in or away from the boundary for either Fe or Cr, suggests that the chemical nature of the incoherent boundary appears to influence the Cr segregation.

In the case of the $\Sigma 5(012)//(021)$, the grain boundary energy is relatively invariant with Cr content, Fig. 7(a), but a modest reduction in excess volume with Cr segregation is predicted, Fig. 7(c). One could speculate that a reduction in excess volume at this boundary would promote segregation and manifest itself with a reduction in grain boundary energy. However the Gibbsian interfacial excess is at or near zero up to ~ 8 at.% Cr, Fig. 7(b), demonstrating no clear thermodynamic preference for Cr. The energetic distribution, Fig. 8, reveals a higher energy for these Cr atoms to be at this $\Sigma 5(012)//(021)$ boundary evident by the linear collection of red spheres at the boundary. It is interesting to note that this is the only boundary studied that showed such a distinct (red) energy value for Cr at a boundary. Upon increasing the Cr content above this value, the interfacial excess, Fig. 7(b), becomes negative indicating a strong tendency for this boundary to reject Cr. Collectively, these results reveal the Cr is not preferred at $\Sigma 5(012)//(021)$, which was also seen experimentally albeit at a $\Sigma 5$ with a different inclination angle.

The most favorable energy state for Cr to be located in the boundary is seen for the $\Sigma 9(1\bar{1}4)//(\bar{1}14)$ and $\Sigma 11(1\bar{1}3)//(\bar{1}13)$, with a linear cluster of white spheres at these boundaries. The corresponding Fe were noted to be red (having a higher energy) in these boundaries. This is in agreement with the interfacial excess behavior, Fig. 7(b), which showed favorable segregation. The rapid increase of these excess values at lower Cr concentrations is likely associated with highly favorable energetics for Cr segregation to these particular boundaries with their excess volume reduction at those particular concentrations.

Returning to Fig. 6, we now address the low and high angle grain boundaries. For the LAGBs, experimentally, the interfacial excess is higher than what was predicted. A low interfacial excess would likely be expected since these boundaries have very good lattice alignment between the grains⁶⁵. And in particular, the simulation was based on a symmetric tilt GB was used which may not properly capture

the true experimental LAGB structure. In contrast, the high interfacial excess for both the experimental and simulated Cr segregations in the HAGBs is suspected to be associated with Cr's clustering. As shown in Fig. 9(a)-(b), experimentally identified clusters were observed in these boundaries. These clusters were defined in the reconstruction to have a threshold value of 20 at.% Cr or higher within a predefined spherical sampling volume of 1 nm³. The vast majority of these clusters were noted in the HAGBs (whose boundaries were verified by the prior cross-correlated PED scan of the APT tip). The balance of the other clusters (which were few) were observed to be within the grains themselves and no clusters were noted in the other types of boundaries. This clustering behavior is believed to be the early onset of phase separation, which has been similarly reported in prior APT studies for various aged Fe(Cr) specimens^{36,66}. The onset of clustering, even in the sputter deposited film, could be expected since this alloy's composition (~ 8 at. %Cr) exceeded the solubility limit of Cr in Fe at room temperature (~5 at.% Cr)³⁴. Since HAGBs provide pathways for rapid diffusion⁶⁷ coupled with larger excess volumes and higher grain boundary energies as compared to special character boundaries⁶⁸, they provide a favorable kinetic and thermodynamic site to initiate the precipitation of the Cr phase. To further corroborate this behavior, a polycrystalline simulation of a HAGB network was performed.

We initiated this polycrystalline simulation by using the experimental composition of Fe-8 at.%Cr. Unfortunately, we were unable to identify similar clusters at this overall composition. This was contributed to the limitations of the simulation time to initiate clustering for this particular composition. However, by increasing the Cr content to 14 at.% within our available simulation time, clustering was detected. As seen in Fig. 9(c), the simulated clusters were observed and compared to the experimental APT boundaries in Fig. 9(a). The interfacial excess values for these simulated boundaries are plotted in Fig. 6. Similar to the experimental findings for the HAGBs, the Gibbsian excess value's standard deviation was large. This larger excess value spread is contributed to the dilute and highly enriched Cr within the boundary and between the different clusters. Hence, depending on where the interfacial excess is

measured, the values would vary considerably and is manifested in the larger error around the average value. Hence, in both the simulation and experimental APT data, the relative amount of interfacial excess was then dependent on the size and location of the cluster with values ranging from a few to tens of atoms/nm². This simulation confirmed that HAGBs were a preferred segregation boundary in the alloy where clustering occurred as compared to the other identified special character boundaries.

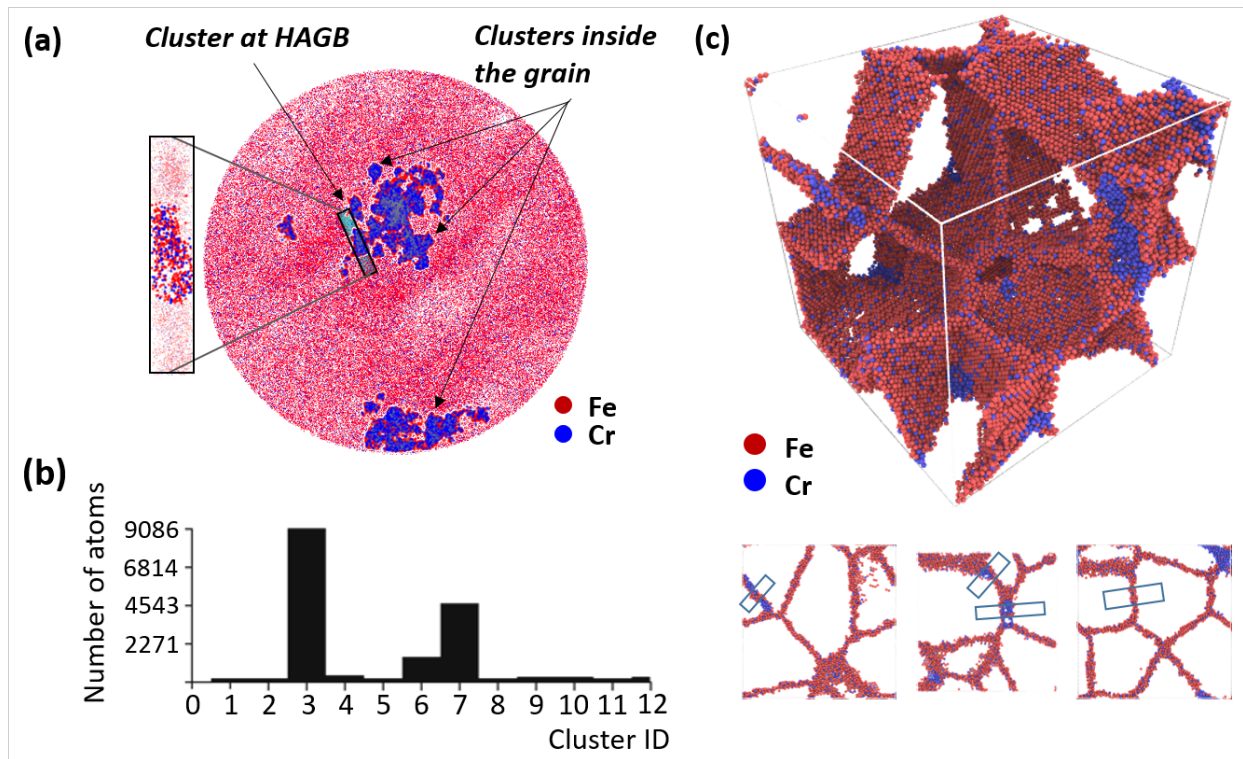


Figure 9: (a) Experimental result of cluster analysis laid over a 10 nm thick atom map (top view) extracted from the original APT data set (b) The histogram of cluster size from (a). (c) Simulation result of clusters forming at polycrystalline GBs with selected images of the clustering at the boundaries shown below the volumetric rendering of all the boundaries. (Color available on-line).

Conclusions

The comparative simulations with correlated TEM and APT has provided experimental verification of grain boundary type dependencies for segregation. The experimental interfacial excess values are similar to the predicted values and exhibit the equivalent trends in segregation to certain types of Σ -boundaries. This provided confidence in simulated understanding and predictions of segregation in Fe(Cr) for other types of specific boundaries.

Our findings confirm that $\Sigma 3$ boundaries are most sensitive to inclination angles changes. This resulted in a larger spread in Cr interfacial excess values, both experimentally and predicted by the simulation. Both the experiments and simulations revealed similar trends in interfacial excess values for the other special character boundaries, though, in general, the experimental absolute values were slightly larger. Of all the types of grain boundaries studied, the HAGBs had a higher Cr solute concentration. This was contributed to these features being preferred sites for clustering and the eventual initiation sites for Cr precipitation, which was confirmed by simulations. The direct and consistent linkage of experimental and simulation findings for the Fe-8%Cr alloy gave confidence in the simulation predictions.

Consequently, the segregation behavior of Cr from 0 to 14 at% was undertaken for other types of specific grain boundaries. The solute-boundary segregation behavior was then discussed in terms of both volume excess reduction and the energetic distribution of Fe and Cr in and away from the boundaries. For the special boundaries, the twin $\Sigma 3(2\bar{1}\bar{1})//(\bar{1}\bar{2}1)$ and $\Sigma 5(012)//(021)$ grain boundary energies were relatively invariant to the Cr content with little to no segregation of Cr to their boundaries. This was in agreement with the prior experiments. In contrast the $\Sigma 3(111)//(111)$ had the highest interfacial excess, for all special character boundaries, with a linear decrease in grain boundary energy with increasing Cr content. The $\Sigma 9(1\bar{1}4)//(\bar{1}14)$, $\Sigma 9(2\bar{2}\bar{1})//(\bar{2}\bar{2}1)$, and $\Sigma 11(1\bar{1}3)//(\bar{1}13)$ revealed a

positive interfacial excess, though at a lower positive value, and a reduction of grain boundary energy whose change was more pronounced at lower Cr contents.

The evidence of specific grain boundary segregation, even in an as-deposited room temperature film, demonstrated the energy preference for grain boundary specific segregation. The added simulations have provided insights into why specific boundaries are more or less favorable for this segregation.

Acknowledgement:

The authors gratefully recognize support from the Army Research Office, grant W911NF1310436, as well as the University of Alabama's Central Analytical Facility.

Reference

- 1 Lu, L., Chen, X., Huang, X. & Lu, K. Revealing the Maximum Strength in Nanotwinned Copper. *Science* **323**, 607-610 (2009).
- 2 King, A., Johnson, G., Engelberg, D., Ludwig, W. & Marrow, J. Observations of Intergranular Stress Corrosion Cracking in a Grain-Mapped Polycrystal. *Science* **321**, 382-385 (2008).
- 3 Grantab, R., Shenoy, V. B. & Ruoff, R. S. Anomalous Strength Characteristics of Tilt Grain Boundaries in Graphene. *Science* **330**, 946-948 (2010).
- 4 Tsen, A. W. *et al.* Tailoring Electrical Transport Across Grain Boundaries in Polycrystalline Graphene. *Science* **336**, 1143-1146 (2012).
- 5 Chookajorn, T., Murdoch, H. A. & Schuh, C. A. Design of Stable Nanocrystalline Alloys. *Science* **337**, 951-954, doi:10.1126/science.1224737 (2012).
- 6 Trelewicz, J. R. & Schuh, C. A. Grain boundary segregation and thermodynamically stable binary nanocrystalline alloys. *Physical Review B* **79**, 094112, doi:10.1103/PhysRevB.79.094112 (2009).
- 7 Darling, K. A., Tschopp, M. A., VanLeeuwen, B. K., Atwater, M. A. & Liu, Z. K. Mitigating grain growth in binary nanocrystalline alloys through solute selection based on thermodynamic stability maps. *Computational Materials Science* **84**, 255-266, doi:10.1016/j.commatsci.2013.10.018 (2014).
- 8 Darling, K. A. *et al.* Stabilized nanocrystalline iron-based alloys: Guiding efforts in alloy selection. *Materials Science and Engineering: A* **528**, 4365-4371, doi:10.1016/j.msea.2011.02.080 (2011).
- 9 Upmanyu, M., Srolovitz, D. J., Shvindlerman, L. S. & Gottstein, G. Misorientation Dependence of Intrinsic Grain Boundary Mobility: Simulation and Experiment. *Acta Materialia* **47**, 3901-3914 (1999).
- 10 Upmanyu, M. *et al.* Boundary Mobility and Energy Anisotropy Effects on Microstructural Evolution During Grain Growth. *Interface Science* **10**, 201-216 (2002).
- 11 Dillon, S. J. & Rohrer, G. S. Mechanism for the development of anisotropic grain boundary character distributions during normal grain growth. *Acta Materialia* **57**, 1-7, doi:10.1016/j.actamat.2008.08.062 (2009).
- 12 Holm, E. A., Hassold, G. N. & Miodownik, M. A. On Misorientation distribution evolution during anisotropic grain growth. *Acta Materialia* **49**, 2981-2991 (2001).

- 13 Yao, L., Ringer, S. P., Cairney, J. M. & Miller, M. K. The anatomy of grain boundaries: Their structure and atomic-level solute distribution. *Scripta Materialia* **69**, 622-625, doi:10.1016/j.scriptamat.2013.07.013 (2013).
- 14 Miller, M. K., Kelly, T. F., Rajan, K. & Ringer, S. P. The future of atom probe tomography. *Materials Today* **15**, 158-165, doi:10.1016/s1369-7021(12)70069-x (2012).
- 15 Dickey, E. C. & Fan, X. Yttria-Stabilized Cubic-Zirconia Symmetric Tilt Grain Boundaries. *Journal of the American Ceramic Society* **84**, 1361-1368 (2001).
- 16 Dillon, S. J., Tang, M., Carter, W. C. & Harmer, M. P. Complexion: A new concept for kinetic engineering in materials science. *Acta Materialia* **55**, 6208-6218, doi:10.1016/j.actamat.2007.07.029 (2007).
- 17 Dillon, S. & Harmer, M. Multiple grain boundary transitions in ceramics: A case study of alumina. *Acta Materialia* **55**, 5247-5254, doi:10.1016/j.actamat.2007.04.051 (2007).
- 18 Li, Y. J., Ponge, D., Choi, P. & Raabe, D. Segregation of boron at prior austenite grain boundaries in a quenched martensitic steel studied by atom probe tomography. *Scripta Materialia* **96**, 13-16, doi:10.1016/j.scriptamat.2014.09.031 (2015).
- 19 Herbig, M., Choi, P. & Raabe, D. Combining structural and chemical information at the nanometer scale by correlative transmission electron microscopy and atom probe tomography. *Ultramicroscopy* **153C**, 32-39, doi:10.1016/j.ultramic.2015.02.003 (2015).
- 20 Brons, J. G. & Thompson, G. B. Orientation Mapping via Precession-Enhanced Electron Diffraction and Its Applications in Materials Science. *JOM* **66**, 165-170, doi:10.1007/s11837-013-0799-5 (2013).
- 21 Moeck, P. *et al.* High spatial resolution semi-automatic crystallite orientation and phase mapping of nanocrystals in transmission electron microscopes. *Crystal Research and Technology* **46**, 589-606, doi:10.1002/crat.201000676 (2011).
- 22 Rauch, E. F. *et al.* Automated nanocrystal orientation and phase mapping in the transmission electron microscope on the basis of precession electron diffraction. *Zeitschrift für Kristallographie* **225**, 103-109, doi:10.1524/zkri.2010.1205 (2010).
- 23 Tomozawa, M., Miyahara, Y. & Kako, K. Solute segregation on $\Sigma 3$ and random grain boundaries in type 316L stainless steel. *Materials Science and Engineering: A* **578**, 167-173, doi:10.1016/j.msea.2013.04.048 (2013).
- 24 Pirgazi, H., Glowinski, K., Morawiec, A. & Kestens, L. A. I. Three-dimensional characterization of grain boundaries in pure nickel by serial sectioning via mechanical polishing. *Journal of Applied Crystallography* **48**, 1672-1678, doi:10.1107/s1600576715017616 (2015).
- 25 Kiss, A. K. & Labar, J. L. Determining Projections of Grain Boundaries from Diffraction Data in Transmission Electron Microscope. *Microscopy and microanalysis : the official journal of Microscopy Society of America, Microbeam Analysis Society, Microscopical Society of Canada* **22**, 551-564, doi:10.1017/S1431927616000684 (2016).
- 26 Kiss, A. K., Rauch, E. F. & Labar, J. L. Highlighting material structure with transmission electron diffraction correlation coefficient maps. *Ultramicroscopy* **163**, 31-37, doi:10.1016/j.ultramic.2016.01.006 (2016).
- 27 Kiss, A. K., Rauch, E. F., Pecz, B., Szivos, J. & Labar, J. L. A Tool for Local Thickness Determination and Grain Boundary Characterization by CTEM and HRTEM Techniques. *Microscopy and microanalysis : the official journal of Microscopy Society of America, Microbeam Analysis Society, Microscopical Society of Canada* **21**, 422-435, doi:10.1017/S1431927615000112 (2015).
- 28 Tschopp, M. A. & McDowell, D. L. Asymmetric tilt grain boundary structure and energy in copper and aluminium. *Philosophical Magazine* **87**, 3871-3892, doi:10.1080/14786430701455321 (2007).

- 29 Tschopp, M. A. & McDowell, D. L. Structures and energies of $\Sigma 3$ asymmetric tilt grain boundaries in copper and aluminium. *Philosophical Magazine* **87**, 3147-3173, doi:10.1080/14786430701255895 (2007).
- 30 Zhang, L., Lu, C. & Tieu, K. Atomistic simulation of tensile deformation behavior of summation operator5 tilt grain boundaries in copper bicrystal. *Sci Rep* **4**, 5919, doi:10.1038/srep05919 (2014).
- 31 Tschopp, M. A., Coleman, S. P. & McDowell, D. L. Symmetric and asymmetric tilt grain boundary structure and energy in Cu and Al (and transferability to other fcc metals). *Integrating Materials and Manufacturing Innovation* **4**, doi:10.1186/s40192-015-0040-1 (2015).
- 32 Homer, E. R., Patala, S. & Priedeman, J. L. Grain Boundary Plane Orientation Fundamental Zones and Structure-Property Relationships. *Sci Rep* **5**, 15476, doi:10.1038/srep15476 (2015).
- 33 Zhou, X., Kaub, T., Martens, R. L. & Thompson, G. B. Influence of Fe(Cr) miscibility on thin film grain size and stress. *Thin Solid Films* **612**, 29-35 (2016).
- 34 Malerba, L., Caro, A. & Wallenius, J. Multiscale modelling of radiation damage and phase transformations: The challenge of FeCr alloys. *Journal of Nuclear Materials* **382**, 112-125, doi:10.1016/j.jnucmat.2008.08.014 (2008).
- 35 Klueh, R. L. & Nelson, A. T. Ferritic/martensitic steels for next-generation reactors. *Journal of Nuclear Materials* **371**, 37-52, doi:10.1016/j.jnucmat.2007.05.005 (2007).
- 36 Danoix, F. & Auger, P. Atom Probe Studies of the Fe–Cr System and Stainless Steels Aged at Intermediate Temperature: A Review. *Materials Characterization* **44**, 177-201 (2000).
- 37 Miller, M. K. *et al.* Spinodal Decomposition in Fe–Cr Alloys: Experimental Study at the Atomic Level and Comparison with Computer Models-I. Introduction and Methodology. *Acta Metall. Mater.* **43**, 3385-3401 (1995).
- 38 Hyde, J. M. *et al.* Spinodal Decomposition in Fe–Cr Alloys: Experimental Study at the Atomic Level and Comparison with Computer Models-II. Development of Domain Size and Composition Amplitude. *Acta Metall. Mater.* **43**, 3403-3413 (1995).
- 39 Hyde, J. M. *et al.* Spinodal Decomposition in Fe–Cr Alloys: Experimental Study at the Atomic Level and Comparison with Computer Models-III. Development of Morphology. *Acta Metall. Mater.* **43**, 3415-3426 (1995).
- 40 Bachhav, M., Robert Odette, G. & Marquis, E. A. Microstructural changes in a neutron-irradiated Fe–15at.%Cr alloy. *Journal of Nuclear Materials* **454**, 381-386, doi:10.1016/j.jnucmat.2014.08.026 (2014).
- 41 Bachhav, M., Robert Odette, G. & Marquis, E. A. α' precipitation in neutron-irradiated Fe–Cr alloys. *Scripta Materialia* **74**, 48-51, doi:10.1016/j.scriptamat.2013.10.001 (2014).
- 42 Hu, R., Smith, G. D. W. & Marquis, E. A. Effect of grain boundary orientation on radiation-induced segregation in a Fe–15.2at.% Cr alloy. *Acta Materialia* **61**, 3490-3498, doi:10.1016/j.actamat.2013.02.043 (2013).
- 43 Bhattacharya, A. *et al.* Chromium enrichment on the habit plane of dislocation loops in ion-irradiated high-purity Fe–Cr alloys. *Acta Materialia* **78**, 394-403, doi:10.1016/j.actamat.2014.06.050 (2014).
- 44 Kuksenko, V., Pareige, C. & Pareige, P. Intra granular precipitation and grain boundary segregation under neutron irradiation in a low purity Fe–Cr based alloy. *Journal of Nuclear Materials* **425**, 125-129, doi:10.1016/j.jnucmat.2011.10.031 (2012).
- 45 Marquis, E. A., Hu, R. & Rousseau, T. A systematic approach for the study of radiation-induced segregation/depletion at grain boundaries in steels. *Journal of Nuclear Materials* **413**, 1-4, doi:10.1016/j.jnucmat.2011.03.023 (2011).

- 46 Hu, R., Smith, G. D. W. & Marquis, E. A. Atom probe study of radiation induced grain boundary segregation/depletion in a Fe-12%Cr alloy. *Progress in Nuclear Energy* **57**, 14-19, doi:10.1016/j.pnucene.2011.10.011 (2012).
- 47 Barr, C. M. *et al.* Anisotropic radiation-induced segregation in 316L austenitic stainless steel with grain boundary character. *Acta Materialia* **67**, 145-155, doi:10.1016/j.actamat.2013.11.060 (2014).
- 48 Han, W. Z., Demkowicz, M. J., Fu, E. G., Wang, Y. Q. & Misra, A. Effect of grain boundary character on sink efficiency. *Acta Materialia* **60**, 6341-6351, doi:10.1016/j.actamat.2012.08.009 (2012).
- 49 <http://estore.omniprobe.com/m1webgear/ProductDetails.aspx?PartUniqueID=20A12D71-F8A4-4987-9F9A-D96CC909AEE2>.
- 50 Thompson, K. *et al.* In situ site-specific specimen preparation for atom probe tomography. *Ultramicroscopy* **107**, 131-139, doi:10.1016/j.ultramic.2006.06.008 (2007).
- 51 Hartshorne, M. I., Isheim, D., Seidman, D. N. & Taheri, M. L. Specimen preparation for correlating transmission electron microscopy and atom probe tomography of mesoscale features. *Ultramicroscopy* **147**, 25-32, doi:10.1016/j.ultramic.2014.05.005 (2014).
- 52 Ogawa, H. GBstudio: A Builder Software on Periodic Models of CSL Boundaries for Molecular Simulation. *Materials Transactions* **47**, 2706-2710, doi:10.2320/matertrans.47.2706 (2006).
- 53 Terentyev, D., He, X., Serra, A. & Kuriplach, J. Structure and strength of $\langle 110 \rangle$ tilt grain boundaries in bcc Fe: An atomistic study. *Computational Materials Science* **49**, 419-429, doi:10.1016/j.commatsci.2010.05.033 (2010).
- 54 Olmsted, D. L., Foiles, S. M. & Holm, E. A. Survey of computed grain boundary properties in face-centered cubic metals: I. Grain boundary energy. *Acta Materialia* **57**, 3694-3703, doi:10.1016/j.actamat.2009.04.007 (2009).
- 55 Li, J. AtomEye: an efficient atomistic configuration viewer. *Modelling and Simulation in Materials Science and Engineering* **11**, 173-177, doi:citeulike-article-id:572390 doi: 10.1088/0965-0393/11/2/305 (2003).
- 56 Sadigh, B. *et al.* Scalable parallel Monte Carlo algorithm for atomistic simulations of precipitation in alloys. *Physical Review B* **85**, 184203, doi:10.1103/PhysRevB.85.184203 (2012).
- 57 Plimpton, S. Fast Parallel Algorithms for Short-Range Molecular Dynamics. *Journal of Computational Physics* **117**, 1-19 (1995).
- 58 Stukowski, A., Sadigh, B., Erhart, P. & Caro, A. Efficient implementation of the concentration-dependent embedded atom method for molecular-dynamics and Monte-Carlo simulations. *Modelling and Simulation in Materials Science and Engineering* **17**, 075005, doi:10.1088/0965-0393/17/7/075005 (2009).
- 59 Randle, V. A Methodology for Grain Boundary Plane Assessment by Single-section Trace Analysis. *Scripta Materialia* **44**, 2789-2794 (2001).
- 60 Samudrala, S. K. *et al.* New atom probe approaches to studying segregation in nanocrystalline materials. *Ultramicroscopy* **132**, 158-163, doi:10.1016/j.ultramic.2012.12.013 (2013).
- 61 Herbig, M. *et al.* Atomic-Scale Quantification of Grain Boundary Segregation in Nanocrystalline Material. *Physical Review Letters* **112**, 126103, doi:10.1103/PhysRevLett.112.126103 (2014).
- 62 Chang, L. S., Rabkin, E., Straumal, B. B., Baretzky, B. & Gust, W. Thermodynamic Aspects of the Grain Boundary Segregation in Gu(Bi) Alloys. *Acta Materialia* **47**, 4041-4046 (1999).
- 63 Pauling, L. Atomic Radii and Interatomic Distances in Metals. *Journal of the American Chemical Society* **69**, 542-553, doi:10.1021/ja01195a024 (1947).
- 64 Terentyev, D., He, X., Zhurkin, E. & Bakaev, A. Segregation of Cr at tilt grain boundaries in Fe-Cr alloys: A Metropolis Monte Carlo study. *Journal of Nuclear Materials* **408**, 161-170, doi:10.1016/j.jnucmat.2010.11.024 (2011).

- 65 Hull, D. & Bacon, D. J. *Introduction to Dislocations (Fifth Edition)*. (Butterworth-Heinemann, 2011).
- 66 Danoix, F., Auger, P. & Blavette, D. Hardening of aged duplex stainless steels by spinodal decomposition. *Microscopy and microanalysis : the official journal of Microscopy Society of America, Microbeam Analysis Society, Microscopical Society of Canada* **10**, 349-354, doi:10.1017/S1431927604040516 (2004).
- 67 Koblinski, P., Wolf, D., Phillpot, S. R. & Gleiter, H. Self-diffusion in high-angle fcc metal grain boundaries by molecular dynamics simulation. *Philosophical Magazine A* **79**, 2735-2761, doi:10.1080/01418619908212021 (1999).
- 68 Wolf, D. & Yip, S. *Materials Interfaces: Atomic-level Structure and Properties*. (Springer, 1992).

Supplementary Material for:
Grain Boundary Specific Segregation in Nanocrystalline Fe(Cr)

Xuyang Zhou¹, Xiao-xiang Yu¹, Tyler Kaub¹, Richard L. Martens¹, and Gregory B. Thompson^{1*}

¹The University of Alabama, Department of Metallurgical & Materials Engineering, Box 870202, Tuscaloosa, AL 35401-0202

*Correspondence to: gthompson@eng.ua.edu

1. Quantifying the experimental grain boundary normal and inclination angle:

To measure the inclination angle, we utilized the technique reported by Kiss *et al.*¹. This method measures the inclination angle based on the projected width of the boundary as determined by the overlapping Precession Electron Diffraction (PED) patterns that would occur as the beam rasters over the boundary, i.e. whenever the grain boundary plane is oriented oblique to the electron beam, the overlapping area of neighboring grains can be discerned. The projected width of the GB is then measured using the following equation

$$\tan \omega = \frac{d}{t} \dots \dots \dots (S1)$$

where d is the projected width of grain boundary and t is the thickness of the sample, as shown in Fig. S1. For our work, the thickness refers to the diameter of the APT tip. The experimental GB inclination, Fig. S2(a)-(b), was determined by plotting the weight-factors of each diffracted intensity contribution from either grain on each side of the boundary, Fig. S2(c) and (d). As the beam rastered closer to the other grain, more of the diffracted pattern from that grain will be observed in the pattern. As that pattern becomes more pronounced, it is weighted more. IN this method, one can then quantify the diffraction pattern differences in overlapping patterns which can then be used to estimate the GB inclination. The average distance between the two fitted lines in Fig. S2(c) and (d) defines the projection width of the grain boundary, albeit based on the resolution of the electron probe, which was ~ 2.5 nm. In the case shown, the width was approximately 16 nm with a scanning step size of 2 nm. Assuming that the diameter of the APT tip was approximately 100 nm (based on the TEM image, Fig. 3(a)), the experimental inclination angle is approximately 9° . Due to the experimental limitations of either a very fine grain sizes and/or low image quality factors for the PED pattern captured, it was not possible to provide the

inclination angle for each and every grain. In those cases, as mentioned in the paper, we have assumed that the grain boundary plane is parallel to the electron beam or, alternatively, we assumed no inclination to the boundary in the viewed projection. This was a reasonable assumption based on the cross-sectional TEM image, Fig. 4(a). The inclination angles that were measured are tabulated in Table 2, under the column ‘Inclination angle (PED)’.

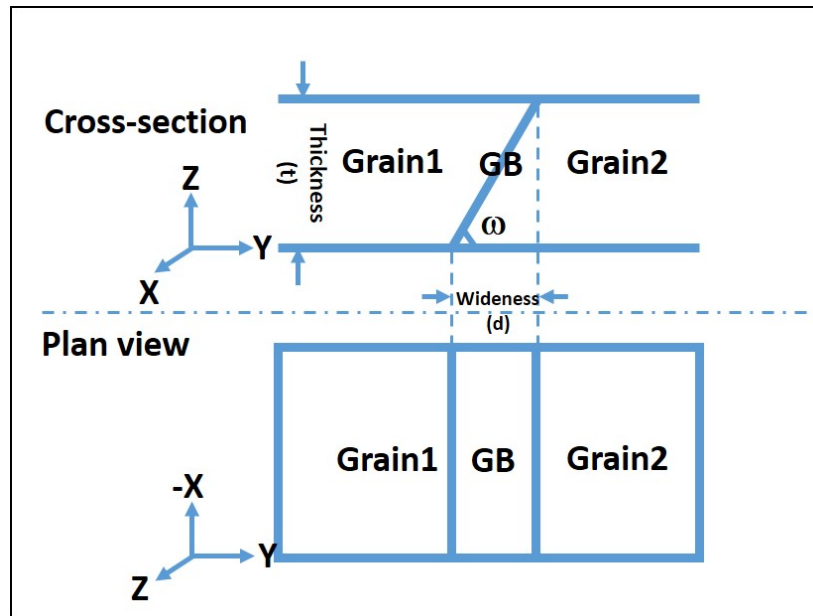


Fig. S1: Schematic of the cross section and projected boundary with designated variable to define the boundary width and inclination from a PED scan.

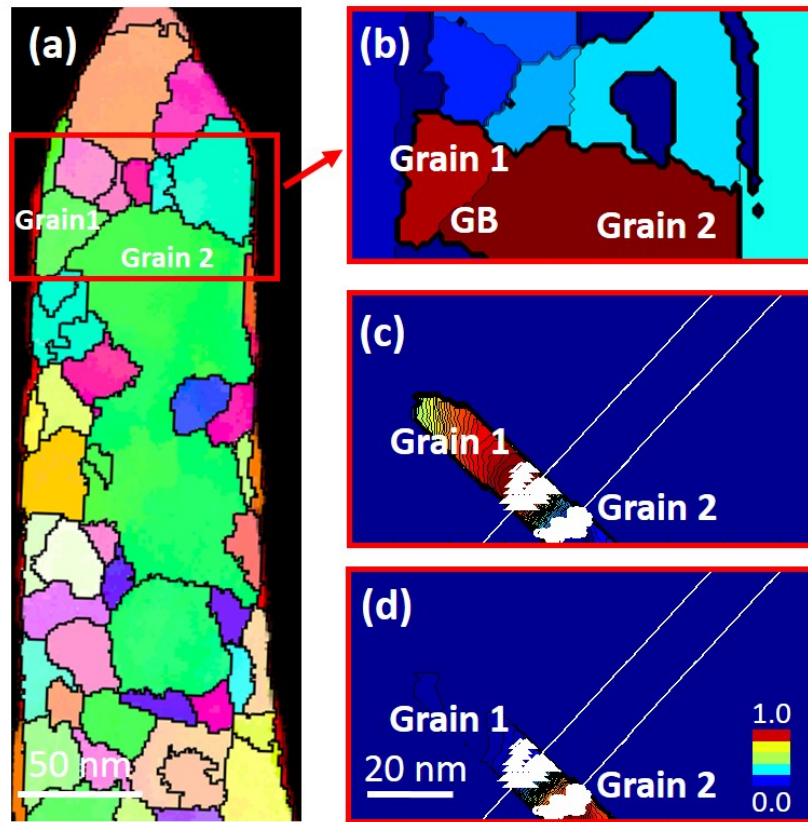


Fig. S2: (a) Orientation map of the APT tip (Fig. 3(b)) (b) Magnified image of a region of interest from (a) (c) the change in diffracted intensity (weight factor) of Grain 1 as it approaches the grain boundary projection, indicated by the white line (d) the change in diffracted intensity (weight factor) of Grain 2 as it approaches the grain boundary projection, indicated by the white line. The white marked features represent the weight factor values used to fit the projected boundary line. The method for (c) and (d) were taken from Kiss *et al.*¹

2. Determining a common reference system for inclination angles – computed and measured:

Though the experimental grain boundary inclination angle is important, it does not necessarily provide the common reference plane from which the inclination angle relative to the two fixed lattices can be compared. In order for one to determine this inclination angle, a reference plane must be defined.

2.1 Reference inclination angle for simulated grain boundaries

For the simulated images, this was done by establishing the position within the lattice from which the angle of inclination, Θ , to the GB plane's projection can be measured. To determine the grain boundary inclination angle an appropriate and common viewing direction based on the CSL type is required. For example, we used the [110] viewing direction for the $\Sigma 3$, $\Sigma 9$, and $\Sigma 11$ and [100] viewing direction for $\Sigma 5$. The choice of viewing direction was largely based on our ability to readily identify a series of parallel planes between each grain that would form the grain boundary between the two grains.

With the grain boundary now defined by the two sets of parallel planes in each grain, the reference plane was then required. This was done by defining a unit cell in each grain after which the symmetric plane between the two grains could be determined. This symmetric plane then served as the reference plane to the grain boundary plane created by the parallel planes from the viewing direction. Using the reference plane and grain boundary plane, the grain boundary inclination angle can then be measured.

These concepts are illustrated in Fig. S3 for an asymmetric $\Sigma 3$ boundary. Here, the boundary is being viewed along the [110] direction for BCC Fe. The grain boundary, represented by the projected orange line, was formed by the two parallel planes listed in the figure, i.e. $(55\bar{1})$ and (711) . After which, the repeating unit cell in each grain, highlighted by the green boxes, was identified along with the symmetric plane between these two unit cells. This is graphically illustrated by the projected blue line in Fig. S3. The angle of inclination was then measured from the blue projected line to the projected orange line.

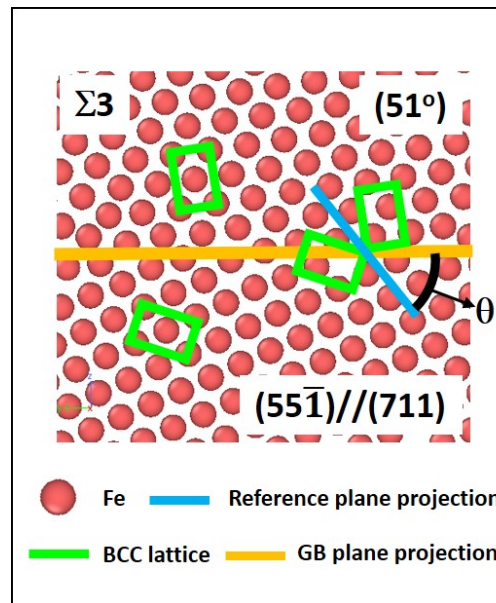


Fig. S3: A simulated inclination angle measurement from a $\Sigma 3$ boundary created by the abutment of $(55\bar{1})$ parallel with (711) . The green lines guide the eye for the unit lattice structure whereas the orange line is a projection of the GB plane and the blue lines being the projection of the symmetric plane between the two unit cells. The measurement of the blue projection line and orange projection line provides a common reference position of the inclination angle, Θ , determination.

In Fig. S4, four types of simulated Σ boundaries are shown, with the theoretical inclination angle changed from 0° to 90° . For $\Sigma 5$, we only tilted to 45° because above this angle, the conditions are symmetric to the values below this angle. Using specific tilt angles, we then were able to calculate the grain boundary energy, excess volume, and interfacial excess for each of these asymmetric (as well as symmetric) boundary structures shown in Fig. 5, where property values between these angles could be interpolated and compared to the experiments.

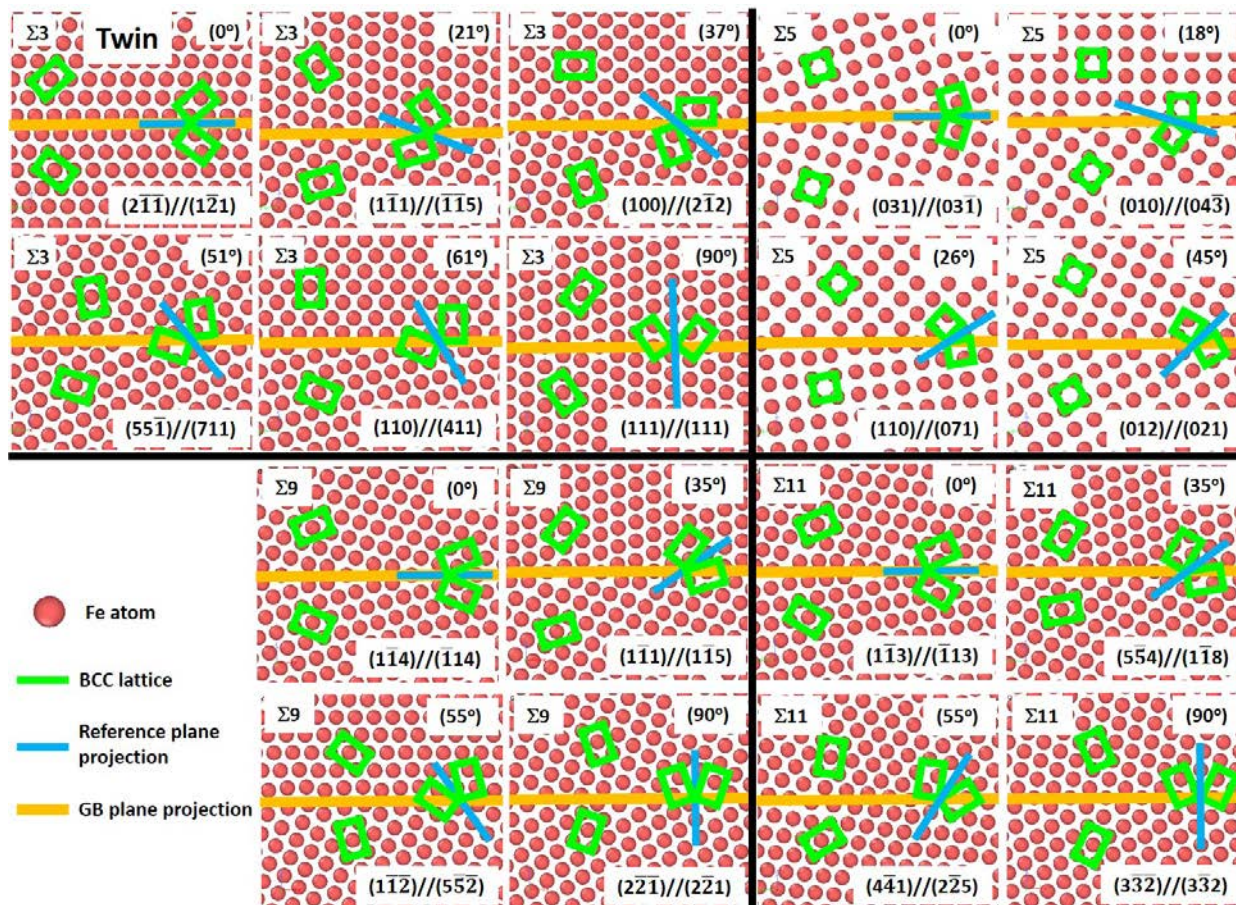


Fig. S4: Structural views of asymmetric $\Sigma 3$, $\Sigma 5$, $\Sigma 9$ and $\Sigma 11$ CSL grain boundaries. The green lines guides the eye for the lattice structure whereas the orange lines reveal the GB plane projection and the blue lines are the projected symmetric plane between the two unit cells between the two adjacent grains.

2.2 Reference inclination angle for experimental grain boundaries

To determine the grain boundary inclination angle from the experimental PED patterns, a reference plane must also be established between the two grains' orientations. To do this, the following procedure was performed. First, the grain boundary was defined by the grain boundary normal, which is represented by the red line in Fig. S5. This line can be assumed to be normal to the electron beam since the GB planes are reasonably parallel to the viewing direction, as described above and shown in Fig. 4(a), or determined by the PED scan that

provided the weighted diffraction patterns across the boundary that revealed the projection of the boundary¹. The PED scan also provided the quantitative indices for each grain's texture relative to the beam's projection. This information was then exported and used to create the projection of the unit cell referenced to this texture using a crystallographic software package². This is schematically shown in Fig. S5(a). Knowing the texture, the unit cells on either side of the CSL boundary are then rotated to a common viewing direction based on the CSL type as described above and is schematically shown in Fig. S5(b). After titling to this common viewing direction, the symmetric plane between the two unit cells is readily identified and can now serve as the reference plane needed to measure against the physical grain boundary as done for the computed asymmetric boundary types described above in 2.1. This is the projected blue line in Fig. S5(b). Since the grain boundary normal will rotate with the unit cell to the appropriate viewing direction, the GB plane is readily identified after rotation as the orange projected plane as schematically shown in Fig. S5(b). If the boundary was inclined (as measured by PED), then upon rotation of the unit cell to the common viewing direction, the grain boundary normal was adjusted accordingly to the inclination angle relative to the grain texture. For conditions where the GB was parallel to the beam (little to no inclination), this made the texture rotation, coupled with the grain boundary normal, straightforward because one does not need to be concerned with how much the boundary itself is inclined to the grain's texture orientation. The experimental angle of inclination between the two grains that created the CSL type can then be measured between the reference (blue projected line trace) and the GB plane (projected orange surface) as shown in Fig. S5(b). The results of these findings are tabulated in Table 2 under the column 'Inclination angle (REF).'

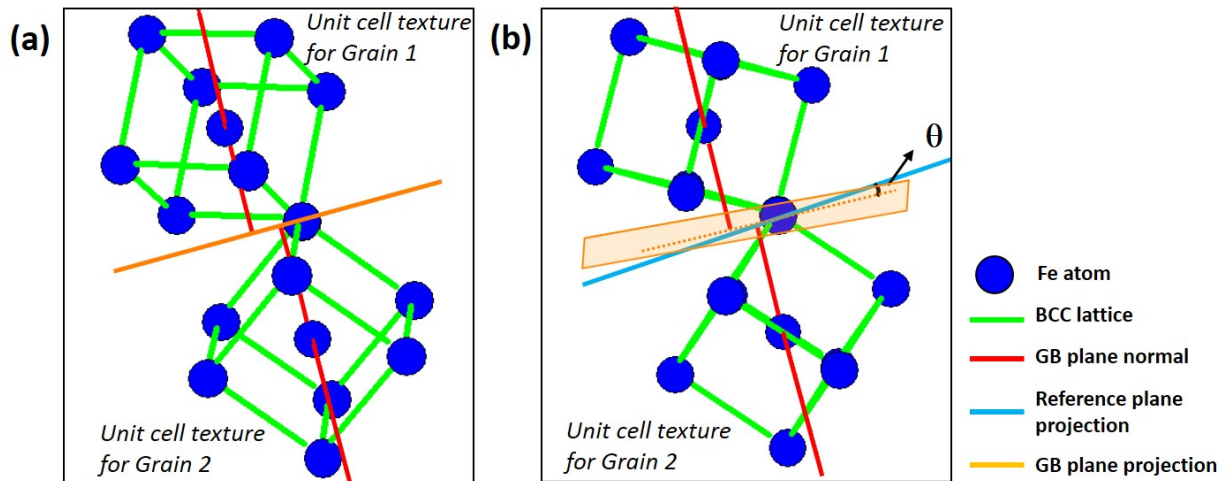


Fig. S5: (a) Schematic representation of the unit cell texture determined by the PED scan for a Σ_3 twin. The red lines represent the normal to the grain boundary to each of the unit cell for each grain. (b) Schematic representation of the unit cell texture rotated to a common viewing direction from which the symmetric plane, represented by the projected blue line, can be found. The orange plane represents the projected grain boundary determined from the GB normal (red lines). The inclination angle, θ , is measured from the projected symmetric plane (blue line trace) and the projected grain boundary plane (orange surface), represented by the dashed orange line.

3. Simulations result of additional CSL grain boundaries

Though these boundaries were not found in the experimental film, we have provided a series of additional simulations of GB energy, excess volume, and interfacial excess for other specific types of symmetric Σ -boundaries that are noted to occur in BCC Fe. This information is solely given to the reader as a larger data base or predicted Cr segregation in Fe based for those specific boundary types as shown in Fig. S6.

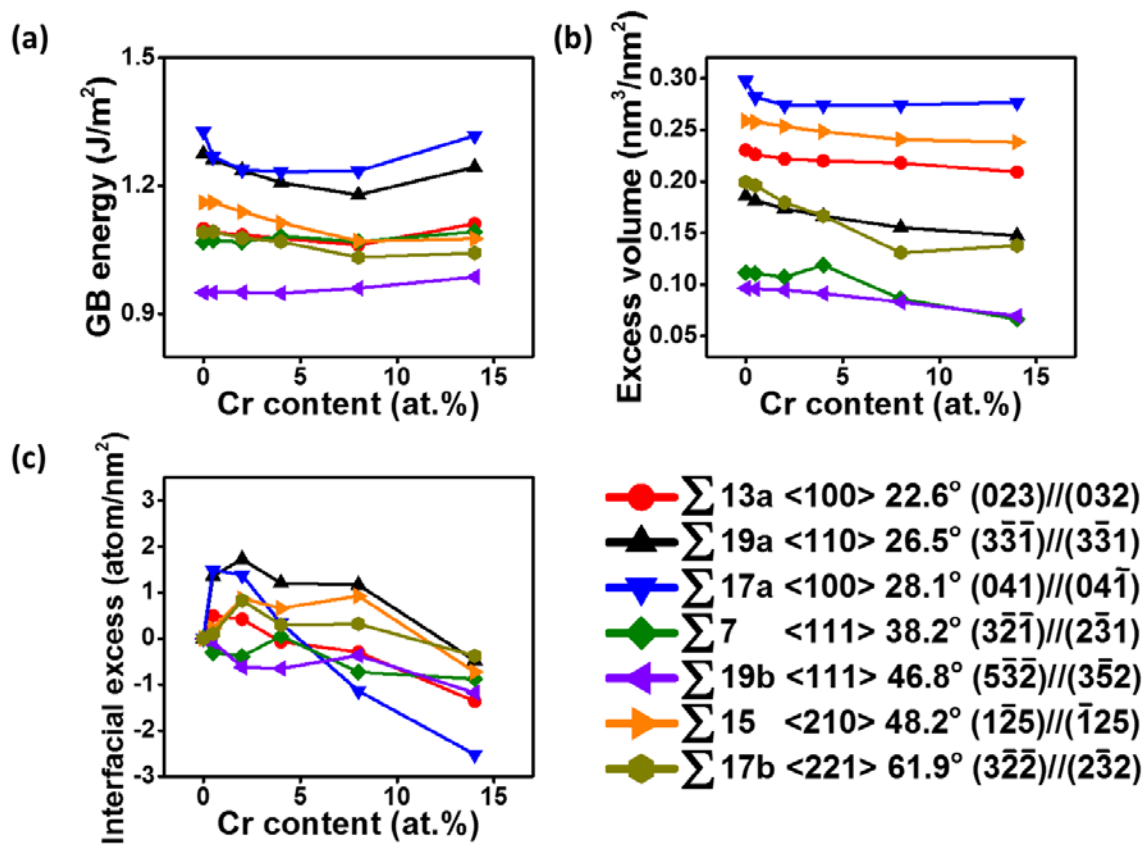


Fig. S6: (a) Calculated grain boundary energy (b) Excess volume (c) Interfacial excess for other Σ -GBs listed in the legend.

References

- 1 Kiss, A. K. & Labar, J. L. Determining Projections of Grain Boundaries from Diffraction Data in Transmission Electron Microscope. *Microscopy and microanalysis : the official journal of Microscopy Society of America, Microbeam Analysis Society, Microscopical Society of Canada* **22**, 551-564, doi:10.1017/S1431927616000684 (2016).
- 2 Boudias, C. & Monceau, D. *CaRine Crystallography*, Compiègne: DIVERGENT SA. (1998).

CHAPTER 7

Influence of Solute Partitioning on the Microstructure and Growth Stresses in Nanocrystalline Fe(Cr) Thin Films

Xuyang Zhou¹ and Gregory B. Thompson¹

1. The University of Alabama, Department of Metallurgical & Materials Engineering,
Tuscaloosa, AL USA

Abstract:

This paper addresses how solute segregation and phase separation evolves the intrinsic growth stresses for Fe-4Cr and Fe-16Cr (at%) nanocrystalline films. Ambient temperature deposition resulted in both alloys exhibiting a near equivalent tensile stress though the average grain sizes were approximately 50 nm and 100 nm respectively. Upon annealing during deposition to 523K and 673K, the tensile stress was reduced in each film and it eventually became compressive for the higher deposition temperature. Interestingly, the Fe-16Cr film, at the higher annealing temperature, diverted from the steady state compressive stress towards a tensile stress after approximately 150 nm of growth. The collective stress evolution of these films is discussed in terms of their phase separation as a function of Cr content and processing temperature. It was found that Cr acted as a grain refiner which appeared to dominate the film microstructure and associated stress response.

Key words: segregation, grain boundary, stress, in situ annealing, FeCr, PED, APT

1. Introduction

Thin films are a technologically important material structure for a variety of industries including protective wear resistance surfaces in the tool and die industries, reflective coatings for optics, and electrical conduction control of logic devices for semiconductors [1-8]. These physical properties are influenced by the intrinsic residual stresses that are generated during deposition of the film [9-15]. In extreme cases, these stresses result in film delamination, buckling, and micro-cracking from the substrate causing device failures.

Thin film stress development is related to the adatom mobility and the competition between coalescence-induced tensile stress and compressive stress generation as these adatoms diffuse into grain boundaries [16-21]. These effects have been studied intently by controlling various deposition parameters including pressure [22] and growth rate [23]. *in situ* annealing has also been shown to promote stress

evolution by providing thermal energy that will exponentially increase the adatom mobility and change the thin films stress state. For example, Thurner [24] reported that low adatom mobility species, e.g. Fe or Cr, which nominally show tensile growth can transition to compressive growth with increasing deposition temperature. In many of these studies, a single element system was used. However, multi-species systems or alloys could offer an additional variable of control through the cooperative adatom diffusivity behavior between different atoms. Here, the thermodynamic tendencies for solid solution formation, phase separation, or the precipitation of a new crystalline phase would dramatically affect the film stress evolution. This would be particularly pronounced by providing additional heating during deposition that would assist the system towards equilibrium. This would be especially relevant in thin film growth where physical vapor deposition can yield non-equilibrium phases by the rapid “quenching” of the species from the vapor to solid state [25, 26].

In an alloy, one can expect the segregation of a particular species to grain boundaries. Such segregation could be a viable route for stress state manipulation through microstructural control of grain boundary chemistries as well as grain size, where solute could pin grains from growing [25-27]. We have recently reported growing a series of low Cr content Fe(Cr) thin films at room temperature and found an inverse relationship between the grain size and tensile stress with Cr content up to 8 at.% [27]. When Cr was below the solubility limit, the Fe(Cr) grains grew whereas as upon exceeding the solubility limit, the Cr concentration within the grain boundaries was noted to increase and refine the grain size. Collectively this resulted in a varied stress response with composition.

In this work, we continue our investigations into the alloying effects of Fe(Cr) but with temperature during deposition. Fe(Cr) is a spinodal decomposition system [28-30] and has been well studied in bulk because of its interest in irradiation based steels [29, 31]. In our initial thin film studies, the early onset of phase separation was noted with an increased presence of Cr in the high angle grain boundaries [32]. With the use of *in situ* annealing done in this study, this phase separation should be even more pronounced and have a much more dramatic effect on the grain size, morphology, and stress states. For example, one can easily speculate that intrinsic Cr clustering within the grains created by the initial deposition but now heated by the substrate would stimulate the creation of new interfaces besides the island-to-island contacts during deposition. Such interfaces would change how the grains evolve and grow resulting in yet to be studied stress responses during deposition. Furthermore, depending on the film’s composition within or outside the miscibility gap, the phase separation of Fe and Cr via spinodal decomposition, which does not have a thermodynamic barrier for phase separation [33], or nucleation and growth could give another interesting variable for early onset stress evolution in the deposition films.

Though both species will phase separate from each other, Fe does tolerate a limited solubility of Cr within its phase at room temperature, with such solubility increasing with temperature. Though the exact extent of solubility varies among different reports [28-30, 34], an agreeing explanation was found that the change in the enthalpy of mixing from negative to positive is around 5. at.% Cr. Thus, an ideally lower solute Fe(Cr) thin film, such as Fe-4Cr, would be in equilibrium as a solid solution at either room temperature or elevated temperature whereas a higher solute film, Fe-16Cr, would be well within the miscibility gap and phase separate. Using these two compositions, we aim to better understand the intrinsic links of phase separation on nanocrystalline film morphology and accompanying residual stress development during the film deposition process.

2. Experimental

The two alloy films - Fe-4Cr or Fe-16Cr (at.%) - were magnetron sputter deposited in an AJA ATC-1500 system using 99.95% pure pre-alloyed targets. The films were grown to an approximate thickness of 300 nm onto 300 μm thick silicon [100] substrates which had a protective 100 nm amorphous silicon oxide surface to prevent deleterious reactions with the substrate with annealing. The temperature was calibrated using a k-Space[®] Bandit system on a previous Si substrate where the Si wafer's band edge changed with known temperature values. The sputtering rate was found to be approximately 0.100 nm/s for Fe-4Cr and 0.106 nm/s for Fe-16Cr and was relatively invariant to changes over the *in situ* deposition temperatures studied. The deposition rates were determined by dividing the film thickness, measured from x-ray reflectivity (XRR) [35] and confirmed by the transmission electron microscopy (TEM) cross-sectional micrographs, by the deposition time. XRR was performed on an X'pert Philips diffractometer operated with Cu $K\alpha$ radiation ($\lambda = 0.15406$ nm) at 40 kV and 30 mA. Prior to deposition, the chamber had a base pressure $< 6 \times 10^{-6}$ Pa evacuated by mechanical and turbo-pumps. High-purity Argon then flowed into the sputtering chamber as a working gas at a rate of 10 standard cubic centimeters per minutes to a pressure of 0.27 Pa.

The *in situ* stress state was measured through a k-Space[®] Multi-beam Optic Sensor attached to the base of the chamber [36]. By reflecting a series of laser spots from the substrate to a charge-coupled detector, the relative position of the spots moved as the substrate bends in response to the growth stresses. Using the Stoney equation, given below, the stress within the film was calculated.

$$\sigma_f = \frac{E_s}{6(1-\nu_s)} \frac{t_s^2}{t_f} \left(\frac{1}{R} - \frac{1}{R_0} \right) \quad (1)$$

where σ_f is the average films stress, ν_s and E_s are the Poisson ratio and Young's modulus of the substrate respectively, t_s is the substrate thickness, t_f is the film thickness, and $1/R_0$ and $1/R$ are measured curvatures of the films before and during the deposition.

The phase identification of the films was characterized by X-ray diffraction (XRD) via a Philips diffractometer with Cu $K\alpha$ radiation as the source operated at 45 kV and 40 mA as well as by electron diffraction using an FEI Tecnai F20 (scanning) transmission electron microscope ((S)TEM). The in-plane and out-plane microstructures were also characterized in the TEM from either traditional cutting, dimpling, and ion-milling 3 mm discs (plan-view) or focus ion beam (FIB) extraction and milling techniques (for the cross-sections). With the assistance of the NanoMEGA ASTARTM platform [37-39], the grain sizes, grain boundary character, as well as grain orientation distribution, were quantified using precession electron diffraction (PED) in the TEM. The PED scanning was operated with a 0.2° precession angle and a scanning step size of 3 nm, in the same regions of interest (ROI), which was 0.9 μm \times 0.9 μm for in-plane, 1.4 μm \times 0.3 μm for out-of-plane. After scanning, the data was converted for analysis using TSL OIM Analysis 7 software. Grain based and kernel based misorientation analyses were employed to identify grains and any varying local misorientations within the grains respectively. The Local Orientation Spread (LOS) method was used to calculate the misorientation between each point in the kernel with LOS maps created used those averaged values for the kernel. In this paper, the first nearest neighbor at a maximum misorientation spread of 5° was employed. Pole figures were also constructed from the PED data for texture analysis and compared to the XRD data collected on a Bruker D8 GADDS diffractometer.

The overall composition and local element distribution in the films were characterized by Atom Probe Tomography (APT). The required needle-shaped geometry for these specimens was prepared in the film's cross-section using a FIB lift-out technique and annular milling procedure described in reference [40] in either a TESCAN LYRA FIB- Field Emission Scanning Electron Microscope (SEM) or an FEI Quanta 3D dual beam FIB-SEM. With the APT tip prepared, the specimen was loaded into a Hummingbird TEM holder and placed into the FEI Tecnai F20 S(TEM) operated at 200 keV. The grain-to-grain mapping of the film was conducted using the PED at a precessed angle again of 0.2° but now at a scanning step size of 2 nm. Afterwards, the tip was field evaporated in a Cameca Instruments Local Electrode Atom Probe (LEAP[®]) 5000 XS operated at a specimen set point of 57 K, 500 kHz laser pulse repetition rate for a 1.0% atoms per pulse detection rate with a laser energy of 50 pJ. The prior PED analysis of the tips grain structure was then overlaid onto the APT reconstructed chemical map with further details on this procedure found in reference [32].

3. Results

Figure 1 shows the *in situ* stress evolution of the 300 nm thick Fe-4Cr and Fe-16Cr films deposited at room temperature (RT), 523K, and 673K. The RT films for both alloys exhibited near equivalent steady-state tensile stress, ~ 0.65 GPa, in the post coalescence regime evident by the linear response. This is more clearly plotted as the instantaneous stress, Figure 1(b). At the higher deposition temperatures, the tensile stress was reduced and even became compressive for the highest deposition temperature of 673K. But, unlike the RT deposition, the instantaneous stress response varied with thickness.

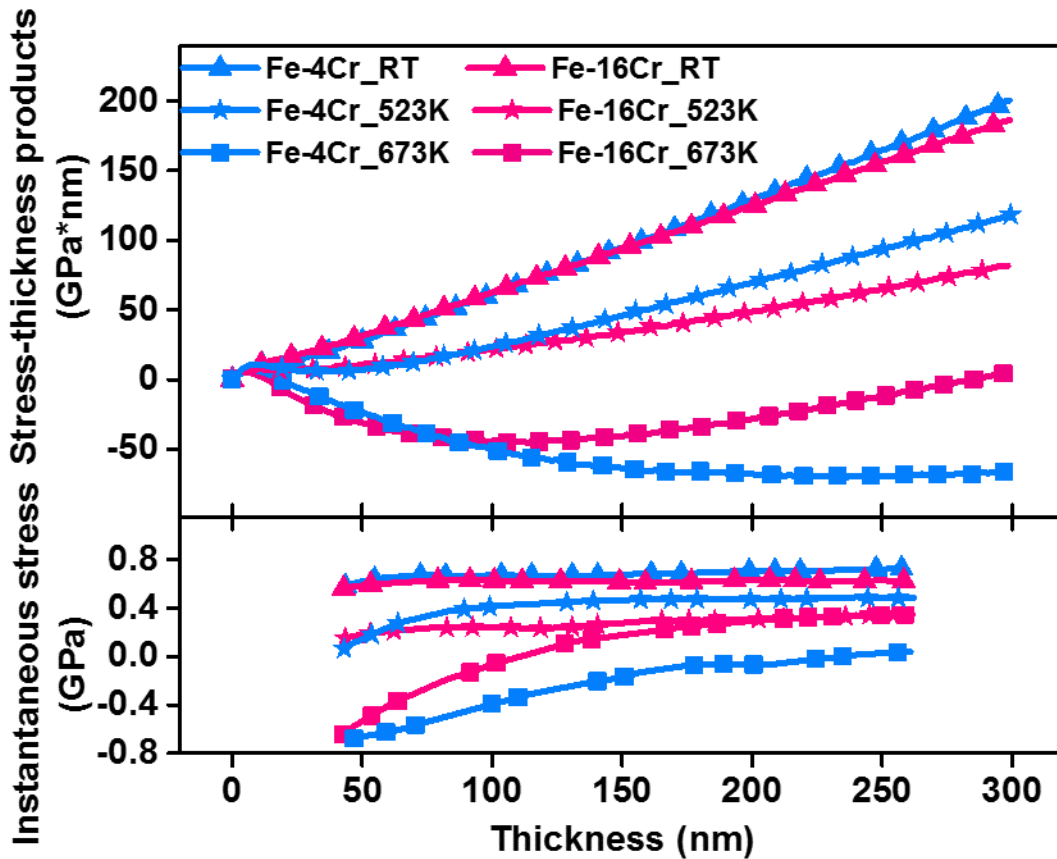


Figure 1 (a) Stress thickness products and (b) Instantaneous stress varying with film thickness for Fe-4Cr and Fe-16Cr thin films deposited at room temperature (RT), 523K, and 673K.

At 523K, both alloy films retained the tensile stress states with near invariant instantaneous stress responses after the early stages of post-coalescence growth ($> \approx 100$ nm), Figure 1(a). However, the increased temperature lowered the overall absolute stress value. Upon *in situ* depositing at 673K, a more dramatic change in the stress

evolution was found. Both films exhibited an evolving growth stress during deposition, with the stress values over the thickness range studied being compressive. Of the two films, the Fe-16Cr did reveal a more dramatic change in stress with thickness with a trend to revert back to a tensile state for thicknesses beyond ≈ 150 nm. This type of non-steady state stress is indicative of an evolving grain size with growth [23, 41-43], which will be further elaborated below.

Figure 2 is the PED cross-sectional orientation maps of Fe-4Cr and Fe-16Cr films deposited at RT, 523K, and 673K. In this view, one can begin to ascertain how the grains developed as the film thickened. With increasing deposition temperature, the films would move from the Zone 1 to Zone T designation as described in the model by Thornton [44]. All of these films revealed a relatively columnar morphology; however, the columnar diameters, as well as the prevalence of some polycrystalline grains within the columnar structure, varied. At RT, the columnar grain sizes of the RT Fe-4Cr film were relatively similar in diameter and much thinner than those in the RT Fe-16Cr film (compare Figure 2(a) vs. Figure 2(d)), where the columnar morphology exhibited an abnormal grain size distribution with both large and refined columnar granular structures. Within the discussion section below, the grain sizes have been quantified and will be further elaborated upon in understanding how these changes are linked to the stress states.

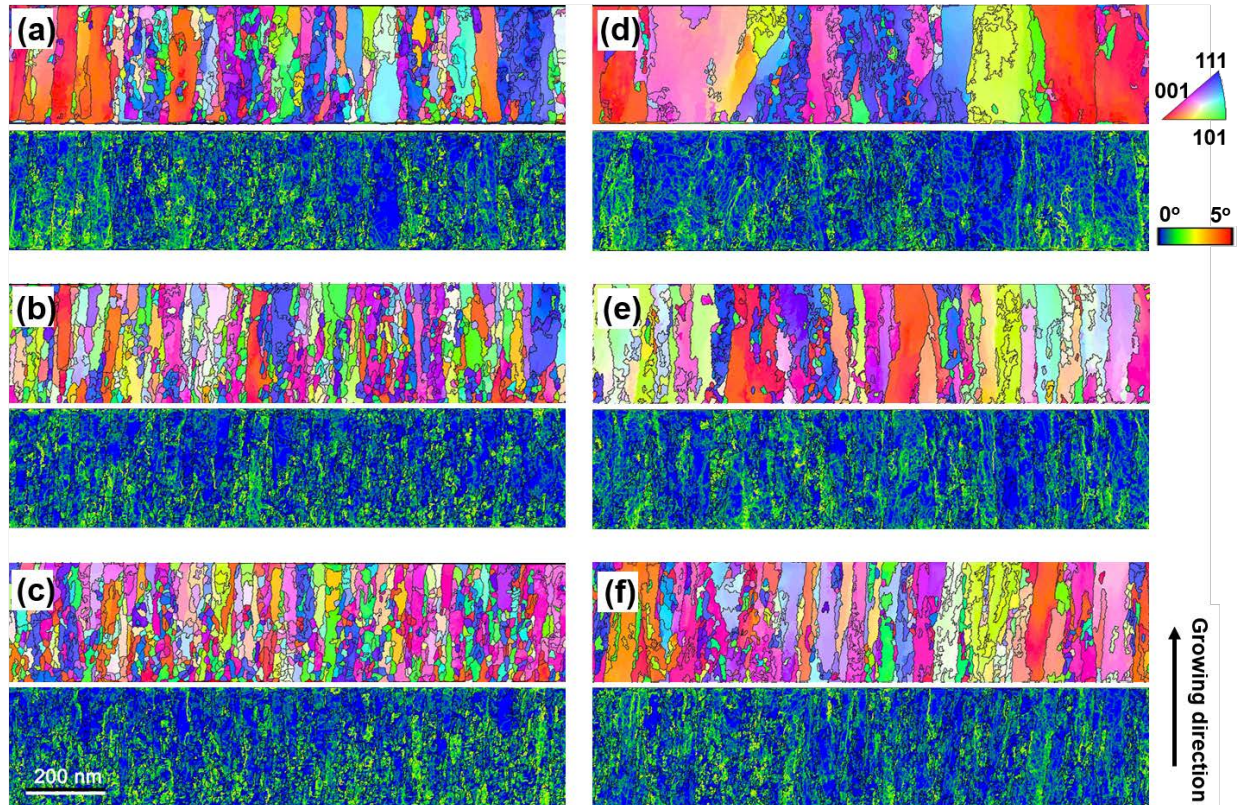


Figure 2 PED reconstructed orientation maps and corresponding local orientation spread maps showing cross-section information of Fe-4Cr films deposited **(a)** at room temperature (RT); **(b)** at 523K; **(c)** at 673K; and Fe-16Cr thin films deposited **(d)** at RT; **(e)** at 523K; **(f)** at 673K.

Upon *in situ* heating during growth, the Fe-4Cr films did not indicate any substantial grain growth in the columnar diameter, Figure 2(b)-(c). In prior studies by Thurner et al. [24], annealing of elemental Fe films to 473 K resulted in a clear onset of grain growth [24]. What is apparent in the Fe-4Cr films is that the annealing resulted in the onset of a more polycrystalline granular morphology within each of the columns. For the Fe-16Cr film, the annealing resulted in an apparent refinement of the columnar grain sizes and, unlike, the Fe-4Cr film, these columns did not have a large fraction, polycrystalline granular morphology within their structure, Figure 2(e)-(f). The corresponding local orientation spread or LOS maps, found under the inverse (or multicolor) map for each film and condition, is plotted in Figure 2. Here we note that many of the columnar grains revealed a continuous (but small) crystalline rotation throughout the vertical growth direction of the grain.

Figure 3 is a series of plan-view PED scans for each alloy and temperature. The plan-view grain sizes showed good agreement with the columnar diameter widths for

each of these films and provided a more robust means of analysis of grain size. Qualitatively, it is clear that the Fe-4Cr film was relatively equiaxed in grain shape for all three deposition conditions. In contrast, the RT Fe-16Cr film contained a range of grain sizes and shapes and only upon annealing did the grain morphology evolve towards a more equiaxed and uniform grain size distribution. Figure 4 is the the grain size distributions in this viewing direction. These histograms were calculated by the area fraction distribution, $F_A(D_i)$, given as

$$f_A(D_i)\delta D_i = \frac{A_i}{A_{total}} \quad (2)$$

where A_i is the area of grain ' i ', A_{total} is the total area occupied by the grains which are equal to the surface of the measurement of all the pixels belonging to grains [45], and δD_i is the bin size. The Fe-4Cr film at all temperatures retained an equiaxed grain size with their histograms being fitted to a lognormal function, superimposed in Figure 4(a) [45, 46]. Unlike Fe-4Cr, the Fe-16Cr revealed a wide distribution of gain sizes at all deposition conditions. Though, at 673 K, the Fe-16Cr grain size distribution did narrow. Similar grain refinement can also be seen for the Fe-4Cr films with increasing deposition temperature. The cumulative grain size distribution, Figure 4(b), and the average grain size diameter, Figure 4(c), taken from these histograms readily confirm this refinement, with the largest changes occurring in the Fe-16Cr film.

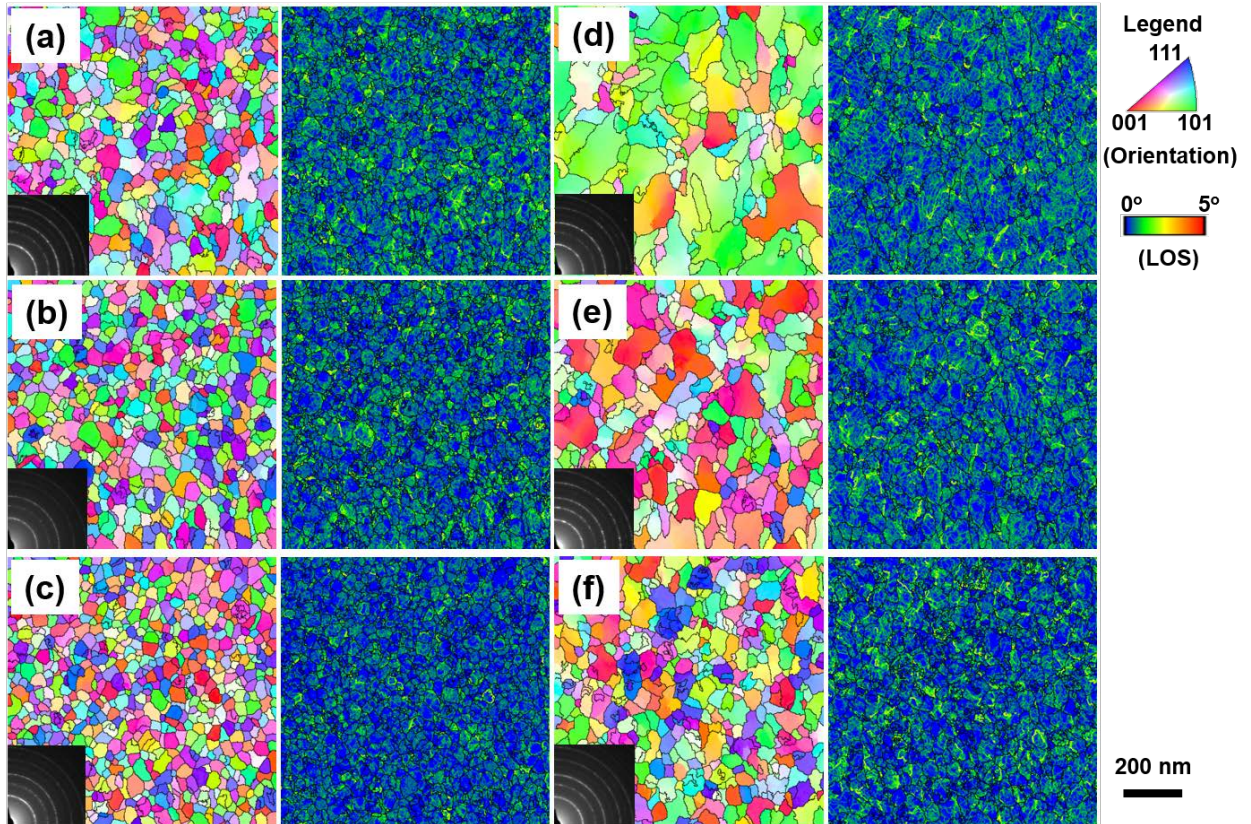


Figure 3 PED reconstructed orientation maps and corresponding local orientation spread maps showing plan-view information of Fe-4Cr films deposited **(a)** at room temperature (RT); **(b)** at 523K; **(c)** at 673K; and Fe-16Cr thin films deposited **(d)** at RT; **(e)** at 523K; **(f)** at 673K. The diffraction pattern of each specimen is included.

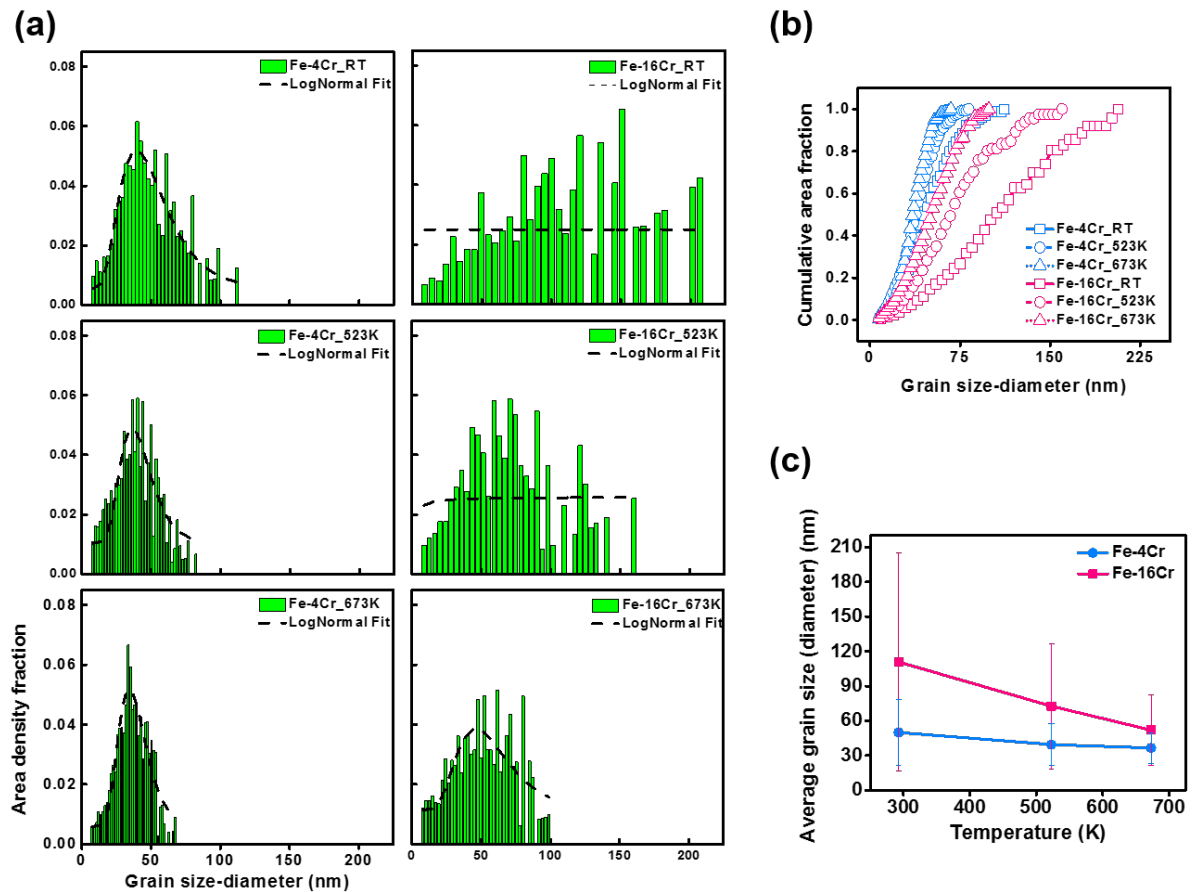


Figure 4 (a) Grain size distribution for Fe-4Cr and Fe-16Cr thin films deposited at room temperature (RT), 523K and 673K. Log normal function was used for grain size distribution fitting. **(b)** Cumulative grain size distribution plot quantifying each of these thin films. **(c)** Average grain size varying with deposition temperature for Fe-4Cr and Fe-16Cr thin films. The error bars show the standard deviation of grain size

Similar to cross-section analysis, the LOS maps are presented to the left of orientation maps in Figure 3 in the plan view condition. At RT, both the Fe-4Cr and Fe-16Cr samples showed a sub-grain structure within the grain evident by the prevalent green tint in the LOS maps of Figure 3. This would be expected as this modest crystalline tilt was prevalent throughout the columnar grain structure in Figure 2. As the annealing temperature increased for the Fe-4Cr film, qualitatively, the extent of this small crystalline misorientation decreased evident in the reduction of the green tint in the LOS maps between Figure 3(a)-(c). This is quantified in the plot of average misorientation with annealing temperature, Figure 5, where a $\sim 27\%$ reduction was noted to occur between RT and 673K. In contrast, the Fe-16Cr film did not show a substantial reduction in this small misorientation reduction with temperature, Figure 5.

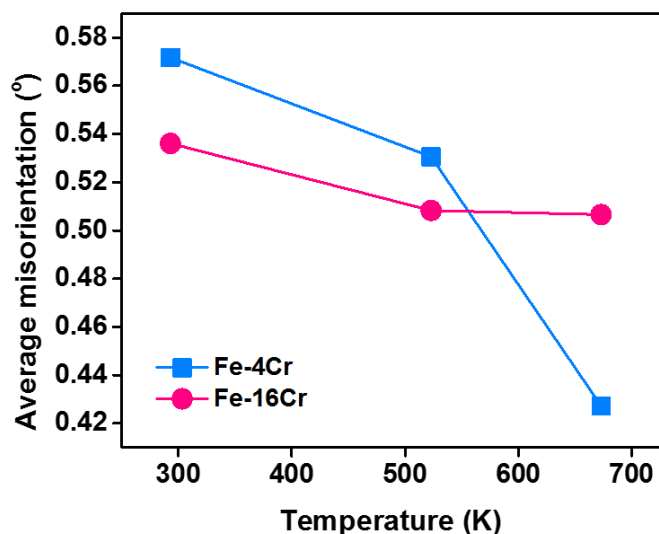


Figure 5 Average misorientation vary with temperature and composition. The average misorientation was drawn from local orientation spread maps of plan-view thin films.

All of the electron diffraction, embedded in Figure 3, and XRD scans (not shown) confirmed a single BCC phase for all alloys and temperature conditions. That would be expected since both phases are BCC. However, the films did experience an evolving texture evolution. At RT, the Fe-16Cr film revealed a much more predominate $\langle 101 \rangle$ fiber structure than Fe-4Cr indicated by the high-intensity region in the center of XRD pole figures for the $\langle 101 \rangle$ orientation, Figure 6. Upon annealing, each of the films exhibited a gradual texture change from $\langle 101 \rangle$, but this change was much more pronounced in the Fe-16Cr alloy. This change, particularly for Fe-16Cr, can be inferred from the clear color variation seen in the IPF in Figure 3(d)-(f). The detailed texture evolution, Figure 6, quantifies this change for all alloys and conditions. When the temperature was elevated to 673K, both Fe-4Cr and Fe-16Cr films did not show a strong, preferential texture.

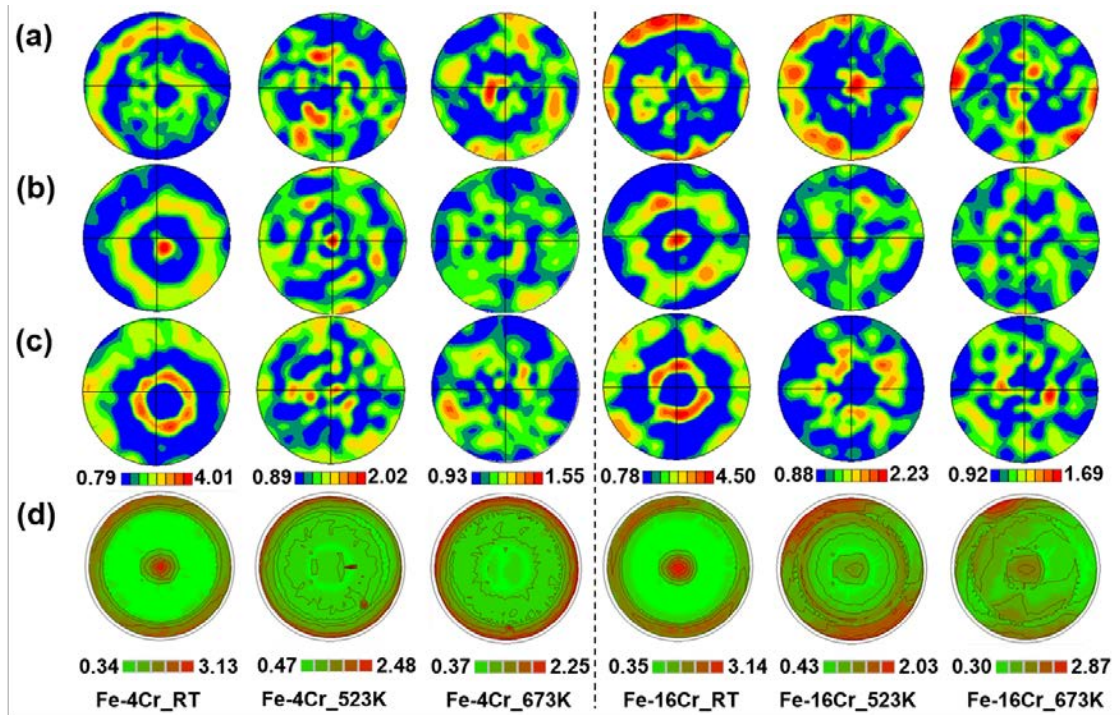


Figure 6 PED pole figures (first three rows, **(a)** $\langle 001 \rangle$, **(b)** $\langle 101 \rangle$ and **(c)** $\langle 111 \rangle$, respectively) from the Fe-4Cr and Fe-16Cr films deposited at room temperature (RT), 523K and 673K with the corresponding **(d)** X-ray diffraction pole figures (fourth row): $\langle 101 \rangle$ texture.

Figure 7 (a)-(d) are the PED-atom probe cross-correlative study from four separate atom probe tips prepared for each alloy at either RT or 673K. Each atom probe data set contained over 40 million ions, with the overall composition confirmed by APT. Grain boundaries in the atom probe data sets are observed through the Cr solute segregation decorating the boundaries and/or density variations created by the evaporation field differences between the grains under the single field reconstruction assumption [47, 48]. The sensitivity of the atom probe allowed FeO ion complexes to be found within the film; however, one should note that they were at a very low concentration, i.e. 0.05 at. %. These oxides were found to be at the grain boundaries, dashed arrows, and along other linear features, double headed arrows, in Figure 7(a) & (c), and provided ideal markers within the reconstructions. Looking carefully at the cross-correlative atom probe tips, one can ascertain several subtle features within the grain itself. For example, Figure 7(a) and (c) reveal orthogonal viewing directions where one can see both a point like feature and then a linear feature when the data sets rotated 90° , indicated by the double arrowhead. As these features are within the grain itself, it is suggestive that they may be decorating dislocations [49]. This could be further inferred as the grains themselves are revealing changes in the LOS maps within those

grains and dislocations themselves are responsible mechanisms for such subtle crystalline rotations. To our surprise, we did not observe any significant Cr segregation on or near these defects. Upon annealing, clear Cr enrichment was observed within the grains and on the grain boundaries themselves which is revealed as the red (or hot spots) in the 2D compositional maps shown in Figure 7(b) and (d).

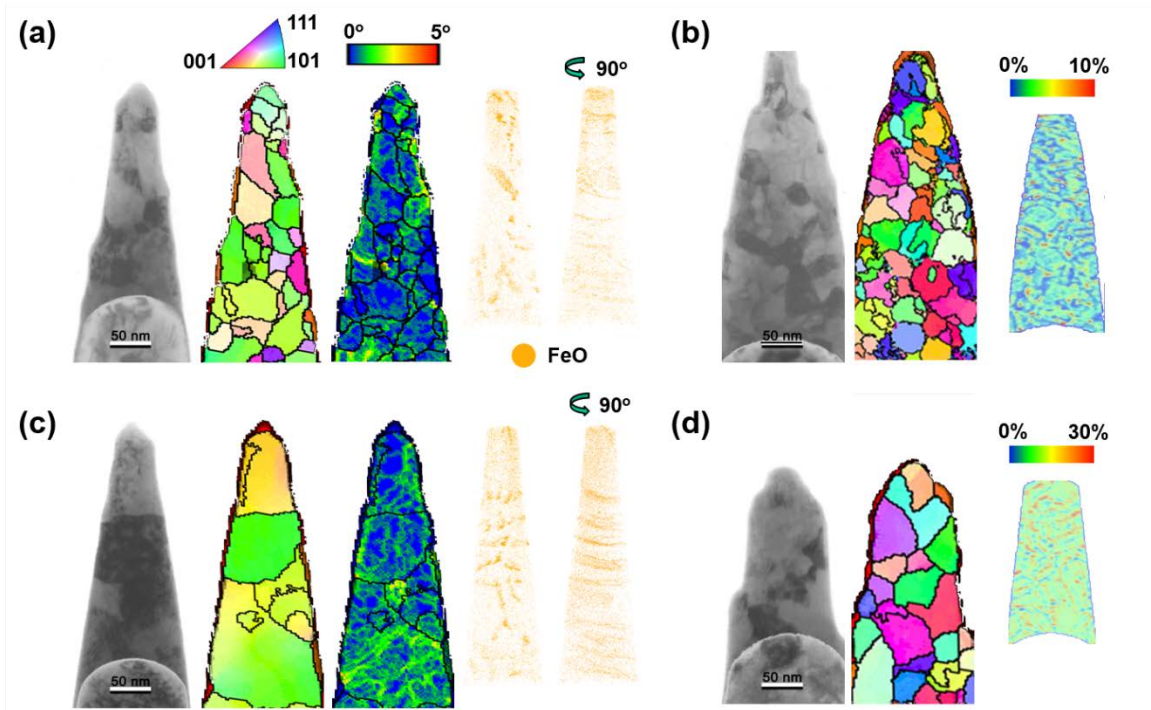


Figure 7 Cross-correlative study of Fe-4Cr films deposited **(a)** at room temperature (RT); **(b)** at 673K and Fe-16Cr films deposited **(c)** at RT; **(d)** at 673K. In **(a)** and **(c)**, bright field TEM image, PED reconstructed orientation maps, local orientation spread maps, and corresponding 3-D atom probe reconstructions of FeO ions were chosen to show. In **(b)** and **(d)**, bright field TEM image, PED reconstructed orientation maps, and corresponding 2D (1nm thick thin slides) Cr composition profile maps from 3-D atom probe reconstructions were chosen to show.

Figure 8 quantifies the Gibbisan interfacial excess of Cr, Γ_{Cr} , at these grain boundaries as a function of composition and temperature. Each data point represents an individual excess value. The interfacial excess was measured by placing a fixed cylinder through the atom probe imaged grain boundary and quantifying the Cr solute on either side of the boundary and within the boundary itself using a procedure similar to that by Krakauer et al. [27, 50]. Cr segregation was noted in all films, even the Fe-4Cr film, which would be the solid solution alloy. As the either the Cr content increased and/or the temperature, Γ_{Cr} , increased as well as evident in the spread in its values. As

previously reported by the authors, this large variation in excess is contributed to local clustering within the grain boundaries [32].

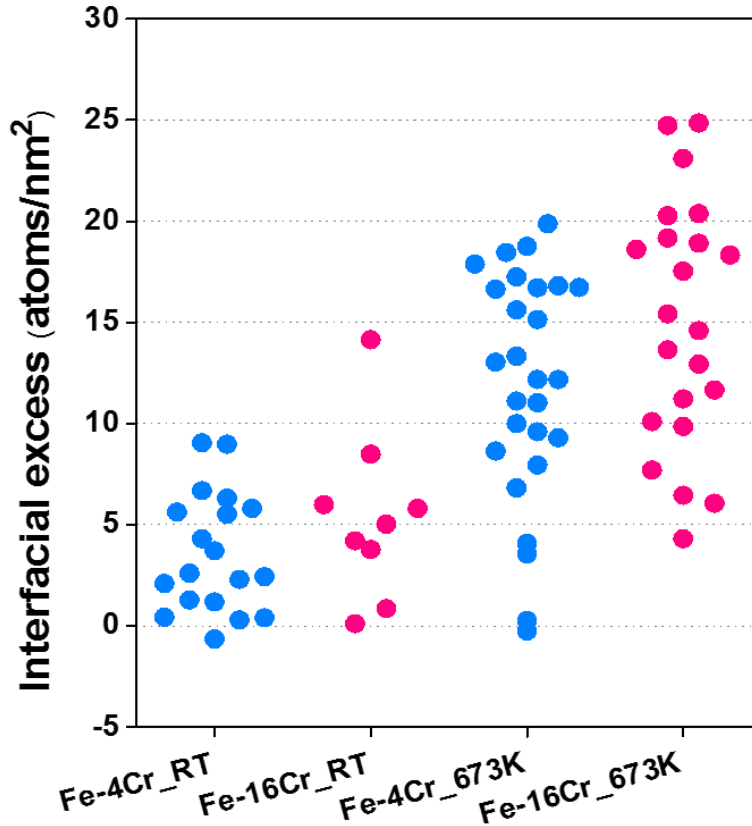


Figure 8 Statistical chart of interfacial excesses calculated from different grain boundaries found in tips shown in Figure 7. RT is short for room temperature.

4. Discussion

The findings from this study suggests that alloy composition and deposition temperature create a variation in microstructure, i.e. grain structure, growth texture, and local elemental partitioning. Those differences individually or jointly have influenced the thin films stress response. With the results from the different characterization methods presented, along with the residual growth stresses observed, the linkage of how the structure and corresponding stress is now discussed.

At RT, both Fe-4Cr and Fe-16Cr films displayed a constant tensile stress, Figure 1, with TEM-PED revealing a columnar structure, Figure 2. What is particularly striking is

that both films exhibited nearly identical (steady-state) stress values but had very different grain sizes and distributions, i.e. normal vs. abnormal for the Fe-4Cr and Fe-16Cr respectively. Grain size has been historically linked to the stress responses in thin films [27]. According to island-based growth models [18, 19, 51], tensile stress is inversely related to the grain size. The larger grain sizes, observed in the Fe-16Cr film as compared to Fe-4Cr, would suggest that it would have a lower tensile stress yet it was observed to have a steady-stress state comparable to the smaller grain size Fe-4Cr film. To explain this peculiar behavior, we review the differences in the microstructures between the two films.

Both films showed a similar local misorientation, Figure 5, at RT, which is related to the crystalline imperfections within the grains, such as sub-grain formations. The distribution of these local misorientations were seen in both plan-view and cross sections, Figures 2 and 3, and appeared throughout the granular morphologies. Thus, this effect is likely not a contributing factor to explain the similar stress states for the different size grains. These same grains also revealed similar $\langle 011 \rangle$ fiber textures in the pole figures in Figure 6. Though the IPF grain map in Figure 3(a) reveals, qualitatively, more dispersion of colored textures in the grains; the pole figure taken from that image, Figure 6, quantifies a strong $\langle 011 \rangle$ fiber texture. The potential confusion in the granular map resides in that foil was not ideally orthogonal to the electron beam when it was scanned. This can be inferred by the off-centric high intensity ring pattern in the $\langle 111 \rangle$ pole figure in Figure 6(c) for the RT Fe-4Cr film. In contrast, the Fe-16Cr film, which showed a granular color map texture of $\langle 011 \rangle$ in Figure 3(d), has its $\langle 111 \rangle$ pole figure intensity's ring pattern uniformly centric around the pole's center point. Since both of these films exhibit near equivalent fiber textures, this too cannot explain the peculiar stress behavior. Thus, the difference in the grain size in yielding a similar tensile stress must have been offset by the composition effect within the film. This can be understood by recognizing that the Γ_{Cr} between the two films is nearly equivalent, Figure 8. With the Cr not strongly partitioned into the grain boundaries for the Fe-16Cr film, the matrix is in a super-saturated condition. Consequently, the excess Cr would produce local strains within the matrix grains of the Fe-16Cr film which potentially helps to offset the tensile reduction in the overall film stress behavior.

The next logical question would then follow how the Cr content facilitated such large grain growth. The grain sizes within a thin film is driven by the mobility of the adatoms on the surface to coalesce together and form impinging islands. This ultimately develops the final grain structure. In the case of Fe-4Cr, the alloy is in a thermodynamic equilibrium composition for a solid solution. Since Fe is reported to grow as equiaxed grains [27], it reasons that if a solute is thermodynamically stable in solution, changes in the grain morphology would not necessarily be expected. However, the Fe-16Cr is a composition is far from equilibrium but has been processed into a supersaturated solid solution. Thus, differences in Fe and Cr intrinsic adatom motilities would be much more

interactive because of the much higher solute concentration. Considering that the solute itself would partition from the solvent, one can image the cooperative adatom behavior on the growth surface to be complex in how islands impinge, rotate and diffuse atoms between each feature. In prior work by the authors [27], we noted that an equiaxed Fe(Cr) grain size could be maintained up to 8 % Cr; however, once the Cr exceeded the ~ 5 at.% Cr solubility limit, these grains refined. The refinement was reported to be a result of Cr adatoms producing a Zener-like solute drag on the grains as the solute partitioned to the grain boundaries. In this new case, where the solute content is so sufficiently high, and the interfacial excess nearly equivalent to the Fe-4Cr film (Figure 8), the grains must be growing through some other competing factor.

The lowest surface energy for bcc metals is the {011} surface [52]. Wang *et al.* [53] have used molecular dynamics studies to demonstrate that the diffusion barrier for Fe on the {011} surface is lower than that of the {001} and {111} surfaces. Though surface energy is often the energetic term that will control surface (facet) formations; other considerations can alter the texture development. For example, in face centered cubic (FCC) metal films, the lowest surface energy is {111} but many films will also exhibit a minor {002} peak, which is the elastically soft direction in FCC [54, 55]. Hence, strain energy can also compete with texture development.

Though the Fe-4Cr and Fe-16Cr both show equivalent textures in the pole figures in Figure 6, the differences in their elastic strains is suspected to be contributing to how the grains are growing these particular surfaces. Fe's elastically soft direction is <001> [56] whereas it is <011> for Cr [56]. Consequently, as the Cr content increased, the alloy ever more favors a different elastically softer direction that also happens to match the lowest energy surface, i.e. {011}. This change is believed to have help promote the increased grain sizes and spread in the grain size distribution in the higher Cr content film.

Upon annealing the substrate to 523K during deposition, the alloy films retained a tensile stress response, albeit at a lower absolute value, Figure 1. This stress finally became compressive at 673K. The grain size distribution for both Fe-4Cr and Fe-16Cr refined with each successive increase in temperature, Figure 4(b), with the Fe-16Cr showing a dramatic reduction in the average grain size, Figure 4(c). Furthermore, the Fe-4Cr films retained the log normal grain size distribution indicating a resistance to abnormal grain growth. Interestingly, the Fe-16Cr grains, which had a large distribution of grain sizes trended towards a more uniform, log normal grain size distribution at the highest substrate temperature, Figure 4(a).

It is common to observe a tensile stress reduction with elevated temperature in thin films because the thermal energy promotes grain growth which in turn reduces the grain boundary density within the film. Such behavior has been confirmed by Thurner [24] for both elemental Fe and Cr films. What is less common to observe, as seen here,

is a reduction (or static) grain size with temperature that results in a corresponding reduction in the tensile stress. This is plotted in Figure 9 as grain size verses the stress at 200 nm. Though it would be more ideal to plot steady-state stress, the highest temperature films showed a stress variation with thickness making this not possible for all films. Regardless of this issue, the plot does reveal, for the thicknesses studied, a reduction of stress with either a static or decreasing grain size. One would normally assume a smaller grain size would promote an opposite trend or no change if the grain size did not vary. At this point, we do note that the varying stress state for Fe-16Cr at 673K did exhibit a trend back towards a tensile stress state. This particular reversion will be elaborated upon further in the subsequent paragraphs. We will first address Fe-4Cr, as it provides a composition where ideally a solid solution is in thermodynamic equilibrium under all conditions and it did retain a consistent, equiaxed grain size through all the annealing temperatures.

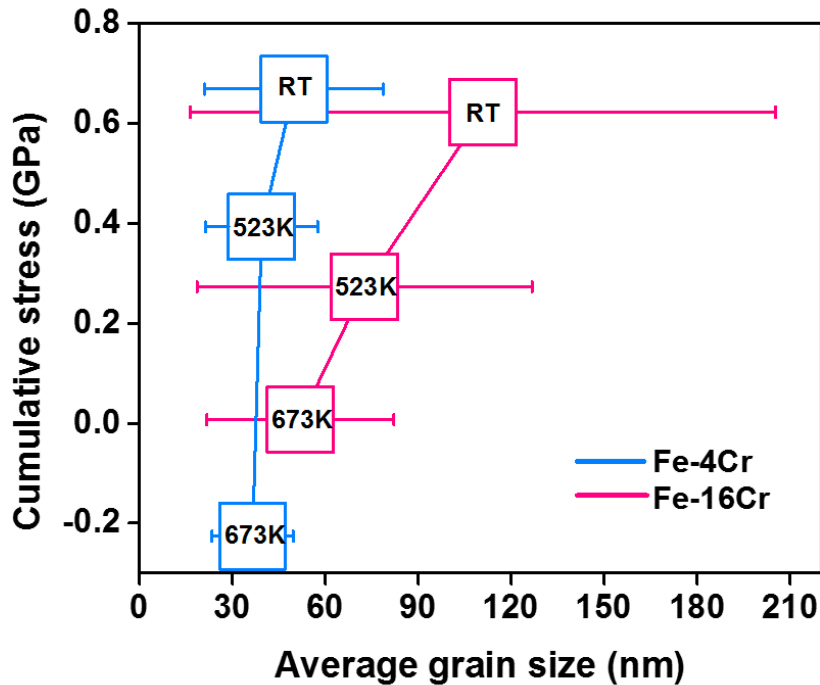


Figure 9 Thin film stress varying with average grain size.

Though Fe-4Cr is ideally in solution, the binary system is a phase separating alloy at higher Cr concentrations. Consequently, it is not surprising that the solute, even at low concentrations, would have some preferential segregation to the grain boundaries. For example, Cu-Ni forms a solid solution but solute Ni has been reported to be weakly segregating [57] with experimental verification to that effect [58]. Here, we have

observed excess Cr in the grain boundaries, Figure 8, for an ideal solid solution Fe-4Cr film. Upon annealing, more of this Cr content increased in the grain boundary, Figure 8, evident by the increase in the interfacial excess at 673K. Interestingly, this increase did not result in any further refinement of the grain sizes, Figure 4(c), but randomized the texture evident by the loss of the strong $\langle 011 \rangle$ intensity in the pole figures of Figure 6. Thus, the reduction of the tensile stress here does not appear to trend with grain size but rather the nature of the grain boundary itself and the loss of the fiber texture.

According to thin film stress models proposed by Chason [43], the insertion of excess adatoms into the grain boundaries is proposed as a potential mechanism for compressive stress generation. The increased migration of Cr into these boundaries, even at the lower solute concentration, may be assisting in the reduction of the tensile stresses that form across impinging islands. As the boundary density has not changed, but the Γ_{Cr} has, this would lend support to that notation.

To address the Fe-16Cr film, several interesting microstructural and stress responses are observed with the increase in temperature. Similar to Fe-4Cr, excess Cr in the grain boundaries were observed. Unlike Fe-4Cr, the Fe-16Cr average grain size value did refine and the grain size distribution did tighten, Figure 4. Though the standard deviation for these grain sizes would imply overlap, a review of the PED scans in Figure 3 and the average values clearly reveal a grain size reduction between all three films. Thus, the reduced grain size and the reduction of the tensile stress does not follow conventional understanding. However, at 673K, which is the smallest grain size for all of these films, the Fe-16Cr film's stress trended back towards a tensile stress condition. The lack of a steady-state stress during this particular growth provides clues that an evolving microstructure is contributing to the complex and peculiar stress responses. Upon reviewing the cross-sectional TEM micrographs, Figure 2, the Fe-16Cr film at 673K exhibit a rather continuous columnar grain size throughout the thickness of the film. Though some grain growth could be occurring, dependent on film thickness and post-growth observations, a more likely contribution would be the alloy system itself being driven towards thermodynamic equilibrium.

At 16 at.% Cr, the alloy, in a sputter deposited solid solution BCC phase, is far from equilibrium. Heating such a system would help drive the system towards a lower energy state. Using atom probe tomography, we have been able to quantify the onset of phase separation within the grains of the film. Though Cr segregation to the grain boundaries is occurring, evident by the increase in the Γ_{Cr} , the high solute within the grain itself is also phase separating. Figure 10(a) reveals a layering of Cr concentrations within the grains. In Figure 10(b), three orthogonal cylinders – denoted as x, y, and z - are placed through the same interior portion of the grain. The compositional profiles in all three directions reveal a sinusoidal fluctuation, Figure 10(c), suggestive of a spinodal decomposition reaction, even though the enthalpy of mixing is only slightly positive at

1.1 kJ/mol [59]. If the reaction was by nucleation and growth, one would expect a very Cr-rich phase to be present by virtue that it nucleated within the grain. Using the cross-correlative indexing of the grain orientation, the compositional layers appeared to be systematically separating on $\{112\}$ planes, Figure 10(d). The $\{112\}$ planes were determined through the cross-correlative use of precession electron diffraction of the atom probe tip prior to field evaporation. With increasing the temperature, sufficient thermal energy was clearly present to assist the film to phase separate. The creation of these interphase boundaries, where the film wants to phase separate (creating new interfaces) while retaining a coalesced, continuous film, and may explain the varied stress response with growth thickness. Since the 523K stress response was linear or in steady state, the thermal energy must not have been sufficient to promote a sufficient onset of phase separation and microstructural evolution with growth.

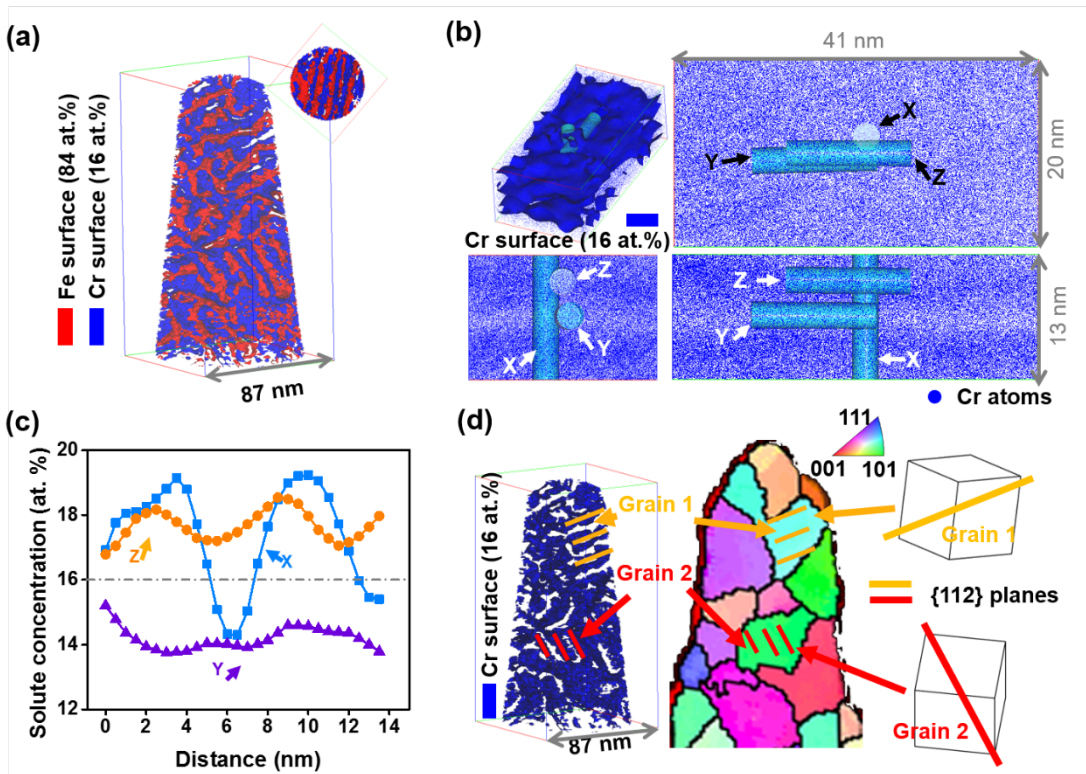


Figure 10 (a) Atom probe tomography results of the same tips shown in Figure 7 (d) using 16 at.% Cr & 84 at.% Fe iso-concentration surfaces, respectively (16 atomic % Cr & 84 atomic% Fe were chosen as a threshold value to highlight different regions). (b) Different views of Cr atom in Fe-16Cr films with three different cylinders embedded. Those cylinders were used to show (c) local concentration variation. (d) 16 at.% Cr iso concentration surfaces map and PED reconstructed orientation maps of the Fe-16Cr tip. Orange lines are from grain one, and red lines are from grain two. The sketches of grain orientations were also included. The Cr atoms preferred to segregate into the planes lose to $\{112\}$ crystalline plane.

Upon further inspection of the Fe-4Cr film's 673 K stress data, it too revealed a non-steady state stress response, though the film did not appear to trend towards a tensile stress state at the layer thicknesses studied. Figure 11 is the atom probe reconstruction of its morphology at 673K. Though this film is thermodynamically predicted to be an equilibrium solid solution, it too revealed a Cr layering structure, Figure 11(a). Again, three orthogonal cylinders are placed through a grain, shown in Figure 11(b), and a compositional fluctuation was measured, Figure 11(c). The cross-correlative microscopy revealed that these layers too favored the {112} planes. Unlike the Fe-16Cr film, which had a higher Cr content amplitude, the Fe-4Cr's equivalent species amplitude was lower which is contributed to the lower Cr content within the film; but we do note that the wavelength of fluctuations are very similar. This lower Cr content may explain why this film was not (yet) trending towards a tensile stress state. Regardless of the non-steady state stress behavior, this finding does suggest that the thermodynamically equilibrium concentration of Cr in solution with bcc Fe may be lower than previously expected and/or the effects of a nanocrystalline granular film have altered the bulk thermodynamic equilibrium conditions.

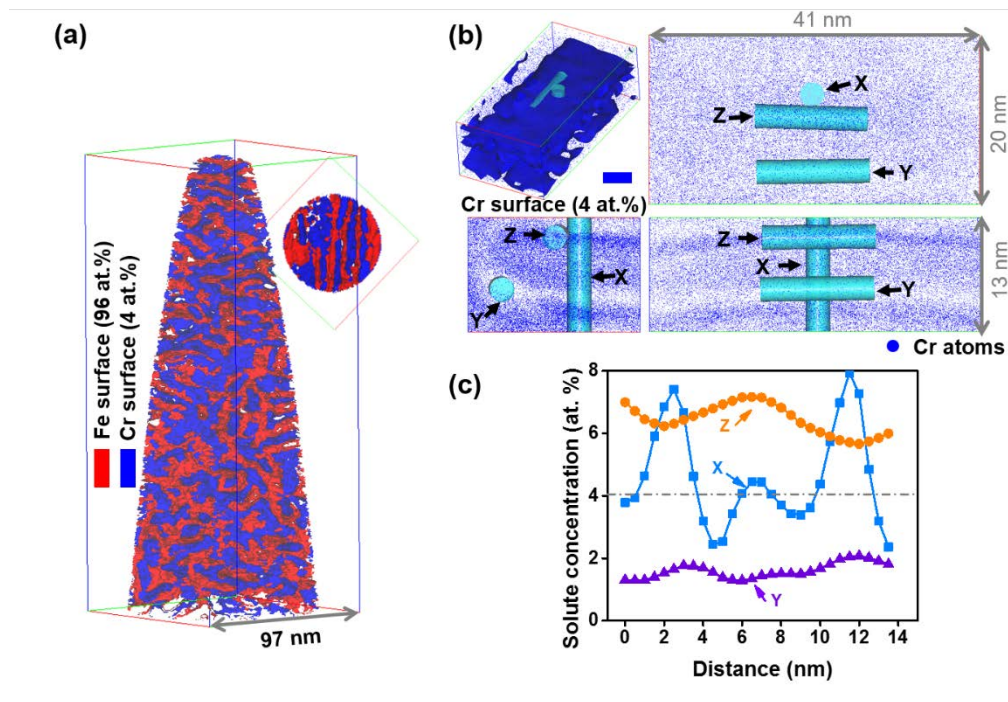


Figure 11 (a) Atom probe tomography results of the same tips shown in Figure 7 (b) using 4 at.% Cr & 96 at.% Fe iso-concentration surfaces, respectively (4 atomic % Cr & 96 atomic% Fe were chosen as a threshold value to highlight different regions). **(b)** Different views of Cr atom in Fe-4Cr films with three different cylinders embedded. Those cylinders were used to show **(c)** local concentration variation.

5. Conclusion

A series of Fe-4Cr and Fe-16Cr thin films have been sputter-deposited onto surface oxidized [001] Si substrates at different growth temperatures. The *in situ* growth stress response was measured and films at RT and 523 revealed steady-state, tensile growth stresses. Interestingly, the stress reduced with temperature, which could be expected; however, the grains were either static or refined. Nominally, with temperature, grains grow reducing the grain boundary area with an associated reduction in tensile stress. Thus, the mechanism of stress reduction here has been proposed to be related to the grain boundary chemical structure, where excess Cr adatoms segregated. This segregation was associated in providing a solute drag effect that either kept the grain size static or helped refine the grain size and grain size distribution. Further increases in Cr were shown to promote a loss of the <011> fiber texture with an equiaxed, tighter grain size distribution.

Upon further increases in temperature to 673K, the films continued to reduce in stress; nonetheless, the stress was no longer in steady state. Atom probe tomography revealed a Cr compositional fluctuation within the grains that was reminiscent of a spinodal decomposition reaction. Though this could be expected for the Fe-16Cr film, which is far from equilibrium and well within a two phase region, the Fe-4Cr film is predicted to be in solution. The presence of phase separation in this alloy suggest that either Fe does not have as high solid solubility as predicted and/or the nanocrystalline effects of the thin film have altered the equilibrium composition conditions. Regardless, this evolving phase separation in both films is believed to have contributed to the changing stress state with growth. The competition between phase separation and maintaining a continuous coalescence film provides for a complex stress-microstructure interaction. The results of this work further identifies that alloy compositions can provide for an interesting and intriguing means of microstructural and stress control in thin films.

Acknowledgements

The authors gratefully recognize support from the Army Research Office, grant W911NF1310436, Dr. Michael Bakas program manager. The authors thank Dallin Barton and Ty Prosa for their technical discussions. The UA Central Analytical Facility is recognized for additional assistance and access to the microscopes used in this research.

Reference

- [1] F.J. Himpsel, J.E. Ortega, G.J. Mankey, R.F. Willis, Magnetic nanostructures, *Advances in Physics* 47(4) (1998) 511-597.
- [2] P.K. Tien, Light Waves in Thin Films and Integrated Optics, *Appl. Opt.* 10(11) (1971) 2395-2413.

- [3] K. Nomura, H. Ohta, A. Takagi, T. Kamiya, M. Hirano, H. Hosono, Room-temperature fabrication of transparent flexible thin-film transistors using amorphous oxide semiconductors, *Nature* 432(25) (2004) 488-492.
- [4] S. Kovesnikov, W. Tsai, I. Ok, J.C. Lee, V. Torkanov, M. Yakimov, S. Oktyabrsky, Metal-oxide-semiconductor capacitors on GaAs with high-k gate oxide and amorphous silicon interface passivation layer, *Applied Physics Letters* 88(2) (2006) 022106.
- [5] B. Radisavljevic, A. Radenovic, J. Brivio, V. Giacometti, A. Kis, Single-layer MoS₂ transistors, *Nature nanotechnology* 6(3) (2011) 147-150.
- [6] X. Chen, S.S. Mao, Titanium dioxide nanomaterials: synthesis, properties, modifications, and applications, *Chemical reviews* 107(7) (2007) 2891-959.
- [7] I. Repins, M.A. Contreras, B. Egaas, C. DeHart, J. Scharf, C.L. Perkins, B. To, R. Noufi, 19.9%-efficient ZnO/CdS/CuInGaSe² solar cell with 81.2% fill factor, *Progress in Photovoltaics: Research and Applications* 16(3) (2008) 235-239.
- [8] P.H. Mayrhofer, C. Mitterer, L. Hultman, H. Clemens, Microstructural design of hard coatings, *Progress in Materials Science* 51(8) (2006) 1032-1114.
- [9] M.A. Steiner, R.B. Comes, J.A. Floro, W.A. Soffa, J.M. Fitz-Gerald, L1' ordering: Evidence of L₁₀-L₁₂ hybridization in strained Fe_{38.5}Pd_{61.5} epitaxial films, *Acta Materialia* 85 (2015) 261-269.
- [10] M. Seita, C.M. Pecnik, S. Frank, R. Spolenak, Direct evidence for stress-induced texture evolution and grain growth of silver thin films upon thermal treatment and self-ion bombardment, *Acta Materialia* 58(19) (2010) 6513-6525.
- [11] K. Yalamanchili, I.C. Schramm, E. Jiménez-Piqué, L. Rogström, F. Mücklich, M. Odén, N. Ghafoor, Tuning hardness and fracture resistance of ZrN/Zr_{0.63}Al_{0.37}N nanoscale multilayers by stress-induced transformation toughening, *Acta Materialia* 89 (2015) 22-31.
- [12] K.S. Park, J.K. Park, Effect of thin film stress on the elastic strain energy of Cr thin film on substrate, *Acta Materialia* 47(7) (1999) 2177-2184.
- [13] D. Sander, The correlation between mechanical stress and magnetic anisotropy in ultrathin films, *Reports on Progress in Physics* 62 (1999) 809-858.
- [14] T. Shibata, H. Irie, D.A. Tryk, K. Hashimoto, Effect of Residual Stress on the Photochemical Properties of TiO₂ Thin Films, *The Journal of Physical Chemistry C* 113(29) (2009) 12811-12817.
- [15] R.C. Cammarata, Surface and interface stress effects in thin films, *Progress in Surface Science* 46(1) (1994) 1-38.
- [16] J. Leib, R. Mönig, C. Thompson, Direct Evidence for Effects of Grain Structure on Reversible Compressive Deposition Stresses in Polycrystalline Gold Films, *Physical Review Letters* 102(25) (2009) 256101.
- [17] D. Flototto, Z.M. Wang, L.P.H. Jeurgens, E.J. Mittemeijer, Kinetics and magnitude of the reversible stress evolution during polycrystalline film growth interruptions, *Journal of Applied Physics* 118(5) (2015).
- [18] R.W. Hoffman, Stresses in thin films: The relevance of grain boundaries and impurities, *Thin Solid Films* 34 (1976) 185-190.
- [19] L.B. Freund, E. Chason, Model for stress generated upon contact of neighboring islands on the surface of a substrate, *Journal of Applied Physics* 89(9) (2001) 4866-4872.
- [20] G. Abadias, A. Fillon, J.J. Colin, A. Michel, C. Jaouen, Real-time stress evolution during early growth stages of sputter-deposited metal films: Influence of adatom mobility, *Vacuum* 100 (2014) 36-40.
- [21] H.Z. Yu, J.S. Leib, S.T. Boles, C.V. Thompson, Fast and slow stress evolution mechanisms during interruptions of Volmer-Weber growth, *Journal of Applied Physics* 115(4) (2014).

- [22] Y.G. Shen, Y.W. Mai, Q.C. Zhang, D.R. McKenzie, W.D. McFall, W.E. McBride, Residual stress, microstructure, and structure of tungsten thin films deposited by magnetron sputtering, *Journal of Applied Physics* 87(1) (2000) 177-187.
- [23] H.Z. Yu, C.V. Thompson, Grain growth and complex stress evolution during Volmer–Weber growth of polycrystalline thin films, *Acta Materialia* 67 (2014) 189-198.
- [24] G. Thurner, R. Abermann, Internal stress and structure of ultrahigh vacuum evaporated chromium and iron films and their dependence on substrate temperature and oxygen partial pressure during deposition, *Thin Solid Films* 192(2) (1990) 277-285.
- [25] B. Fu, G.B. Thompson, In situ growth stresses during the phase separation of immiscible FeCu thin films, *Applied Surface Science* 257(5) (2010) 1500-1505.
- [26] B. Fu, W. An, C.H. Turner, G.B. Thompson, In Situ Thin Film Growth Stresses during Chemical Ordering, *Physical Review Letters* 105(9) (2010) 096101.
- [27] X. Zhou, T. Kaub, R.L. Martens, G.B. Thompson, Influence of Fe(Cr) miscibility on thin film grain size and stress, *Thin Solid Films* 612(1) (2016) 29-35.
- [28] W. Xiong, M. Selleby, Q. Chen, J. Odqvist, Y. Du, Phase Equilibria and Thermodynamic Properties in the Fe-Cr System, *Critical Reviews in Solid State and Materials Sciences* 35(2) (2010) 125-152.
- [29] L. Malerba, A. Caro, J. Wallenius, Multiscale modelling of radiation damage and phase transformations: The challenge of FeCr alloys, *Journal of Nuclear Materials* 382(2-3) (2008) 112-125.
- [30] O. Kubaschewski, *IRON—Binary Phase Diagrams*, Springer Berlin Heidelberg 2013.
- [31] R.L. Klueh, A.T. Nelson, Ferritic/martensitic steels for next-generation reactors, *Journal of Nuclear Materials* 371(1-3) (2007) 37-52.
- [32] X. Zhou, X.-x. Yu, T. Kaub, R.L. Martens, G.B. Thompson, Grain Boundary Specific Segregation in Nanocrystalline Fe(Cr), *Scientific Reports* 6 (2016) 34642.
- [33] D.A. Porter, K.E. Easterling, M. Sherif, *Phase Transformations in Metals and Alloys*, Third Edition (Revised Reprint), CRC Press 2009.
- [34] F. Danoix, P. Auger, Atom Probe Studies of the Fe–Cr System and Stainless Steels Aged at Intermediate Temperature: A Review, *Materials Characterization* 44 (2000) 177-201.
- [35] Y. Sasanuma, M. Uchida, K. Okada, K. Yamamoto, Y. Kitano, A. Ishitani, Characterization of long-periodic layered structures by X-ray diffraction IV: Small angle X-ray diffraction from a superlattice with non-ideal interfaces, *Thin Solid Films* 203(1) (1991) 113-120.
- [36] C. Taylor, D. Barlett, E. Chason, J. Floro, A Laser-Based Thin-Film Growth Monitor, *Industrial Physicist* 4(1) (1998) 25.
- [37] J.G. Brons, G.B. Thompson, Orientation Mapping via Precession-Enhanced Electron Diffraction and Its Applications in Materials Science, *JOM* 66(1) (2013) 165-170.
- [38] P. Moeck, S. Rouvimov, E.F. Rauch, M. Véron, H. Kirmse, I. Häusler, W. Neumann, D. Bultreys, Y. Maniette, S. Nicolopoulos, High spatial resolution semi-automatic crystallite orientation and phase mapping of nanocrystals in transmission electron microscopes, *Crystal Research and Technology* 46(6) (2011) 589-606.
- [39] E.F. Rauch, J. Portillo, S. Nicolopoulos, D. Bultreys, S. Rouvimov, P. Moeck, Automated nanocrystal orientation and phase mapping in the transmission electron microscope on the basis of precession electron diffraction, *Zeitschrift für Kristallographie* 225(2-3) (2010) 103–109.
- [40] K. Thompson, D. Lawrence, D.J. Larson, J.D. Olson, T.F. Kelly, B. Gorman, In situ site-specific specimen preparation for atom probe tomography, *Ultramicroscopy* 107(2-3) (2007) 131-9.
- [41] E. Chason, A kinetic analysis of residual stress evolution in polycrystalline thin films, *Thin Solid Films* 526 (2012) 1-14.

- [42] E. Chason, P. Guduru, Tutorial: Understanding residual stress in polycrystalline thin films through real-time measurements and physical models, *Journal of Applied Physics* 119(19) (2016).
- [43] E. Chason, B. Sheldon, L. Freund, J. Floro, S. Hearne, Origin of Compressive Residual Stress in Polycrystalline Thin Films, *Physical Review Letters* 88(15) (2002) 156103.
- [44] J.A. Thornton, Influence of apparatus geometry and deposition conditions on the structure and topography of thick sputtered coatings, *Journal of vacuum Science & Technology* 11(4) (1974) 666-670.
- [45] L.S. Toth, S. Biswas, C. Gu, B. Beausir, Notes on representing grain size distributions obtained by electron backscatter diffraction, *Materials Characterization* 84 (2013) 67-71.
- [46] K. Okazaki, H. Conrad, Recrystallization and Grain Growth in Titanium: I. Characterization of the Structure, *Metallurgical Transactions* 3 (1972) 1972-2411.
- [47] M. Herbig, M. Kuzmina, C. Haase, R.K.W. Marceau, I. Gutierrez-Urrutia, D. Haley, D.A. Molodov, P. Choi, D. Raabe, Grain boundary segregation in Fe–Mn–C twinning-induced plasticity steels studied by correlative electron backscatter diffraction and atom probe tomography, *Acta Materialia* 83 (2015) 37-47.
- [48] D.J. Larson, T.J. Prosa, R.M. Ulfig, B.P. Geiser, T.F. Kelly, *Local Electrode Atom Probe Tomography: A User's Guide*, Springer, New York, 2013.
- [49] M. Kuzmina, M. Herbig, D. Ponge, S. Sandlobes, D. Raabe, Linear complexions: Confined chemical and structural states at dislocations, *Science* 349(6252) (2015) 1080-1083.
- [50] B.W. Krakauer, D.N. Seidman, Absolute atomic-scale measurements of the Gibbsian interfacial excess of solute at internal interfaces, *Physical Review B* 48(9) (1993) 6724-6727.
- [51] W.D. Nix, B.M. Clemens, Crystallite coalescence: A mechanism for intrinsic tensile stresses in thin films, *Journal of Materials Research* 14(8) (1999) 3467-3473.
- [52] G. Grochola, S.P. Russo, I. Yarovsky, I.K. Snook, "Exact" surface free energies of iron surfaces using a modified embedded atom method potential and lambda integration, *J Chem Phys* 120(7) (2004) 3425-30.
- [53] C. Wang, D. Chang, C. Tang, J. Su, Y. Zhang, Y. Jia, Single Adatom Adsorption and Diffusion on Fe Surfaces, *Journal of Modern Physics* 2(9) (2011) 1067-1072.
- [54] C. Thompson, On the grain size and coalescence stress resulting from nucleation and growth processes during formation of polycrystalline thin films, *Journal of Materials Research* 14(7) (1999) 3164-3168.
- [55] C. Thompson, Structure evolution during processing of polycrystalline films, *Annu. Rev. Mater. Sci.* 30 (2000) 159-190.
- [56] K. Barmak, K. Coffey, *Metallic Films for Electronic, Optical and Magnetic Applications: Structure, Processing and Properties*, Elsevier Science 2014.
- [57] M. Janda, On the Intrinsic Stress in Thin Chromium Films, *Thin Solid Films* 142(1) (1986) 37-45.
- [58] H.A. Murdoch, C.A. Schuh, Estimation of grain boundary segregation enthalpy and its role in stable nanocrystalline alloy design, *Journal of Materials Research* 28(16) (2013) 2154-2163.

CHAPTER 8

Phase and Microstructural evolution in sputtered Fe-Cr films

Xuyang Zhou¹ and Gregory B. Thompson¹

1. The University of Alabama, Department of Metallurgical & Materials Engineering,
Tuscaloosa, AL USA

Abstract:

A series of $\text{Fe}_x\text{Cr}_{1-x}$ thin films (where $X = 0$ to 1) were magnetron sputter deposited onto ambient temperature substrates. The elemental films adopted the BCC structure with a tens of nanometer-sized equiaxed grains. The Fe-49Cr (at%) film grew as the high temperature σ -phase, with similar but smaller equiaxed grain sizes. All other alloy compositions deposited as the A2 solid solution BCC phase. The Fe-5Cr film was found to have ordering through atom probe tomography (APT) analysis and confirmed prior modeling and diffuse neutron diffraction results. However, upon depositing this film at 673 K, this ordering is lost. Films of Fe-16Cr, Fe-24Cr, and Fe-72Cr increased in grain size, with the -24Cr and -72Cr films exhibiting abnormal grain sizes that were hundreds of nanometers in size. It is suspected that the thermodynamic driving force to phase separate has contributed to the increased adatom mobility. Furthermore, these films revealed a peculiar 'star-burst' contrast pattern within their grains that has been associated with a modest orientation shift which too is contributed to the early onset of phase separation evident in our APT clustering analysis of these alloy films.

Keywords: Fe-Cr, structure evolution, atom probe, ordering and clustering

1. Introduction

Thin film deposition is a highly dynamic process which can yield a variety of microstructures with several of the phases being different from those nominally observed in bulk, equilibrium phase diagrams [1]. For example, amorphous phases can be fabricated by vapor quenching techniques [2-4], high-temperature phases can be stabilized in the films deposited at room temperature [5], and supersaturated solid solutions are often achieved beyond bulk solubility limits [6-9]. By understanding the structural evolution during thin film growth, and even controlling the structural evolution, one can generate unique mechanical and functional properties [10-17].

The Fe-Cr alloy is an important engineering material because of its combined corrosion and oxidation resistance coupled to good mechanical strength [18-21]. As a thin film, Fe-Cr have been able to exhibit several other unique properties that are not normally associated with its bulk form [6, 7, 22-24]. For example, Fe-Cr multilayers

exhibit the giant magnetoresistance effect [22]. The alloy is also reported to be a topologically close-packed (TCP) phase film with excellent tribology properties because of its large hardness-to-elastic ratio [23]. Sputtered nanocrystalline Fe-Cr films also exhibit improvements in pitting resistance [24-27]. When sputter deposited, these films often extend solid solubility ranges not observed in the bulk which has been contributed to some of the aforementioned properties [6, 7, 24].

The Fe-Cr system exhibits a miscibility gap with its phase separation characteristics attracting the research interests since the mid-twenty century [28, 29]. From theoretical calculations, the enthalpy of mixing was reported to change from a negative to positive value near 5 at.% Cr at or below ambient temperature [30-32]. Interestingly, in solution, Fe-rich Fe(Cr) has even been suggested to have local short range ordering reported from diffuse-neutron-scattering measurements [30, 33] as well as modeling predictions [30, 34]. To date there has been little additional experimental studies that have explored this ordering behavior in the dilute Cr solute limit. Often the behavior is considered to be associated with clustering [35-37]. Consequently, this ordered structure is not readily reported on Fe-Cr binary phase diagrams. Upon extending Cr's composition beyond the solubility limit, the alloy will proceed to phase separate by either nucleation and growth or spinodal decomposition dependent on its compositional location within the miscibility gap's spinodal. [38].

One way to study these early stages of phase separation is by atom probe tomography (APT). APT provides 3D reconstructions of individual atoms with near perfect lattice rectification. Its high chemical and spatial resolution (around 0.1-0.3 nm in depth and 0.3-0.5nm laterally with equal sensitivity for all elements [39, 40]) offers scientists a technique to probe the very fine scale behavior of phase forming a phase separating behavior [39, 40]. As a result, this technique has been extensively used to quantify the spinodal decomposition of Fe-Cr alloys in its bulk form [39-47] but has had rather limited application to Fe-Cr thin films [9] where several highly nonequilibrium phase states can be achieved as mentioned above. A Thus APT characterization offers potentially interesting opportunities to study phase equilibria in this alloy as a thin film as well as new insights into how systems, far from equilibrium, migrate towards thermodynamic equilibrium.

Several methods have been developed to detect phase separation behavior using APT. These include the Johnson and Klotz (JK) ordering parameters [48, 49], Langen, Bar-on, and Miller (LBM) method [44, 45], the contingency table [50], the radial distribution function method (RDF) [41, 51], and the three-dimensional Markov field (3DMF) approach [42, 43, 47]. In this paper, we have explored the use of the LBM method, radial distribution method, and the 3DMF to discuss the early stages of phase

separation in a series of nanocrystalline Fe-Cr films. The aim of which is to understand how phase separation initiates as a function of composition as well as compare which of these methods yields data-sets most respective of the physical system's behavior.

In the LBM method, a pair of Gaussian distributions of the solute concentrations are used to fit an experimental probability distribution [44, 45]. Those two Gaussian distributions share the same width, σ , but are centered at different concentrations, μ_1 and μ_2 , respectively. This is described using the formulation of equation (1)

$$P(c) = \frac{\mu_2 \exp\left[-\frac{(c-\mu_1)^2}{2\sigma^2}\right] + \mu_1 \exp\left[-\frac{(c-\mu_2)^2}{2\sigma^2}\right]}{(\mu_1 + \mu_2)\sigma\sqrt{2\pi}} \quad (1)$$

where μ_1 and μ_2 are the peak and trough compositions, respectively; σ^2 is the variance of each Gaussian distribution. The amplitude is $\mu_2 - \mu_1$.

In the RDF method, a radial concentration profile is constructed for every detected atom for the chosen element [41, 51]. Specifically, an atom i is selected as the origin and the probability density to find another atom j is calculated in a sequence spherical shells. (In this work we divided the shells to be of 0.2 nm thick and ranged to 10 nm). This probability density plot is then averaged over all the atoms for a chosen element and it was normalized to the average bulk concentration. The RDF is expressed as:

$$RDF(r) = \frac{C_E(r)}{C_0} = \frac{N_E(r)/N(r)}{C_0} \quad (3)$$

where $C_E(r)$ is the atomic composition of element E at the distance of r , C_0 is the average composition of element E in the studied volume, $N_E(r)$ and $N(r)$ is the total number of atoms of element E and all elements at the distance of r , respectively.

Finally, the 3DMF is adapted for the determination of the Warren-Cowley (W-C) parameter [52], α_{BA}^k . The W-C quantifies near neighbor solute atom interactions by describing the distribution of atoms within a binary AB system, as

$$\alpha_{BA}^k = 1 - \frac{P_{BA}^k}{X_A} = 1 - \frac{1 - P_{BB}^k}{1 - X_B} \quad (2)$$

where P_{BA}^k or P_{BB}^k are the probabilities of finding an A-type matrix atom or a B-type solute atom in the k th shell of atoms surrounding a B-type solute atom, respectively, given X_A the overall concentration of A atoms in the system [40]. The P_{BB}^k is calculated by

$$P_{BB}^k = \frac{1}{N_B} \sum_{i=1}^{N_B} \frac{n_i}{c_i} \quad (3)$$

where c_i is the number of nearest neighbors and n_i is the number of solute nearest neighbors around a solute atoms i [47]. If α_{BA}^k is positive, then there is a preference for like atoms to cluster whereas a negative value means a preference for dissimilar atoms to order. The application of the 3DMF method will be used to explore the aforementioned ordering of the dilute Fe(Cr) system. Rather than inferring this ordering from a magnetic property response that was an outcome of the diffuse neutron diffraction experiment [33], the APT would provide a complimentary structural characterization of the atomic distributions and further confirm if such ordering does occur. Such short-range ordering information would be then be valuable as forward feeding data for thermodynamic models that calculate configurational entropy and the lowest energy states in this system for dilute Cr additions to Fe [47]. These types of results would then lend to new insights and information to better understating phase stability in Fe-Cr alloy films.

2. Experimental

Elemental Fe, Cr, and alloyed Fe_{1-x}Cr_x (0<x<1) nanocrystalline thin films were sputter deposited from 99.95 at.% pure Fe and Cr targets in an AJA ATC-1500 stainless steel magnetron-sputtering system to an approximate thickness of 300 nm onto 300 μm thick Si [001] substrates at ambient temperature. A quartz crystal SQM-160 sensor determined the deposition rates for each elemental films to be ~ 0.1 nm/sec. Alloy films, with each of the different compositions, was achieved through co-sputtering two elemental targets with various sputtering power combinations. The base vacuum pressure prior deposition was $< 6 \times 10^{-6}$ Pa. During deposition, a pressure of 0.27 Pa was maintained using ultra-high purity argon flowed as the working gas at ten standard cubic centimeters per minute flow rate. For in-situ annealing experiment, the reported temperature was calibrated by using a k-Space[®] Bandit system.

A series of θ -2 θ x-ray diffraction (XRD) scans was conducted post-growth using a X'pert Philips diffractometer operated with Cu K α radiation ($\lambda = 1.5406 \text{ \AA}$) at 45 kV and 40 mA for phase identification. Microstructure characterization was performed in an FEI Tecnai Super twin F20 (S)TEM using plan-view TEM foils, which were prepared by cutting, dimpling and ion-milling a 3 mm disc taken from the substrate. Precession Electron Diffraction (PED) scans, performed in the TEM, provided grain orientation mapping via the NanoMEGAS platform [53-55]. The PED was operated with a 0.3 $^\circ$ precession angle at a step size of 3 nm on a region as large as 1.2 $\mu\text{m} \times 1.2 \mu\text{m}$. After scanning, the data was converted for analysis using TSL OIM Analysis 7 software. Grain size distributions were plotted based on the orientation map that optimized via grain dilation.

The composition of each alloy film was confirmed by APT in a Cameca® Scientific Instruments Local Electrode Atom Probe (LEAP) 5000 XS. The required needle-shaped geometries were prepared for atom probe analysis using a focus ion beam (FIB) cross-sectional lift-out technique and annular milling procedure described in reference [9, 56] in either the TESCAN LYRA FIB- Field Emission Scanning Electron Microscope (SEM) or an FEI Quanta 3D dual beam FIB-SEM. The specimens were field evaporated with a laser energy of 50 pJ for a 0.5 % targeted evaporation rate at a base temperature 37 K. The APT data was reconstructed using the IVAS 3.8 software platform. As noted in the introduction, the LBM [44, 45], RDF [41, 51], and 3DMF [42, 43, 47] methods were chosen to detect the phase separation behavior.

3. Result and discussion

A series of elemental and alloy thin films spanning Fe, Fe-5 at.%Cr, Fe-16 at.%Cr, Fe-24 at.%Cr, Fe-49at.%Cr, Fe-72at.%Cr, and Cr, were grown. The XRD scans, Figure 1, confirmed that the elemental films were BCC and the alloy films adopted the solid solution BCC A2 phase revealing a strong {011} fiber texture. The only exception was the Fe-49Cr film which diffracted two strong reflections at 39° and 85° 2Θ , respectively. According to the binary phase diagram, an ordered intermetallic FeCr phase, denoted as σ , is present in the miscibility gap but decomposes and phase separates into two BCC phases below $\sim 700\text{K}$. When compositions within the σ -phase are processed, it has been reported to be the equilibrium σ -phase, which is a tetragonal P 42/mn structure [57] or a metastable A15 phase [5, 23, 57-62], which is a cubic Pm3n structure [60, 62]. Since both these two structures have very similar reflections near 39° (002) and 85° (004), we are unable to determine the crystal structure from XRD alone, but will be determined from proceeding electron diffraction experiments. Regardless of the ambiguity in the structure from the XRD scans, it is clear that a high temperature, ordered phase was able to be sputter deposited onto an ambient temperature substrate. This demonstrates that the negative enthalpy of formation of this ordered phase is sufficient to avoid forming a simple solid solution. What is also particularly striking is that the ordered phase is a higher temperature phase and it was able to be formed at room temperature by this process from two separate sputtering sources.

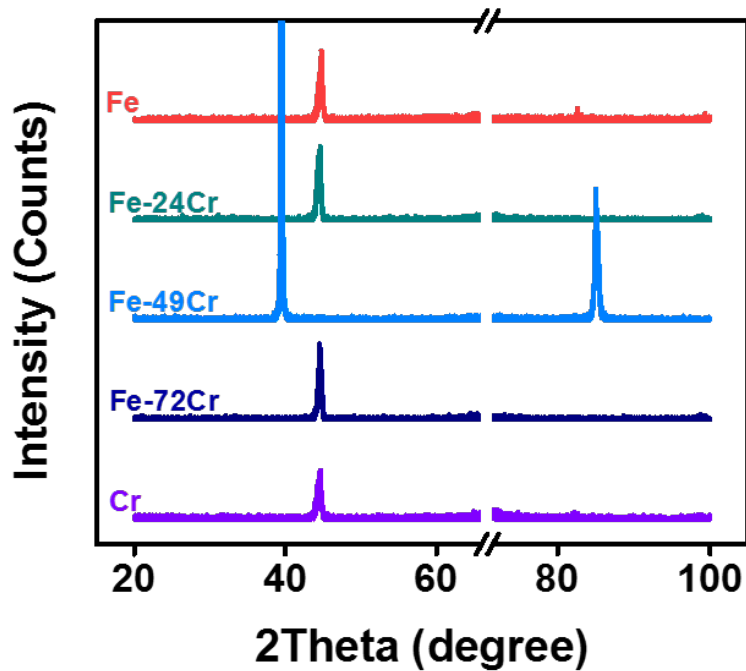


Figure 1 X-ray spectrums of Fe-Cr alloying films with different solute concentrations

Figure 2(a) shows the simulated polycrystalline diffraction patterns of {001} textured σ -phase and A15 phase as well as the experimentally measured selected area diffraction (SAD). When one compares the experimentally diffracted inner most ring and the most intense ring, we note that the pattern matches the σ -phase. The A15 phase does not have a reflection that matches the inner most ring whereas the σ -phase does. Furthermore, the most intense ring for A15 is composed of two reflections where the experimental diffraction revealed a single reflection whose ring spacing matched the single ring spacing of the σ -phase. Upon closer inspection, all other simulated σ -phase rings were consistently matched with the experimental diffraction pattern. We also tilted the films 30° away from the {001} zone axis, which was the fiber texture of this film, and found that the simulated diffraction patterns continued to match well with the experimental observations, Figure 2(b).

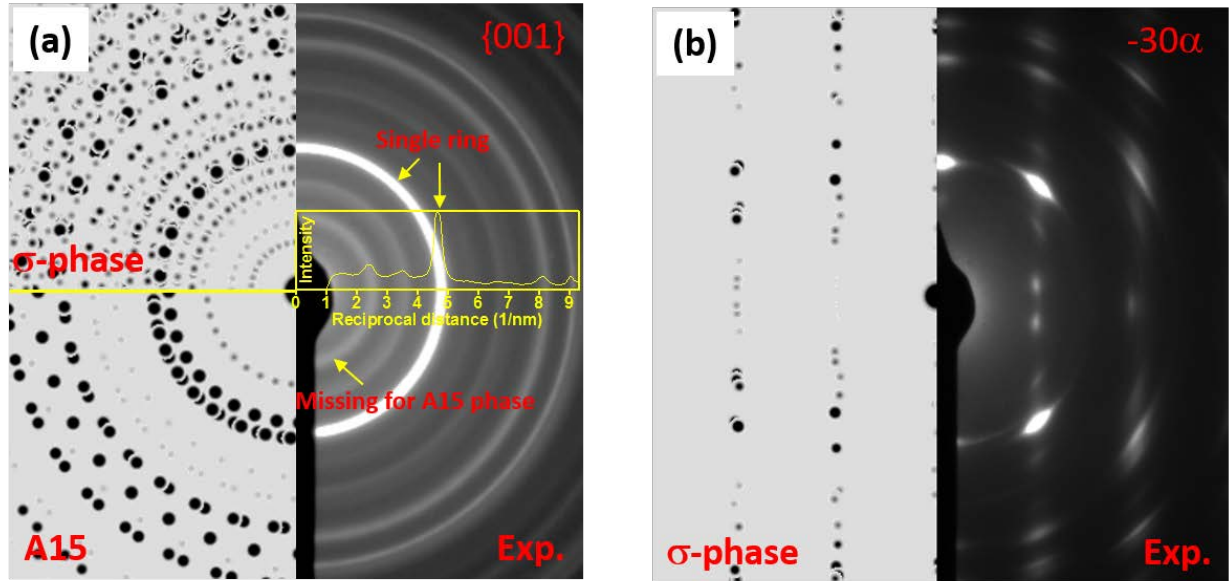


Figure 2 (a) The simulated polycrystalline diffraction patterns of $\{001\}$ textured σ -phase and A15 phase as well as the experimentally measured one. **(b)** The simulated polycrystalline diffraction patterns of textured σ -phase and the experimental observation 30° away from the $\{001\}$ zone axis.

Figure 3(a) and (b) are the bright field and dark field images of the Fe-49Cr film which revealed that this σ -phase has grown with a very fine nanocrystalline grain size, in contrast the solid solution A2 phases for the Fe-Cr alloys revealed much larger grain sizes, plotted in Figure 4. An HRTEM lattice fringe image, Figure 3(c), indicated that even in the small gains, multiple structural defects were present indicated the partitioning of the lattice fringes in different directions. The PED orientation map has been employed to identify the phase, grain size distribution, and texture. The templates of a σ -phase and an A15 phase were used and over 98% area was identified to have a σ -phase with the balance being the A15 phase. This result further confirmed that the dominate phase of the Fe-49Cr film is the high temperature σ -phase. The PED orientation map also revealed a high degree of $[001]$ texture, which is in agreement with the XRD scan in Figure 1, where the two peaks can now be identified as $[002]$ and $[004]$ fiber textures.

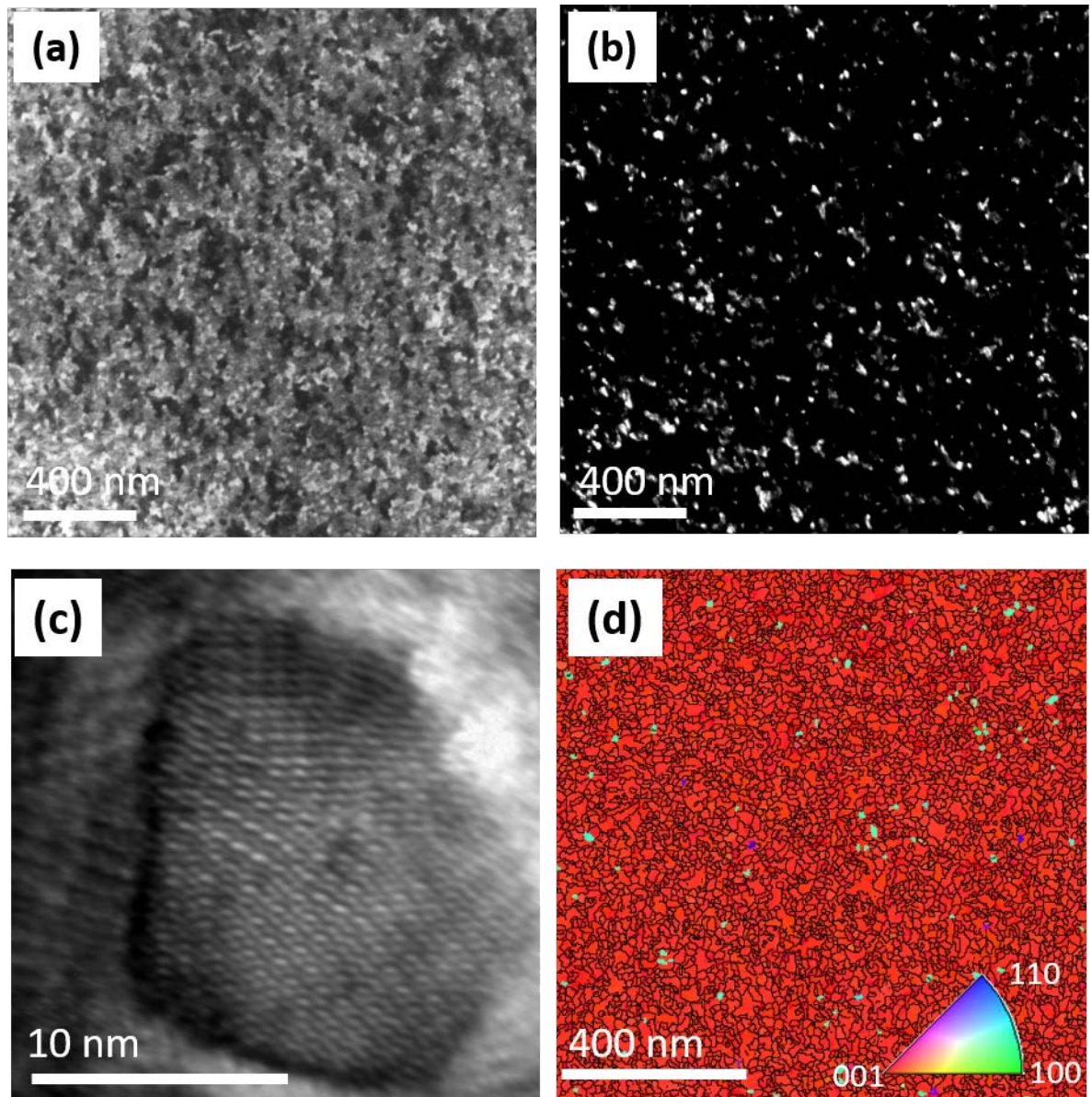


Figure 3 (a) Bright field image (b) dark field image (c) HRTEM and (d) PED reconstructed orientation maps of the Fe-49Cr film.

Similar PED scans for all of the other films was done (appendix), with the grain sizes plotted in Figure 4 as a cumulative grain size distribution. Table 1 also contains a tabulation of the As shown in this figure, the elemental films – Fe and Cr – as well as the Fe-49Cr film grew with the smallest grain sizes and a narrow gain size distribution, evident by the near vertical cumulative area fraction at a specific grain size suggesting normal grain growth behavior. Upon alloying Fe to Fe-16Cr, the grain size is still relatively equiaxed but its distribution has now widened and the sizes have grown. Unlike

this and the other aforementioned films, the Fe-24Cr and Fe-72Cr films revealed the most dramatic grain size shifts with several very large grains and very clear abnormal grain growth behavior evident by the horizontal shifts in the grain sizes as a function of the cumulative grain size area.

Table 1 Phase, grain size, and segregation amplitude varying with alloy concentration and deposition temperature in the Fe-Cr films. AGG is abnormal grain growth

Temperature	Concentration	Phase	Grain size distribution	Grain size	Amplitude
RT	Fe	BCC	Equiaxed	39 ± 22 nm	-
	Fe-5Cr	BCC	Equiaxed	50 ± 29 nm	-
	Fe-16Cr	BCC	AGG	111 ± 94 nm	3 at.%
	Fe-24Cr	BCC	AGG	422 ± 280 nm	6 at.%
	Fe-49Cr	σ-phase	Equiaxed	30 ± 16 nm	2 at.%
	Fe-72Cr	BCC	AGG	291 ± 199 nm	4 at.%
	Cr	BCC	Equiaxed	33 ± 14 nm	-
673K	Fe-5Cr	BCC	Equiaxed	37 ± 13 nm	3 at.%

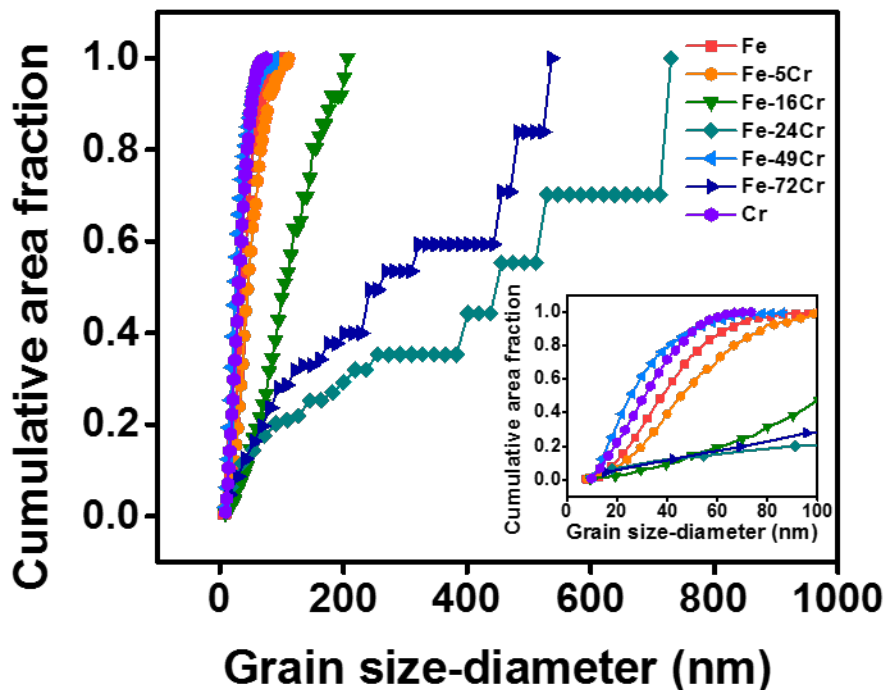


Figure 4 Cumulative grain size distribution plots for Fe-Cr alloying films with different solute concentrations. Grain size was measured from precession electron diffraction scans with 1.2X1.2 mm² and 3 nm step size.

The increase in Fe's grain size with Cr additions has been previously reported by the authors for a series of films with low Cr solute concentrations [8]. In that work, with Cr in solution with Fe, the grain size increased (up to ~ 4 at.% Cr) whereas once the Cr partitioned strongly to the grain boundaries, the grain size then refined for a 8 at.% Cr composition. This refinement was contributed to a solute drag effect. What is particularly interesting in these new films, further increasing the solute Cr content from the prior 8% to now 16% does not continue a grain refinement. Rather the grains appear to increase in grain size suggesting a solute concentration limit for grain refinement in Fe-Cr thin films.

The onset of the increase in the grain size is suspected to be linked to the phase separating behavior of the film. As the solute content increases, the driving force for the two species to partition becomes ever stronger within the microstructure. This thermodynamic driving force would then contribute to the adatom mobility during growth which would then explain the increase in grain sizes once a critical concentration of solutes was present. One can infer that conclusion when considering either the Fe-24Cr or Fe-72Cr films. Here the grains are very large and show a variety of large sizes. Though the XRD and PED scattering identified a single A2 phase, to confirm that the system is (starting to) chemically partition and drive these microstructural changes, we have performed APT.

Figure 5(a) plots the three types of distributions for each composition quantified by the APT datasets. The binomial distributions in Figure 5(a) represent the condition where the system is a single phase or, in other words, no partitioning between the species. It provides a reference from which distributions can be compared to and reveal chemical partitioning. The observed distributions is the raw data and has been computed by binning the compositions into $0.5 \times 0.5 \times 0.5$ nm voxel sizes and comparing each voxel to the other. Finally, the LBM model used two Gaussian functions based on the concentration of each species to fit the observed data, with the details of the LBM model previously discussed. Using the two Gaussian distributions, the relative concentration difference between each fit was found and plotted as an amplitude difference between each distribution, Figure 5(b). The larger the amplitude difference, the greater the partitioning in the system. These amplitude values are tabulated in Table 1. The Fe-rich alloys revealed the highest extent of partitioning at 24% Cr. At 49%Cr, which is the σ -phase, the partitioning value is low and would be exhibited as the atoms are in an ordered intermetallic phase. The presence of some 'partitioning' at the σ -phase composition is contributed to the lack of perfect atom-to-lattice rectification in the APT data sets as well as the σ -phase not being a line compound. What is particularly

interesting is that at 5%Cr, there is no notable partitioning which implies that Cr is in solution. This agrees with prior modeling that Cr would be in solution at this composition for low temperatures [30-32]. For all the other compositions, even though the film is deposited onto an ambient temperature substrate, the thermodynamic energies to phase separate are sufficiently large enough to promote the early onset of chemical partitioning even at low homologous temperatures. These APT results confirm that partitioning has indeed occurred and likely has contributed to the energies needed to facilitate the observed grain growth in the disordered solid solution. The only exception is the Fe-49Cr film, which readily adopted the σ -phase and was no longer in a disordered phase state.

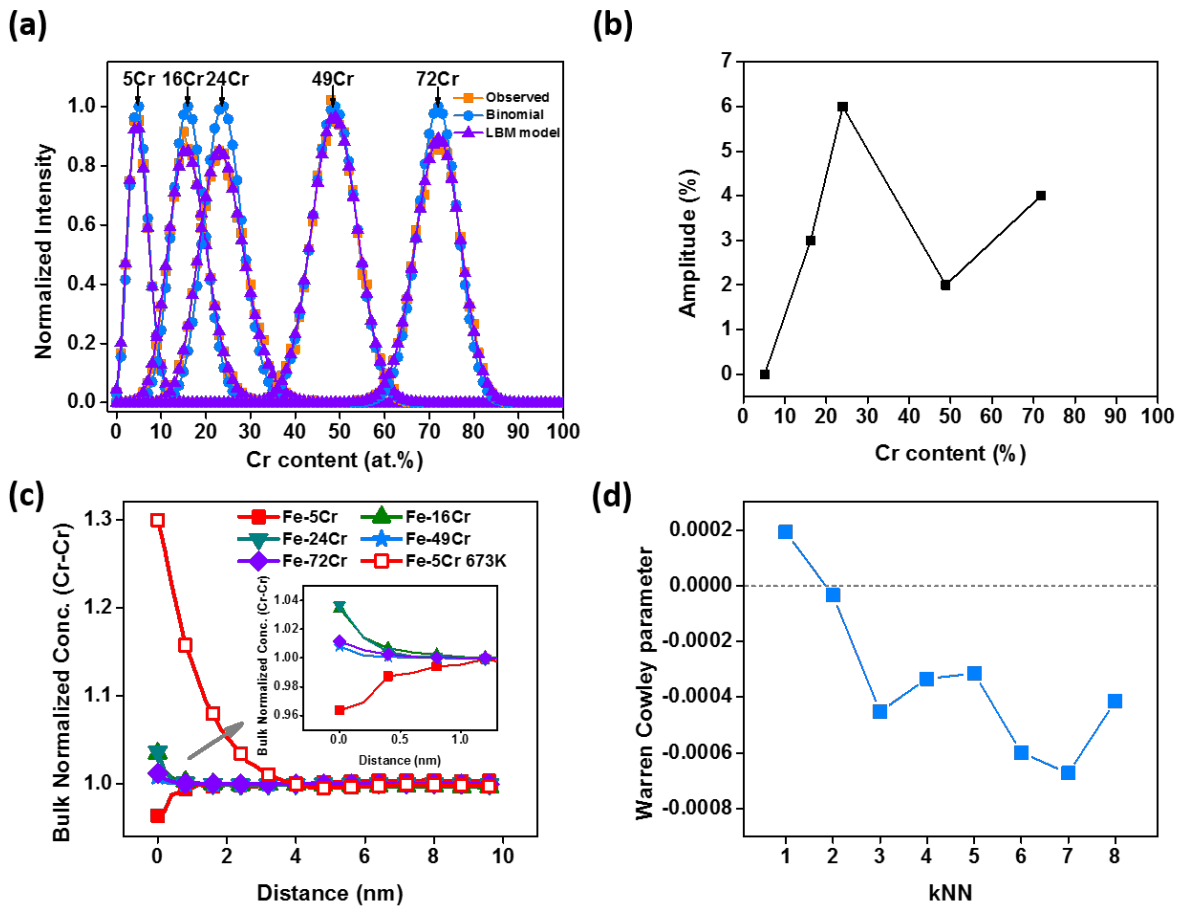


Figure 5 (a) Normalized Cr concentration frequency diagram. The binomial distribution and Langer, Bar-on, and Miller (LBM) model fitting were also included. (b) Composition evolution of amplitudes obtained using LBM method. (c) Radial distribution functions (RDFs) of Cr-Cr used to evaluate atom distribution for the Fe-Cr films with different compositions. (d) Warren Cowley parameters for the Fe-5Cr films with different nearest

neighboring shells. Atom probe data was drawn from a 25X25X25 nm³ cubic of each composition.

Now that we have confirmed partitioning, we have further examined the distributions of the atoms in and near these partitioned clusters. Figure 5(c) is bulk normalized Cr concentration varying with the radial distance, r . The surrounding environment of Cr atoms is changing with Cr concentration. When the Cr concentration is low, the solute concentration of the first several shells of neighboring atoms is 4 % percent lower than the average composition for the solute atoms in the alloy. This means that a slightly ordered structure has indeed formed in the low Cr content Fe-Cr film. As the Cr content increased to 16 % or higher, the neighboring environment of Cr atoms changed from ~ 0.96 of the normalized bulk concentration (or, in other words, ~ 4 % lower than the overall composition) to ~ 1.04 of the normalized bulk concentration (or to a value 4 % higher than the bulk composition). In this case, Cr atoms tend to segregate together and form initial phase separation behavior. This APT results are consistent with the amplitude analysis, Figure 5(b), in which a slightly phase-separated structures was noticed in Fe-16Cr, Fe-24Cr, and Fe-72Cr thin films. It can also be seen from the plot in Figure 5(c) that a limited concentration variation was noticed also noted in the intermetallic σ -phase Fe-49Cr film.

Finally, we have applied the W-C method to our APT data sets to look at the potential short range order in the dilute Fe-5Cr film. The W-C parameter of the Fe-5Cr alloy is close to zero, but the RDF plot shows a Cr-Fe nearest neighbor (NN) environment suggesting a slightly ordered structure. We calculated the W-C parameter for Fe-5Cr with NN shells going from $k = 1$ to 8 shells and noted that the W-C parameter was negative which indicates an ordered structure and would be consistent with the RDF findings in Figure 5(c). Interestingly, some fluctuations in the W-C parameter is noted as a function of the NN shells. It is not clear what this potentially fine structure may imply towards the ordering behavior.

We recently reported the growth stresses for a series of Fe-Cr thin films deposited at ambient and elevated temperatures (673K) [63]. One of these films was the Fe-5Cr alloy. Applying the above mentioned APT analysis methods to the 673 K Fe-5Cr film's APT data set, we noted a loss in the ordered structure, Figure 5(c). This annealed film, like its ambient temperature counterpart, was the A2 phase. The loss in order is evident by the neighboring concentration being nearly 1.3 times higher than the nominal bulk concentration (the unfilled red square marker in Figure 5(c)). Recall that the ambient Fe-5Cr value was slightly less than the normalized bulk concentration (filled

red square in Figure 5(c)). One could expect an order-disorder behavior for this phase, as already noted, it is most often observed in the disordered state.

The microstructure that has formed from the strongly partitioning alloy, Fe-24Cr, is shown in Figure 6. A ‘star burst-like’ pattern throughout the microstructure was observed in the bright field image, as shown in Figure 6(a). Similar features were seen in the Fe-16Cr and Fe-72Cr films, which like Fe-24Cr were all the highly supersaturated A2 structures. By tilting the foil along the α tilt axis in the TEM, the outline of the black patterns of the ‘star burst’ changed position and shape accordingly, Figure 6(b-e). This ‘star-burst pattern’ phenomenon is believed to be generated from a modest orientation rotation within the grains, likely created by the onset of partitioning. It is not believed to be from a large scale compositional fluctuation as such were not observed in the APT datasets nor bend contrast from electron diffraction.

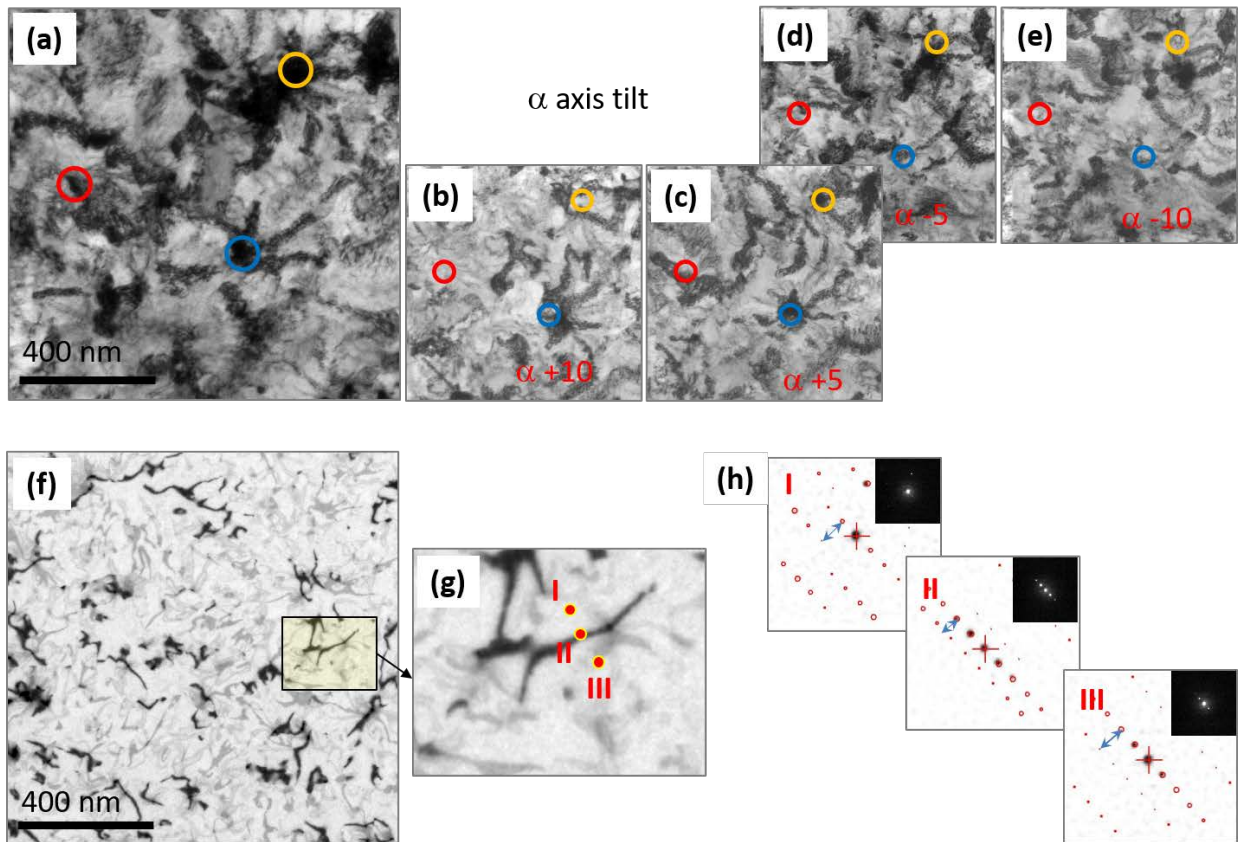


Figure 6 Bright field image of the Fe-24Cr film with (a) 0 tilt (b) +5 a tilt (c) +10 a tilt (d) -5 a tilt (e) -10 a tilt. (f) Bright field image of the Fe-24Cr film with a thickness of 10 nm (g) Magnified view of Figure 5(f) (h) Diffraction patterns from points showing in Figure 5(g).

To study this peculiar microstructural feature further and confirm if it is indeed a grain rotation effect, a 10 nm thick Fe-24Cr film was grown onto a SiN_x window, Figure 6(f). The aim of which was to capture the early onset of this feature with film growth. Figure 6(g) revealed a series of black and grey contrast lines taken from a region of interest shown in Figure 6(f). Here, we implemented a PED scan across each feature, Figure 6(h), with the associated diffraction patterns for each point labeled in Figure 6(g). The I, II, and III points are each respectively located in the white, black, and white contrast regions, respectively. In all the diffraction patterns, a systematic row of reflections is shown to go from the upper left corner to the lower right corner for this A2 phase orientation. The consistency of a similar set of reflections confirms that the points are within the same grain. However, the spacing between the systematic row of these reflections narrows or widens based on the point location in the microstructure, which is illustrated by the double arrow label from between the rows of reflections for each I, II, and III point. This variation, for the same phase, indicates a slight orientation change in the diffracted beam through the foil. Rather than is contrast being associated with a large compositional effect, it does appear to a crystalline orientation effect.

4. Conclusion

A series of Fe_{1-x}Cr_x (0<x<1) films have been sputter-deposited onto ambient temperature [001] Si substrates with its phase and microstructure quantified. . Each of the elemental films deposited as a BCC structure with a narrow grain size distribution.

The Fe-5Cr film formed an A2 solid solution BCC phase also with an equiaxed grain size with a narrow grain size distribution. APT analysis confirmed prior neutron diffraction experiments that this composition yielded an ordered structure; however, if this film is deposited at 673 K, the ordering is lost. To the authors' knowledge, this ordering phase has been previously confirmed by diffuse neutron scattering [30, 33] and modeling studies [30, 34]. To the authors' knowledge, this report provides the first confirmation of it through an APT analysis where it is more often reported as a cluster behavior in similar studies [35-37].

The Fe-49Cr film adopted the σ -phase, which is a high temperature ordered phase, even in the ambient temperature deposition. These grains were equiaxed and fine in size.

For the remaining films, Fe-16Cr, Fe-24Cr, and Fe-72Cr, all deposited as the A2 phase with the grain sizes being larger than the prior films discussed above. Of these films, the Fe-24Cr and Fe-72 films exhibited significant abnormal grain growth. This behavior has been contributed to the system being driven to chemical partition by providing an additional thermodynamic contributor to the adatom mobility. APT analysis confirmed this partitioning and onset of clustering, even though it was not

readily observed in the TEM images and associated diffraction patterns. These films exhibited a peculiar 'star-burst' contrast pattern within the grains. Through localized diffraction patterns in and away from this contrast, it was found to be a modest orientation tilt within the grain and is not believed to be associated with a particular chemical contrast. However, these changes in orientation are likely contributed to the system being kinetically constrained by the lower temperature to phase separate, as it is clear from the Fe-49Cr σ -phase that significant adatom interactions can occur to yield ordered intermetallic phase formations.

Acknowledgement

The authors gratefully recognize support from the Army Research Office, grant W911NF1310436, as well as the University of Alabama's Central Analytical Facility. Thank Dr. Anna Ceguerra and Dr. Simon Ringer for providing us the access to use MASSIVE atom probe data analysis software package.

Reference

- [1] J.A. Venables. Introduction to Surface and Thin Film Processes, Cambridge University Press, Cambridge, 2000.
- [2] M. Lu, C.L. Chien. Structural and Magnetic-Properties of Fe-W Alloys, Journal of Applied Physics 67 (1990) 5787-5789.
- [3] R. Banerjee, S. Bose, A. Genc, P. Ayyub. The microstructure and electrical transport properties of immiscible copper-niobium alloy thin films, Journal of Applied Physics 103 (2008).
- [4] R. Banerjee, A. Puthucode, S. Bose, P. Ayyub. Nanoscale phase separation in amorphous immiscible copper-niobium alloy thin films, Applied Physics Letters 90 (2007).
- [5] N.H. Duc, A. Fnidiki, J. Teillet, J. Ben Youssef, H. Le Gall. Structural and magnetic studies of sputtered Fe_{1-x}Cr_x thin films, Journal of Applied Physics 88 (2000) 4778-4782.
- [6] G. Meng, Y. Li, F. Wang. The corrosion behavior of Fe-10Cr nanocrystalline coating, Electrochimica Acta 51 (2006) 4277-4284.
- [7] K. Wasa, S. Hayakawa. Special features of thin compound films prepared by magnetron sputtering, Surface Science 86 (1979) 300-307.
- [8] X. Zhou, T. Kaub, R.L. Martens, G.B. Thompson. Influence of Fe(Cr) miscibility on thin film grain size and stress, Thin Solid Films 612 (2016) 29-35.
- [9] X. Zhou, X.-x. Yu, T. Kaub, R.L. Martens, G.B. Thompson. Grain Boundary Specific Segregation in Nanocrystalline Fe(Cr), Scientific Reports 6 (2016) 34642.
- [10] P.H. Mayrhofer, C. Mitterer, L. Hultman, H. Clemens. Microstructural design of hard coatings, Progress in Materials Science 51 (2006) 1032-1114.
- [11] F.J. Himpsel, J.E. Ortega, G.J. Mankey, R.F. Willis. Magnetic nanostructures, Advances in Physics 47 (1998) 511-597.
- [12] S. Koveshnikov, W. Tsai, I. Ok, J.C. Lee, V. Torkanov, M. Yakimov, S. Oktyabrsky. Metal-oxide-semiconductor capacitors on GaAs with high-k gate oxide and amorphous silicon interface passivation layer, Applied Physics Letters 88 (2006) 022106.
- [13] B. Radisavljevic, A. Radenovic, J. Brivio, V. Giacometti, A. Kis. Single-layer MoS₂ transistors, Nature nanotechnology 6 (2011) 147-150.
- [14] P.K. Tien. Light Waves in Thin Films and Integrated Optics, Appl. Opt. 10 (1971) 2395-2413.

- [15] K. Nomura, H. Ohta, A. Takagi, T. Kamiya, M. Hirano, H. Hosono. Room-temperature fabrication of transparent flexible thin-film transistors using amorphous oxide semiconductors, *Nature* 432 (2004) 488-492.
- [16] X. Chen, S.S. Mao. Titanium dioxide nanomaterials: synthesis, properties, modifications, and applications, *Chemical reviews* 107 (2007) 2891-2959.
- [17] I. Repins, M.A. Contreras, B. Egaas, C. DeHart, J. Scharf, C.L. Perkins, B. To, R. Noufi. 19.9%-efficient ZnO/CdS/CuInGaSe² solar cell with 81.2% fill factor, *Progress in Photovoltaics: Research and Applications* 16 (2008) 235-239.
- [18] R.L. Klueh, A.T. Nelson. Ferritic/martensitic steels for next-generation reactors, *Journal of Nuclear Materials* 371 (2007) 37-52.
- [19] E.A. Little. Void-swelling in irons and ferritic steels I. Mechanisms of swelling suppression, *Journal of Nuclear Materials* 87 (1979) 11-24.
- [20] R.A. Lula, J.G. Parr. *Stainless steel*, American Society for Metals, 1986.
- [21] D. Terentyev, P. Olsson. Radiation damage in FeCr alloys for nuclear applications: Addressed problems and open issues, (2008).
- [22] M.N. Baibich, J.M. Broto, A. Fert, F.N. Van Dau, F. Petroff, P. Etienne, G. Creuzet, A. Friederich, J. Chazelas. Giant Magnetoresistance of (001)Fe/(001)Cr Magnetic Superlattices, *Physical Review Letters* 61 (1988) 2472-2475.
- [23] W. Al-Khoury, J.P. Eymery, P. Goudeau. Phase transformation of the A15 metastable phase of Fe-Cr thin films prepared by ion-beam sputtering, *Journal of Applied Physics* 102 (2007).
- [24] R.K. Gupta, N. Birbilis. The influence of nanocrystalline structure and processing route on corrosion of stainless steel: A review, *Corrosion Science* 92 (2015) 1-15.
- [25] R.B. Inturi, Z. Szklarska-Smialowska. Localized Corrosion of Nanocrystalline 304 Type Stainless Steel Films, *CORROSION* 48 (1992) 398-403.
- [26] L. Liu, Y. Li, F. Wang. Pitting mechanism on an austenite stainless steel nanocrystalline coating investigated by electrochemical noise and in-situ AFM analysis, *Electrochimica Acta* 54 (2008) 768-780.
- [27] C. Pan, L. Liu, Y. Li, F. Wang. Pitting corrosion of 304ss nanocrystalline thin film, *Corrosion Science* 73 (2013) 32-43.
- [28] J.W. Cahn. On Spinodal Decomposition, *Acta Metallurgica* 9 (1961) 795-801.
- [29] J. Cahn. 1967 Institute of metals lecture spinodal decomposition, *Transactions of the Metallurgical Society of Aime* 242 (1968) 89-103.
- [30] L. Malerba, A. Caro, J. Wallenius. Multiscale modelling of radiation damage and phase transformations: The challenge of FeCr alloys, *Journal of Nuclear Materials* 382 (2008) 112-125.
- [31] A. Caro, D. Crowson, M. Caro. Classical Many-Body Potential for Concentrated Alloys and the Inversion of Order in Iron-Chromium Alloys, *Physical Review Letters* 95 (2005).
- [32] P. Erhart, A. Caro, M. Serrano de Caro, B. Sadigh. Short-range order and precipitation in Fe-rich Fe-Cr alloys: Atomistic off-lattice Monte Carlo simulations, *Physical Review B* 77 (2008).
- [33] I. Mirebeau, M. Hennion, G. Parette. First Measurement of Short-Range-Order Inversion as a Function of Concentration in a Transition Alloy, *Physical Review Letters* 53 (1984) 687-690.
- [34] M. Hennion. Chemical SRO effects in ferromagnetic Fe alloys in relation to electronic band structure, *J. Phys. F: Met. Phys* 13 (1983) 2351-2358.
- [35] M.K. Miller, M.G. Hetherington. Morphology and scaling behavior of ultrafine isotropic microstructures in Fe-Cr alloys from atom probe field ion microscopy data, *Scripta Materialia* 24 (1990) 1375-1380.
- [36] R. Okano, K. Hono, K. Takanashi, H. Fujimori, T. Sakurai. Magnetoresistance and phase decomposition in Cr-Fe bulk alloys, *Journal of Applied Physics* 77 (1995) 5843.

- [37] M. Bachhav, G. Robert Odette, E.A. Marquis. Microstructural changes in a neutron-irradiated Fe–15at.%Cr alloy, *Journal of Nuclear Materials* 454 (2014) 381-386.
- [38] D.A. Porter, K.E. Easterling, M. Sherif. *Phase Transformations in Metals and Alloys*, Third Edition (Revised Reprint), CRC Press, 2009.
- [39] D.J. Larson, T.J. Prosa, R.M. Ulfing, B.P. Geiser, T.F. Kelly. *Local Electrode Atom Probe Tomography: A User's Guide*. New York: Springer, 2013.
- [40] M.K. Miller, R.G. Forbes. *Atom-Probe Tomography: The Local Electrode Atom Probe*, Springer US, 2014.
- [41] J. Zhou, J. Odqvist, M. Thuvander, P. Hedström. Quantitative Evaluation of Spinodal Decomposition in Fe-Cr by Atom Probe Tomography and Radial Distribution Function Analysis, *Microscopy and Microanalysis* 19 (2013) 665-675.
- [42] A.V. Ceguerra, M.P. Moody, R.C. Powles, T.C. Petersen, R.K.W. Marceau, S.P. Ringer. Short-range order in multicomponent materials, *Acta Crystallographica Section A* 68 (2012) 547-560.
- [43] A.V. Ceguerra, R.C. Powles, M.P. Moody, S.P. Ringer. Quantitative description of atomic architecture in solid solutions: A generalized theory for multicomponent short-range order, *Physical Review B* 82 (2010).
- [44] J.S. Langer, M. Bar-on, H.D. Miller. New computational method in the theory of spinodal decomposition, *Physical Review A* 11 (1975) 1417-1429.
- [45] W. Xiong, J. Ågren, J. Zhou. An effective method to estimate composition amplitude of spinodal decomposition for atom probe tomography validated by phase field simulations, *arXiv preprint arXiv:1205.4195* (2012).
- [46] J. Zhou, J. Odqvist, L. Høglund, M. Thuvander, T. Barkar, P. Hedstrom. Initial clustering - a key factor for phase separation kinetics in Fe-Cr-based alloys, *Scripta Materialia* 75 (2014) 62-65.
- [47] A.V. Ceguerra, M.P. Moody, L.T. Stephenson, R.K.W. Marceau, S.P. Ringer. A three-dimensional Markov field approach for the analysis of atomic clustering in atom probe data, *Philosophical Magazine* 90 (2010) 1657-1683.
- [48] C.A. Johnson, J.H. Klotz. *The Atom Probe and Markov Chain Statistics of Clustering*, *Technometrics* 16 (1974) 483-493.
- [49] M.K. Miller, T.D. Shen, R.B. Schwarz. Atom probe tomography study of the decomposition of a bulk metallic glass, *Intermetallics* 10 (2002) 1047-1052.
- [50] M.P. Moody, L.T. Stephenson, P.V. Liddicoat, S.P. Ringer. Contingency table techniques for three dimensional atom probe tomography, *Microscopy research and technique* 70 (2007) 258-268.
- [51] X. Xu, J. Odqvist, M.H. Colliander, M. Thuvander, A. Steuwer, J.E. Westraadt, S. King, P. Hedstrom. Structural Characterization of Phase Separation in Fe-Cr: A Current Comparison of Experimental Methods, *Metallurgical and Materials Transactions a-Physical Metallurgy and Materials Science* 47a (2016) 5942-5952.
- [52] J.M. Cowley. An Approximate Theory of Order in Alloys, *Phys Rev* 77 (1950) 669-675.
- [53] J.G. Brons, G.B. Thompson. Orientation Mapping via Precession-Enhanced Electron Diffraction and Its Applications in Materials Science, *JOM* 66 (2013) 165-170.
- [54] P. Moeck, S. Rouvimov, E.F. Rauch, M. Véron, H. Kirmse, I. Häusler, W. Neumann, D. Bultreys, Y. Maniette, S. Nicolopoulos. High spatial resolution semi-automatic crystallite orientation and phase mapping of nanocrystals in transmission electron microscopes, *Crystal Research and Technology* 46 (2011) 589-606.

- [55] E.F. Rauch, J. Portillo, S. Nicolopoulos, D. Bultreys, S. Rouvimov, P. Moeck. Automated nanocrystal orientation and phase mapping in the transmission electron microscope on the basis of precession electron diffraction, *Zeitschrift für Kristallographie* 225 (2010) 103–109.
- [56] K. Thompson, D. Lawrence, D.J. Larson, J.D. Olson, T.F. Kelly, B. Gorman. In situ site-specific specimen preparation for atom probe tomography, *Ultramicroscopy* 107 (2007) 131-139.
- [57] H.L. Yakel. Atom Distributions in Sigma-Phases .1. Fe and Cr Atom Distributions in a Binary Sigma-Phase Equilibrated at 1063-K,1013-K and 923-K, *Acta Crystallogr B* 39 (1983) 20-28.
- [58] S.M. Dubiel, J. Cieslak. Sigma-Phase in Fe-Cr and Fe-V Alloy Systems and its Physical Properties, *Critical Reviews in Solid State and Materials Sciences* 36 (2011) 191-208.
- [59] B.F.O. Costa, G. Le Caer, J.M. Loureiro, V.S. Amaral. Mechanically induced phase transformations of the sigma phase of nanograined and of coarse-grained near-equiatomic FeCr alloys, *Journal of Alloys and Compounds* 424 (2006) 131-140.
- [60] J.P. Eymery, W. Al-Khoury, P. Goudeau, A. Fnidiki. Mossbauer investigation of $Fe_{1-x}Cr_x$ films grown by ion-beam sputter deposition, *Physica B* 381 (2006) 297-305.
- [61] K. Sumiyama, N. Ohshima, Y. Nakamura. Nonequilibrium Fe-Cr Alloys Produced by Vapor Quenching, *T Jpn I Met* 28 (1987) 699-705.
- [62] N. Yukawa, M. Hida, T. Imura, M. Kawamura, Y. Mizuno. Structure of Chromium-Rich Cr-Ni, Cr-Fe, Cr-Co, and Cr-Ni-Fe Alloy Particles Made by Evaporation in Argon, *Metallurgical Transactions* 3 (1972) 887-&.
- [63] X. Zhou, G. Thompson. Influence of Solute Partitioning on the Microstructure and Growth Stresses in Nanocrystalline Fe(Cr) Thin Films, *Thin Solid Films* Submitted (2017).

Supplementary Information:

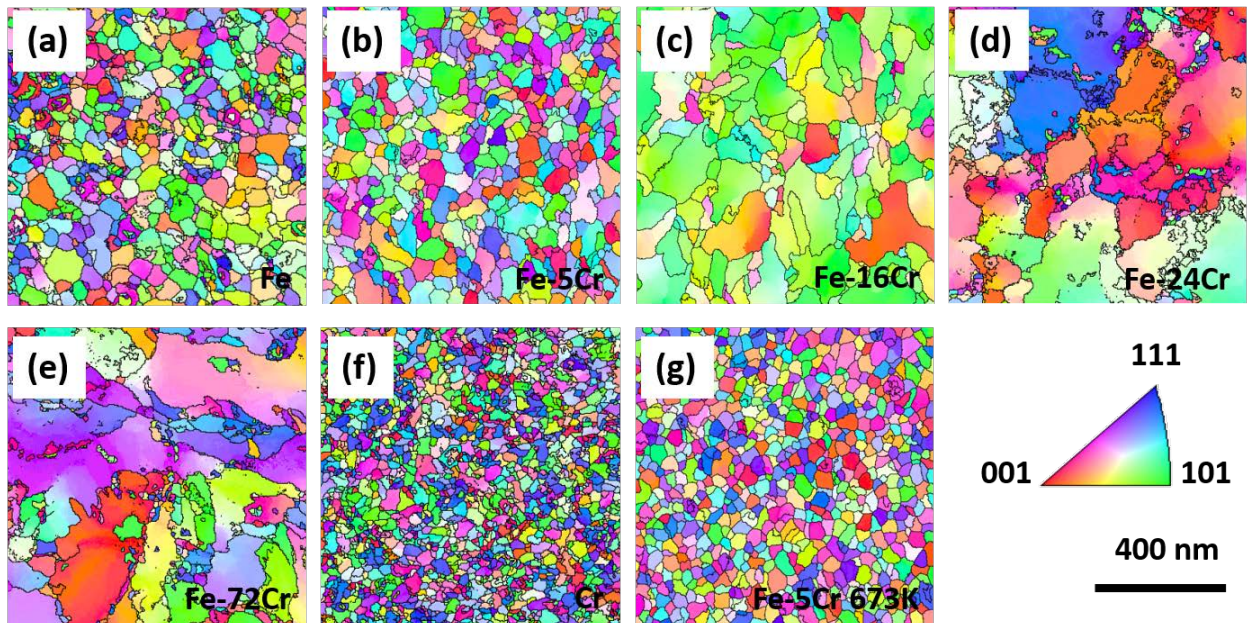


Figure S1 PED reconstructed orientation maps of the room temperature deposited (a) Fe (b) Fe-5Cr (c) Fe-16Cr (d) Fe-24Cr (e) Fe-72Cr (f) Cr, and (g) 673K annealed Fe-5Cr films.

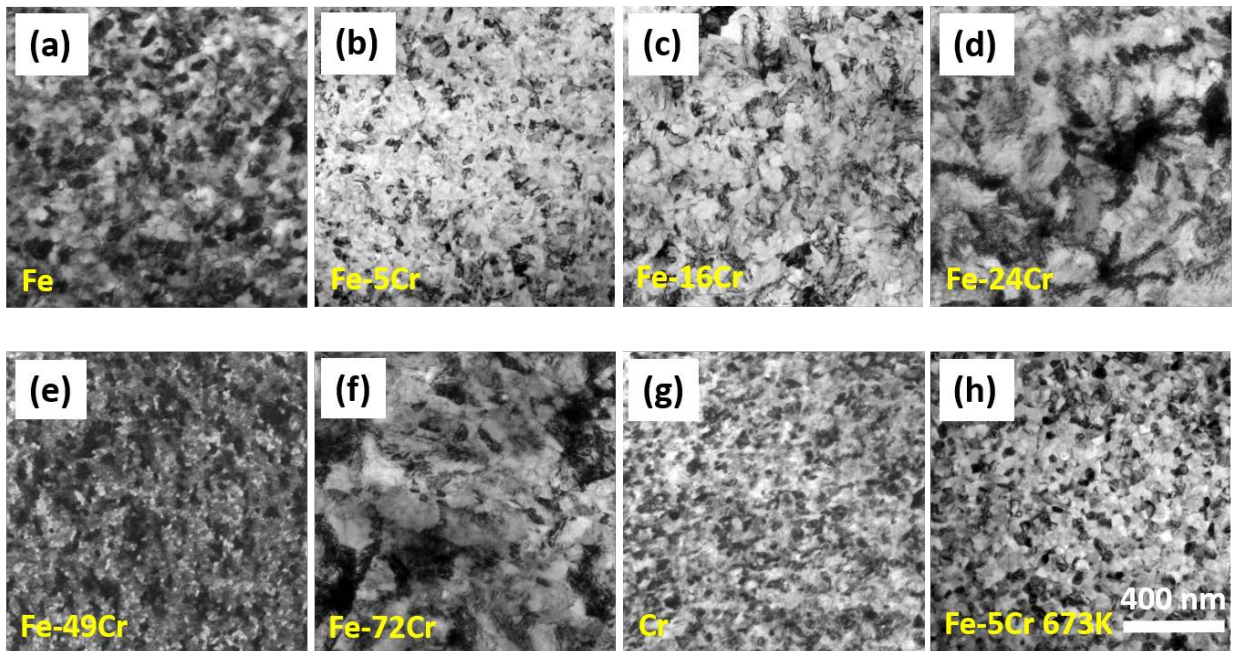


Figure S2 Bright field images of the room temperature deposited (a) Fe (b) Fe-5Cr (c) Fe-16Cr (d) Fe-24Cr (e) Fe-49Cr (f) Fe-72Cr (g) Cr and (h) 673K annealed Fe-5Cr films.

CHAPTER 9

***In situ* TEM observations of initial oxidation behavior in Fe-rich Fe-Cr alloys**

Xuyang Zhou^{*,1} and Gregory B. Thompson¹

¹The University of Alabama, Department of Metallurgical & Materials Engineering, Tuscaloosa, AL USA

* Address correspondence to E-mail: xzhou41@crimson.ua.edu, Phone: +1 205-887-3194

ABSTRACT: Two nanocrystalline alloys of Fe-4Cr and Fe-16Cr were sputter deposited and formed a solid solution A2 phase. Each alloy was then *in situ* annealed up to 800°C with the phase and microstructure quantified by transmission electron microscopy (TEM). The low partial pressure of oxygen in the TEM column ($\sim 2.6 \times 10^{-6}$ Pa) oxidized both films at temperatures at and above 700°C. However, the oxide morphologies were quite different. The Fe-4Cr revealed nanosphere Cr oxide clusters within the grains which has been explained by the thermodynamic preference for Cr to be in solution. The Fe-16Cr precipitated distinct Cr₂O₃ grains which has been described by Cr phase separation at the grain boundaries. Iron oxide was not observed and demonstrating Cr's strong preference for oxygen, even in very low oxygen environments. Using precession electron diffraction (PED), the grain characters of these boundaries were determined revealing a significant effect of high angle grain boundaries on the growth and precipitation behavior of the oxides. The collective results reveal the initial stages of oxidation evolution in nanocrystalline grains, the role of Cr content on such behavior.

KEYWORDS: *in situ* transmission electron microscopy, FeCr, oxidation, X-ray energy dispersion spectroscopy, precession electron diffraction

1. Introduction

The Fe-rich Cr alloys provide two of the major constituent components in stainless steels enabling these materials to exhibit decent corrosion resistance and good mechanical properties [1-4]. As a result, these alloys are a critical material for a variety of technologies used in the nuclear, manufacturing, and energy industries [1, 3, 5-8]. Once the Cr content extends 11 at.% in these steels [1], a stable chromia (Cr₂O₃) surface scale will form and

provide for passivity protection to the metal [9-13]. If the diffusion is predominated by metal ion transport, this oxide scale, on low-alloy steels, will grow outward by the metal diffusion; if the diffusion is predominated by oxygen ion diffusion, the oxide scale will then grow inwards into the metal [14]. Besides the metal or oxygen transport type, the formation of the oxide scale is also a kinetic process that will also be related to the temperature and oxygen partial pressure, with the oxidation rates being linear, logarithmic or parabolic dependent on the active mechanism [14]. At high temperatures, the oxidation rate is typically parabolic and is regulated by diffusion through the scale. At such temperatures, the inward diffusion mentioned above contributes substantially to the overall oxidation process by the fast oxygen diffusion along grain boundaries [15]. Since grain boundaries provide high diffusivity pathways, the amount of grain boundary area will then play a critical role in controlling oxidation behavior. This is particularly relevant for nanocrystalline alloys, whose small grain size may be advantageous for higher strengthening but may be more susceptible to rapid oxidation [15]. Besides grain boundaries, phase boundaries can also contribute to enhanced diffusivities as noted in the work by Golden *et al.* who reported a fast path for oxygen to diffuse along phase boundaries [16].

Despite the extensive studies of oxidation and corrosion behavior on Fe-Cr alloys [17-20], capturing the initial stages of oxidation and its effects on the microstructure is still relatively elusive. To date, most characterization of oxidation is done post-mortem requiring one to infer how the final structure was achieved. However, *in situ* microscopy can enable one to track and even quantify real-time reactions, as well as observing potential mechanisms that are only active during the time of the event, that can lead to final microstructure [21-23]. Such imaging capability can provide for new and unique insights to behaviors that can be lost in post-mortem analysis [24-27]. The advent of various temperature and now liquid and gas stages has enabled many of these observations that were previously not seen, to be elucidated. For example, Banerjee *et al.* employed *in situ* environmental transmission electron microscopy (TEM) to monitor the nanoscale growth of Ni on silica-supported metal model catalysts [28] and Unocic *et al.* directly visualized the dynamic structural and chemical changes during high-temperature oxidation of β -NiAl nanoparticles [29].

Here, we extend these studies to quantify how oxidation initiates and evolves as a function of nanocrystalline granular evolution for a low (4 at.%Cr) and high (16 at.% Cr) binary Fe(Cr) alloy. The aim of the study is then to better understand how the initial stages of passivation occurs for different Cr contents and how that evolves in a nanocrystalline metal, as most efforts have been directed towards ‘bulk’ stainless steels. By using a binary system, we also reduce the complexity of additional interactions with other solutes that may complicate the observed interaction and structural evolution and provide a basis for future studies to compare too. Furthermore, by annealing in a low partial pressure oxygen environment, the rate of oxidation can be reduced enabling the ability to capture this reaction with respect to potential chemical partitioning and structural changes, such as grain growth or grain boundary re-orientations. To quantify these effects, *in situ* imaging needs to be coupled with, for example, rapid X-ray energy dispersion spectroscopy (XEDS) for compositional measurements. To quantify microstructural changes, precession electron diffraction (PED) can provide quantification for both nanoscale grain boundary and grain texture imaging. In particular, both of these techniques – XEDS and PED - are amenable to TEM, which provides the ability to regularly image nanocrystalline granular structures. By applying these complementary techniques, as will be developed in this paper, one will be able to quantitatively understand nanocrystalline stability during passivation and how Cr solute concentration partitions in response for a series of low and high Cr content Fe(Cr) samples.

2. Materials and methods

To fabricate the nanocrystalline alloy, thin films of either Fe-4 at.% Cr or Fe-16 at.% Cr were magnetron sputter deposited in an AJA ATC-1500 system from 99.95% pure pre-alloyed targets. The sputtering rates were found to be approximately 0.100 nm/s for Fe-4Cr and 0.106 nm/s for Fe-16Cr with the deposition rates determined by dividing the film thickness, measured from x-ray reflectivity (XRR) [30], by the deposition time. The XRR was performed on an X’pert Philips diffractometer operated with Cu $K\alpha$ radiation ($\lambda = 0.15406$ nm) at 40 kV and 30 mA. Before deposition, the chamber had a base pressure $< 6 \times 10^{-6}$ Pa evacuated by mechanical and turbo-pumps. High-purity Argon then flowed into the sputtering chamber as the working gas at a rate of 10 standard cubic centimeters per minute to a pressure of 0.27 Pa. The films were grown to an approximate thickness of 40

nm onto SiN_x windows in a DENS[®] chip [31] at room temperature, which ensured direct electron transparency in the TEM. The DENS[®] chip is based on a microelectromechanical systems (MEMS) chip that can provide rapid heating/cooling with 0.001 °C temperature stability, in set images in Figure 1(a) [31]. The low amount of thermal mass to heat also ensures very stable positioning for imaging at temperature (negligible thermal drift) which is advantageous to both chemical mapping and PED collection [32]. The Fe(Cr) films were annealed *in situ* using the chip in the TEM with the heating cycles shown in Figure 1(a). The oxidation behavior occurred from the partial pressure of oxygen that is present in the TEM column, Figure 1(b), which will further be discussed shortly.

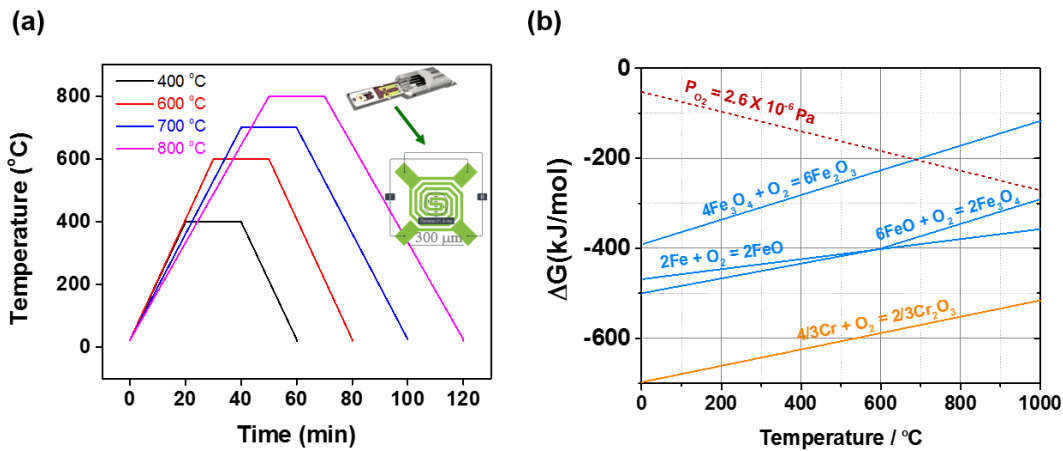


Figure 1 (a) *in situ* heat treatment history and the sketch of a DENS chip included (b) Ellingham diagram of Fe and Cr

After deposition, the Fe(Cr) films were immediately transferred into a FEI Tecnai SupertwinF20 (S)TEM. The TEM column evacuated pressure was $\sim 1.2 \times 10^{-5} \text{ Pa}$, and assuming an air mixture of 78%N₂-22%O₂, the oxygen partial pressure was $\sim 2.6 \times 10^{-6} \text{ Pa}$. The Ellingham diagram, Figure 1(b), shows that the thermodynamic driving force for oxidation will change with temperature. Thus, the lower oxygen content and the ability to anneal the film provides an ideal situation where the rate of oxidation can be slowed such that the initial stages of oxidation can be captured. Furthermore, under these controlled conditions, the immiscible phase separation between Fe-Cr prior to and after oxidation would reveal the hierarchy of microstructure evolution in these nanocrystalline alloys.

Therefore, we can provide for a very controlled (slow) rate of oxidation by increasing the temperature. Considering that the material is very minimal (required to be a thin foil), this provides a mechanism to study these effects in a controlled manner, particularly if one does not have a specialized gas reaction system. Also, by providing a low O₂ environment, we can observe the phase separation of the Fe-Cr (immiscible system) prior to and after oxidation initiates to determine the hierarchy of the microstructure evolution.

A NanoMEGAS platform on the TEM was employed to conduct PED scans [33-35]. The PED scans were collected using a 0.3° procession angle and a scanning step size of 3 nm, in the same size of region of interest (ROI), which was 800 × 800 nm². After scanning, the data was converted for analysis using TSL OIM Analysis 7 software and analyzed after grain dilation optimization. The composition, in the same ROI, was characterized by XEDS mapping using an EDAX[®] silicon drift detector (SDD).

3. Results and discussion

Figure 2(a) shows the series of bright field images, diffraction patterns, and PED orientation maps for the Fe-4Cr and Fe-16Cr films at room temperature and annealed settings at 400°C, 600°C, 700°C, and 800°C. Each image is from the same ROI so specific microstructural features can be tracked. From the diffraction patterns, the Fe-4Cr films only revealed a single body center cubic (bcc) solid solution A2 phase for all temperature conditions. Similarly, the Fe-16Cr film revealed an A2 phase but only up to 600°C after which additional reflections indexed for the Cr₂O₃ phase [36] were noted at 700°C and 800°C.

Orientation maps for the nanocrystalline Fe-4Cr sample revealed a mixture of grain textures evident by the multiple colors seen in the PED scan, Figure 2(a; i-v). Interestingly, as the temperature increased, the grain size was rather invariant with only modest increase in the mean grain size occurred at the highest temperatures, Figure 2(b), which was only a 10% increase from the room temperature film. Furthermore, the multiple textures within the film were maintained. The Fe-16Cr film was quite different. Here, the film adopted a strong [001] fiber texture, Figure 2(a; vi-x), which was also retained throughout the annealing stages. What is particularly interesting in the PED scans is the presence of much smaller [101] grains. As the temperature increased, evident grain growth occurred at 700°C,

Figure 2(b), with several of these smaller [101] grains now consumed by the [001] grains shown in sequence of images in Figure 2(a; vi-viii). With this grain growth, the grain shapes also changed. In the room temperature and lower annealed samples, the grains boundaries are curved; with increasing temperature, these boundaries become much more faceted (linear) between each other, Figure 2(a; x). By 800°C, the Fe-16Cr mean grain size was ~ 50% larger than the initial grain size with clear oxidation and formation of Cr₂O₃ over portions of the grains, Figure 2(a; x).

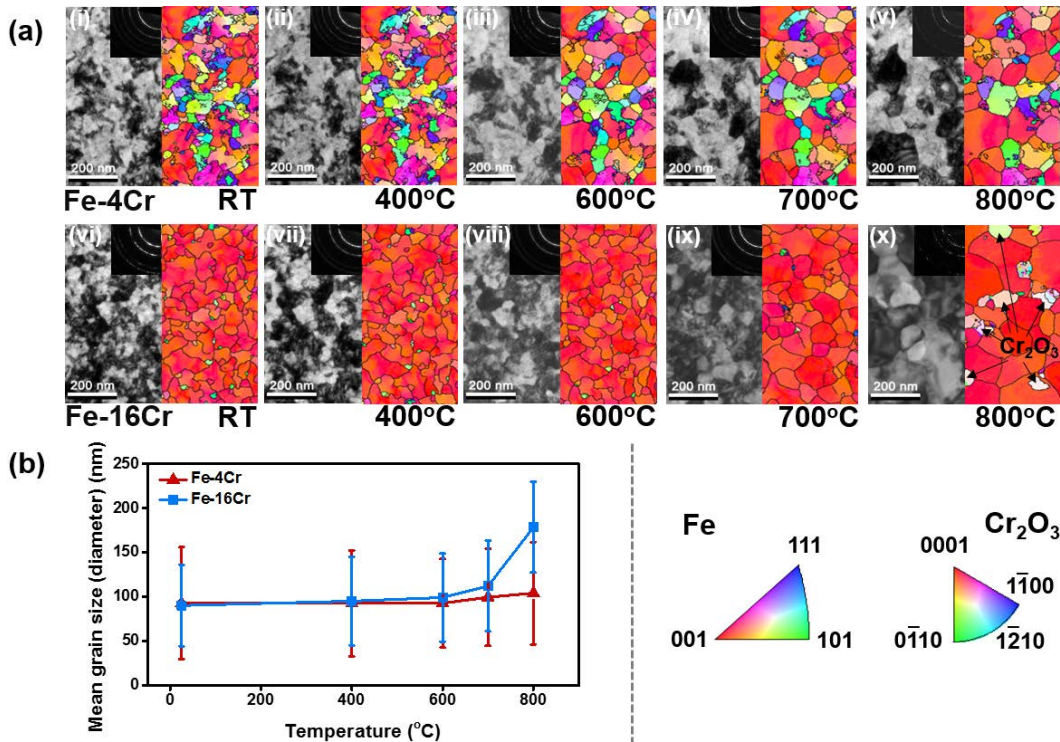


Figure 2 (a) Bright field images, diffraction patterns, and orientation maps of the (i)-(v) Fe-4Cr films and the (vi)-(x) Fe-16Cr films at RT or annealed at 400°C, 600°C, 700°C, 800°C (b) Mean grain size varying with temperatures for the Fe-4Cr and Fe-16Cr films.

This Cr₂O₃ phase was only resolved in the PED scan at the 700°C and 800°C for Fe-16Cr films. However, the favorable formation of chrome oxide as compared to iron oxide, Figure 1(b), would suggest that it should have also reacted with the Fe-4Cr film. A high angle annular dark field (HAADF) image taken over a larger ROI than the prior PED scans is shown in Figure 3(a)-(b). The image clearly reveals dark, very small nanosphere features within the grains. As will be shown later through XEDS analysis, these feature are indeed oxides and such contrast in the HAADF would be expected since the image's

contrast will scale as $\sim Z^2$, where Z is the atomic number. The small scale of these oxide clusters did not provide sufficient diffraction volume in the SAD pattern, but it is clear that the initial stages of oxidation were initiated in this particular nanocrystalline Fe-4Cr sample. In comparison, similar dark features are seen for the Fe-16Cr film, but are much larger in size and appear as independent grains, Figure 3(c), which would be in agreement with the PED and XEDS images in Figure 4. To further verify that the dark features are a result of the Cr content in either film, an elemental Fe nanocrystalline film annealed in an equivalent means to 800°C is shown in Figure 3(d). This HAADF feature does not show any dark contrast nano-spheres within the grains nor any large grains with comparable dark contrast as seen in Figure 3(c). Thus, one can conclude from the microstructure, that the oxidation is facilitated by the presence of the Cr content in the nanocrystalline alloys but the morphological evolution of the oxide is composition dependent.

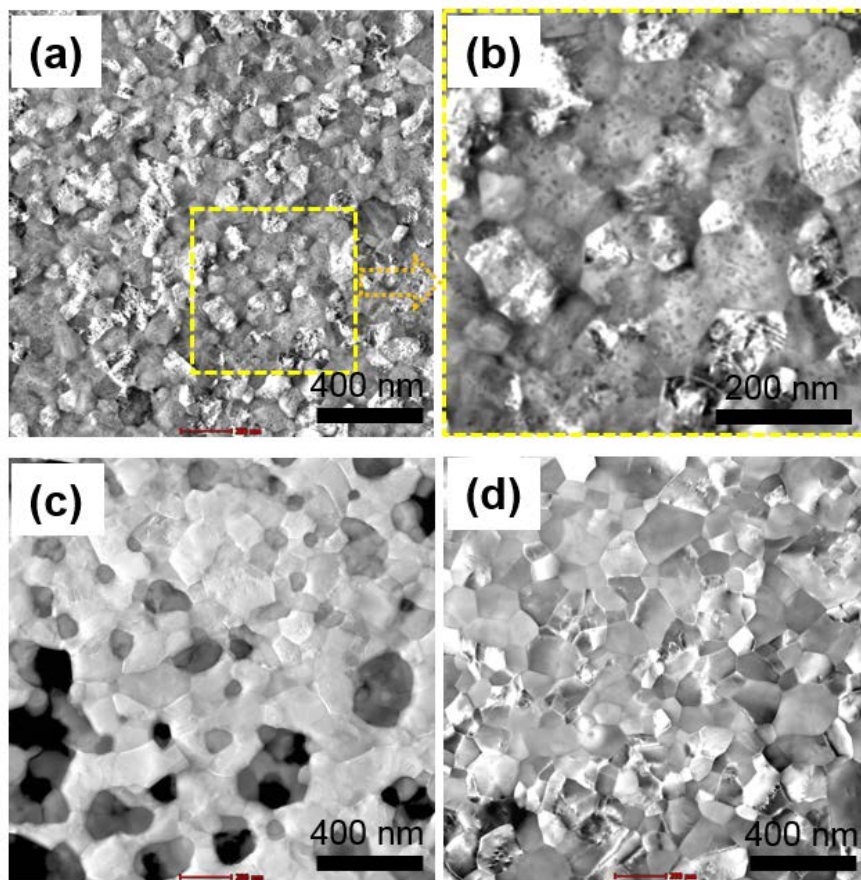


Figure 3 HAADF image of the (a) Fe-4Cr annealed at 800°C. (b) is a magnified view of (a). HAADF images of the (c) Fe-16Cr and (d) Fe films annealed at 800°C.

To better understand the oxygen migration that created these different oxide morphologies in each alloy, an XEDS scan was done at each sequential step of annealing with the amount of oxygen content quantified. A negligible amount of oxygen is observed in the as-deposited Fe-4Cr film and Fe-16Cr film with both films retaining this near zero value up to 600°C, Figure 4(a). At 600°C, a clear increase of oxygen to ~1.5 at.% is observed in the Fe-4Cr film and an increase to ~ 5 at.% was measured in the Fe-16Cr film. This uptake in oxygen is noted to occur in distinct regions within each alloy. Upon raising the temperature, the oxygen levels further increased for both films, Figure 4(a). With this increase in oxygen, it occurred in distinct regions within each film. As noted in Figure 3, the Fe-4Cr film revealed the oxygen within the grains as small clusters (or nano-spheres) whereas the Fe-16Cr film revealed dominate oxygen content as a distinct Cr₂O₃ granular phases. These specific compositional distinctions can be observed in the representative XEDS maps in Figure 4(b). Based on the XEDS quantification of the oxygen content, Figure 4(a), it is clear that the Cr₂O₃ phase formed in the Fe-16Cr film, in agreement with the prior diffraction results in Figure 2. The much lower oxygen content in the Fe-4Cr film was not the Cr₂O₃ phase and would also be in agreement with the diffraction findings that did not reveal such reflections. Thus, the uptake of oxygen and the formation of Cr₂O₃ is dependent on both Cr composition, as noted in the bulk alloys [1], and temperature.

This dependence is further confirmed in tracking the Cr content in the Fe-16Cr film. Figure 4(c) is a plot of how the Cr/(Fe+Cr) ratio changes with temperature. With the onset of Cr₂O₃ precipitation in the Fe-16Cr film at 800°C, the Cr content within the bulk of the alloy decreases with a corresponding increase in the precipitate composition. Thus, the oxide extracts out the Cr from the bulk of the film to grow the oxide phase. At 800°C, the Cr₂O₃ phase occupied approximately 12 vol.% of the sample based on the XEDS compositional map, Figure 4(b) and PED scan in Figure 2(a; x). In contrast, the deviation of the Cr content at the clusters and within the alloy only revealed a much smaller deviation.

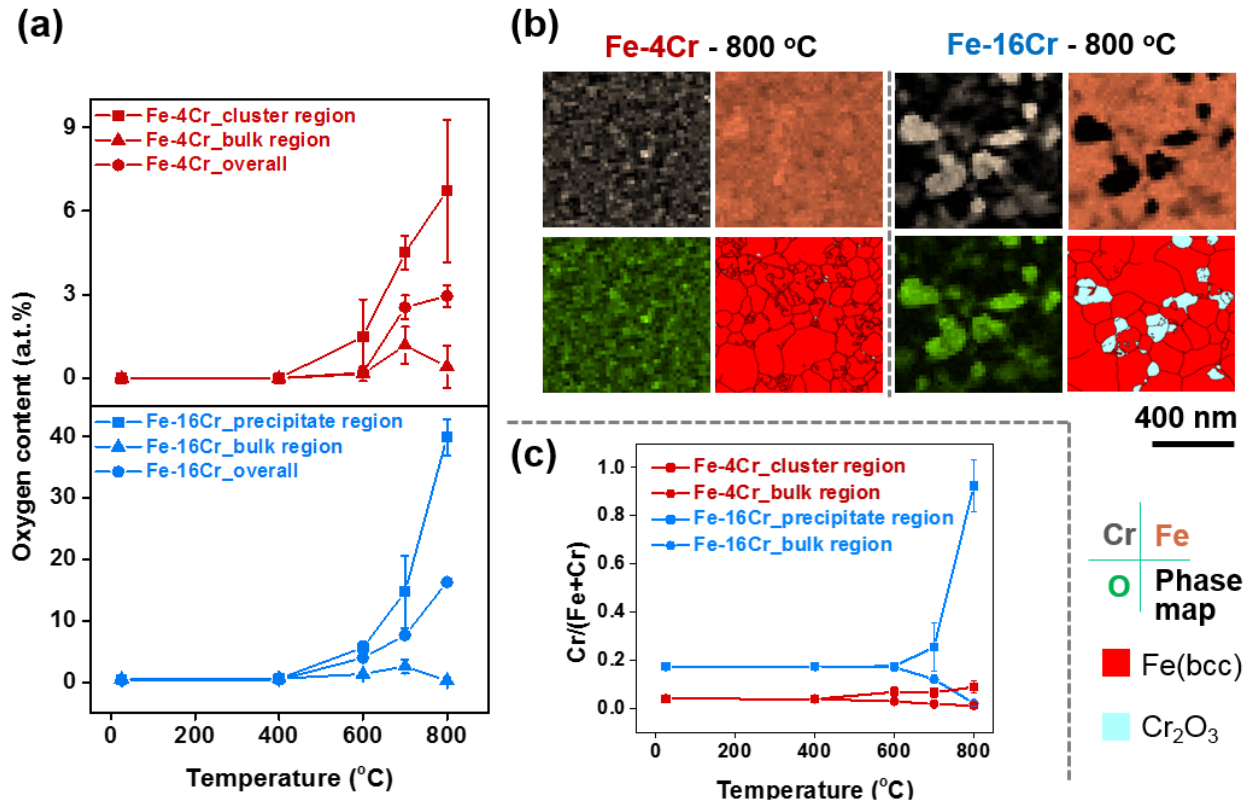


Figure 4 (a) The overall oxygen content, oxygen content of low and high Cr regions of the Fe-4Cr and Fe-16Cr films at different annealing temperature (b) Cr, Fe, O elemental distribution maps and phase map of the Fe-4Cr and Fe-16Cr films annealed at 800°C (c) the ratio of Cr/(Fe+Cr) in low and high Cr region of the Fe-4Cr and Fe-16Cr films at different annealing temperatures. bcc represents body center cubic.

The formation of the nanoscale clusters reveals an interesting thermodynamic competition that controls the morphology of the oxidation in the microstructure. The solubility of Cr in Fe, at ambient temperatures, is approximately 5 at.% and increases with temperature. Thus, the Fe-4Cr alloy is within this single phase field with no driving force for phase separation. However, the thermodynamic preference for Cr to react with oxygen has allowed it to occur within the grains itself. What is particularly interesting is that the elemental Fe film, annealed at 800°C, did not oxidize further confirming the strong preference of Cr to react with oxygen even when in solution and at very low concentrations.

Unlike the Fe-4Cr alloy, the Fe-16Cr reaction with oxygen yielded a distinct phase that had separated itself from the Fe-rich matrix microstructure. The Cr₂O₃ scale had grown into grains. Since sputtering yielded a supersaturated solid solution, upon annealing, the

Fe-16Cr system was driven to phase separate. However, as the Cr came out of solution, it reacted with the oxygen as no distinct bcc Cr reflections. The differences in the oxide morphology (clusters vs. distinct grains) is driven by this phase separation behavior. In a complimentary study to this in situ work, a 200 nm Fe-16Cr film was annealed at 700°C under an equivalent vacuum condition as the TEM and a cross-sectional foil was extracted using a focus ion beam lift out method similar to that reported in [37]. Figure 5(a) reveals the XEDS cross section where one can clearly see the formation of the scale between the grains and its migration towards the surface of the film. As the Cr phase separated into the grain boundaries, it reacted with the oxygen whereupon the Cr₂O₃ consumed the grain as it grew until the Cr was depleted out of the grain. Since the Fe was less reactive to oxygen at these partial pressures and temperatures, the oxidation appeared to cease once the Cr had reacted. We can better understand this migration of the oxide along the boundaries by considering the boundary types themselves.

Using PED, the various boundary types have been identified. Figure 5(b) and (c) shows the grain boundary maps for the *in situ* 700°C and 800°C annealed Fe-16Cr film respectively. By comparing the ROI-A between the 700°C and 800°C, the Cr₂O₃ phase precipitation evolution is evident in multi-grain boundary junction, pointed to by the larger solid red arrow. At 700°C, no oxides was yet present at this junction which composed three high angle grain boundaries (HAGBs, labeled #1-#3) and one Σ 5 boundary (labeled #4). Also note that a low angle grain boundary (LAGB) is very near this junction (labeled #5). Upon annealing to 800°C, the Cr₂O₃ precipitate became readily apparent at this former junction as well as a few other smaller oxide precipitates along one of the HAGBs (#1). The larger oxide at the junction would not be unexpected as a multi-boundary junction would be the convergence point for Cr solute from multiple sources as well as provide multiple interfaces from which the oxide could heterogeneously nucleate from and remove prior grain boundaries, albeit replacing it with an inter-phase boundary. At 800°C, we can see that two of the HAGBs (#2 and #3) are now replaced by a LAGB. Upon annealing, the LAGB noted at 700°C (#5) appears to have swept through the microstructure. The oxide is now bridging three distinct boundary types – LAGB (#5), a Σ 5 boundary (#4), and a HAGB (#1) This convergence allows us to measure the dihedral angle at all three (different) boundary types, shown in Figure 5(d), with those values found to be 149°, 116°, and 97°

respectively. When all three boundaries are 120°, the boundary energies are in geometrically stable condition; however, this is not the case. The lower 97° angle for the HAGB, which is the lowest among the three, suggests that it is the preferred (or fastest) growing direction for the oxide. A HAGB can readily transport Cr solute to the precipitate because of its higher diffusivity [38, 39]. Furthermore, a LAGB and a $\Sigma 5$ boundary have lower segregation of Cr solutes to it, as previously reported by the authors [39]. Collectively this would then explain why additional oxides, pointed to by the smaller dash red arrow in Figure 5(c), were only observed on the HAGB and not on the LAGB or $\Sigma 5$. Using Young's equation [38],

$$\frac{\gamma_{12}}{\sin\alpha_3} = \frac{\gamma_{23}}{\sin\alpha_1} = \frac{\gamma_{31}}{\sin\alpha_2} \quad (1)$$

where γ is the interfacial energy, α is the contact angle of grain boundary. The relative boundary energies for the three different boundary types at each junction with the oxide were computed and tabulated in Table 1 and angle as labeled in Figure 5(e).

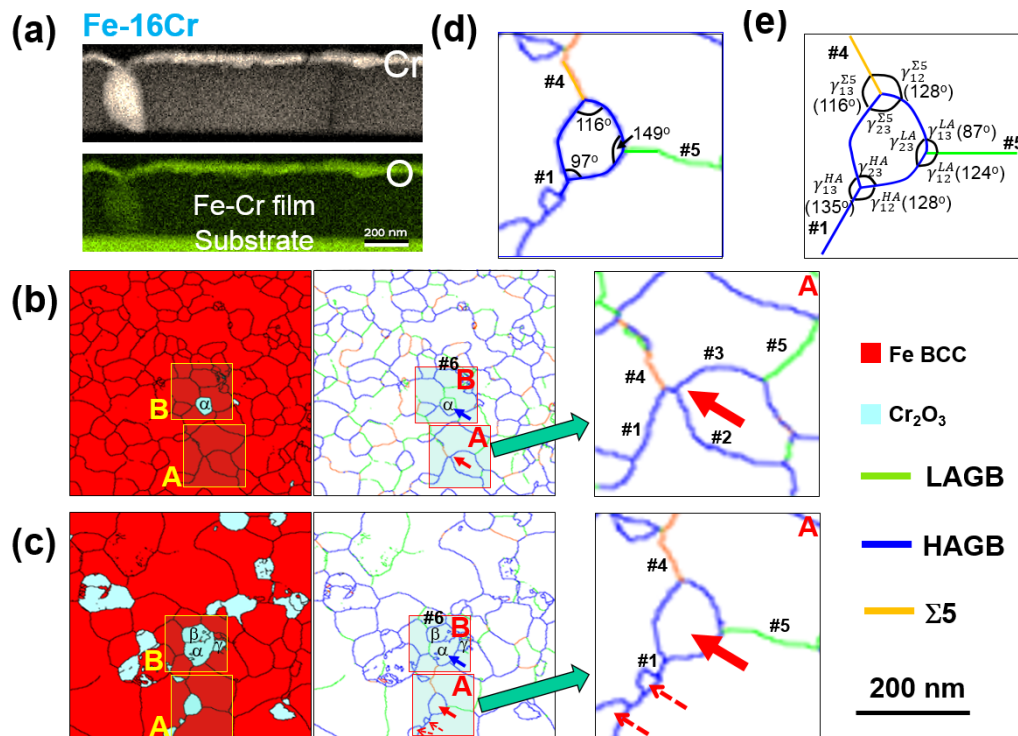


Figure 5 (a) XEDS cross section map of the Fe-16Cr film annealed at 700°C for 1 hour. Phase maps and grain boundary evolution of Fe-16Cr film after annealing at (b) 700°C, and (c) 800°C. Two cyan rectangular blocks locate ROI-A and ROI-B. (d) and (e) are the magnified grain boundary map of ROI-A of the 800°C annealed Fe-16Cr film

Table 1. The relative boundary energies for the three different boundary types at each junction with the oxide.

$\gamma_{23}^{GB} - \gamma_{12}^{GB} - \gamma_{13}^{GB}$	$\gamma_{23}^{GB} / \gamma_{12}^{GB}$	$\gamma_{23}^{GB} / \gamma_{13}^{GB}$	$\gamma_{12}^{GB} / \gamma_{13}^{GB}$
LAGB-HAGB-HAGB	0.62	0.52	0.83
HAGB-HAGB-HAGB	1.26	1.40	1.11
$\Sigma 5$ - HAGB - HAGB	1.14	1.00	0.88

Looking ROI-B, Figure 5(b), we can note that a Cr_2O_3 precipitate (labeled α) was already present in a junction at 700°C , unlike ROI-A where an oxide precipitate had not yet nucleated. This α oxide was bounded between LAGBs and HAGBs. After annealing at 800°C , the size of the oxide phase increased from ~ 50 nm to ~ 100 nm and was still bounded by the same types of GBs but a part of the LAGB, which was just above the α -designated precipitate in the ROI-B, has been consumed by Cr_2O_3 growth creating a HAGB that separate itself from another Cr_2O_3 precipitate, denoted as β in ROI-B in Figure 5(c). This new Cr_2O_3 precipitate (β), as well as another Cr_2O_3 precipitate labeled γ in the same ROI-B in Figure 5(c) are all now in contact with each other as separate grains, with the contact boundaries between each being a HAGB, Figure 5(c). For these oxides to now have formed, the β and γ oxide particles must have grown from a different direction and then impinged into the α oxide particle to create a HAGB. If the α oxide particle had facilitated their nucleation, one would not expect a boundary between the oxides. Upon closer inspection of the PED scan at 700°C , the region from which the β and γ oxides originated from had HAGBs (labeled #6 in Figure 5(b)) which are is still present at 800°C , Figure 5(c). This again provides strong experimental evidence of the dominance of HAGBs in the evolution of the oxide growth.

4. Conclusion

Two nanocrystalline alloys of Fe-4Cr and Fe-16Cr were sputter deposited and formed a solid solution A2 phase. Each alloy was then in situ annealed in a TEM. At temperatures at and above 700°C, both alloys revealed Cr oxidation. The oxygen source was from the low partial pressure of oxygen presence in the TEM column. Though both alloys oxidized, the morphology of the oxide was different. For the Fe-4Cr, nanoscale oxide clusters were characterized to be within the Fe matrix grains whereas large, distinct granular Cr₂O₃ phases present in the Fe-16Cr alloy. Neither oxide produced a continuous passive layer for the Fe-rich matrix. Though Fe oxide is also a favorable reaction, at these temperatures and partial pressures of oxygen, no Fe oxides were not observed. This demonstrates the very strong oxidation tendencies of Cr, even in environments that are not necessary oxygen-rich.

The formation of the oxide clusters in Fe-4Cr was contributed to Cr being thermodynamically favorable in solution with Fe. However, for Fe-16Cr, the solid solution was supersaturated and upon annealing, the Cr would be driven to phase separate from Fe. However, upon separating, the Cr reacted with the low partial pressure of oxygen in the column and formed Cr₂O₃. This phase separation and oxidation reaction occurred at the grain boundaries within the microstructure. With the higher Cr content, this alloy was able to continue to provide sufficient Cr content for the scale in the boundary to grow and become distinct grains within the microstructure. Furthermore, through the use of in situ analysis, coupled with PED for grain boundary character quantification, the evolution of the oxide from these boundaries was tracked and measured. The oxides most readily grow from HAGBs. The dominance of the HAGB was noted for a particular oxide precipitate that was connected to a HABG, a LAGB, and a $\Sigma 5$. Upon annealing, the oxide demonstrated preference for growth along the HAGB evident by a lower dihedral angle and the additional precipitation of oxides on the same boundary. This has been contributed to the higher Cr diffusivity of this boundary compared to the other types. In this case, the lower oxygen content within the TEM column provided a controlled oxidation response in the material allowing us to observe these initial stages of reactions and nucleation. Such reactions should be expected to occur even if the diffraction does not indicate it, as evident

by our Fe-4Cr alloy which formed clusters but no clear diffraction change in the A2 solid solution.

ACKNOWLEDGMENT

The authors gratefully recognize support from the Army Research Office, grant W911NF1310436, as well as the University of Alabama's Central Analytical Facility. The SDD for the EDS and DENS heating stage was purchased under the DURIP award W911NF1510405:

REFERENCES

- [1] KH Lo, CH Shek, JKL Lai (2009) *Materials Science & Engineering R-Reports* 65: 39. Doi:10.1016/j.mser.2009.03.001
- [2] RL Klueh, AT Nelson (2007) *Journal of Nuclear Materials* 371: 37. Doi:10.1016/j.jnucmat.2007.05.005
- [3] EA Little (1979) *Journal of Nuclear Materials* 87: 11. Doi:[https://doi.org/10.1016/0022-3115\(79\)90122-3](https://doi.org/10.1016/0022-3115(79)90122-3)
- [4] RA Lula, JG Parr (1986) *Stainless steel*. American Society for Metals,
- [5] RK Gupta, N Birbilis (2015) *Corrosion Science* 92: 1. Doi:10.1016/j.corsci.2014.11.041
- [6] T Horita, Y Xiong, H Kishimoto, K Yamaji, N Sakai, H Yokokawa (2004) *Journal of Power Sources* 131: 293. Doi:<https://doi.org/10.1016/j.jpowsour.2003.10.017>
- [7] D Terentyev, P Olsson (2008).
- [8] M Ziętała, T Durejko, M Polański, et al. (2016) *Materials Science and Engineering: A* 677: 1. Doi:<https://doi.org/10.1016/j.msea.2016.09.028>
- [9] K Sugimoto, S Matsuda (1980) *Materials Science and Engineering* 42: 181. Doi:10.1016/0025-5416(80)90027-0
- [10] B Pujilaksono, T Jonsson, H Heidari, M Halvarsson, JE Svensson, LG Johansson (2011) *Oxid Met* 75: 183. Doi:10.1007/s11085-010-9229-z
- [11] HJ Grabke (2000) *Surface and Interface Analysis* 30: 112. Doi:10.1002/1096-9918(200008)30:1
- [12] A Ponomareva, E Isaev, N Skorodumova, Y Vekilov, I Abrikosov (2007) *Physical Review B* 75: 245406. Doi:10.1103/PhysRevB.75.245406
- [13] M Ropo, K Kokko, M Punkkinen, et al. (2007) *Physical Review B* 76: 220401(R). Doi:10.1103/PhysRevB.76.220401
- [14] P Alnegren (2012) *Institutionen för kemi- och bioteknik Chalmers tekniska högskola, Göteborg*
- [15] VB Trindade, U Krupp, PEG Wagenhuber, HJ Christ (2005) *Materials and Corrosion* 56: 785. Doi:10.1002/maco.200503879
- [16] RA Golden, EJ Opila (2018) *Journal of Materials Science* 53: 3981. Doi:10.1007/s10853-017-1823-x
- [17] N Das, T Shoji, Y Takeda (2010) *Corrosion Science* 52: 2349. Doi:10.1016/j.corsci.2010.04.006
- [18] S Lozano-Perez, D Saxey, T Yamada, T Terachi (2010) *Scripta Materialia* 62: 855. Doi:10.1016/j.scriptamat.2010.02.021

- [19] M Punkkinen, K Kokko, H Levamaki, et al. (2013) *Journal of Physics-Condensed Matter* 25: 495501. Doi:10.1088/0953-8984/25/49/495501
- [20] COA Olsson, D Landolt (2003) *Electrochimica Acta* 48: 1093. Doi:10.1016/S0013-4686(02)00841-1
- [21] CR Xue, T Narushima, Y Ishida, T Tokunaga, T Yonezawa (2014) *Acs Appl Mater Inter* 6: 19924. Doi:10.1021/am505333v
- [22] GH Cui, DZ Wu, SL Qi, S Jin, ZP Wu, RG Jin (2011) *Acs Appl Mater Inter* 3: 789. Doi:10.1021/am1011468
- [23] CM Wang, DK Schreiber, MJ Olszta, DR Baer, SM Bruemmer (2015) *Acs Appl Mater Inter* 7: 17272. Doi:10.1021/acsami.5b04341
- [24] DE Eakins, DF Bahr, MG Norton (2004) *Journal of Materials Science* 39: 165. Doi:DOI 10.1023/B:JMSC.0000007741.97288.bd
- [25] BA Cook, XZ Wei, JL Harringa, MJ Kramer (2007) *Journal of Materials Science* 42: 7643. Doi:10.1007/s10853-007-1898-x
- [26] ARS Gautam, JM Howe (2009) *Journal of Materials Science* 44: 601. Doi:10.1007/s10853-008-3080-5
- [27] MY Zheng, WC Zhang, K Wu, CK Yao (2003) *Journal of Materials Science* 38: 2647. Doi:Doi 10.1023/A:1024486619379
- [28] R Banerjee, PA Crozier (2012) *Journal of Physical Chemistry C* 116: 11486. Doi:10.1021/jp2073446
- [29] K Unocic, D Shin, R Unocic, L Allard (2017) *Oxid Met* 88: 495. Doi:10.1007/s11085-016-9676-2
- [30] Y Sasanuma, M Uchida, K Okada, K Yamamoto, Y Kitano, A Ishitani (1991) *Thin Solid Films* 203: 113. Doi:[http://dx.doi.org/10.1016/0040-6090\(91\)90522-Y](http://dx.doi.org/10.1016/0040-6090(91)90522-Y)
- [31]
- [32] J Brons, G Thompson (2014) *Jom* 66: 165. Doi:10.1007/s11837-013-0799-5
- [33] JG Brons, GB Thompson (2013) *JOM* 66: 165. Doi:10.1007/s11837-013-0799-5
- [34] P Moeck, S Rouvimov, EF Rauch, et al. (2011) *Crystal Research and Technology* 46: 589. Doi:10.1002/crat.201000676
- [35] EF Rauch, J Portillo, S Nicolopoulos, D Bultreys, S Rouvimov, P Moeck (2010) *Zeitschrift für Kristallographie* 225: 103. Doi:10.1524/zkri.2010.1205
- [36] AH Hill, A Harrison, C Dickinson, WZ Zhou, W Kockelmann (2010) *Micropor Mesopor Mat* 130: 280. Doi:10.1016/j.micromeso.2009.11.021
- [37] LA Giannuzzi, FA Stevie (1999) *Micron* 30: 197. Doi:[https://doi.org/10.1016/S0968-4328\(99\)00005-0](https://doi.org/10.1016/S0968-4328(99)00005-0)
- [38] G Gottstein (2004) *Physical Foundations of Materials Science*. Springer Berlin Heidelberg,
- [39] X Zhou, X-x Yu, T Kaub, RL Martens, GB Thompson (2016) *Scientific Reports* 6: 34642. Doi:10.1038/srep34642

CHAPTER 10

Phase and Microstructural evolution in sputtered Fe-Cr films

Xuyang Zhou¹ and Gregory B. Thompson¹

1. The University of Alabama, Department of Metallurgical & Materials Engineering,
Tuscaloosa, AL USA

Abstract:

A series of $\text{Fe}_x\text{Cr}_{1-x}$ thin films (where $X = 0$ to 1) were magnetron sputter deposited onto ambient temperature substrates. The elemental films adopted the BCC structure with a tens of nanometer-sized equiaxed grains. The Fe-49Cr (at%) film grew as the high temperature σ -phase, with similar but smaller equiaxed grain sizes. All other alloy compositions deposited as the A2 solid solution BCC phase. The Fe-5Cr film was found to have ordering through atom probe tomography (APT) analysis and confirmed prior modeling and diffuse neutron diffraction results. However, upon depositing this film at 673 K, this ordering is lost. Films of Fe-16Cr, Fe-24Cr, and Fe-72Cr increased in grain size, with the -24Cr and -72Cr films exhibiting abnormal grain sizes that were hundreds of nanometers in size. It is suspected that the thermodynamic driving force to phase separate has contributed to the increased adatom mobility. Furthermore, these films revealed a peculiar 'star-burst' contrast pattern within their grains that has been associated with a modest orientation shift which too is contributed to the early onset of phase separation evident in our APT clustering analysis of these alloy films.

Keywords: Fe-Cr, structure evolution, atom probe, ordering and clustering

1. Introduction

Thin film deposition is a highly dynamic process which can yield a variety of microstructures with several of the phases being different from those nominally observed in bulk, equilibrium phase diagrams [1]. For example, amorphous phases can be fabricated by vapor quenching techniques [2-4], high-temperature phases can be stabilized in the films deposited at room temperature [5], and supersaturated solid solutions are often achieved beyond bulk solubility limits [6-9]. By understanding the structural evolution during thin film growth, and even controlling the structural evolution, one can generate unique mechanical and functional properties [10-17].

The Fe-Cr alloy is an important engineering material because of its combined corrosion and oxidation resistance coupled to good mechanical strength [18-21]. As a thin film, Fe-Cr have been able to exhibit several other unique properties that are not

normally associated with its bulk form [6, 7, 22-24]. For example, Fe-Cr multilayers exhibit the giant magnetoresistance effect [22]. The alloy is also reported to be a topologically close-packed (TCP) phase film with excellent tribology properties because of its large hardness-to-elastic ratio [23]. Sputtered nanocrystalline Fe-Cr films also exhibit improvements in pitting resistance [24-27]. When sputter deposited, these films often extend solid solubility ranges not observed in the bulk which has been contributed to some of the aforementioned properties [6, 7, 24].

The Fe-Cr system exhibits a miscibility gap with its phase separation characteristics attracting the research interests since the mid-twenty century [28, 29]. From theoretical calculations, the enthalpy of mixing was reported to change from a negative to positive value near 5 at.% Cr at or below ambient temperature [30-32]. Interestingly, in solution, Fe-rich Fe(Cr) has even been suggested to have local short range ordering reported from diffuse-neutron-scattering measurements [30, 33] as well as modeling predictions [30, 34]. To date there has been little additional experimental studies that have explored this ordering behavior in the dilute Cr solute limit. Often the behavior is considered to be associated with clustering [35-37]. Consequently, this ordered structure is not readily reported on Fe-Cr binary phase diagrams. Upon extending Cr's composition beyond the solubility limit, the alloy will proceed to phase separate by either nucleation and growth or spinodal decomposition dependent on its compositional location within the miscibility gap's spinodal. [38].

One way to study these early stages of phase separation is by atom probe tomography (APT). APT provides 3D reconstructions of individual atoms with near perfect lattice rectification. Its high chemical and spatial resolution (around 0.1-0.3 nm in depth and 0.3-0.5nm laterally with equal sensitivity for all elements [39, 40]) offers scientists a technique to probe the very fine scale behavior of phase forming a phase separating behavior [39, 40]. As a result, this technique has been extensively used to quantify the spinodal decomposition of Fe-Cr alloys in its bulk form [39-47] but has had rather limited application to Fe-Cr thin films [9] where several highly nonequilibrium phase states can be achieved as mentioned above. A Thus APT characterization offers potentially interesting opportunities to study phase equilibria in this alloy as a thin film as well as new insights into how systems, far from equilibrium, migrate towards thermodynamic equilibrium.

Several methods have been developed to detect phase separation behavior using APT. These include the Johnson and Klotz (JK) ordering parameters [48, 49], Langen, Bar-on, and Miller (LBM) method [44, 45], the contingency table [50], the radial distribution function method (RDF) [41, 51], and the three-dimensional Markov field (3DMF) approach [42, 43, 47]. In this paper, we have explored the use of the LBM

method, radial distribution method, and the 3DMF to discuss the early stages of phase separation in a series of nanocrystalline Fe-Cr films. The aim of which is to understand how phase separation initiates as a function of composition as well as compare which of these methods yields data-sets most respective of the physical system's behavior.

In the LBM method, a pair of Gaussian distributions of the solute concentrations are used to fit an experimental probability distribution [44, 45]. Those two Gaussian distributions share the same width, σ , but are centered at different concentrations, μ_1 and μ_2 , respectively. This is described using the formulation of equation (1)

$$P(c) = \frac{\mu_2 \exp\left[\frac{-(c-\mu_1)^2}{2\sigma^2}\right] + \mu_1 \exp\left[\frac{-(c-\mu_2)^2}{2\sigma^2}\right]}{(\mu_1 + \mu_2)\sigma\sqrt{2\pi}} \quad (1)$$

where μ_1 and μ_2 are the peak and trough compositions, respectively; σ^2 is the variance of each Gaussian distribution. The amplitude is $\mu_2 - \mu_1$.

In the RDF method, a radial concentration profile is constructed for every detected atom for the chosen element [41, 51]. Specifically, an atom i is selected as the origin and the probability density to find another atom j is calculated in a sequence spherical shells. (In this work we divided the shells to be of 0.2 nm thick and ranged to 10 nm). This probability density plot is then averaged over all the atoms for a chosen element and it was normalized to the average bulk concentration. The RDF is expressed as:

$$RDF(r) = \frac{C_E(r)}{C_0} = \frac{N_E(r)/N(r)}{C_0} \quad (3)$$

where $C_E(r)$ is the atomic composition of element E at the distance of r , C_0 is the average composition of element E in the studied volume, $N_E(r)$ and $N(r)$ is the total number of atoms of element E and all elements at the distance of r , respectively.

Finally, the 3DMF is adapted for the determination of the Warren-Cowley (W-C) parameter [52], α_{BA}^k . The W-C quantifies near neighbor solute atom interactions by describing the distribution of atoms within a binary AB system, as

$$\alpha_{BA}^k = 1 - \frac{P_{BA}^k}{X_A} = 1 - \frac{1 - P_{BB}^k}{1 - X_B} \quad (2)$$

where P_{BA}^k or P_{BB}^k are the probabilities of finding an A-type matrix atom or a B-type solute atom in the k th shell of atoms surrounding a B-type solute atom, respectively, given X_A the overall concentration of A atoms in the system [40]. The P_{BB}^k is calculated by

$$P_{BB}^k = \frac{1}{N_B} \sum_{i=1}^{N_B} \frac{n_i}{c_i} \quad (3)$$

where c_i is the number of nearest neighbors and n_i is the number of solute nearest neighbors around a solute atoms i [47]. If α_{BA}^k is positive, then there is a preference for like atoms to cluster whereas a negative value means a preference for dissimilar atoms to order. The application of the 3DMF method will be used to explore the aforementioned ordering of the dilute Fe(Cr) system. Rather than inferring this ordering from a magnetic property response that was an outcome of the diffuse neutron diffraction experiment [33], the APT would provide a complimentary structural characterization of the atomic distributions and further confirm if such ordering does occur. Such short-range ordering information would be then be valuable as forward feeding data for thermodynamic models that calculate configurational entropy and the lowest energy states in this system for dilute Cr additions to Fe [47]. These types of results would then lend to new insights and information to better understating phase stability in Fe-Cr alloy films.

2. Experimental

Elemental Fe, Cr, and alloyed Fe_{1-x}Cr_x (0<x<1) nanocrystalline thin films were sputter deposited from 99.95 at.% pure Fe and Cr targets in an AJA ATC-1500 stainless steel magnetron-sputtering system to an approximate thickness of 300 nm onto 300 μ m thick Si [001] substrates at ambient temperature. A quartz crystal SQM-160 sensor determined the deposition rates for each elemental films to be \sim 0.1 nm/sec. Alloy films, with each of the different compositions, was achieved through co-sputtering two elemental targets with various sputtering power combinations. The base vacuum pressure prior deposition was $< 6 \times 10^{-6}$ Pa. During deposition, a pressure of 0.27 Pa was maintained using ultra-high purity argon flowed as the working gas at ten standard cubic centimeters per minute flow rate. For in-situ annealing experiment, the reported temperature was calibrated by using a k-Space[®] Bandit system.

A series of θ -2 θ x-ray diffraction (XRD) scans was conducted post-growth using a X'pert Philips diffractometer operated with Cu K α radiation ($\lambda = 1.5406 \text{ \AA}$) at 45 kV and 40 mA for phase identification. Microstructure characterization was performed in an FEI Tecnai Super twin F20 (S)TEM using plan-view TEM foils, which were prepared by cutting, dimpling and ion-milling a 3 mm disc taken from the substrate. Precession Electron Diffraction (PED) scans, performed in the TEM, provided grain orientation mapping via the NanoMEGAS platform [53-55]. The PED was operated with a 0.3 $^\circ$ precession angle at a step size of 3 nm on a region as large as 1.2 μ m \times 1.2 μ m. After scanning, the data was converted for analysis using TSL OIM Analysis 7 software. Grain size distributions were plotted based on the orientation map that optimized via grain dilation.

The composition of each alloy film was confirmed by APT in a Cameca® Scientific Instruments Local Electrode Atom Probe (LEAP) 5000 XS. The required needle-shaped geometries were prepared for atom probe analysis using a focus ion beam (FIB) cross-sectional lift-out technique and annular milling procedure described in reference [9, 56] in either the TESCAN LYRA FIB- Field Emission Scanning Electron Microscope (SEM) or an FEI Quanta 3D dual beam FIB-SEM. The specimens were field evaporated with a laser energy of 50 pJ for a 0.5 % targeted evaporation rate at a base temperature 37 K. The APT data was reconstructed using the IVAS 3.8 software platform. As noted in the introduction, the LBM [44, 45], RDF [41, 51], and 3DMF [42, 43, 47] methods were chosen to detect the phase separation behavior.

3. Result and discussion

A series of elemental and alloy thin films spanning Fe, Fe-5 at.%Cr, Fe-16 at.%Cr, Fe-24 at.%Cr, Fe-49at.%Cr, Fe-72at.%Cr, and Cr, were grown. The XRD scans, Figure 1, confirmed that the elemental films were BCC and the alloy films adopted the solid solution BCC A2 phase revealing a strong {011} fiber texture. The only exception was the Fe-49Cr film which diffracted two strong reflections at 39° and 85° 2Θ , respectively. According to the binary phase diagram, an ordered intermetallic FeCr phase, denoted as σ , is present in the miscibility gap but decomposes and phase separates into two BCC phases below $\sim 700\text{K}$. When compositions within the σ -phase are processed, it has been reported to be the equilibrium σ -phase, which is a tetragonal P 42/mn structure [57] or a metastable A15 phase [5, 23, 57-62], which is a cubic Pm3n structure [60, 62]. Since both these two structures have very similar reflections near 39° (002) and 85° (004), we are unable to determine the crystal structure from XRD alone, but will be determined from proceeding electron diffraction experiments. Regardless of the ambiguity in the structure from the XRD scans, it is clear that a high temperature, ordered phase was able to be sputter deposited onto an ambient temperature substrate. This demonstrates that the negative enthalpy of formation of this ordered phase is sufficient to avoid forming a simple solid solution. What is also particularly striking is that the ordered phase is a higher temperature phase and it was able to be formed at room temperature by this process from two separate sputtering sources.

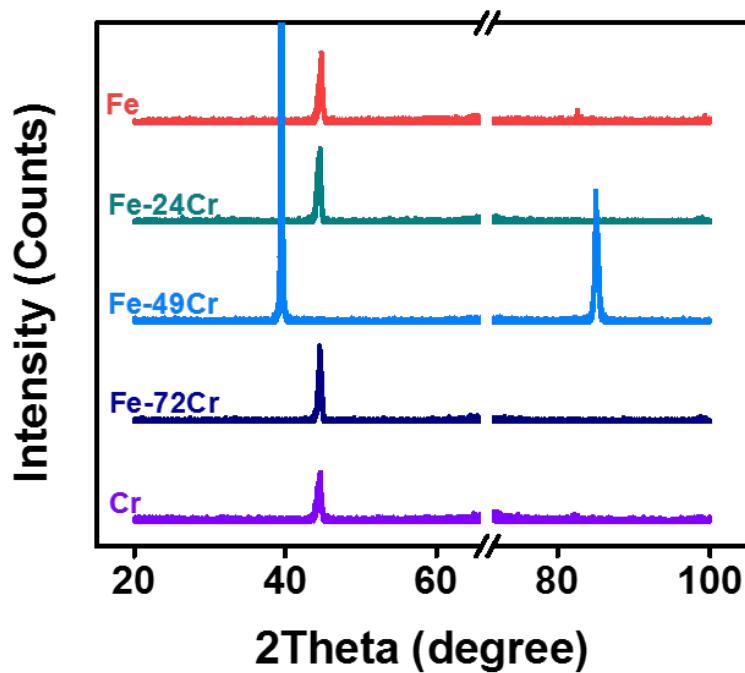


Figure 1 X-ray spectrums of Fe-Cr alloying films with different solute concentrations

Figure 2(a) shows the simulated polycrystalline diffraction patterns of {001} textured σ -phase and A15 phase as well as the experimentally measured selected area diffraction (SAD). When one compares the experimentally diffracted inner most ring and the most intense ring, we note that the pattern matches the σ -phase. The A15 phase does not have a reflection that matches the inner most ring whereas the σ -phase does. Furthermore, the most intense ring for A15 is composed of two reflections where the experimental diffraction revealed a single reflection whose ring spacing matched the single ring spacing of the σ -phase. Upon closer inspection, all other simulated σ -phase rings were consistently matched with the experimental diffraction pattern. We also tilted the films 30° away from the {001} zone axis, which was the fiber texture of this film, and found that the simulated diffraction patterns continued to match well with the experimental observations, Figure 2(b).

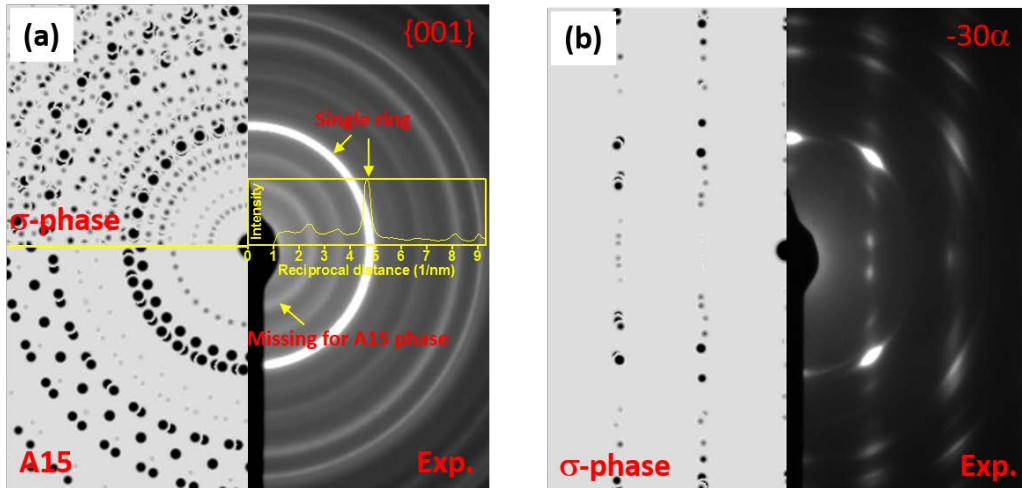


Figure 2 (a) The simulated polycrystalline diffraction patterns of $\{001\}$ textured σ -phase and A15 phase as well as the experimentally measured one. **(b)** The simulated polycrystalline diffraction patterns of textured σ -phase and the experimental observation 30° away from the $\{001\}$ zone axis.

Figure 3(a) and (b) are the bright field and dark field images of the Fe-49Cr film which revealed that this σ -phase has grown with a very fine nanocrystalline grain size, in contrast the solid solution A2 phases for the Fe-Cr alloys revealed much larger grain sizes, plotted in Figure 4. An HRTEM lattice fringe image, Figure 3(c), indicated that even in the small gains, multiple structural defects were present indicated the partitioning of the lattice fringes in different directions. The PED orientation map has been employed to identify the phase, grain size distribution, and texture. The templates of a σ -phase and an A15 phase were used and over 98% area was identified to have a σ -phase with the balance being the A15 phase. This result further confirmed that the dominate phase of the Fe-49Cr film is the high temperature σ -phase. The PED orientation map also revealed a high degree of $[001]$ texture, which is in agreement with the XRD scan in Figure 1, where the two peaks can now be identified as $[002]$ and $[004]$ fiber textures.

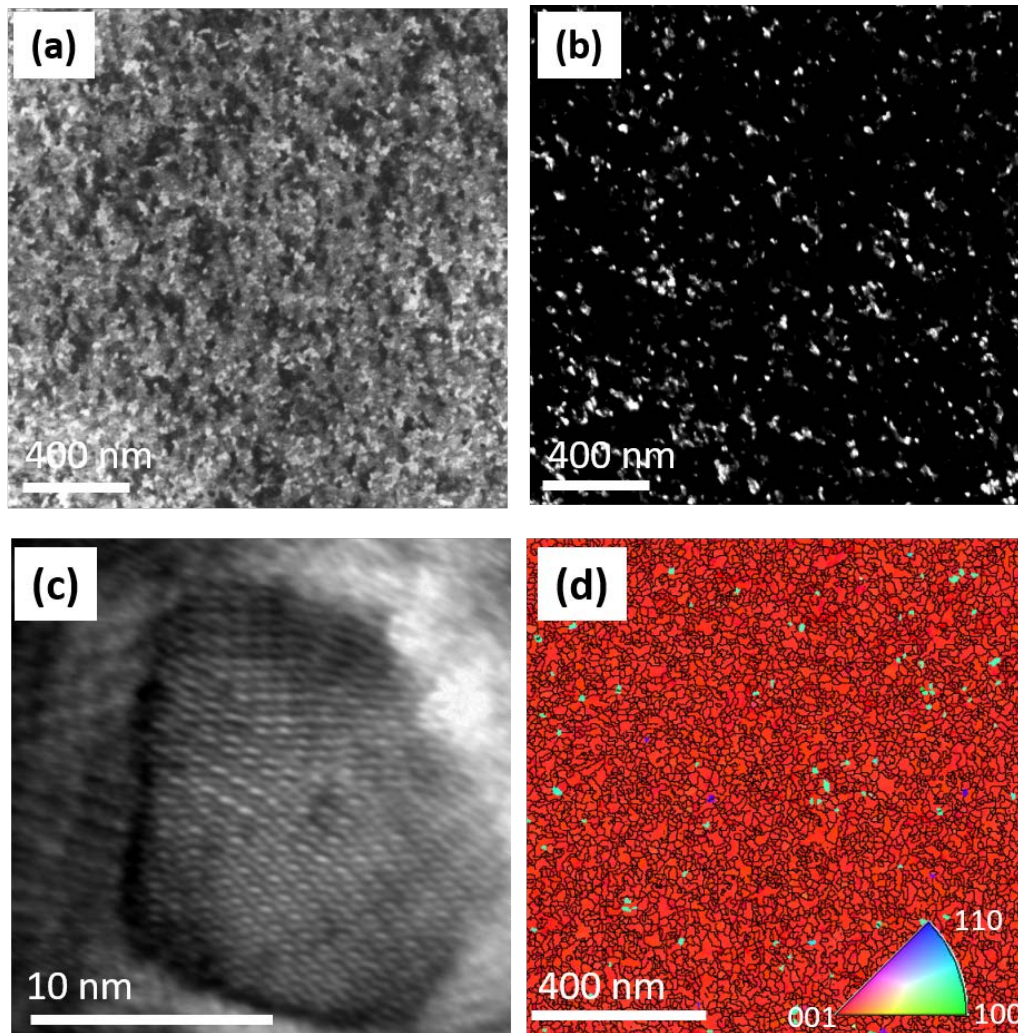


Figure 3 (a) Bright field image (b) dark field image (c) HRTEM and (d) PED reconstructed orientation maps of the Fe-49Cr film.

Similar PED scans for all of the other films was done (appendix), with the grain sizes plotted in Figure 4 as a cumulative grain size distribution. Table 1 also contains a tabulation of the As shown in this figure, the elemental films – Fe and Cr – as well as the Fe-49Cr film grew with the smallest grain sizes and a narrow gain size distribution, evident by the near vertical cumulative area fraction at a specific grain size suggesting normal grain growth behavior. Upon alloying Fe to Fe-16Cr, the grain size is still relatively equiaxed but its distribution has now widened and the sizes have grown. Unlike this and the other aforementioned films, the Fe-24 Cr and Fe-72Cr films revealed the most dramatic grain size shifts with several very large grains and very clear abnormal

grain growth behavior evident by the horizontal shifts in the grain sizes as a function of the cumulative grain size area.

Table 1 Phase, grain size, and segregation amplitude varying with alloy concentration and deposition temperature in the Fe-Cr films. AGG is abnormal grain growth

Temperature	Concentration	Phase	Grain size distribution	Grain size	Amplitude
RT	Fe	BCC	Equiaxed	39 ± 22 nm	-
	Fe-5Cr	BCC	Equiaxed	50 ± 29 nm	-
	Fe-16Cr	BCC	AGG	111 ± 94 nm	3 at.%
	Fe-24Cr	BCC	AGG	422 ± 280 nm	6 at.%
	Fe-49Cr	σ-phase	Equiaxed	30 ± 16 nm	2 at.%
	Fe-72Cr	BCC	AGG	291 ± 199 nm	4 at.%
	Cr	BCC	Equiaxed	33 ± 14 nm	-
673K	Fe-5Cr	BCC	Equiaxed	37 ± 13 nm	3 at.%

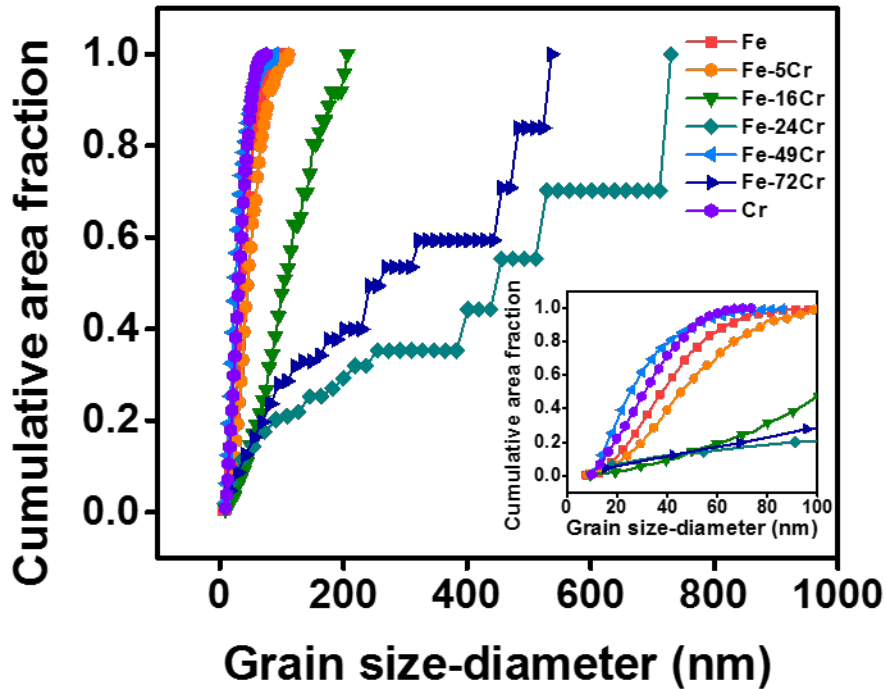


Figure 4 Cumulative grain size distribution plots for Fe-Cr alloying films with different solute concentrations. Grain size was measured from precession electron diffraction scans with 1.2X1.2 mm² and 3 nm step size.

The increase in Fe's grain size with Cr additions has been previously reported by the authors for a series of films with low Cr solute concentrations [8]. In that work, with Cr in solution with Fe, the grain size increased (up to ~ 4 at.% Cr) whereas once the Cr partitioned strongly to the grain boundaries, the grain size then refined for a 8 at.% Cr composition. This refinement was contributed to a solute drag effect. What is particularly interesting in these new films, further increasing the solute Cr content from the prior 8% to now 16% does not continue a grain refinement. Rather the grains appear to increase in grain size suggesting a solute concentration limit for grain refinement in Fe-Cr thin films.

The onset of the increase in the grain size is suspected to be linked to the phase separating behavior of the film. As the solute content increases, the driving force for the two species to partition becomes ever stronger within the microstructure. This thermodynamic driving force would then contribute to the adatom mobility during growth which would then explain the increase in grain sizes once a critical concentration of solutes was present. One can infer that conclusion when considering either the Fe-24Cr or Fe-72Cr films. Here the grains are very large and show a variety of large sizes. Though the XRD and PED scattering identified a single A2 phase, to confirm that the system is (starting to) chemically partition and drive these microstructural changes, we have performed APT.

Figure 5(a) plots the three types of distributions for each composition quantified by the APT datasets. The binomial distributions in Figure 5(a) represent the condition where the system is a single phase or, in other words, no partitioning between the species. It provides a reference from which distributions can be compared to and reveal chemical partitioning. The observed distributions is the raw data and has been computed by binning the compositions into $0.5 \times 0.5 \times 0.5$ nm voxel sizes and comparing each voxel to the other. Finally, the LBM model used two Gaussian functions based on the concentration of each species to fit the observed data, with the details of the LBM model previously discussed. Using the two Gaussian distributions, the relative concentration difference between each fit was found and plotted as an amplitude difference between each distribution, Figure 5(b). The larger the amplitude difference, the greater the partitioning in the system. These amplitude values are tabulated in Table 1. The Fe-rich alloys revealed the highest extent of partitioning at 24% Cr. At 49%Cr, which is the σ -phase, the partitioning value is low and would be exhibited as the atoms are in an ordered intermetallic phase. The presence of some 'partitioning' at the σ -phase composition is contributed to the lack of perfect atom-to-lattice rectification in the APT data sets as well as the σ -phase not being a line compound. What is particularly interesting is that at 5%Cr, there is no notable partitioning which implies that Cr is in

solution. This agrees with prior modeling that Cr would be in solution at this composition for low temperatures [30-32]. For all the other compositions, even though the film is deposited onto an ambient temperature substrate, the thermodynamic energies to phase separate are sufficiently large enough to promote the early onset of chemical partitioning even at low homologous temperatures. These APT results confirm that partitioning has indeed occurred and likely has contributed to the energies needed to facilitate the observed grain growth in the disordered solid solution. The only exception is the Fe-49Cr film, which readily adopted the σ -phase and was no longer in a disordered phase state.

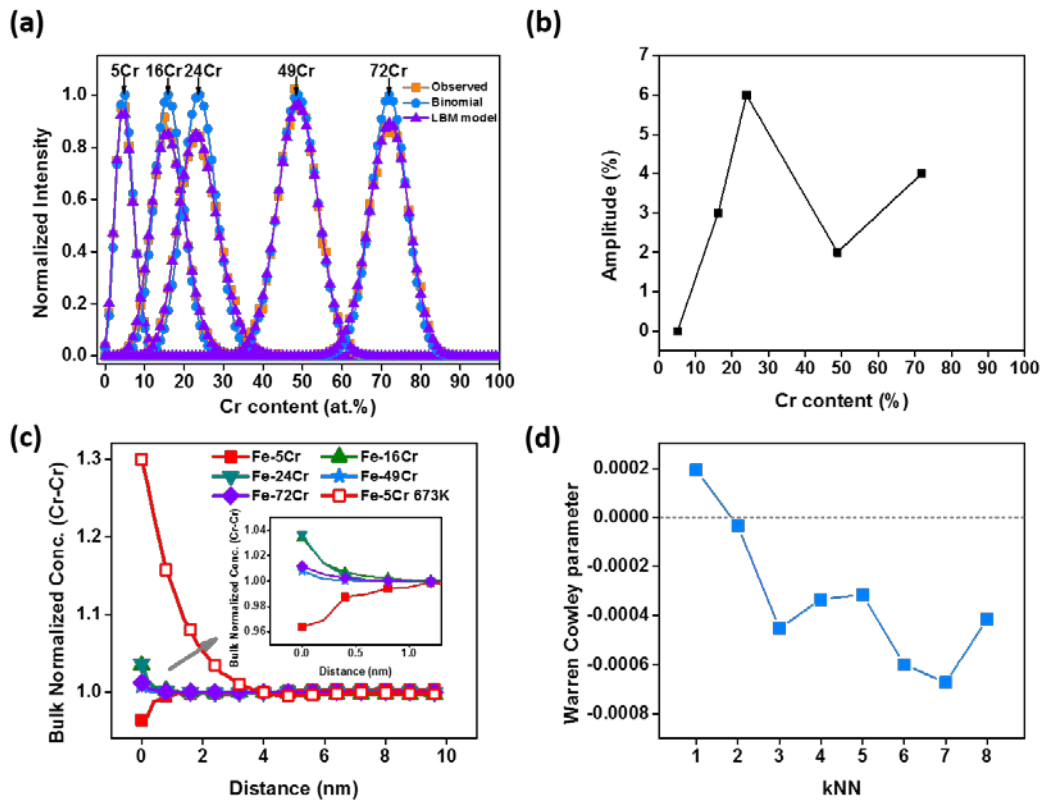


Figure 5 (a) Normalized Cr concentration frequency diagram. The binomial distribution and Langer, Bar-on, and Miller (LBM) model fitting were also included. **(b)** Composition evolution of amplitudes obtained using LBM method. **(c)** Radial distribution functions (RDFs) of Cr-Cr used to evaluate atom distribution for the Fe-Cr films with different compositions. **(d)** Warren Cowley parameters for the Fe-5Cr films with different nearest neighboring shells. Atom probe data was drawn from a 25X25X25 nm³ cubic of each composition.

Now that we have confirmed partitioning, we have further examined the distributions of the atoms in and near these partitioned clusters. Figure 5(c) is bulk normalized Cr concentration varying with the radial distance, r . The surrounding environment of Cr atoms is changing with Cr concentration. When the Cr concentration is low, the solute concentration of the first several shells of neighboring atoms is 4 % percent lower than the average composition for the solute atoms in the alloy. This means that a slightly ordered structure has indeed formed in the low Cr content Fe-Cr film. As the Cr content increased to 16 % or higher, the neighboring environment of Cr atoms changed from ~ 0.96 of the normalized bulk concentration (or, in other words, ~ 4 % lower than the overall composition) to ~ 1.04 of the normalized bulk concentration (or to a value 4 % higher than the bulk composition). In this case, Cr atoms tend to segregate together and form initial phase separation behavior. This APT results are consistent with the amplitude analysis, Figure 5(b), in which a slightly phase-separated structures was noticed in Fe-16Cr, Fe-24Cr, and Fe-72Cr thin films. It can also be seen from the plot in Figure 5(c) that a limited concentration variation was noticed also noted in the intermetallic σ -phase Fe-49Cr film.

Finally, we have applied the W-C method to our APT data sets to look at the potential short range order in the dilute Fe-5Cr film. The W-C parameter of the Fe-5Cr alloy is close to zero, but the RDF plot shows a Cr-Fe nearest neighbor (NN) environment suggesting a slightly ordered structure. We calculated the W-C parameter for Fe-5Cr with NN shells going from $k = 1$ to 8 shells and noted that the W-C parameter was negative which indicates an ordered structure and would be consistent with the RDF findings in Figure 5(c). Interestingly, some fluctuations in the W-C parameter is noted as a function of the NN shells. It is not clear what this potentially fine structure may imply towards the ordering behavior.

We recently reported the growth stresses for a series of Fe-Cr thin films deposited at ambient and elevated temperatures (673K) [63]. One of these films was the Fe-5Cr alloy. Applying the above mentioned APT analysis methods to the 673 K Fe-5Cr film's APT data set, we noted a loss in the ordered structure, Figure 5(c). This annealed film, like its ambient temperature counterpart, was the A2 phase. The loss in order is evident by the neighboring concentration being nearly 1.3 times higher than the nominal bulk concentration (the unfilled red square marker in Figure 5(c)). Recall that the ambient Fe-5Cr value was slightly less than the normalized bulk concentration (filled red square in Figure 5(c)). One could expect an order-disorder behavior for this phase, as already noted, it is most often observed in the disordered state.

The microstructure that has formed from the strongly partitioning alloy, Fe-24Cr, is shown in Figure 6. A 'star burst-like' pattern throughout the microstructure was

observed in the bright field image, as shown in Figure 6(a). Similar features were seen in the Fe-16Cr and Fe-72Cr films, which like Fe-24Cr were all the highly supersaturated A2 structures. By tilting the foil along the α tilt axis in the TEM, the outline of the black patterns of the 'star burst' changed position and shape accordingly, Figure 6(b-e). This 'star-burst pattern' phenomenon is believed to be generated from a modest orientation rotation within the grains, likely created by the onset of partitioning. It is not believed to be from a large scale compositional fluctuation as such were not observed in the APT datasets nor bend contrast from electron diffraction.

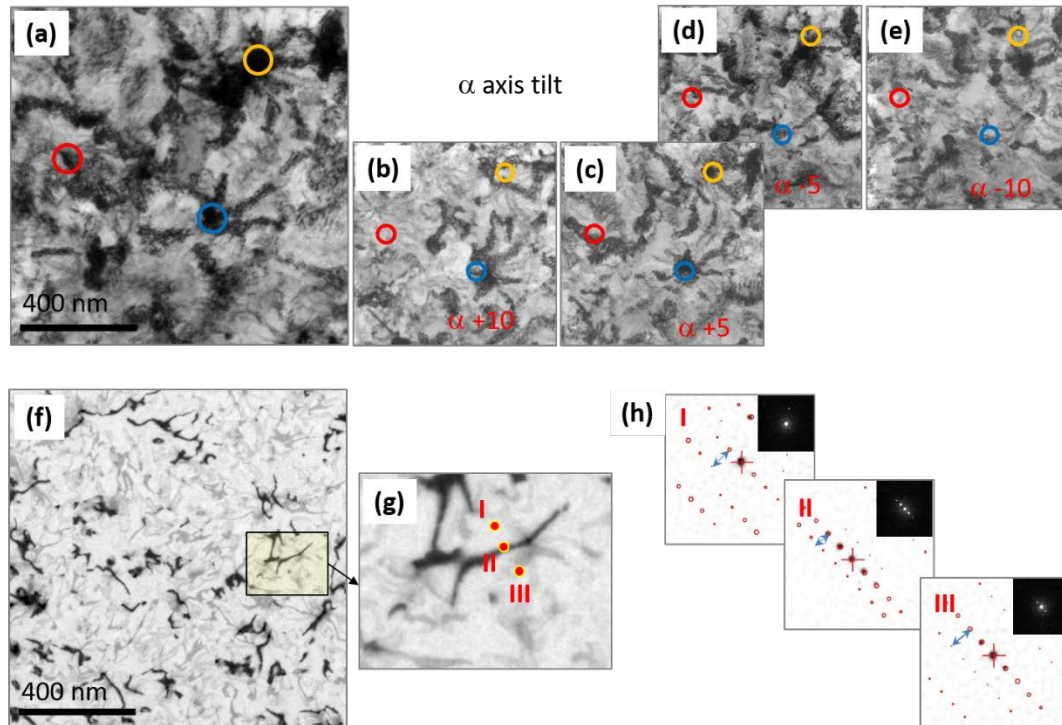


Figure 6 Bright field image of the Fe-24Cr film with (a) 0 tilt (b) +5 a tilt (c) +10 a tilt (d) -5 a tilt (e) -10 a tilt. (f) Bright field image of the Fe-24Cr film with a thickness of 10 nm (g) Magnified view of Figure 5(f) (h) Diffraction patterns from points showing in Figure 5(g).

To study this peculiar microstructural feature further and confirm if it is indeed a grain rotation effect, a 10 nm thick Fe-24Cr film was grown onto a SiN_x window, Figure 6(f). The aim of which was to capture the early onset of this feature with film growth. Figure 6(g) revealed a series of black and grey contrast lines taken from a region of interest shown in Figure 6(f). Here, we implemented a PED scan across each feature, Figure 6(h), with the associated diffraction patterns for each point labeled in Figure 6(g). The I, II, and III points are each respectively located in the white, black, and white

contrast regions, respectively. In all the diffraction patterns, a systematic row of reflections is shown to go from the upper left corner to the lower right corner for this A2 phase orientation. The consistency of a similar set of reflections confirms that the points are within the same grain. However, the spacing between the systematic row of these reflections narrows or widens based on the point location in the microstructure, which is illustrated by the double arrow label from between the rows of reflections for each I, II, and III point. This variation, for the same phase, indicates a slight orientation change in the diffracted beam through the foil. Rather than contrast being associated with a large compositional effect, it does appear to be a crystalline orientation effect.

4. Conclusion

A series of $\text{Fe}_{1-x}\text{Cr}_x$ ($0 < x < 1$) films have been sputter-deposited onto ambient temperature [001] Si substrates with its phase and microstructure quantified. Each of the elemental films deposited as a BCC structure with a narrow grain size distribution.

The Fe-5Cr film formed an A2 solid solution BCC phase also with an equiaxed grain size with a narrow grain size distribution. APT analysis confirmed prior neutron diffraction experiments that this composition yielded an ordered structure; however, if this film is deposited at 673 K, the ordering is lost. To the authors' knowledge, this ordering phase has been previously confirmed by diffuse neutron scattering [30, 33] and modeling studies [30, 34]. To the authors' knowledge, this report provides the first confirmation of it through an APT analysis where it is more often reported as a cluster behavior in similar studies [35-37].

The Fe-49Cr film adopted the σ -phase, which is a high temperature ordered phase, even in the ambient temperature deposition. These grains were equiaxed and fine in size.

For the remaining films, Fe-16Cr, Fe-24Cr, and Fe-72Cr, all deposited as the A2 phase with the grain sizes being larger than the prior films discussed above. Of these films, the Fe-24Cr and Fe-72 films exhibited significant abnormal grain growth. This behavior has been contributed to the system being driven to chemical partition by providing an additional thermodynamic contributor to the adatom mobility. APT analysis confirmed this partitioning and onset of clustering, even though it was not readily observed in the TEM images and associated diffraction patterns. These films exhibited a peculiar 'star-burst' contrast pattern within the grains. Through localized diffraction patterns in and away from this contrast, it was found to be a modest orientation tilt within the grain and is not believed to be associated with a particular chemical contrast. However, these changes in orientation are likely contributed to the system being kinetically constrained by the lower temperature to phase separate, as it is

clear from the Fe-49Cr σ -phase that significant adatom interactions can occur to yield ordered intermetallic phase formations.

Acknowledge

The authors gratefully recognize support from the Army Research Office, grant W911NF1310436, as well as the University of Alabama's Central Analytical Facility. Thank Dr. Anna Ceguerra and Dr. Simon Ringer for providing us the access to use MASSIVE atom probe data analysis software package.

Reference

- [1] J.A. Venables. Introduction to Surface and Thin Film Processes, Cambridge University Press, Cambridge, 2000.
- [2] M. Lu, C.L. Chien. Structural and Magnetic-Properties of Fe-W Alloys, *Journal of Applied Physics* 67 (1990) 5787-5789.
- [3] R. Banerjee, S. Bose, A. Genc, P. Ayyub. The microstructure and electrical transport properties of immiscible copper-niobium alloy thin films, *Journal of Applied Physics* 103 (2008).
- [4] R. Banerjee, A. Puthucode, S. Bose, P. Ayyub. Nanoscale phase separation in amorphous immiscible copper-niobium alloy thin films, *Applied Physics Letters* 90 (2007).
- [5] N.H. Duc, A. Fnidiki, J. Teillet, J. Ben Youssef, H. Le Gall. Structural and magnetic studies of sputtered Fe_{1-x}Cr_x thin films, *Journal of Applied Physics* 88 (2000) 4778-4782.
- [6] G. Meng, Y. Li, F. Wang. The corrosion behavior of Fe-10Cr nanocrystalline coating, *Electrochimica Acta* 51 (2006) 4277-4284.
- [7] K. Wasa, S. Hayakawa. Special features of thin compound films prepared by magnetron sputtering, *Surface Science* 86 (1979) 300-307.
- [8] X. Zhou, T. Kaub, R.L. Martens, G.B. Thompson. Influence of Fe(Cr) miscibility on thin film grain size and stress, *Thin Solid Films* 612 (2016) 29-35.
- [9] X. Zhou, X.-x. Yu, T. Kaub, R.L. Martens, G.B. Thompson. Grain Boundary Specific Segregation in Nanocrystalline Fe(Cr), *Scientific Reports* 6 (2016) 34642.
- [10] P.H. Mayrhofer, C. Mitterer, L. Hultman, H. Clemens. Microstructural design of hard coatings, *Progress in Materials Science* 51 (2006) 1032-1114.
- [11] F.J. Himpsel, J.E. Ortega, G.J. Mankey, R.F. Willis. Magnetic nanostructures, *Advances in Physics* 47 (1998) 511-597.
- [12] S. Kovesnikov, W. Tsai, I. Ok, J.C. Lee, V. Torkanov, M. Yakimov, S. Oktyabrsky. Metal-oxide-semiconductor capacitors on GaAs with high-k gate oxide and amorphous silicon interface passivation layer, *Applied Physics Letters* 88 (2006) 022106.
- [13] B. Radisavljevic, A. Radenovic, J. Brivio, V. Giacometti, A. Kis. Single-layer MoS₂ transistors, *Nature nanotechnology* 6 (2011) 147-150.
- [14] P.K. Tien. *Light Waves in Thin Films and Integrated Optics*, *Appl. Opt.* 10 (1971) 2395-2413.
- [15] K. Nomura, H. Ohta, A. Takagi, T. Kamiya, M. Hirano, H. Hosono. Room-temperature fabrication of transparent flexible thin-film transistors using amorphous oxide semiconductors, *Nature* 432 (2004) 488-492.
- [16] X. Chen, S.S. Mao. Titanium dioxide nanomaterials: synthesis, properties, modifications, and applications, *Chemical reviews* 107 (2007) 2891-2959.

- [17] I. Repins, M.A. Contreras, B. Egaas, C. DeHart, J. Scharf, C.L. Perkins, B. To, R. Noufi. 19.9%-efficient ZnO/CdS/CuInGaSe² solar cell with 81.2% fill factor, *Progress in Photovoltaics: Research and Applications* 16 (2008) 235-239.
- [18] R.L. Klueh, A.T. Nelson. Ferritic/martensitic steels for next-generation reactors, *Journal of Nuclear Materials* 371 (2007) 37-52.
- [19] E.A. Little. Void-swelling in irons and ferritic steels I. Mechanisms of swelling suppression, *Journal of Nuclear Materials* 87 (1979) 11-24.
- [20] R.A. Lula, J.G. Parr. *Stainless steel*, American Society for Metals, 1986.
- [21] D. Terentyev, P. Olsson. Radiation damage in FeCr alloys for nuclear applications: Addressed problems and open issues, (2008).
- [22] M.N. Baibich, J.M. Broto, A. Fert, F.N. Van Dau, F. Petroff, P. Etienne, G. Creuzet, A. Friederich, J. Chazelas. Giant Magnetoresistance of (001)Fe/(001)Cr Magnetic Superlattices, *Physical Review Letters* 61 (1988) 2472-2475.
- [23] W. Al-Khoury, J.P. Eymery, P. Goudeau. Phase transformation of the A15 metastable phase of Fe-Cr thin films prepared by ion-beam sputtering, *Journal of Applied Physics* 102 (2007).
- [24] R.K. Gupta, N. Birbilis. The influence of nanocrystalline structure and processing route on corrosion of stainless steel: A review, *Corrosion Science* 92 (2015) 1-15.
- [25] R.B. Inturi, Z. Szklarska-Smialowska. Localized Corrosion of Nanocrystalline 304 Type Stainless Steel Films, *CORROSION* 48 (1992) 398-403.
- [26] L. Liu, Y. Li, F. Wang. Pitting mechanism on an austenite stainless steel nanocrystalline coating investigated by electrochemical noise and in-situ AFM analysis, *Electrochimica Acta* 54 (2008) 768-780.
- [27] C. Pan, L. Liu, Y. Li, F. Wang. Pitting corrosion of 304ss nanocrystalline thin film, *Corrosion Science* 73 (2013) 32-43.
- [28] J.W. Cahn. On Spinodal Decomposition, *Acta Metallurgica* 9 (1961) 795-801.
- [29] J. Cahn. 1967 Institute of metals lecture spinodal decomposition, *Transactions of the Metallurgical Society of Aime* 242 (1968) 89-103.
- [30] L. Malerba, A. Caro, J. Wallenius. Multiscale modelling of radiation damage and phase transformations: The challenge of FeCr alloys, *Journal of Nuclear Materials* 382 (2008) 112-125.
- [31] A. Caro, D. Crowson, M. Caro. Classical Many-Body Potential for Concentrated Alloys and the Inversion of Order in Iron-Chromium Alloys, *Physical Review Letters* 95 (2005).
- [32] P. Erhart, A. Caro, M. Serrano de Caro, B. Sadigh. Short-range order and precipitation in Fe-rich Fe-Cr alloys: Atomistic off-lattice Monte Carlo simulations, *Physical Review B* 77 (2008).
- [33] I. Mirebeau, M. Hennion, G. Parette. First Measurement of Short-Range-Order Inversion as a Function of Concentration in a Transition Alloy, *Physical Review Letters* 53 (1984) 687-690.
- [34] M. Hennion. Chemical SRO effects in ferromagnetic Fe alloys in relation to electronic band structure, *J. Phys. F: Met. Phys* 13 (1983) 2351-2358.
- [35] M.K. Miller, M.G. Hetherington. Morphology and scaling behavior of ultrafine isotropic microstructures in Fe-Cr alloys from atom probe field ion microscopy data, *Scripta Materialia* 24 (1990) 1375-1380.
- [36] R. Okano, K. Hono, K. Takanashi, H. Fujimori, T. Sakurai. Magnetoresistance and phase decomposition in Cr-Fe bulk alloys, *Journal of Applied Physics* 77 (1995) 5843.
- [37] M. Bachhav, G. Robert Odette, E.A. Marquis. Microstructural changes in a neutron-irradiated Fe-15at.%Cr alloy, *Journal of Nuclear Materials* 454 (2014) 381-386.
- [38] D.A. Porter, K.E. Easterling, M. Sherif. *Phase Transformations in Metals and Alloys*, Third Edition (Revised Reprint), CRC Press, 2009.

- [39] D.J. Larson, T.J. Prosa, R.M. Ulfing, B.P. Geiser, T.F. Kelly. Local Electrode Atom Probe Tomography: A User's Guide. New York: Springer, 2013.
- [40] M.K. Miller, R.G. Forbes. Atom-Probe Tomography: The Local Electrode Atom Probe, Springer US, 2014.
- [41] J. Zhou, J. Odqvist, M. Thuvander, P. Hedström. Quantitative Evaluation of Spinodal Decomposition in Fe-Cr by Atom Probe Tomography and Radial Distribution Function Analysis, *Microscopy and Microanalysis* 19 (2013) 665-675.
- [42] A.V. Ceguerra, M.P. Moody, R.C. Powles, T.C. Petersen, R.K.W. Marceau, S.P. Ringer. Short-range order in multicomponent materials, *Acta Crystallographica Section A* 68 (2012) 547-560.
- [43] A.V. Ceguerra, R.C. Powles, M.P. Moody, S.P. Ringer. Quantitative description of atomic architecture in solid solutions: A generalized theory for multicomponent short-range order, *Physical Review B* 82 (2010).
- [44] J.S. Langer, M. Bar-on, H.D. Miller. New computational method in the theory of spinodal decomposition, *Physical Review A* 11 (1975) 1417-1429.
- [45] W. Xiong, J. Ågren, J. Zhou. An effective method to estimate composition amplitude of spinodal decomposition for atom probe tomography validated by phase field simulations, arXiv preprint arXiv:1205.4195 (2012).
- [46] J. Zhou, J. Odqvist, L. Hoglund, M. Thuvander, T. Barkar, P. Hedstrom. Initial clustering - a key factor for phase separation kinetics in Fe-Cr-based alloys, *Scripta Materialia* 75 (2014) 62-65.
- [47] A.V. Ceguerra, M.P. Moody, L.T. Stephenson, R.K.W. Marceau, S.P. Ringer. A three-dimensional Markov field approach for the analysis of atomic clustering in atom probe data, *Philosophical Magazine* 90 (2010) 1657-1683.
- [48] C.A. Johnson, J.H. Klotz. The Atom Probe and Markov Chain Statistics of Clustering, *Technometrics* 16 (1974) 483-493.
- [49] M.K. Miller, T.D. Shen, R.B. Schwarz. Atom probe tomography study of the decomposition of a bulk metallic glass, *Intermetallics* 10 (2002) 1047-1052.
- [50] M.P. Moody, L.T. Stephenson, P.V. Liddicoat, S.P. Ringer. Contingency table techniques for three dimensional atom probe tomography, *Microscopy research and technique* 70 (2007) 258-268.
- [51] X. Xu, J. Odqvist, M.H. Colliander, M. Thuvander, A. Steuwer, J.E. Westraadt, S. King, P. Hedstrom. Structural Characterization of Phase Separation in Fe-Cr: A Current Comparison of Experimental Methods, *Metallurgical and Materials Transactions a-Physical Metallurgy and Materials Science* 47a (2016) 5942-5952.
- [52] J.M. Cowley. An Approximate Theory of Order in Alloys, *Phys Rev* 77 (1950) 669-675.
- [53] J.G. Brons, G.B. Thompson. Orientation Mapping via Precession-Enhanced Electron Diffraction and Its Applications in Materials Science, *JOM* 66 (2013) 165-170.
- [54] P. Moeck, S. Rouvimov, E.F. Rauch, M. Véron, H. Kirmse, I. Häusler, W. Neumann, D. Bultreys, Y. Maniette, S. Nicolopoulos. High spatial resolution semi-automatic crystallite orientation and phase mapping of nanocrystals in transmission electron microscopes, *Crystal Research and Technology* 46 (2011) 589-606.
- [55] E.F. Rauch, J. Portillo, S. Nicolopoulos, D. Bultreys, S. Rouvimov, P. Moeck. Automated nanocrystal orientation and phase mapping in the transmission electron microscope on the basis of precession electron diffraction, *Zeitschrift für Kristallographie* 225 (2010) 103-109.
- [56] K. Thompson, D. Lawrence, D.J. Larson, J.D. Olson, T.F. Kelly, B. Gorman. In situ site-specific specimen preparation for atom probe tomography, *Ultramicroscopy* 107 (2007) 131-139.

- [57] H.L. Yakel. Atom Distributions in Sigma-Phases .1. Fe and Cr Atom Distributions in a Binary Sigma-Phase Equilibrated at 1063-K,1013-K and 923-K, Acta Crystallogr B 39 (1983) 20-28.
- [58] S.M. Dubiel, J. Cieslak. Sigma-Phase in Fe-Cr and Fe-V Alloy Systems and its Physical Properties, Critical Reviews in Solid State and Materials Sciences 36 (2011) 191-208.
- [59] B.F.O. Costa, G. Le Caer, J.M. Loureiro, V.S. Amaral. Mechanically induced phase transformations of the sigma phase of nanograined and of coarse-grained near-equiatomic FeCr alloys, Journal of Alloys and Compounds 424 (2006) 131-140.
- [60] J.P. Eymery, W. Al-Khoury, P. Goudeau, A. Fnidiki. Mossbauer investigation of $Fe_{1-x}Cr_x$ films grown by ion-beam sputter deposition, Physica B 381 (2006) 297-305.
- [61] K. Sumiyama, N. Ohshima, Y. Nakamura. Nonequilibrium Fe-Cr Alloys Produced by Vapor Quenching, T Jpn I Met 28 (1987) 699-705.
- [62] N. Yukawa, M. Hida, T. Imura, M. Kawamura, Y. Mizuno. Structure of Chromium-Rich Cr-Ni, Cr-Fe, Cr-Co, and Cr-Ni-Fe Alloy Particles Made by Evaporation in Argon, Metallurgical Transactions 3 (1972) 887-&.
- [63] X. Zhou, G. Thompson. Influence of Solute Partitioning on the Microstructure and Growth Stresses in Nanocrystalline Fe(Cr) Thin Films, Thin Solid Films Submitted (2017).

Supplementary Information:

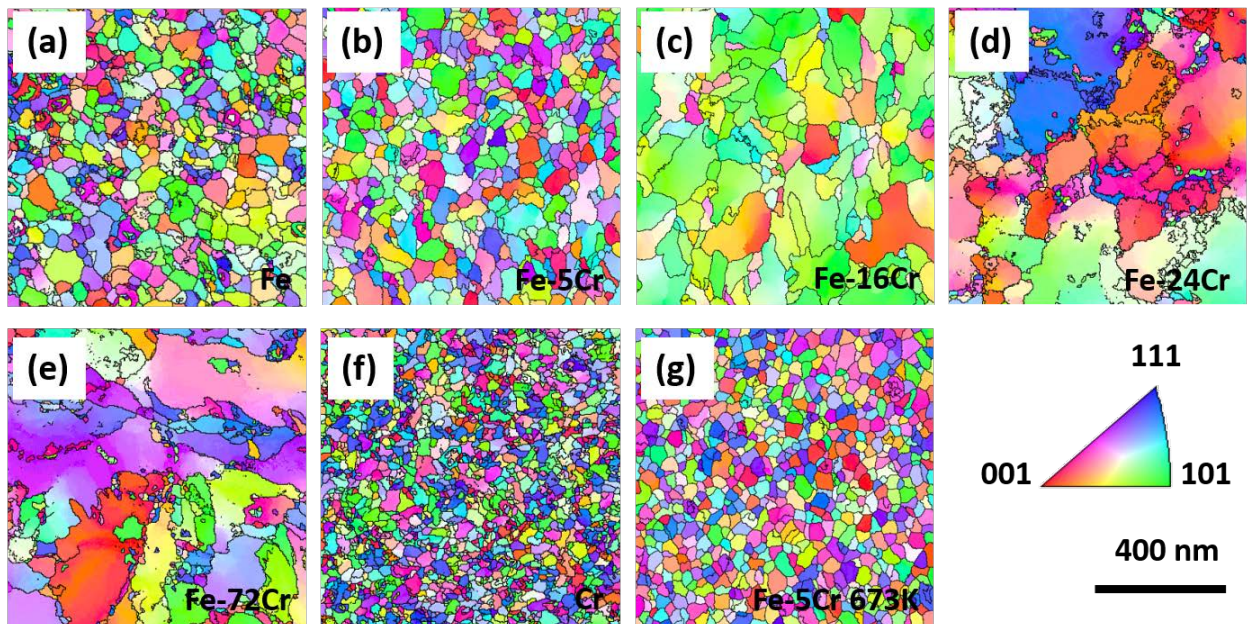


Figure S1 PED reconstructed orientation maps of the room temperature deposited (a) Fe (b) Fe-5Cr (c) Fe-16Cr (d) Fe-24Cr (e) Fe-72Cr (f) Cr, and (g) 673K annealed Fe-5Cr films.

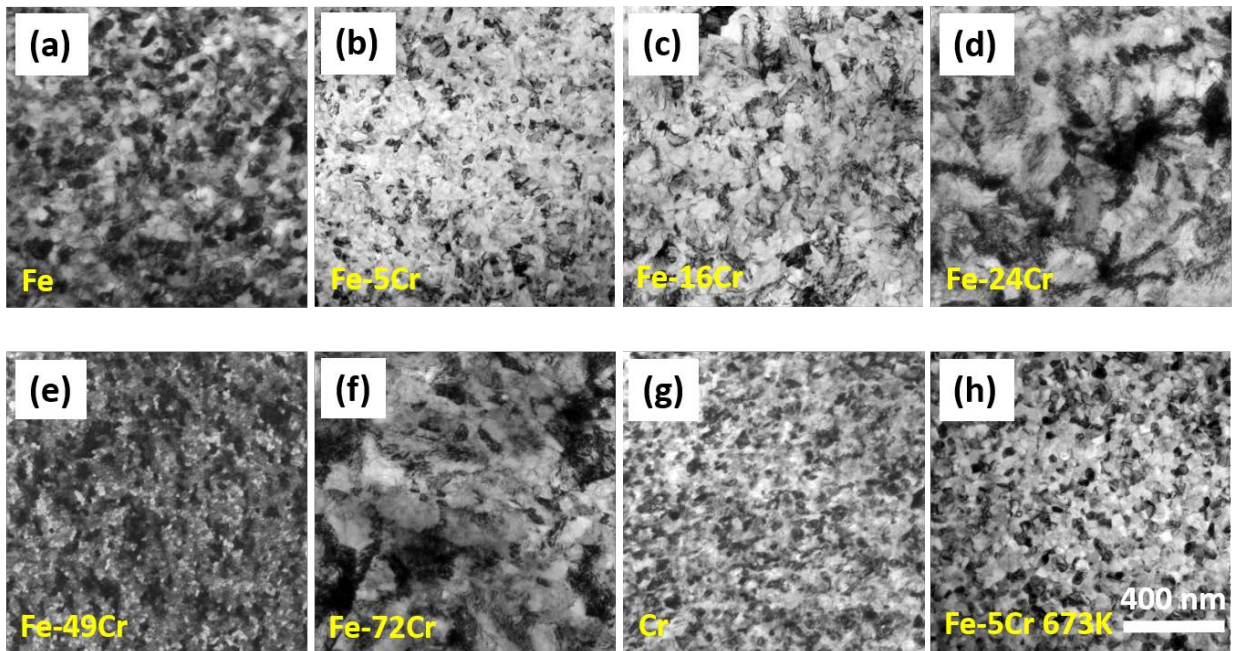


Figure S2 Bright field images of the room temperature deposited (a) Fe (b) Fe-5Cr (c) Fe-16Cr (d) Fe-24Cr (e) Fe-49Cr (f) Fe-72Cr (g) Cr and (h) 673K annealed Fe-5Cr films.

CHAPTER 10

Ti Segregation in Regulating the Stress and Microstructure Evolution in W-Ti Nanocrystalline Films

Tyler Kaub¹ and Gregory Thompson¹

¹*Department of Materials and Metallurgical Engineering, University of Alabama, Tuscaloosa, Alabama 35401*

Abstract

This paper explores the effect of Ti's segregation and corresponding effect on the intrinsic thin film growth stress and microstructural evolution in a series of $W_{1-x}(Ti)_x$ alloys where x varied from 0 to 20 at.%. We report that the addition of the Ti solute reduces the compressive W growth stress, with further reductions achieved through *in-situ* annealing during growth. Upon examination of the microstructure, Ti did not appear to have a dramatic effect in altering the film's grain size and distribution, but it did increase the fraction of low angle grain boundaries. We confirmed that the A15 to bcc W phase transformation, which occurs in the early stages of W growth, was diminished with increasing Ti content. This has been explained with respect to Ti's preference for getting residual oxygen, a known stabilizer for the A15 phase. Collectively, this work demonstrates the impact of solute segregation in the control of residual stresses, specific grain boundary formations, and phase transformation control in growing thin films.

Introduction

For most metallic thin film growth, a Volmer-Weber growth morphology is observed during deposition. Under such growth, large residual stresses can develop¹⁻³ which can lead to thin film failures such as buckling, delamination⁴, and cracking⁵. Consequently, there has been intense effort to understand and control thin film stress evolution. In particular to the Volmer-Weber behavior, a compressive-to-tensile-to-compressive stress evolution for high adatom mobility species and a compressive-to-tensile evolution for low adatom mobility species is noted to occur as the thin film thickens^{2,6}. To explain this evolving stress, several models have been proposed^{1,7-11}. While general agreement exists for the mechanisms generating the initial compressive and tensile stresses¹², the secondary post-coalescence compressive stress, seen in high adatom mobility species, remains an area of active discussion. One of the proposed mechanisms for the formation of this secondary post-coalescence compressive stress involves the

insertion of excess adatoms into grain boundaries during growth. The driving force for this insertion is created by differences in chemical potentials between the surface and grain boundaries^{10,13}. Utilizing this mechanism, Chason *et al.*¹ have developed a kinetic based model, where the tensile stress generating mechanism of grain boundary formation and the compressive stress generation mechanism of excess adatom insertion into grain boundaries is described. Thus, by changing the grain boundaries themselves (structurally, chemically, and/or the number density of boundaries in the film) the stress state is altered implying that grain boundaries themselves act as a potential microstructural pathway forward to influence the residual stress.

Arguably, the major means of controlling grain boundaries have come from regulating the growth conditions¹⁴. This can be achieved through changes in deposition pressure (where the mean free path length (number of collisions of the species) from the target to the substrate varies the arrival energy), the deposition rate of species onto the substrate, substrate bias, and *in-situ* heating of the substrate¹⁵⁻¹⁷. More recently, attempts in the use of alloying have been shown to promote another means of stress regulation via grain control and phase formation¹⁸. In the work by Fu and Thompson¹⁹, the extent of preferential species type segregation into the grain boundaries was shown to control the stress. More recently Zhou *et al.*²⁰ reported how Cr solutes can regulate the Fe grain size which correlated directly with the stress evolution. Interestingly, in this latter work, a change in the fraction of special character grain boundaries was also noted to influence the stress. Kaub *et al.*²¹ have also shown that small amounts of solute can dramatically alter the compressive stresses by achieving a thermodynamically equilibrium of segregation into the grain boundaries for a series of Cu-Ni thin films.

In this work, we expand upon these earlier alloy studies but into the W-Ti system. The W-Ti system presents an interesting case study because the phase diagram predicts a region of W solid solubility up to ~ 12 at.% Ti at room temperature²². Above this solubility limit, the two species phase separate with no competing intermetallic compounds. In addition, W-Ti alloys has been noted to yield nanocrystalline stable grain sizes when subjected to thermal annealing²³. Shaginyan et al.²⁴ grew a W-30Ti (at.%) film as a control for a study of micro-hardness changes with nitrogen doping in W-Ti-N. This film exhibited preferential surface segregation of Ti, as compared to the film-substrate interface, which changed the size and widths of the crystallites within the film microstructure.

Of the refractory species, W films have been extensively studied because of their attributes for the integrated circuit industry. Its high melting temperature, high electrical conductivity, high mechanical strength, good metal barrier performance and fine patternability²⁵

have found it to be an ideal film in the construction of these devices. It has even found uses in spin transfer torque architectures²⁶. As discussed above, changes in the deposition parameters have been used to control the stress state of elemental W films. These studies include sputtering-gas pressure^{27,28}, substrate bias²⁹, and temperature³⁰. Both compressive and tensile stress states were observed, dependent upon process conditions, and found to correlate with the resulting W film's microstructure. At low sputtering gas-pressures, the W films exhibited large compressive stresses and grew as dense columnar grains. Films at higher pressures displayed tensile growth stresses and a columnar structure with voids along the grain boundaries. With further increases in the gas pressure, the films even exhibited dendritic-like growth morphologies as well as an amorphous structure^{27,28}. Sun *et al.*³⁰ found that increasing the W deposition rate resulted in larger compressive stresses with a correlated reduction in the W grain size. When the substrate temperature was increased, they reported that the compressive stress state of the W film relaxed³⁰. Through the proposed use of solute alloying of W, we aim to continue to broaden upon these previous W film studies.

Experimental

A series of W (control), W-5 at% Ti (W5Ti) and W-20 at% Ti (W20Ti) films were deposited in an AJA ATC-1500 stainless-steel chamber through co-sputtering >99.95% pure elemental targets. The respective alloy compositions were chosen based on the predicted solubility limit from the W-Ti phase diagram, so that a sample below and above the solubility limit could be investigated. Each film was deposited to a thickness of 300 nm onto a Si [001] wafer with a 100 nm thermally grown SiO₂ surface layer. The base pressure prior to deposition was < 1.33 x10⁻⁵ Pa, whereupon ultrahigh purity Ar was flowed at 10 standard cubic centimeters per minute to 0.266 Pa as the working gas. The deposition rates ranged from 0.075 nm/sec to 0.114 nm/sec dependent on the alloy composition, with the W deposition rate held constant. The growth rates were determined by dividing the final film thickness by the growth time with the thickness verified by small angle x-ray reflectivity using an X'Pert Philips x-ray diffractometer (XRD) operated with a Cu K_α source at 45 kV and 40 mA. The substrate temperatures were calibrated using a non-contact K-Space Bandit® unit that measures the Si band edge of the substrate upon heating.

The stress evolution during deposition was measured *in situ* using a K-Space Associates multibeam optical sensor system (MOS)®. The MOS measures the change in wafer curvature

using a reflected laser beam passed through an echelon to form an array of spots collected on a charge coupled device camera³¹. The reflected laser spots relative displacement is used to calculate the average stress using the Stoney equation,

$$\sigma = -\frac{1}{12} \frac{E_s}{1-\nu_s} \frac{\cos(\alpha)t_s^2}{Lt_f} \left(\frac{1}{R_1} - \frac{1}{R_0} \right) \quad (1)$$

where $\frac{E_s}{1-\nu_s}$ is the biaxial modulus of the substrate, t_s and t_f are the thickness of the substrate (250 μm) and thin film respectively, α is the angle of incidence of the laser beam (2°), L is the substrate detector optic length (88 cm) and R_0 and R_1 are the radii of curvature of the substrate before and during film deposition³².

Phase determination was carried out using a combination of XRD on a Bruker D8 Discover with a Co K α source and electron diffraction using an FEI TECNAI G² Supertwin (Scanning) Transmission Electron Microscope ((S)TEM). Grain sizes and morphology were determined by TEM micrographs and using the automated crystal orientation mapping (ACOM) platform by NanoMegas ASTAR based on precession electron diffraction³³. These scans contained a 1 μm^2 region using a 3 nm step size. Orientation Imaging Microscopy (OIM) – version 8 – software was then used to compile and reconstruct the data for grain size/distribution and grain boundary type identification. Atom probe tomography (APT) was performed in a Cameca LEAP 5000 XS at 50 K at a laser energy setting of 200 pJ with a pulse rate of 333 kHz. The thin film samples were prepared into the required needle like geometry for APT field evaporation using a dual beam Focus Ion Beam (FIB) described in reference³⁴.

Results

The *in-situ* growth stress measurements are displayed in Figure 1, which shows the stress thickness plots. The numbers labeled next to each curve corresponds to the steady-state stress values for each alloy. A linear slope, which occurred after ~ 50 nm of growth for all the films, indicates that the incremental stress does not change with thickness and is in steady-state. The elemental (non-alloyed) W film exhibited the largest compressive steady-state stress with this stress being reduced with increasing Ti content, Figure 1(a). When viewing the initial growth regime of the elemental W film, a modulation in the stress response is observed up to thicknesses less than ~ 50 nm. This modulation of stress is a result of a structural phase change the film is undergoing with growth and will be further discussed in detail below.

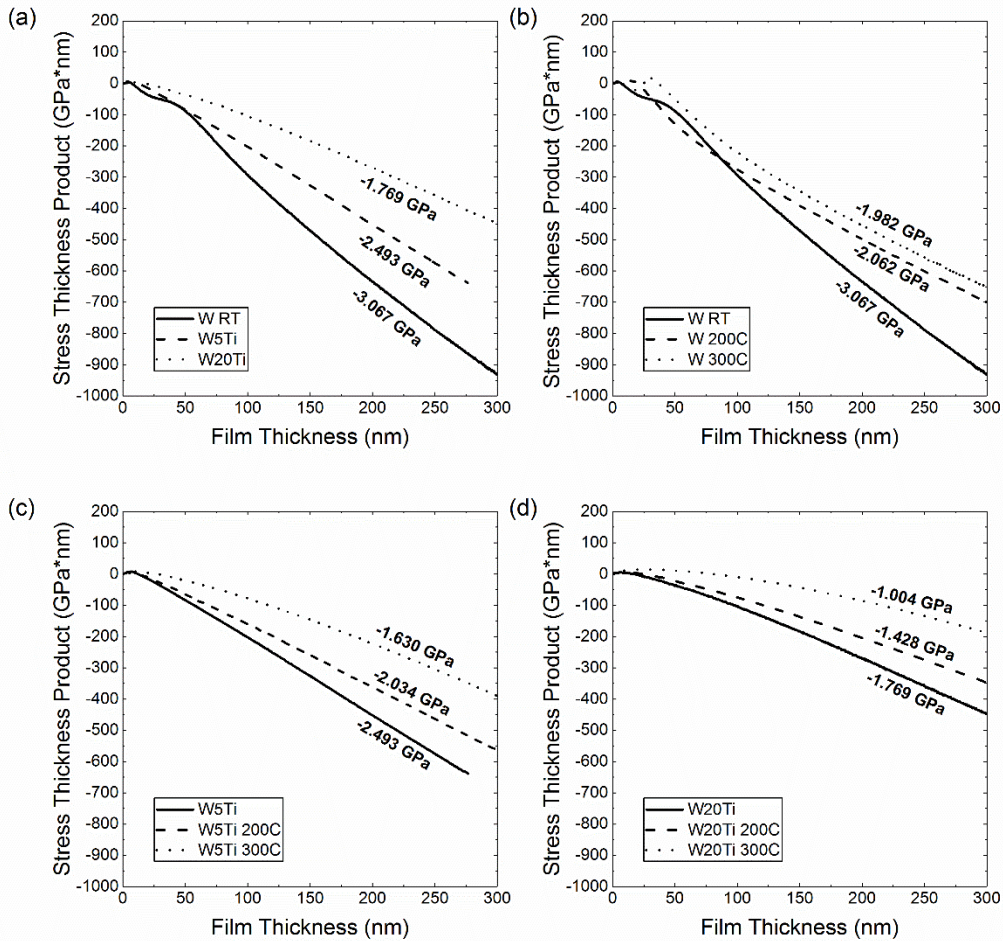


Figure 1. Growth stress evolution and steady-state stress values of W-Ti films (a) W, W5Ti and W20Ti deposited at room temperature (RT) (b) W-RT, W-200°C, and W-300°C (c) W5Ti-RT, W5Ti-200°C, and W5Ti-300°C and (d) W20Ti-RT, W20Ti-200°C and W20Ti-300°C .

Figure 1(b) illustrates the effect of substrate heating on the stress state for the elemental W film. At a substrate temperature of 200 °C, the steady-state compressive stress was observed to decrease by ~1 GPa from the room temperature deposition condition. Interestingly, a further increase in substrate temperature from 200 °C to 300 °C resulted in a rather limited reduction in the steady-state stress of the film, i.e. -2.062 GPa vs. -1.982 GPa respectively. These results are now compared to the substrate heating for the W5Ti and W20Ti alloys, Figure 1(c) and Figure 1(d) respectively. As with the elemental film, both alloy films revealed a reduction of stress with heating. However, when compared to their respective room temperature deposition stress state, the magnitude of this stress relaxation difference at 200 °C was smaller for both alloys, approximately 0.5 GPa for W5Ti and 0.3 GPa for W20Ti, than that of the elemental W deposition's reduction for an equivalent temperature change. Upon increasing the substrate

temperature to 300°C, a further and more pronounced compressive stress relaxation occurred for both alloys that was ~0.4 GPa lower than the prior 200 °C steady-state stress. This change in steady-state stress was much larger than the change observed for elemental W (~0.08 GPa reduction) between 200 °C and 300 °C.

As noted above, during the initial growth of elemental W, the stress thickness product exhibited a double tensile maxima, with the first maxima indicated by the dashed arrow and the second maxima indicated by the solid arrows in Figure 2. This first stress maxima is associated with the initial film coalescence or (first concave maxima³⁵), which was relatively equivalent in its stress maxima and thickness values for all films and temperatures studied. The second maxima was observed to vary with film composition and deposition temperature. Interestingly, this second maxima was not observed in the W20Ti films, which is clearly seen upon enlarging the stress thickness plot for the early stages of film growth in Figure 2(c). For the elemental W film, this double tensile maxima was most pronounced when the substrate was heated, Figure 2(a), with its position shifted in thickness with temperature. When looking at the secondary tensile maxima for the W5Ti film, Figure 2(b), two notable differences from the elemental W are observed. The first is a shift in the location of the tensile maxima to a much thinner film thickness of ~8 nm for all substrate deposition temperatures (compared to either ~ 50 nm (room temperature), ~ 17 nm (200°C) and ~30 nm (300°C) for W). And second, upon increasing the deposition temperature, the relative height of the secondary maxima peak decreased.

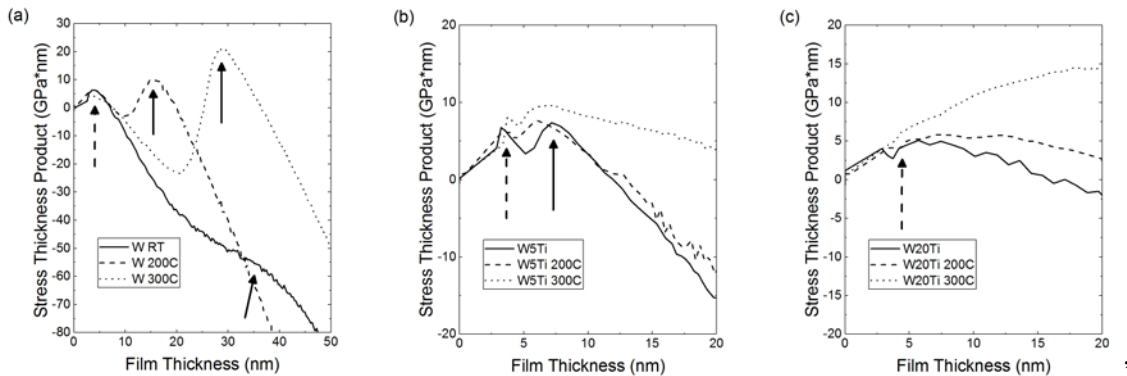


Figure 2. Intrinsic stress evolution of the early stages of film growth for (a) W-RT, W-200°C and W-300°C (b) W5Ti-RT, W5Ti-200°C and W5Ti-300°C (c) W-20Ti, W-20Ti 200°C and W-2-Ti-300°C

While the phase diagram predicts α bcc W to be the only phase formed, it has been widely observed that the A15 (also referred to as β) W forms under a variety of deposition conditions³⁶⁻³⁸ and grows with a tensile stress state²⁹. The metastable β phase has been reported to depend on film thickness, oxygen partial pressure³⁶, substrate bias, temperature, and deposition power^{29,39}. A critical thickness of around 50 nm is often reported as the upper bound for β -W stability. For films below this critical thickness, the transformation to α -W can still occur at room temperature but requires tens to hundreds of hours to transform, which can be accelerated by external annealing. To confirm the phase change, XRD was performed at a film thickness of 20 nm for room temperature W and W5Ti film. This thickness and these compositions were chosen to determine if the stress response at these film thicknesses were indeed linked to the presence of β -W.

The top two XRD scans shown in Figure 3 are for these two 20 nm thick films. It is clear that the W film diffracted the β -W phase whereas the W5Ti film, which is now at a thickness beyond its second stress maxima (Figure 2(b)), does not. This phase confirmation also supports the prior reports of β -W exhibiting a tensile behavior as it grows²⁹. It indicates that the slope of the stress response can then be used as an indicator to estimate the thickness regime of the β -W stability. The XRD scans for all other films grown to a thickness of 300 nm are shown on the bottom of Figure 3. As can be observed, all of these films revealed unambiguous diffraction of the α -W phase with a strong {110} bcc texture peak. The XRD results also did not reveal any hcp α -Ti indicating that the films were in solid solution with Ti and/or any phase separation was not sufficient to yield a secondary phase for diffraction identification. The lack of Ti clustering into the α -Ti phase may be associated with its decoration of the nanoscale grain boundaries where it has been associated with nanocrystalline grain stabilization²³.

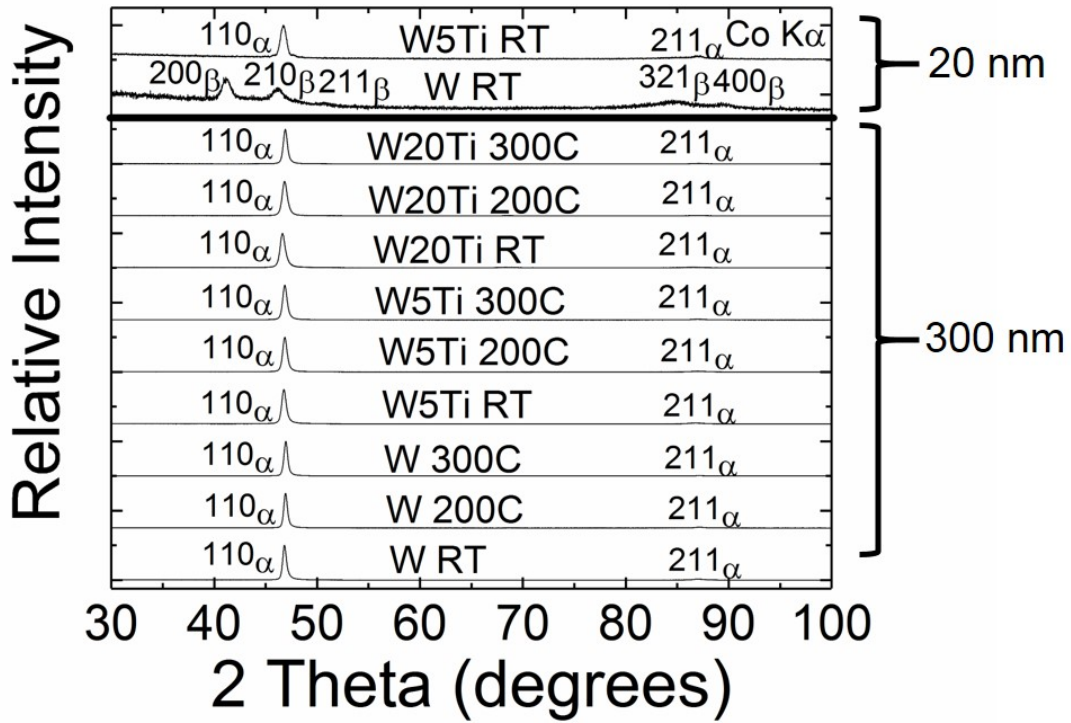


Figure 3. X-ray diffraction of W and W5Ti deposited at room temperature grown to a thickness of 20 nm above and of W, W5Ti and W20Ti deposited at room temperature, 200°C and 300°C to a thickness of 300 nm below.

Table I. Diffraction angle and lattice parameter a calculated from the d_{110} spacing for the films at 300 nm thickness.

Composition	2 theta (Degrees)	a (Å)
W	46.83	3.185
W 200C	46.92	3.179
W 300C	46.96	3.176
95W5Ti RT	46.80	3.186
95W5Ti 200C	46.84	3.183
95W5Ti 300C	46.87	3.182
80W20Ti RT	46.63	3.198
80W20Ti 200C	46.82	3.185
80W20Ti 300C	46.90	3.181

Table 1 is a tabulation of the shift in the diffraction peak for the d_{110} lattice spacing as well as the corresponding a -lattice parameter taken from Figure 3. We can note that as the W film is annealed the lattice parameter relaxes towards its bulk equilibrium value of 3.165 \AA^{40} . Similar trends can be seen in the alloy films, though they are not able to achieve the same elemental lattice parameter relaxation. This difference is attributed to the bcc W lattice having some solubility for Ti, which would be consistent with the thermodynamic equilibrium phase diagram of W-Ti as well as Vegard's law predictions⁴¹ that the lattice parameter shifts with composition. Through annealing, it is evident that the super saturation of Ti in the as-deposited W-Ti film is reduced by the shift of the lattice parameter created by the available thermal energy to facilitate segregation of Ti to the boundaries.

Table II. Grain size measured from automated crystal orientation mapping at a film thickness of 300 nm.

Composition	Average Grain Size (nm)
W	60.2 ± 44.9
W 200C	57.4 ± 44.9
W 300C	68.7 ± 46.0
95W5Ti RT	65.5 ± 62.4
95W5Ti 200C	59.6 ± 54.7
95W5Ti 300C	68.3 ± 49.0
80W20Ti RT	52.4 ± 49.0
80W20Ti 200C	56.5 ± 55.6
80W20Ti 300C	57.0 ± 44.9

Grain size determination, acquired by ACOM, showed that all of the films have an average grain size around 60 nm with the individual grain sizes tabulated in Table 2. The large standard deviations in the grain size was associated with a large range of grain sizes in the deposited films, as shown in the representative grain size histograms for the room temperature deposited films, Figure 4. Interestingly, the increase in deposition temperature did not appear to help narrow the distribution of the grain sizes during growth evident by the continued large standard deviations observed and tabulated in Table 2. The representative bright field images, Figure 5(a), and the grain boundary mapping images, Figure 5(b), revealed similar grain sizes and varied size distributions.

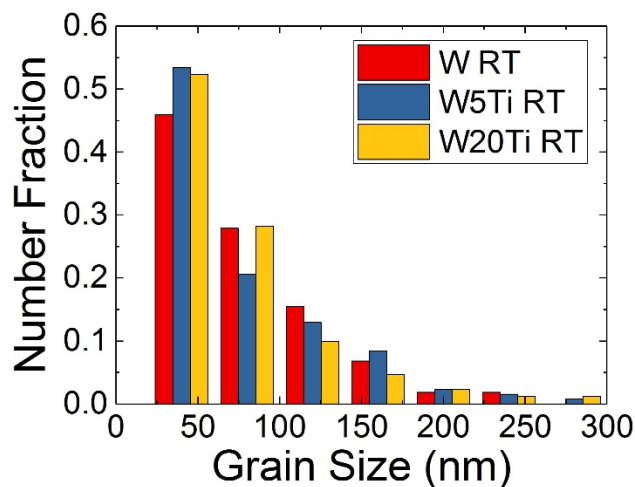


Figure 4. Histogram of grain size distributions of W, W5Ti and W20Ti deposited at room temperature. The histogram reveals a wide range of observed grain sizes across all film compositions. Color available on line.

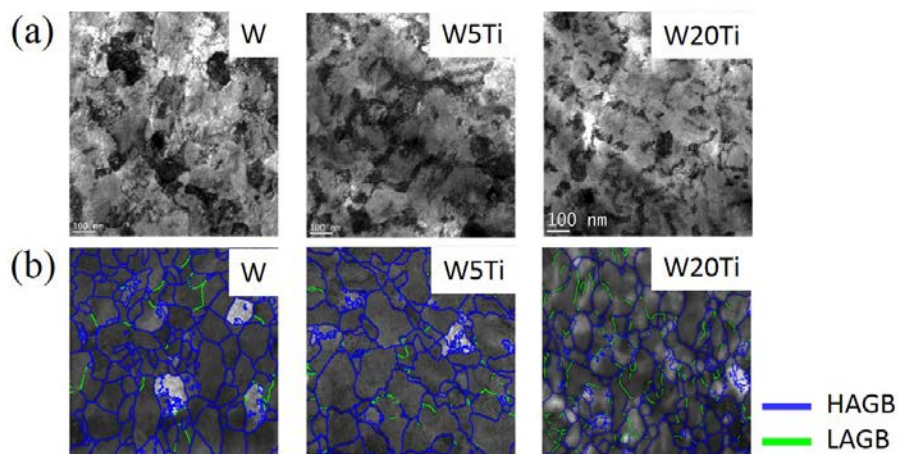


Figure 5. (a) Bright field TEM micrographs of W, W5Ti, and W20Ti deposited at room temperature to a film thickness of 300 nm, (b) grain boundary maps illustrating HAGBs (blue) and LAGBs (green) for room temperature W, W5Ti and W20Ti. Color available on line.

The majority of grain boundaries in all the films were high angle grain boundaries (HAGBs); however, the fraction of low angle grain boundaries (LAGBs) as well as $\Sigma 3$ and $\Sigma 11$ special character grain boundaries did reveal trends in either composition or deposition temperature, Figure 6. These three grain boundary types – LAGBs, $\Sigma 3$, and $\Sigma 11$ – comprise the next highest fraction of boundary types in the films. As the Ti content increased, the fraction of LAGBs increased from 0.070 (W) to 0.117 (W5Ti) to 0.212 (W20Ti), with the values given averaged over all three temperatures for each composition. Interestingly, as the Ti content increased the relative fraction of $\Sigma 3$ boundaries remained similar between each film at each specific composition but upon annealing, in all three films, the $\Sigma 3$ fraction decreased. Finally, the $\Sigma 11$ appeared to be more prevalent with either lower Ti contents and/or annealing. For the W20Ti film, the presence of $\Sigma 11$ was a relatively low fraction of boundary types for all deposition temperatures, with such behavior not observed for the other two films.

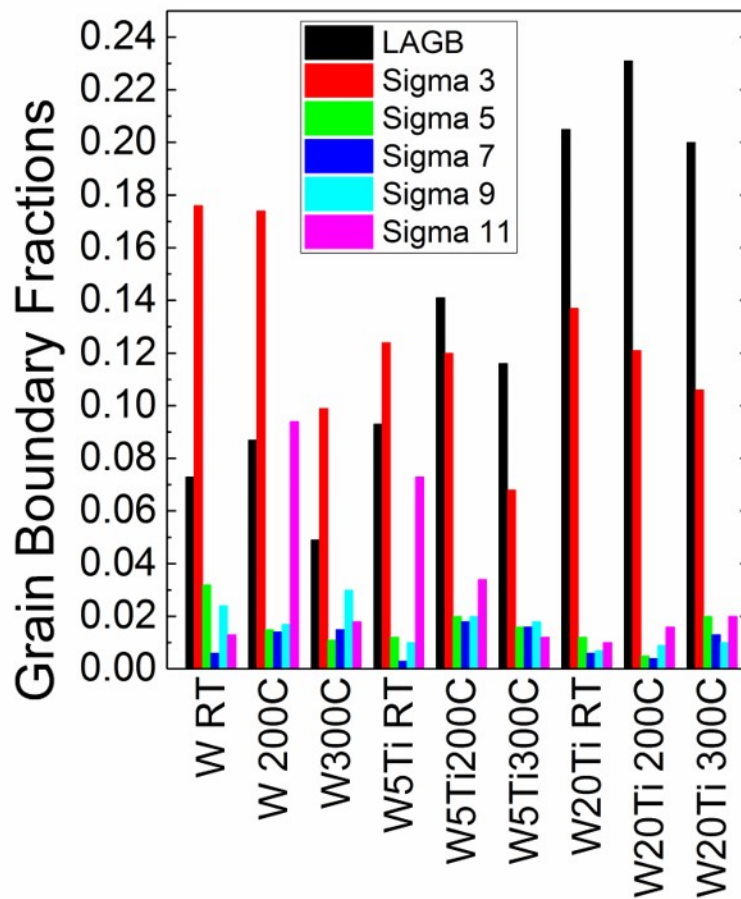


Figure 6. Fraction of low angle grain boundaries and the special grain boundary types of Sigma's 3, 5, 7, 9 and 11. Color available on line.

Discussion

The reduction in the magnitude of the compressive growth stress upon adding Ti demonstrates that alloying can have a significant effect on intrinsic growth stress and microstructure development, even when the average grain sizes (with large standard deviations) being relatively similar between compositions. There have been numerous studies on how grain size can influence the resultant stress state of a film^{11,42,43}. Here, the differences between W and its alloyed films' average grain sizes are relatively minor ($\Delta < \sim 8$ nm). Furthermore, the W5Ti film's average grain size at room temperature is actually larger than that of W whereas the W20Ti film's average grain size at room temperature is less than elemental W. Yet, each alloy film has a lower steady-state compressive stress and the trend of reduction follows with increasing Ti content. The wide distribution of grain sizes retained for all the films further complicates the ability to link a specific grain size as the primary factor influencing the stress differences between each film.

Regardless of the complications of grain size to stress, a clear trend in Ti content with compressive stress reduction was observed. Prior work has shown that deposition rate can also influence W's compressive stress state³⁰. One could potentially suggest that the modest increase in deposition rate created by the solute addition could be a contributing factor. However, in the prior deposition rate study, the compressive stress increased with rate, which is the opposite trend observed here.

As discussed in the introduction, compressive stress has been suggested to originate from the migration of excess adatoms into the grain boundaries created by a chemical potential driving force between the surface and grain boundaries during growth¹⁰. Though this model was constructed for single species films, it was expanded by Fu and Thompson¹⁹ to include a chemical potential driving force from intrinsic segregation enthalpies. This would suggest that the grain boundary environment is key to determining the stress state. Prior work into the nanocrystalline stability in the W-Ti system by Chookajorn *et al*²³ has shown that Ti will decorate the grain boundaries because of its ~ 50 kJ/mol enthalpy of segregation with W. Also, as noted in the introduction, Shaginyan *et al*.²⁴ noted preferential Ti partitioning in W-Ti films. Thus having a solute that preferentially locates in and around the grain boundary region would contribute to control of the grain boundary chemical potential.

To determine if the predicted segregation occurs (even at room temperature deposition) in our sputter deposited films, atom probe tomography was performed. Figure 7 is an atom map from a representative W(Ti) alloy at a grain boundary triple point. An isoconcentration surface of Ti enrichment is revealed along the grain boundaries within this film confirming Ti solute segregation to the grain boundaries does occur. With further increases in Ti content increases, this boundary enrichment further increases. From the XRD as well as TEM diffraction data, the clustering of the Ti and subsequent precipitation of a secondary α -Ti phase did not occur at the composition and annealing conditions studied.

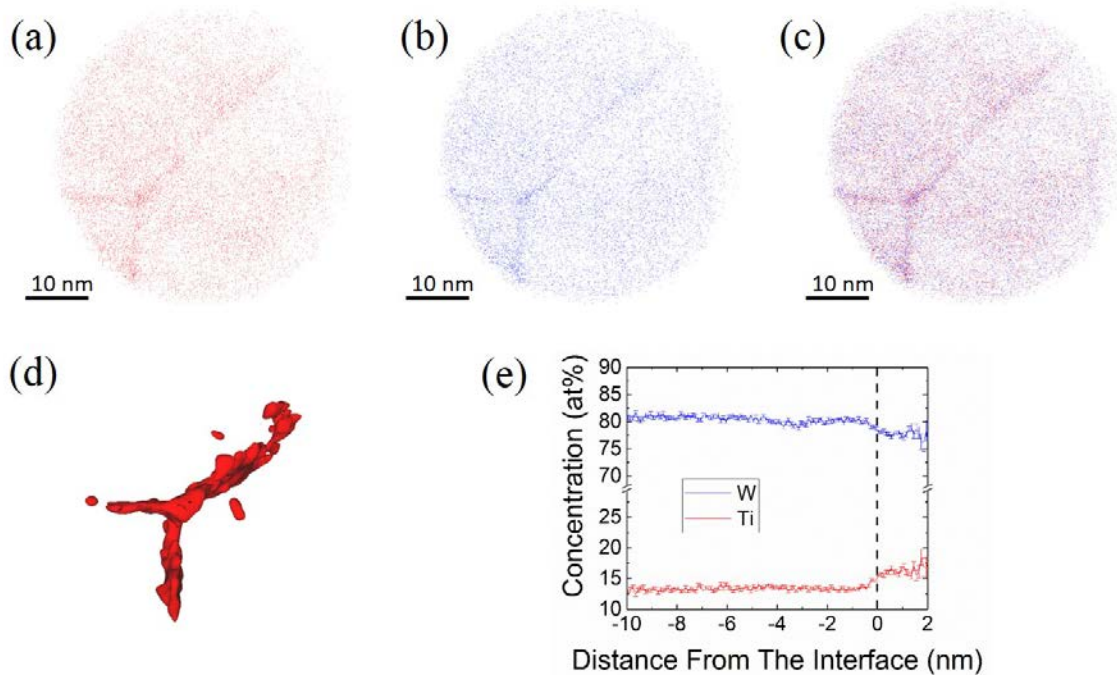


Figure 7. Representative atom probe reconstruction form a W15Ti film deposited at room temperature. (a) atom map of Ti (b) atom map of W (c) atom map of W-Ti (d) isoconcentration surface of Ti showing enrichment along the grain boundaries and (e) proximity histogram quantifying Ti enrichment along the boundary region. Color available on line.

This segregation suggests a possible mechanism resulting in the observed reduction of compressive stress with increasing Ti content. The presence of Ti in the grain boundary provides a thermodynamic barrier for the further insertion of excess W adatoms into the grain boundaries. Thus, as the amount of Ti in the film increases, a corresponding increase in Ti segregation to the grain boundaries occurs. The overall fraction of excess W atoms inside the grain boundary will

reduce resulting in a reduction in the compressive force created by W adatoms, particularly when one recognizes that Ti is a smaller atom than W⁴⁴.

Besides the overall steady-state compressive stress behavior with Ti, the initial growth stresses where the β -to- α W transition occurred also tracked with Ti content. As the Ti content increased, the critical thickness for β -Ti stability was reduced and eventually was not observed for the highest solute content alloy. Figure 8 contains TEM micrographs for a 20 nm elemental W and W20Ti films grown at room temperature. Recall that at 20 nm, W was indexed by XRD as β -W and W5Ti was α -W, Figure 3. In the W film micrograph, Figure 8(a), a dominate β -W phase with grain sizes of 8.8 ± 1.4 nm was observed. This very fine microstructure (small grain size) exhibited by β -W would explain the tensile stress behavior observed when this phase is present²⁹. However, upon closer inspection of Figure 8(a), a few larger ‘bright grains’ can also be seen. A careful measurement of the selected area diffraction pattern, Figure 8(b), revealed a ring consistent with the α -W phase, which coincides through dark field imaging (not shown) of these bright grains as nucleated α -W. Their relatively low volume fraction inhibited them from sufficient diffraction intensity in the prior XRD scan. The addition of Ti appears to be thermodynamically favoring the formation of α -W over β -W. This was ascertained by noting the stress response of the secondary tensile peak; this peak decreased in relative height and thickness between the elemental and alloy films seen in Figure 2. This α -W stabilization was further confirmed by the TEM micrographs in Figure 8, which showed a complete transition to α -W, and no secondary tensile peak, Figure 2(c), observed in the W20Ti film.

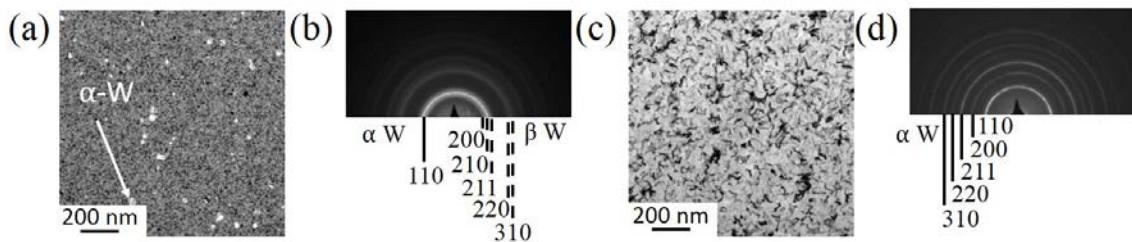


Figure 8. TEM of (a) 20 nm W-RT bright field showing fine β W grains and large α W grains (b) corresponding diffraction of 20 nm W-RT showing β -W and a small fraction of α -W (c) 20 nm W20Ti-RT bright field image revealing larger α -W grains (d) corresponding diffraction revealing only bcc α -W reflections.

The grain sizes at 20 nm for the W20Ti film (38.57 ± 27.76 nm) does reveal a smaller average size than those reported for it at 300 nm thick (52.4 ± 49.0 nm), Table 2. Furthermore, the collective grain sizes for 20 nm W (8.8 ± 1.4 nm) are smaller than the 20 nm W20Ti film, Figure 8(c). This difference in grain sizes between these two films is explained though the phases they form and the structure zone model of thin film growth⁴⁵. It is clear that if β -W forms, it does so as fine grains, which ultimately transform to larger α -W, as one can infer from Figure 8(a) where larger α -W grains are observed in the presence of β -W. However, these initial α -W in-plane grain sizes, Figure 8(c), are still smaller than their final average grain size measured at 300 nm thickness (68.7 ± 46.0 nm), Table 2 and Figure 5. The cross-sectional microstructure for the films, with a representative image shown in Figure 9 for W5Ti, revealed the films all grow in the zone T region of the Thornton structure zone model. In this region, a competitive grain growth process develops in the initial stages, evident by the v-shaped grains. Eventually a preferred orientation or grain is adopted whereupon that grain dominates and grows creating the final, larger grain size than those that nucleated during the early stages of deposition⁴⁶. The nonlinear slope from the stress measurements, Figure 1, during the early film growth also supports the notion of the zone T behavior because the changing slope is related to evolving grain sizes⁴⁷. Most interesting, by adding Ti to the W film, and bypassing or at least restricting the thickness stability range of β -W initial growth, the type of grain boundaries that formed in coalescence stages of growth changed. Since W20Ti bypassed completely the β -to- α W transition, a clear increase in LAGBs was created. This 20 nm W20Ti film, Figure 8(c), exhibited a LAGB fraction of 0.224, which is approximately the same fraction exhibited at the 300 nm. Thus as the film thickened, this grain boundary type does not appear to change with film thickness.

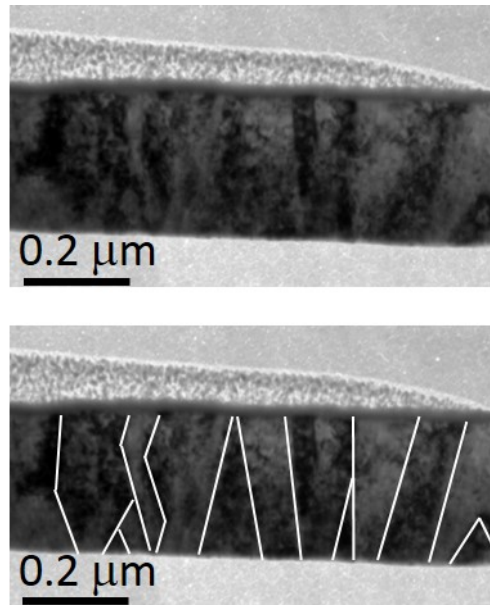


Figure 9. Bright field image of W5Ti cross section (300 nm thick film) showing zone T growth with some v-shaped grain morphologies traced in the image below by the white lines.

Though these are interesting observations, it does not explain how Ti is reducing the stability of the β -W phase. Upon adding Ti, the phase stability can be altered by changes in the free energies associated with solid solution mixing between α and β W. In addition, strain may influence this phase stability, albeit the effect is minimal because of the relatively small changes in lattice parameters tabulated in Table 1. Interestingly, β -W stability has been linked to oxygen content³⁹. Though each film was grown in vacuum, some amount of deleterious background oxygen will still be present. The time of flight mass spectrum from the prior atom probe experiments revealed an oxygen content that varied between ~ 0.5 to ~ 0.9 at.% in these films. It is well known that Ti has a much stronger affinity for oxygen than W⁴⁸. Thus, it is reasonable to assume that as the Ti content increased, the excess Ti was able to getter this residual oxygen from W, which would mitigate its ability to stabilize the β -W phase. This gettering difference was observed in the atom probe mass spectrum, where the detected complex ions with oxygen were in a larger fraction for the titanium based complexes than the tungsten based complexes, i.e. $\sim 0.63\%$ TiO₂ versus 0.01% WO₂ for the room temperature W5Ti film. For the elemental W films, there is a slight shift in the secondary tensile stress condition with deposition temperature. These shifts are less prevalent for the alloy films. This difference in behavior is contributed to Ti's ability to getter oxygen. Recall that oxygen is a known stabilizer for β -W, and at elevated

temperature, minor outgassing within the vacuum chamber can occur, which would explain the apparent shift behavior in the elemental W films where oxygen's influence would be more pronounced. Thus, not only has Ti influenced the steady-state stress but also influenced the phase stability behavior of the W alloy films.

Finally, the heating of the substrate during deposition resulted in the reduction of the compressive stress for all of the films, which is consistent with prior work of elevated temperature deposited elemental W films³⁰. In Sun *et al.*³⁰ study, the reduction of the compressive stress was linked to larger grain sizes. From Table 2, we can see that the average grain size did increase for the W film, which may have contributed to the compressive reduction, though the large standard deviation in grain sizes convolutes this link. Interestingly, the average grain size of the W20Ti film showed the least variation in grain size with annealing and is likely contributed to the aforementioned nanocrystalline stability behavior. As mentioned above, the heating of the film did result in changes in the bcc phase lattice parameter, Table 1, with this behavior contributed to the thermally assisted further migration of Ti to the grain boundaries to achieve equilibrium solubility within the W grains. This migration would then change the unit cell strain of W-Ti and also assist in the reduction of the compressive stress state of the film.

Conclusion

In this paper, we have explored the effect Ti additions on the intrinsic growth stress and microstructural evolution in the W-Ti system. Increasing Ti content in the films resulted in a reduction in the magnitude of the observed compressive stress. This reduction occurred without significant changes to the average grain size, with the grain sizes exhibiting a large size distribution independent of composition or the deposition substrate temperature studied. The stress reduction is attributed to Ti segregation to the grain boundaries, which was confirmed by APT. This segregation of Ti would provide a thermodynamic barrier for the insertion of excess W adatoms to the grain boundaries as well as a notable atomic volume size difference between the types of adatoms in the grain boundaries themselves. Upon heating the films at each composition, a reduction in the compressive stress was observed. This change was attributed to further Ti enrichment of the grain boundaries as well as a lattice relaxation towards equilibrium.

The addition of Ti was noted to modify the stability of the metastable formation of A15 or β -W that can form in the early stages of growth. With increasing Ti content, the thickness stability regime of β -W decreased and eventually, at the highest Ti content, did not form. This has been attributed to Ti's preference to getter oxygen from W, where oxygen is known to help

stabilize β -W. The removal of initially nucleating β -W resulted in both larger initial grain sizes upon growth and an order of magnitude increase in the fraction of LAGBs.

Collectively, this work has demonstrated that Ti solutes can have a dramatic effect on the stress and microstructure of W-based thin films. Not only can Ti be used to tune the stress evolution of the sputter deposited films, but it can also control the phase stability and grain boundary character types within these films. This indicates that composition can be an equally important variable in the process control and tailoring of residual thin film stress and thin film structure.

Acknowledgement

The authors gratefully acknowledge the Army Research Office, grant W911NF1310436, Dr. Michael Bakas program manager. The UA Central Analytical Facility is recognized for additional assistance and access to the microscopes used in this research.

References

- ¹ E. Chason, M. Karlson, J.J. Colin, D. Magnfält, K. Sarakinos, and G. Abadias, *Journal of Applied Physics* **119**, 145307 (2016).
- ² R. Abermann, *Vacuum* **41**, 1279 (1990).
- ³ R.W. Hoffman, *Thin Solid Films* **34**, 185 (1976).
- ⁴ M.-W. Moon, J.-W. Chung, K.-R. Lee, K.H. Oh, R. Wang, and A.G. Evans, *Acta Materialia* **50**, 1219 (2002).
- ⁵ J.S. Wang and A.G. Evans, *Acta Materialia* **47**, 699 (1999).
- ⁶ R. Koch, *Journal of Physics: Condensed Matter* **6**, 9519 (1994).
- ⁷ F. Spaepen, *Acta Materialia* **48**, 31 (2000).
- ⁸ A. González-González, C. Polop, and E. Vasco, *Phys. Rev. Lett.* **110**, 056101 (2013).
- ⁹ C. Friesen and C.V. Thompson, *Phys. Rev. Lett.* **89**, 126103 (2002).
- ¹⁰ E. Chason, B.W. Sheldon, L.B. Freund, J.A. Floro, and S.J. Hearne, *Phys. Rev. Lett.* **88**, 156103 (2002).
- ¹¹ R. Koch, D. Hu, and A.K. Das, *Phys. Rev. Lett.* **94**, 146101 (2005).
- ¹² W.D. Nix and B.M. Clemens, *Journal of Materials Research* **14**, 3467 (1999).
- ¹³ A. Saedi and M.J. Rost, *Nature Communications* **7**, 10733 (2016).
- ¹⁴ L. Shaginyan, J.G. Han, and H.M. Lee, *Jpn. J. Appl. Phys.* **43**, 2594 (2004).
- ¹⁵ A.L.D. Vecchio and F. Spaepen, *Journal of Applied Physics* **101**, 063518 (2007).
- ¹⁶ G. Thurner and R. Abermann, *Thin Solid Films* **192**, 277 (1990).
- ¹⁷ M. Pletea, W. Brückner, H. Wendrock, and R. Kaltofen, *Journal of Applied Physics* **97**, 054908 (2005).
- ¹⁸ H.S. Myung, H.M. Lee, L.R. Shaginyan, and J.G. Han, *Surface and Coatings Technology* **163**, 591 (2003).
- ¹⁹ B. Fu and G.B. Thompson, *Journal of Applied Physics* **108**, 043506 (2010).
- ²⁰ X. Zhou, T. Kaub, R.L. Martens, and G.B. Thompson, *Thin Solid Films* **612**, 29 (2016).

- ²¹ T.M. Kaub, P. Felfer, J.M. Cairney, and G.B. Thompson, *Scripta Materialia* **113**, 131 (2016).
- ²² J.L. Murray, *Bulletin of Alloy Phase Diagrams* **2**, 192 (n.d.).
- ²³ T. Chookajorn and C.A. Schuh, *Acta Materialia* **73**, 128 (2014).
- ²⁴ L.R. Shaginyan, M. Mišina, J. Zemek, J. Musil, F. Regent, and V.F. Britun, *Thin Solid Films* **408**, 136 (2002).
- ²⁵ R. Shohji, in *Proceedings of ISSM2000. Ninth International Symposium on Semiconductor Manufacturing (IEEE Cat. No.00CH37130)* (2000), pp. 165–168.
- ²⁶ C.-F. Pai, L. Liu, H.W. Tseng, and D.C. Ralph, *Appl. Phys. Lett.* **101**, 122404 (2012).
- ²⁷ Y.G. Shen, Y.W. Mai, Q.C. Zhang, D.R. McKenzie, W.D. McFall, and W.E. McBride, *Journal of Applied Physics* **87**, 177 (1999).
- ²⁸ T.J. Vink, W. Walrave, J.L.C. Daams, A.G. Dirks, M.A.J. Somers, and K.J.A. van der Aker, *Journal of Applied Physics* **74**, 988 (1993).
- ²⁹ P. Petroff, T.T. Sheng, A.K. Sinha, G.A. Rozgonyi, and F.B. Alexander, *Journal of Applied Physics* **44**, 2545 (1973).
- ³⁰ R.C. Sun, T.C. Tisone, and P.D. Cruzan, *Journal of Applied Physics* **46**, 112 (1975).
- ³¹ Taylor, C., Bartlett, D., Chason, E., and Floro, J., *The Industrial Physicists* **4**, 25 (1998).
- ³² G.G. Stoney, *Proceedings of the Royal Society A: Mathematical, Physical and Engineering Sciences* **82**, 172 (1909).
- ³³ J.G. Brons and G.B. Thompson, *JOM* **66**, 165 (2014).
- ³⁴ K. Thompson, D. Lawrence, D.J. Larson, J.D. Olson, T.F. Kelly, and B. Gorman, *Ultramicroscopy* **107**, 131 (2007).
- ³⁵ R. Abermann and R. Koch, *Thin Solid Films* **142**, 65 (1986).
- ³⁶ S.M. Rossnagel, I.C. Noyan, and C. Cabral Jr., *Journal of Vacuum Science & Technology B: Microelectronics and Nanometer Structures Processing, Measurement, and Phenomena* **20**, 2047 (2002).
- ³⁷ M.J. O’Keefe and J.T. Grant, *Journal of Applied Physics* **79**, 9134 (1996).
- ³⁸ J.-S. Lee, J. Cho, and C.-Y. You, *Journal of Vacuum Science & Technology A: Vacuum, Surfaces, and Films* **34**, 021502 (2015).
- ³⁹ I.A. Weerasekera, S. Ismat Shah, D.V. Baxter, and K.M. Unruh, *Appl. Phys. Lett.* **64**, 3231 (1994).
- ⁴⁰ H.E. Swanson and E. Tatge, *NBS Circular 539* **1**, (1953).
- ⁴¹ L. Vegard, *Zeitschrift Fur Physik* **5**, 17 (1921).
- ⁴² D. Magnfält, A. Fillon, R.D. Boyd, U. Helmerson, K. Sarakinos, and G. Abadias, *Journal of Applied Physics* **119**, 055305 (2016).
- ⁴³ E. Chason, J.W. Shin, S.J. Hearne, and L.B. Freund, *Journal of Applied Physics* **111**, 083520 (2012).
- ⁴⁴ E. Clementi, D.L. Raimondi, and W.P. Reinhardt, *The Journal of Chemical Physics* **47**, 1300 (1967).
- ⁴⁵ J.A. Thornton, *Annual Review of Materials Science* **7**, 239 (1977).
- ⁴⁶ I. Petrov, P.B. Barna, L. Hultman, and J.E. Greene, *Journal of Vacuum Science & Technology A: Vacuum, Surfaces, and Films* **21**, S117 (2003).
- ⁴⁷ H.Z. Yu and C.V. Thompson, *Acta Materialia* **67**, 189 (2014).
- ⁴⁸ D. Gaskell, *Introduction to the Thermodynamics of Materials*, 5th ed. (Taylor & Francis, 2008).

CHAPTER 11

The influence of alloy atoms interactions on thin films stress

Xuyang Zhou¹ and Gregory B. Thompson¹

1. The University of Alabama, Department of Metallurgical & Materials Engineering,
Tuscaloosa, AL USA

Abstract

A series of W-Fe and W-Cr thin films were sputter deposited and the intrinsic growth stresses measured. The elemental W film, under the growth conditions studied, grew compressive whereas the elemental Fe and Cr films grew tensile. By mixing these elements, the alloy stress state was bounded between the two elemental stresses. Both alloys revealed a zero or cross-over stress state. This zero-stress did not trend linearly to the compositions but was effected by chemical partitioning and/or by the grain size and shape. Interestingly, we noted that alloying W(Fe), Fe(W), W(Cr) or Cr(W), where (element) is the solute species, promoted some extent of grain growth across all alloy systems. Dependent on composition, lath-like partitioning was quantified within the grains for the W-Fe and W-Cr films by atom probe tomography. Using the zero-stress composition, the films were re-deposited at 673K to drive the microstructure towards equilibrium and monitor the associated stress evolution. Under these conditions, both alloys exhibited a similar compressive stress state during post-coalescence growth, with the post-deposition stress recovery being much greater in the W-Fe film than that of the W-Cr film. This was contributed to a difference in grain sizes between the two films.

Keyword: Stress evolution; Thin films; W-Fe; W-Cr; Atom probe; Segregation

1. Introduction

Thin films are a vital architecture in several technologically important applications including tribological coatings [1], information storage [2], semiconductor transistor design [3, 4], optical devices [5, 6], and energy harvesting [7, 8]. During thin film deposition, the thin films can generate significantly large intrinsic stresses that can lead to thin film device failures. For example tensile stresses can lead to cracking [9, 10] with compressive stresses often associated with delamination, buckling, and blistering of the film from the substrate [10-12]. Stresses in interconnect conductor films has been shown to promote the nucleation of whiskers and hillocks which result in short circuit failures [13, 14]. Thus, the ability to control the residual stress in a thin film is vitally important to enhance the reliability of thin film based devices.

When a thin film is deposited, the intrinsic stress state evolves based on different stages of growth. In the embryonic stage, nuclei clusters of atoms migrate together generating a compressive stress from the Laplacian stress. As they embryonic islands approach each other, they elastically strain to connect with each other reverting the stress state to become tensile. [15-17]. After coalescence of the islands, elemental films with high adatom mobility, such as Cu [18], Ag [19] and Co [20], then experience a compressive stress state while films with low adatom mobility, like Fe [21] and Cr [21] tend to retain the coalescence-induced tensile condition with continued growth. To date, the post-coalescences compressive stress is still a matter of much research and discussion. It has been proposed that the chemical potential differences on the surface, during deposition, with respect to the grain boundaries, results excess adatoms diffusing into the grain boundaries to create the compressive stress [19]. Under that idea, a few papers have been reported in how the solute in the boundary can be used to tune the stress state. For example, Fu and Thompson [22, 23] reported how preferential segregation of the Pt solute in a grain boundary could make a nominally tensile retaining film, like Fe become compressive. Similarly, Kaub and Thompson have shown how solute enrichment based on Gibbsian interfacial excess can be used to control the intrinsic deposition film stress [24]. The authors here have reported how the solute in Fe(Cr) can be used to manipulate the grain size and regulate the stress state [25]. In all of these cases, the grain size and/or grain boundary composition have been identified as key variables in controlling the thin film stress in multi-component films. Thus, composition, much like deposition rate, pressure, and substrate temperature can act as a processing variable to regulate the resulting thin film residual stress.

One of the intriguing findings in the Fu and Thompson [22] paper, where Pt segregation was found to occur in an Fe-Pt film, was a zero stress state. While in the “zero-state” stress state, the grain boundaries and interior of the film grains were compositionally equivalent suggesting no preferential segregation. Thus, Fu and Thompson’s work [26] concluded that grain boundary chemistry was critical. Of the prior alloy work mentioned above, the Cu-Ni work [24] was in two nominally compressive growing films and the Fe-Cr work was in two nominally tensile growing films. To date, a follow-on study to the original Fe and Thompson [22] work, where a nominally compressive growing film, i.e. Pt, and a tensile growing film, i.e. Fe, are mixed to further explore zero stress cross-overs and what compositions would resides at such positions within the interior of the grains and the grain boundaries. Clearly, depending on the interaction between the solvent and solute atoms, the microstructure and grain boundary chemistry of such an alloy thin film will vary dependent on the intrinsic thermodynamics of the system itself. Such variations could generate different stress responses and/or new insights in how alloying is controlling the grain boundary composition and resultant stress.

In this work, we extend these previous alloying studies and explore the relationship between composition and stress in other mixed compressive-tensile systems. Here, W-Fe and W-Cr systems were selected as the case studies. The W elemental film is nominally compressive growing [27] whereas the Fe and Cr elemental films are nominally tensile. [21]. Thus, using the same compressive forming film, one can ascertain how different tensile growing species alters the alloy stress state. All three species are body-centered cubic (BCC) phases at room temperature. However, based on the thermodynamic equilibrium phase diagram, the interactions between these species is different. In the W-Cr is a phase separation system, where the species have a positive enthalpy of mixing exists, whereas W-Fe yields several intermetallic phases such as the Laves phase (Fe_2W) and the mu (μ) phase (Fe_7W_6) [28], indicative of composition dependent negative enthalpy of formation behavior. Though both systems provide a different phase equilibrium responses, the highly dynamic processing of sputtering often places multiple elements into a single solid solution upon deposition. Thus, under a metastable state of a single solid solution, body-centered cubic (A2) phase, these potential multi-phase complications can be reduced and the effect of composition on stress can be studied. To drive the system to equilibrium, or in other words promote a more dramatic interaction between the solvent and solute species, we will also anneal the films during deposition to quantify how that changes the stress state as the film is thermally driven to equilibrium.

2. Experimental

Elemental and alloyed thin films of Fe, Cr, W, $\text{W}_{1-x}\text{Fe}_x$, and $\text{W}_{1-x}\text{Cr}_x$ ($0 < x < 1$) were sputter deposited from 99.95% pure Fe, Cr, and W elemental targets in an AJA ATC-1500 stainless steel magnetron-sputtering system. The films grew to an approximate thickness of 200 nm onto 300 μm thick silicon [100] substrates which had a 100 nm thick thermally grown amorphous surface oxide. The base vacuum pressure prior deposition was $< 6 \times 10^{-6}$ Pa. For sputtering, ultra-high purity argon flowed as the working gas at ten standard cubic centimeters per minute flow rate to a pressure of 0.27 Pa. The deposition rates of elemental films were determined by SQM-160 thin films deposition monitor using quartz crystal sensor technology. By adjusting sputtering power, the sputtering rates for all films set as 0.1 nm/s. Alloy films with the different compositions were achieved through co-sputtering the respective two elemental targets at various sputtering power combinations to yield a deposition rate that gave the targeted composition. The composition of each alloy film was then verified by energy-dispersive X-ray spectroscopy (EDX) using an EDAX[®] Company detector in a FEI Quanta 3D Dual electron-focus ion beam system. For the *in situ* annealing experiments, the reported temperatures were calibrated by using a k-Space[®] Bandit system that provides a non-contact measurement of the Si band edge responses with temperature. The *in situ*

stress state during deposition was monitored using a k-Space Associates (kSA®) Multi-beam Optic Sensor (MOS) [29]. The details about this wafer curvature-based stress measurement technique can be found elsewhere [22, 30]. Concisely stated, this technology shines a two dimensional laser array onto a substrate surface and measures the displacement of reflective rays as the substrate bends in response to the film's growth on the substrate. Using the Stoney equation [31], given below, the stress within the film is then measured and calculated.

$$\sigma_f = \frac{E_s}{6(1-\nu_s)} \frac{t_s^2}{t_f} \left(\frac{1}{R} - \frac{1}{R_0} \right) \quad (1)$$

where σ_f is the average films stress, ν_s and E_s are the Poisson ratio and Young's modulus of the substrate respectively, t_s is the substrate thickness, t_f is the film thickness, and $1/R_0$ and $1/R$ are measured curvatures of the films before and during the deposition.

A series of θ - 2θ scans of x-ray diffraction (XRD) was conducted post deposition and ex-situ on an X'pert Philips diffractometer operated with Cu K α radiation ($\lambda = 1.5406$ Å) that was operated at 45 kV and 40 mA for phase identification. Electron diffraction patterns were also taken in the plan-view orientation (normal to the substrate) in an FEI Tecnai F20 Scanning Transmission Electron Microscope, (S)TEM, to examine both phase and microstructure.. The plan-view foils were prepared by cutting, dimpling, and ion-milling a 3 mm disc cut from the substrate containing the film. From the same foils, the grain morphology and size was imaged in the bright field as well as the atomic number, Z, -contrast image collected on a high angle annual dark field (HAADF) detector.. When taking the HAADF images, the camera length was set to 80 mm to eliminate the contribution of Bragg diffraction to the contrast. Grain sizes and orientation distributions were further quantified by using the precession electron diffraction (PED) technique on a NanoMEGA ASTARTM platform [32-34]. The PED scans operated with a 0.3° precession angle at a scanning step size of 3 nm over a $1.2 \mu\text{m} \times 1.2 \mu\text{m}$ regions of interest (ROI) in the in-plane orientation. After scanning, the data was converted for analysis using TSL OIM Analysis 7 software. Grain based and kernel based misorientation analyses have been employed to identify the grains with varying local misorientation and the local orientation variations within each grain, respectively. The Local Orientation Spread (LOS) method was calculated to determine the misorientation between each point in the kernel and all others in the kernel with the LOS maps created using those averaged values for the kernel. In this paper, the 1st nearest neighbor algorithm with a maximum misorientation set as 5° .

The alloy films were also characterized by atom probe tomography (APT) performed on a Cameca Instruments Local Electrode Atom Probe (LEAP®) 5000 XS. The atom probe provides a 3D representation of the placement of the various atoms with near perfect lattice rectification. A FIB lift-out technique [35, 36] was employed to

prepare the atom probe tips using the aforementioned FEI Quanta 3D dual beam FIB-SEM. The extracted tips were sharpened into needle-like geometries necessary for field evaporation with a 5 keV clean-up step to move Ga⁺ implanted surface damage in a TESCAN LYRA FIB- Field Emission Scanning Electron Microscope (SEM). Once sharpened, the tips were field evaporated in the LEAP operated with a specimen set point of 40 K, laser pulse energy of 100-200 pJ at a pulse repetition rate of 500 kHz for a 0.5% atoms per pulse detection rate.

Furthermore, a correlative microscopy technique between the TEM-PED and the LEAP samples were conducted for selected samples. Here, the FIB extracted tips were mounted on a Si half grid holder rather than the normal used coupon [36, 37] and loaded onto a Hummingbird TEM holder and placed into the TEM for imaging. The grain-to-grain mapping of the film was again conducted using the PED technique on the Nanomegas ASTARTM platform. The beam was precessed at 0.3° at a scanning step size of 2 nm. Further detailed PED and APT cross-correlative information can be found in [36].

3. Results and discussion

3.1 Stress evolution at room temperature

The *in situ* stress evolution of 200 nm thick W, W-14 at.% Fe, W-40 at.% Fe, W-76 at.% Fe, W-95 at.% Fe, and Fe are displayed in Figure 1(a). From Figure 1(a), the W thin film revealed a post-coalescence compressive growth stress whereas the Fe thin film exhibited a post-coalescence tensile growth stress state, all of which would be consistent with prior literature [21, 27]. The tensile stress for Fe is nominally linked to its low adatom mobility [21]. Conversely compressive stresses are often discussed in terms of higher mobility species [18-20]. However, W having a very high melting point (~3300°C), could be assumed to have rather limited surface diffusivity. To rationalize its compressive stress, one must consider the sputtering energy distribution from a polycrystalline target, $F(E)$. Here $F(E)$ is proportional to $E/(E+U)^3$ where E is the energy of sputtered atoms, and U is the binding force normal to the surface, normally represented as a binding energy [38]. Typically, sputtered atom energies have a maximum near $U/2$ (which is several eV) and a dissipating energy tail extending to tens to hundreds of eV. When comparing W's higher binding energy to Fe atoms, it lends itself to having a higher probability in generating atoms with higher energies [27, 39]. This increase in energy is suspected to assist adatom diffusion into the grain boundary regions that have been proposed to create a compressive response [19] as well as the impact energies of W adatoms creating peening effects that can also lead to compressive stresses [27].

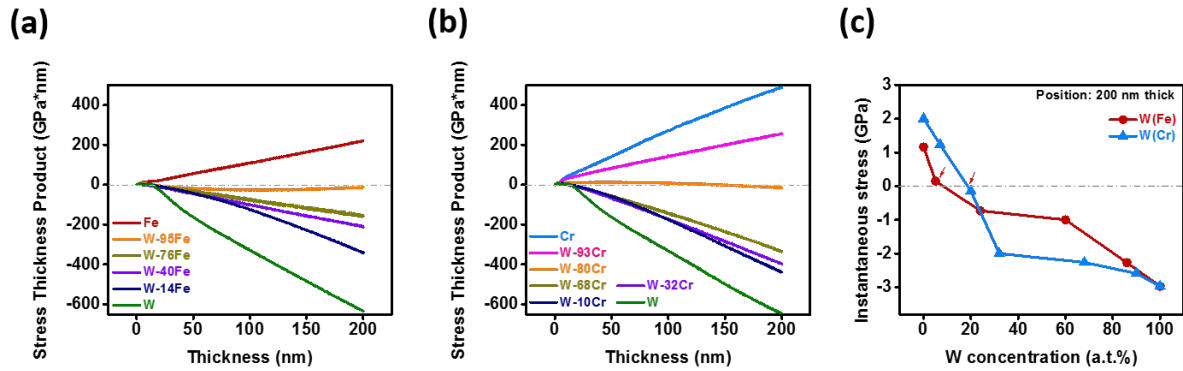


Figure 1 Stress thickness product varying with thin films thickness in **(a)** W-Fe system and **(b)** W-Cr system. **(c)** The instantaneous stress of 200 nm thick film varying with solute concentrations in W-Fe system and W-Cr system.

For the alloy films, a stress dependent response is observed with composition and the alloy stress states are bounded between the elemental W and Fe stress conditions. The stress thickness product, plotted in Figure 1(a). Of these alloy compositions, the W-95Fe film revealed an instantaneous residual stress near zero as it grew. Further increases in W content resulted in this alloy film becoming ever compressive.

XRD, with selected area diffraction patterns, confirmed that nearly all these alloys formed either the bcc phase in the single element state or an A2 phase for the alloys, Figure 2. The only exception of this was the W-40Fe and W-76Fe films which vitrified. Lu *et al.* [40] reported in Fe_xW_{100-x} alloy films, the composition between $40 \leq x \leq 70$ at.% Fe were amorphous. Our experiments are in agreement with their experimental findings [40]. In the phenomenological theory proposed by Egami and Waseda [41], this vitrification has been explained as a size difference between the two elements. Each of crystallized thin film exhibited a fiber texture of $\{110\}$. Of the films, only the W and W-14Fe revealed additional reflections in this Bragg-Brenato scattering configuration, with those reflections being the $\{211\}$ and $\{220\}$ planes. The presence of these additional textures is indicative of an energetic competition between the lowest surface energy and elastically soft growth directions in thin films [42]. Note that the reason the intensities of W-rich thin films are much higher than the intensities of Fe-rich thin films is because of its higher scattering factor. Using the $\{110\}$ peak, it was fitted to a Gaussian profile where upon the lattice parameter was determined from Bragg's law. In Figure 3, the lattice parameters of the BCC alloys decreased monotonically with Fe content which is associated with the smaller atomic size of Fe than that of W. This trend fits well with Vegard's law [43]. For the same reason, the position of the main scattered peak of the amorphous alloys was also found to shift to a high q value when more Fe was added.

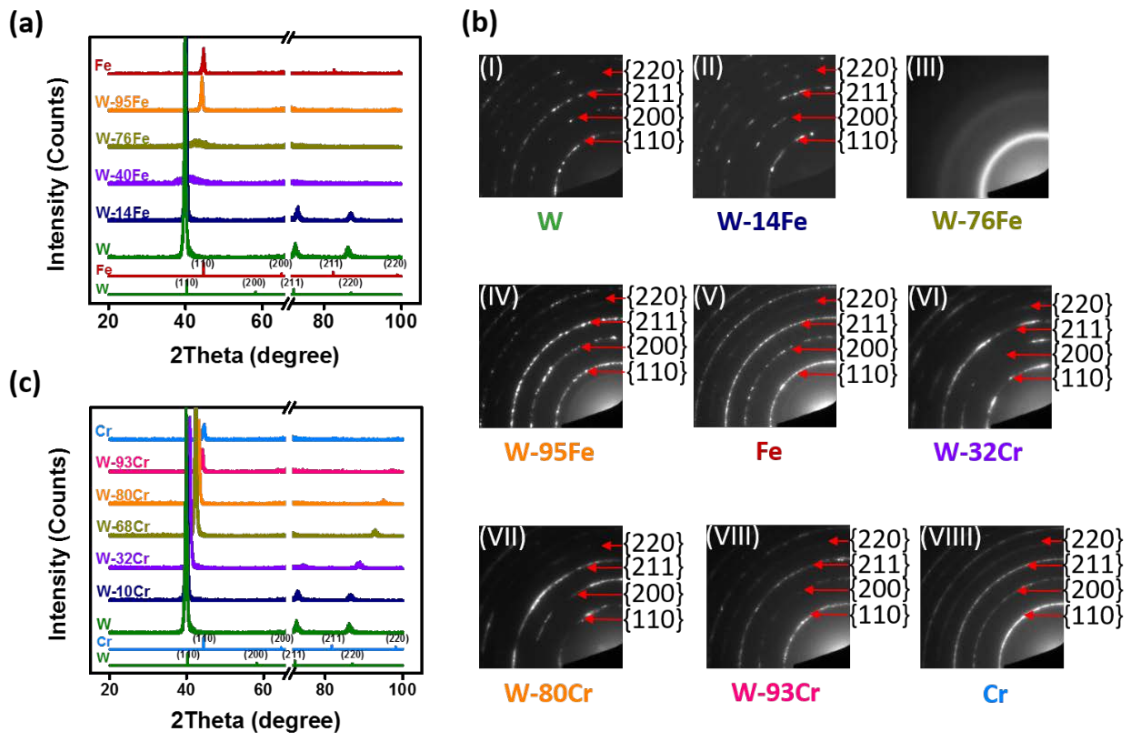


Figure 2 (a) X-ray spectrums for W-Fe alloying films with different solute concentrations. (b) SAED pattern of the (I) W (II) W-14Fe (III) W-76Fe (IV) W-95Fe (V) Fe (VI) W-32Cr (VII) W-80Cr (VIII) W-93Cr (VIII) Cr. The diffraction pattern indexes W-76Fe thin film to an amorphous structure while the other alloy thin films to BCC symmetry. (c) X-ray spectrums for W-Cr alloying films with different solute concentrations.

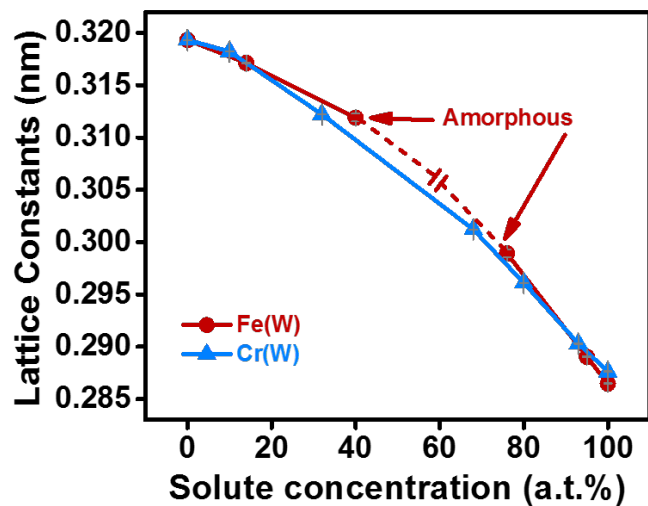


Figure 3 Lattice constants varying with solute concentration in the W-Fe and W-Cr system

Similar to the W-Fe system, the W-Cr system's alloy compositions' growth stresses - which spans W-10Cr, W-32Cr, W-68Cr, W-80Cr, and W-93Cr - are bounded between W and Cr. Here, the near zero growth stress was found to occur for the W-80Cr film. Since the Cr elemental film has a higher tensile stress than that of the Fe elemental film, it appears that the mixing of a larger amount of W was required in order to reduce the tensile stress to zero. Interestingly, the compositions where zero stress is observed are not at a composition that would be a linear connection between the two elemental films' stress values, Figure 1(c). As will be developed in section 3.2, grain structure and size along with grain boundary composition is believed to contribute to the zero-stress response and not just a simple bulk composition. Further referring to Figure 1(c), a distinct slope change in the stress with bulk composition is observed with ever increasing Cr content. In contrast. The W-Fe films revealed a more gradual increase of the tensile stresses with Fe content. XRD diffraction and electron diffraction, Figure 2, confirmed that the single elemental film of Cr was BCC and the W-Cr alloys were the A2 structure. Unlike W-Fe, the W-Cr alloys did not form an amorphous phase. The alloys also trended well with a rules of mixture Vegard's law approximation to the A2 lattice parameter, Figure 3.

3.2 The influence of phase separation on grain structure and stress evolution

The stress state of a thin film has been shown to be related to its grain size [10, 25, 44]. As alluded to in the introduction, the use of solutes has been reported to both regulate the grain size [25] as well as segregate to the grain boundaries [22, 24], all of which has contributed to the growth stresses [22, 24, 25]. Figure 4 is the cumulative grain size area plot for both alloys; the grain sizes were quantified by the PED mapping with representative images shown in the same figure. Depending on the composition, the grain size varied and even the distribution of grain sizes within specific alloys showed significant variance.

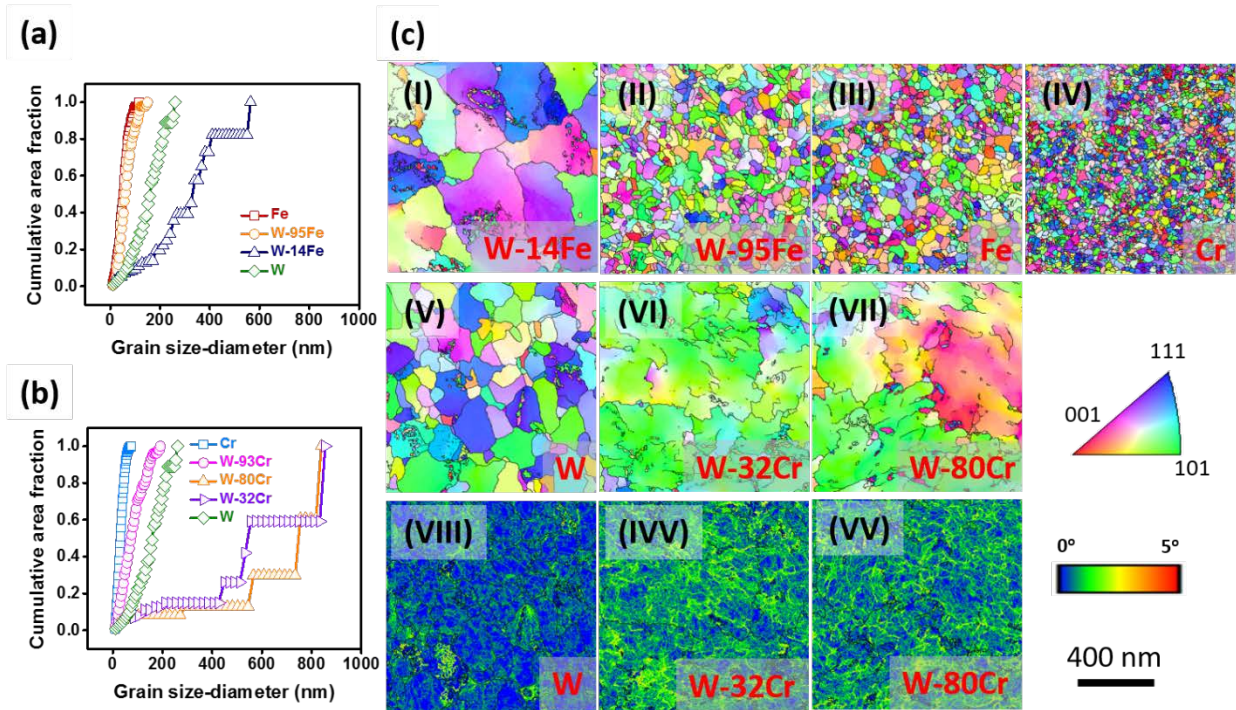


Figure 4 Cumulative grain size distribution plots for **(a)** W-Fe and **(b)** W-Cr films with different compositions. **(c)** Precession electron diffraction reconstructed orientation maps of **(I)** W-14Fe film **(II)** W-95Fe film **(III)** Fe film **(IV)** Cr film **(V)** W film **(VI)** W-32Cr film **(VII)** W-80Cr film and local orientation spread maps of **(VIII)** W film **(IVV)** W-32Cr film **(VV)** W-80Fe film.

For the W-Fe films, we noted a reasonably tight grain size distribution for the W, Fe, and W-95Fe films, evident by the near vertical area fraction for a specific grain size for each film. With a very modest amount of W added to the Fe film increased the adatom mobility with the W-95Fe film grain size shifted to ~ 66 nm which was slightly larger in size ($\sim 1.2X$) than Fe, yet this composition was no longer in a tensile state but exhibited a near zero stress condition. An APT reconstruction of this film is shown in Figure 5(a). A 1-dimensional cross sectional profile across the grains did not reveal a notable increase in the W solute content in the grain boundaries. Rather the grain boundary composition and that of the interior of the grains was equivalent, Figure 5(d). Such a finding would be consistent with the prior work of Fu and Thompson in the Fe-Pt system where the zero stress state, for near equivalent grain sizes, occurred when there was no solute segregation in the boundaries [22]. Further APT reconstructions of the W-76Fe film also revealed a compositional uniformity through the film. Here, this film was compressive; however, the alloy was amorphous, which also explains the lack of plotting its grain size in Figure 4(a). Though no discernable grain size was quantified, the

generation of the compressive stress is regarded to be related to the peening effect from high energy adatoms [27].

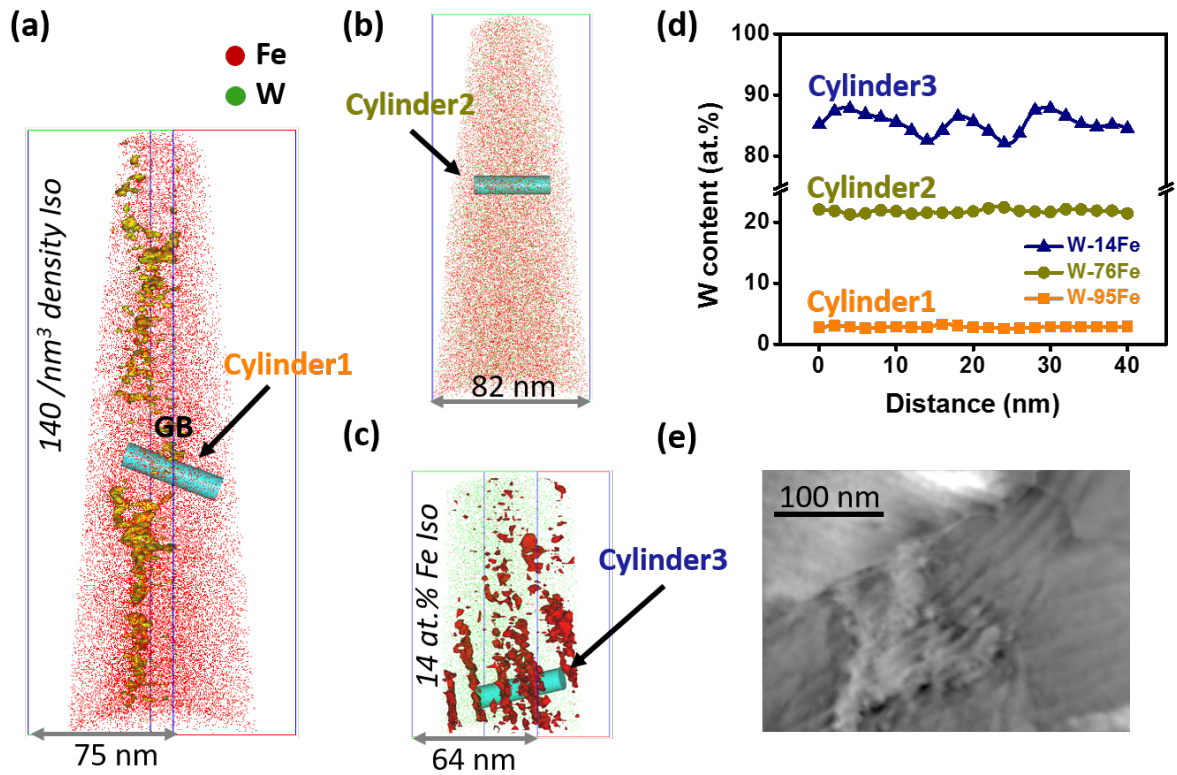


Figure 5 Atom probe reconstructions of (a) the W-95Fe film with 140 /nm³ density isosurface embedded (b) the W-76Fe film (c) the W-14Fe film with 16 at.% Fe isosurface embedded. (d) 1-D composition variations from pX5²X40 nm³ cylinders showing in Figure 5(a-c). (e) High angle annual dark field image of the W-14Fe film.

Returning back to the cumulative area fraction grain sizes, Figure 4(a), the W-14Fe film, which is now crystalline, exhibited a much larger grain size than the prior elemental or alloy compositions as well as an abnormal grain size distribution evident by the horizontal shift between grain sizes at the larger length scale regime. This film, like the amorphous films, was in a compressive residual stress state. Upon closer inspection of its stress thickness product, Figure 1(a), one can observe a subtle change in slope between the initial stages of growth and thicknesses > ~70 nm. A change in this slope product is usually indicative of a microstructural evolution during growth and well could be associated with these growing grains, with specific grains growing much more rapidly than others. It appears that the solute additions of Fe to W provided a much more dramatic change in grain size than W being added to the Fe-rich films. The APT reconstruction, Figure 5(c), and its 1-dimensional profile, Figure 5(d), with a

corresponding STEM high angle annular dark field image in Figure 5(e), confirmed that this alloy is phase separating. The film's microstructure appears to be forming a layered laminate morphology within the grains themselves. Interestingly the authors have reported a similar morphology in phase separating Fe-Cr films which also corresponded to films with larger grain sizes and abnormal grain size distributions [45]. It would appear that the onset of this type of phase separation morphology is linked this particular type of grain size development. We suspect that the thermodynamic energies present to phase separate provides an additional driving force for adatom mobility that can spur the larger grain sizes. Interestingly, this film has the largest grain sizes of all the films but did not exhibit the highest compressive stress, which is W. Thus, grain size alone is not sufficient in predicting an ever increasing compressive stress state for this system.

The W-Cr films exhibited a similar grain size distribution, with both normal and abnormal grain size distributions dependent on composition, Figure 4(b). The elemental Cr films exhibited the smallest grain sizes, which would consistent with low adatom mobility films that also experience a tensile growth state [21]. Like the W-95Fe film, a small amount for W to Cr shifted the grain size to a larger value while retaining a relatively narrow distribution for the W-93Cr alloy. The APT profile of its grain boundary composition, Figure 6(a) and (d), revealed a modest enrichment of W in the boundary. Unlike the W-Fe system, which can form a variety of intermetallic phases, the W-Cr system exhibits a miscibility gap with a positive enthalpy of formation. This may explain the tendency, even in low solute concentrations for the W to partition to the grain boundaries. The increase in the grain size (less grain boundary area) as well as the presence of a larger solute atom in the boundary would then explain the reduction of the tensile stress from that of the elemental Cr film.

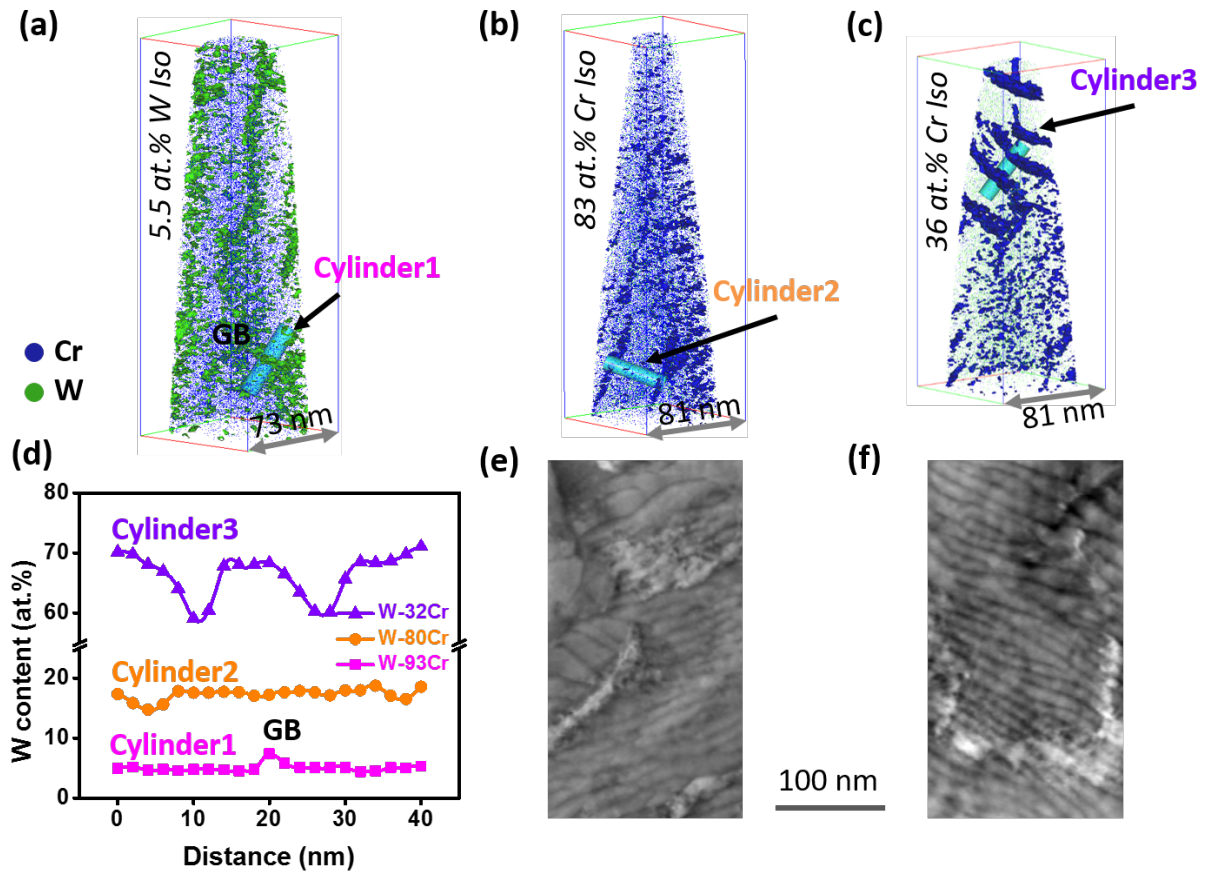


Figure 6 Atom probe reconstructions of (a) the W-93Cr film with 5.5 at.% W isosurface embedded (b) the W-80Cr film with 83 at.% Cr isosurface embedded (c) the W-32Cr film with 36 at.% Cr isosurface embedded (e) 1-D composition variations from $pX5^2 \times 40 \text{ nm}^3$ cylinders across boundaries showing in Figure 6(a-c). High angle annual dark field image of (e) the W-80Cr film and (f) the W-32Cr film.

Interestingly, at W-80Cr and W-32Cr, where either element is the solvent, the grain sizes increased dramatically and exhibited a large size distribution. APT analysis confirmed, like that of the W-14Fe, a microstructure with a laminated morphology with compositional profiles confirming the phase separation. Once again, this structure is linked to films with larger sizes and distributions. What is particularly noteworthy is that the W-80Cr is the film with the near zero stress state. Unlike prior films in this study and other alloys, the grain size distribution and the solute enrichment in the interfaces were not homogeneous. This suggests that the microstructure control of stress, particularly at the zero stress, is complex. It is possible that the formation of the laminated morphology from phase separation may balance the effects of a varied grain size. The evolution of this morphology will be further elaborated upon with annealing during deposition in section 3.3 below.

Using the LOS from the PED scans, shown in Figure 4(c), one can note a qualitative increase in small misorientation, or sub-grain size structure, with mixing content. The W film revealed a relevantly low degree of misorientation evident by the ‘blue’ tint in Figure 4(c). With mixing, both as the solvent and solute containing species, the larger grains contained a significant fraction of ‘green’ tint or small misorientations around $\sim 2^\circ$. This likely is a result of the migration of the two species from each other as observed in the phase separating laminate microstructure.

3.3 Stress evolution at elevated temperature

In all alloy compositions studied, the film was in a metastable state evident by the A2 phase. To understand how the stress state would evolve as the system is driven towards equilibrium, we have deposited the two ‘zero-stress’ compositions at 673K and measured both the growth stress and post-deposition stress recovery, Figure 7. Chason *et al.* [19] have proposed that during deposition, in the presence of the growth flux, the chemical potential of the surface is higher than that in equilibrium which is responsible for driving the excess atoms into the grain boundaries. By removing the deposition flux, the chemical potential of the surface is reduced which will facilitate excess adatom to migrate out of the boundaries to relieve the compressive stress. This can give insights in to the stability of a film’s stress state.

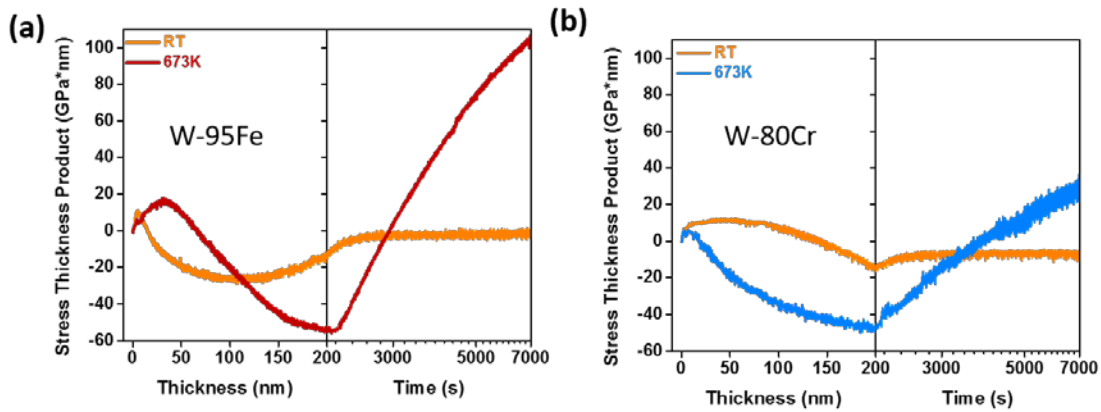


Figure 7 Stress thickness products varying with thin films thickness and relaxing time at different deposition temperatures for **(a)** W-95Fe films and **(b)** W-80Cr films.

As noted in Figure 7(a) and (b), both of the near ‘zero’ films exhibited very minimal compressive stress recovery after ceasing deposition. This could be expected as the compressive stress was near zero. One can infer from the deposition growth stress regime, a very modest varying slope suggesting that the films microstructure was undergoing some structural evolution, which could be expected by mixing the two species together. Once these films were deposited at temperature, they readily became

compressive in the post-coalescence regime. The W-95Fe film showed a marked tensile growth ‘hump’ during the early stages of growth before coalescence indicating, even with temperature, the adatom mobility was hindered by the presence of W and the desire for the two species to phase separate, as Fe has no bulk solubility for W at this temperature [28]. This can be inferred from the APT sample of the same film, Figure 8.

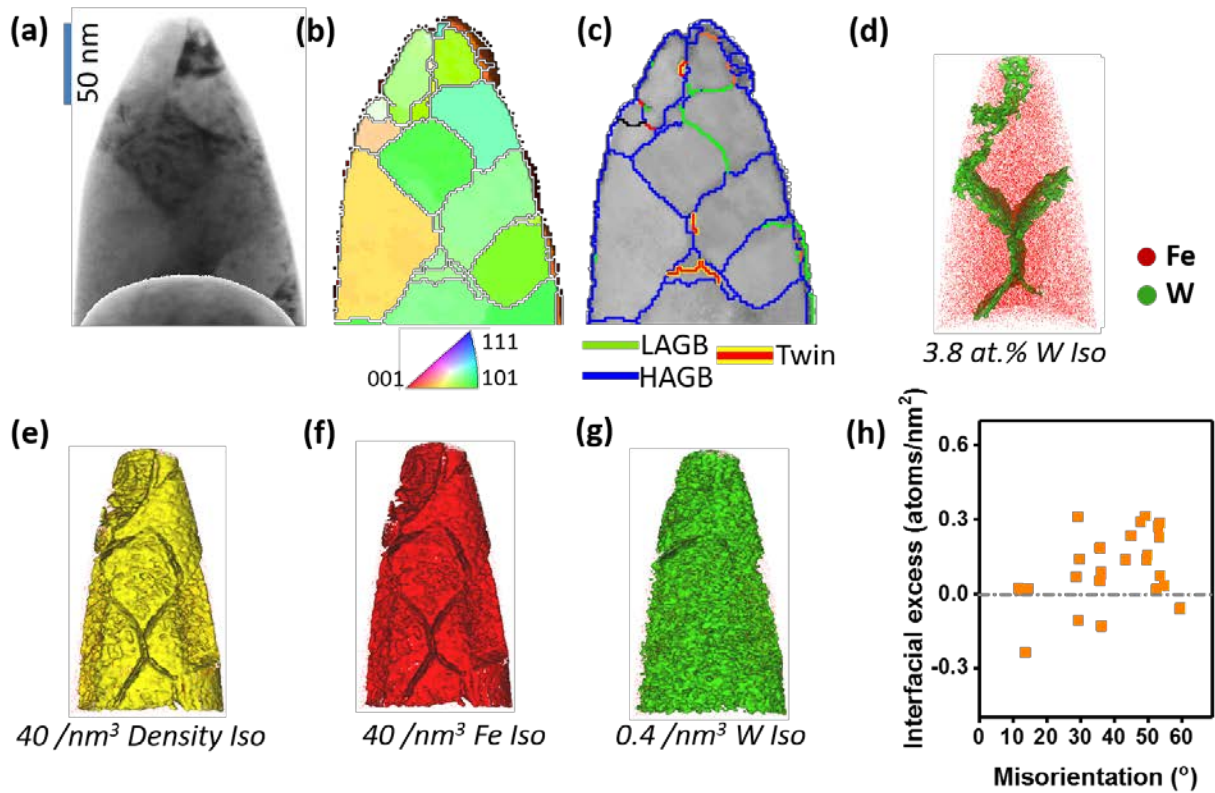


Figure 8 Correlative transmission electron microscopy and atom probe tomography study of W-95Fe film annealed at 673K: **(a)** bright field image **(b)** orientation map **(c)** grain boundary map and Fe & W atoms map with **(d)** 3.8 at.% isosurface embedded **(e)** 40 /nm³ density isosurface embedded **(f)** 40 /nm³ Fe density isosurface embedded **(g)** 0.4 /nm³ W density isosurface embedded **(h)** Interfacial excesses are varying with misorientations.

Using a correlative PED-APT technique [36], we have quantified the boundary types and observed a significant fraction of W in the high angle grain boundaries. However, based on the solute concentration, the W appeared to ‘wet’ the boundaries rather than cluster-up at the triple junctions. At the low angle grain boundary in Figure 8(c), one can note a very low quantity of W when comparing it to Figure 8(d). The Gibbsian interfacial excess for this film is plotted in Figure 8(h).

The onset of annealing has clearly promoted phase separation but has not resulted in a significant increase in grain size. The 673K W-95Fe grains are ~ 77 nm and only 1.15X larger than its room temperature deposit. Thus, we did not believe that grain size played a significant role in the change in stress state. Rather the enrichment of the W in the grain boundaries, Figure 8, would suggest that the grain boundary chemistry played a more significant effect in making the film more compressive. As the heat was applied, sufficient thermal energy promoted the W to the grain boundaries to yield a compressive stress state. Upon ceasing deposition, the film then showed a rapid relaxation of this compressive stress even to a residual tensile stress condition. The tensile stress is then contributed energetic competition between coalescing the boundaries while such mating surfaces are being in contact with a solute species that it wants to thermodynamically be driven from. When annealed during deposition, this effect was overcome.

Similar to the room temperature W-80Cr film, the 673K annealed deposited film revealed large grain sizes and distributions, with such effect increased by the thermal effects. The PED LOS mapping also retained the high extent of sub-grain structure that was noted to occur in the room temperature film, compare Figure 9(d) vs. Figure 4(c). This film went from a near 'zero' stress state to a compressive stress condition with annealing and upon ceasing deposition, the film exhibited a post-compressive stress relaxation similar to the prior annealed W-95Fe film. But, unlike the W-95Fe film, the rate of this relaxation and the magnitude of the recovered stress was less. APT and STEM-HAADF imaging, Figure 10, reveal the laminated phase separating morphology similar to that which was observed in the room temperature deposition. However, with annealing these lathes or laminates have thickened. Thus, the annealing has promoted further phase separation and growth. With these thicker laminates, the extent of post-deposition recovery was dimensioned because each species is coalesced more with the species it thermodynamically prefers.

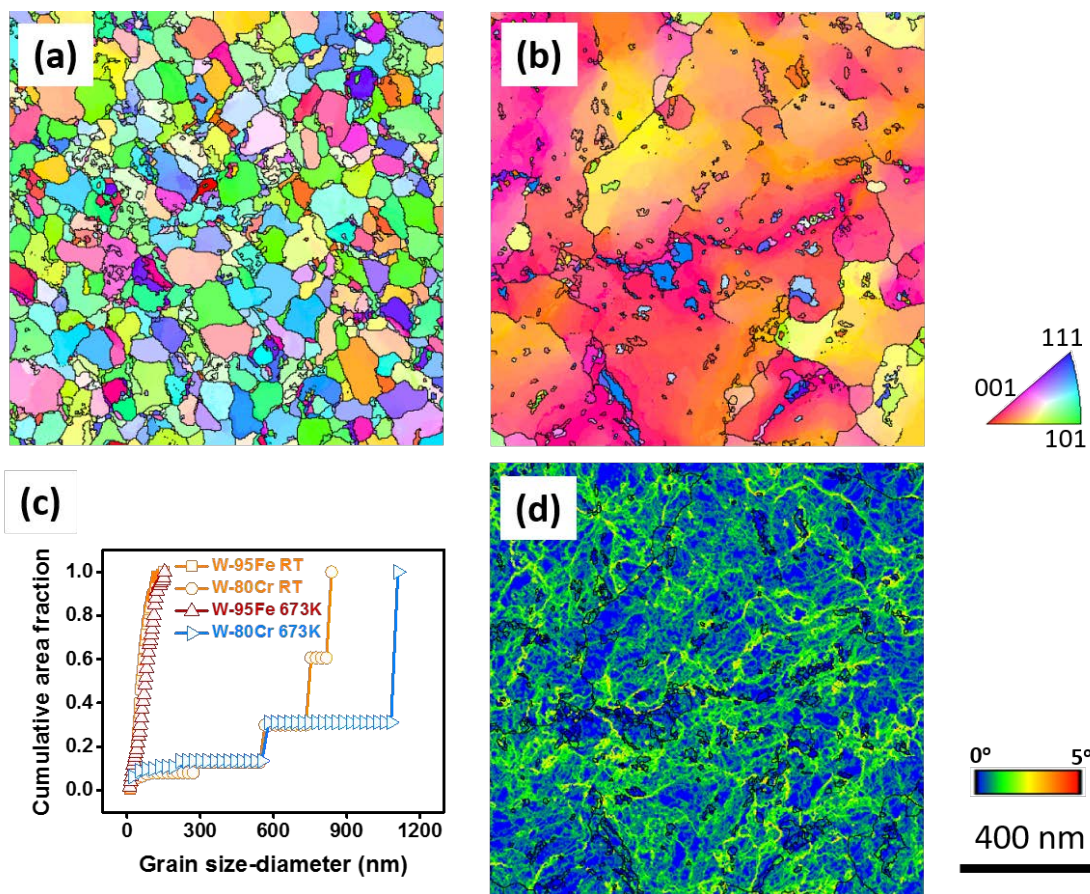


Figure 9 Precession electron diffraction reconstructed orientation maps of (a) W-95Fe and (b) W-80Cr films (c) Cumulative grain size distribution plots for RT W-95Fe, RT W-80Cr, 673K 95Fe, and 673K W-80Cr (d) Local orientation spread map of the W-80Cr films deposited at 673K.

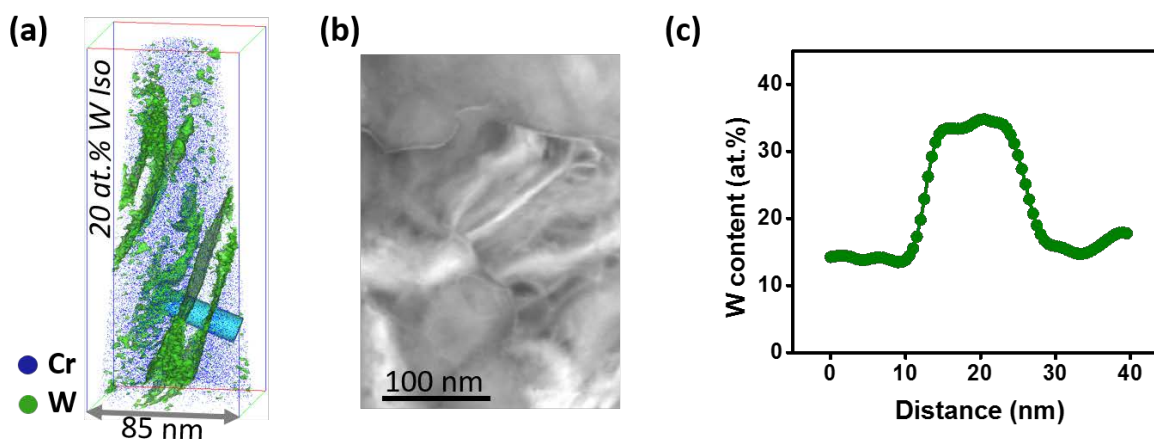


Figure 10 (a) Atom probe reconstructions and (b) High angle annular dark field image of the W-80Cr film deposited at 673K. 20 at% W isosurface was embedded in Figure 10(a). (c) 1-D composition variations from $pX5^2 \times 40 \text{ nm}^3$ cylinders across grain boundaries showing in Figure 10(a).

4. Conclusion

A series of W-Fe and W-Cr thin films have been sputter-deposited onto surface oxidized [001] Si substrates at either room temperature or 673K. The *in situ* growth stress has been measured, and their microstructures have been characterized. The major findings include the following:

- The residual stress of an alloy composed of a nominal tensile and compressive elemental film is bound by the elemental stress values.
- A “zero-stress” film does not necessarily trend with a linear approximation of composition between the elemental tensile and compressive stress values. The grain size and grain boundary composition can contribute to the stress state. For W-95Fe, which is the near zero stress condition for this alloy, the grain boundaries and matrix composition was equivalent, or, that the solute segregation was not present in the boundaries. Conversely, for the W-80Cr film, a much wider grain size distribution of sizes were found with a laminate phase separating morphology observed in the grains. These differences demonstrate the diversity of microstructures that form and achieve this cross over stress state.
- The laminate phase separating morphology with larger and wide grain size distributions has been seen in other room temperature deposited films suggesting that these features are linked to grain growth. This has been attributed to excess adatom mobility because of the strong enthalpies to phase separate.
- Upon annealing the ‘zero-stress’ room temperature compositions during growth, both W-95Fe and W-80Cr films became compressive. Interestingly, the grain size for the W-95Fe film did not grow significantly and retained an equiaxed grain size. APT confirmed the segregation of W to the boundaries, with the solute appearing to ‘wet’ the boundaries. The invariance of the grain size and the enrichment of the boundaries with the solute suggests that the grain boundary composition was significant in the change in the stress state. The W-80Cr film retained the similar large grain sizes and distributions, with such features increased by the temperature. The laminate phase separating morphology was still present, with the solute lathes thickened.
- The present work demonstrates that alloy composition can be used to regulate the film stress, with such stress being tuned near a zero stress state. However, the complications of predicting the ‘zero stress’ composition is complicated by potential phase separation as well as varied grain sizes and grain boundary compositions. Of the two systems studied here, the W-Fe was the most ‘well-behaved’ in observing how grain boundary composition regulates thin film stress

near the zero-stress condition while making other microstructure features relatively invariant.

Acknowledge

The authors gratefully recognize support from the Army Research Office, grant W911NF1310436, Dr. Micheal Bakas program manager. The UA Central Analytical Facility is recognized for additional assistance and access to the microscopes used in this research.

References

- [1] P.H. Mayrhofer, C. Mitterer, L. Hultman, H. Clemens, Microstructural design of hard coatings, *Progress in Materials Science* 51(8) (2006) 1032-1114.
- [2] F.J. Himpsel, J.E. Ortega, G.J. Mankey, R.F. Willis, Magnetic nanostructures, *Advances in Physics* 47(4) (1998) 511-597.
- [3] S. Koveshnikov, W. Tsai, I. Ok, J.C. Lee, V. Torkanov, M. Yakimov, S. Oktyabrsky, Metal-oxide-semiconductor capacitors on GaAs with high-k gate oxide and amorphous silicon interface passivation layer, *Applied Physics Letters* 88(2) (2006) 022106.
- [4] B. Radisavljevic, A. Radenovic, J. Brivio, V. Giacometti, A. Kis, Single-layer MoS₂ transistors, *Nature nanotechnology* 6(3) (2011) 147-150.
- [5] P.K. Tien, *Light Waves in Thin Films and Integrated Optics*, *Appl. Opt.* 10(11) (1971) 2395-2413.
- [6] K. Nomura, H. Ohta, A. Takagi, T. Kamiya, M. Hirano, H. Hosono, Room-temperature fabrication of transparent flexible thin-film transistors using amorphous oxide semiconductors, *Nature* 432(25) (2004) 488-492.
- [7] X. Chen, S.S. Mao, Titanium dioxide nanomaterials: synthesis, properties, modifications, and applications, *Chemical reviews* 107(7) (2007) 2891-959.
- [8] I. Repins, M.A. Contreras, B. Egaas, C. DeHart, J. Scharf, C.L. Perkins, B. To, R. Noufi, 19.9%-efficient ZnO/CdS/CuInGaSe² solar cell with 81.2% fill factor, *Progress in Photovoltaics: Research and Applications* 16(3) (2008) 235-239.
- [9] I. Mizushima, P. Tang, H. Hansen, M. Somers, Residual stress in Ni-W electrodeposits, *Electrochimica Acta* 51(27) (2006) 6128-6134.
- [10] E. Chason, P. Guduru, Tutorial: Understanding residual stress in polycrystalline thin films through real-time measurements and physical models, *Journal of Applied Physics* 119(19) (2016).
- [11] M. Moon, J. Chung, K. Lee, K. Oh, R. Wang, A. Evans, An experimental study of the influence of imperfections on the buckling of compressed thin films, *Acta Materialia* 50(5) (2002) 1219-1227.
- [12] J. Wang, A. Evans, Effects of strain cycling on buckling, cracking and spalling of a thermally grown alumina on a nickel-based bond coat, *Acta Materialia* 47(2) (1999) 699-710.
- [13] I. Blech, Electromigration in thin aluminum films on titanium nitride, *Journal of Applied Physics* 47(4) (1976) 1203-1208.
- [14] E. Chason, N. Jadhav, F. Pei, E. Buchovecky, A. Bower, Growth of whiskers from Sn surfaces: Driving forces and growth mechanisms, *Progress in Surface Science* 88(2) (2013) 103-131.

- [15] W.D. Nix, B.M. Clemens, Crystallite coalescence: A mechanism for intrinsic tensile stresses in thin films, *Journal of Materials Research* 14(8) (1999) 3467-3473.
- [16] R.W. Hoffman, Stresses in thin films: The relevance of grain boundaries and impurities, *Thin Solid Films* 34 (1976) 185-190.
- [17] L.B. Freund, E. Chason, Model for stress generated upon contact of neighboring islands on the surface of a substrate, *Journal of Applied Physics* 89(9) (2001) 4866-4872.
- [18] F. Spaepen, Interfaces and stresses in thin films, *Acta Materialia* 48 (2000) 31-42.
- [19] E. Chason, B. Sheldon, L. Freund, J. Floro, S. Hearne, Origin of Compressive Residual Stress in Polycrystalline Thin Films, *Physical Review Letters* 88(15) (2002) 156103.
- [20] T. Zhi Luo, L. Guo, R.C. Cammarata, Real-time intrinsic stress generation during Volmer–Weber growth of Co by electrochemical deposition, *Journal of Crystal Growth* 312(8) (2010) 1267-1270.
- [21] G. Thurner, R. Abermann, Internal stress and structure of ultrahigh vacuum evaporated chromium and iron films and their dependence on substrate temperature and oxygen partial pressure during deposition, *Thin Solid Films* 192(2) (1990) 277-285.
- [22] B. Fu, G.B. Thompson, Compositional dependent thin film stress states, *Journal of Applied Physics* 108(4) (2010).
- [23] B. Fu, W. An, C.H. Turner, G.B. Thompson, In Situ Thin Film Growth Stresses during Chemical Ordering, *Physical Review Letters* 105(9) (2010) 096101.
- [24] T.M. Kaub, P. Felfer, J.M. Cairney, G.B. Thompson, Influence of Ni Solute segregation on the intrinsic growth stresses in Cu(Ni) thin films, *Scripta Materialia* 113 (2016) 131-134.
- [25] X. Zhou, T. Kaub, R.L. Martens, G.B. Thompson, Influence of Fe(Cr) miscibility on thin film grain size and stress, *Thin Solid Films* 612(1) (2016) 29-35.
- [26] B. Fu, G. Thompson, Compositional dependent thin film stress states, *Journal of Applied Physics* 108(4) (2010).
- [27] Y.G. Shen, Y.W. Mai, Q.C. Zhang, D.R. McKenzie, W.D. McFall, W.E. McBride, Residual stress, microstructure, and structure of tungsten thin films deposited by magnetron sputtering, *Journal of Applied Physics* 87(1) (2000) 177-187.
- [28] J. Vreštal, M. Materials Science International Team, Phase diagram of the Fe-W system: Datasheet from MSI Eureka in SpringerMaterials (http://materials.springer.com/msi/phase-diagram/docs/sm_msi_r_10_013708_01_full_LnkDia0), in: G. Effenberg (Ed.) MSI, Materials Science International Services GmbH, Stuttgart.
- [29] C. Taylor, D. Barlett, E. Chason, J. Floro, A Laser-Based Thin-Film Growth Monitor, *Industrial Physicist* 4(1) (1998) 25.
- [30] L. Wan, X.-x. Yu, X. Zhou, G. Thompson, Interrelationship of in situ growth stress evolution and phase transformations in Ti/W multilayered thin films, *Journal of Applied Physics* 119(24) (2016) 245302.
- [31] G.G. Stoney, The Tension of Metallic Films Deposited by Electrolysis, *Proceedings of the Royal Society of London. Series A* 82(553) (1909) 172-175.
- [32] J.G. Brons, G.B. Thompson, Orientation Mapping via Precession-Enhanced Electron Diffraction and Its Applications in Materials Science, *JOM* 66(1) (2013) 165-170.
- [33] P. Moeck, S. Rouvimov, E.F. Rauch, M. Véron, H. Kirmse, I. Häusler, W. Neumann, D. Bultreys, Y. Maniette, S. Nicolopoulos, High spatial resolution semi-automatic crystallite orientation and phase mapping of nanocrystals in transmission electron microscopes, *Crystal Research and Technology* 46(6) (2011) 589-606.
- [34] E.F. Rauch, J. Portillo, S. Nicolopoulos, D. Bultreys, S. Rouvimov, P. Moeck, Automated nanocrystal orientation and phase mapping in the transmission electron microscope on the basis of precession electron diffraction, *Zeitschrift für Kristallographie* 225(2-3) (2010) 103–109.

- [35] K. Thompson, D. Lawrence, D.J. Larson, J.D. Olson, T.F. Kelly, B. Gorman, In situ site-specific specimen preparation for atom probe tomography, *Ultramicroscopy* 107(2-3) (2007) 131-9.
- [36] X. Zhou, X.-x. Yu, T. Kaub, R.L. Martens, G.B. Thompson, Grain Boundary Specific Segregation in Nanocrystalline Fe(Cr), *Scientific Reports* 6 (2016) 34642.
- [37] Commercial product - Silicon half grids. Available at:
<http://www.microscopyconsumables.com/product-p/grd-0002.04.10.htm>.
- [38] M.W. Thompson, The contribution of collision cascades to sputtering and radiation damage, *Philosophical Transactions of the Royal Society a-Mathematical Physical and Engineering Sciences* 362(1814) (2004) 5-28.
- [39] M. Itoh, M. Hori, S. Nadahara, The Origin of Stress in Sputter-Deposited Tungsten Films for X-Ray Masks, *Journal of Vacuum Science & Technology B* 9(1) (1991) 149-153.
- [40] M. Lu, C.L. Chien, Structural and Magnetic-Properties of Fe-W Alloys, *Journal of Applied Physics* 67(9) (1990) 5787-5789.
- [41] T. Egami, Y. Waseda, Atomic Size Effect on the Formability of Metallic Glasses, *Journal of Non-Crystalline Solids* 64(1-2) (1984) 113-134.
- [42] C. Thompson, Structure evolution during processing of polycrystalline films, *Annu. Rev. Mater. Sci.* 30 (2000) 159-190.
- [43] L. Vegard, Die Konstitution der Mischkristalle und die Raumfüllung der Atome, *Zeitschrift für Physik* 5(1) (1921) 17-26.
- [44] J. Leib, R. Mönig, C. Thompson, Direct Evidence for Effects of Grain Structure on Reversible Compressive Deposition Stresses in Polycrystalline Gold Films, *Physical Review Letters* 102(25) (2009) 256101.
- [45] X. Zhou, G. Thompson, Influence of Solute Partitioning on the Microstructure and Growth Stresses in Nanocrystalline Fe(Cr) Thin Films, *Thin Solid Films Submitted* (2017).

CHAPTER 12

Stress Evolution and Microstructure in Ag-Al Thin Films

Tyler Kaub¹, Bhargava Samanthula², and Gregory Thompson¹

*¹Department of Materials and Metallurgical Engineering, University of Alabama,
Tuscaloosa, Alabama 35401*

²New Albany High School, New Albany, Ohio 43054

Abstract

Intrinsic stress measurements in the Al-Ag system explores how the formation of an intermetallic phase influences the intrinsic stress evolution and optical properties of the films. The addition of Al results in increasing compressive stress with increasing Al content. It was shown that the formation of Ag₂Al resulted in a reduction of grain size that corresponded with decreased surface roughness. Optical reflectivity measurements show that increasing Al content can blue shift the local minima observed in elemental Ag. This paper illustrates how precipitation of a second phase influences growth behavior.

Introduction

Metallic thin films have found a wide array of uses in nanoplasmonic and nanophotonic applications, electrical interconnections, and more recently in uses in optical cloaking and superlensing [1–4]. Of the metallic thin films Ag provides an excellence balance of optical reflectivity and high electrical conductivity as well as plasmonic properties making it well suited to the aforementioned applications[5]. However, with prolonged atmospheric exposure, a thin layer of corrosion may form on the surface, often referred to as tarnishing in the case of Ag. To improve the tarnishing resistance of Ag it can be alloyed with Al [6]. Al, like Ag, has high optical reflectivity and only suffers a small initial drop in this reflectivity when exposed to air [6]. Additionally, Al alloying can reduce cost and increase the hardness of a Ag film. In this paper, we explore the growth stresses, phase evolution, and optical reflective for a series of Ag-Al sputter deposited films. As an optical coating, the intrinsic growth stresses that result from the deposition process are critical as these stresses can lead to the film bulging, cracking, and/or catastrophic delamination.

The development of the intrinsic growth stress in metallic thin films is related to the growth mechanisms of the film along with the adatom mobility on the surface of the growing film. For metallic thin films deposited by physical vapor deposition on Si substrates Volmer-Weber [7] growth is the primary mechanism and is defined by the film nucleating three-dimensional islands on the substrate surface. This island nucleation is followed by growth, and subsequent island coalescence into a continuous film that continues to thicken. The stress evolution associated with this growth is typically a compressive-to-tensile evolution followed by either the retention of the tensile stress or the development of a secondary post-coalescence compressive stress. The deposition parameters and adatom mobility determine whether the film will remain tensile or become compressive. The initial compressive stress is believed to result

from the compression of the islands in response to minimizing the surface area in the early stages of nucleation. The tensile formation arises from elastic strain as these islands come in proximity to each other and elastically deform to reduce their surface area by forming new segments of grain boundary. The post-coalescence stress evolution is an area of active research with leading theories involving chemical potential differences between the surface and newly formed grain boundaries leading to the insertion of excess adatoms into the grain boundaries resulting in the compressive stress [8]. Other mechanisms to account for this compressive stress involve the inclusion of excess defects on the surface of the film [9], interaction forces between grains [10,11], and excess atoms trapped on surface ledges [12].

To alter the intrinsic stress state, deposition processing conditions are traditionally adjusted including substrate temperature [13,14], deposition rate [8,15] and sputter pressure [16,17]. Adjusting the deposition parameters modifies the microstructure of the film, particularly the fraction of grain boundary-to-grain size ratio, which has been shown to directly correlate with film stress [18,19]. This ratio, along with the mechanisms proposed in the above models for the origins of the post-coalescence compressive stress state, indicates that control of interfaces plays a vital role in film stress evolution. In more recent work, the use of alloying has also been shown to be a viable means of stress control. For example, in Cu(Ag) and Cu(V), an increase in solute content refines the grain size and adjusts the stress state [20].

The Ag-Al system is a classical precipitation case material with prior work showing two different precipitate structures at low temperature the hcp Ag_2Al γ phase and the Ag_3Al μ a complex cubic structure [21]. The Ag_2Al is known to nucleate out of the α -Al matrix from partial dislocations. Additionally, phase formation could have an impact on the surface roughness, grain size and optical properties of the thin film. Thus, depositing a system with no barrier to form a second phase presents an interesting opportunity for study to see how the nucleation of a second phase affects film properties and growth stress. To date there has not been a holistic study linking intrinsic film stress, composition and phase formation in Ag-Al.

Experimental details:

The Ag-Al films were deposited in an AJA ATC-1500 stainless-steel chamber through co-sputtering >99.95% pure elemental targets. The films were grown to a thickness of 300 nm onto a Si[100] substrate with a native surface oxide at room temperature. The base pressure prior to deposition was $< 1.33 \times 10^{-5}$ Pa and the working gas was ultrahigh purity Ar at 0.266 Pa. The sputtering power for the two elemental stress measurements was held constant, but resulted in differing deposition rates of 0.19 nm/sec for Al and 1.6 nm/sec for Ag. In the case of the alloys, the corresponding Al deposition rate was held constant at 0.19 nm/s and the Ag rate was varied to achieve the desired composition resulting in a range of Ag deposition rates of 0.19 nm/sec to 1.6 nm/sec. Determination of the growth rates was done by dividing the final film thickness by the growth time and verified by small angle x-ray reflectivity [22] using an X'Pert Philips x-ray diffractometer (XRD) operated with a $\text{Cu } K_\alpha$ source at 45 kV and 40 mA.

The growth stresses during deposition was measured *in situ* using a K-Space Associates multibeam optical sensor system (MOS). The MOS measures changes in wafer curvature using a reflected laser beam passed through an etalon to form an array of spots collected on a charge coupled device camera [23]. The reflected laser spots relative displacement is then used to calculate the average stress using the Stoney equation,

$$\sigma t_f = \frac{\delta d M_s t_s^2 \cos \alpha}{d 12L} \quad (1)$$

where M_s is the biaxial modulus of the substrate, t_s and t_f are the thickness of the substrate (250 μm) and thin film respectively, α is the angle of incidence of the laser beam (2°), L is the substrate detector optic length (88 cm) and $\frac{\delta d}{d}$ is the differential laser spot spacing on the detector [24].

Phase identification and grain size was determined using a combination of X-ray diffraction performed on a Bruker D8 Discover with a Co $K\alpha$ source and electron diffraction and imaging in a FEI TECNAI G2 Supertwin (scanning) transmission electron microscope ((S)TEM). Cross-sectional TEM foils were prepared using a focused ion beam lift out technique [25] using an FEI Quanta 3D dual beam FIB/SEM. Atom probe tomography (APT) was performed using a Cameca LEAP 3000XS Si in laser mode at a temperature of 50 K. Samples were prepared using a FIB liftout technique [26] using a FEI Quanta and a TESCAN Lyra Dual beam FIB/SEM for annular milling to sharpen the tips. The surface roughness along with a secondary grain size measurement was acquired using a Digital Instruments Dimension 3100 atomic force microscope in tapping mode. Reflectivity measurements were made using a Woolam VASE spectroscopic ellipsometer.

Results and Discussion:

The intrinsic stress measurements for the Ag, 79Ag21Al (at.%), 66Ag34Al (at.%), 34Ag66Al (at.%) and Al films are shown in Figure 1. All of the films displayed similar behavior until the post-coalescence regime were differences in the secondary compressive stress as the film thickened can be seen in Figure 1(a). All the alloy films appear to exhibit a constant slope as the film thickens indicating that the stress has reached a steady state. This indicates that there is little to no microstructural change with thickness occurring in the films and that stress trends with composition. The grain size displayed in Table 1 indicates that the grain size decreases as the Al content increases in the alloys. However, in the case of the elemental films pure Al has a much larger grain size than any of the other films likely due to its lower melting point compared to Ag. When comparing the grain size and stress of the films as the Al content increased in the alloys the stress became more compressive and the grain size decreases. Interestingly, the Al and Ag films exhibit nearly equivalent steady state stress while Al's grain size is nearly twice the size of Ag. The slight change in slope for the Al film stress indicates the Al film was likely undergoing grain growth during film deposition [27], which may have led to the difference in observed grain sizes. The stress relaxation data shown in Figure 1(b) illustrates that the silver and silver rich alloys have a similar amount of stress relaxation, whereas Al has a somewhat lower relaxation, \pm rich alloy may impede the mobility of the atoms. However, all of the films exhibit relatively low levels of stress recovery for high mobility materials indicating that driving force for precipitation may be altering the surface mobility of the adatoms.

Table 1: AFM showing the surface roughness versus the Al content

Al content (%)	Surface roughness (RMS)	Grain size (nm)
0	4.38 nm	59 ± 5.6
21	2.02 nm	58 ± 7.6

34	3.99 nm	56.6 ± 3.1
66	1.46 nm	39.7 ± 4.9
100	5.15 nm	133.8 ± 13.5

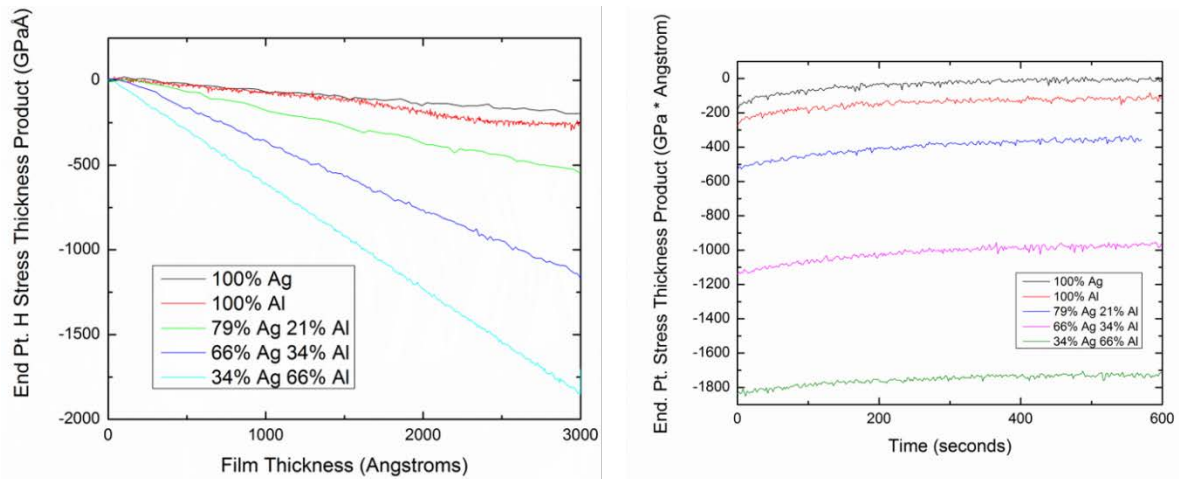


Figure 1. (a) Intrinsic growth stress for Ag-Al alloys and elemental films (b) Stress relaxation of films showing Al rich alloy has less relaxation

The X-ray diffraction results in Figure 2, show all of the films exhibit a primary 111 growth texture, which is common in FCC metals due to the 111 plane having the lowest surface energy. The Ag film exhibited some 200 and 311 growth texture as well indicating strain energy minimization is competing with surface energy minimization [28]. The 66Ag34Al alloy shows an extra peak corresponding to Ag_2Al which is an intermetallic phase predicted to form in this compositional region and is present over a wide range of Al composition 22.9 to 41.9 at% [21]. The Ag_2Al peak has a very low intensity in 79Ag21Al indicating that a small amount of the intermetallic is forming at that composition. HAADF images shown in Figure 3 revealed a distinct two phase microstructure with the Ag_2Al dispersed in an Aluminum rich matrix. An energy dispersive spectroscopy map of the region confirms the two phases observed in XRD with a Ag rich phase and Al rich phase forming.

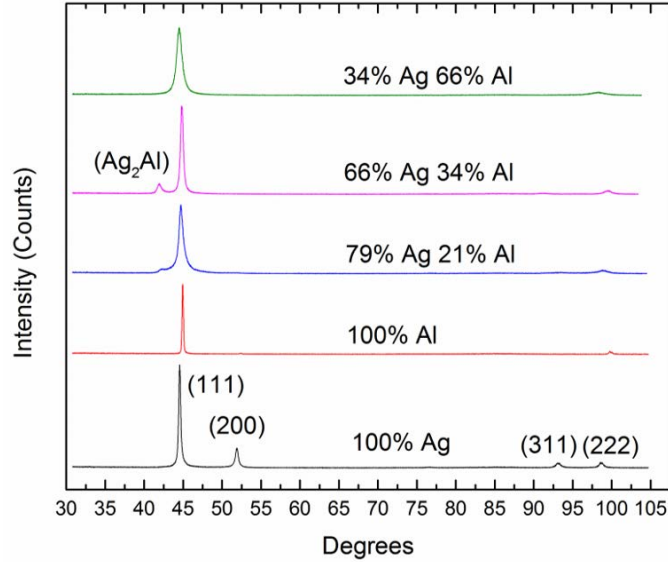


Figure 2. X-ray diffraction showing FCC 111 texture and formation of Ag_2Al in 66Ag34Al and 79Ag21Al films

Atom probe tomography performed on the 66Al33Ag sample and the atom maps are displayed in Figure 4. Upon examining the bulk composition of two APT tips evaporated from the sample the average bulk composition was 66.19 ± 0.007 at% Al, 29.95 ± 0.035 at% Ag and 3.4 ± 0.7 at% Ga. The large amount of Ga is due to the strong affinity between Ga and Al making it difficult to avoid this artifact from sample preparation. Examining the atom maps in Figure 3 where Al is shown in green and Ag in light blue it immediately becomes obvious that the samples are not homogeneous. The samples contain Al rich regions with an average composition of 92.2 ± 1.6 at% Al and 3.5 ± 1.5 at% Ag and regions that correspond to Ag_2Al with a composition of 40.98 ± 1.31 at% Al and 54.84 ± 2.29 at% Ag. Considering the composition for the intermetallic phase is not at stoichiometry it is believed that the intermetallic is forming over a wide range of compositional regions as indicated by the phase diagram. The prior TEM on the sample reflected a similar microstructure and chemical distribution indicating that while XRD did not detect an intermetallic peak microstructural characterization indicates the presence of an intermetallic phase.

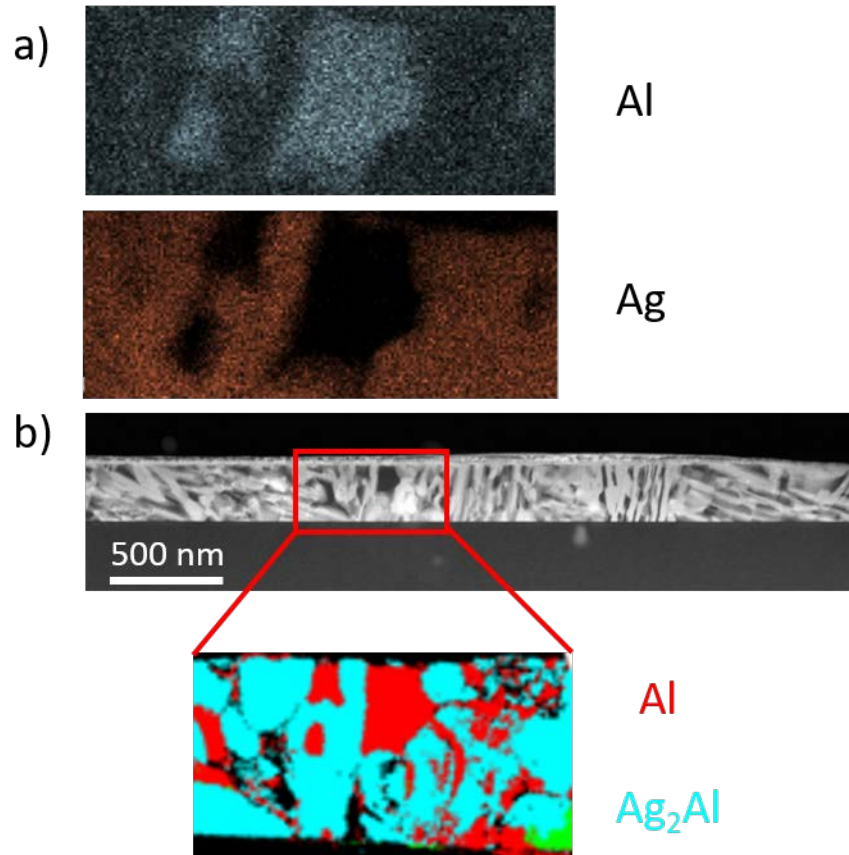


Figure 3. EDS Maps (a) showing formation of Al rich region and intermetallic region (b) HAADF image confirming phase separate as observed in XRD for Ag₃₄Al₆₆

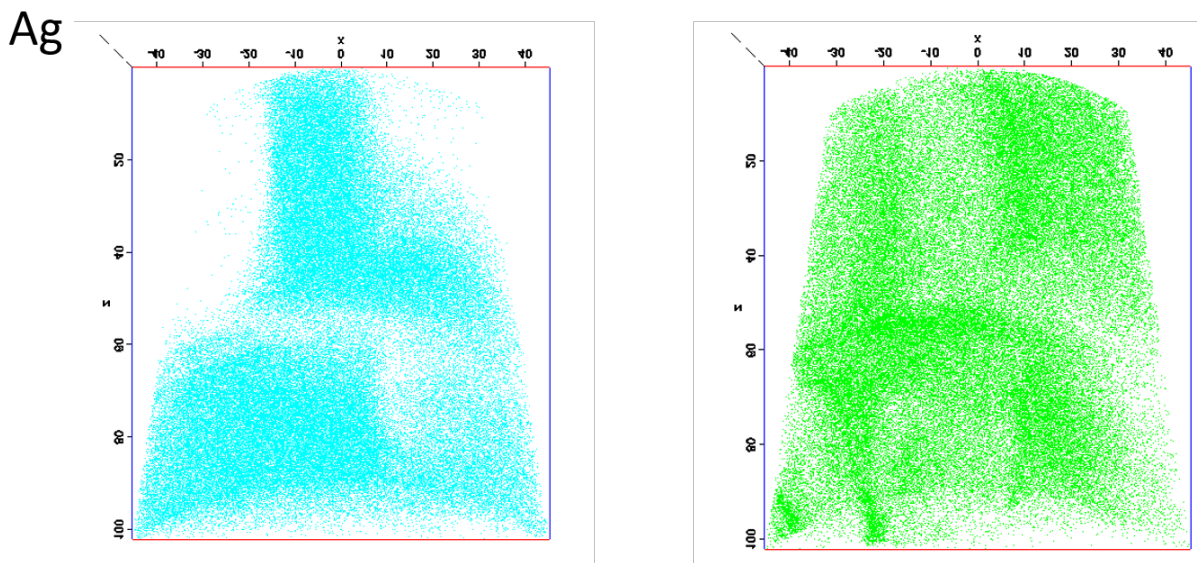


Figure 4. Atom maps of the 66Al₃₃Ag sample illustrating the phase separation occurring and highlighting the formation of Al rich regions.

Atomic force microscopy was performed to determine the effect of alloy content on the surface roughness of the films. Table 1 illustrates the surface roughness and grain size for the films as deposited. The alloy films all exhibited lower surface roughness than the elemental films. 66Ag34Al was the roughest of the alloy films followed by 79Ag21Al. The roughness data for the alloys correspond with the strength of the Ag_2Al peak observed by XRD indicating that as the amount of the intermetallic increased the films became rougher. Grain size did not appear to correspond with surface roughness, but a reduction in grain size was observed with increasing Al content in the alloys. Elemental Al had the largest grain size of all the films, which is likely due to it being deposited at approximately $0.5T_H$ its homologous temperature.

Reflectance measurements on the Ag-Al films are shown in Figure 5 for a wavelength range of 250-800nm. The Ag reflectance curve shows a reflectance minimum at 320nm which corresponds to the bulk plasma resonance of silver which has been reported to be 3.8 eV [29]. It has been previously reported that the bulk plasma frequency of Al is significantly larger than Ag resulting in a blue shift of the observed minima with increasing Al alloying content [29,30]. The Ag-Al alloy films in this study all exhibited this blue shift behavior and for 34Ag66Al film no minima was observed.

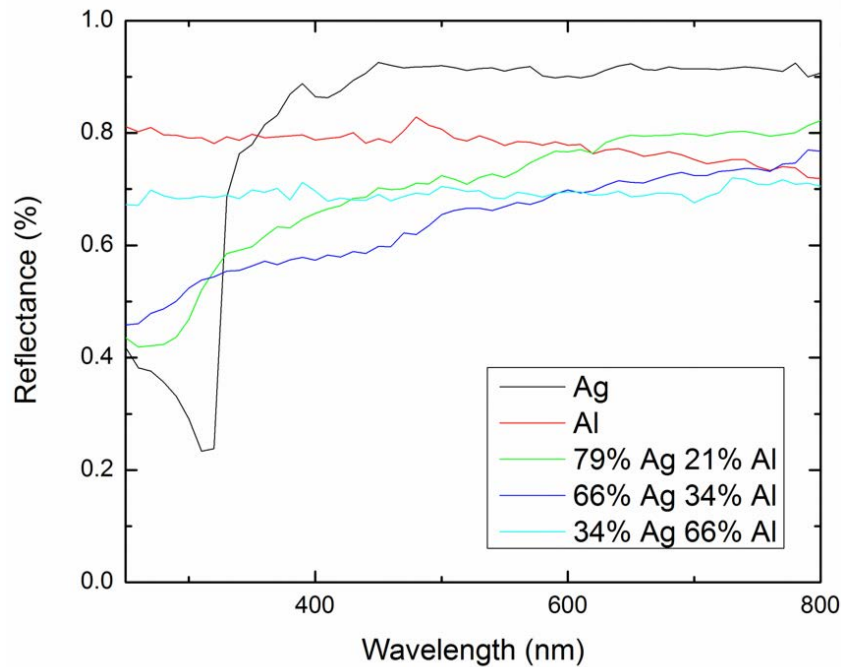


Figure 5. Optical reflectance spectra for Ag-Al films showing a minima around 300nm for the Ag rich films

The large increase in compressive stress in the alloy thin films indicates that the addition of a second element is changing the growth behavior. The compressive stress scales with grain size thus indicating Al additions result in grain refinement and thus more grain boundaries. The increase in grain boundary area results in more sites for excess adatom insertion and thus a larger

compressive stress. This excess adatom insertion can be facilitated in this system because Al has a lower surface energy 1.143 J/M^2 than Ag 1.246 J/M^2 [31] resulting in Al wanting to migrate to the interfaces in the system. In addition, to this Ag has a lower solubility in Al $\sim 1 \text{ at\%}$ versus Al in Ag $\sim 10 \text{ at\%}$. The differences in solubility are reflected in grain size refinement as Al content increases. This results in an increased driving force for phase separation and thus higher compressive stresses due to the resulting grain refinement. Finally, it appears that the compressive stress in the alloy films appears to be invariant to the formation of the Ag_2Al intermetallic forming.

The formation of Ag_2Al may not influence the stress behavior of the system because of its formation mechanism. Ag_2Al could be said to precipitate homogeneously because it has an energy of formation barrier of $\sim 0 \text{ KJ/mol}$ and the formation process relies on dislocations. In the system the dissociation of the $(1/2)[110]$ slip dislocation in either the Ag or Al fcc lattice into two $(1/6)\langle 112 \rangle$ partial dislocations results in a stacking fault that generates a strip of hcp lattice. When we deposit alloys in the compositional range where the $\gamma \text{ Ag}_2\text{Al}$ phase is stable all the stacking fault has to do is absorb some Ag atoms to replace Al to precipitate out the phase (cite book). The dynamic nature of sputter deposition can help facilitate the replacement of Al atoms and explains how a large amount of intermetallic was formed in the films during deposition.

The Al-Ag system shows that alloying Ag with Al increases the compressive stress with increasing Al content. It was found that addition of Al resulted in grain refinement leading to increased compressive stress and the formation of Ag_2Al had little to no influence on the compressive stress but did correspond with increased surface roughness. Increasing the Al content lowered the reflectivity of the films but blue shifted the minima observed in Ag resulting in a more uniform reflectivity over the measured range.

Acknowledgement:

The authors gratefully recognize ARO-W911NF-13-1-0436 for support of this research.

References:

- [1] S. A. Maier, *Plasmonics: Fundamentals and Applications* (Springer Science & Business Media, 2007).
- [2] A. K. Sarychev and V. M. Shalaev, *Electrodynamics of Metamaterials* (World Scientific, 2007).
- [3] D. O. S. Melville and R. J. Blaikie, *Opt. Express*, OE **13**, 2127 (2005).
- [4] J. B. Pendry, *Phys. Rev. Lett.* **85**, 3966 (2000).
- [5] R. E. Hummel, *Solar Energy* **27**, 449 (1981).
- [6] R. O. Adams, C. W. Nordin, F. J. Fraikor, and K. D. Masterson, *Thin Solid Films* **63**, 151 (1979).
- [7] E. Bauer, *Zeitschrift Für Kristallographie* **110**, 372 (1958).
- [8] E. Chason, B. W. Sheldon, L. B. Freund, J. A. Floro, and S. J. Hearne, *Phys. Rev. Lett.* **88**, 156103 (2002).
- [9] C. Friesen and C. V. Thompson, *Phys. Rev. Lett.* **89**, 126103 (2002).
- [10] A. González-González, G. M. Alonzo-Medina, A. I. Oliva, C. Polop, J. L. Sacedón, and E. Vasco, *Phys. Rev. B* **84**, 155450 (2011).

- [11] A. González-González, C. Polop, and E. Vasco, *Phys. Rev. Lett.* **110**, 056101 (2013).
- [12] F. Spaepen, *Acta Materialia* **48**, 31 (2000).
- [13] G. Thurner and R. Abermann, *Thin Solid Films* **192**, 277 (1990).
- [14] R. Koch, D. Hu, and A. K. Das, *Physical Review Letters* **94**, 146101 (2005).
- [15] A. L. D. Vecchio and F. Spaepen, *Journal of Applied Physics* **101**, 063518 (2007).
- [16] M. Pletea, W. Brückner, H. Wendrock, and R. Kaltofen, *Journal of Applied Physics* **97**, 054908 (2005).
- [17] M. Pletea, W. Brückner, H. Wendrock, R. Kaltofen, and R. Koch, *Journal of Applied Physics* **99**, 033509 (2006).
- [18] J. Leib, R. Mönig, and C. V. Thompson, *Phys. Rev. Lett.* **102**, 256101 (2009).
- [19] R. Koch, *Journal of Physics: Condensed Matter* **6**, 9519 (1994).
- [20] T. Kaub, R. Anthony, and G. B. Thompson, *Journal of Applied Physics* **122**, 225302 (2017).
- [21] A. J. McAlister, *Bulletin of Alloy Phase Diagrams* **8**, 526 (1987).
- [22] Y. Sasanuma, M. Uchida, K. Okada, K. Yamamoto, Y. Kitano, and A. Ishitani, *Thin Solid Films* **203**, 113 (1991).
- [23] Taylor, C., Bartlett, D., Chason, E., and Floro, J., *The Industrial Physicists* **4**, 25 (1998).
- [24] G. G. Stoney, *Proceedings of the Royal Society A: Mathematical, Physical and Engineering Sciences* **82**, 172 (1909).
- [25] L. A. Giannuzzi and F. A. Stevie, *Micron* **30**, 197 (1999).
- [26] K. Thompson, D. Lawrence, D. J. Larson, J. D. Olson, T. F. Kelly, and B. Gorman, *Ultramicroscopy* **107**, 131 (2007).
- [27] H. Z. Yu and C. V. Thompson, *Acta Materialia* **67**, 189 (2014).
- [28] C. V. Thompson, *Scripta Metallurgica et Materialia* **28**, 167 (1993).
- [29] D. A. Bobb, G. Zhu, M. Mayy, A. V. Gavrilenko, P. Mead, V. I. Gavrilenko, and M. A. Noginov, *Applied Physics Letters* **95**, 151102 (2009).
- [30] S. Auer, W. Wan, X. Huang, A. G. Ramirez, and H. Cao, *Applied Physics Letters* **99**, 041116 (2011).
- [31] W. R. Tyson and W. A. Miller, *Surface Science* **62**, 267 (1977).

CHAPTER 13

Role of Atomic Migration in Nanocrystalline Stability: Grain Size and Thin Film Stress States

Monica Kapoor and Gregory B. Thompson*

The University of Alabama

Department of Metallurgical & Materials Engineering

Tuscaloosa, AL USA 35487-0202

[*Gthompson@eng.ua.edu](mailto:Gthompson@eng.ua.edu)

Abstract

As the length scale of materials decreases to the nanometer regime, grain boundaries occupy a relatively larger volume fraction. Consequently, they play an important role in stabilizing nanocrystalline systems. This review looks at the role of solute segregation to grain boundaries in stabilizing such systems. In recent years, grain size stabilization from solute segregation has led to new types of thermodynamic stability maps as a materials design tool. We propose to extend and adapt these concepts of grain boundary solute segregation as a stabilizing effect to thin film stress states. A recent study on Fe-Pt alloy films, where one species enriched the boundaries, was shown to manipulate the stress from tensile-to-compressive as a function of composition. This suggests that intrinsic segregation can be used as a tunable variable to manipulate stress states, analogous to changing film processing parameters, such as deposition rate, pressure, etc. The application of such solute segregation is at the precipice of new opportunities in materials design of thin films.

1. Introduction

When the grain size of a material is reduced to nanometer regime, interfaces constitute a large part of the overall structure [1]. This is aptly illustrated in Fig. 1, which shows how the fraction of intercrystalline regions (the lattice volume near the grain boundaries which differs from the equilibrium structure), the grain boundaries, and the triple junctions (where three grains/crystals intersect) varies as a function of the grain size. When the grain size decreases from 100 nm to 3 nm, the grain boundary fraction increases from 3 % to 44 %, or, alternatively, a larger fraction of the atoms is at the interfaces. Consequently, nanocrystalline materials can and often

do exhibit different properties - such as crystallographic structure [2], solubility [3] or mechanical properties [4] - than their bulk forms.

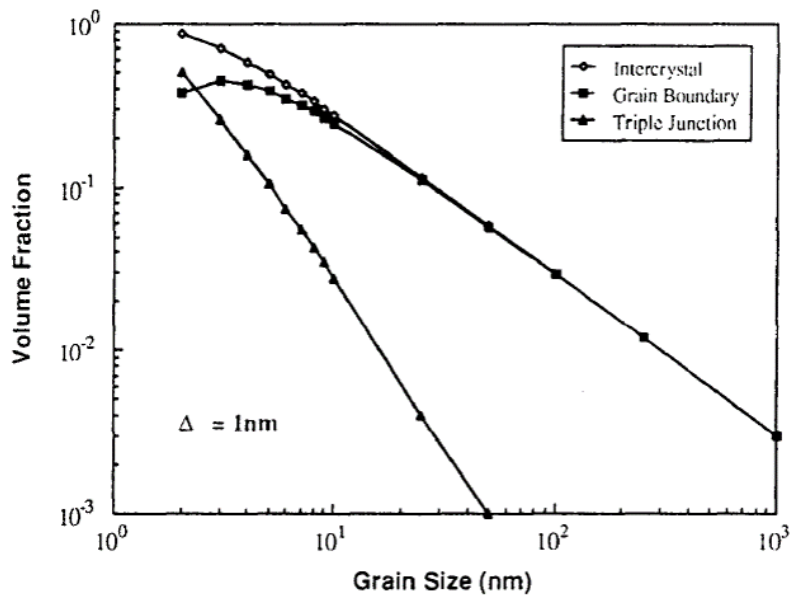


Fig. 1: Volume fraction of intercrystalline regions, grain boundary, and triple junctions as a function of grain size in nano-crystalline Fe [1].

These nanocrystalline materials are processed in a variety of methods, including physical or chemical vapor deposition and electro-deposition [5] as thin films as well as ball-milling and sintering of powders into monolithic forms [6]. In each case, the stability of the nanocrystalline structure is necessary for the processed material to maintain a desired set of properties or attributes. Understanding this nanocrystalline stability has been an area of active research for several decades [5, 7-9]. Most recently, several researchers across different disciplines have been addressing how atomic segregation to grain boundaries contributes to nanocrystalline stability.

The motivation of this review is to understand how such atomic migration and segregation to nanocrystalline grain boundaries evolves and contributes to the stability in thin films and nanocrystalline alloy materials. In particular, thin films and coatings are sensitive to delamination and cracking, which is a product of the residual stress [5]. Recent work in nanocrystalline alloys, in both thin film and monolithic forms, has shown that segregation to grain boundaries can have a stabilizing effect [10, 11]. These studies have primarily addressed stability against grain growth. Interestingly, the role of segregation has largely been overlooked as a

means to stabilize the stress state in nanocrystalline grains in post-coalesced thin films. In this review, the current status of atomic migration and segregation as a stabilizing effect on grain size and thin film stress states is addressed.

First, we will discuss how solute segregation to grain boundaries stabilizes grain size in nanocrystalline systems. The high surface area-to-volume ratio in such structures leads to a larger fraction of non-equilibrium grain boundary sites, altering the 'bulk' thermodynamics. A number of experiments on stabilizing nanocrystalline alloys, ranging from strongly segregating systems such as Ni-P to weakly segregating systems such as Ni-W, have provided new insights into the factors that contribute to stabilization [8, 10]. These efforts in conjunction with computational modeling have very recently culminated in thermodynamic stability maps which appear to be a promising design tool [12-16].

Second, we will discuss the role of grain boundaries in the stress generation in a growing thin film. The generation of intrinsic or residual stress in thin films has been debated upon for several years with recent experiments and simulations providing evidence to support the importance of grain boundaries in the stress evolution [17-27].

In both topics, the role of atomic migration into and out of a nanocrystalline boundary is paramount in the stability of the structure.

2. Segregation-induced nanocrystalline stability

In a polycrystalline system, the free energy will decrease by reducing the grain boundary area. This results in an inherent driving force to reduce the grain boundary area by grain growth and thereby creating instability with respect to the grain size. Two primary approaches have been used to stabilize the nanocrystalline alloys [6, 9, 28] – (1) The kinetic approach, which is pinning the boundaries to reduce their mobility. This pinning is accomplished by forming precipitates (Zener pinning), solute drag, and/or chemical ordering [29, 30]. Unfortunately, these approaches are overcome at high temperatures and the grain stability is lost [6, 11]. (2) The thermodynamic approach, which is stabilizing the nanocrystalline alloy by reducing the driving force for growth. This can be achieved by allowing a solute to segregate to the grain boundary and altering the thermodynamic energy balance [31-33]. This latter concept is the primary focus below.

1. Thermodynamics of grain size stabilization

Some 20 years ago, the concept of solute segregation to the grain boundaries to stabilize nanocrystalline alloys was proposed and eventually developed by other researchers [3, 7, 8, 10-

14, 16, 31-38]. One of the earliest attempts to study and quantify the effect of solute segregation was in Ni-P system [8, 35]. In a Ni-3.6 at. %P alloy, grain size increased from ~9 nm to ~25 nm after annealing at 400°C. The limited grain growth was attributed to P segregation [35] with atom probe tomography revealing that P was inhomogeneously distributed at the grain boundaries. Using a mass balance for the solute, Kirchheim group derived an equation which relates the solute content to the grain size by the empirical equation -

$$d(c_0) = \frac{\Delta}{1 - \left(\frac{c_0 - c_{gb}}{c_g - c_{gb}}\right)^{\frac{1}{3}}} \quad (1)$$

where d = grain size, Δ = grain boundary width, c_0 = bulk solute concentration, c_g = solute concentration in the grain interior, and c_{gb} = solute concentration at the grain boundary. This equation predicted that the stable grain size would decrease as a function of increasing P content. This relationship, with subsequent modifications by several other groups, has been shown to predict the stable grain sizes in Ni-P alloys as well as being consistent with the newer observations in Ni-W and Fe-Zr systems [7, 39].

This stabilization is explained by thermodynamics as follows [31, 33, 36]: The change in Gibbs free energy, G , of a polycrystalline material due to the change in grain boundary area, a , is given by -

$$dG = \gamma da \quad (2)$$

where γ = grain boundary energy. In single-component systems the grain boundary energy, γ , is positive, so the only way to lower the free energy is by reducing the grain boundary area, hence an inherent driving force for grain growth. However, if the grain boundary energy can somehow be reduced to zero, then there is no driving force and the system will be stable. This reduction in grain boundary energy can be accomplished in an alloy system by allowing a solute to segregate to the grain boundaries and alter γ [31, 33, 36]. The grain boundary energy due to segregation is then given as -

$$\gamma = \gamma_0 - \Gamma (\Delta G_{seg} + RT \ln X) \quad (3)$$

where γ_0 = grain boundary energy of the pure element, Γ = specific excess of solute atoms located at the grain boundary area, ΔG_{seg} = segregation energy, R = gas constant, T = temperature and X = global composition. This equation shows that grain boundary energy of a pure element, γ_0 , can be reduced by the energy needed to move the solute atoms to the grain boundary. With a

sufficiently high segregation energy, the solute excess can actually reduce the grain boundary energy, γ , to zero thereby eliminating the driving force for grain growth.

2. *Factors affecting stabilization*

Equation (3) has been fitted to Fe-P, Ni-P, and Pd-Zr experimental data and showed good agreement [32]. An outcome of that work demonstrated that as the solute content increased, the grain boundary reached a saturation value with respect to solute atoms it can accommodate. At this saturation point, a stable grain size was achieved [32, 36]. From the results of these particular systems, it was posited that solute segregation in a strongly segregating system will drive the grain boundary energy to zero [32].

More recently, Detor and Schuh reported similar grain size stabilization in Ni-W alloy, which is a weakly segregating system [7]. In such a system, the grain boundary energy would not necessarily have to be zero to achieve stabilization in contrast to prior rationalization for strongly segregating systems. Simulations on Ni-W alloys with 1, 5 and 20 at. % W showed that the tendency of a solute to segregate decreased as the solute concentration increased [10]. For a grain size of 4 nm, the enrichment factor (i.e. ratio of solute concentration at the grain boundary to that in the bulk) decreased from ~ 2.6 to ~ 1 as the bulk solute composition increased from 1 at. % to 20 at. %. This interestingly translated to enthalpy of segregation decreasing as a function of increasing bulk composition, as seen in Fig. 2 [10]. This composition-dependent segregation enthalpy had not been previously considered. This composition-dependent segregation enthalpy was now used to calculate the change in grain boundary energy in Ni-P and in Ni-W. They found that grain boundary energy does indeed go to zero in the Ni-P system but it was still positive in the Ni-W system. Thus, it is insufficient to only consider high enthalpy of segregation as the deciding factor for nanocrystalline stabilization. To rationalize this stabilization, other factors must be considered.

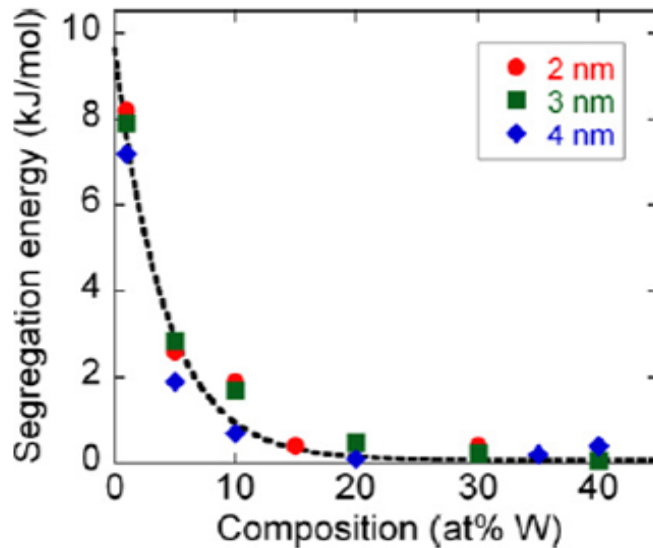


Fig. 2: Segregation energy as a function of bulk composition of W solute [10]. (color available on-line)

It has been proposed that not only energy of segregation but its relation to the energy of mixing determines nanocrystalline stability [14, 15]. For example, there are many systems with high energies of segregation, but at high solute concentrations or high temperatures these solutes agglomerate and form a phase separated microstructure which limits their use in nanocrystalline stabilization [11]. In contrast, there are many alloys with low segregation enthalpies which are successful nanocrystalline alloys, e.g. Ni-W [7]. The competition between these two energies must be considered. By plotting the alloys as a function of the enthalpy of mixing and enthalpy of segregation, a thermodynamic stability map for nanocrystalline alloys can be created [14-16]. These maps can be used as a tool to quickly screen a variety of alloys for nanocrystalline stability. Two general mapping schemes have been proposed and we review both of them below [14, 15].

3. Thermodynamic Stability Maps

Schuh's group used a modified regular nanocrystalline solution (RNS) model and included stability against phase separation as an input to develop the thermodynamic stability maps [12, 15]. The RNS model allows for distinct grain boundary and grain interior regions to be modeled as a system [38]. The RNS model was adapted to calculate segregation enthalpies (independent of grain boundary solute and temperature), which is not an easily available material property and is usually estimated. In their work they have considered ~ 2500 binary alloys and mapped these alloys as a function of enthalpy of mixing and enthalpy of segregation. Fig. 3 is one such

thermodynamic stability map with pink and green regions with a sliver region between the two in yellow. Each of these regions indicate different levels of stability [15]. The solute and the solvent are denoted by a combination of the elemental and geometrical symbols respectively. An alloy in the pink region is not stable as a nanocrystalline system, in the yellow region it is stable as a nanocrystalline system but not against phase separation, and in the green region is stable as a nanocrystalline system and against phase separation.

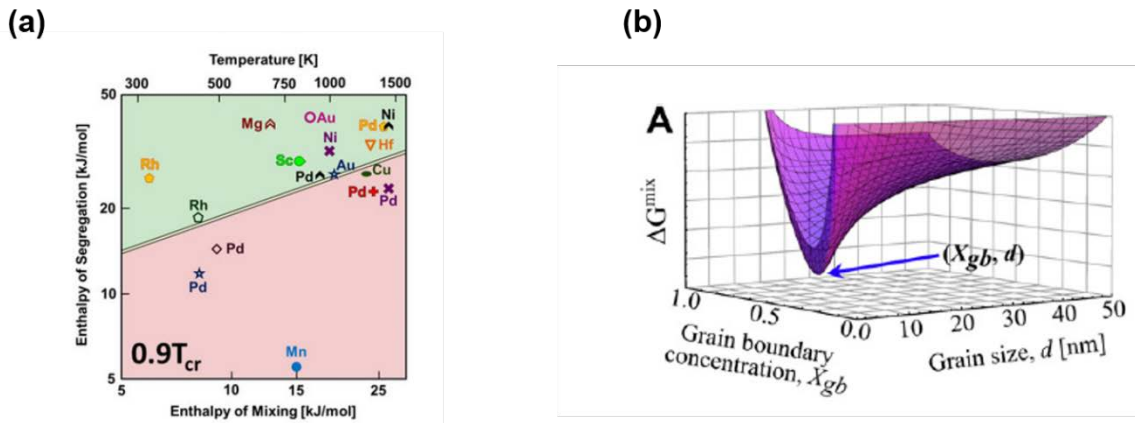


Fig. 3 (a): Thermodynamic stability map showing three regions of stability for various combinations of solute and solvent. The solute is denoted by the element symbol and the solvent by the geometrical symbols [15], (b) Free energy surface with the minimum showing the stable grain size at the bulk solute concentration, at which this surface was calculated [12]. (color available on-line)

To understand these maps, we will go through the highlights of how such a thermodynamic stability map

is obtained – (1) A free energy surface, shown in Fig. 3 (b), is computed in the grain boundary solute concentration and grain size space. If there is no minimum in this surface, then it cannot be stabilized as a nanocrystalline system, and will be plotted in the pink region of the thermodynamic stability map. For example, Mn with a solid blue circle in pink region indicates that Mn solute in Cu (denoted by the blue filled circle) cannot be stabilized as a nanocrystalline system. (2) If there is a minimum in the surface, then it will be stabilized as a nanocrystalline system, at the particular grain size and grain boundary composition. Fig. 3 (b) shows a surface with the minimum, marked by an arrow. If the minimum energy of this surface is lower than that of other possible bulk states, then this system is stable as a nanocrystalline system and against

phase separation and will be plotted in the green region in the map. For example, Au with the open magenta circle in the green region indicates that Au solutes in a Mo solvent alloy will be a stable nanocrystalline system. (3) If the minimum in the surface is not lower than other possible bulk states, then this system will be stable as a nanocrystalline system but not against phase separation.

These types of maps have led to some unexpected predictions. For example, consider the solute additions to W. In general, nanostructural stability has been estimated based on atomic size mismatch or solubility, which are indication of enthalpy of segregation. However, Sr in W has the highest atomic mismatch and Ag and Cu in W have the lowest solubility; but all three of these solutes are predicted to be unstable as nanocrystalline systems in reference [16]. Hence, these prior simple 'rules' do not necessarily provide the correct predictions.

Koch's group have modified the above RNS approach to develop a model specifically for strongly segregating systems [40]. They noted that Schuh group's model did not suitably scale the enthalpy of segregation by the grain boundary volume fraction. To date, Koch's group's modification has been applied to only a few systems (Fe-Zr, Cu-Zr, Cu-Nb, and Ni-W) with some experimental validation of those results [11].

Another set of thermodynamic stability maps has been developed by Darling *et al.* [14]. In their model, they assume no secondary phase precipitation, which is reasonable in a dilute limit. They modified the Wynblatt-Ku model for surface segregation by replacing the surface environment with a grain boundary interface. Darling *et al.* suggested that the elastic misfit between the solute and solvent induces solute segregation [28, 41]. Motivated by prior work on Pd-Zr and their work on Fe-Zr alloys, they used elastic size misfit energies as an indication of energy of segregation [13, 39]. To understand the utility of these maps, we will briefly consider the Fe-Zr alloy.

Fig. 4 (a) shows the normalized grain boundary energy as a function of the solute Zr in Fe for a series of grain sizes, with the calculation performed for 3 at. % Zr at 550°C. It can be seen that a grain size of 23.1 nm gives a zero grain boundary energy and will be the stable at 550°C. These modeling predictions are consistent with experimental grain size and calculated enthalpy of mixing for Fe- 4 at. % Zr [14]. Fig. 4(a) clearly indicates that the bulk solute concentration for stabilization will vary with grain size.

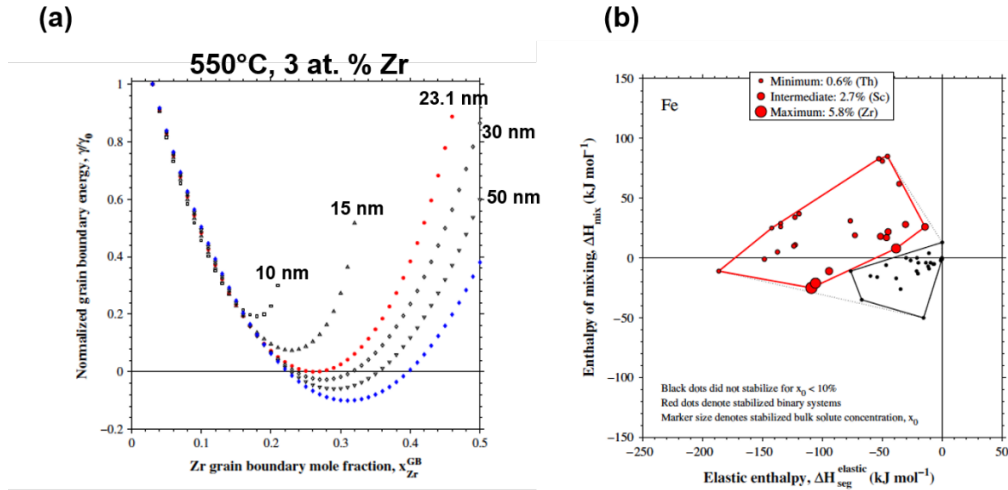


Fig. 4 (a): Normalized grain boundary energy calculated as a function of the grain boundary mole fraction of the solute, Zr, for a series of grain sizes in Fe-Zr, and (b) Stability map for nanocrystalline Fe that plots solutes (stable – red) as a function of enthalpy of mixing and elastic enthalpy. The size of the dot is proportional to the amount of solute needed to stabilize a grain size of 25 nm [14]. (color available on-line)

Taking this concept (obtaining zero grain boundary energy) and applying it to a series of solutes led to the conclusion that stable solutes are a function of elastic enthalpy and enthalpy of mixing. Plotting the solutes as a function of both resulted in stability maps of solutes for a given solvent. Fig 4(b) is such a map of the Fe solvent - with several different solutes – that will stabilize a grain size of 25 nm [14, 42]. The red dots represent the favorable or stabilizing solutes, with the size of the dot corresponding to the minimum amount of solute required to stabilize a particular targeted grain size, i.e. 25 nm in this case.

All of these maps fit the limited experimental data very well giving validity that both the enthalpy of mixing and segregation are critical material properties to determine stability. Though each of these groups approached the issue from a slightly different perspective, i.e. calculations of enthalpy of segregation (Shuch) compared to elastic enthalpy as an indication of enthalpy of segregation (Darlington *et al.*) In all systems, concomitant occurrence of a decreasing grain size with an increasing solute concentration has been used to identify a thermodynamic effect as the mechanism responsible for grain size stabilization.

More recently, Schuh group's has used Monte Carlo analysis to understand the experimental results on ball-milled nanocrystalline W-20 at.% Ti alloy. This alloy had ~20 nm grain sizes after annealing at 1100°C for a week as compared to ~600 nm grain size for an unalloyed W system. They found wide regions of solute depletion and enrichment with a periodicity consistent with the grain size and attributed the thermal stability to these regions of solute enrichment which they called 'grain boundary states'. These results indicate that there are more mechanisms and factors contributing to thermal stability than our current understanding [3, 43]. Clearly more rigorous experimentation is still needed to test the limits of these models.

In the next section, we will discuss how this concept of solute segregation to the grain boundaries can be adapted to stabilize and regulate the stress states in a nanocrystalline thin film.

3. Stress evolution in thin films

In the prior section, we established how the role of solutes in grain boundaries is critical in the stabilization of the grain size. When a thin film is deposited, and is not subjected to single crystal epitaxial growth conditions, a polycrystalline structure forms in the film. These grains are typically nanocrystalline and develop into a columnar morphology as the film thickens. The formation of these grains and their boundaries is a result of the nucleation and growth of isolated clusters which eventually impinge into each other creating these boundaries [5]. It has been found that the grain size correlates with the magnitude of the stress state in the thin film [5, 17, 19, 44]. Hence the stabilization of grain size is crucial to the stress evolution of a film.

In general, the stress state has then been controlled by regulating the grain size via processing, i.e. changing the deposition rate, substrate conditions, vacuum pressure, etc. [19, 22, 44, 45]. In this section of this review, an analogous link to section 2 is given where solute segregation can be now be used as another means of thin film stress state control. In particular, we will address recent models and experiments that discuss how atomic migration in and out of grain boundaries has a stabilizing effect on the nanocrystalline stress states.

1. Primer on film growth and stress evolution

As a thin film grows, three basic modes have been identified: (1) island or Volmer-Weber (2) layer or Frank-van der Merwe and (3) a combination of (1) and (2) termed Stranski-Krastanov [5]. In the Volmer-Weber mode, the island formation occurs because the atoms are more strongly bonded to each other than the substrate. As a result, the film exhibits an initial compressive stress as the atomic-scale migration of these atoms form embryonic islands that minimize surface area-

to-volumetric energies because of surface capillary effects [46]. Fig. 5 is a schematic of this early stage of growth with the slope of the curve indicating compression (negative) or tension (positive). The subsequent tensile stress originates from the elastic strain associated with the coalescence of these islands to minimize the grain boundary energy [47-49]. Films with low atomic mobility, such as Fe [44, 50], Cr [50], and Al [51], tend to retain the tensile condition with continued growth unless acted upon by external stimuli, such as thermal energy. For films with higher intrinsic mobility, the films can exhibit a return to compressive stress which can be partially reduced upon ceasing deposition. If the growth is interrupted at this compressive stress stage, the stress can relax [21, 44, 52]. Upon re-deposition, the compressive stress returns back to the nominal compressive stress measured during growth, hence being a reversible behavior. The mechanisms of post-coalescence compressive stress and stress relaxation are still under discussion.

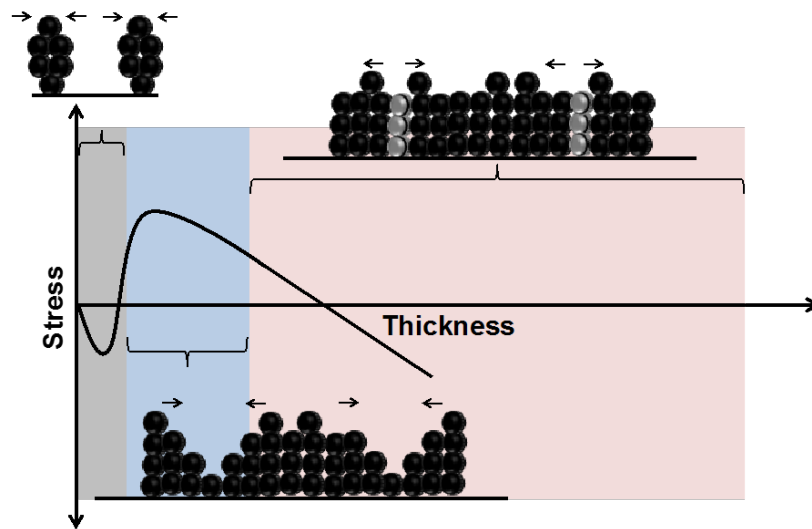


Fig. 5: Schematic cartoon of stress evolution during stress evolution. The grey region shows the initial stage where isolated islands/clusters form and are under compression due to surface capillary effects. The blue region shows the stage where the islands coalesce and form grain boundaries. The pink region represents onset of post-coalescence stress generation. The black dots represent atoms within the grains and grey dots represent atoms at grain boundary. (color available on-line)

Friesen and Thompson [52] proposed that the post-coalescence compressive stress is because of a locked adatom-surface interaction at the substrate. This concept of adatoms trapped

on surface ledges in contributing to the stress generation mechanism appears insufficient in explaining recent experimental results by Shin *et al.* [21]. Pao *et al.* reported the use of molecular dynamics simulations to study the influence of such defect densities, i.e. atomic surface steps and adatoms, on the film stress evolution [24]. From these results, it was concluded that the magnitude of stress due to such defect densities was inadequate to be the dominant mechanism for the observed compressive stress generation [24].

In other work, Koch *et al.* [44] observed that during film growth interruption, the value of the relaxation tensile component increased with thin film thickness and grain size. Thus, they proposed that recrystallization and grain growth played an important role in the latter stages of compressive stress evolution and relaxation. However, as pointed by Thompson *et al.* [53] and Spaepen *et al.* [54], the recrystallization process is not reversible and this mechanism failed to explain the reversible stress evolution during thin film growth interruption [20, 52].

As with Koch *et al.*'s observation, others have also reported experimental evidence that has shown a correlation in the magnitude of film stress with the grain size (or, inversely, the boundary area) [17, 19, 21, 23, 55]. To elaborate on this point, Thompson's group used Au films had a median in-plane grain size of 33, 56 and 94 nm and these were found to have tensile stress relaxation of 80, 46 and 29 MPa respectively [17]. In comparison, the control film, which was an epitaxial film with "infinite" grain size, showed a stress relaxation of less than 1 MPa. Further experimental work in other systems has also shown to exhibit this grain size and stress correlation. Flototto *et al.* reported Ag films deposited on two different substrates, with in-plane grain sizes of 43 nm and 19 nm, which showed a reversible stress change of 13 and 50 MPa respectively [19]. Abadias *et al.* reported that the finer the grain size in Mo films resulted in higher tensile stress recovery during coalescence [55]. From these collective experimental results, the grain boundary area appears to directly correlate to stress and the stress relaxation behavior.

To rationalize these results, an explanation by Chason *et al.* [18] has been proposed that the migration of atoms into and out-of the grain boundaries creates the compressive and relaxation stress recovery, which is developed in detail in the section below.

2. Adatom migration to grain boundaries

We will discuss the highlight of Chason's model with a typical stress-thickness product as a function of time plot, shown in Fig. 6. This plot of Cu films was obtained in the author's work and shows cycles of deposition/film growth (negative slope), interruption/when the deposition is ceased (positive slope), and resuming film growth (negative slope). For clarity, one representative

region each is labeled in Fig. 6. For high mobility atoms, Chason *et al.* hypothesized that the chemical potential on the surface is higher during deposition which provides a thermodynamic driving force for excess atom migration to the grain boundaries [20]. This causes a compressive stress in the grain boundary till the grain boundary saturates and a steady-state is achieved. This region of compression with negative slope is marked with a solid arrow in Fig. 6. When the growth was interrupted (deposition ceased), marked by a dashed arrow in Fig. 6, the chemical potential was lowered on the surface and ‘excess’ adatoms that diffused to the boundaries now flow out of the boundary to the surface and the compressive stress is relaxed (positive slope). When growth is resumed, the compressive stress returns back to the prior value (negative slope). This return to the former stress state is explained by the change in the chemical potential created from the deposition, which provides the driving force for the atoms back into the grain boundaries generating the renewed compressive stress.

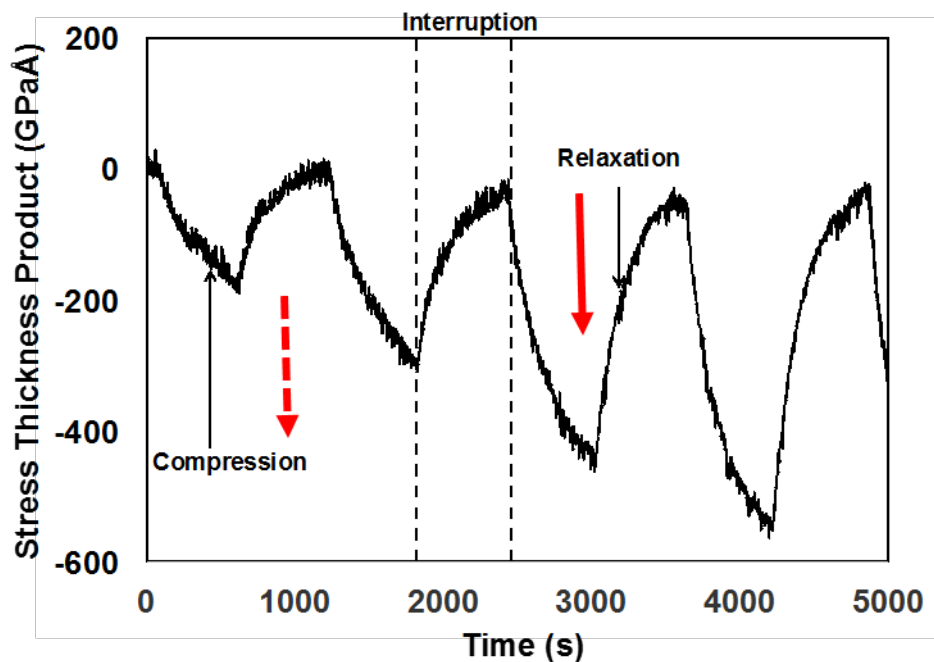


Fig. 6: Stress-thickness as a function of time for Cu films.

Hence, the driving force for the flux of atoms is chemical potential difference between the surface and the grain boundary given by -

$$\Delta\mu = \mu_s - \mu_{gb} = \Delta\mu_0 + \delta\mu_s + \sigma\Omega \quad (4)$$

where $\Delta\mu_0$ = difference between the surface and grain boundary chemical potential in absence of growth (usually negligible), $\delta\mu_s$ = increase in surface chemical potential because of the flux of deposited atoms and accounts for growth conditions, σ = stress across the grain boundary, and Ω

= atomic volume. This chemical potential difference is a balance of growth conditions and the stress in the film. This diffusion-based model predicts that the steady state stress in the film is a function of the tensile stress due to the formation of new grain boundaries and its stress relaxation is due to the atoms diffusing into grain boundaries or trapped in atomic ledges given by –

$$\sigma_{SS} = \frac{\sigma_i R - \sigma_0 \left[\frac{(\Delta\mu_0 + \delta\mu_s)}{kT} \right]}{R + \left[\frac{(\sigma_0 \Omega)}{kT} \right]} \quad (5)$$

where σ_i = tensile stress that develops as a result of the islands coalescing to form grain boundaries, R = normalized growth rate, σ_0 = compressive stress due to adding a single atom to the grain boundary, Ω = atomic volume, T = temperature.

If the steady-state stress is caused by atoms diffusing via grain boundaries, then the time taken to relax this stress (the steady-state time constant) should be proportional to the thickness of the film and the boundary area. In an experimental study with Sn, a very highly mobility species, the films relaxed completely and confirmed this hypothesis that grain boundary diffusion is a dominate mechanism in stress relaxation [21].

Chason *et al.* have recently extended this chemical potential based model to include both high and low mobility species [22]. In this modified model, the residual stress is now a function of a dimensionless parameter (D/LR) where D is an effective diffusivity related to the rate of jumping from the surface to the triple junction (grain boundary intersecting with the surface), R is the growth rate, and L is the grain size [22]. This dimensionless parameter reflects a balance of the kinetic processes, such as film growth, grain size and diffusion.

3. Adatom migration in alloy thin films

The prior sections have reviewed and established that grain size, hence grain boundary area, are dominant microstructural features in regulating the stress generation in thin films. Much of the prior experimental work has been in the use of single species films. In the case of an alloy, with atoms having different diffusivities and segregation energies, mix mobility of multi-component films can offer a tunable variable in the stabilization of stress in nanocrystalline grains. The use of intrinsic segregation in alloys has already been shown to have a stabilizing influence on the grain size via segregation to grain boundaries (Section 2).

Fu *et al.* reported composition-dependent tunable residual stress in Fe-Pt alloy films [56]. When deposited as pure elements, Fe (the low mobility species) retained a tensile stress whereas

Pt (the high mobility species) retained a compressive stress. In a mixed or alloy composition, the differences in mobility caused the higher mobility Pt to enrich the grain boundaries. Fig. 7 shows the effect of composition on the intrinsic stress evolution in the Fe-Pt films. As the amount of Pt was increased (> 35 % Pt), the films became more compressive and did not follow a linear rules of mixture behavior. A wide range of stress, from ~600 MPa for a pure Fe film to ~ - 1600 MPa for a film with ~ 21 at. % Fe, was observed as a function of composition. A near zero stress state is obtained in Fe_{0.65}Pt_{0.35} film, marked by the arrow in Fig. 7.

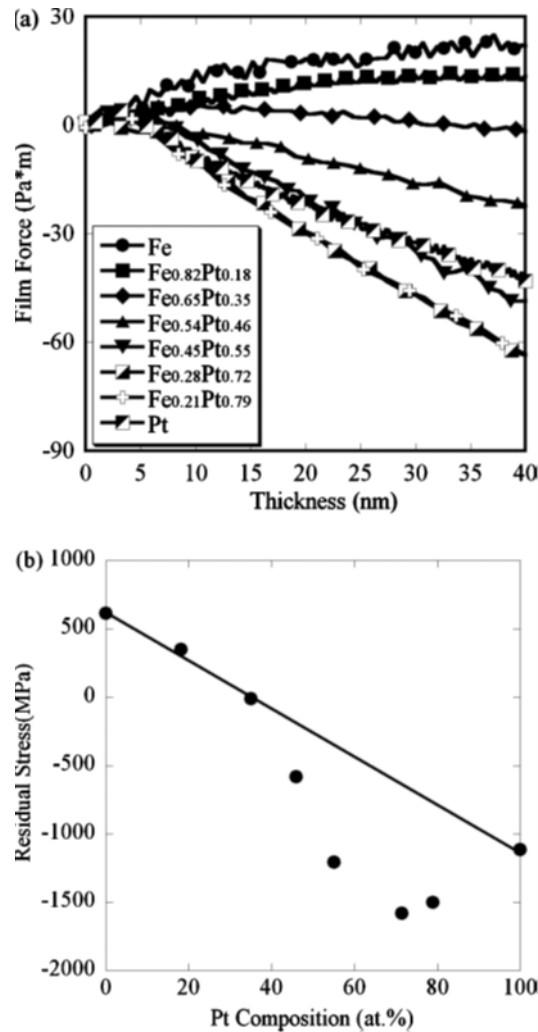


Fig.7: Effect of composition on residual stress evolution in a series of Fe-Pt alloy films. This illustrates the range of stress states as a function of composition with a zero stress state attained in Fe_{0.65}Pt_{0.35} film [56].

Fig. 8 shows the atom maps and 1D composition profiles for $\text{Fe}_{0.54}\text{Pt}_{0.46}$ and $\text{Fe}_{0.65}\text{Pt}_{0.35}$ films, obtained from atom probe tomography. Even in an Fe-rich film ($\text{Fe}_{0.54}\text{Pt}_{0.46}$), Pt being a highly mobile atom and having a thermodynamic preference to enrich an Fe interface is enriched at the grain boundaries. This is visually observed in the atom map seen in Fig. 8 (a) and quantified in 1D composition profile in Fig. 8 (b) [56, 57]. This is consistent with Chason’s model of grain boundary diffusion. This film was reported to have a compressive stress value of ~ -600 MPa. However, the $\text{Fe}_{0.65}\text{Pt}_{0.35}$ film was reported to have a near zero stress state. The atom map of $\text{Fe}_{0.65}\text{Pt}_{0.35}$ film, Fig. 8 (c), showed no visual enrichment of either Fe or Pt at the grain boundary as compared to the grain interior. This is quantified in Fig. 8 (d)’s 1D composition profile.

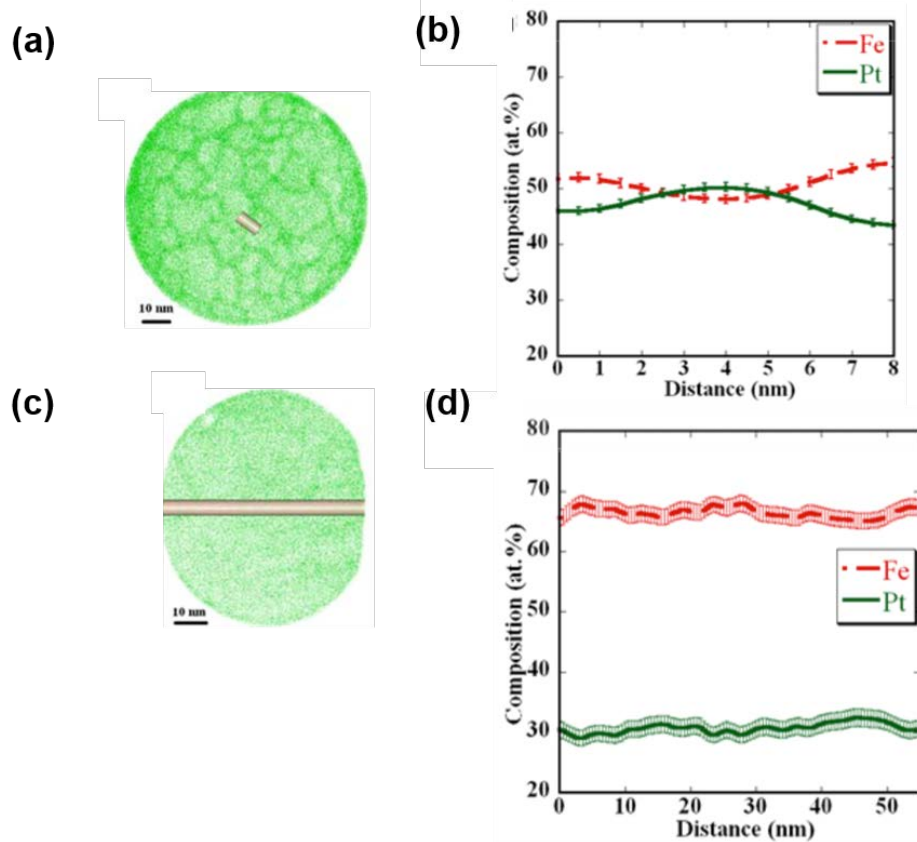


Fig.8: (a) Pt atom map of $\text{Fe}_{0.54}\text{Pt}_{0.46}$ alloy film, (b) 1D composition profile through the grain boundary, obtained from the cylindrical volume, showing Pt enrichment, (c) Pt atom map of $\text{Fe}_{0.65}\text{Pt}_{0.35}$ alloy film, and (d) 1D composition profile throughout the sample, obtained from the cylindrical volume, showing no preferential segregation [56] . (color available on-line)

The results of the Fe-Pt alloy film clearly indicates that stress can be tuned by controlling the number of atoms flowing to the grain boundaries which can be macroscopically tuned by the bulk composition and the enthalpy of mixing and segregation. By increasing the amount of Pt, a higher amount of Pt enriched the grain boundary making the film more compressive. Hence, the difference in the mobility of atoms resulted in a composition-dependent segregation of atoms to the grain boundaries and resulting stress state stabilization.

Using these two findings, Fu *et al.* modified Chason's equation for chemical potential difference which caused the flow of atoms to grain boundaries by adding μ_c , which describes the change in chemical potential due to segregation. This is important because the chemical potential difference is the driving force for the flux of atoms from the surface to the grain boundary. The chemical potential difference between the surface and grain boundary, in the presence of a species that segregates to the grain boundary, would be given as:

$$\Delta\mu' = \mu_s - \mu_{gb} = \Delta\mu_0 + \delta\mu_s + \sigma\Omega - \mu_c \quad (6)$$

where $\Delta\mu_0$ = difference between the surface and grain boundary chemical potential in absence of growth, $\delta\mu_s$ = increase in surface chemical potential because of the flux of deposited atoms, σ = stress along the grain boundary, Ω is the atomic volume, and μ_c = chemical potential rise in the grain boundary because of the segregation of chemically distinct, high mobility adatoms.

To the best of our knowledge, there are no other experimental results on the use of solutes to tune the stress states of a film. Millet *et al.* has reported Monte Carlo simulations of dopants in polycrystalline Cu where the stress changed. The use of such multispecies films, though more complex, has many advantages in elucidating the mechanisms associated with nanocrystalline stability in reference to stress generation. Similar to classic diffusion studies, where tracer atoms allow one to monitor the migration of species in a material, the use of different atoms here allows one to distinguish the chemical character of the nanocrystalline grain boundaries and its contribution to the stress evolution. Even more promising is the mixed mobility behavior between species providing the ability to tune the stress via solute enrichment of the boundaries. By controlling the grain boundary chemistry, a material dependent variable, rather than a processing dependent parameter, a potentially new means to regulate stresses in films is now available. Though these concepts appear simplistic, and film deposition is a complex and dynamical event, the promising results of section 2's thermodynamic stability maps (where

stable segregation is predicted) and the experimental results of Fe-Pt are proof-of-concepts where these two fields can be merged. The thermodynamic maps, developed in the nanocrystalline grain stabilization efforts of Section 2, can provide a design tool for thin films which could help tune the stress and reduce common film failures of delamination and cracking.

4. Conclusions and Future Challenges

As the length scale of materials decreases to the nanometer regime, unique changes in material properties occur. One of the primary changes is the larger fraction of grain boundaries rendering them an important part of stability of nanocrystalline materials. Consequently, the ability to stabilize nanocrystalline grains is an area of active research. This review has provided a summary of highlights in both the nanocrystalline grain growth and nanocrystalline thin film stress evolution. Though each field can be considered distinct; recent developments in understanding the stabilizing impact of solute segregation to grain boundaries provides for an exciting opportunity to unify the two fields. In particular, the grain size stabilization efforts have shown the interrelationship of enthalpy of mixing and enthalpy of segregation to control nano-grain growth. An outcome of this work has been thermodynamic stability maps. At this time, only a handful of systems have been experimentally studied to test and verify these maps as a robust design tool. Direct evidence of solute segregation at the grain boundaries has only been obtained in a very few studies and more computational and experimental work is needed.

Using these thermodynamic maps, one can select systems where grain boundary enrichment could be used to regulate the stress in thin films, which commonly have nanometer grain sizes. Recent experimental and modeling reports have provided a more clear understanding of how grain boundary area (e.g. grain size) contributes to the stress evolution of thin films. The migration of atoms into and out of grain boundaries has been proposed to control the stress and appears to be gaining traction as a valid model. A recent deposition of an alloy film, with one species enriching the boundaries, was shown to manipulate the stress from tensile to compression, with a zero-stress cross over. These results were understood using the grain boundary diffusion model. The zero-stress film showed no preference of segregation of either species to the boundary; this is suggestive that intrinsic material properties, such as thermodynamic segregation and mixing, will have a role in stress generation of thin films, analogous to the grain size stability against growth. To date, more work is still needed to firmly link these connections. Regardless of the current outstanding issues in either field, the promising

results of atomic migration to nanocrystalline grains in regulating their stability appears to be a fruitful area of emerging research for both experiments and modeling.

Acknowledgments:

G.B. Thompson thanks Prof. M. O'Keefe of Missouri Science & Technology for the invitation to write this review. M. Kapoor gratefully acknowledges the support from Sandia National Laboratories through the Department of Energy Office of Basic Energy Sciences and G.B. Thompson acknowledges support from the Army Research Office, grant W911NF1310436, Dr. Suveen Mathaudhu, program manager

References

- (1). G. Palumbo, S. J. Thorpe, et al. *On the contribution of triple junctions to the structure and properties of nanocrystalline materials*. Scripta Metallurgica et Materialia **24** (1990) 1347-1350.
- (2). G. B. Thompson, R. Banerjee, et al. *Phase stability of bcc Zr in Nb/Zr thin film multilayers*. Acta Materialia **51** (2003) 5285-5294.
- (3). T. Chookajorn, C. A. Schuh. *Nanoscale segregation behavior and high-temperature stability of nanocrystalline W–20at.% Ti*. Acta Materialia **73** (2014) 128-138.
- (4). T. J. Rupert, W. Cai, et al. *Abrasive wear response of nanocrystalline Ni–W alloys across the Hall–Petch breakdown*. Wear **298-299** (2013) 120-126.
- (5). R. Koch. *The intrinsic stress of polycrystalline and epitaxial metal thin films*. Journal of Physics: Condensed Matter **6** (1994) 9519-9550.
- (6). C. C. Koch, R. O. Scattergood, et al. *High temperature stabilization of nanocrystalline grain size: Thermodynamic versus kinetic strategies*. Journal of Materials Research **28** (2013) 1785-1791.
- (7). A. Detor, C. A. Schuh. *Tailoring and patterning the grain size of nanocrystalline alloys*. Acta Materialia **55** (2007) 371-379.
- (8). B. Farber, E. Cadel, et al. *Phosphorus segregation in nanocrystalline Ni-3.6 at. % P alloy investigated with the tomographic atom probe (TAP)*. Acta Materialia **48** (2000) 789-796.
- (9). A. Detor, C. A. Schuh. *Microstructural evolution during the heat treatment of nanocrystalline alloys*. Journal of Materials Research **22** (2007) 3233-3248.
- (10). A. Detor, C. A. Schuh. *Grain boundary segregation, chemical ordering and stability of nanocrystalline alloys: Atomistic computer simulations in the Ni–W system*. Acta Materialia **55** (2007) 4221-4232.
- (11). K. A. Darling, B. K. VanLeeuwen, et al. *Thermal stability of nanocrystalline Fe–Zr alloys*. Materials Science and Engineering: A **527** (2010) 3572-3580.
- (12). H. A. Murdoch, C. A. Schuh. *Stability of binary nanocrystalline alloys against grain growth and phase separation*. Acta Materialia **61** (2013) 2121-2132.
- (13). K. A. Darling, B. K. VanLeeuwen, et al. *Stabilized nanocrystalline iron-based alloys: Guiding efforts in alloy selection*. Materials Science and Engineering: A **528** (2011) 4365-4371.
- (14). K. A. Darling, M. A. Tschopp, et al. *Mitigating grain growth in binary nanocrystalline alloys through solute selection based on thermodynamic stability maps*. Computational Materials Science **84** (2014) 255-266.

- (15). H. A. Murdoch, C. A. Schuh. *Estimation of grain boundary segregation enthalpy and its role in stable nanocrystalline alloy design*. Journal of Materials Research **28** (2013) 2154-2163.
- (16). T. Chookajorn, H. A. Murdoch, et al. *Design of stable nanocrystalline alloys*. Science **337** (2012) 951-4.
- (17). J. Leib, R. Mönig, et al. *Direct Evidence for effects of grain structure on reversible compressive deposition stresses in polycrystalline gold films*. Physical Review Letters **102** (2009) 256101-4.
- (18). C.-W. Pao, S. Foiles, et al. *Thin film compressive stresses due to adatom insertion into grain boundaries*. Physical Review Letters **99** (2007) 36102-1-4.
- (19). D. Flötotto, Z. M. Wang, et al. *Effect of adatom surface diffusivity on microstructure and intrinsic stress evolutions during Ag film growth*. Journal of Applied Physics **112** (2012) 043503-1-9.
- (20). E. Chason, B. Sheldon, et al. *Origin of compressive residual stress in polycrystalline thin films*. Physical Review Letters **88** (2002) 156103-1-4.
- (21). J. W. Shin, E. Chason. *Compressive stress generation in Sn thin films and the role of grain boundary diffusion*. Physical Review Letters **103** (2009) 056102-1-4.
- (22). E. Chason, J. W. Shin, et al. *Kinetic model for dependence of thin film stress on growth rate, temperature, and microstructure*. Journal of Applied Physics **111** (2012) 083520-1-10.
- (23). D. Magnfält, G. Abadias, et al. *Atom insertion into grain boundaries and stress generation in physically vapor deposited films*. Applied Physics Letters **103** (2013) 051910-1-4.
- (24). C.-W. Pao, D. Srolovitz, et al. *Effects of surface defects on surface stress of Cu(001) and Cu(111)*. Physical Review B **74** (2006) 155437-1-8.
- (25). M. J. Buehler, A. Hartmaier, et al. *Atomistic and continuum studies of crack-like diffusion wedges and associated dislocation mechanisms in thin films on substrates*. Journal of the Mechanics and Physics of Solids **51** (2003) 2105-2125.
- (26). C.-W. Pao, D. Srolovitz. *Stress and morphology evolution during island growth*. Physical Review Letters **96** (2006) 186103-1-4.
- (27). S. J. Hearne, J. A. Floro. *Mechanisms inducing compressive stress during electrodeposition of Ni*. Journal of Applied Physics **97** (2005) 014901-1-6.
- (28). C. C. Koch, R. O. Scattergood, et al. *Stabilization of nanocrystalline grain sizes by solute additions*. Journal of Materials Science **43** (2008) 7264-7272.
- (29). E. Nes, N. Ryum, et al. *On the Zener drag*. Acta Metallurgica **33** (1985) 11-22.
- (30). J. W. Cahn. *The impurity-drag effect in grain boundary motion*. Acta Metallurgica **10** (1962) 789-798.
- (31). J. Weissmuller. *Alloy effects in nanostructures*. Nanostructured Materials **3** (1993) 261-272.
- (32). F. Liu, R. Kirchheim. *Nano-scale grain growth inhibited by reducing grain boundary energy through solute segregation*. Journal of Crystal Growth **264** (2004) 385-391.
- (33). J. Weissmuller. *Some basic notions on nanostructured solids*. Materials Science and Engineering: A **179-180** (1994) 102-107.
- (34). J. Weissmuller, P. Bunzel, et al. *Two phase equilibrium in small alloy particles*. Journal of Materials Research **9** (1994) 4-7.
- (35). T. Hentschel, D. Isheim, et al. *Nanocrystalline Ni-3.6 at. % P and its transformation sequence studied by atom-probe field ion microscopy*. Acta Materialia **48** (2000) 933-941.
- (36). R. Kirchheim. *Grain coarsening inhibited by solute segregation*. Acta Materialia **50** (2002) 413-419.
- (37). F. Liu, R. Kirchheim. *Grain boundary saturation and grain growth*. Scripta Materialia **51** (2004) 521-525.

- (38). J. Trelewicz, C. A. Schuh. *Grain boundary segregation and thermodynamically stable binary nanocrystalline alloys*. Physical Review B **79** (2009) 94112-1-13.
- (39). K. A. Darling, R. N. Chan, et al. *Grain-size stabilization in nanocrystalline FeZr alloys*. Scripta Materialia **59** (2008) 530-533.
- (40). M. Saber, H. Kotan, et al. *Thermodynamic stabilization of nanocrystalline binary alloys*. Journal of Applied Physics **113** (2013) 063515-1-10.
- (41). P. C. Millett, R. P. Selvam, et al. *Stabilizing nanocrystalline materials with dopants*. Acta Materialia **55** (2007) 2329-2336.
- (42). M. A. Atwater, K. A. Darling, A Visual Library of Stability in Binary Metallic Systems: The Stabilisation of Nanocrystalline Grain Size by Solute Addition: Part 1 (No. ARL-TR-6007), 2012, DTIC#ADA561871.
- (43). T. Chookajorn, C. A. Schuh. *Thermodynamics of stable nanocrystalline alloys: A Monte Carlo analysis*. Physical Review B **89** (2014) 64102-1-10.
- (44). R. Koch, D. Hu, et al. *Compressive stress in polycrystalline Volmer-Weber films*. Physical Review Letters **94** (2005) 146101-1-4.
- (45). R. Abermann, R. Koch. *The internal stress in thin silver, copper and gold films*. Thin Solid Films **129** (1985) 71-78.
- (46). R. C. Cammarata, T. M. Trimble, et al. *Surface stress model for intrinsic stresses in thin films*. Journal of Materials Research **15** (2000) 2468-2474.
- (47). W. D. Nix, B. M. Clemens. *Crystallite coalescence- A mechanism for intrinsic tensile stresses in thin films*. Journal of Materials Research **14** (1999) 3467-3473.
- (48). R. W. Hoffman. *Stresses in thin films: The relevance of grain boundaries and impurities*. Thin Solid Films **34** (1976) 185-190.
- (49). L. B. Freund, E. Chason. *Model for stress generated upon contact of neighboring islands on the surface of a substrate*. Journal of Applied Physics **89** (2001) 4866-73.
- (50). G. Thurner, R. Abermann. *Internal stress and structure of ultrahigh vacuum evaporated Cr and Fe films and their dependence on substrate temperature and oxygen partial pressure during deposition*. Thin Solid Films **192** (1990) 277-285.
- (51). M. Pletea, R. Koch, et al. *In situ stress evolution during and after sputter deposition of Al thin films*. Journal of Physics: Condensed Matter **21** (2009) 225008-1-8.
- (52). C. Friesen, S. C. Seel, et al. *Reversible stress changes at all stages of Volmer-Weber film growth*. Journal of Applied Physics **95** (2004) 1011-20.
- (53). C. Friesen, C. V. Thompson. *Comment on "Compressive Stress in Polycrystalline Volmer-Weber Films"*. Physical Review Letters **95** (2005).
- (54). A. L. Shull, F. Spaepen. *Measurements of stress during vapor deposition of copper and silver thin films and multilayers*. Journal of Applied Physics **80** (1996) 6243-56.
- (55). G. Abadias, A. Fillon, et al. *Real-time stress evolution during early growth stages of sputter-deposited metal films: Influence of adatom mobility*. Vacuum **100** (2014) 36-40.
- (56). B. Fu, G. B. Thompson. *Compositional dependent thin film stress states*. Journal of Applied Physics **108** (2010) 043506-1-6.
- (57). B. Yang, M. Asta, et al. *Equilibrium Monte Carlo simulations of A1-L10 ordering in FePt nanoparticles*. Scripta Materialia **53** (2005) 417-422.

Publications:

In print -

- Xuyang Zhou and Gregory B. Thompson “Influence of solute partitioning on the microstructure and growth stresses in nanocrystalline Fe(Cr) thin films” *Thin Solid Films* **648** (2018) 83-93: 10.1016/j.tsf.2018.01.007
- Grégory Abadias, Eric Chason, Jozef Keckes, Marco Sebastiani, Gregory B. Thompson, Etienne Barthel, Gary L. Doll, Conal E. Murray, Chris H. Stoessel, and Ludvik Martinu “Review Article: Stress in thin films and coatings: Current status, challenges, and prospects” *Journal of Vacuum Science & Technology A: Vacuum, Surfaces, and Films* **36**, 020801 (2018); doi:10.1116/1.5011790 **From the leading work on alloy design of stress evolution, Prof. Thompson was asked to join other leading researchers in film stress evolution to participate in a review article on the status of the field. Through the support of this grant, Prof. Thompson was able to particulate and references the grant in the acknowledgement section.*
- Olivia K. Donaldson, Khalid Hattar, Tyler Kaub, Gregory B. Thompson, and Jason R. Trelewicz “Solute stabilization of nanocrystalline tungsten against abnormal grain growth” *Journal of Materials Research* **33**(1) (2017) 68-80: 10.1557/jmr.2017.296 **From the stress evolution work in W(Ti), the team was asked to collaborate with Prof. J. Trelewicz in the growth of a series of similar films at U of Alabama, as well as providing characterization of them, for a series of studies on thermal stability. This paper references this grant for the support to do this collaborative research.*
- Tyler Kaub and Gregory B. Thompson “Ti segregation in regulating the stress and microstructure evolution in W-Ti nanocrystalline films” *Journal of Applied Physics* **122**(8) (2017) 085301: 10.1063/1.4991880
- Tyler M. Kaub, Ryan Anthony, and Gregory B. Thompson “Intrinsic stress response of low and high mobility solute additions to Cu thin films” *Journal of Applied Physics* **122** (2017) 225302: 10.1063/1.5008269
- Xuyang Zhou and Gregory B. Thompson “Linking experimental solute segregation specificity in nanocrystalline alloys to computational predictions” *Microsc. Microanal.* **23** (suppl. 1) 2017, 704-705: 10.1017/S1431927617004184
- C. Sterwerf, T. Kaub, C. Deng, G.B. Thompson, L. Li "Deformation mode transitions in amorphous-Cu₄₅Zr₅₅/ crystalline-Cu multilayers" *Thin Solid Films* **626** (2017) 184-189: 10.1016/j.tsf.2017.02.035 **Based on Dr. Kaub and Prof. Thompson's work on stress evolution in Cu thin films, they were asked to fabricate and characterize a series of Cu and glassy CuZr films by Prof. Lin Li. Through the support of this grant, which is acknowledge, this synergistic work to the proposed studies were done in this collaboration.*

- X. Zhou, Xuyang Zhou, Xiao-xiang Yu, Tyler Kaub, Richard L. Martens, and Gregory B. Thompson “Grain Boundary Specific Segregation in Nanocrystalline Fe(Cr)” *Scientific Reports* **6** (2016) 34642: 10.1038/srep34642
- T.M. Kaub, P. Felfer, J.M. Cairney, and G.B. Thompson “Influence of Ni solute segregation on the intrinsic growth stresses in Cu(Ni) thin films” *Scripta Materialia* **113** (2016) 131-134: 10.1016/j.scriptamat.2015.10.010
- X. Zhou, T. Kaub, R.L. Martens, and G.B. Thompson “Influence of Fe(Cr) miscibility on thin film grain size and stress” *Thin Solid Films* **612** (2016) 29-35: 10.1016/j.tsf.2016.05.024
- M. Kapoor and G.B. Thompson “Role of atomic migration in nanocrystalline stability: Grain size and thin film stress states” *Current Opinion in Solid State and Materials Science* **19** (2015) 138-146: 10.1016/j.cossms.2014.11.001
- G.B. Thompson, M. Kapoor, T. Kaub, B. Boyce, B. Clarke, K. Darling, P. Felfer, and J. Cairney “Investigations into solute stabilizing effects in nanocrystalline materials: an atom probe characterization study” *Microsc. Microanal.* **21** (suppl. 3) 2015, 357-358: 10.1017/S1431927615002585

Under-review/preparation:

- Xuyang Zhou and Gregory B. Thompson “The influence of alloy atoms interactions on thin films stress” submitted to Applied Surface Science (2018)
- Xuyang Zhou, Xiaoxiang Yu, David Jacobson, and Gregory B. Thompson “Molecular dynamic study of the stress generation during thin film growth” submitted to Physical Review B (2018)
- Xuyang Zhou and Gregory B. Thompson “*In situ* TEM observations of initial oxidation behavior in Fe-rich Fe-Cr alloys” submitted to Journal of Materials Science (2018).
- Xuyang Zhou and Gregory B. Thompson “Phase and Microstructural evolution in sputtered Fe-Cr films” submitted to Materialia (2018)
- Tyler Kaub, Zhaoxia Rao, Eric Chason, and Gregory B. Thompson “The Influence of Deposition Parameters on the Stress Evolution of Sputter Deposited Copper” submitted to Surface Coatings and Technology (2018)
- Tyler Kaub, Bhargava Samanthula, and Gregory Thompson “Stress Evolution and Microstructure in Ag-Al Thin Films” to be submitted to J. Vac. Sci. Techn. A (2018)

Graduation

On May 4th, 2018, Professor Thompson mentored Drs. Tyler Kaub and Xuyang (Rhett) Zhou to their doctoral degrees. Each of these students were supported by this grant.



Tyler Kaub (left) and Xuyang Zhou (right) at the University of Alabama graduation ceremony.

Outreach

Through the support of this grant, Professor Thompson was a recipient of supplementary funds to allow both high school and undergraduate interns to work on this research during the summer months. This enabled them to be given an opportunity to be introduced to opportunities in STEM, with some of these students' contributions sufficient for co-authorship on papers supported by this work. At the end of each summer, the students collected their data and displayed that in a Nanoscience and Engineering Science Fair for other interns during the summer at UA. These students include the following:

Bhargava Samanthula – New Albany High School, New Albany, Ohio - HSAP 2015

Mason McKechnie – University of Alabama - URAP 2015

Ryan Anthony – Northridge High School, Tuscaloosa AL - HSAP 2016

Jaeden Joyner – Northridge High School, Tuscaloosa AL - HSAP 2017

Morgan Ross - University of Alabama - URAP 2017



Collage of images of various high school and undergraduate interns, supported through this grant, working in the lab and presenting their findings.

Awards:

2017 – Professor Gregory B. Thompson was recognized at The Minerals Metals and Materials Society Brimacombe Medalist, with the citation reading “ For notable contributions in linking analytical microscopy with phase and property studies across materials and length scales, commitment to STEM education, and service to TMS.”

2017 – Graduate student Xuyang (Rhett) Zhou was the Microscopy Society of America Student Award winner for his work “Linking Experimental Solute Segregation Specificity in Nanocrystalline Alloys to Computational Predictions”

2014 – Professor Gregory B. Thompson was awarded the Blackmon-Moody Outstanding Professor of the Year – *The Frederick Moody Blackmon and Sarah McCorkle Moody Outstanding Professor Award is presented annually to a UA faculty member judged to have made extraordinary research contributions that reflect credit on the individual, his or her field of study and on the University. It was created by Frederick Moody Blackmon of Montgomery to honor the memory of his grandmother, Sarah McCorkle Moody of Tuscaloosa*



Xuyang (Rhett) Zhou receiving recognition of his research done under this grant at the Annual Microscopy Society of America meeting, August 2017.

Synergy with ARL labs:

Through the support of this award, Professor Thompson has been able to engage with Drs. Kris Darling and B. Chad Hornbuckle at the Army Research Laboratory in the areas of nanocrystalline stability and characterization. Specifically, Professor Thompson's group has been able to provide detailed characterization of nano-scale oxide dispersive alloys being prepared by the Army Research Lab as well as a Cu-based nanogranular stabilized microstructures. The results of which have generated the following papers and new areas of research investigation.

- Dallin J. Barton, Chaitanya Kaleb, B. Chad Hornbuckle, Kristopher A. Darling, Kiran N. Solanki, Gregory B. Thompson "Microstructure and dynamic strain aging behavior in oxide dispersion strengthened 91Fe-8Ni-1Zr (at%) alloy" *Materials Science & Engineering A* 725 (2018) 503–509 10.1016/j.msea.2018.04.016
- K.A. Darling, M. Kapoor, H. Kotan, B.C. Barton, S.D. Walck, G.B. Thompson, M.A. Tschopp, and L.J. Kecskes "Structure and mechanical properties of Fe-Ni-Zr oxide dispersion strengthened (ODS) alloys" *Journal of Nuclear Materials* 467 (2015) 205-213: 10.1016/j.jnucmat.2015.09.011
- M. Kapoor, T. Kaub, K. A. Darling, B.L. Boyce, and G.B. Thompson "An atom probe study on Nb solute partitioning and nanocrystalline grain stabilization in mechanically alloyed Cu-Nb" *Acta Materialia* 126 (2017) 564-575: 10.1016/j.actamat.2016.12.057 (specifically sites this award)

Presentations:

2017

- Xuyang Zhou and Gregory B. Thompson “*Linking Experimental Solute Segregation Specificity in Nanocrystalline Alloys to Computational Predictions*” Microscopy & Microanalysis August 6-10, 2017, St. Louis MO
- T.M. Kaub, D, Jacobson, and GB Thompson “*Influence of Chemical Interface Structure on Thin Film Stress Evolution*” Materials Science & Technology 2017, Pittsburg, PA
- Xuyang Zhou, Tyler Kaub, Florian Vogel, Ryan Anthony, and Gregory B. Thompson “*Correlative Precession Electron Diffraction and Atom Probe Tomography Characterization of Cluster Formations in Nanocrystalline Cu(V)*” Southeastern Microscopy Conference Athens, GA May 24-26, 2017
- Xuyang Zhou, Tyler Kaub, Florian Vogel, Ryan Anthony, and Gregory B. Thompson “*Correlative Precession Electron Diffraction and Atom Probe Tomography Characterization of Cluster Formations in Nanocrystalline Cu(V)*” Southeast Microscopy (SEM) Conference, Athens, Georgia, May 24-26, 2017 (Oral presentation – finalist for the Ruska Award Competition)

2016

- Tyler Kaub, David Jacobson, and Gregory B. Thompson “Use of Solute Segregation to Tune Intrinsic Stress States in Metallic Thin Films” Joint ICMCTC-SVC Workshop on Stress Evolution in Thin Films and Coatings: from Fundamental Understanding to Control, Rosemont, IL October 2-5, 2016 (Poster presentation)
- Xuyang Zhou, Tyler Kaub, and Gregory B. Thompson “Influence of Phase Separation on the Microstructure and Growth Stresses in Nanocrystalline Fe(Cr) Thin Films” Joint ICMCTC-SVC Workshop on Stress Evolution in Thin Films and Coatings: from Fundamental Understanding to Control, Rosemont, IL October 2-5, 2016 (Oral presentation)
- X. Zhou, XX Yu, T Kaub, RL Martens, and GB Thompson “Revealing Specific Grain Boundary Segregation Behavior in Nanocrystalline Fe(Cr)” Atom Probe Tomography & Microscopy 2016, Gyeongju, South Korea, June 12-17, 2016 (Poster presentation)
- X. Zhou, XX Yu, T Kaub, RL Martens, and GB Thompson “Specific Grain Boundary Character Segregation in Nanocrystalline Fe(Cr) Thin Films” EBSD 2016, The University of Alabama, Tuscaloosa, AL (Poster presentation)

2015

- Gregory B. Thompson “Nanoscale Stability: *An investigation of how intermixing and segregation stabilizes nanocrystalline phases*” Department of Chemical Engineering Invited Seminar, University of Melbourne, Australia, April 21st, 2015
- Gregory B. Thompson, Monica Kapoor, Tyler Kaub, Brad Boyce, Blythe Clark, Kris Darling, Peter Felfer and Julie Cairney “Investigation into the solute stabilizing effects in nanocrystalline materials: An atom probe characterization study” Microscopy & Microanalysis, Portland, OR August 2-6, 2015

- X. Zhou T Kaubm RL Martens, and GB Thompson “Growth stress evolution in low adatom mobility Fe(Cr) thin films” American Vacuum Society 62nd International Symposium, October 18-23, 2015, San Jose, CA (Oral presentation)
- T. Kaub, P. Felfer, J Cairney, and GB Thompson “Influence of Ni solute segregation on thin film growth stress states in Cu(Ni)” Center for Materials for Information Technology (MINT), Fall Industrial Review, October 27th, 2015, The University of Alabama (Poster presentation)
- X. Zhou, XX Yu, T Kaub, RL Martens, and GB Thompson “Specific Grain Boundary Character Segregation in Nanocrystalline Fe(Cr) Thin films” Center for Materials for Information Technology (MINT), Fall Industrial Review, October 27th, 2015, The University of Alabama (Poster presentation)
- GB Thompson “Interfacial Solute Segregation Effects on Nanocrystalline Thin Film Growth Stress Evolution” Materials Science & Technology 2015, Columbus, OH, October 4-8th, 2015 (Oral presentation)

2014

- Gregory B. Thompson, Tyler Kaub, Bianzhu Fu, X.X. Yu and Monica Kapoor “Manipulation of Nanocrystalline Stress States via Solute Grain Boundary Segregation” The Atom Probe Tomography & Microscopy Meeting (International Field Emission Society), Stuttgart, Germany August 31st – September 5 2014
- Poster presentation - Gregory B. Thompson, Li Wan, Tyler Kaub, and Xiao-Xiang Yu “Influence of Interfaces on the Intrinsic Growth Stresses in Nanoscale Metallic Thin Films” The 7th International Meeting on Multi-scale Materials Modeling (MMM), October 6-10th, 2014, Berkeley CA
- Gregory B. Thompson, Bianzhu Fu, Tyler Kaub, Xuyang Zhou, Monica Kapoor, and Xiao-xiang “Solute Segregation in Manipulating Intrinsic Stress States in Metallic Thin Films” Materials Science & Technology, Pittsburg, PA October 12 – 16, 2014
- Tyler Kaub, Xiao-xing Yu, and Gregory B. Thompson “Solute segregation in the manipulation of intrinsic stress states in alloy thin films” Materials Research Society Fall Meeting, November 30th – December 5, 2014

The Influence of Solute Additions on Intrinsic Stress in Thin Films

PhD Defense

Tyler Kaub

Committee:

Chair: Gregory B. Thompson¹, Luke Brewer¹, Amber Genau²,
Subhadra Gupta¹, Mark Weaver¹

¹*The University of Alabama Department of Metallurgical & Materials Engineering
Tuscaloosa, Alabama, USA*

²*The University of Alabama at Birmingham Department of Materials Science and Engineering
Birmingham, Alabama, USA*

Acknowledgments:

Army Research Office, ARO-W911NF-13-1-0436



Outline

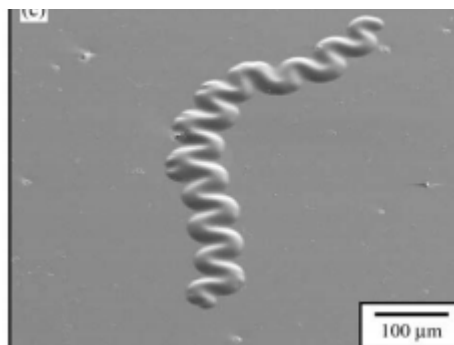
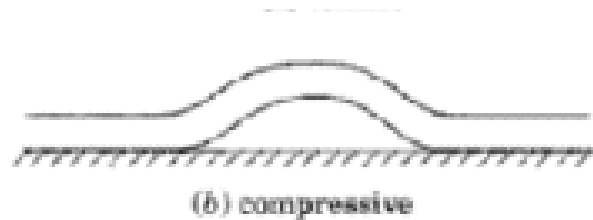
- Primer on Thin Film Stress Evolution
- Stress and Processing Conditions in Sputter Deposited Cu
- Weakly Segregating Solute addition to Cu
- Highly Segregating Solutes in Cu
- Non-Cu Highly Segregating System
- Conclusions

Stress in Thin Films

Stress is a long standing issue

X. *On the Properties of Electro-deposited Antimony.* By G. GORE, Esq.
Communicated by Dr. TYNDALL, F.R.S.

Received December 10,—Read December 10, 1857.



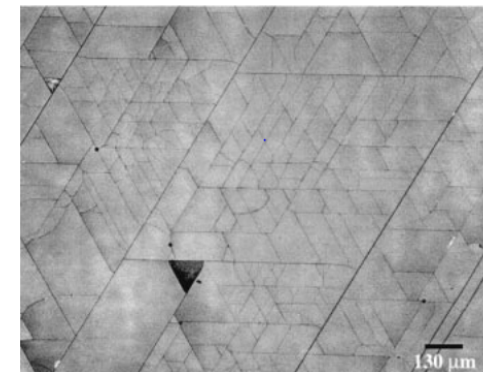
Buckling

The Tension of Metallic Films deposited by Electrolysis.

By G. GERALD STONEY.

(Communicated by the Hon. C. A. Parsons, C.B., V.-P.R.S. Received January 16,
—Read February 4, 1909.)

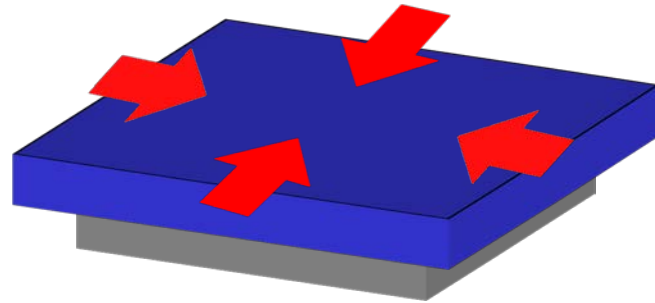
**Stoney discovered film can be in tension
or compression with no external load**



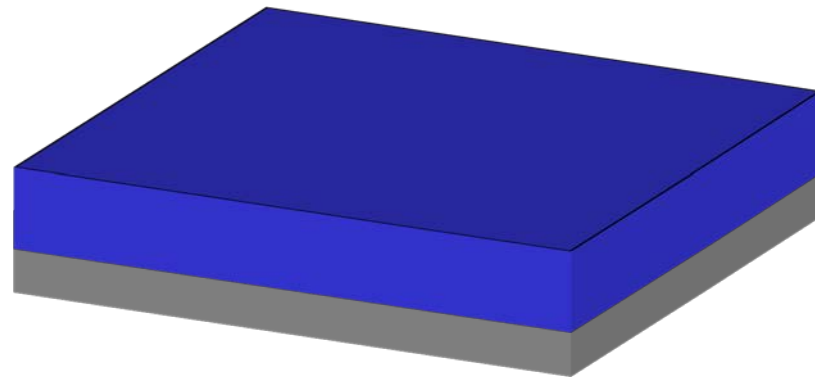
Cracks



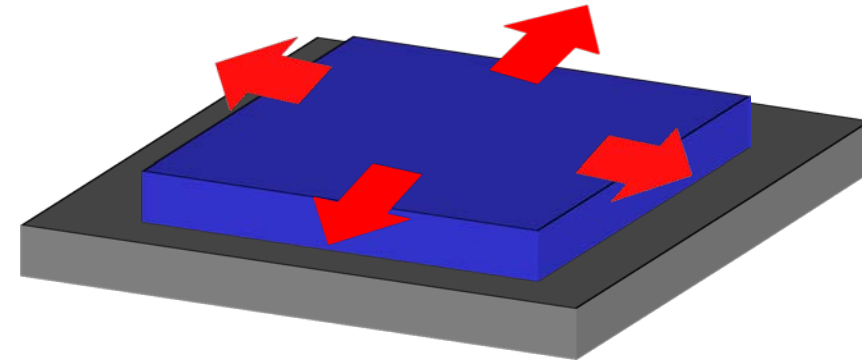
The lateral dimensions of the film are fixed by the rigid substrate



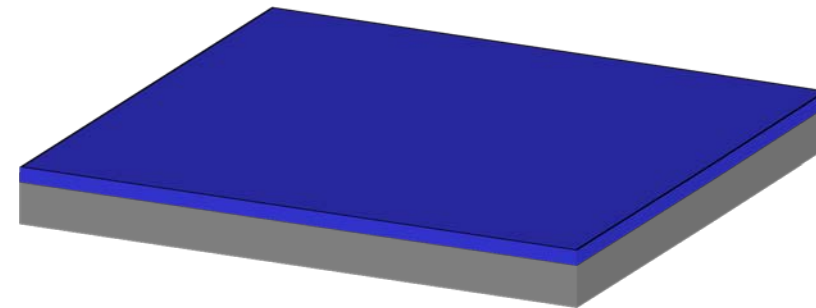
Layer $>$ substrate



Compressive Stress State

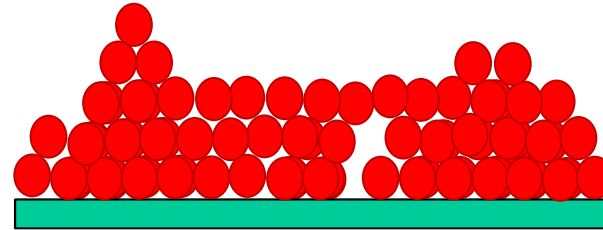


Layer $<$ substrate

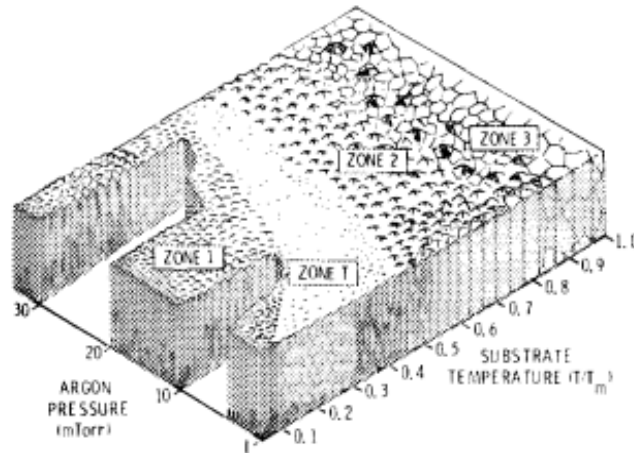


Tensile Stress State

Thin Film Growth and Structure



Structure zone diagram



Thornton, JVST A, 4, 3059 (1986)

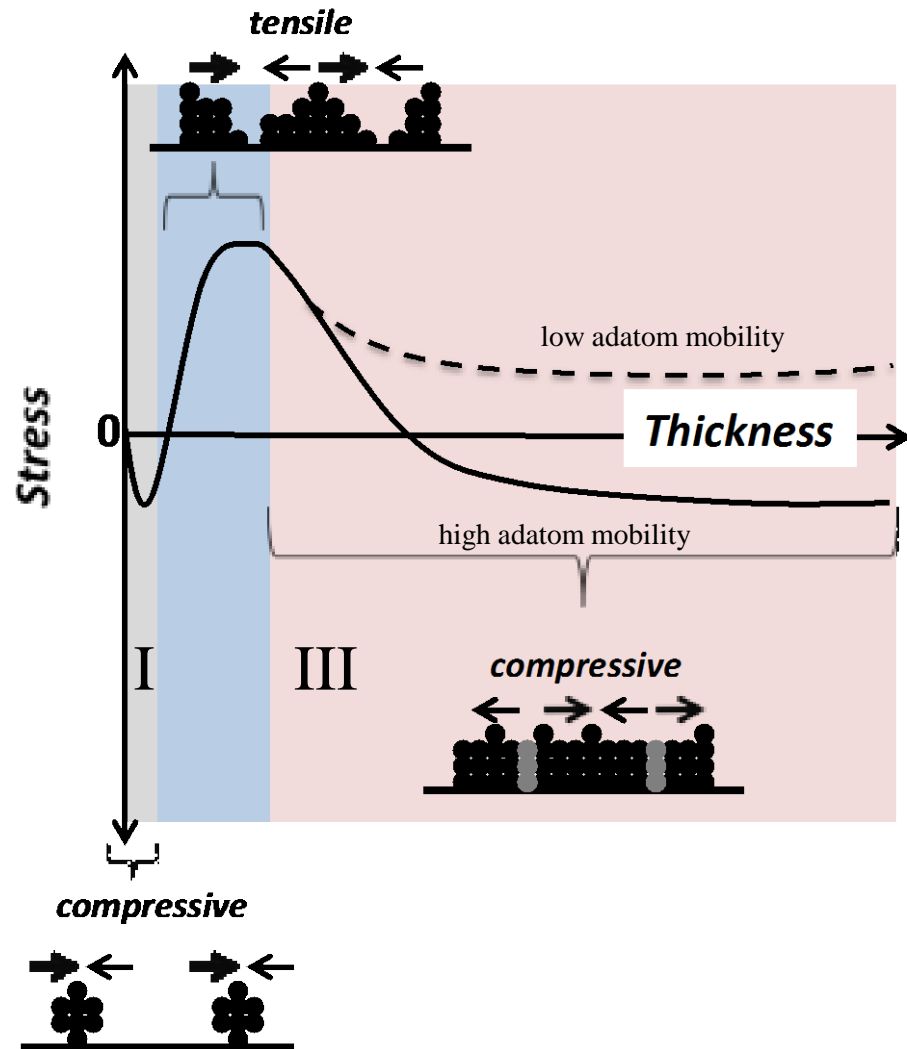
Zone 1: Columnar grains; same size with thickness

Zone T: Grain size changes at surface

Zone 2: Columnar grains; grain growth in the bulk

Zone 3: Equiaxed grains

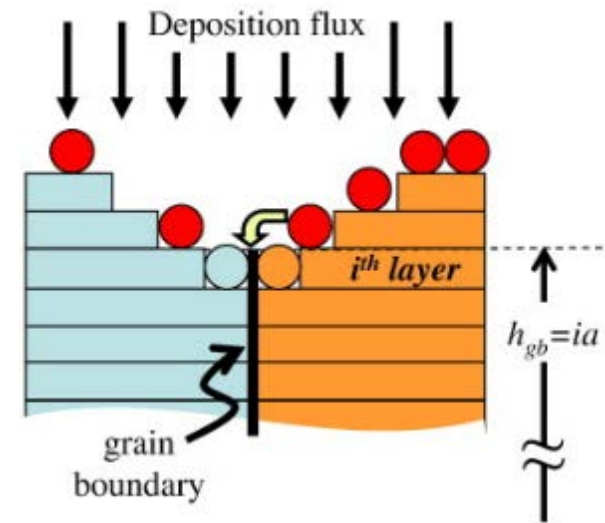
How Thin Film Stress Evolves



- **Stage I:** Initial compressive stress
- **Stage II:** Coalescence results in tensile stress
- **Stage III:** Movement of atoms into and out of grain boundaries (GB) creates compressive stress
- **Adatom mobility** effects stress state conditions
- **Kinetic parameters** of deposition on stress state:
 - *Temperature*
 - *Pressure*
 - *Deposition rate*
 - *Etc.*

Kinetic Model of Film Growth Stress

- *Stress in each layer is independent from other layers*
- *Stress only generated at triple junction*
- *Does not take into account surface stresses*



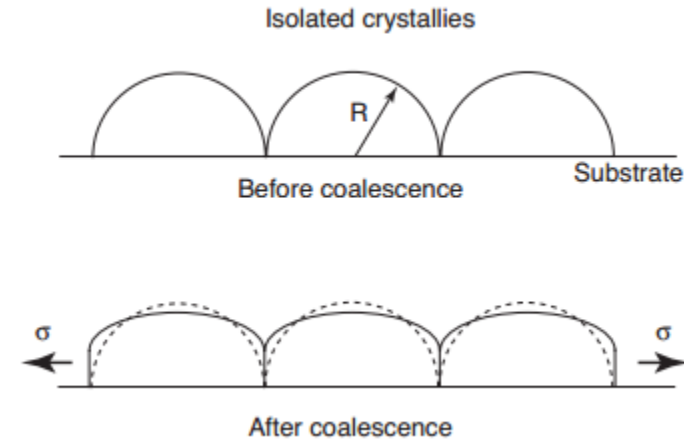
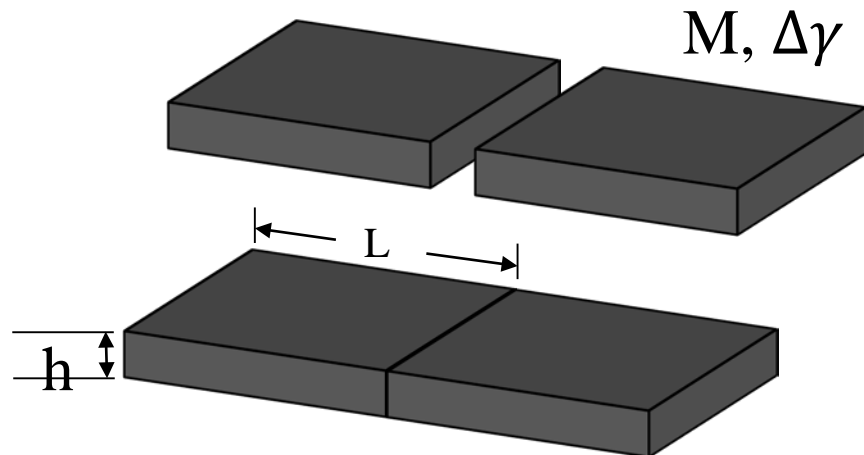
- *Growth rate R*
- *Diffusivity D , temperature T*
- *Grain size L*

*E. Chason, Thin Solid Films 526 (2012) 1–14.

*E. Chason, A.M. Engwall, Thin Solid Films 596 (2015) 2–7.

Tensile Stress Generation

- Gap between grains close to form grain boundaries
- Balance between interfacial and strain energy
- During growth layers zip together

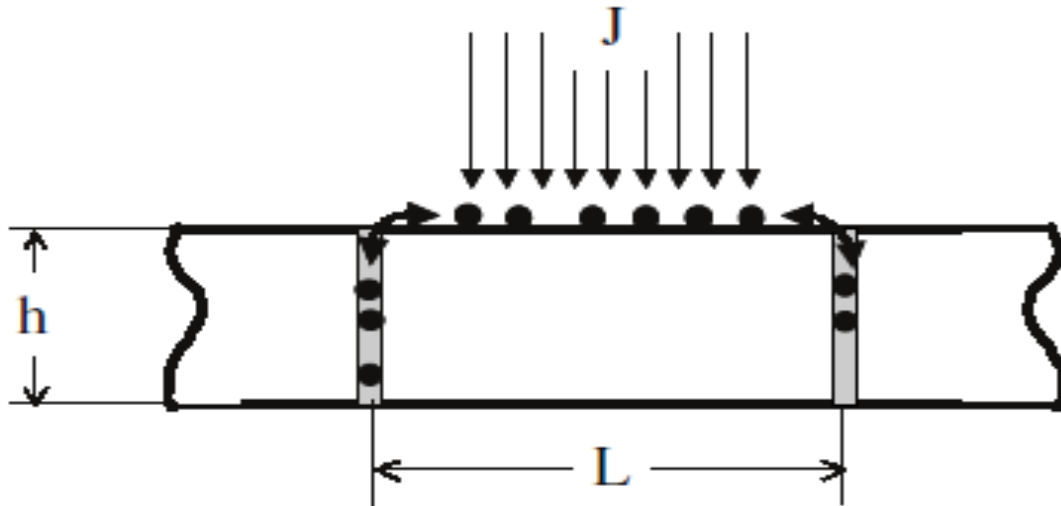


Vlassak, Thin Film Mechanics, Deas Harvard University, Ref: www.mrsec.harvard.edu/education/ap298r2004/Vlassak; 2004.

$$\sigma_T \sim \left(\frac{M\Delta\gamma}{L} \right)^{\frac{1}{2}}$$

Hoffman 1976, Nix and Clemens 1999

Compressive Stress Generation



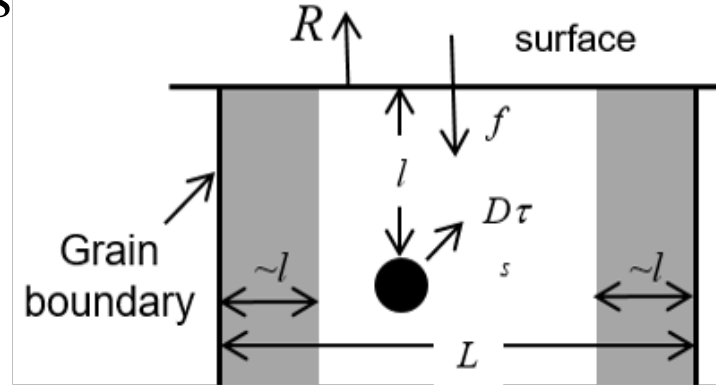
$$\Delta\mu \equiv \mu_s - \mu_{tj} = \delta\mu_s + \sigma_i\Omega$$

Stress changes chemical potential

Energetic Contributions

Collision Induced Densification of Grain Boundary

- Densification induces compressive stress
- Amount of stress relative to particle energy
- A_0 is an adjustable parameter



Incorporation of Defects into the Bulk

- Point defect incorporation induces compressive stress
- Subtracts out contributions from grain boundary region
- B_0 is an adjustable parameter for model fitting accounting for the concentration of defects trapped

$$\sigma_{bulk}^{energetic} = \left(1 - \frac{l}{L}\right) \frac{B_0}{\left(1 + \frac{l}{R\tau_s}\right)}$$

Combined Stress Equation

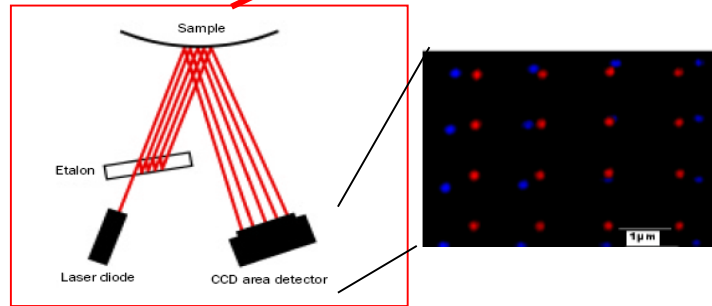
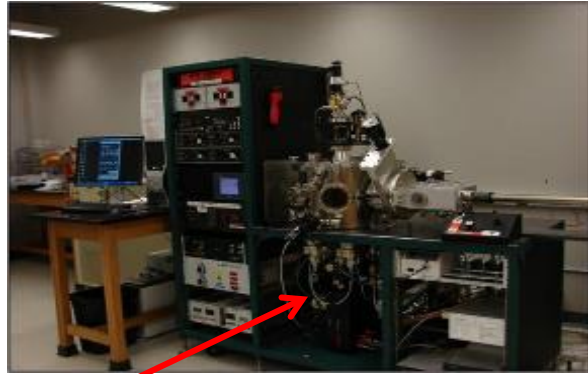
Compressive stress from supersaturation of surface Rate new GB added to film

$$\sigma_{steadystate} = \left[\sigma_c + (\sigma_T - \sigma_c) e^{-\frac{\beta D}{RL}} \right]$$

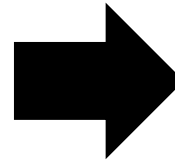
Stress from coalescence

Stress due to GB Densification Stress due to bulk defect incorporation

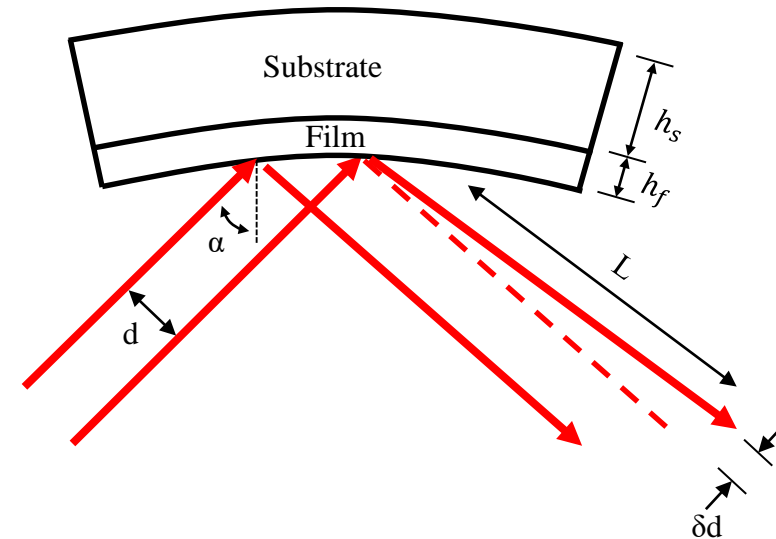
$$\sigma_{steadystate}^{sputtering} = \underbrace{\left[\sigma_c + (\sigma_T - \sigma_c) e^{-\frac{\beta D}{RL}} \right]}_{\text{Growth Stress Effects}} + \underbrace{A_0 \left(\frac{l}{L} \right) + \left(1 - \frac{l}{L} \right) \frac{B_0}{\left(1 + \frac{l}{R\tau_s} \right)}}_{\text{Energetic Stress Effects}}$$



Stressed
film bends
substrate



Curved surface deflects beams



Assumptions:

- Substrate much thicker than film
- Biaxial stress state in film
- Similar elastic properties
- No delamination

Stoney's equation

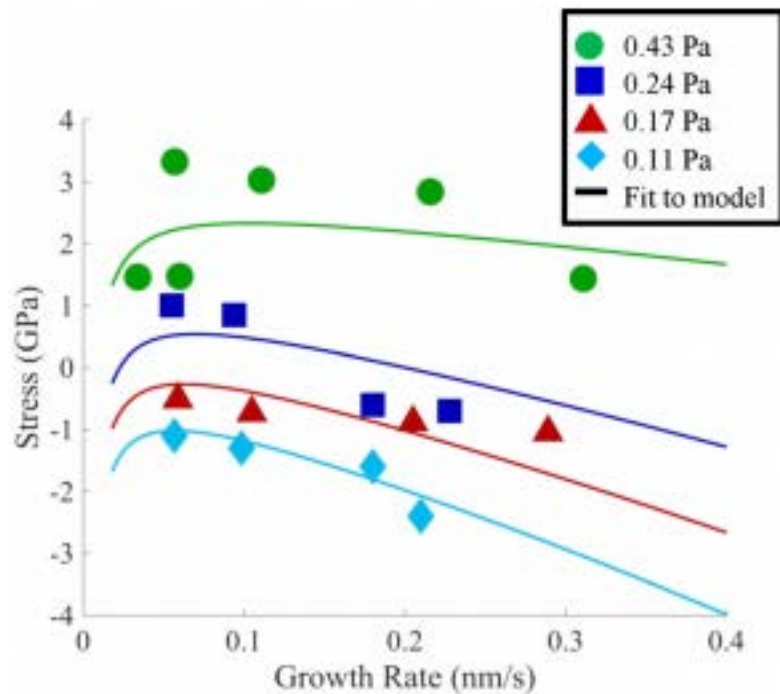
$$\sigma h_f = \frac{\delta d}{d} \frac{M_s h_s^2 \cos \alpha}{12L}$$

Stress Thickness

Stress Evolution of Sputter Deposited Cu

Experimental Design

Sputter Deposited Mo (low mobility)



- Work motivated by a lack of data
- Mo study does not show a compressive stress turn down at low deposition rates
- Sputter deposited Cu (high mobility) can reveal if this turn down will occur

Sputter Deposited Cu (high mobility)

Deposition Pressure (Pa)	Deposition Rate (nm/sec)				
	0.012	0.12	1.0	1.2	2.4
0.267	✓	✓	X	✓	✓
1.333	✓	✓	X	✓	X
2.667	✓	✓	✓	X	X

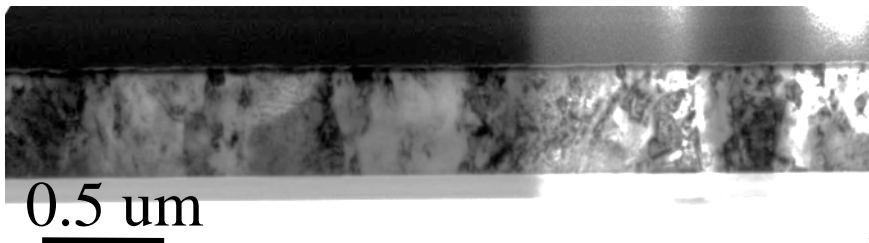
Seed Layer

Without a Seed

High Deposition Rate

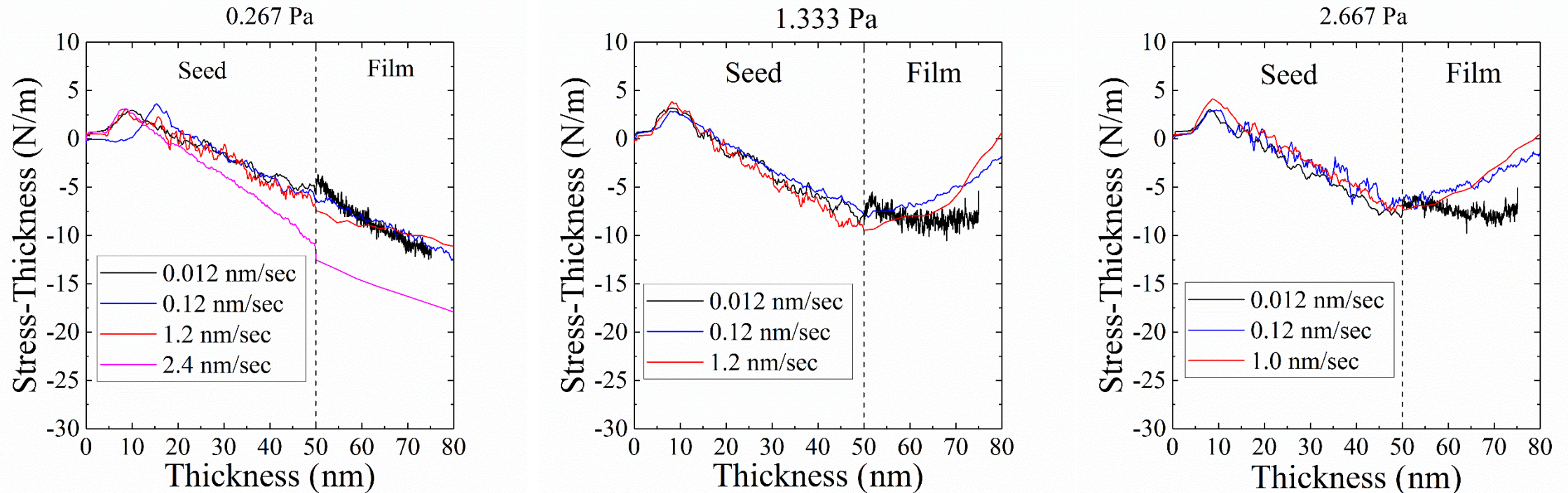


Low Deposition Rate



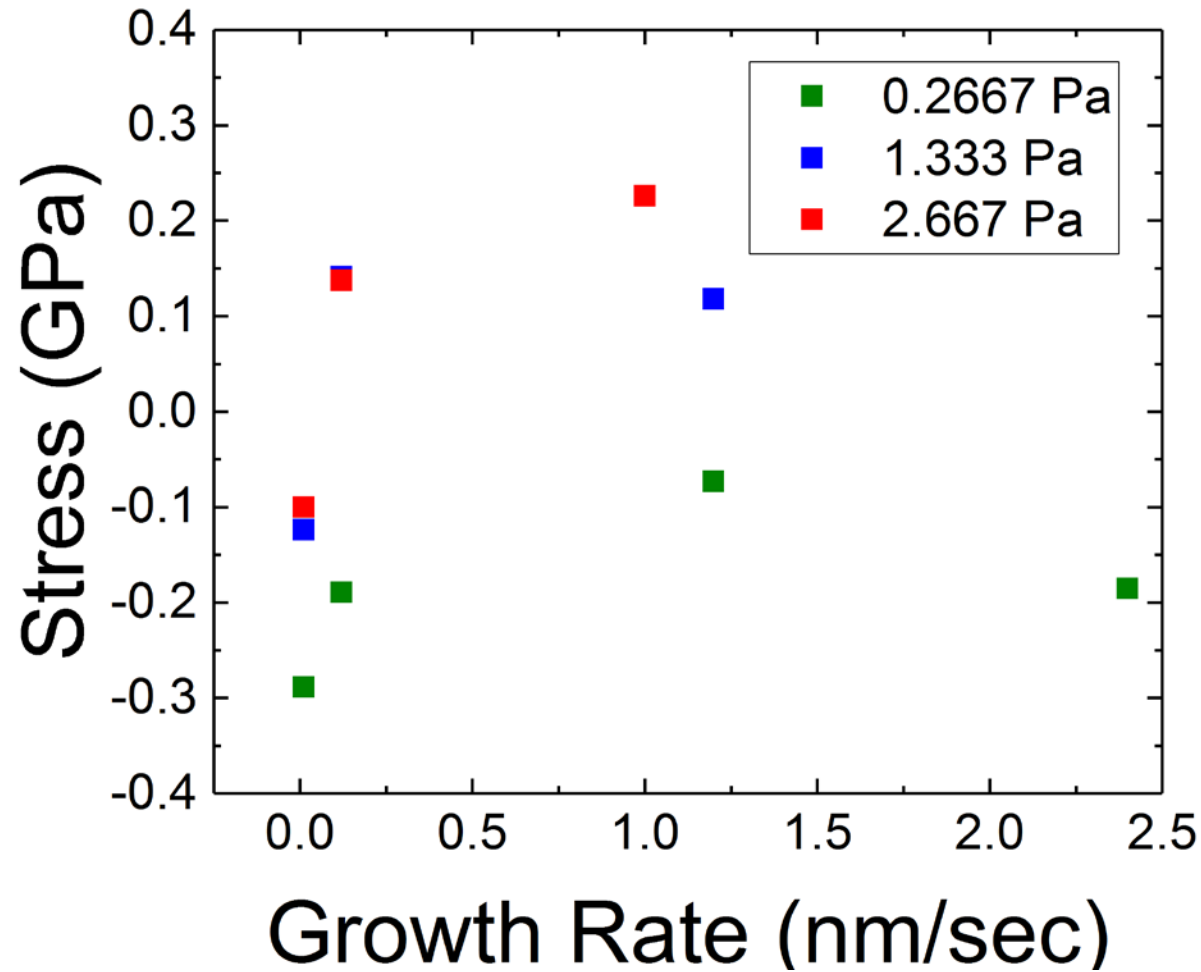
- Different deposition conditions nucleated very different microstructures
- Seed layers were employed in order to control microstructure
- First 50 nm of each deposition used the same parameters, followed by immediate change to the desired deposition condition

Stress Evolution as a Function of Deposition Parameters



- Seed layers demonstrate good stress reproducibility
- As pressure increases the stress shifts to become more tensile

Steady State Stress Trends



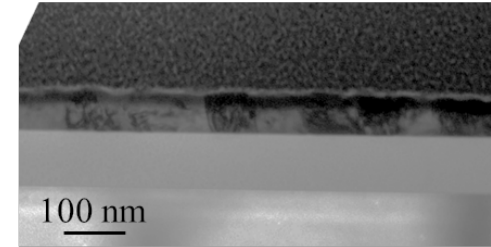
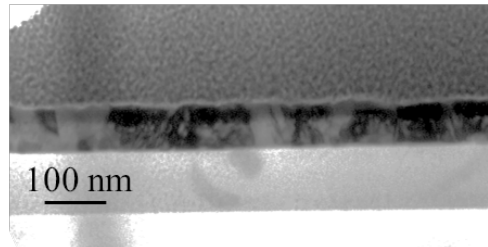
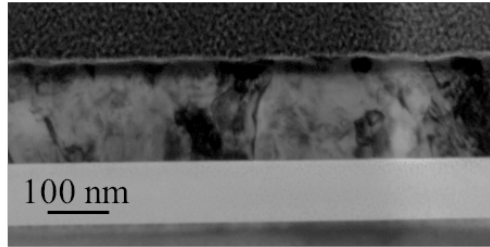
Microstructure

2mtorr

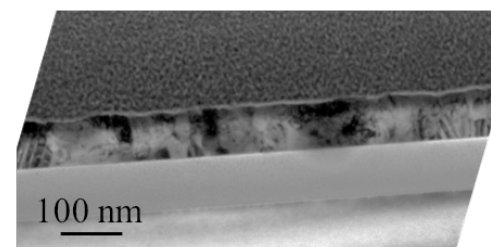
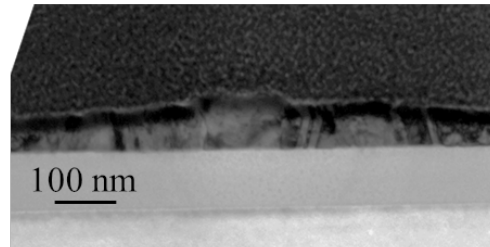
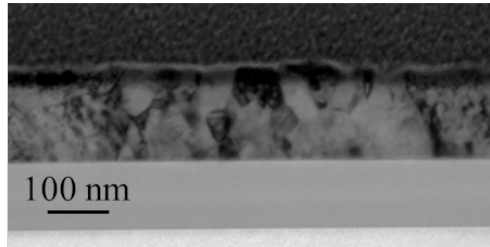
10mtorr

20mtorr

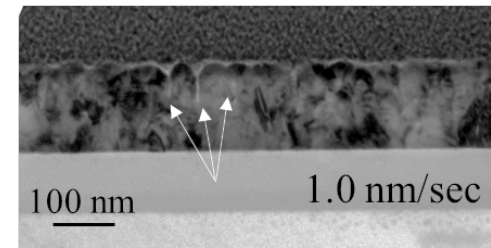
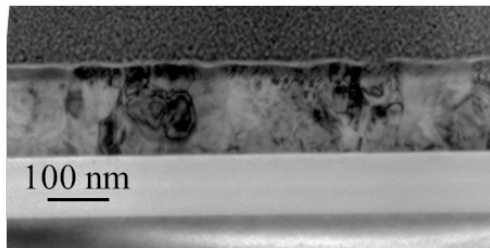
0.012nm/sec



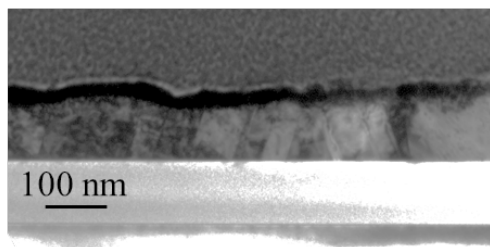
0.12nm/sec



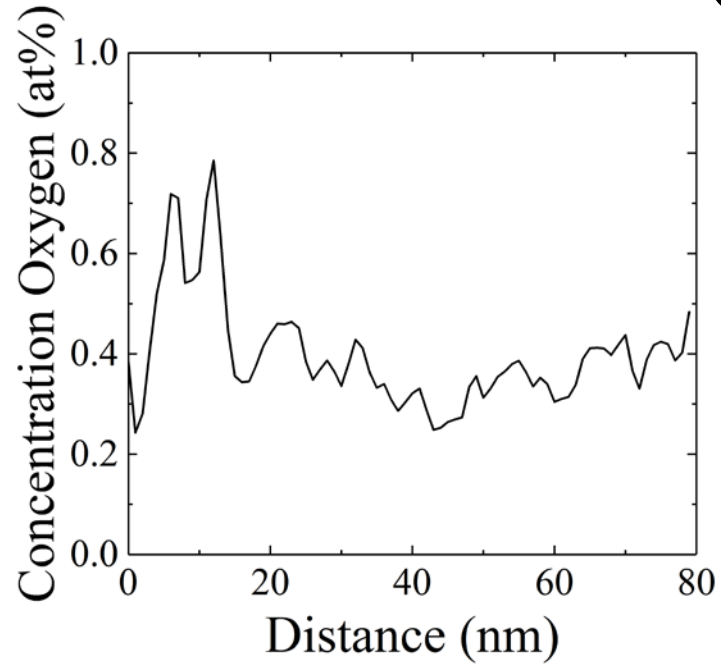
1.2nm/sec



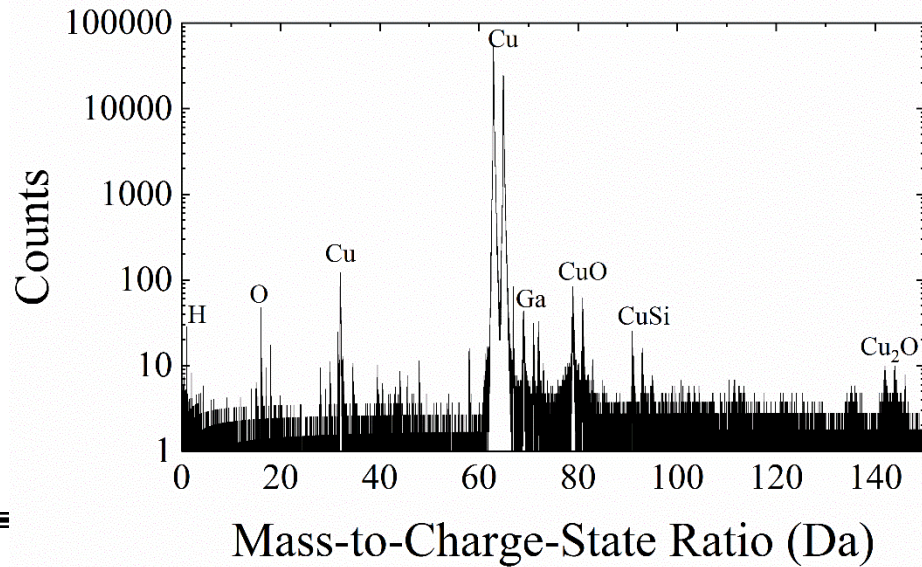
2.4 nm/sec



Oxygen Effects

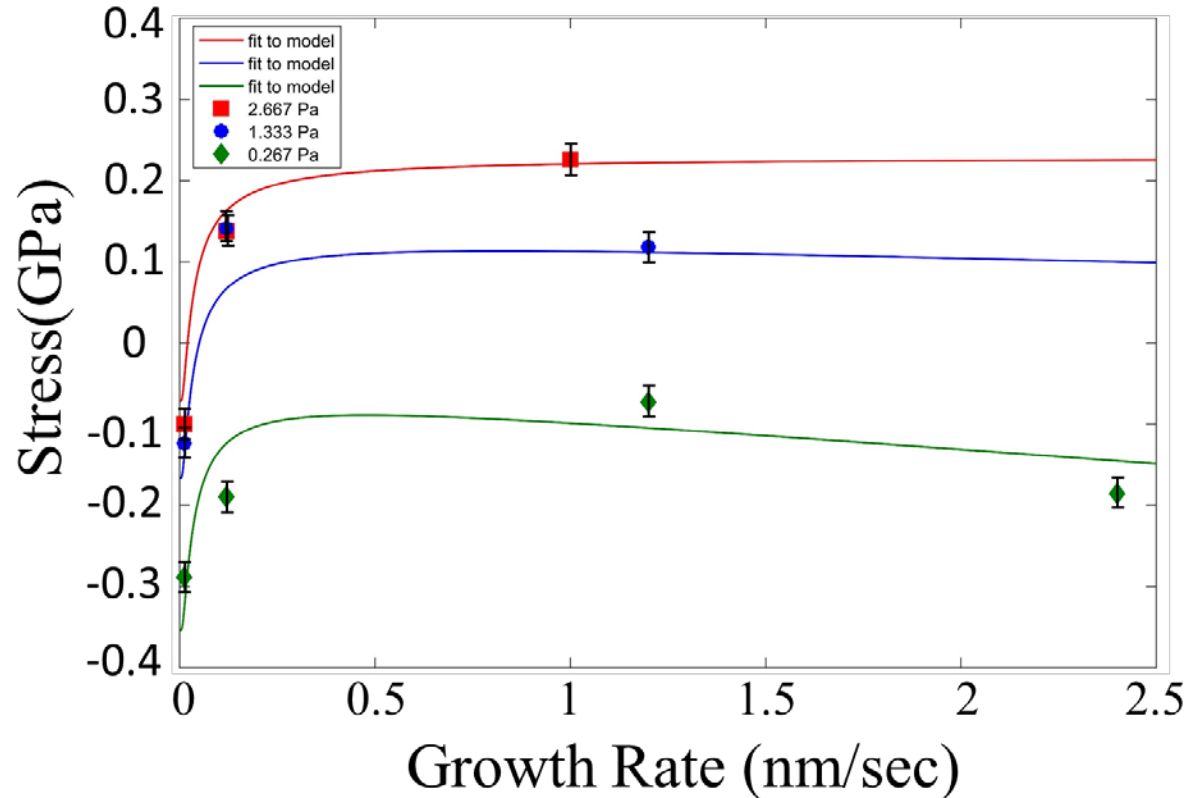


*R. Abermann, R. Koch, Thin Solid Films 142 (1986) 65-76.



Cu Fit to the Kinetic Model

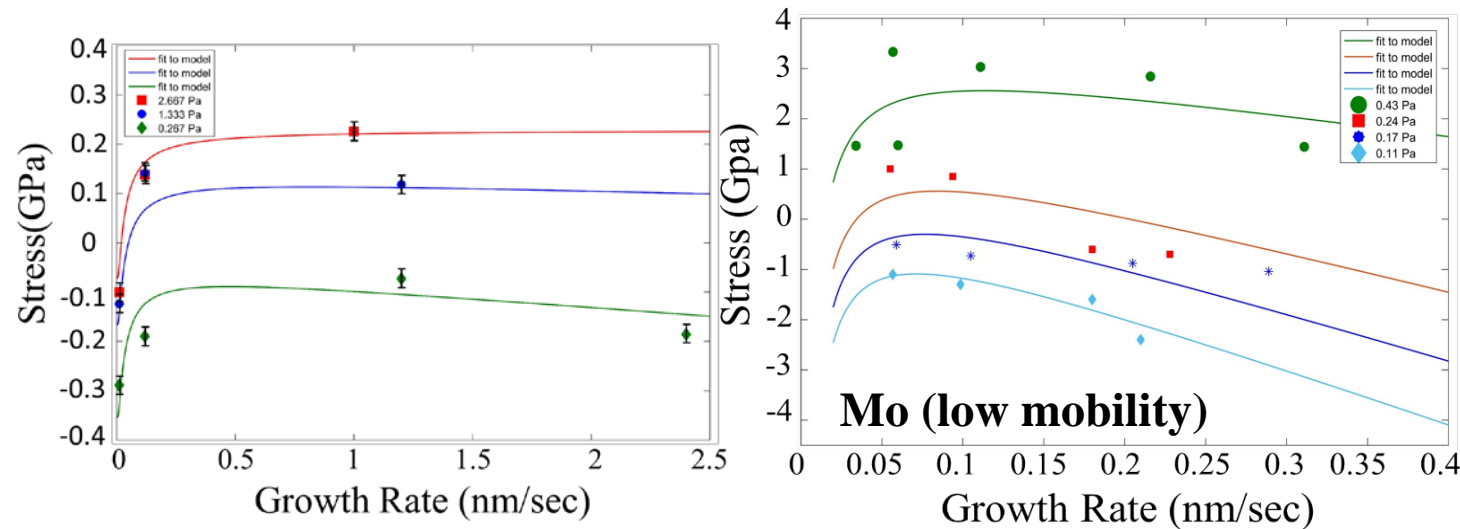
$$\sigma_{\text{steadystate}}^{\text{sputtering}} = \left[\sigma_c + (\sigma_T - \sigma_c) e^{-\frac{\beta D}{RL}} \right] + A_0 \left(\frac{l}{L} \right) + \left(1 - \frac{l}{L} \right) \frac{B_0}{\left(1 + \frac{l}{R\tau_s} \right)}$$



Cu vs. Mo Deposition

Fitting Parameters

$$\sigma_{\text{steady state}}^{\text{sputtering}} = \left[\sigma_c + (\sigma_T - \sigma_c) e^{-\frac{\beta D}{RL}} \right] + A_0 \left(\frac{l}{L} \right) + \left(1 - \frac{l}{L} \right) \frac{B_0}{\left(1 + \frac{l}{R\tau_s} \right)}$$

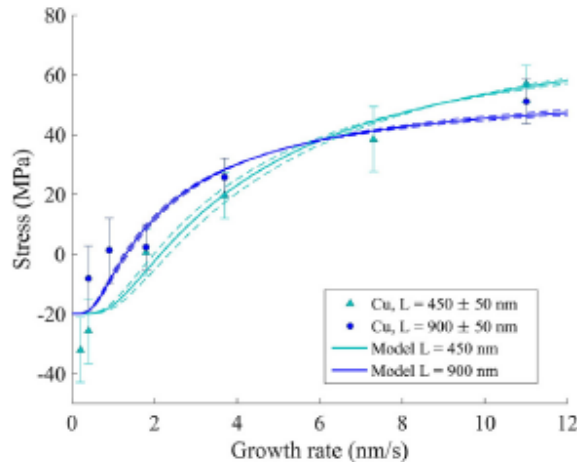
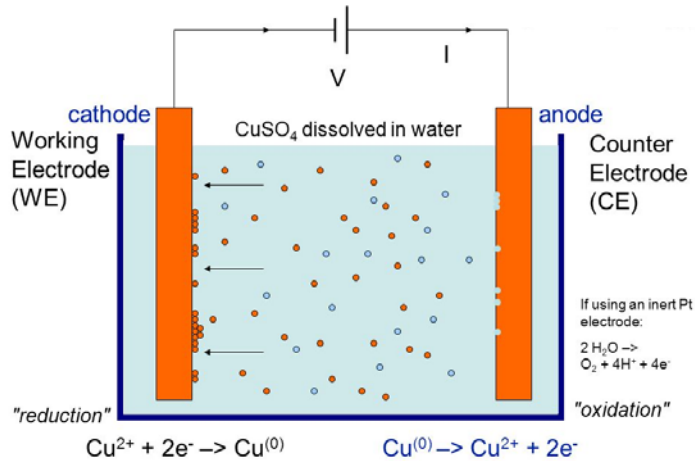


Pressure (Pa)	A ₀ (GPa)	B ₀ (GPa)	βD (nm ² /s)
Cu 0.267	-3.82	-131.19	0.67
Cu 1.333	-2.22	-76.24	0.67
Cu 2.667	-0.22	-7.475	0.67
Mo 0.11	-204.67	-590.08	0.135
Mo 0.24	-190.5	-549.23	0.135
Mo 0.27	-173.97	-501.58	0.135
Mo 0.43	-129.11	-372.23	0.135

- A larger slope is observed in the Mo vs. Cu in the stress vs. growth rate plots
 - This likely indicates that more defects are being incorporated into the Mo film producing compressive stress
 - This is reflected in the model fitting parameters with the B₀ term, which was ~3 times larger for Mo

Deposition Technique Comparison

$$\sigma_{steadystate}^{sputtering} = \left[\sigma_c + (\sigma_T - \sigma_c) e^{-\frac{\beta D}{RL}} \right] + A_0 \left(\frac{l}{L} \right) + \left(1 - \frac{l}{L} \right) \frac{B_0}{\left(1 + \frac{l}{R\tau_s} \right)}$$

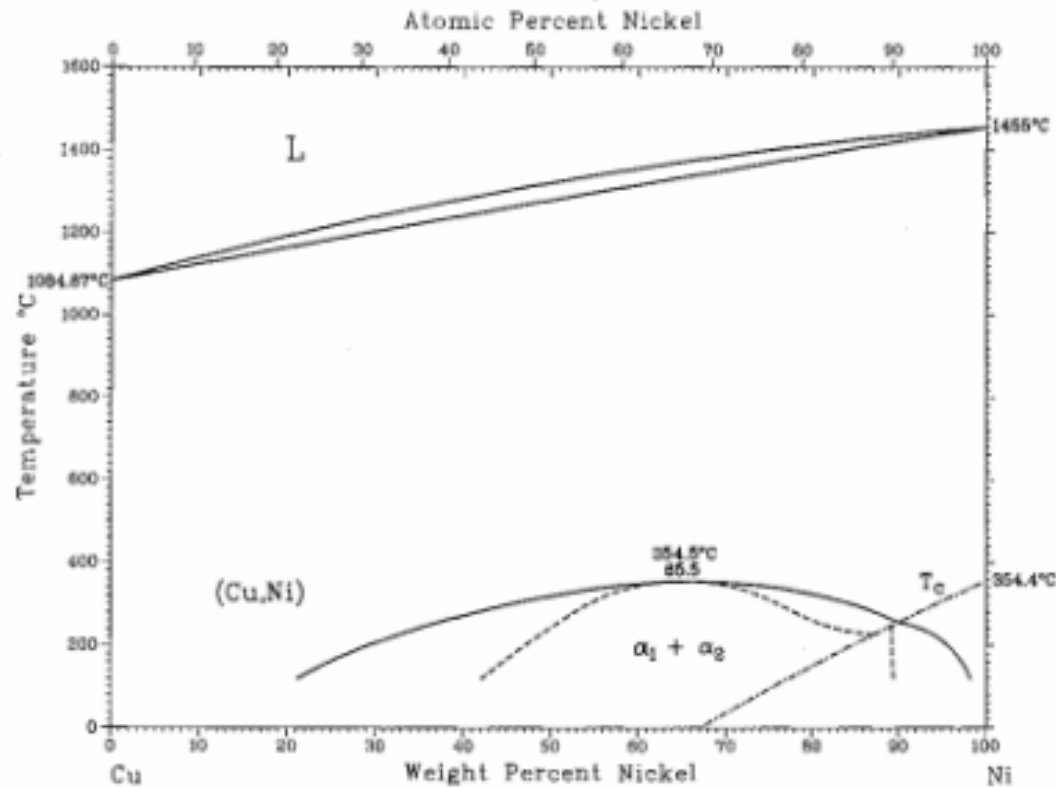


- Electrodeposition only exhibits growth stress
- How do “growth stress” terms compare between different deposition techniques

Technique	σ_c (MPa)	σ_T (MPa)
Electrodeposited Cu	-19.9	380
Sputtered Cu	-70	230
Sputtered Mo	-16,200	5,600

Alloy Thin Film Growth

Cu-Ni

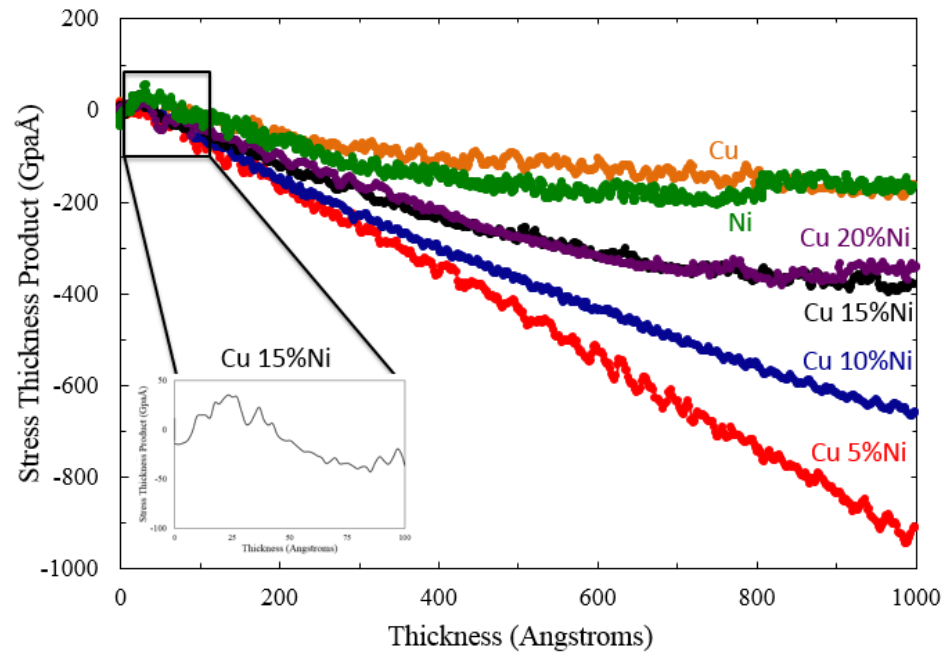


- Forms Solid Solution
- Displays low temperature miscibility gap – solute segregation
- $\Delta H_{\text{seg}} \approx -17 \text{ kJ/mol}$

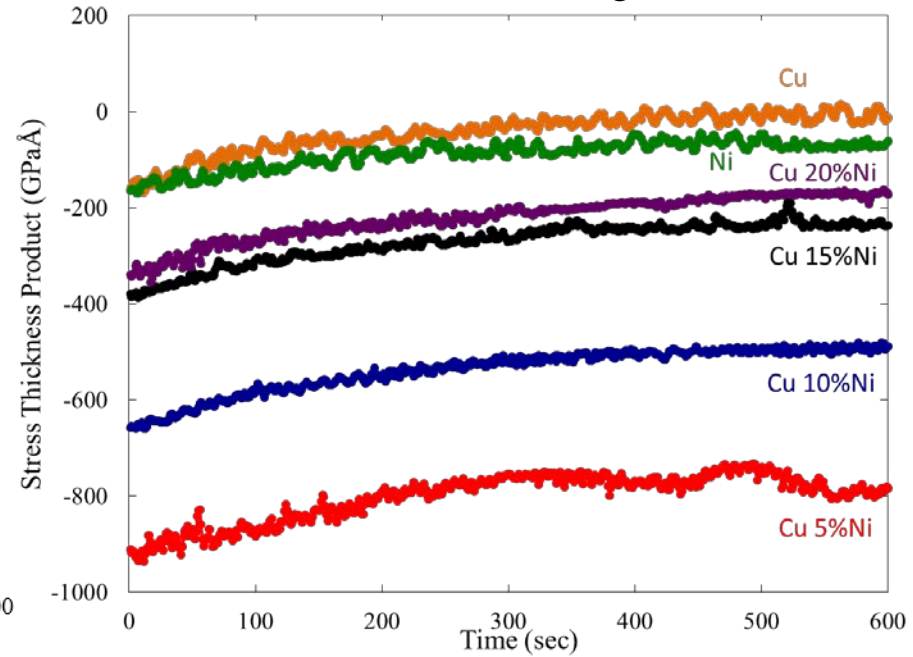
*D.J Chakrabarti, D.E. Laughlin, S.W. Chen, and Y.A. Chang, *Phase Diagrams of Binary Copper Alloys*, ASM International

Cu(Ni) *in situ* Stress Evolution

In situ stress evolution



Stress Relaxation after growth



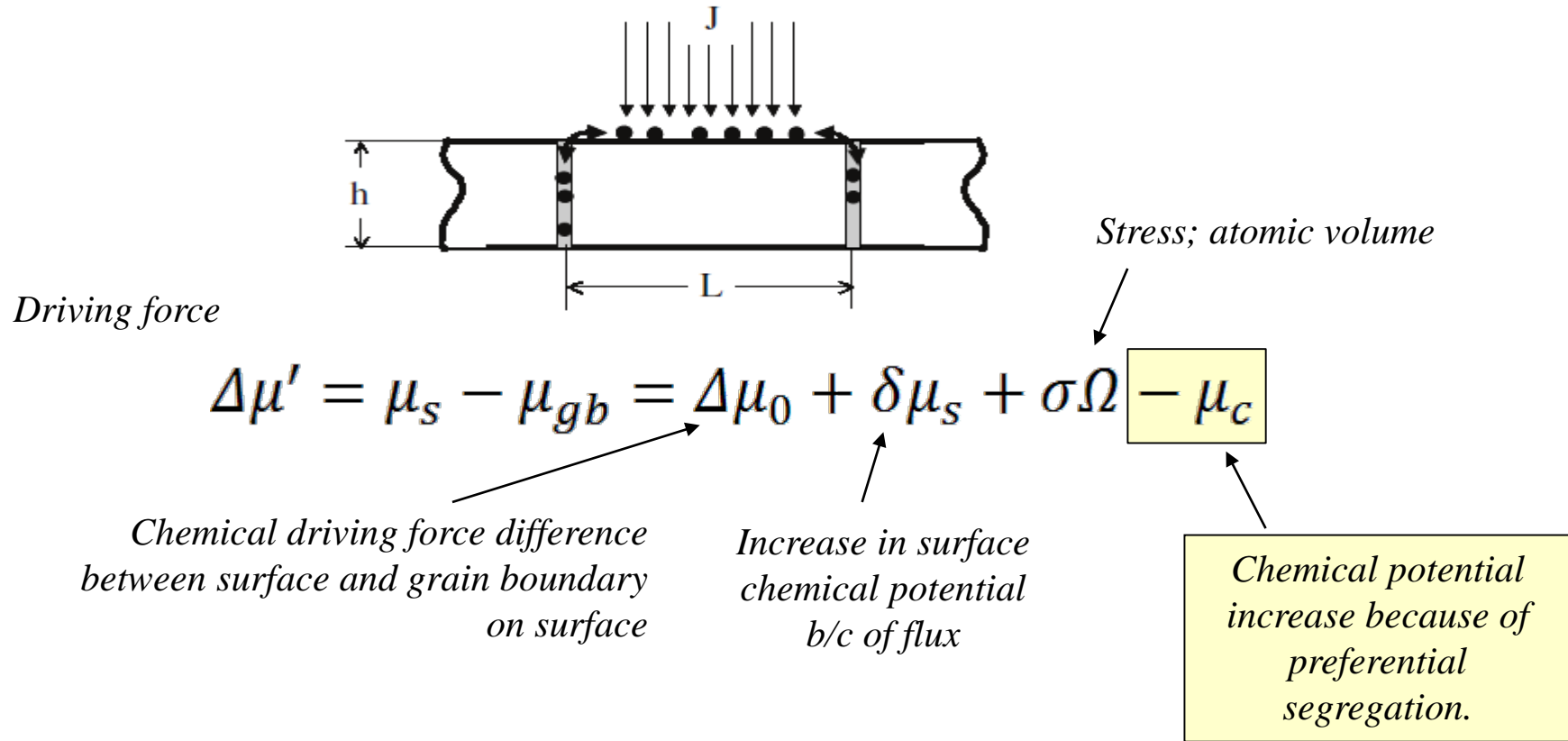
Deposition Rates:

0.211 nm/sec -0.188nm/sec

Composition (at.%)	Cu	Cu ₉₅ Ni ₅	Cu ₉₀ Ni ₁₀	Cu ₈₅ Ni ₁₅	Cu ₈₀ Ni ₂₀	Ni
Average grain size (nm)	44	39	39	35	35	31

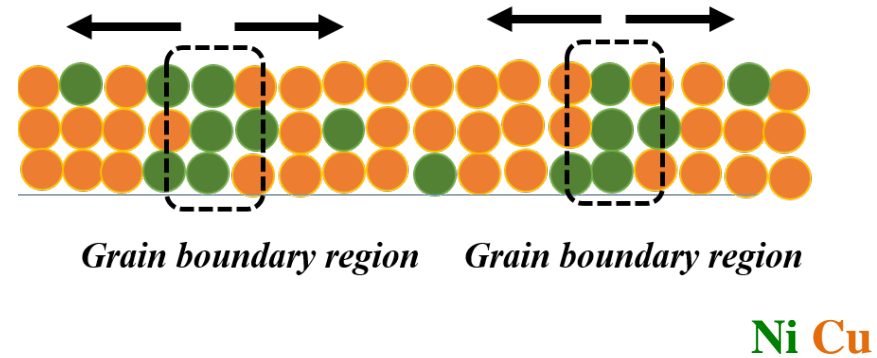
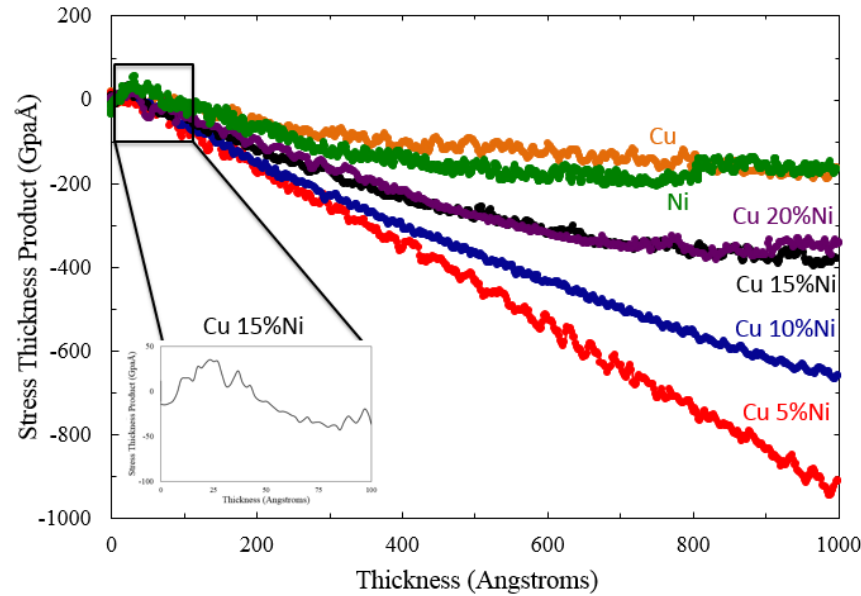
Compositional Dependent Stress States:

Modification of Chason et al. model



Ref: E. Chason *et al.* *Phys. Rev.Lett.* **88**, 156103 (2002)
 D. Fu, G.B. Thompson *J Applied Physics* **108** 043506-1 (2010)

Enrichment of Ni into the Grain Boundaries: *Tuning the Stress States*



Ni segregation enthalpy*:
 $\Delta H_{s \uparrow Ni} = -17 \text{ kJ mol}^{-1}$

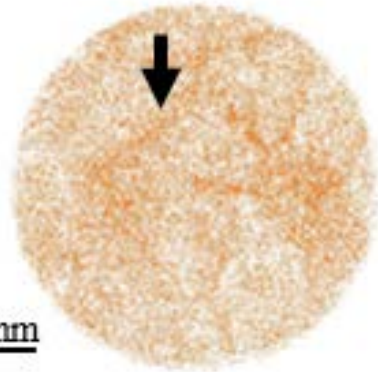
Atomic radii*

$r_{Cu} \sim 145 \text{ pm}$

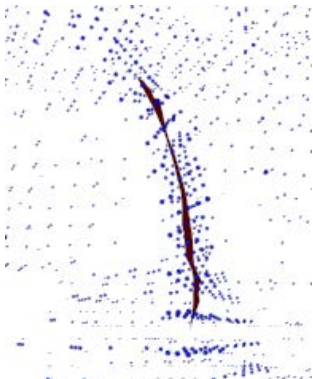
$r_{Ni} \sim 149 \text{ pm}$

*E. Clementi et al J. Chem. Phys. 1963 38, 2686

Cu-5Ni Ni Cu



Density filtered identification of boundary *

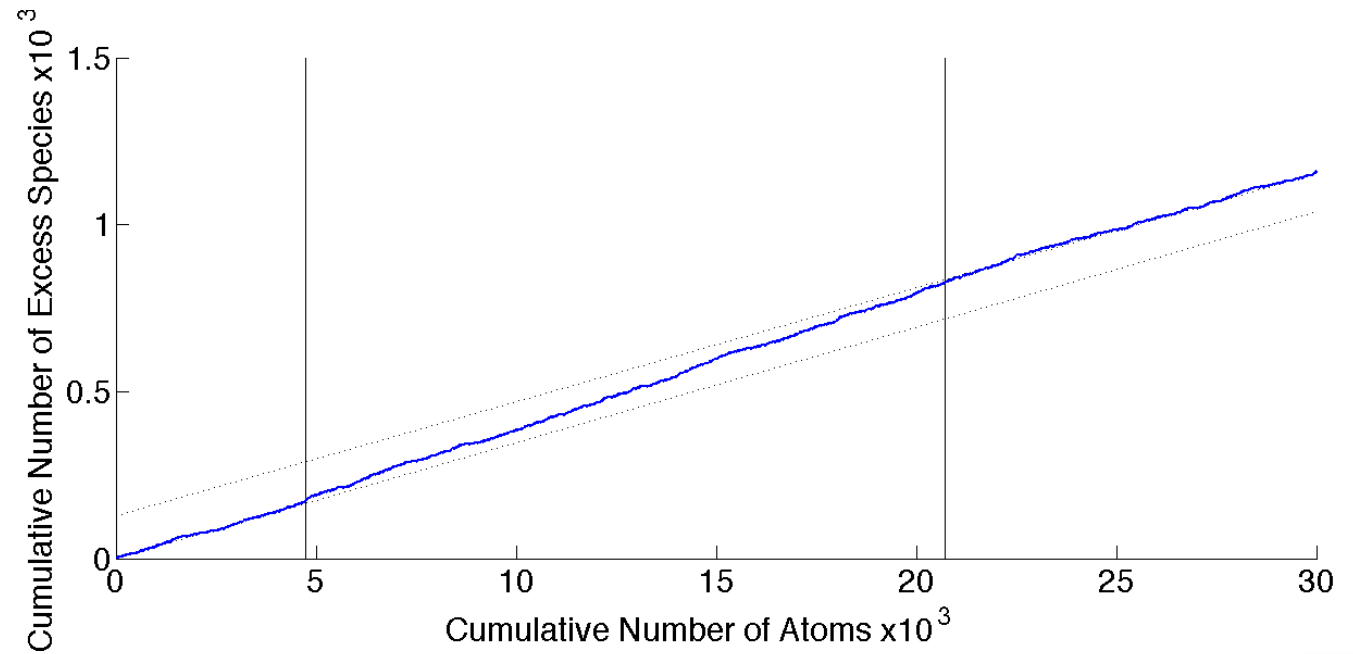


*Ref: P. Felser *et al*,
Ultramicroscopy 2012

Gibbisan Interfacial Excess

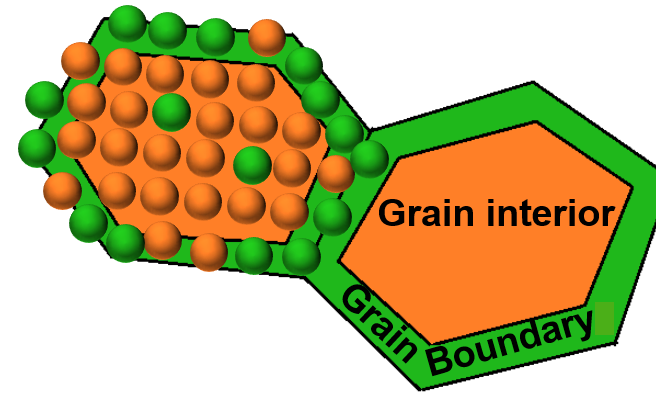
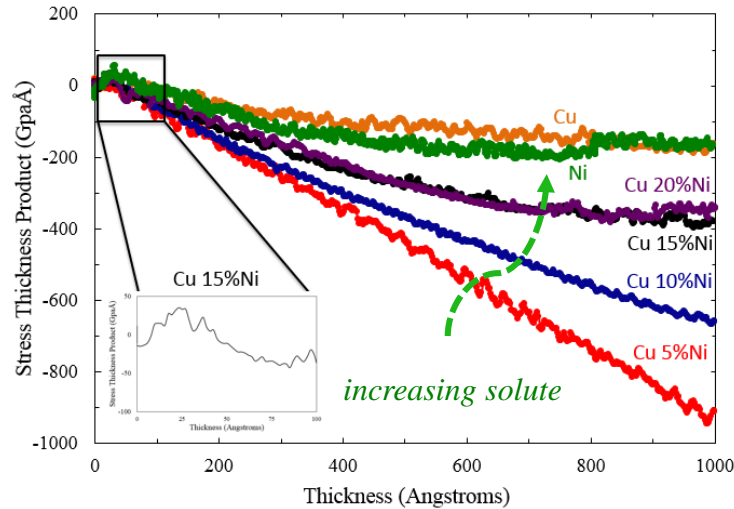
Cu-5Ni $G \sim 0.88 \text{ at/nm}^2 \pm 0.43$

Cu-15Ni $G \sim 0.98 \text{ at/nm}^2 \pm 0.29$



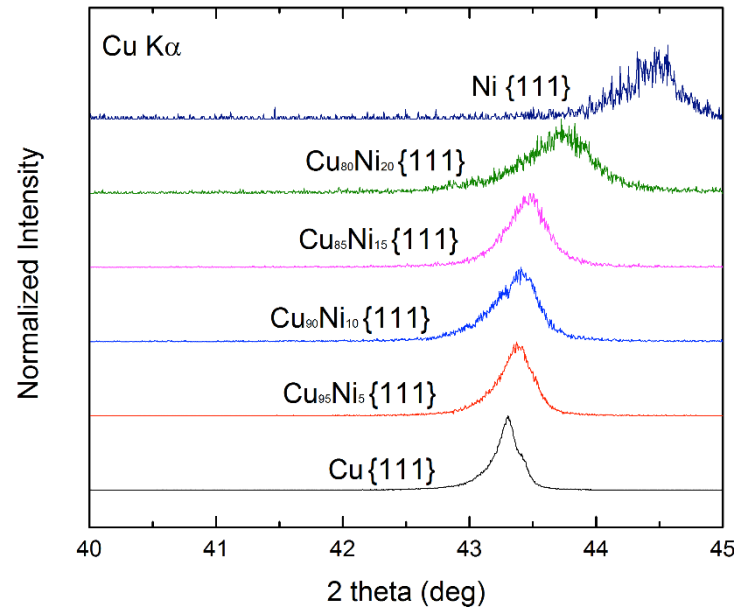
T. Kaub, P. Felser, J.M. Cairney G.B. Thompson *Scripta Materialia* **113** 131-134 (2016)

Solute Saturation



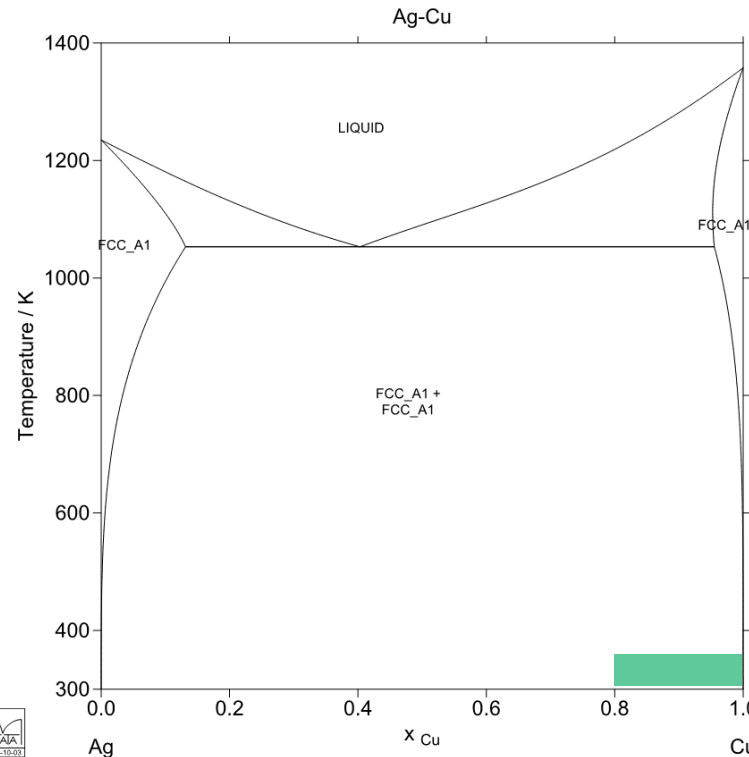
Cu-5Ni $G \sim 0.89 \text{ at/nm}^2$

Cu-15Ni $G \sim 0.98 \text{ at/nm}^2$

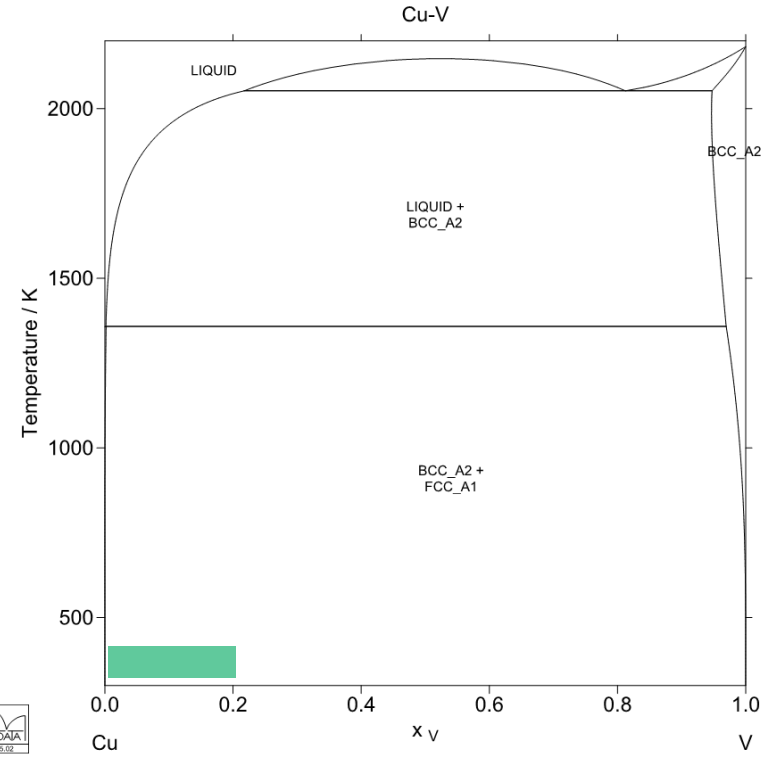


- Low solute additions can segregate to the grain boundary
- When grain boundary saturation is reached, all additional solute goes into the bulk of the grain

Highly Segregating Solutes



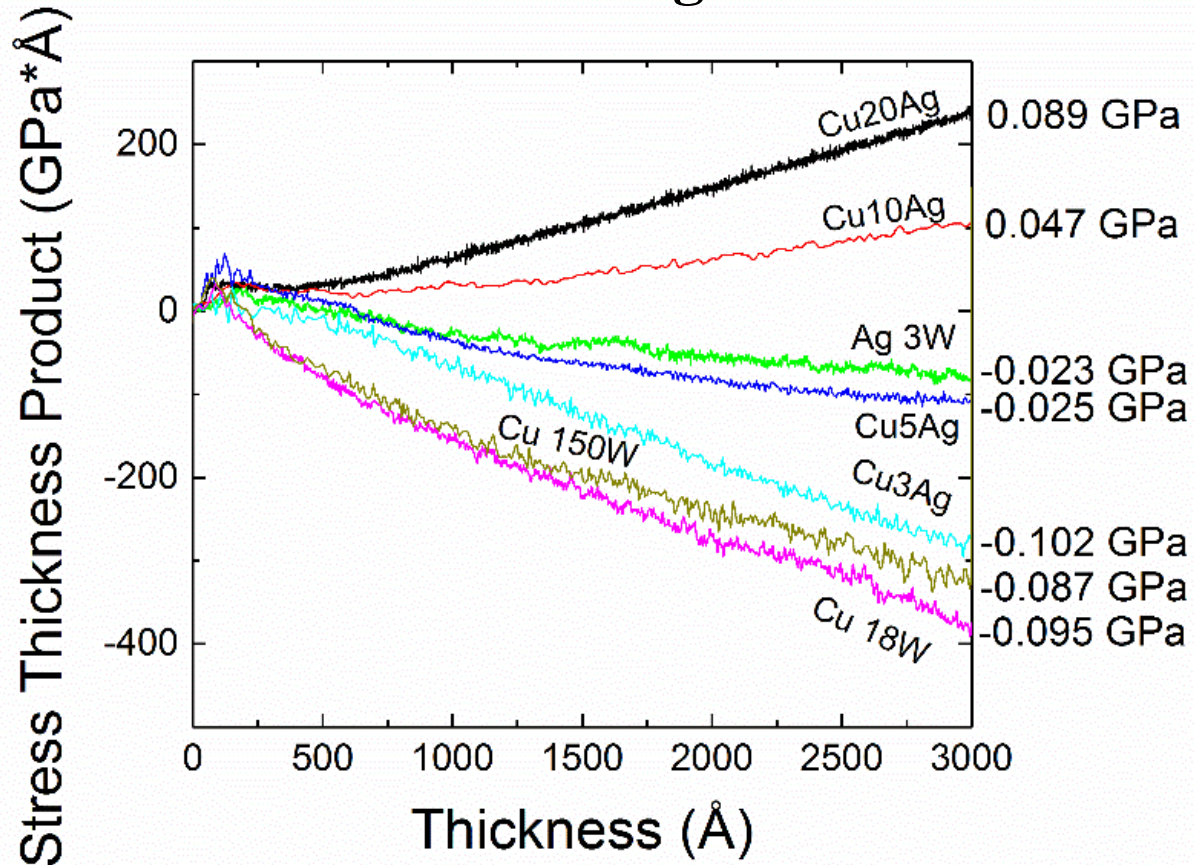
Ag high mobility



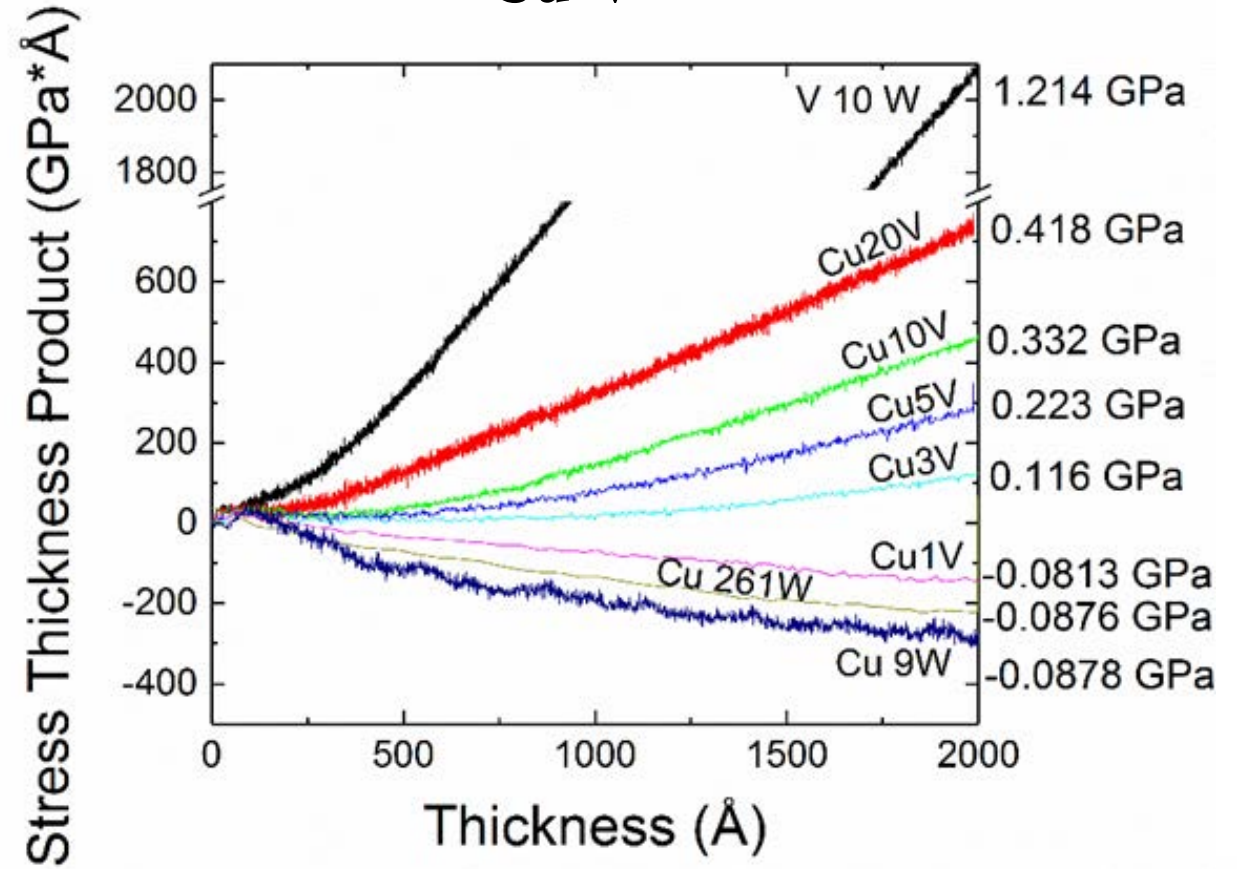
V low mobility



Cu-Ag

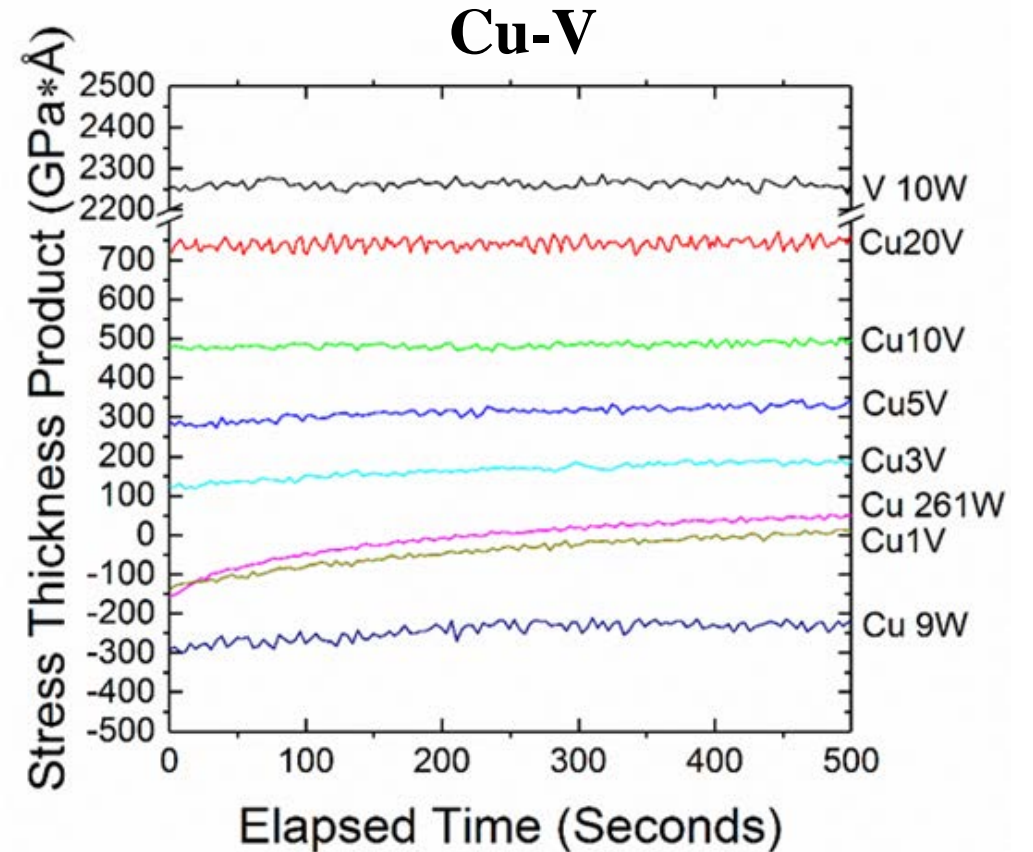
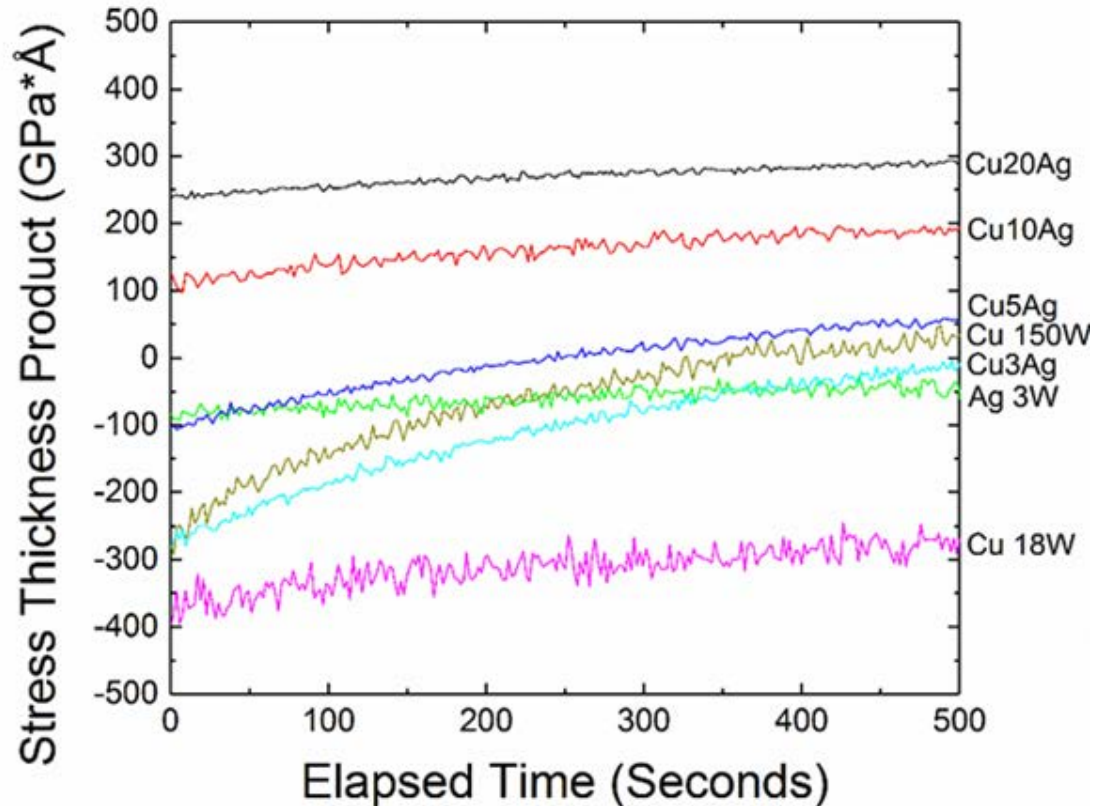


Cu-V

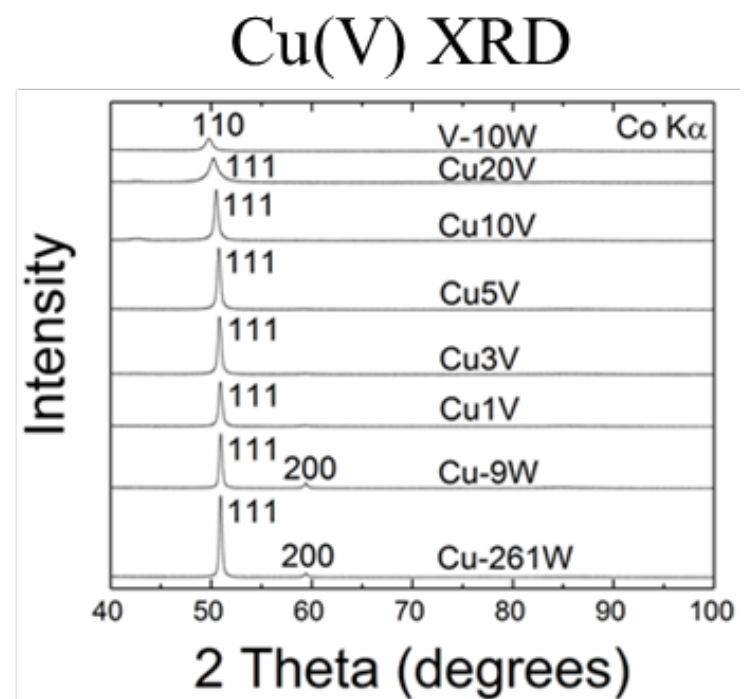
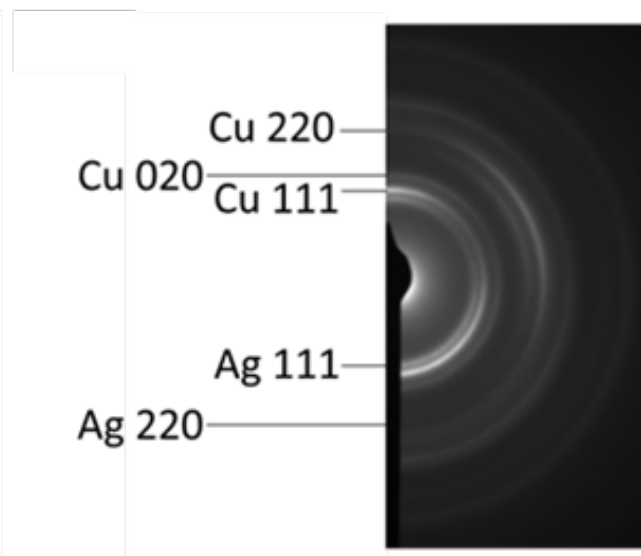
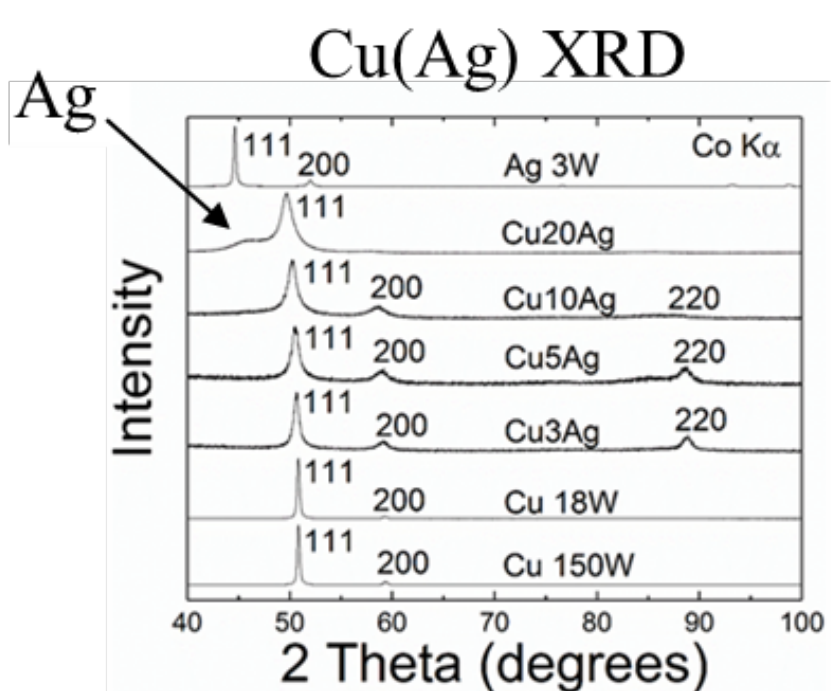


T. Kaub, R. Anthony, G.B. Thompson *J Applied Physics* **122** 225302 (2017)

Stress Relaxation



- Increasing solute content reduces the amount of stress relaxation in both systems
- Cu-V system undergoes no relaxation at ~10 at% V



- Higher enthalpy of mixing for Cu(Ag) ~ 31 kJ/mol* than Cu(V) ~ 5 kJ/mol**
- Diffraction shows at Cu-20 Ag phase separation is starting to occur

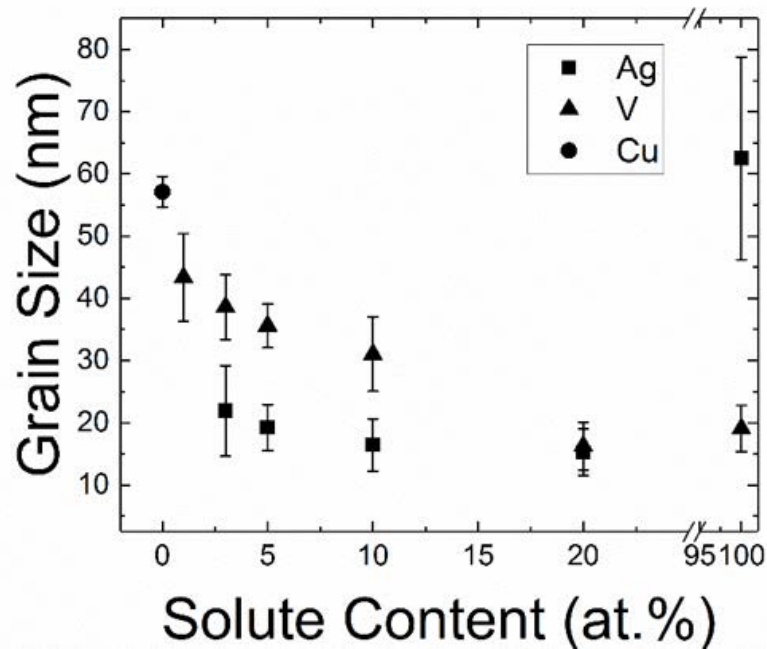
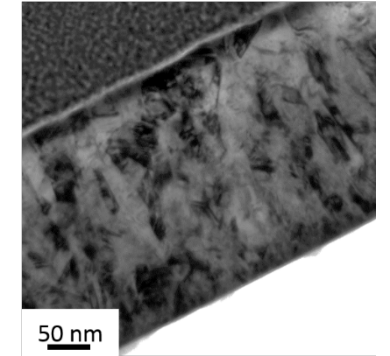
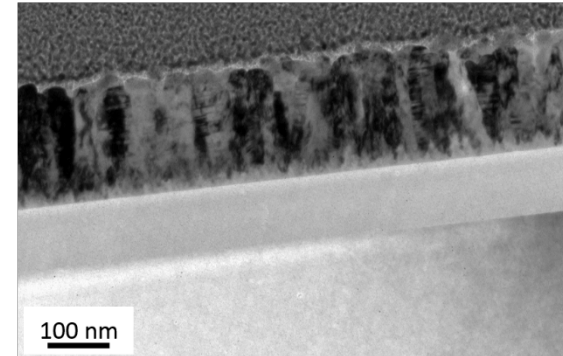
*R. Hultgren *et al.* Selected Values of Thermodynamic Properties of Binary Alloys 1973

**M. A. Atwater and K. A. Darling ARL Tech Report No. ARL-TR-6007, 2012

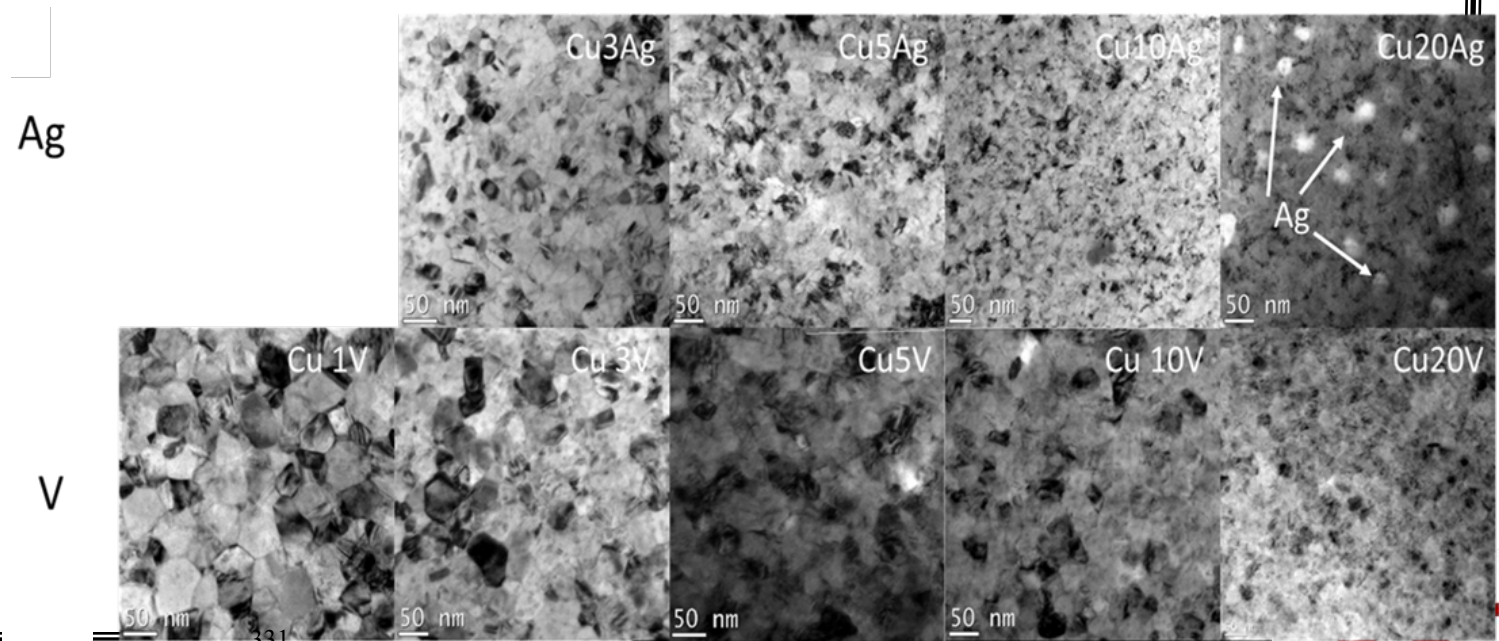


- Solutes refine grain size in both systems
- Refinement is more pronounced in Cu(Ag)
- Ag clusters observed in Cu-20Ag

Cross Section TEM

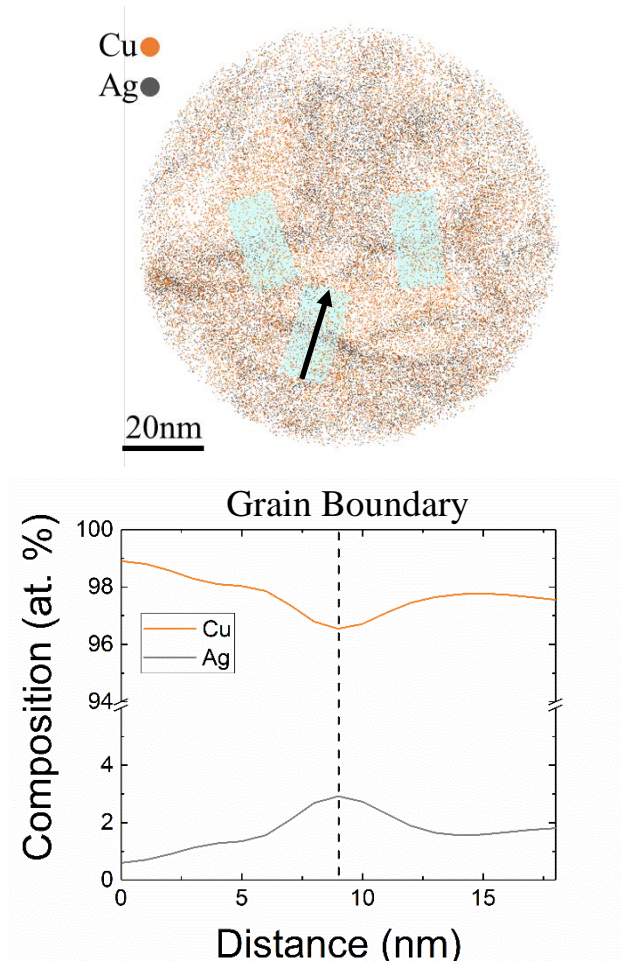


Plan View TEM

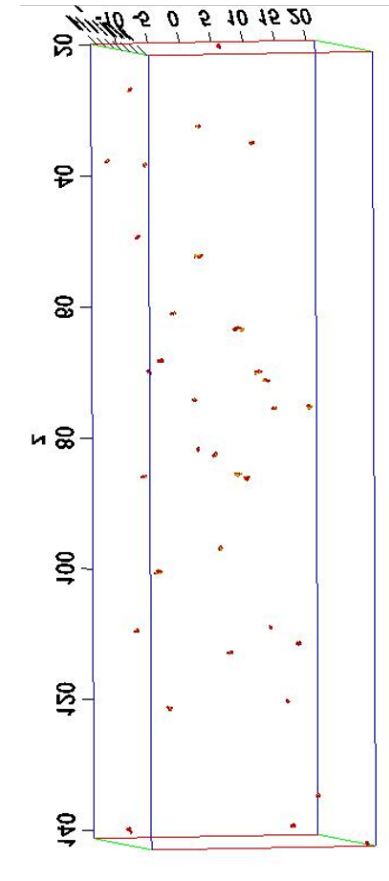


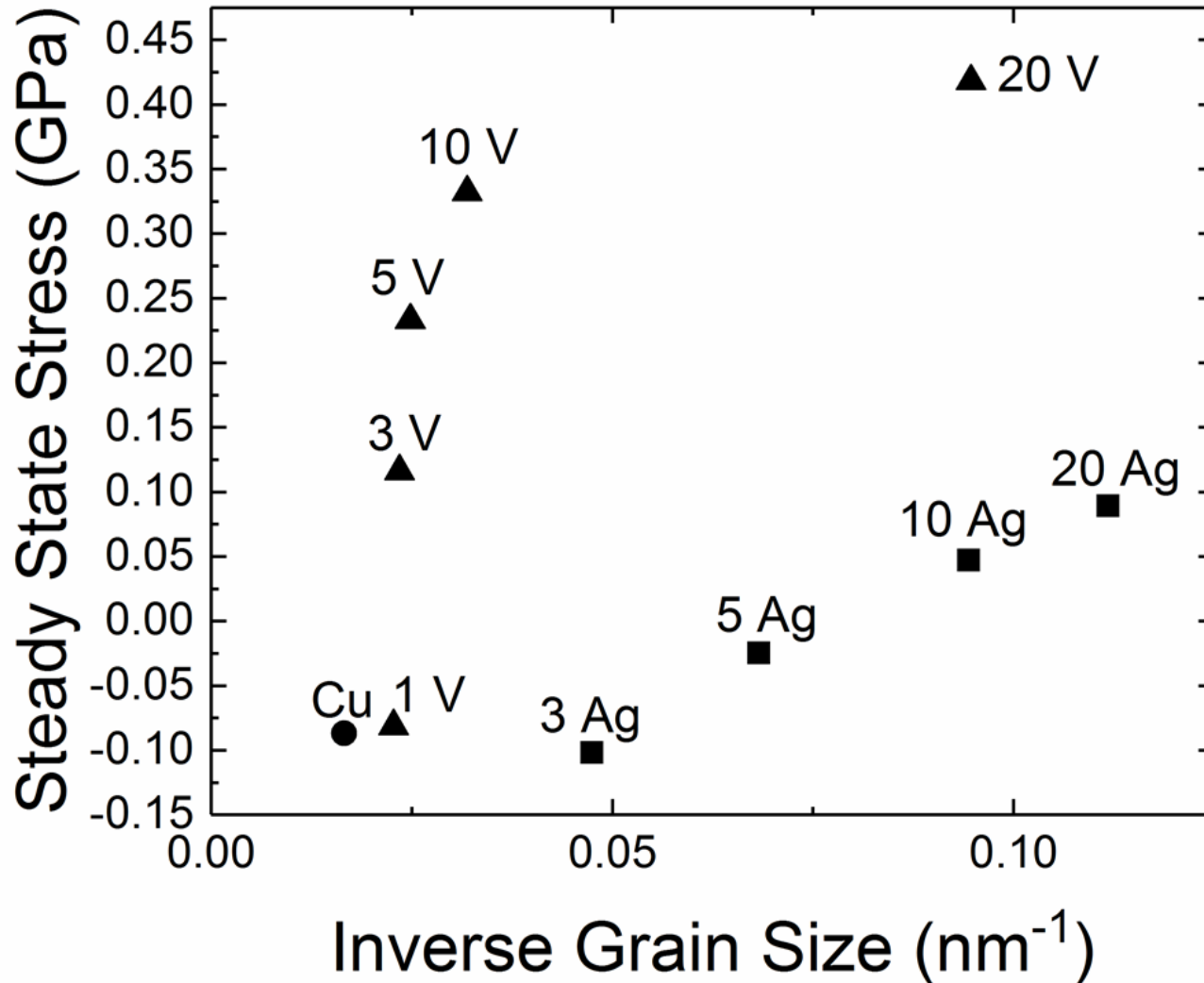
Segregation Observed

Grain Boundary Enrichment in Cu-3Ag



- Ag enrichment in the grain boundaries is observed
- Clustering in low V content film indicates further segregation likely at higher solute content

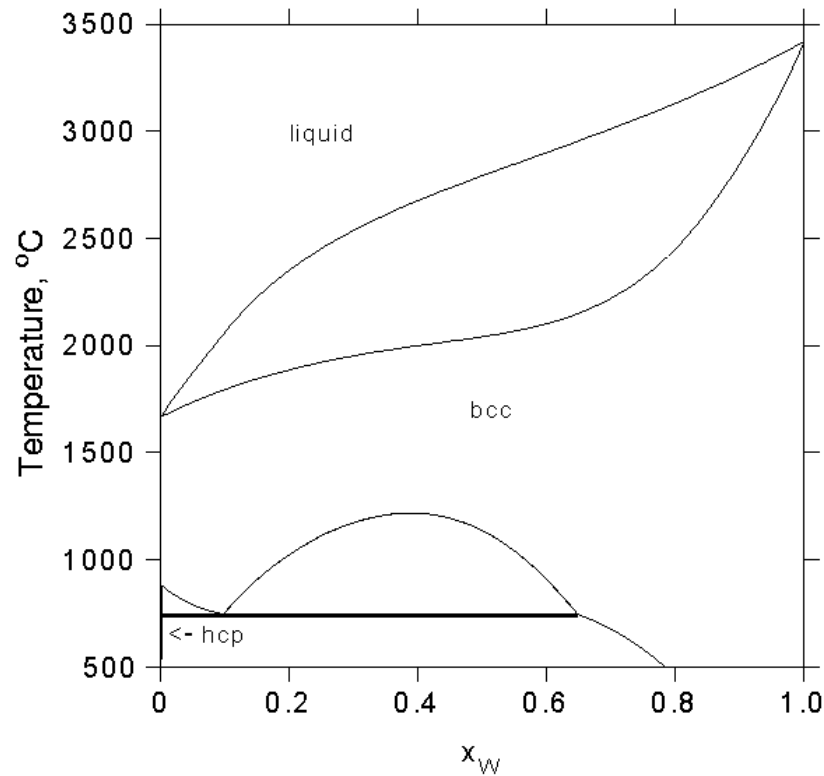




- Tensile stress increases with decreasing grain size
- The rate of change is different between the two systems
- The **stress is different** between the two systems for the **same grain size** indicating an **intrinsic solute effect**
- Intrinsic differences attributed to interatomic potential differences

Non-Cu Segregating System

W-Ti



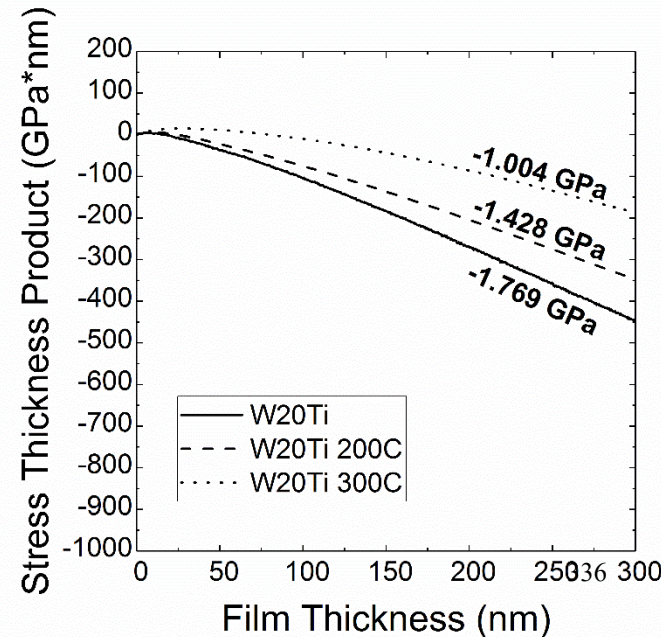
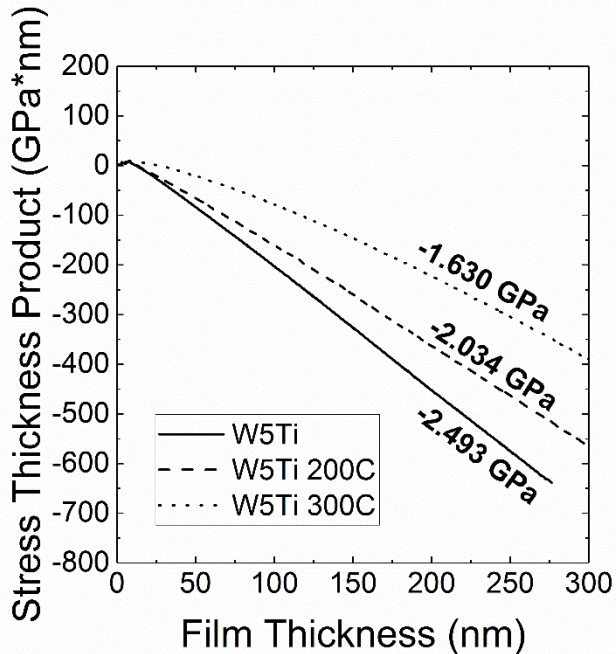
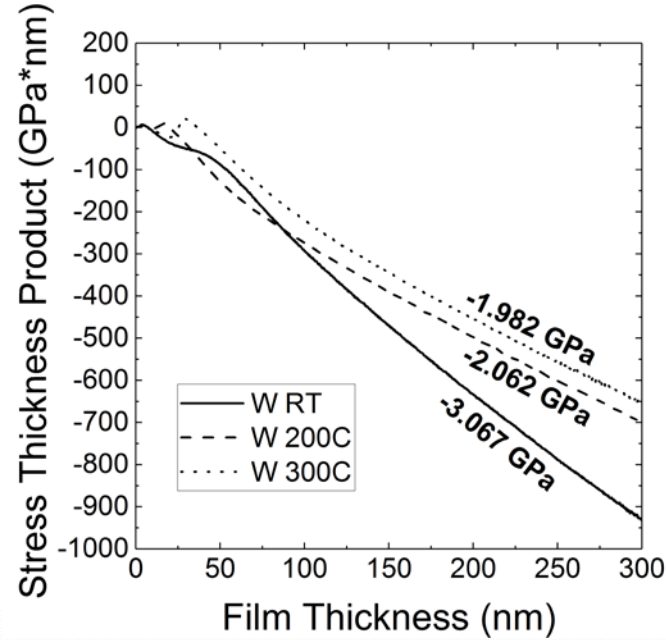
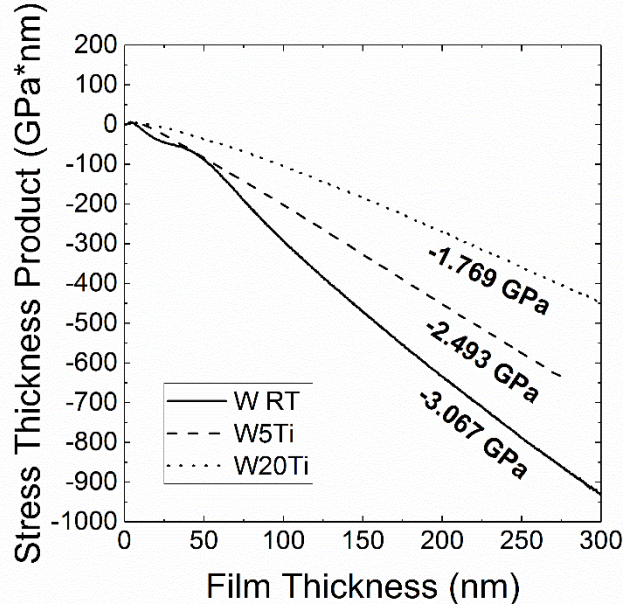
* Murray, *Alloy Phase Diagrams* 1981

- Forms solid solution up to 13 at.% Ti
- $\Delta H_{\text{seg}} \approx -75 \text{ kJ/mol}^*$

*H. A. Murdoch and C.A. Schuh JMR 28(16) (2013) 2154-2163

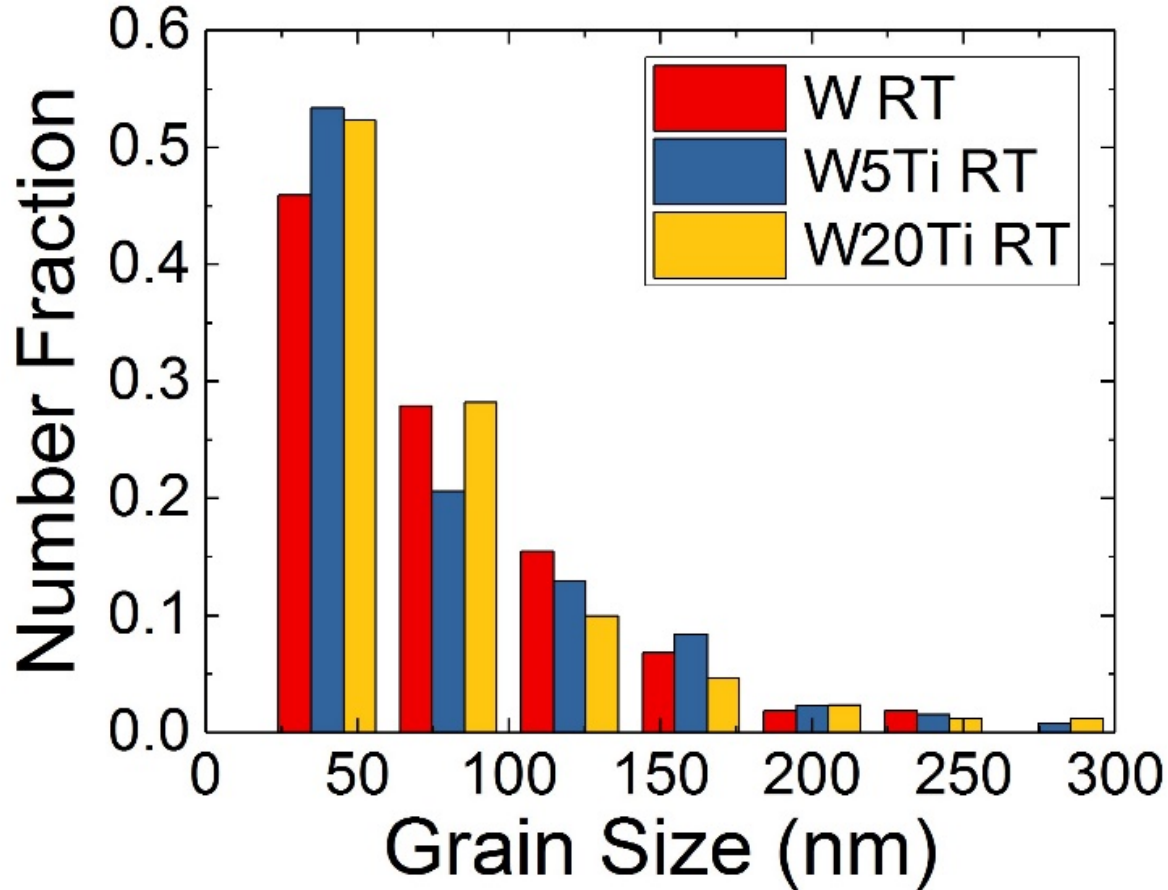
**T. Chookajorn, C.A. Schuh, *Acta Materialia*, 73, (2014) 128-138 reported APT W-Ti phase separation

Solute Additions Reduce Stress



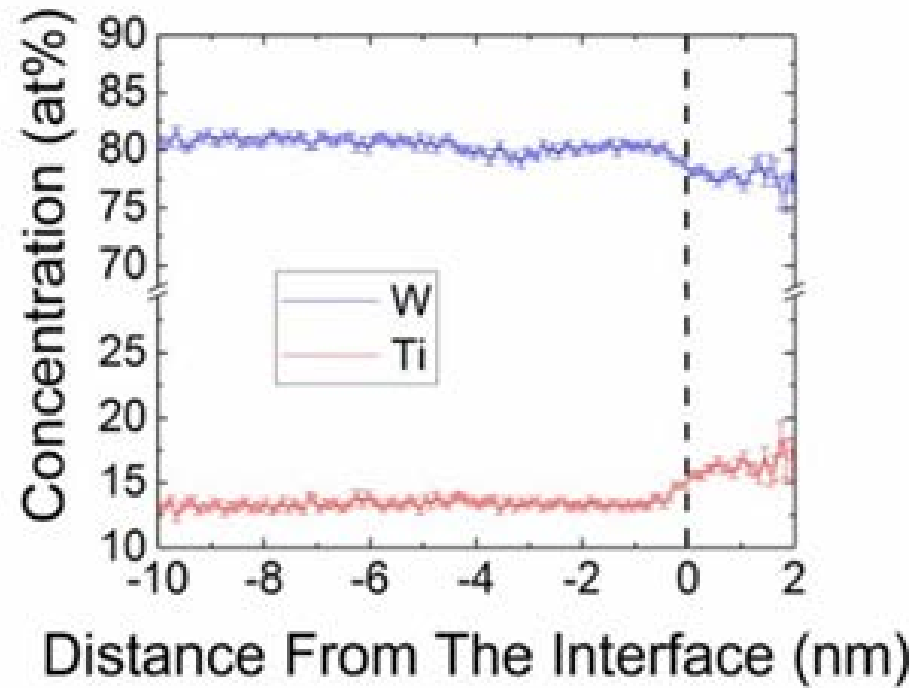
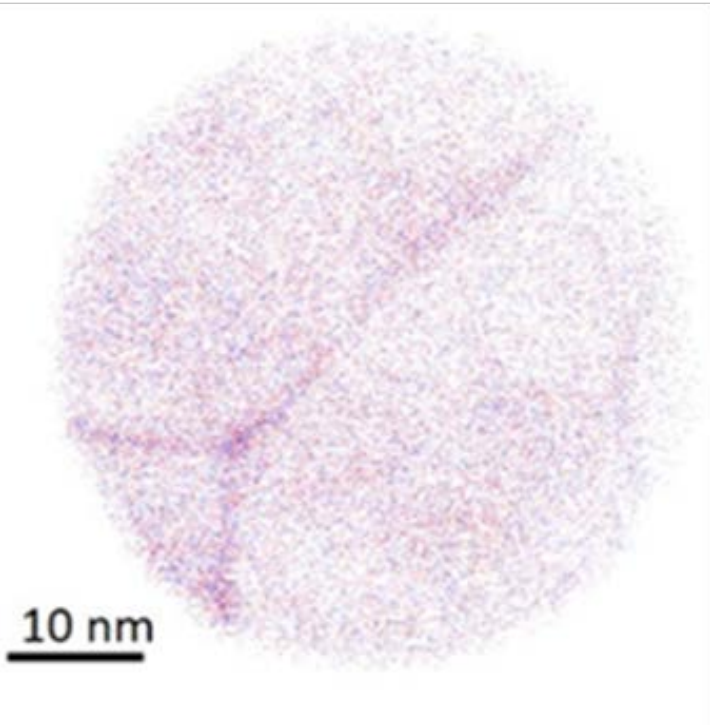
- Increasing Ti content decreased stress
- Higher substrate temperatures resulted in Lower Stresses

Grain Size Does Not Appear to be a Factor



- Grain size approximately the same for all alloys
- Very wide distribution observed

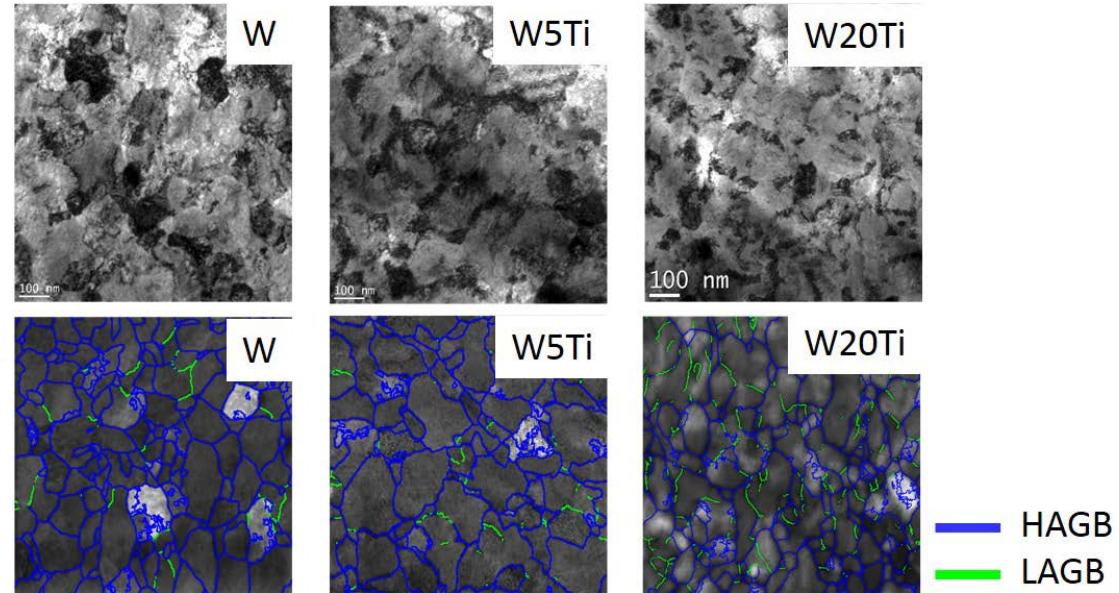
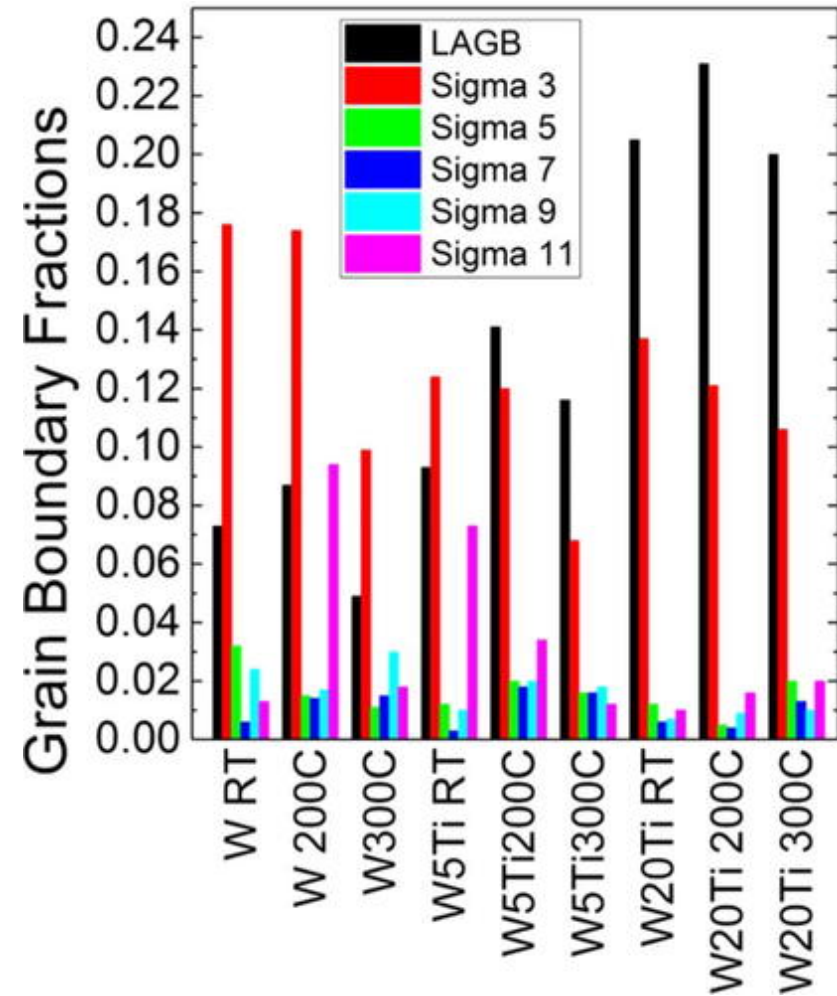
Solute Segregation Occurs



*H. A. Murdoch and C.A. Schuh *JMR* 28(16)
(2013) 2154-2163

T. Kaub, G.B. Thompson *J Applied Physics* 122 085301 (2017)

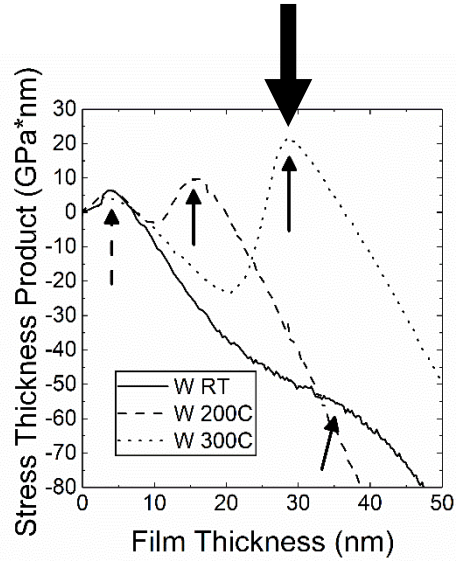
Solute Influence Grain Boundary Structure



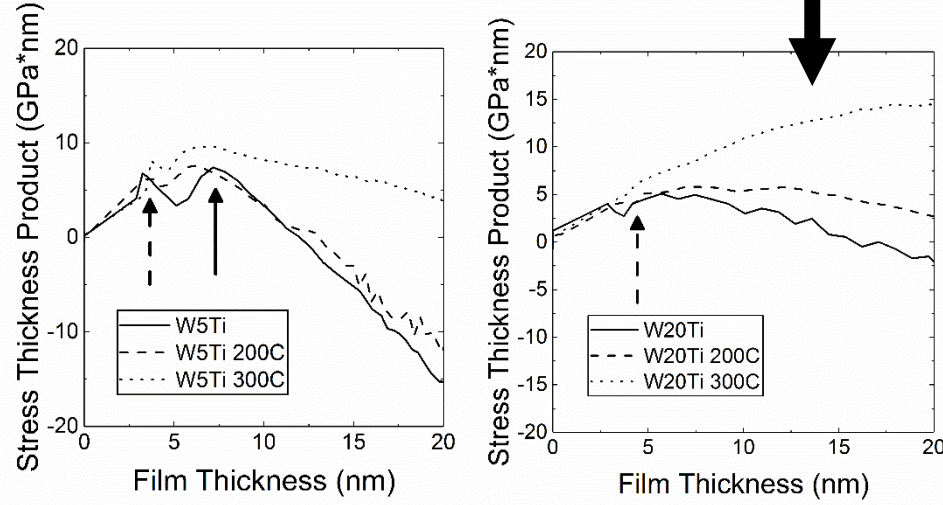
Stress Measurements Reveal Solutes

Alter Phase Stability

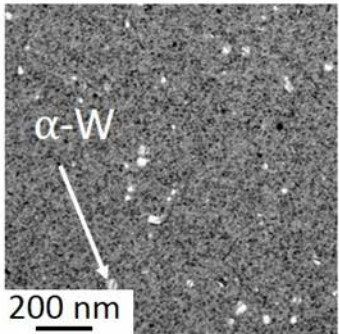
TEM Image



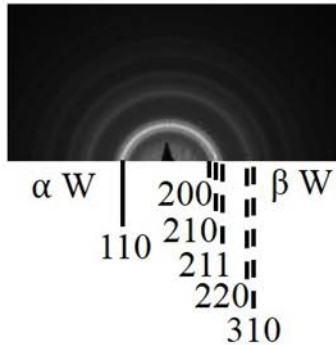
TEM Image



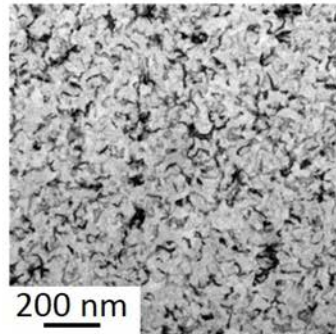
W-30nm



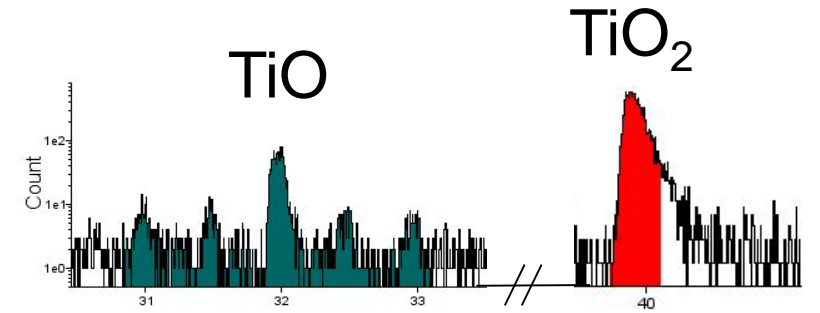
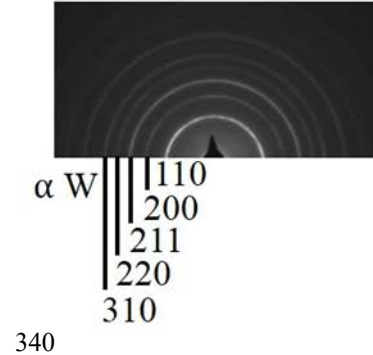
W-30nm



W20Ti-15nm



W20Ti-15nm



Conclusions

- Stress in thin films is strongly related to processing conditions
- Elemental Cu stress measurements matched well with the kinetic model for film stress
 - *At high deposition pressures, tensile stresses increased with deposition rate*
 - *For low deposition pressures a stress “inflection” was observed*
- In multi-component thin films, composition appears to regulate stress state
 - **Cu-Ni**
 - Addition of Ni solute increased compressive stress over elemental levels with further Ni additions resulting in the magnitude of the stress decreasing
 - **Cu-Ag and Cu-V**
 - Solute additions dramatically reduce the grain size and increase the tensile stress
 - Stress is not just a function of grain size but also an intrinsic component from the solutes Ag and V i.e. high vs. low mobility
 - **W-Ti**
 - Ti additions and substrate temperature reduce compressive stress
 - The stability of the β A15 phase is reduced with Ti additions
 - The fraction of low angle grain boundaries increases with Ti additions
 - Ti appears to getter oxygen reducing the β phase stability

Acknowledgments

- I would like to thank Professor Thompson along with the rest of my committee
- Our collaborators Dr.'s Peter Felfer, Julie Cairney and Eric Chason
- The CAF Staff for their help with the microscopes
- Finally my fellow research group members past and present

Chemical Mapping: Atom Probe Tomography

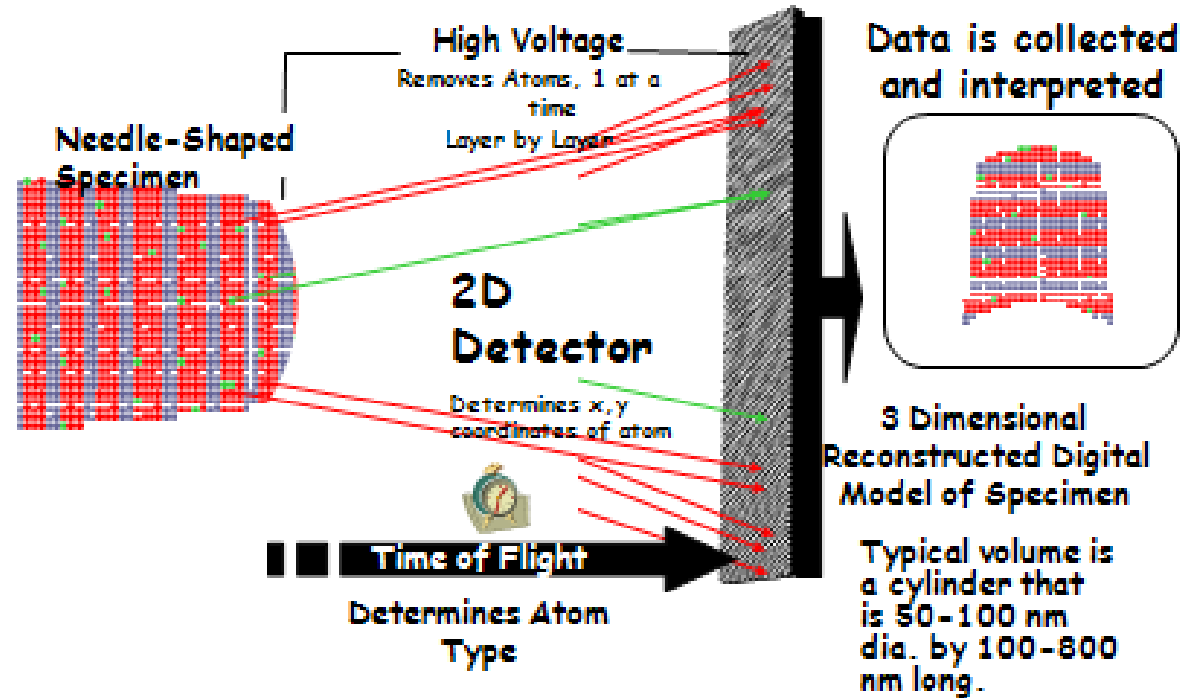
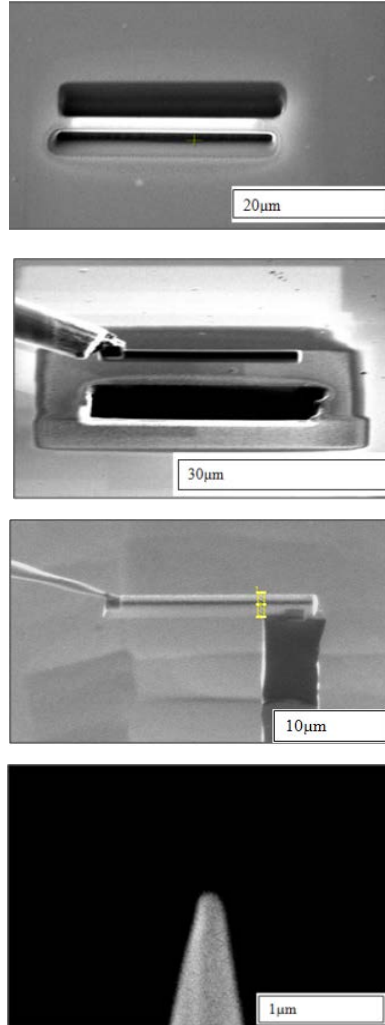
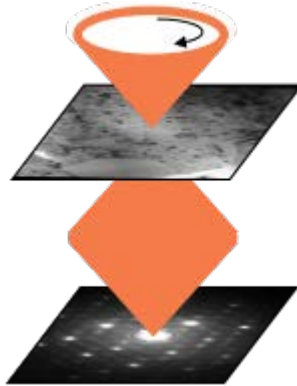


Image courtesy of T. Kelly, Cameca Instruments

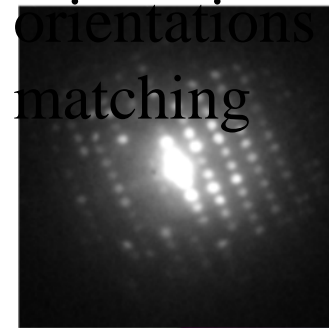
Precession-Electron-Diffraction for Orientation Mapping

Mapping

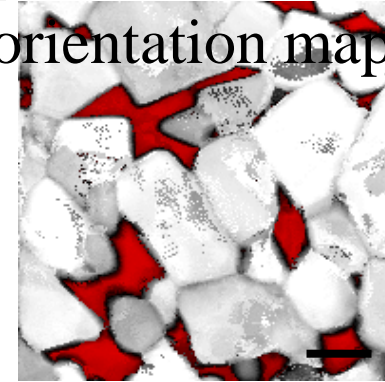
#1: Precess the beam



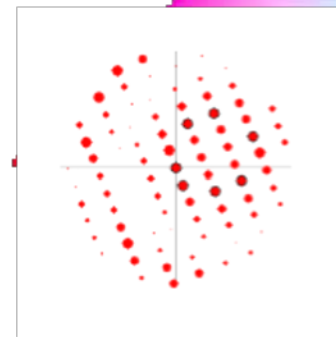
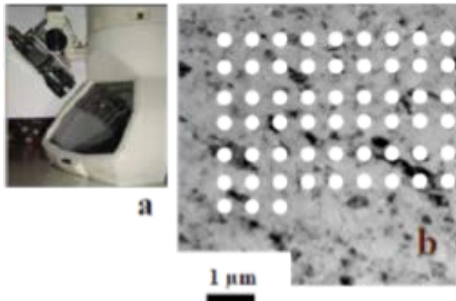
#3: Compare experimental DP to simulated orientations for matching



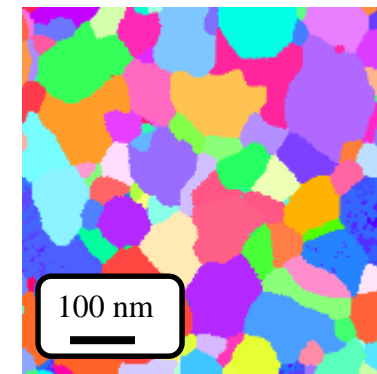
#4: Out put phase and orientation maps



#2: Raster



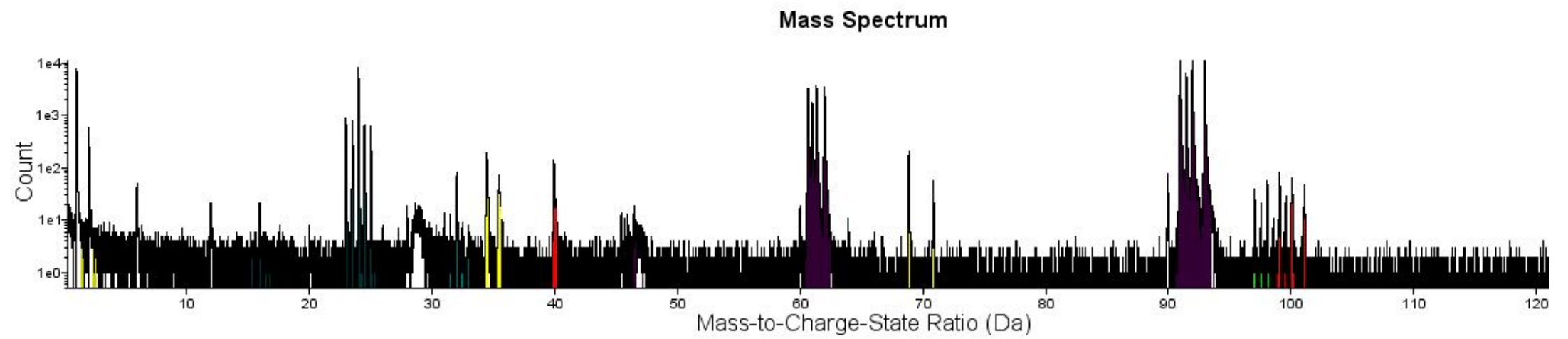
111



100

101

Mass Spectrum W-Ti



Influence of Solute Segregation on Stress and Structure Evolution in Nanocrystalline Thin Films

Xuyang (Rhett) Zhou

*University of Alabama, Materials Science PhD Program
Tuscaloosa, Alabama, USA*

*Committee Members:
Prof. Gregory Thompson, chair
Professor Luke Brewer
Professor Amber Genau (UAB)
Professor Gary Mankey
Professor Mark Weaver*



This work was funded with support from the Army Research Office, ARO-W911NF-13-1-0436.



Acknowledgement

Supervisor:

Professor **Gregory B. Thompson**

Committee members:

Professor **Gregory B. Thompson**

Professor **Luke N. Brewer**

Professor **Amber Genau (UAB)**

Professor **Gary Mankey**

Professor **Mark L. Weaver**

Funding support:

Army Research Office, **ARO-W911NF-13-1-0436.**

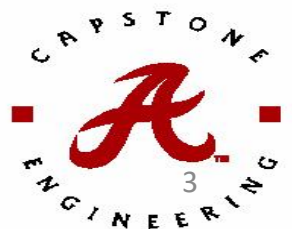


- **Why is stress important and where does it come from in thin films?**

- **Modeling thin film stress as a function of**
 - **Injection energy**
 - **Surface morphology**
 - **Grain size**

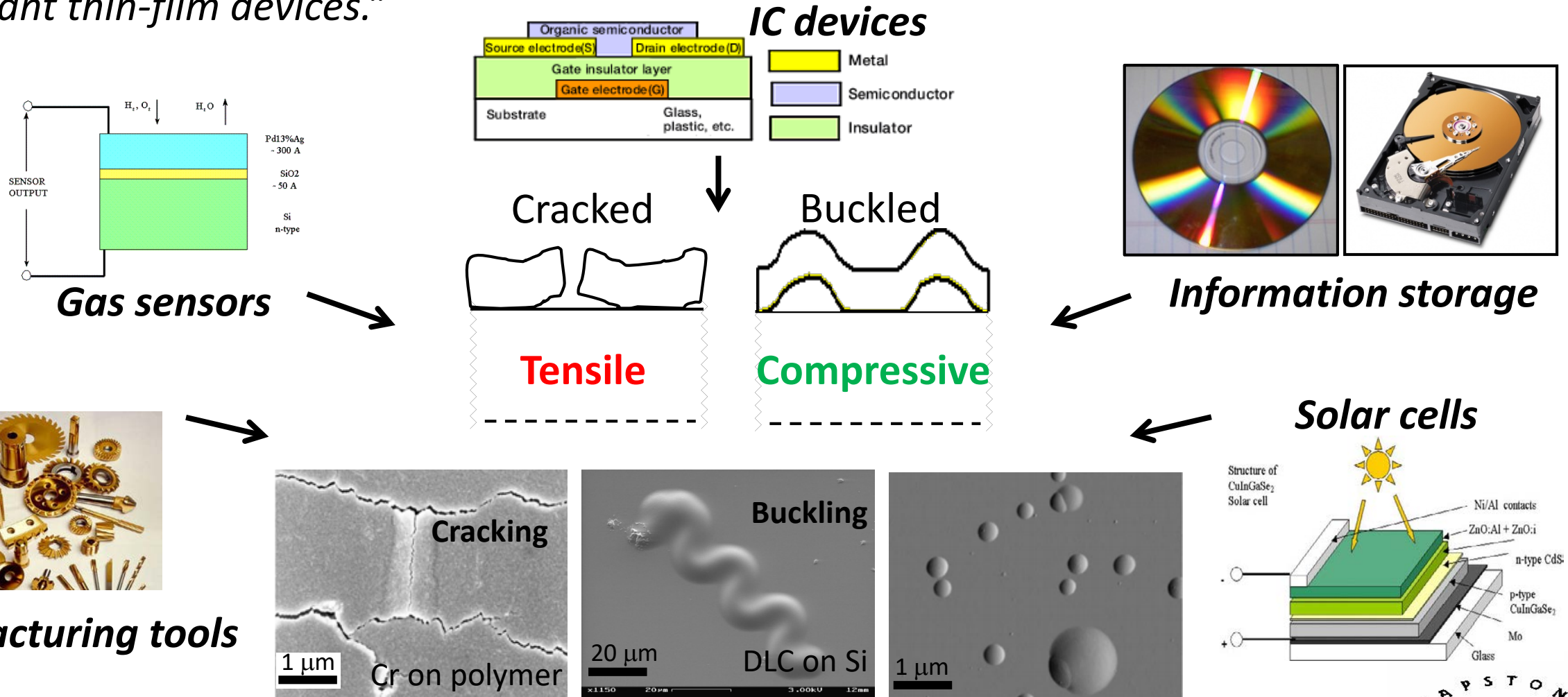
- **Compositional effects on stress evolution**
 - **Mixing tensile-compressive stress states... *seeking zero stress***
 - **Tensile-tensile mixing of stress... *a surprise finding***

- **Specificity of solute segregation to grain boundaries**



Motivation: Thin Film Adhesion and Failures

R. Koch: "Stress is frequently held responsible for malfunction or failure of technologically important thin-film devices."



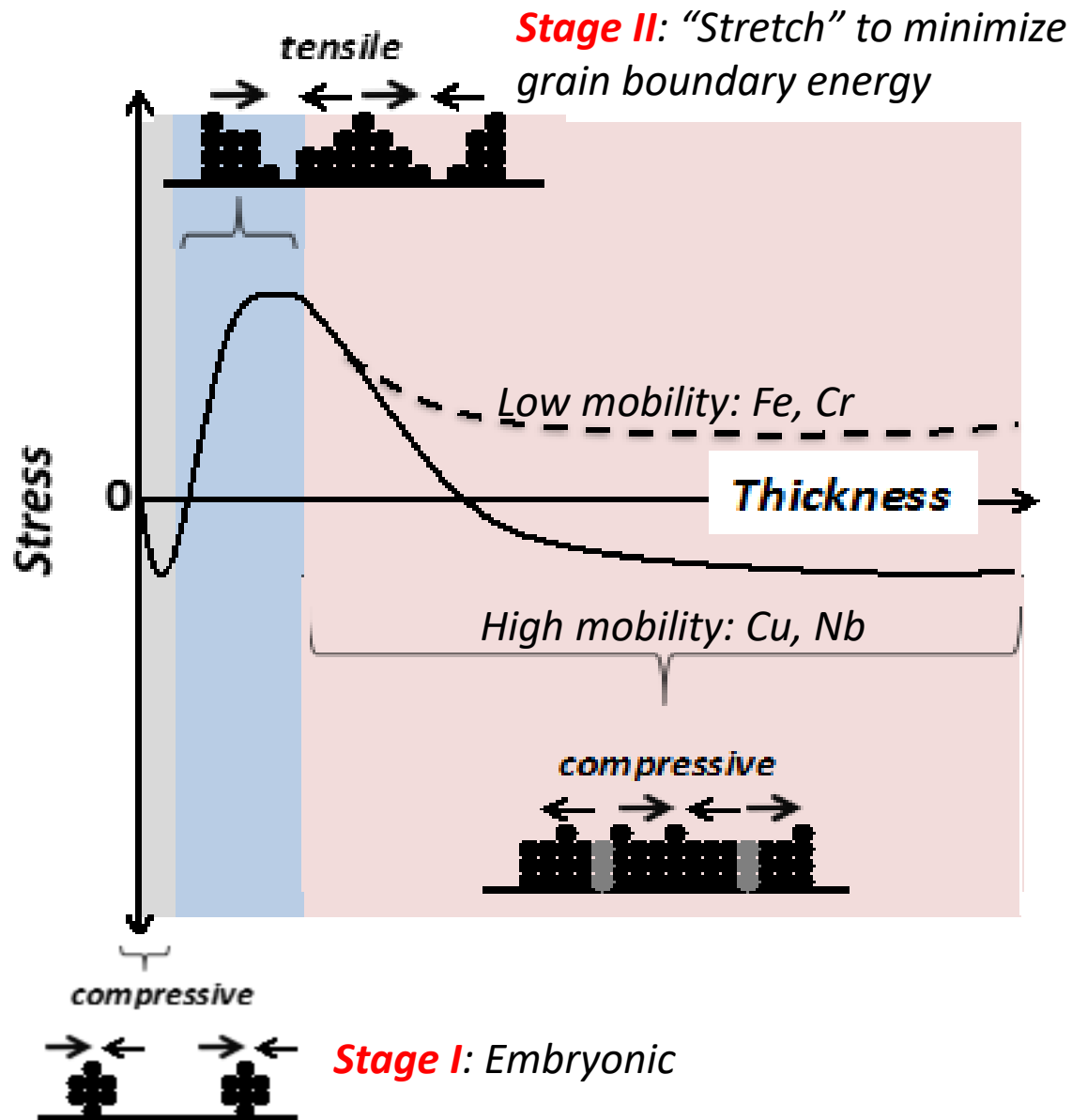
Manufacturing tools

<http://diamond.kist.re.kr/DLC/mwmoon/gallery.htm>

A. Kuznetsov, *Journal of Physics-Condensed Matter*, **24** (2012).

R. Koch, *J. Phys.:Condens. Matter* **6**, 9519 (1994)





In *Stage III*, the steady growth stress is

$$\sigma_{growth} = \sigma_C + (\sigma_T - \sigma_C) e^{\frac{-\beta D}{R_g L}}$$

σ_T : Impinging tensile stress; σ_C : Compressive stress due to adatoms inserting into grain boundaries; R_g : Growth rate; L : Grain size; D : effective diffusivity of atoms from the surface into the grain boundaries; β : concentration of mobile defects and the mechanical properties of the layer

E. Chason, Thin Solid Films, 526 (2012) 1-14.

In a sputtering system, the adatoms are energetic:

$$\sigma^{sputt} = \sigma_{growth} + \sigma_{gb}^{energetic} + \sigma_{bulk}^{energetic}$$

Growth rate dependent

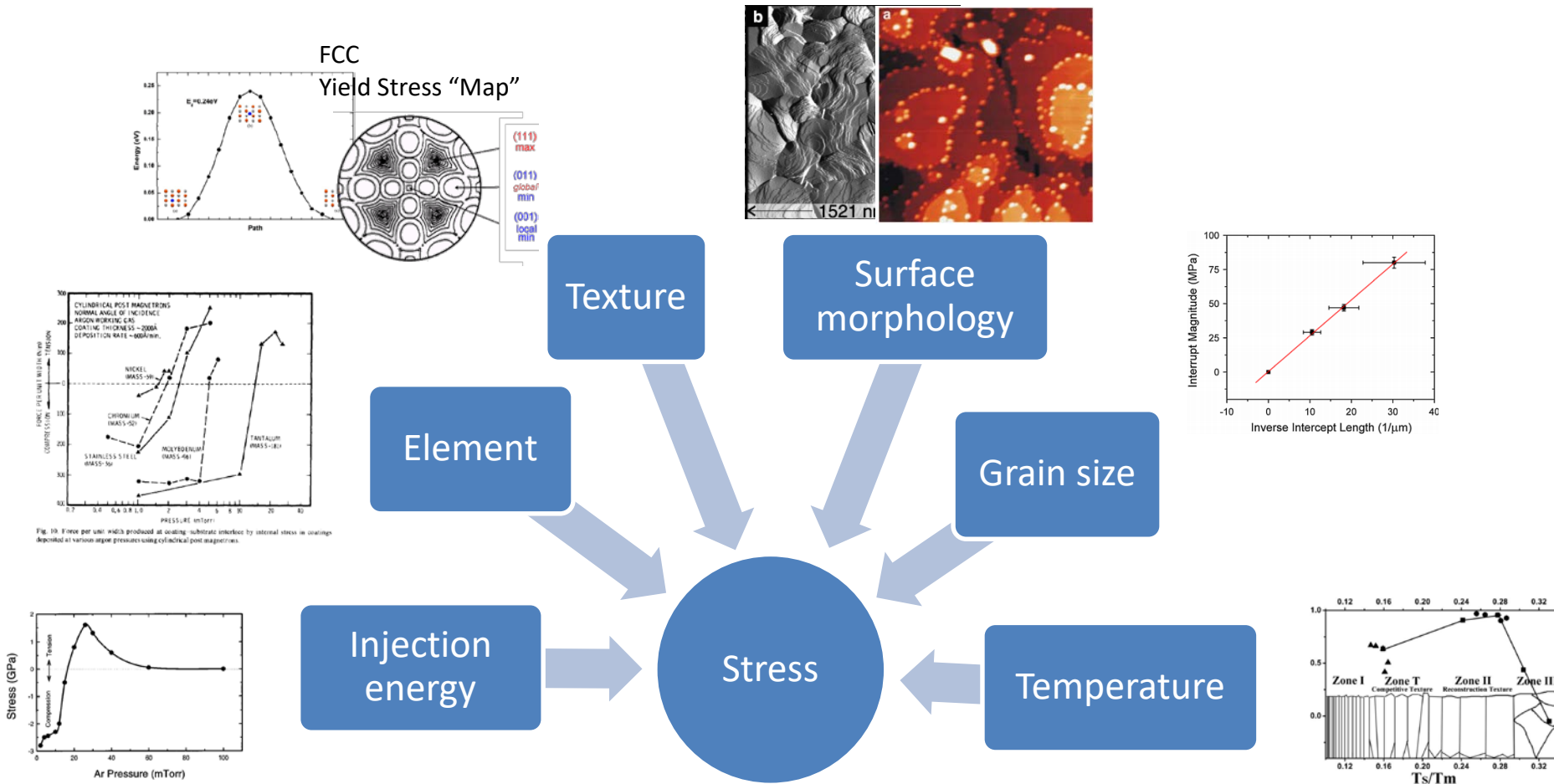
Growth rate dependent

Growth rate independent

Chason, E. et al., Journal of Applied Physics 119 (2016) p. 145307



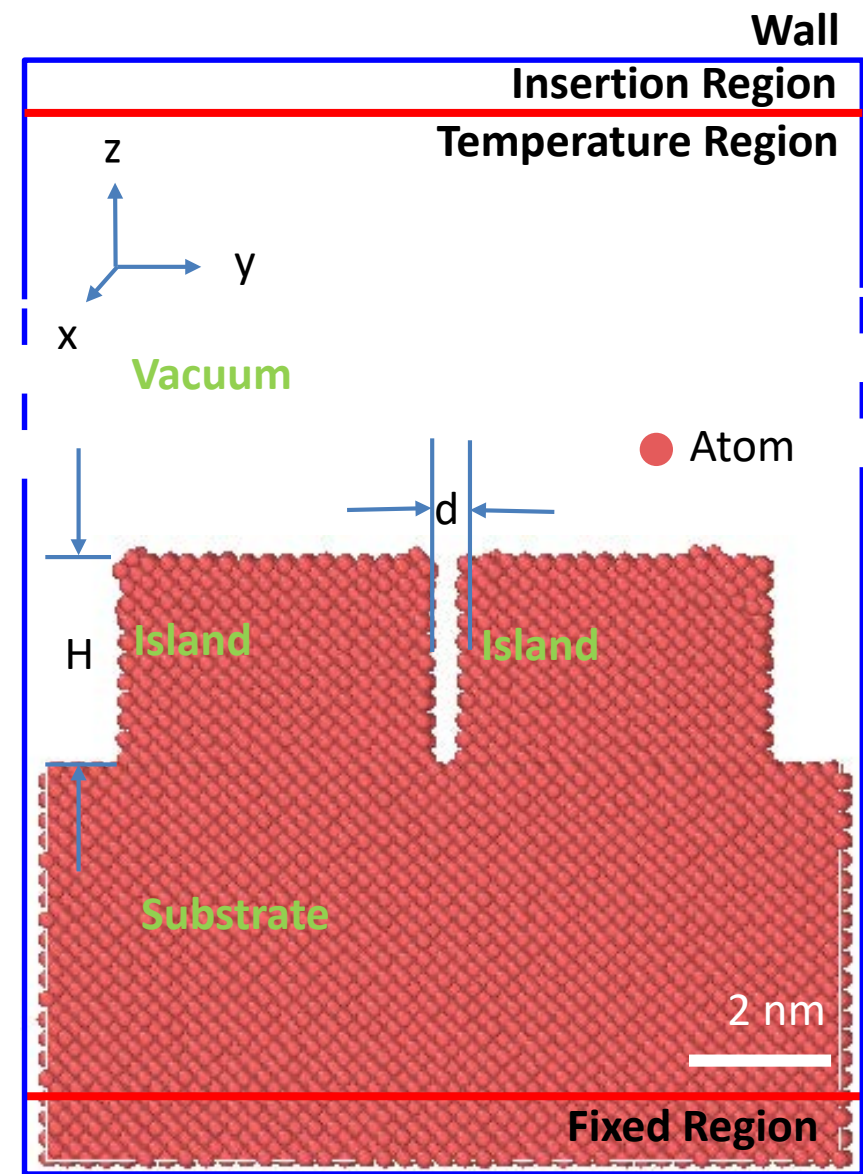
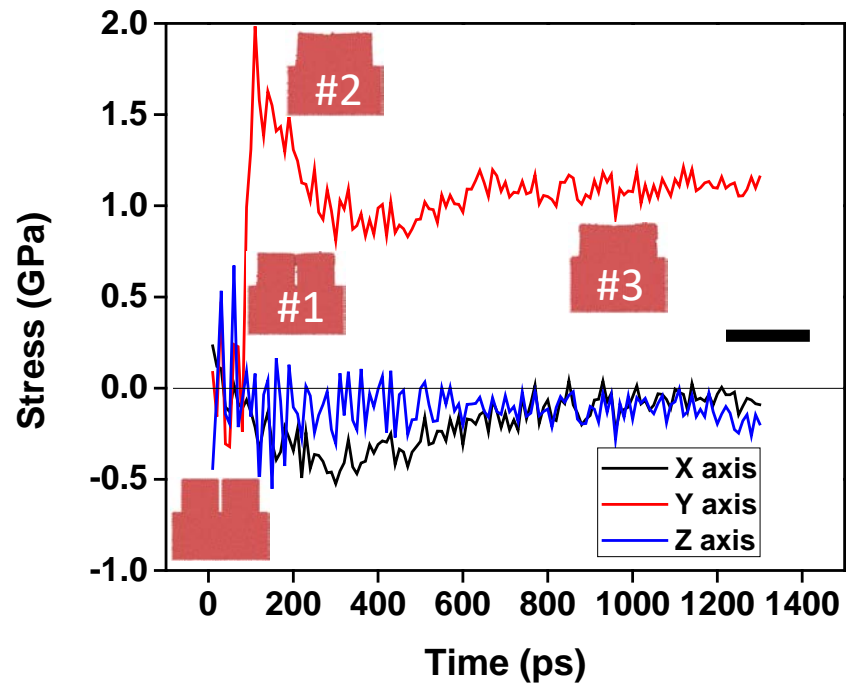
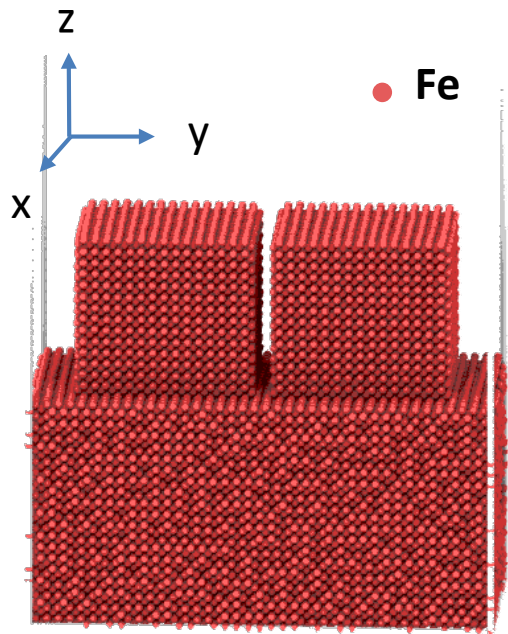
What factors can affect thin film stress?



- Many factors can affect thin film stress;
- All these factors are not independent! Changing one factor might also affect another or more other factors;
- **Can we use a model to study the effect of each factor separately**

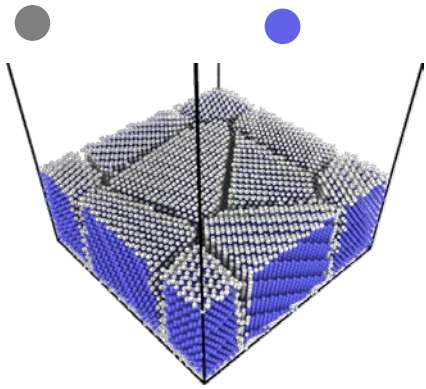
Molecular Dynamics - Structural Model

- A four regions model has been created to mimic the deposition process:
 - **A virtual wall region** to re-sputter the atoms;
 - **An insertion region** where the incident atoms were injected;
 - **A temperature region** where the incoming atoms interacted with the under layer;
 - **A fixed region** to prevent the movement of the initial atoms.

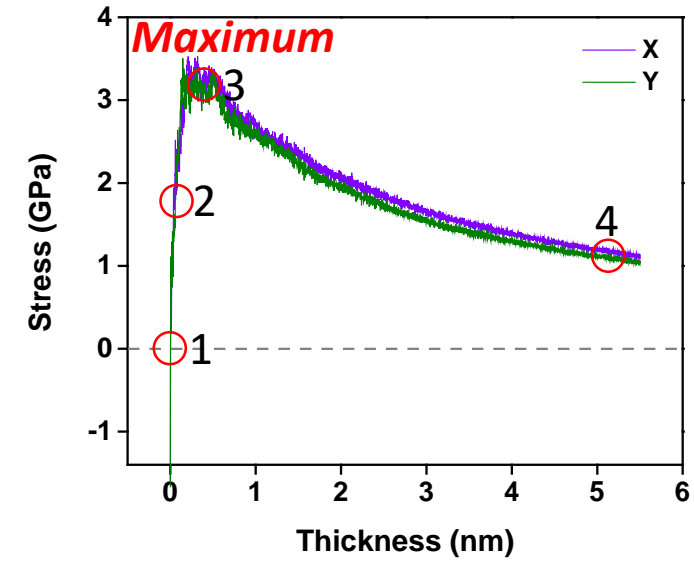
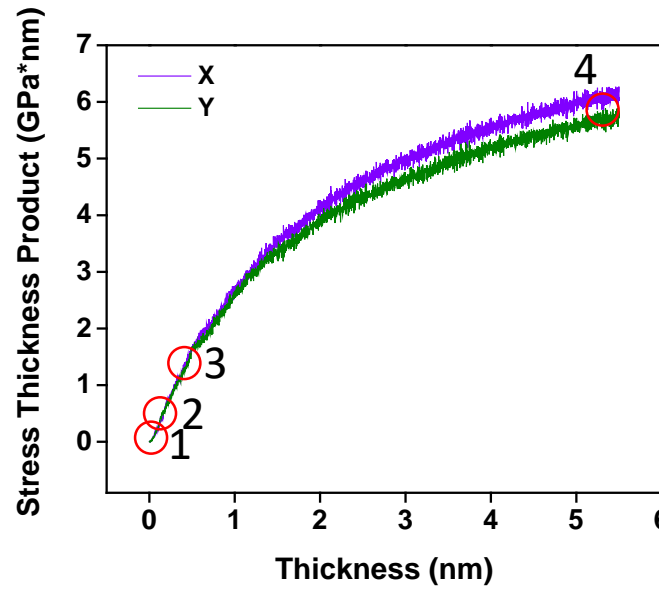


- H is the height of islands;
- d is the distance between two islands.

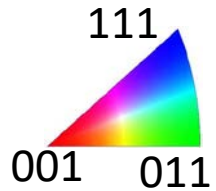
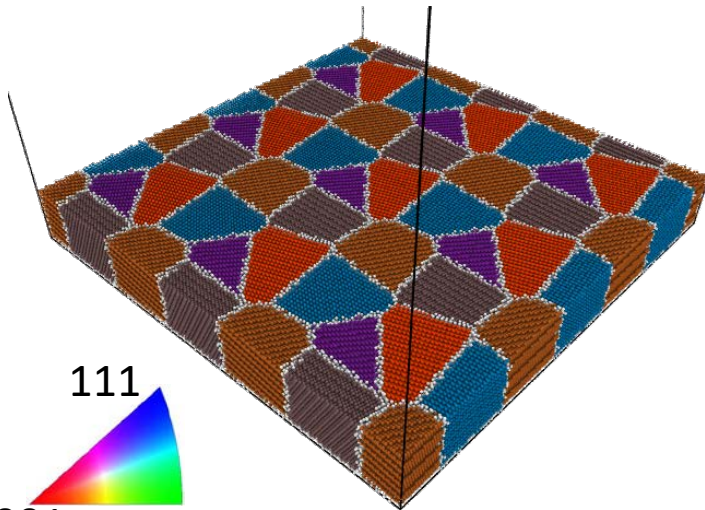
Polycrystalline Model



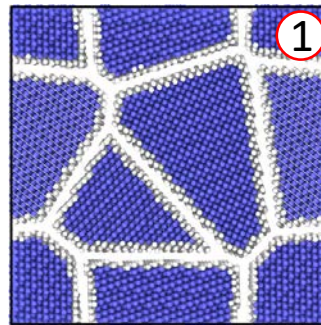
300K, Tungsten, 5eV
Random orientated
Perpendicular edge
structural model



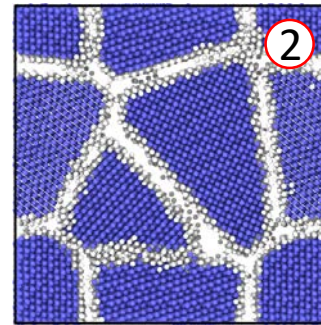
Random Orientation



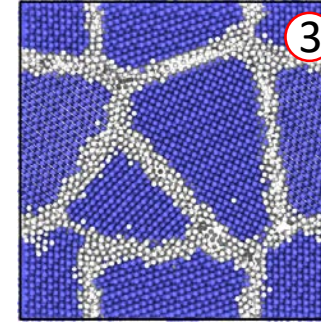
Top view



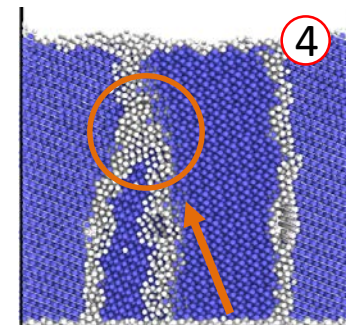
Top view



Top view

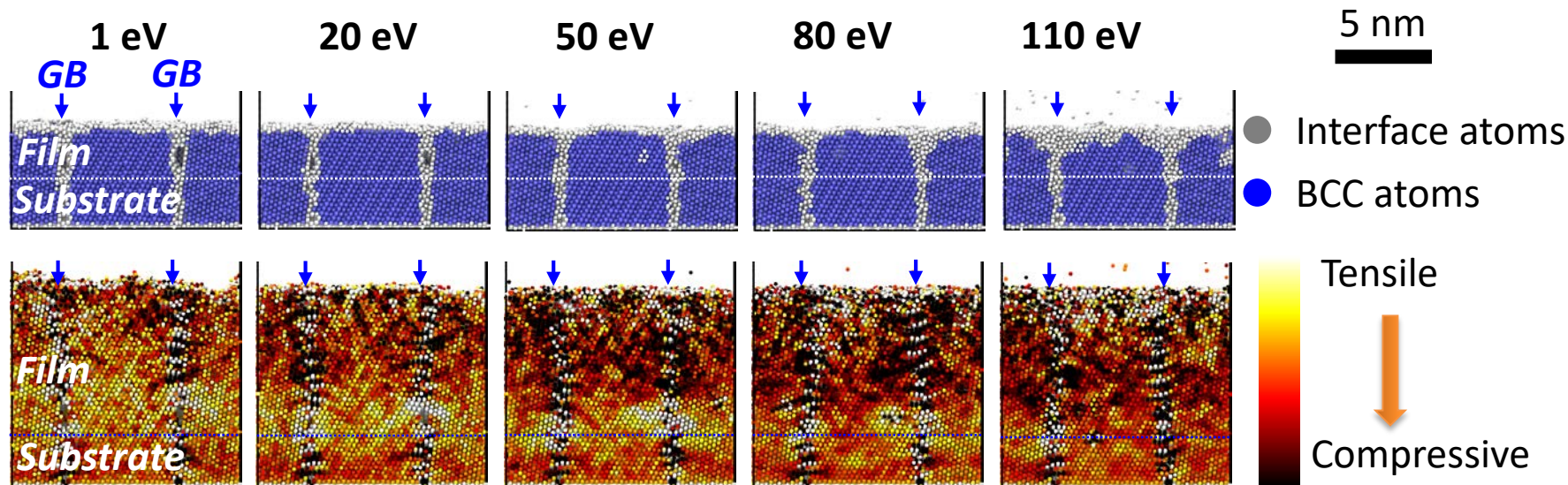
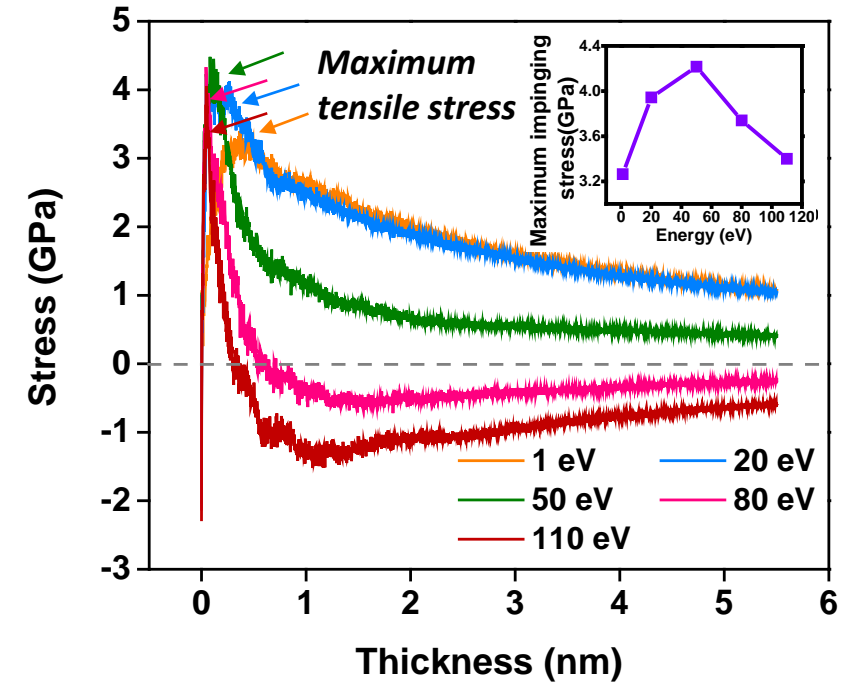
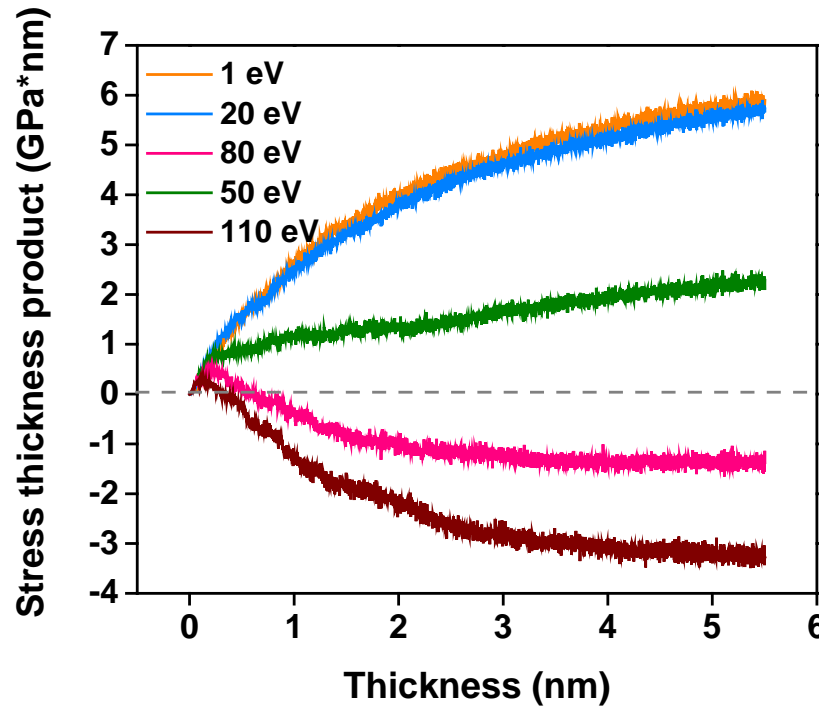
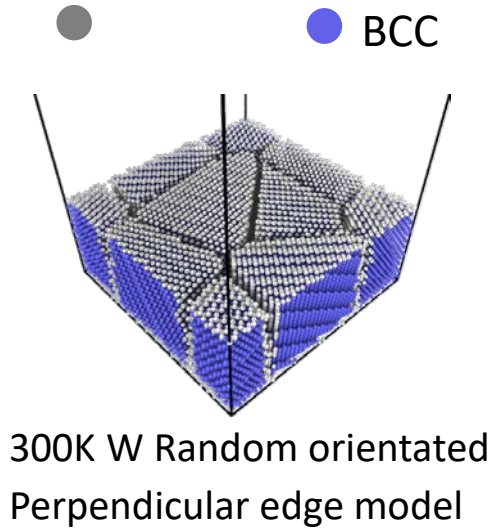


Side view



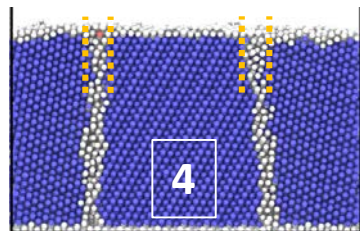
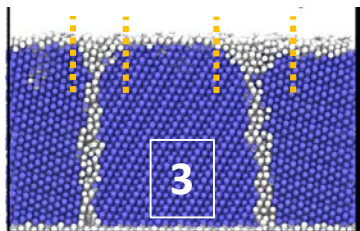
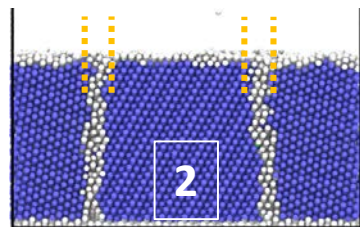
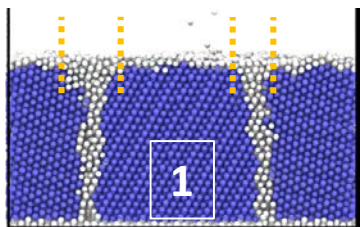
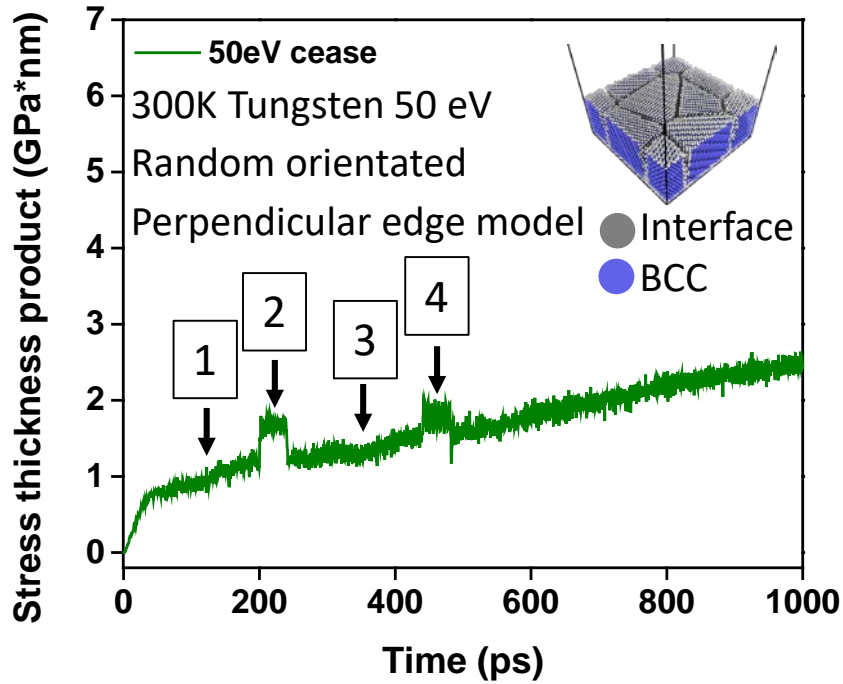
- The tensile stress is generated by the coalescence of adjacent.
- The initial generated tensile stress is averaged by the stress from further growing films





Higher injection energy:

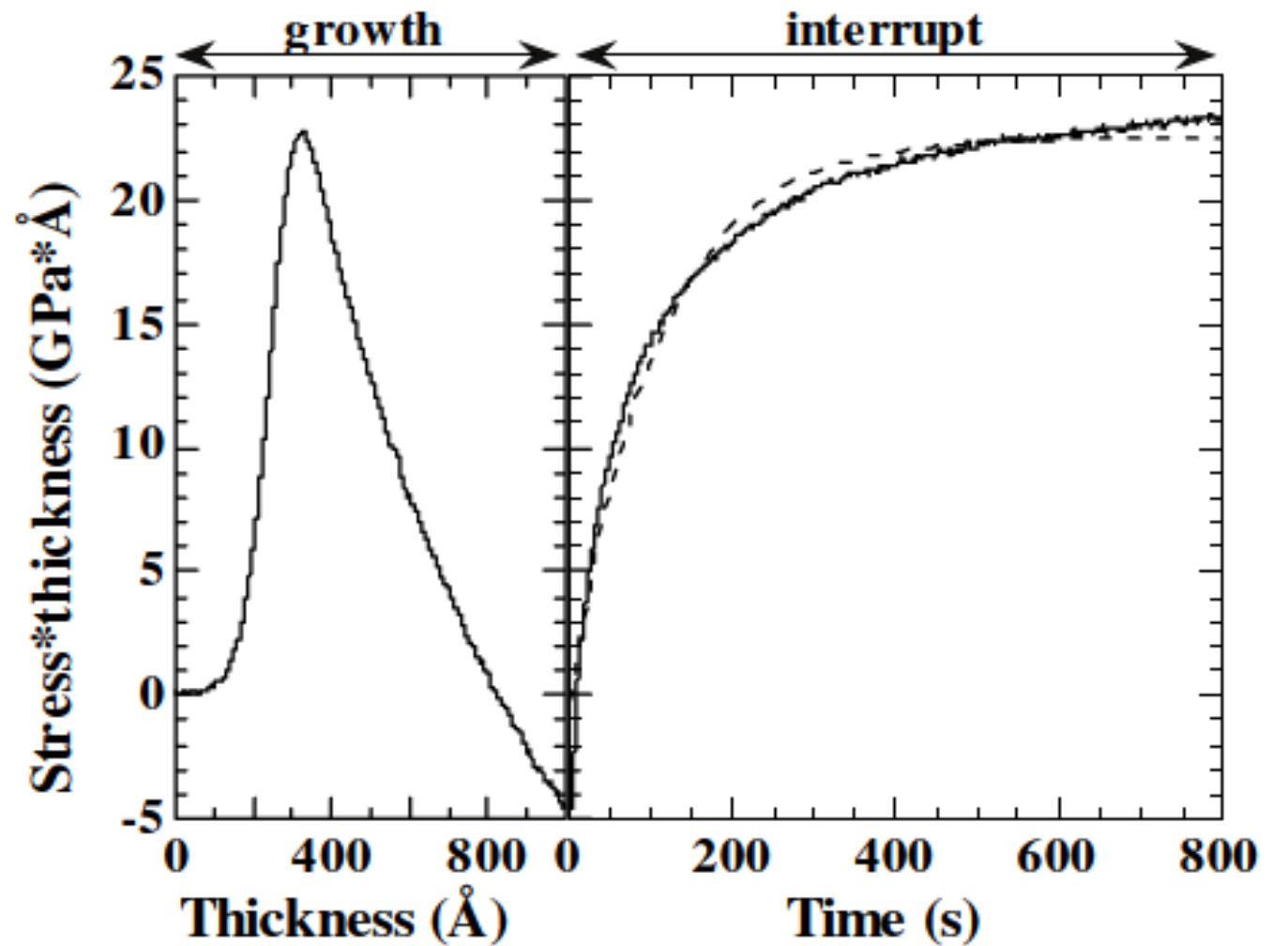
- Can heal defects;
- Generates wider grain boundary;
- Causes injection impact.



● BCC

● Interface atoms

5 nm



- Grain boundaries “tighten up”;
- Surface defects disappeared.

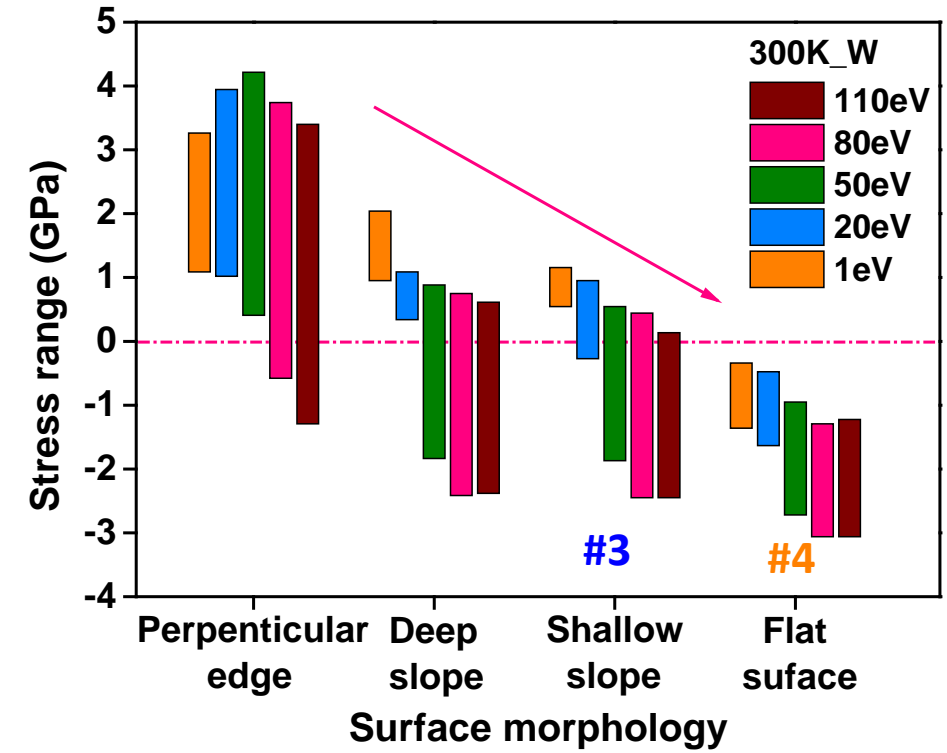
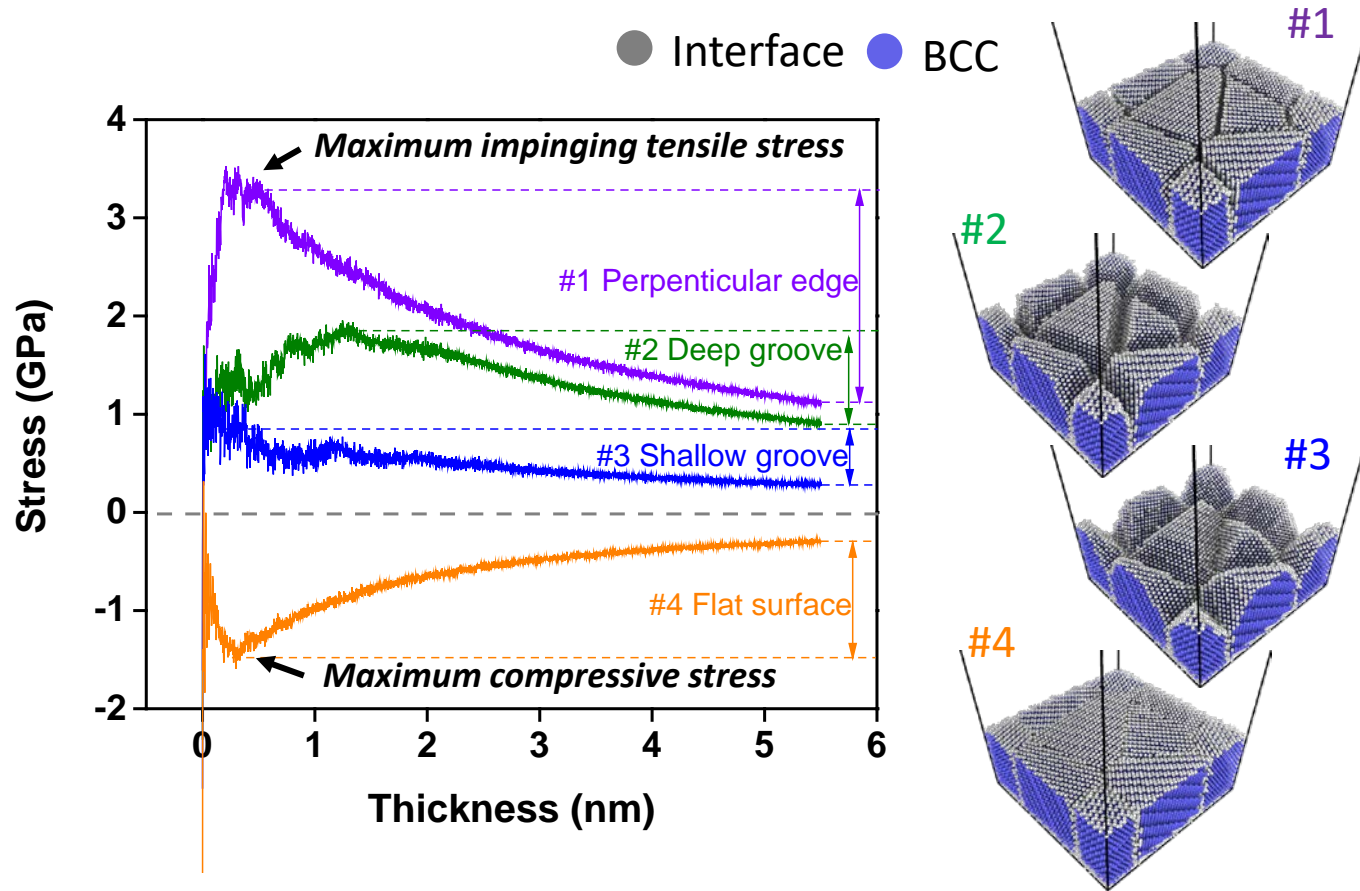
$\sigma_{gb}^{energetic}$

Time dependent

Chason, E. et al., Physical Review Letters **88** (2002) p. 156103.

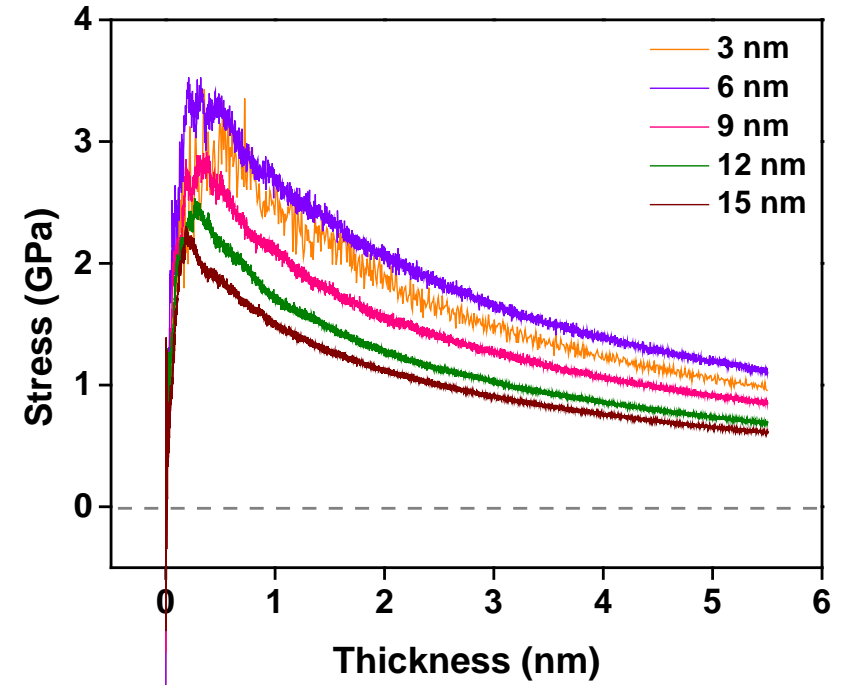
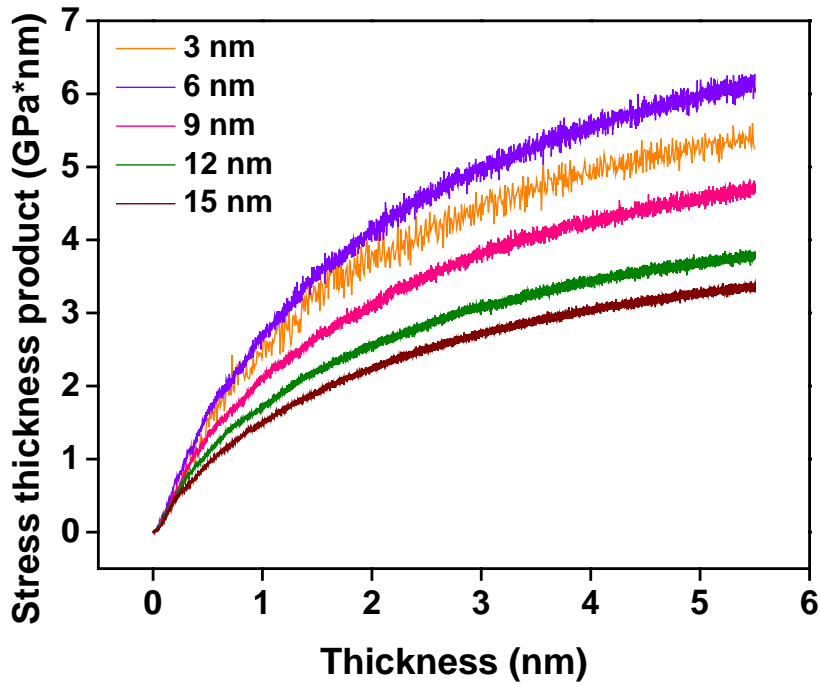
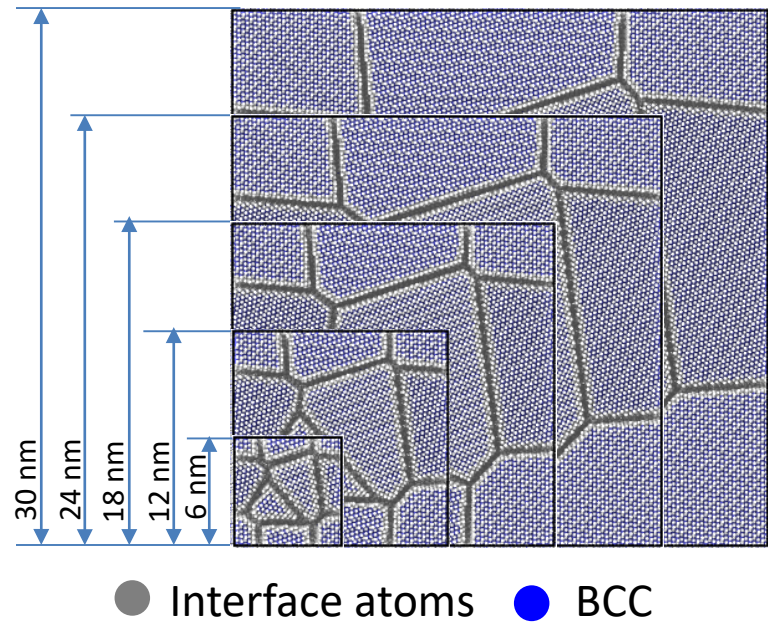


Surface Morphology



- Stress is related to the surface morphology of islands, which can be perpendicular, with a slope, or flat;
- If the islands have a slope, the attraction force will be reduced and less tensile stress can generate;
- Tensile stress cannot be generated on a flat surface. More dominant compressive stress is observed.

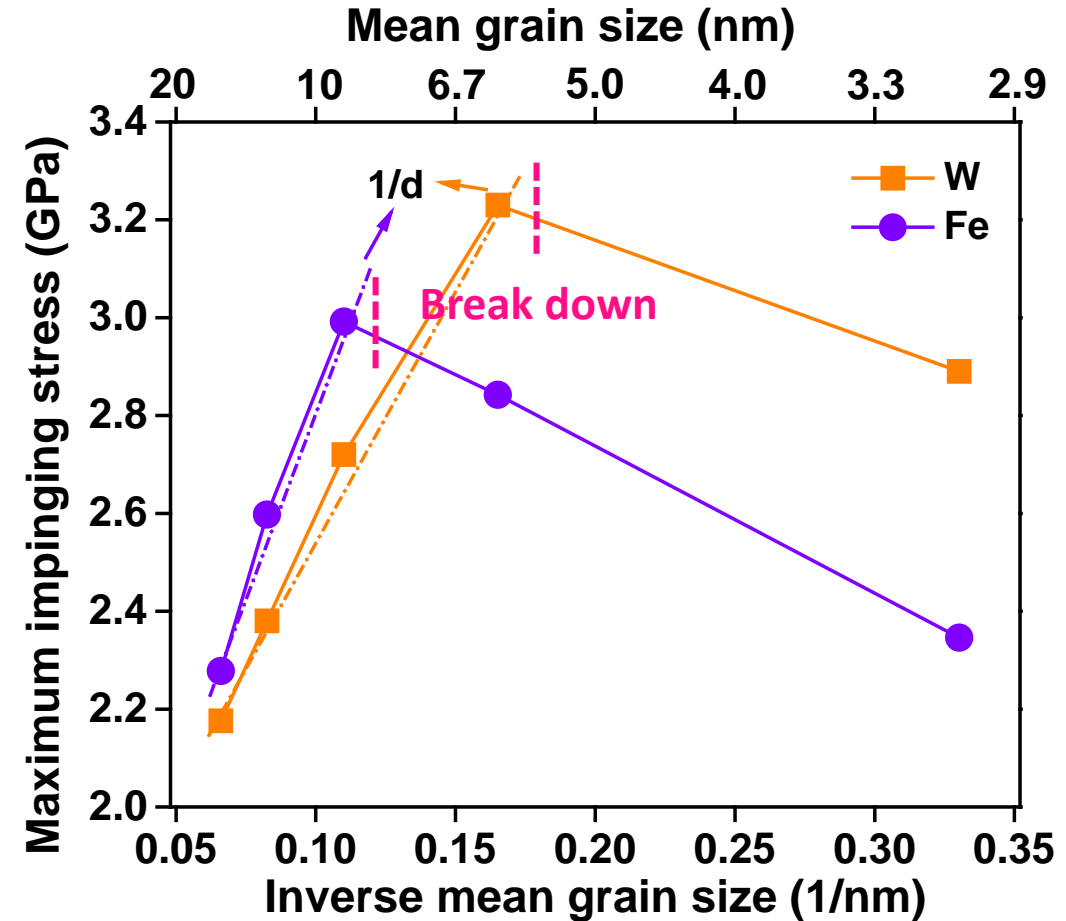
300K Tungsten 5eV Random orientated
 Perpendicular edge model



$$\langle \sigma \rangle = \frac{4(2\gamma_s - \gamma_{gb})}{d}$$

γ_s : Interfacial energy of the surface; γ_{gb} : Interfacial energy of the grain boundaries; d : Grain diameter.

- An inverse relationship was found between the maximum impinging stress and grain size;
- This inverse relationship breaks down when the grain size drops to some critical value;

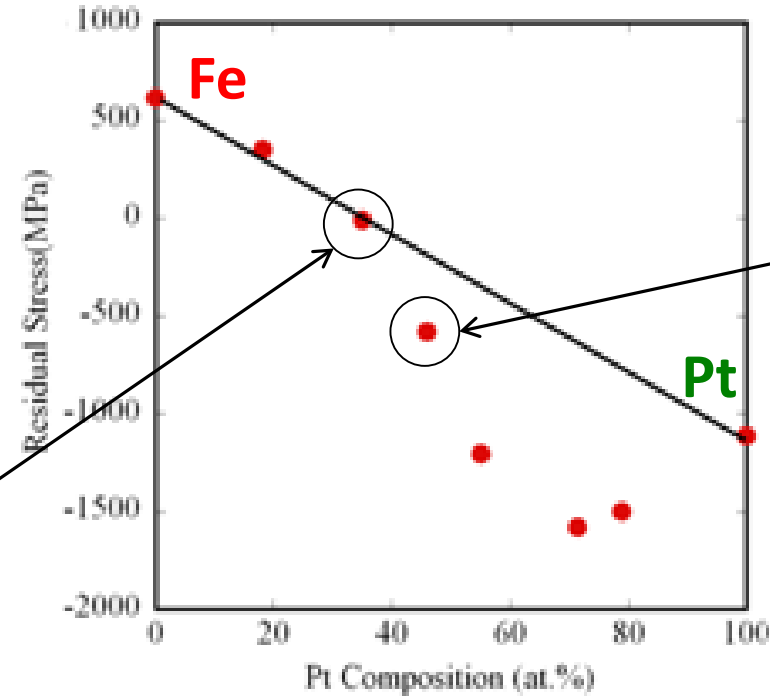
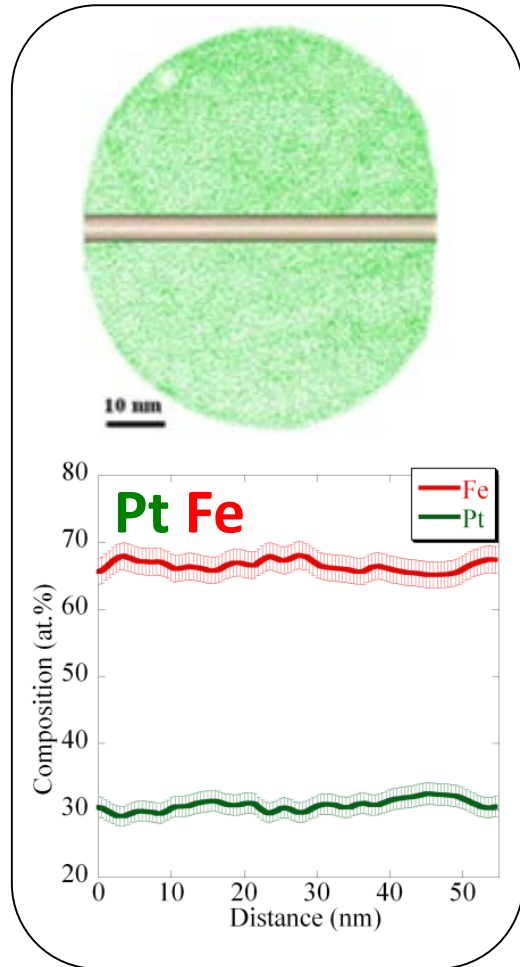


- The generation of tensile stress results from the coalescence of adjacent islands.
- A higher injection energy of adatoms can heal defects to generate a better coalescence of between the adjacent islands resulting in an increase of the maximum impinging tensile stress.
- If the injection energy is too high, a reduction of tensile stress or an increase of compressive stress were observed due to peening effect and grain boundary widening.
- A recovery of tensile stress was observed due to the decrease of grain boundary width and surface defects healing.
- Surface morphology is important to the generation of stress. The steeper the adjacent face is, the stronger tensile stress can generate.
- In general, the large grain size, the higher impinging tensile stress can be generated. However, under some specified limit of grain size, this relationship was not valid due to the yield strength of the studied material and a large fraction of the atoms in the grain boundary.

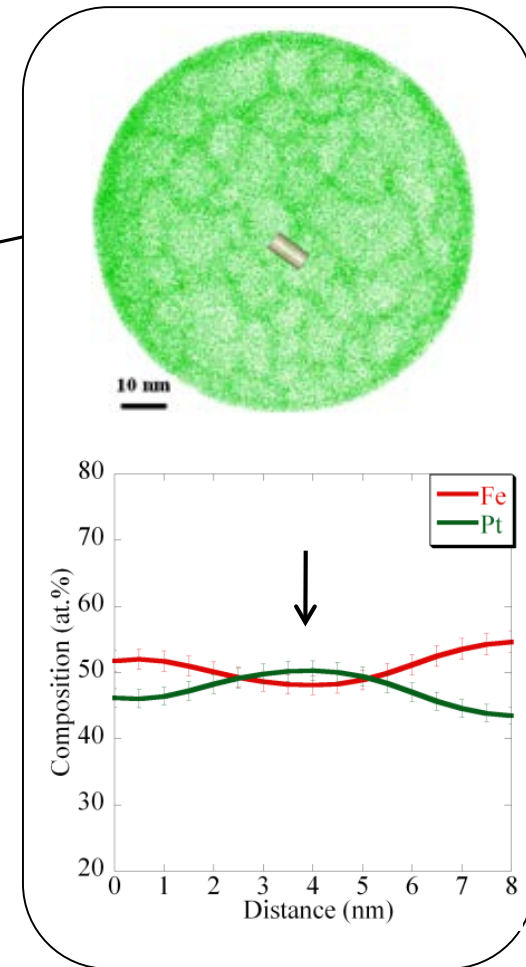
What about compositional effects on stress?

- Not a lot of work done
- Want to build up an experimental data base of this behavior

$\text{Fe}_{0.65}\text{Pt}_{0.35}$: Pt atoms map



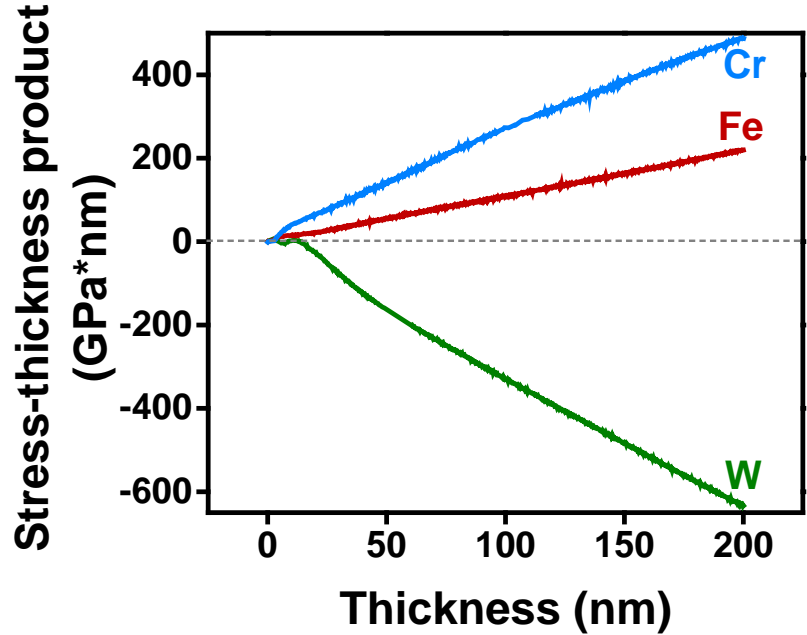
Stress trending with species in the grain boundaries



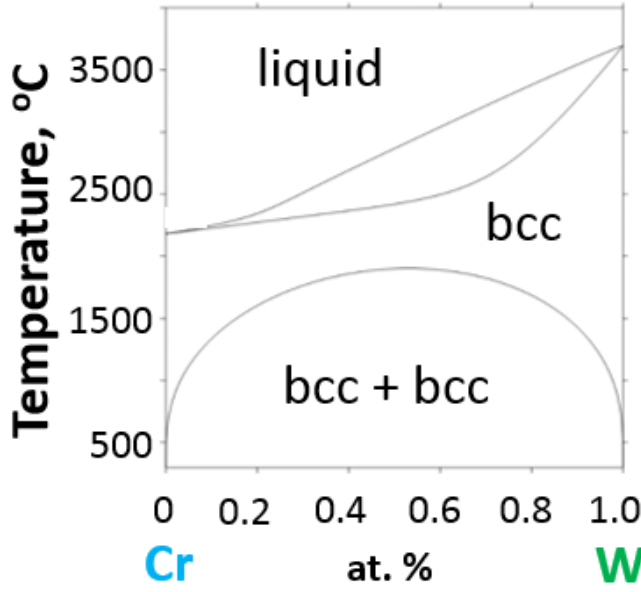
- Can a mix of tensile + compression give you a similar zero stress state?
- If so, what is its chemical structure of the grain boundary like?

Tensile: Fe, Cr

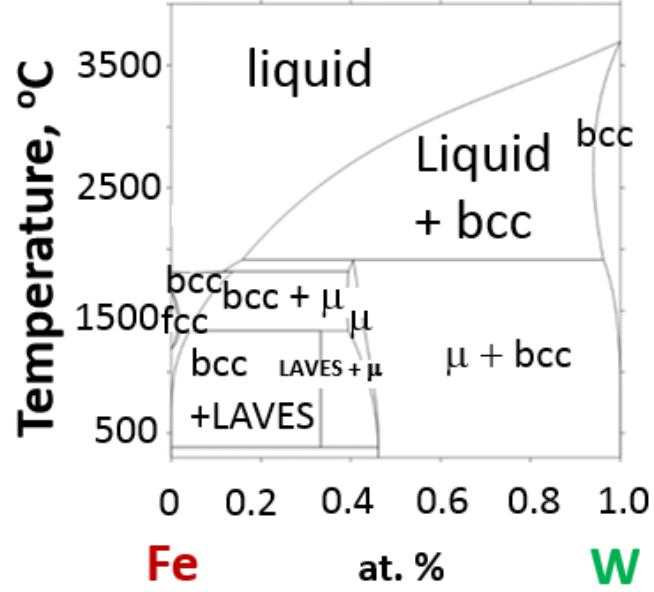
Compressive: W



miscibility gap – segregating behavior



Xu, K. et al., MSI, Stuttgart, 2016

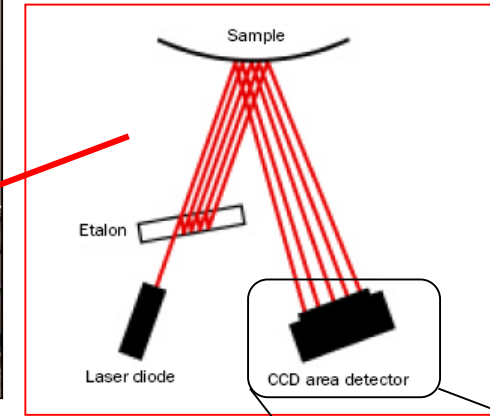
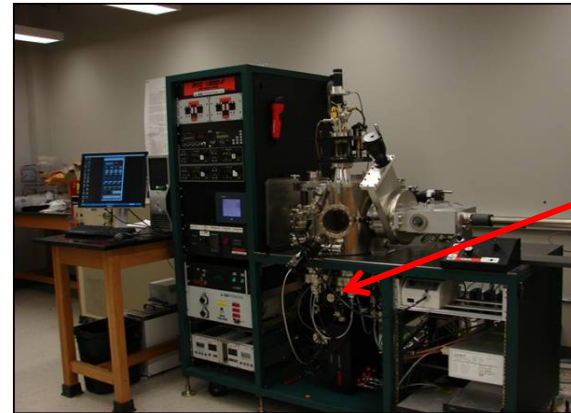


Vreštál, J. et al., MSI, Stuttgart, 2010



In situ Stress Measurement

- AJA ATC-1500 sputtering system
 - 6×10^{-6} Pa
 - Working pressure Ar at 0.27 Pa
 - Co-sputter elemental targets

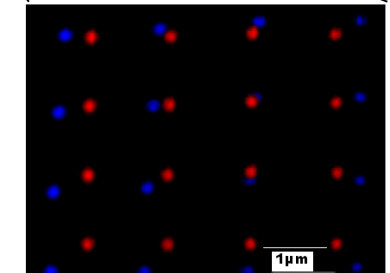
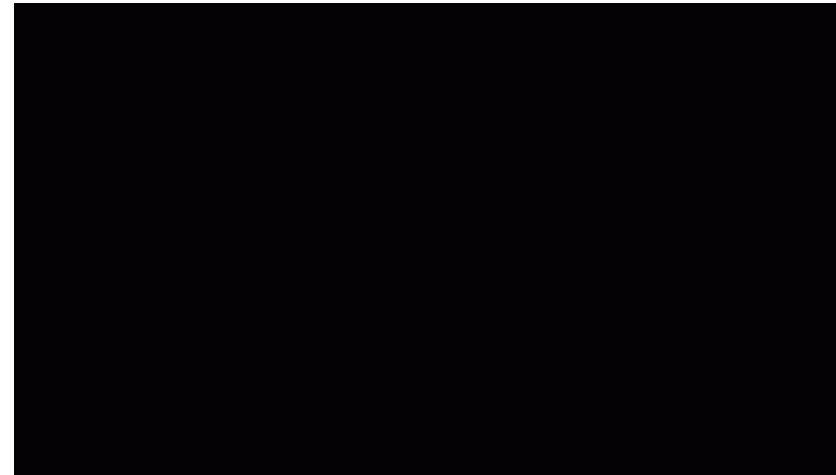


- Using reflected laser beams, the curvature in the substrate caused by the stress induced bending is captured.

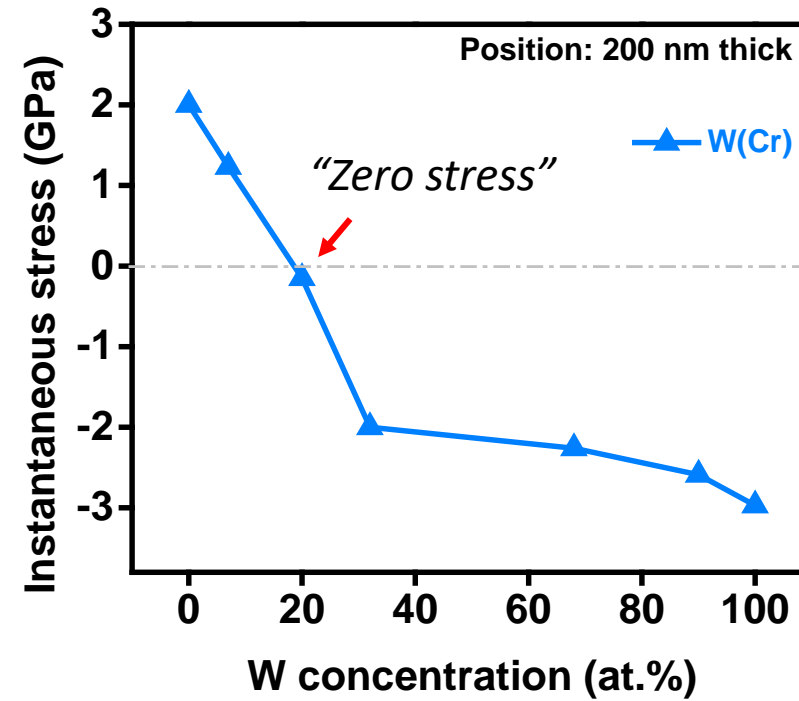
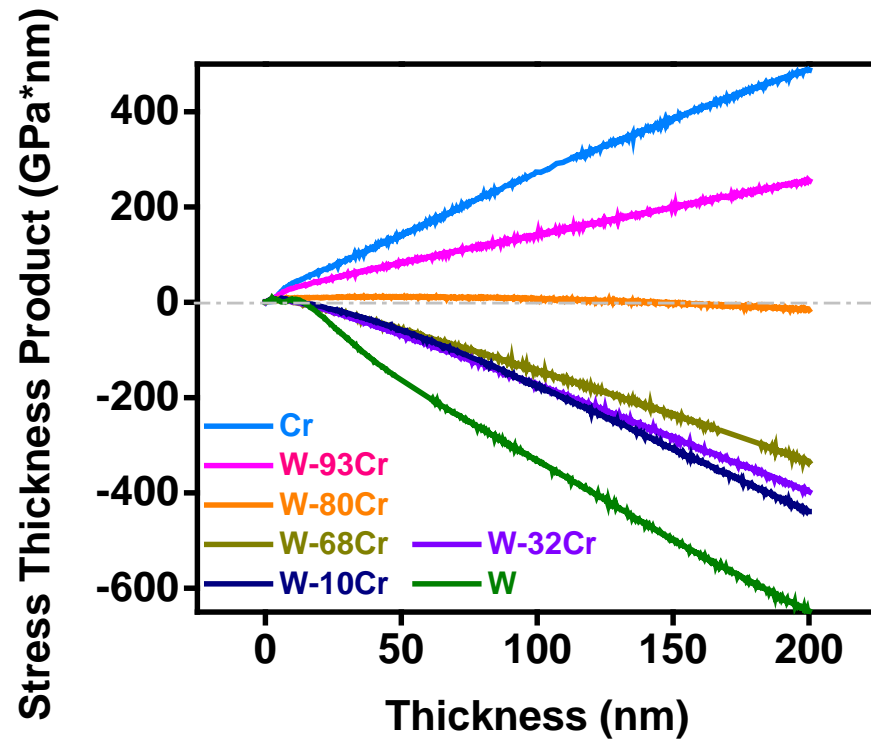
- Stoney equation relates displacement of spots to stress

$$\sigma_f = \frac{E_s}{6(1 - \nu_s)} \frac{t_s^2}{t_f} \left(\frac{1}{R} - \frac{1}{R_0} \right)$$

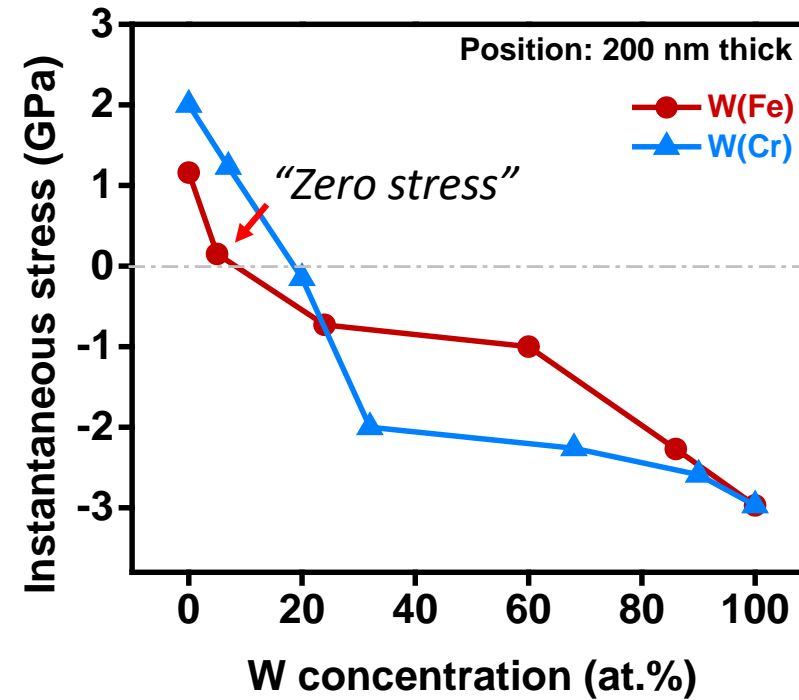
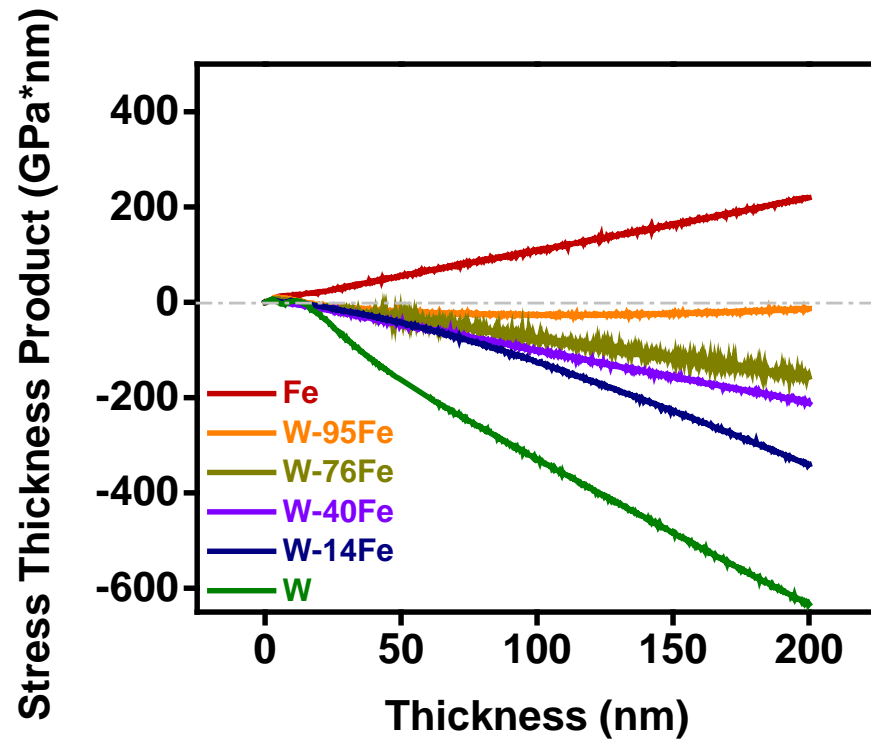
σ_f : Film's stress; ν_s : Poisson's ratio of the substrate; E_s : Young's modulus of the substrate; t_s : Substrate thickness; t_f : Film thickness; $1/R_0$ and $1/R$: Curvatures of the films before and during the deposition.



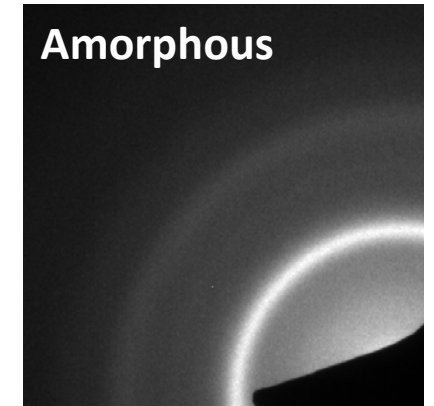
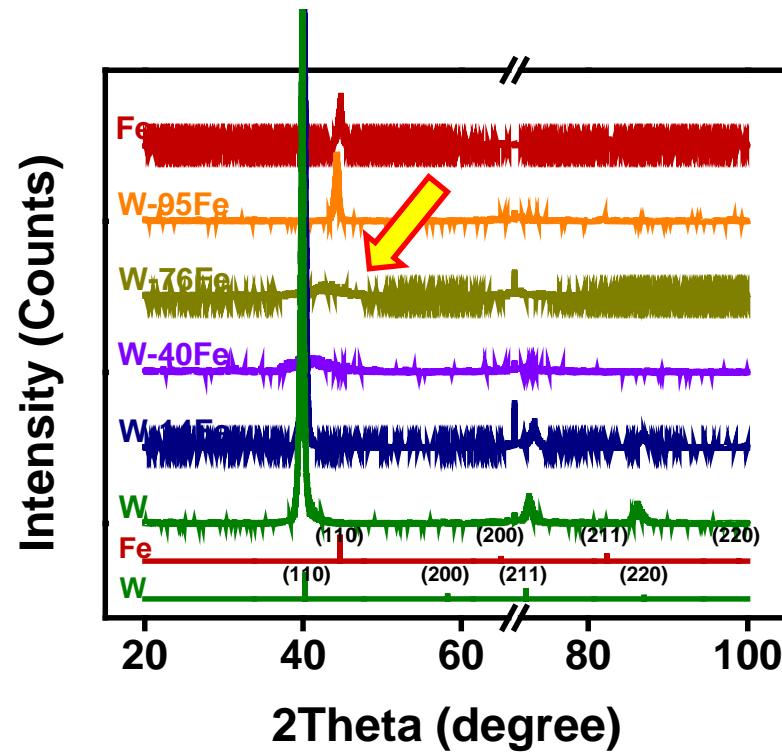
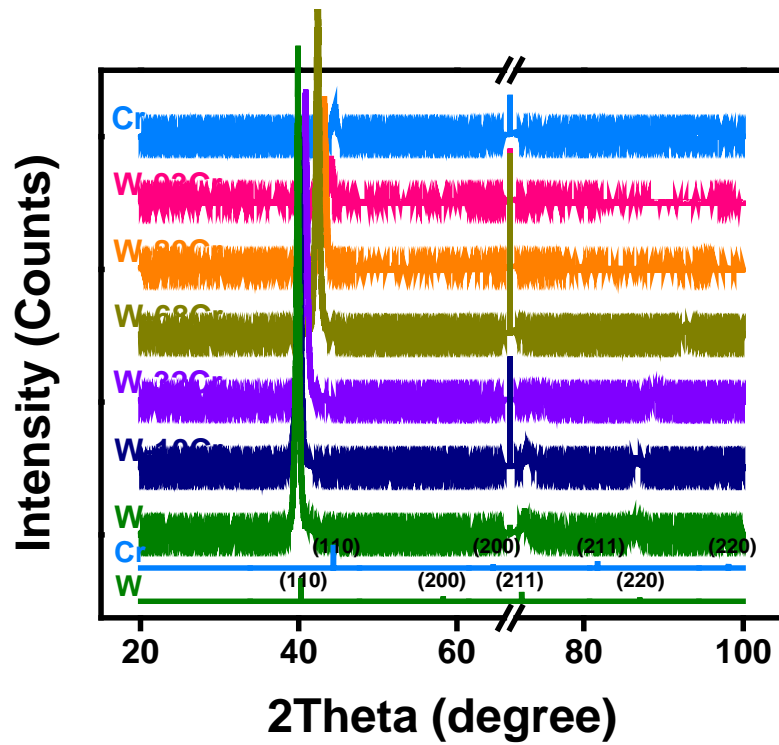
MOS
(Multi-beam Optical Sensor)



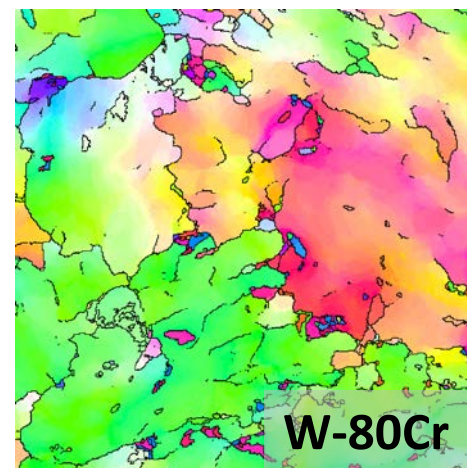
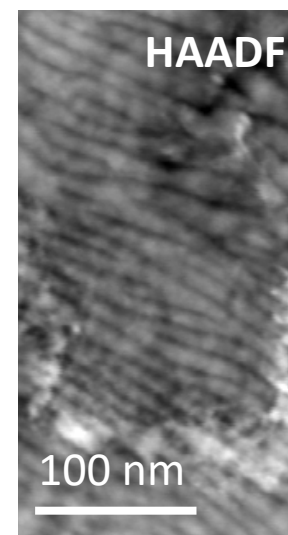
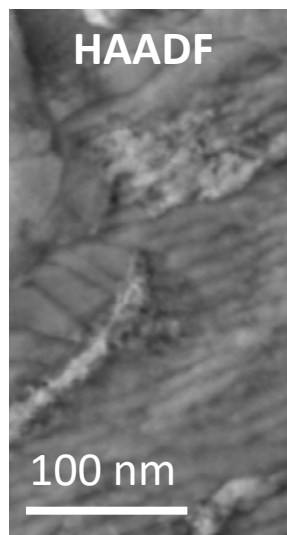
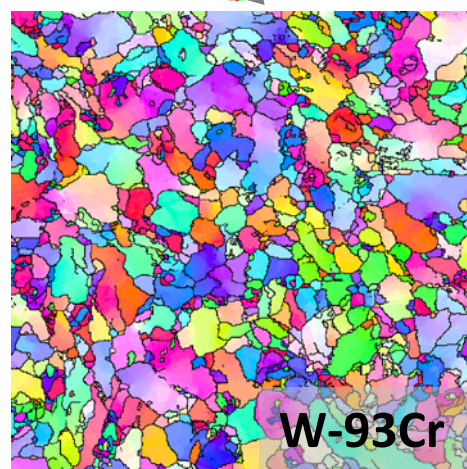
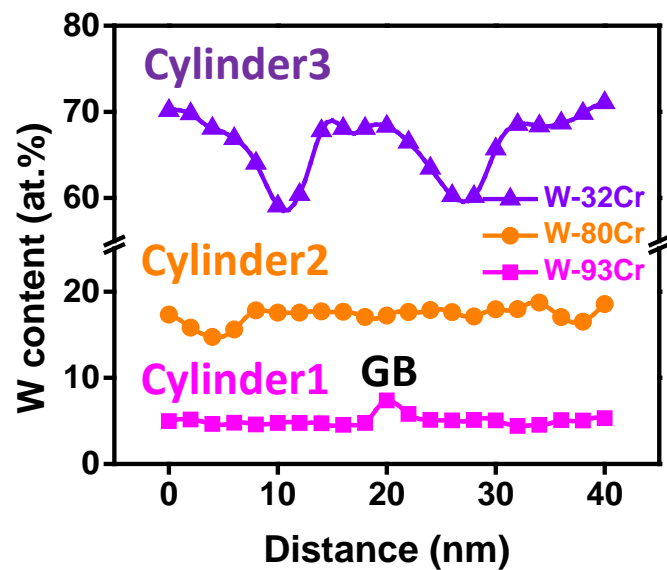
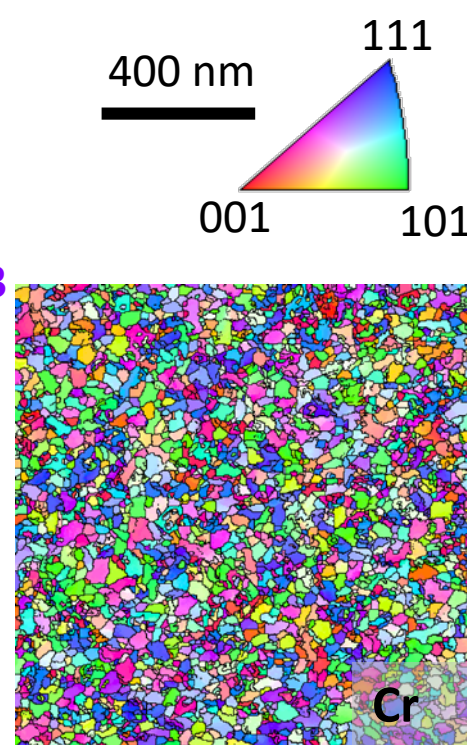
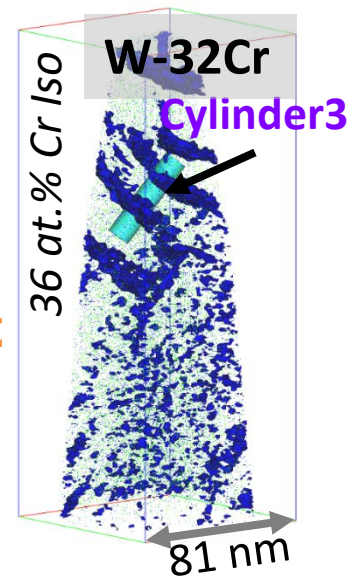
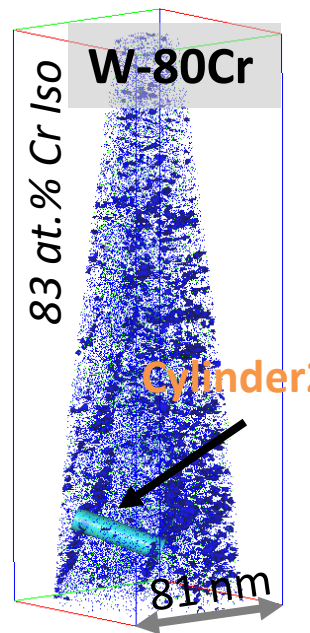
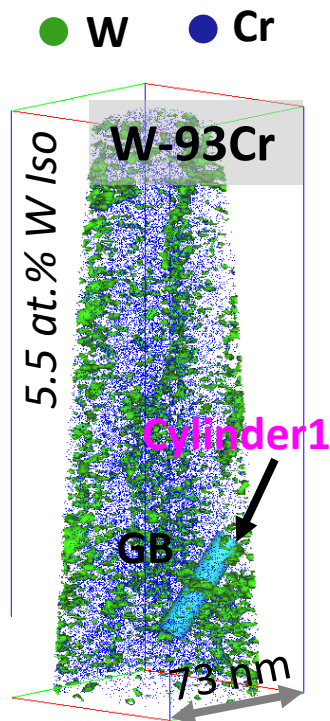
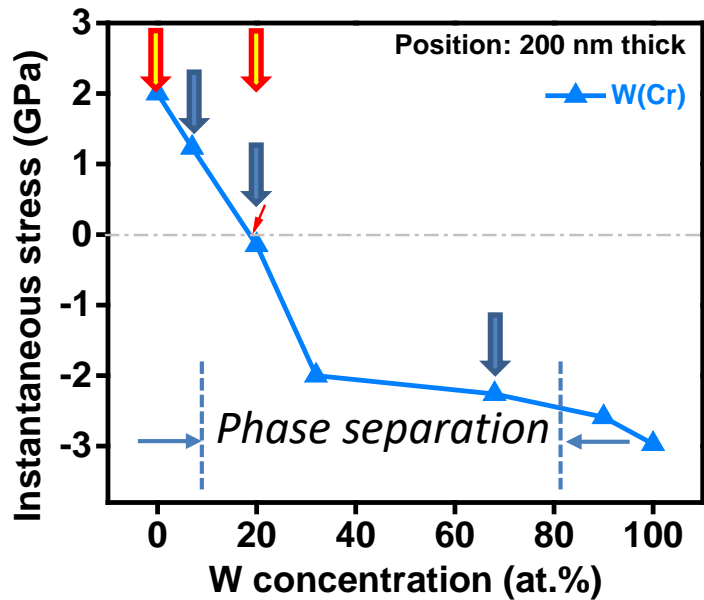
- The near zero growth stress was found to occur for the W-80Cr film;
- The alloy stress is not a linear connection between the two elemental films' stress values.

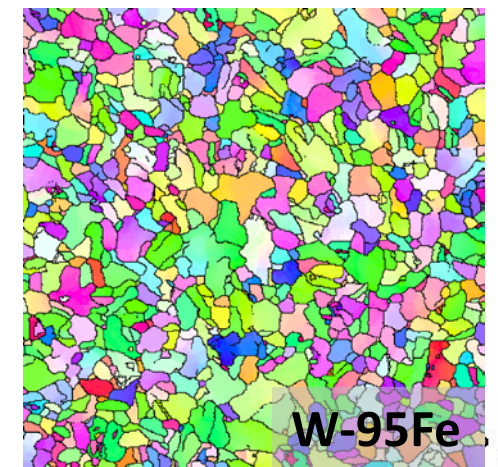
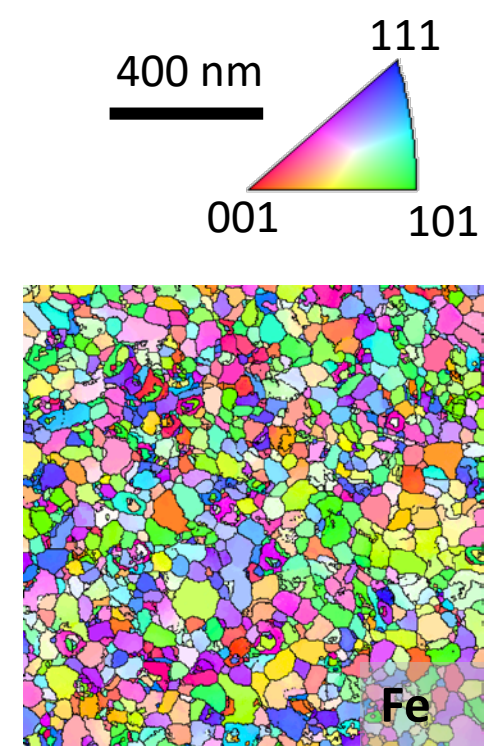
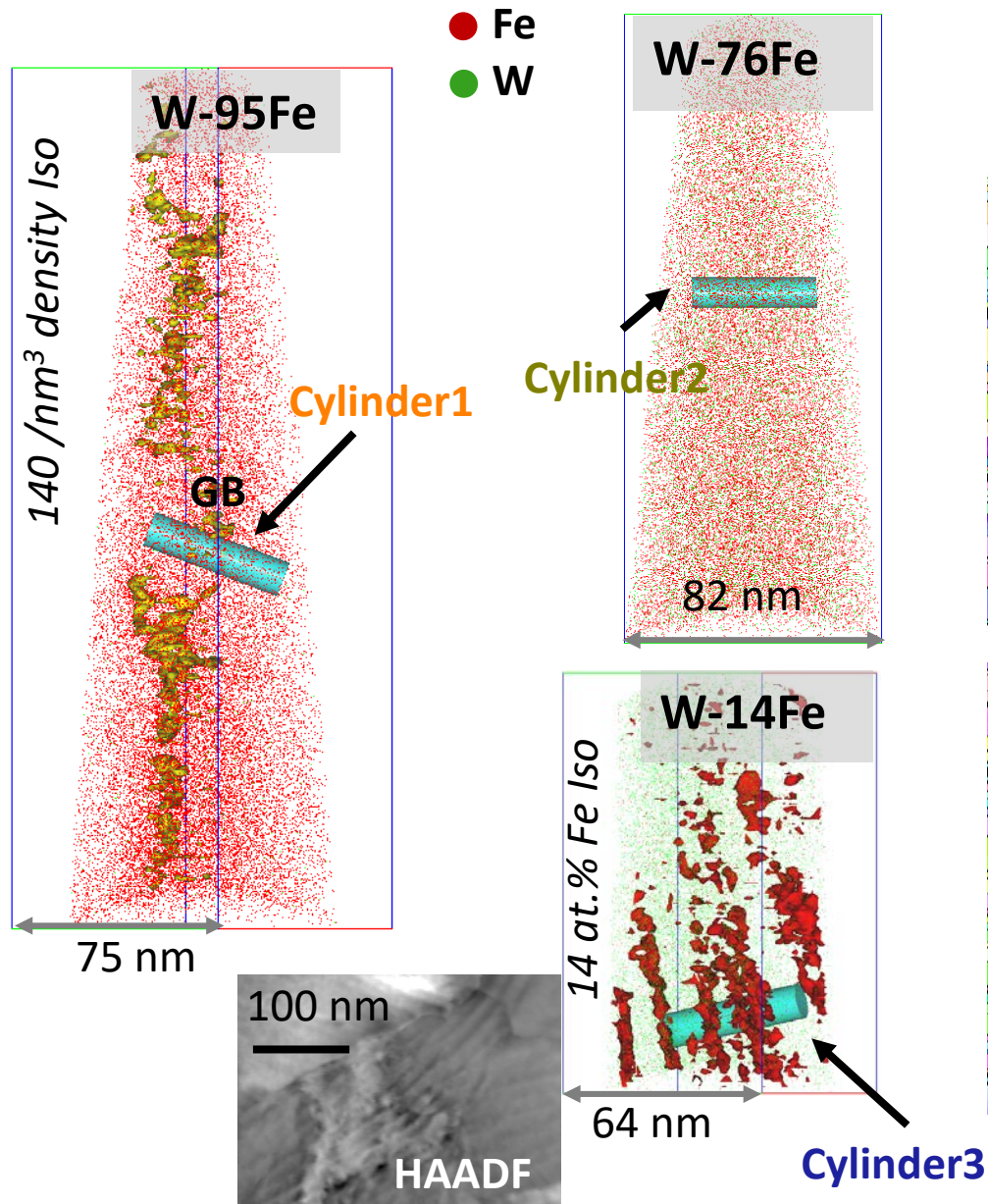
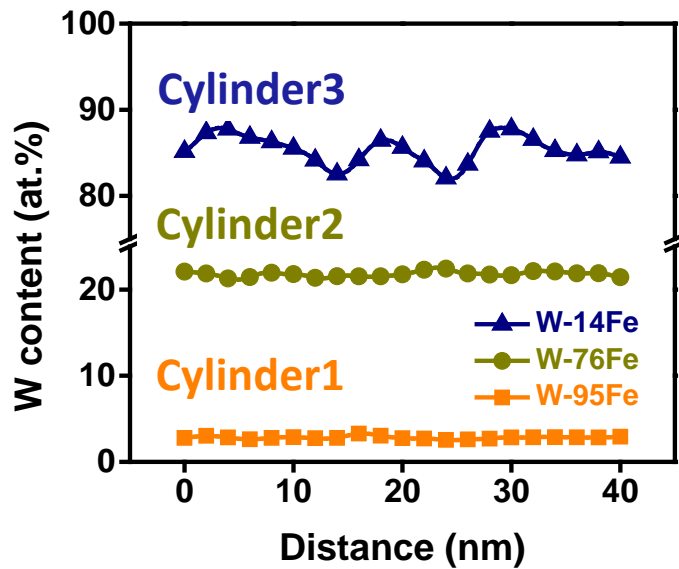
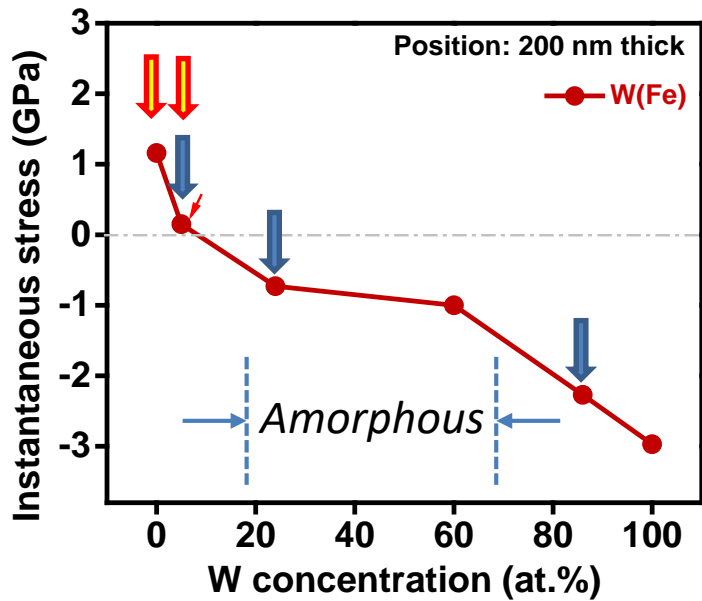


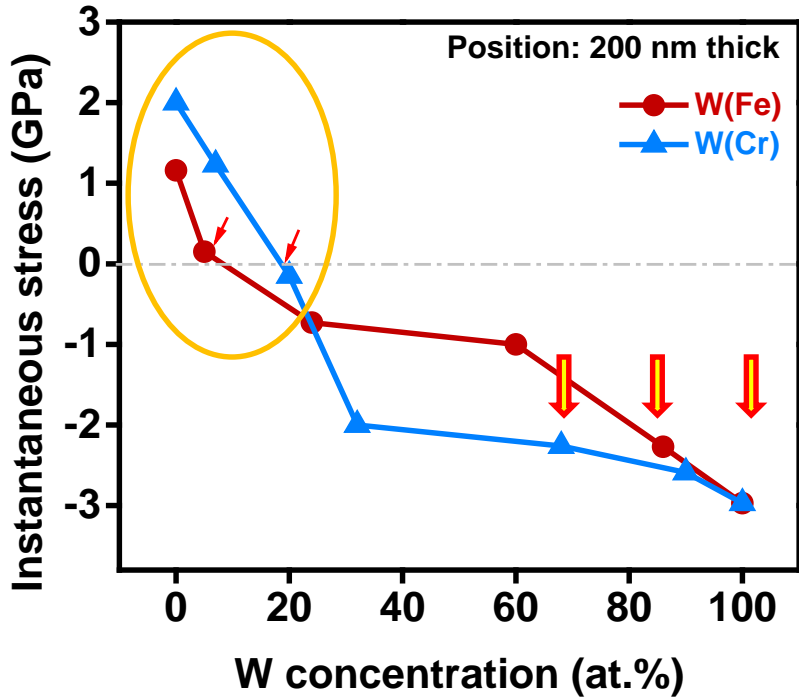
- The near zero growth stress was found to occur for the W-95Fe film;
- The alloy stress is not a linear connection between the two elemental films' stress values.
- W-Fe alloy film required a smaller amount of W to reduce the tensile stress to zero than that of W-Cr alloy film.



- Nearly all these alloys formed either the BCC phase in the single element state or an A2 phase for the alloys;
- The only exceptions were the W-40Fe and W-76Fe films, which were amorphous.

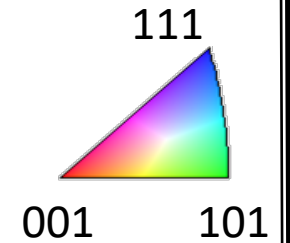
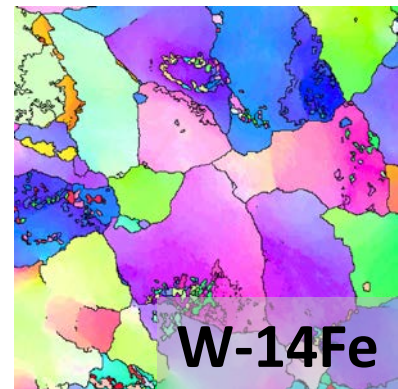
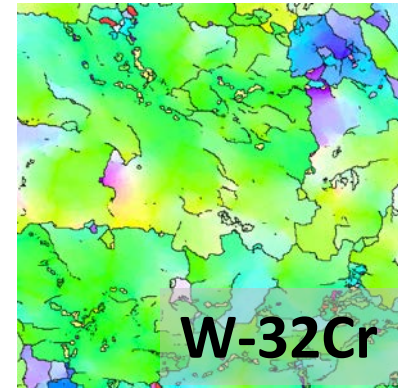
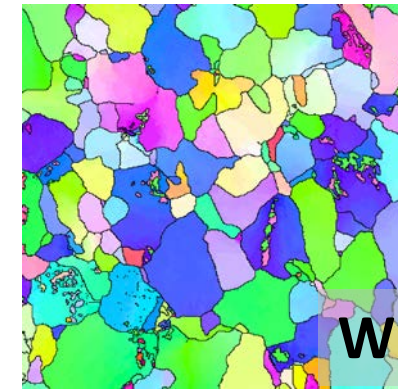
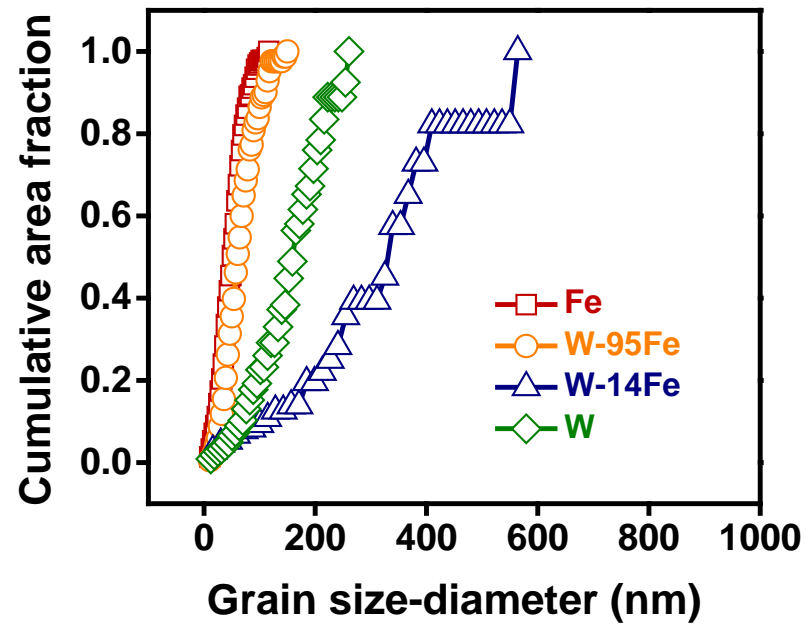
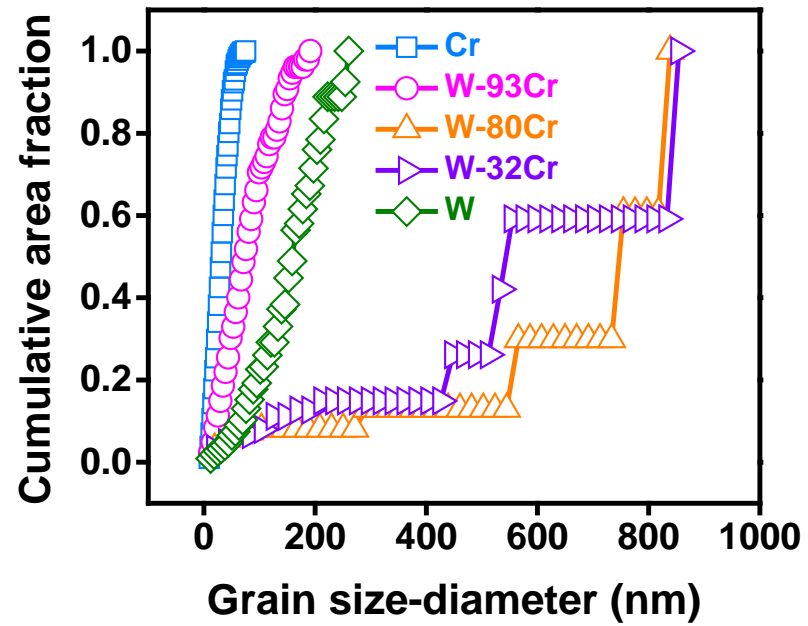




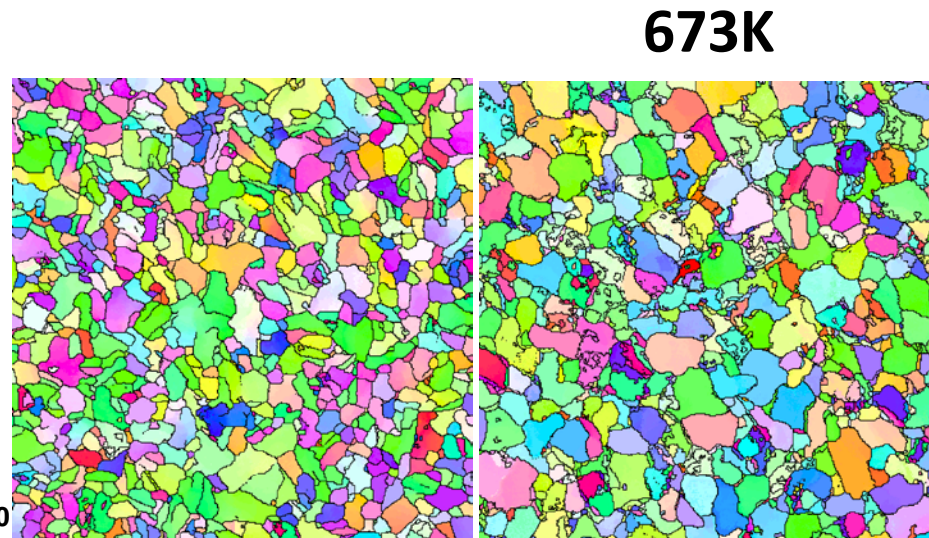
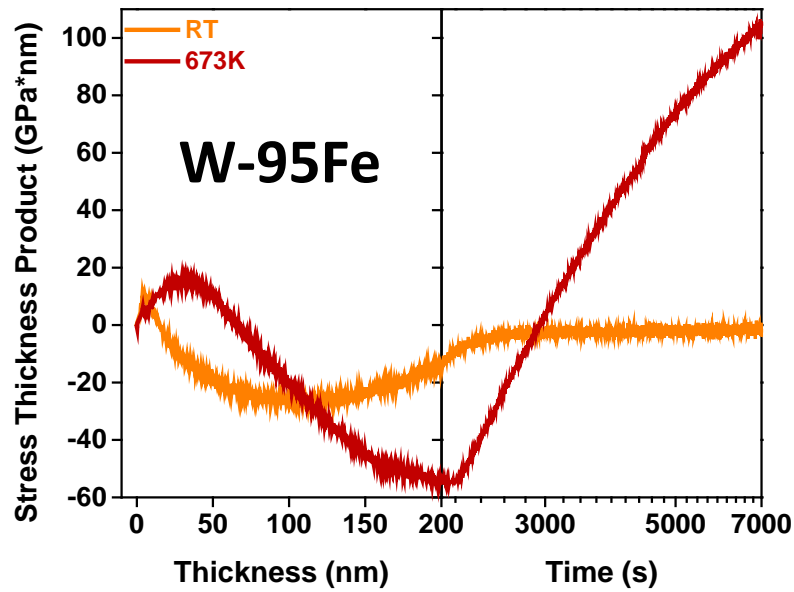
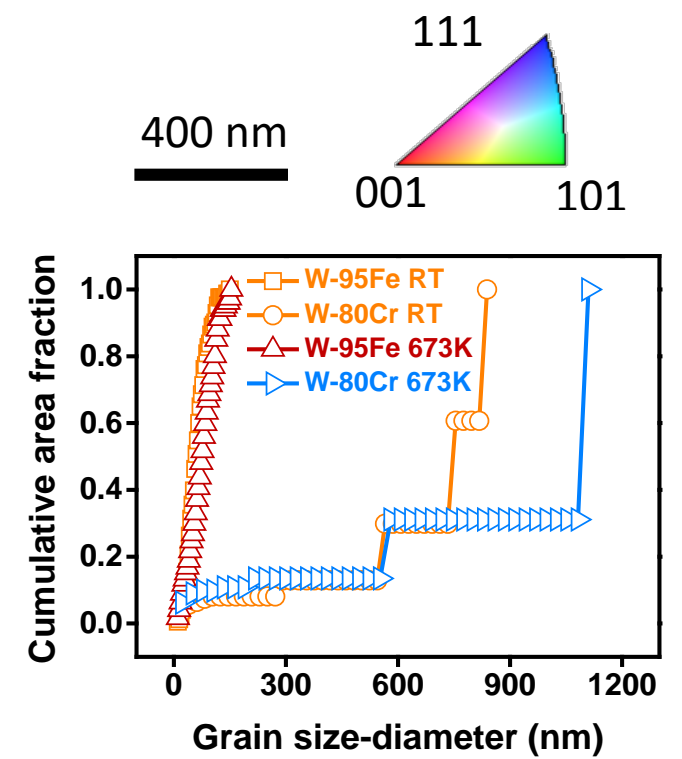
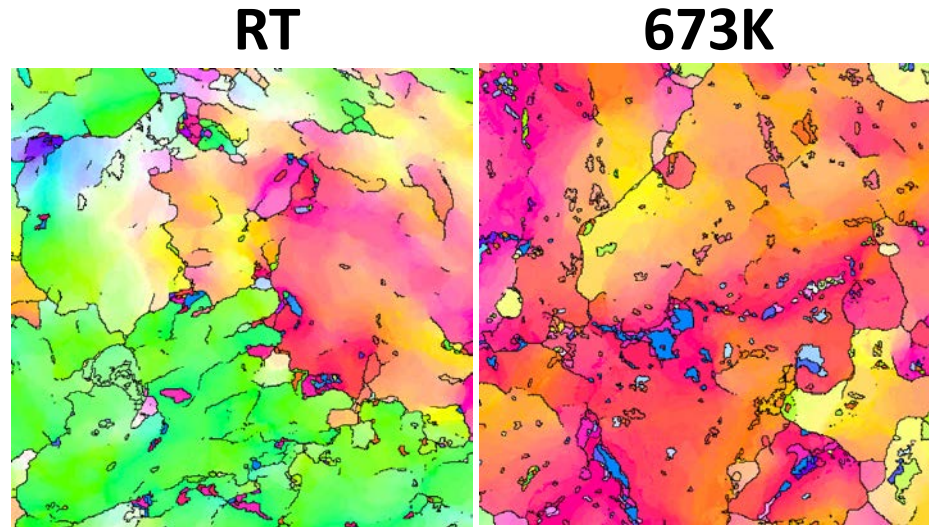
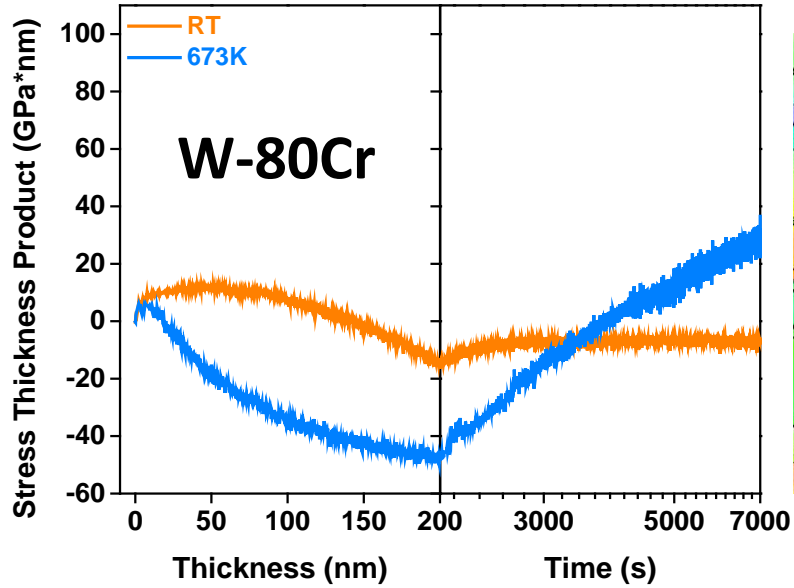


Adding Fe or Cr into the W matrix can:

- Increase the grain size;
- Reduce the compressive stress.

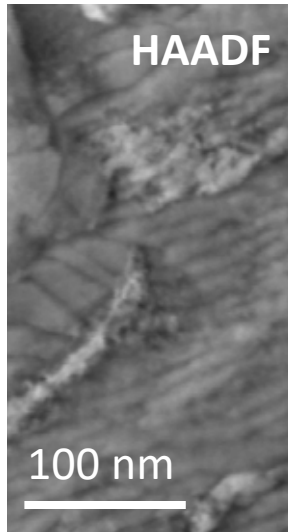
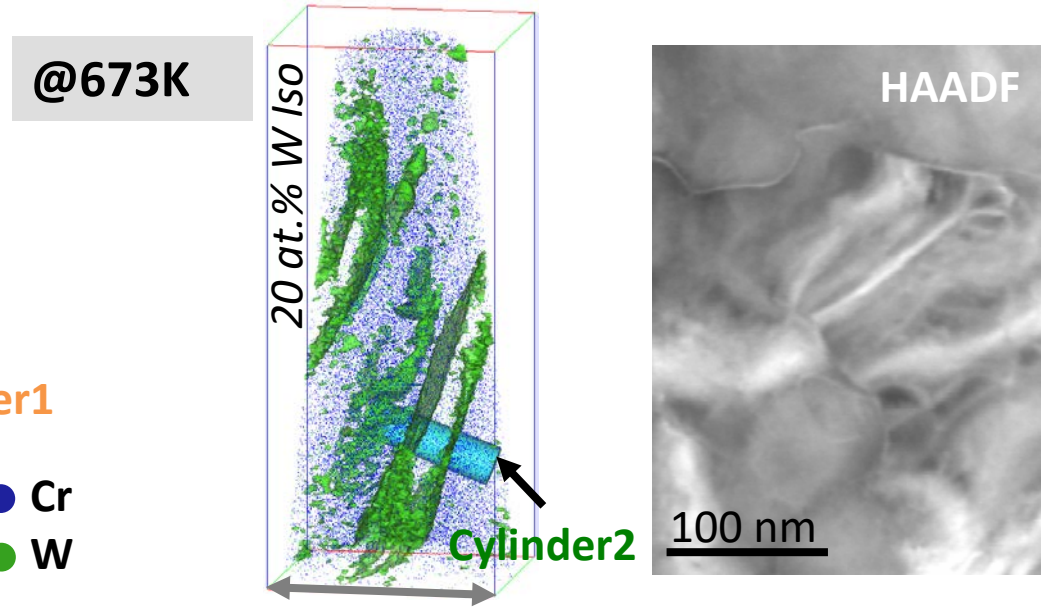
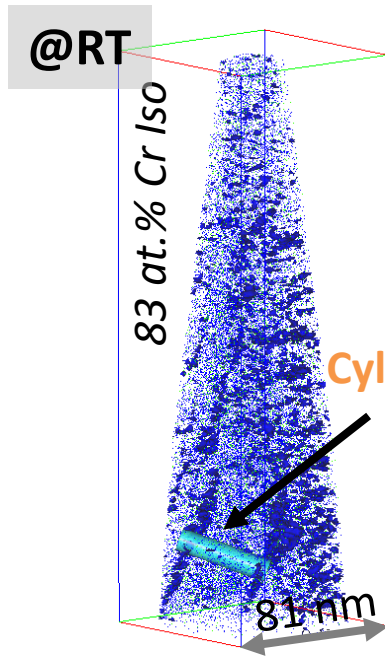
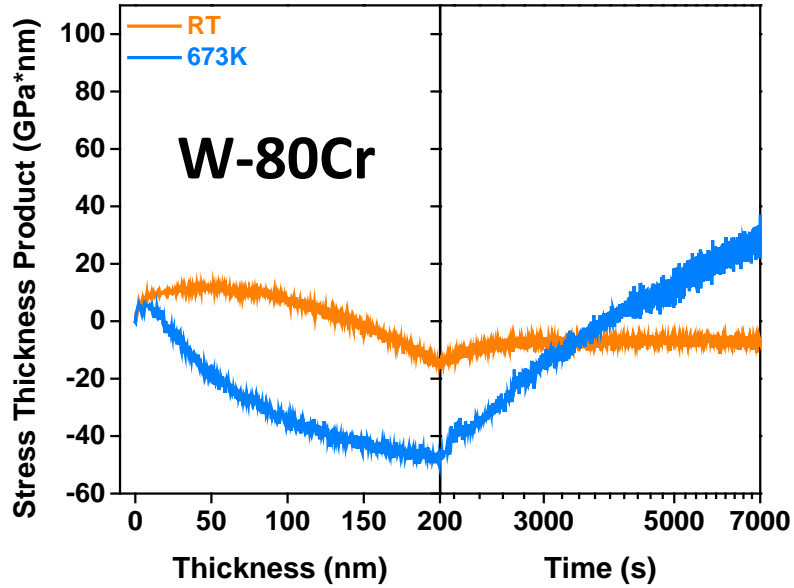






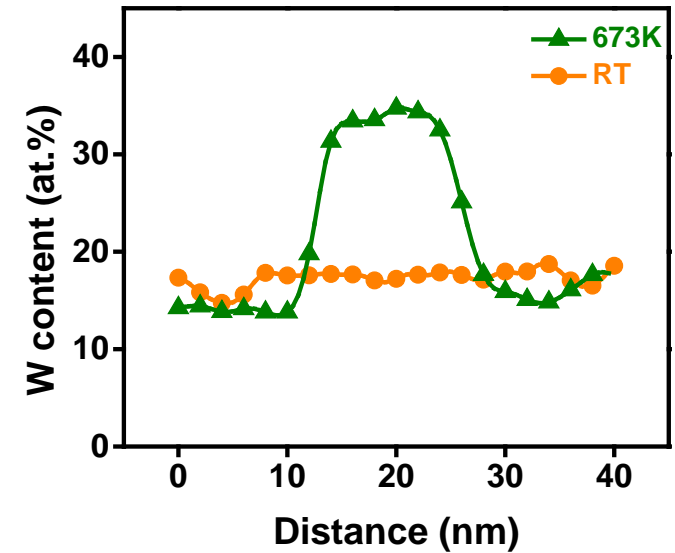
At elevated temperature:

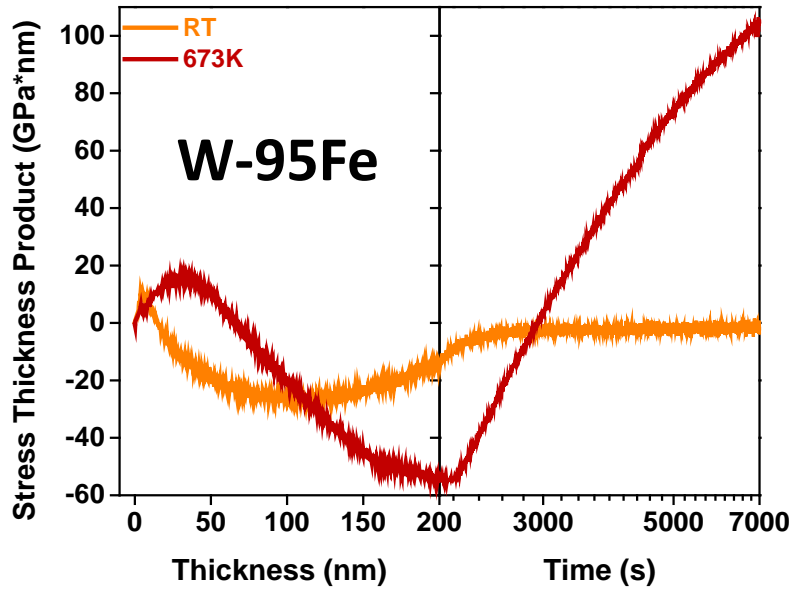
- Grain growth;
- Tensile stress to compressive;
- Strong stress recovery;
- W-Fe film showed larger stress recovery than W-Cr.



Heating film during deposition:

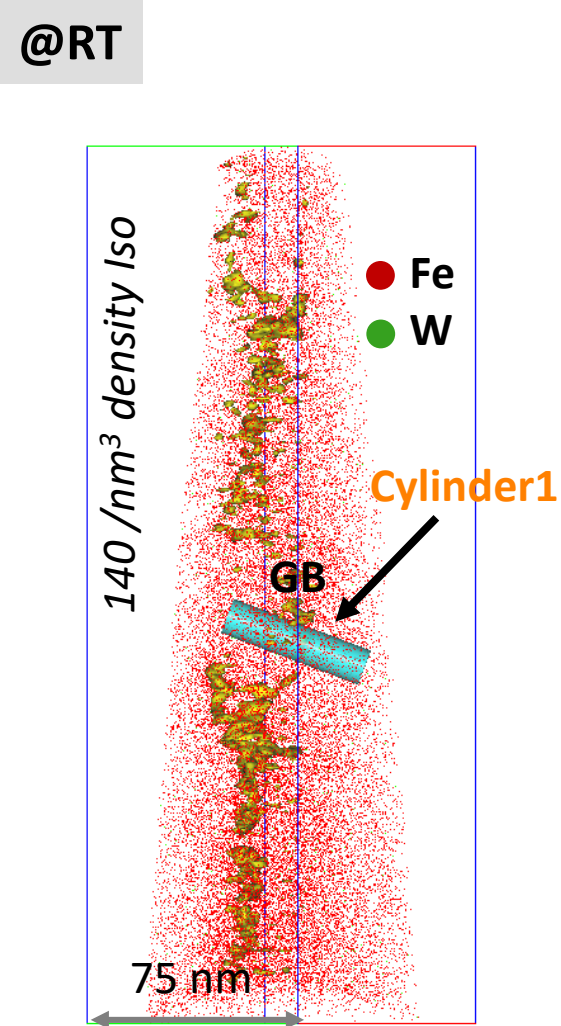
- Promotes higher chemical partitioning
- The lath structures thicken.





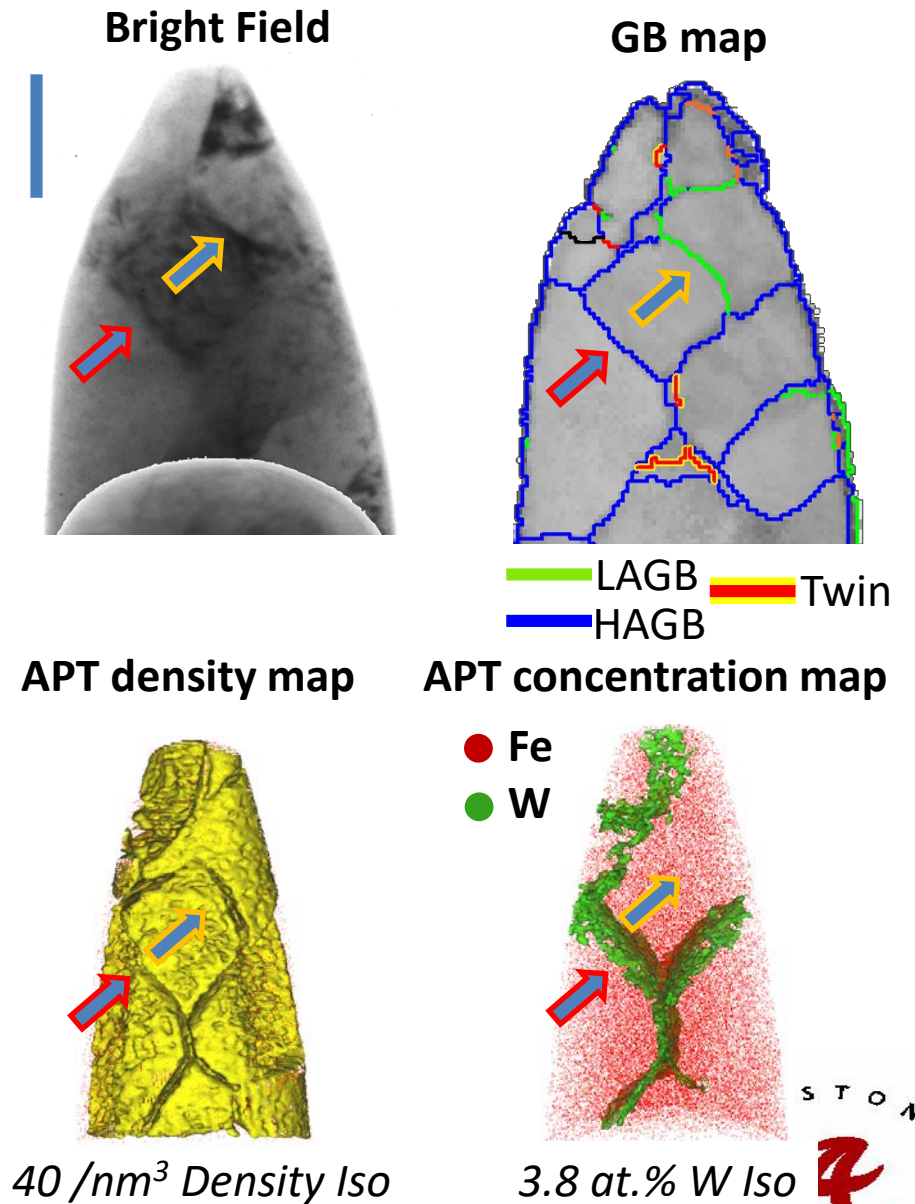
Heating film during deposition:

- W segregates strongly to GBs.
- Segregation is preferred to HAGBs vs. LAGBs.



No grain boundary segregation

@673K



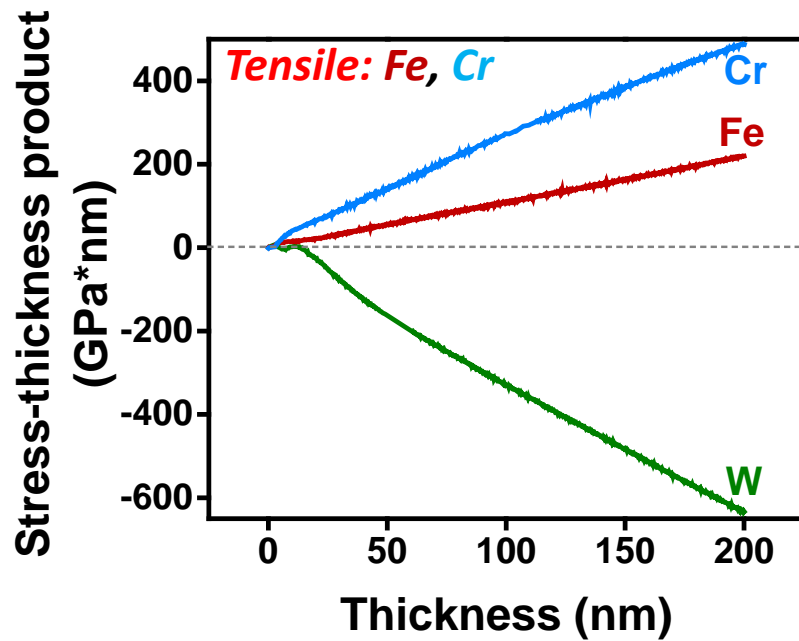
➤ W-Cr and W-Fe films

- Upon heating the ‘zero-stress’ room temperature compositions during growth, both W-80Cr and W-95Fe films became compressive and stress recovery behavior. In W-80Cr film, the laminate phase separating morphology was still present, with the solute lathes thickened and portioning more pronounced. In W-95Fe film, the segregation of W to the boundaries, with the solute appearing to ‘wet’ the HAGBs.

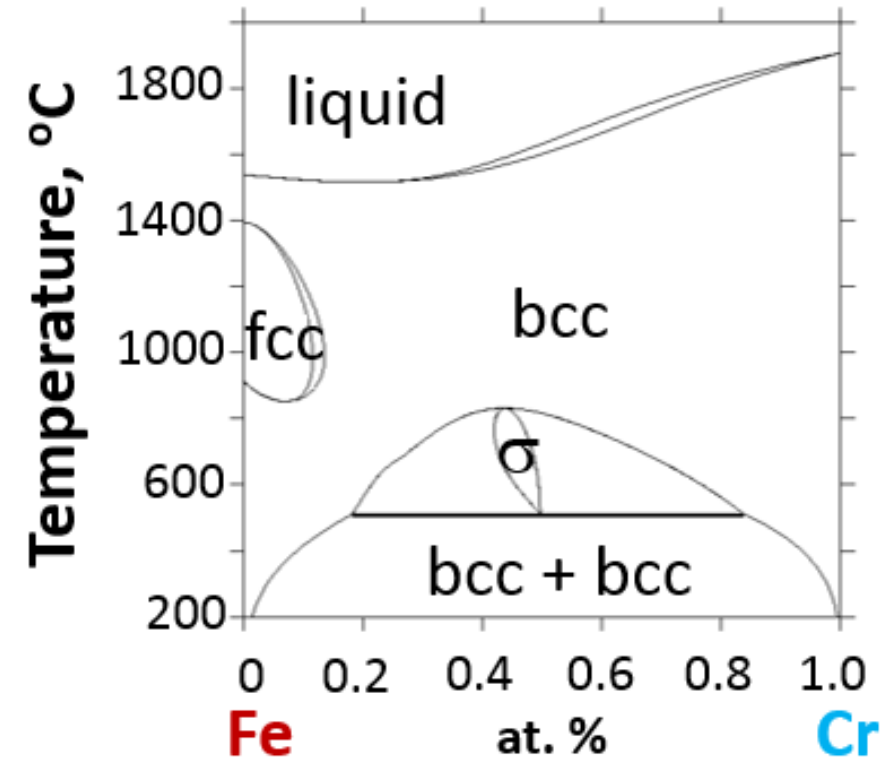
But what happens if mixing two tensile species together?



- From the above learned, the Fe –Cr system was used for case study



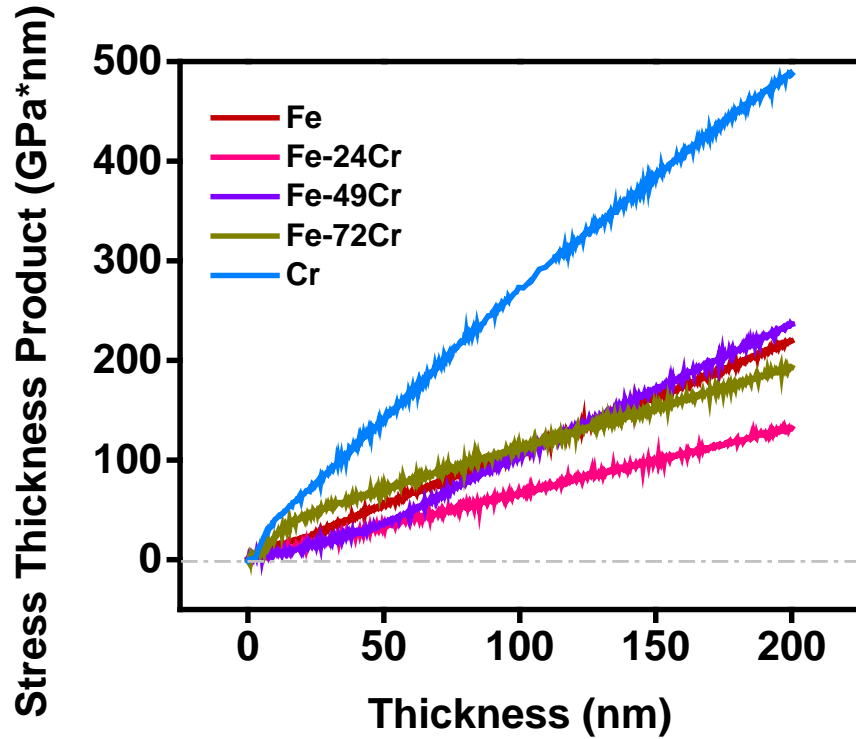
miscibility gap – segregating behavior



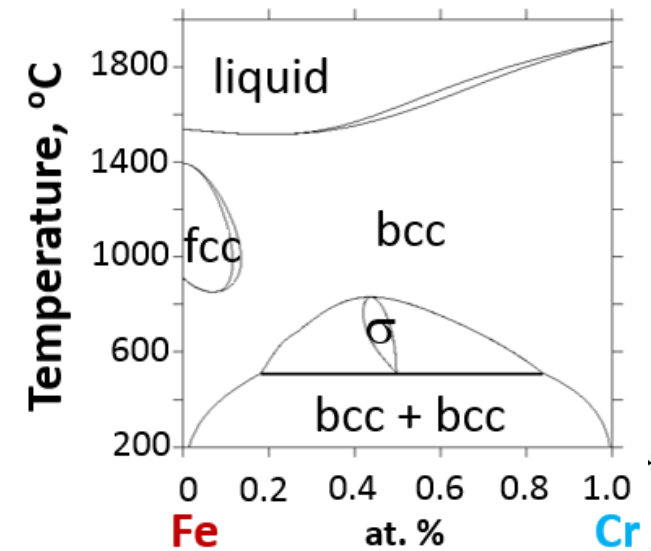
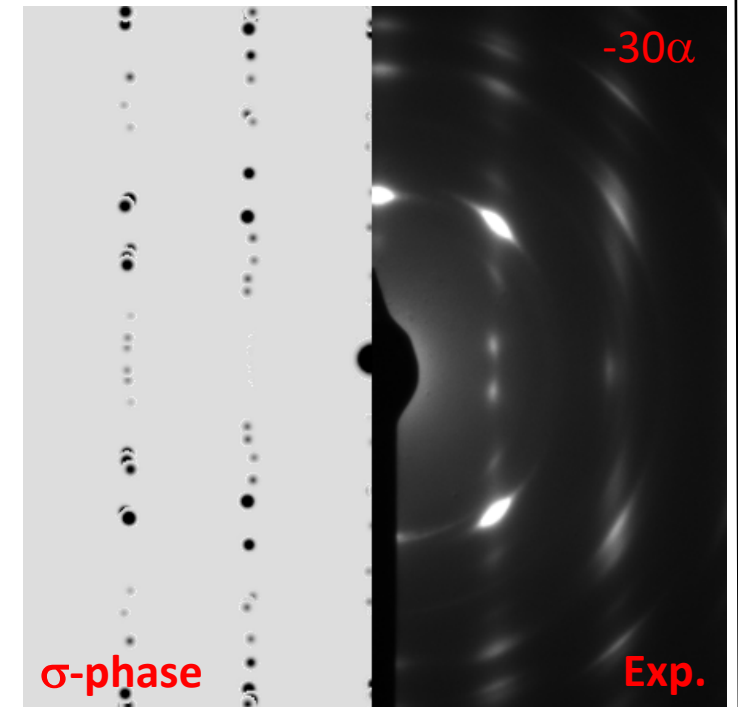
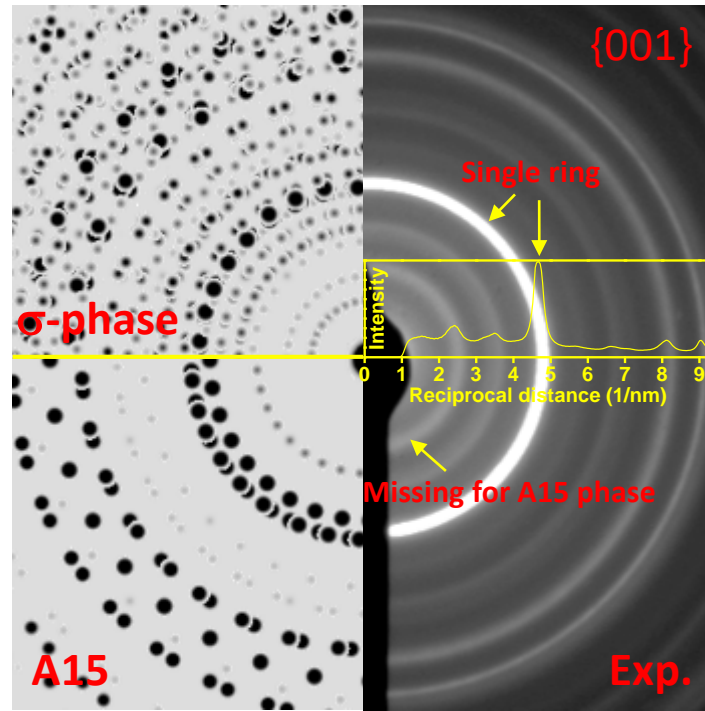
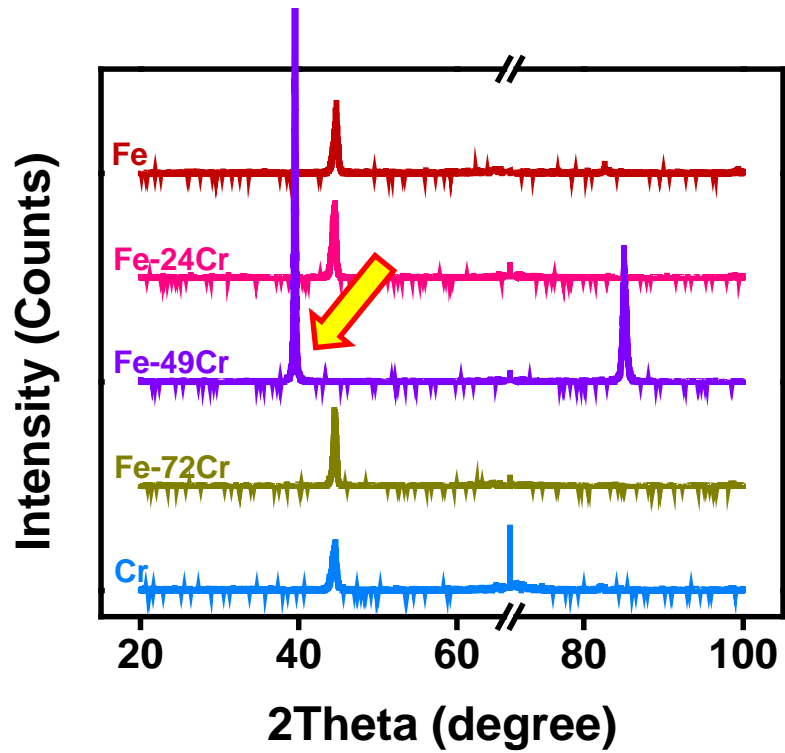
Kubaschewski, O., Springer Berlin Heidelberg 2013.



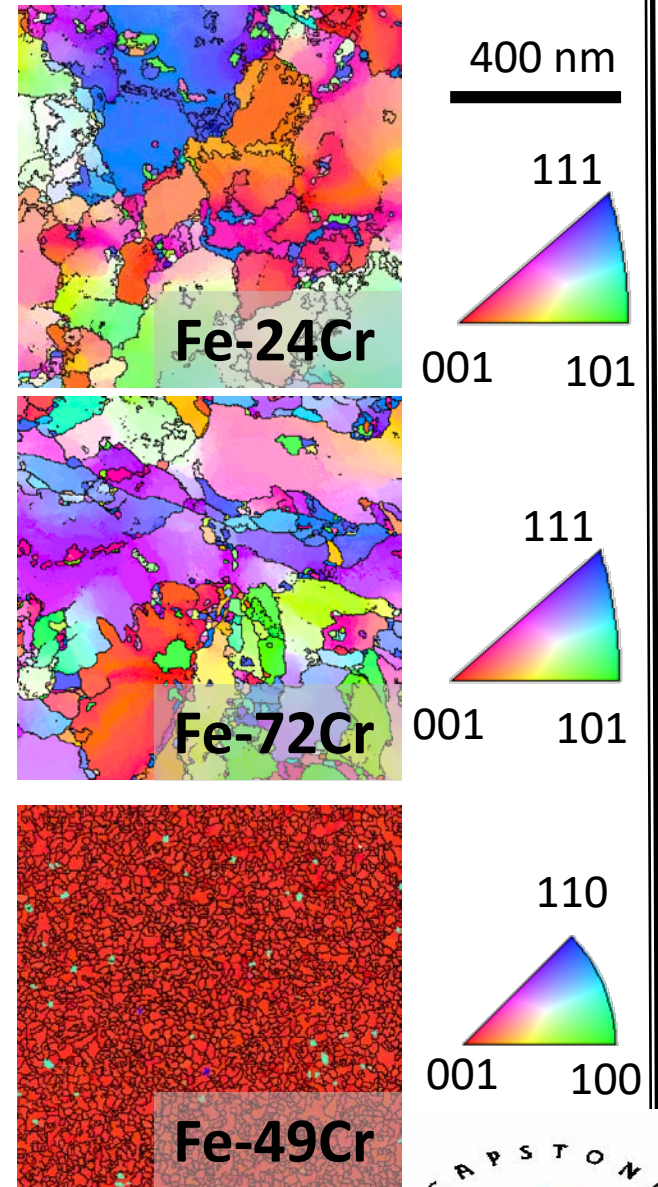
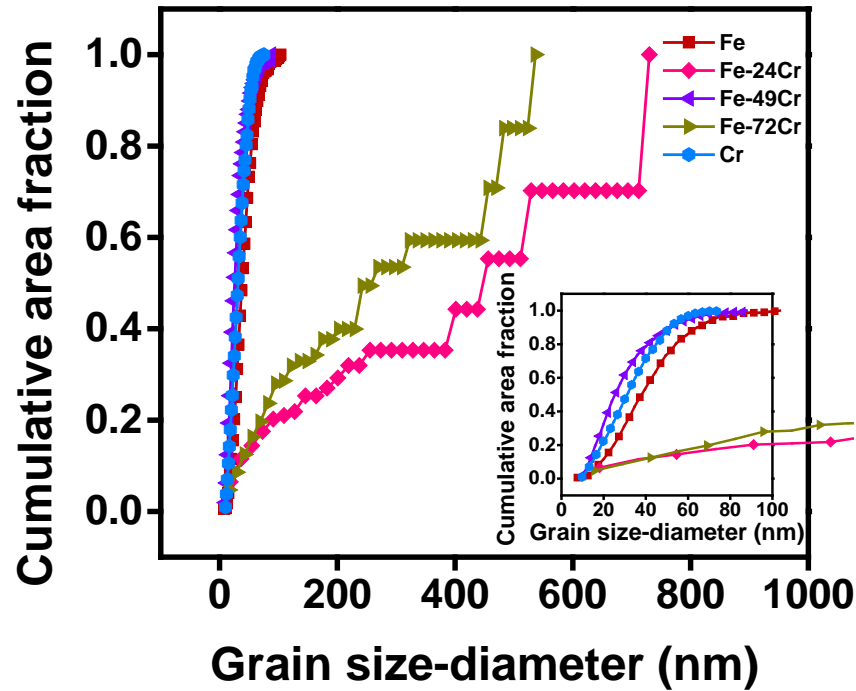
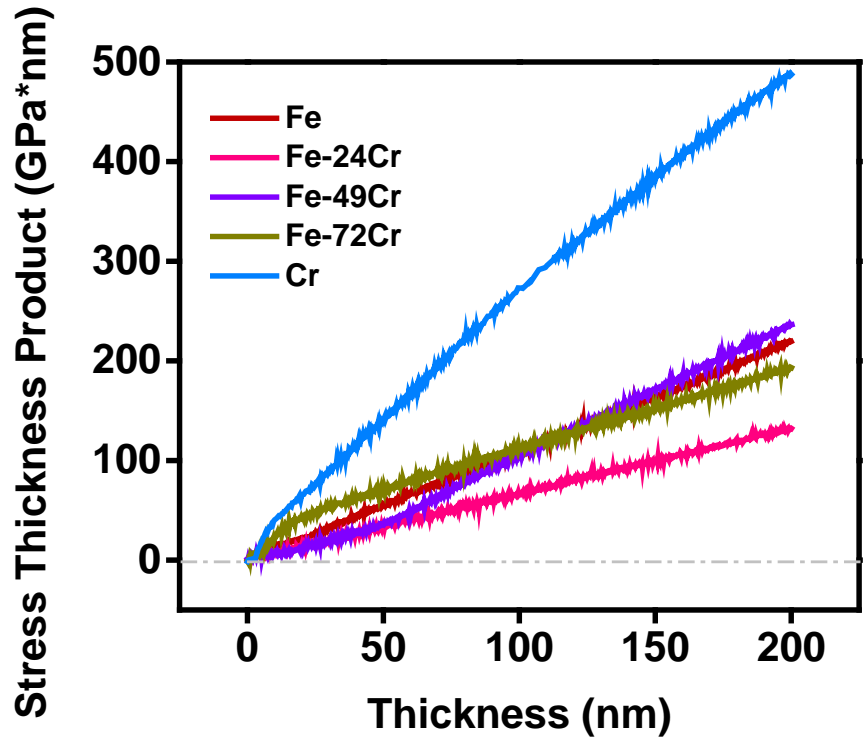
- *a surprise finding*



➤ The alloy stress is not a linear connection between the two elemental films' stress values.

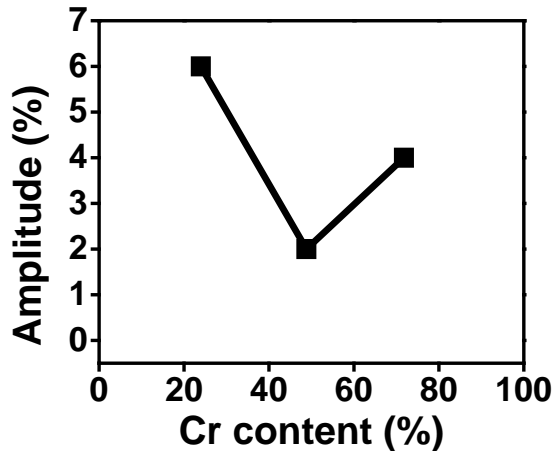
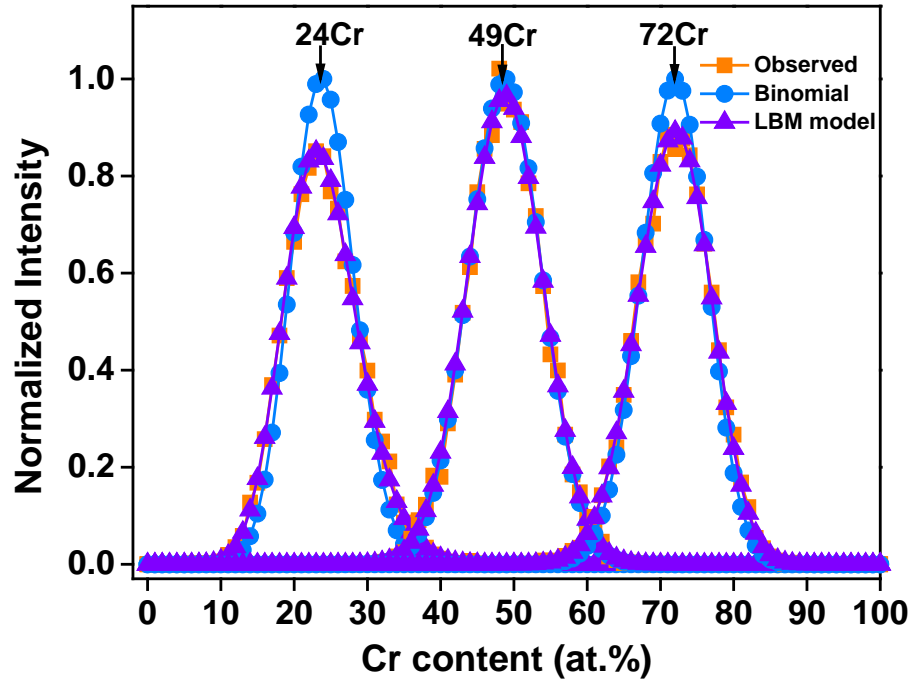


- The only exception was the Fe-49Cr film, which was σ -phase.

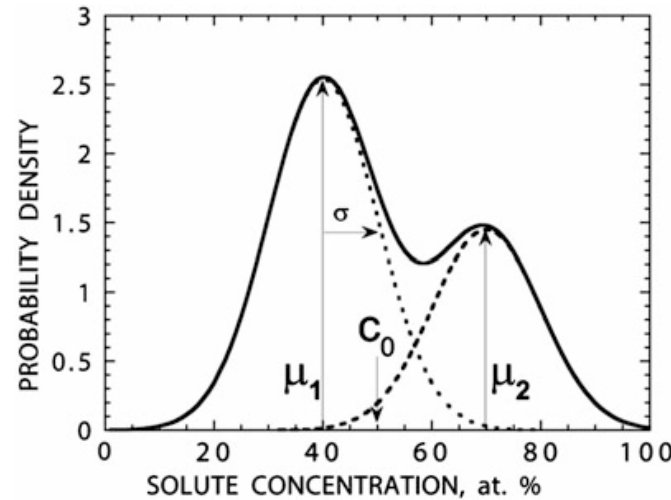


- Adding sufficient Cr into Fe matrix or adding Fe into Cr can cause abnormal grain growth resulting in a reduction of impinging tensile stress.
- σ -phase has very fine grain size that brings the tensile stress up.

Note: Analysis was drawn from 25X25X25 nm³ APT data for each Fe-Cr alloy.



$$P(c) = \frac{\mu_2 \exp \left[\frac{-(c - \mu_1)^2}{2\sigma_{LBM}^2} \right] + \mu_1 \exp \left[\frac{-(c - \mu_2)^2}{2\sigma_{LBM}^2} \right]}{(\mu_1 + \mu_2)\sigma_{LBM}\sqrt{2\pi}}$$

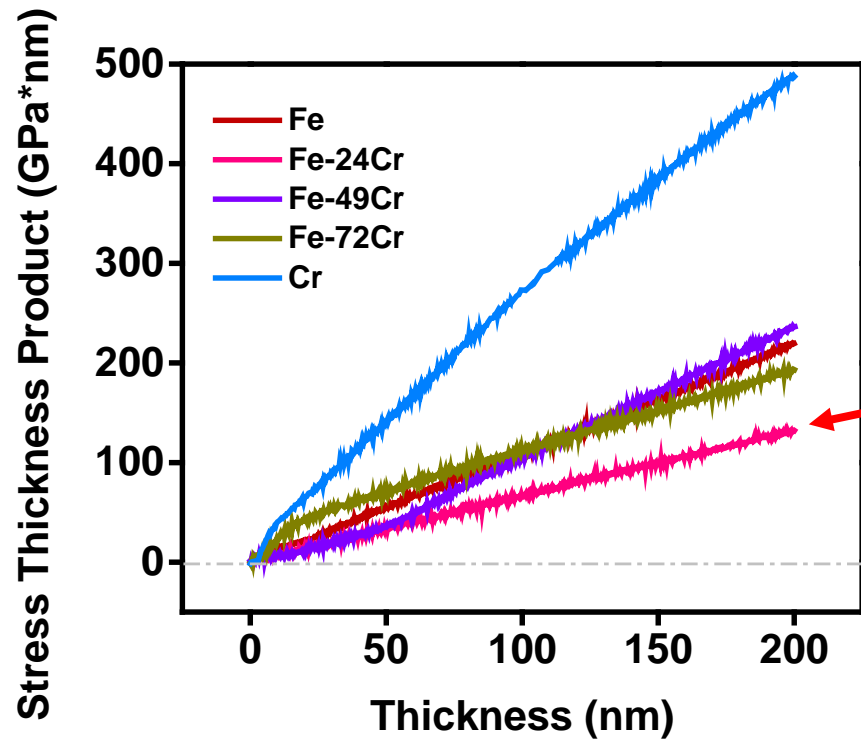


c : Solute concentration; μ_1 and μ_2 : Peak and trough compositions; σ_{LBM}^2 : Variance of each Gaussian distribution. $\mu_2 - \mu_1$: Amplitude.

LBM: Langen, Bar-on, and Miller

- Local segregations were noticed in Fe-24Cr and Fe-72Cr films;
- No compositional variation was noticed in the σ -phase Fe-49Cr film.

Miller, M.K. et al., *Atom-Probe Tomography: The Local Electrode Atom Probe*, Springer US, 2014

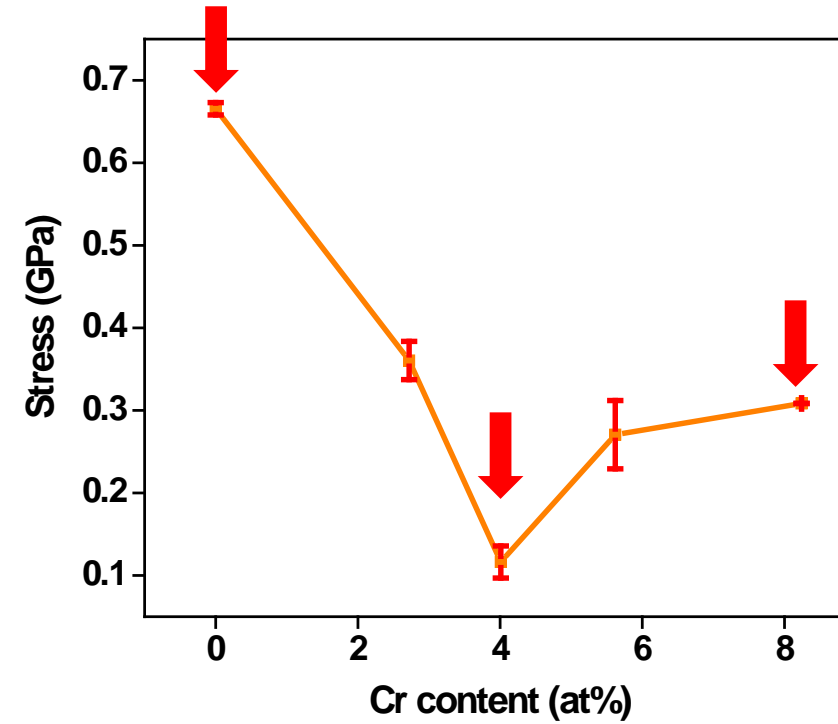
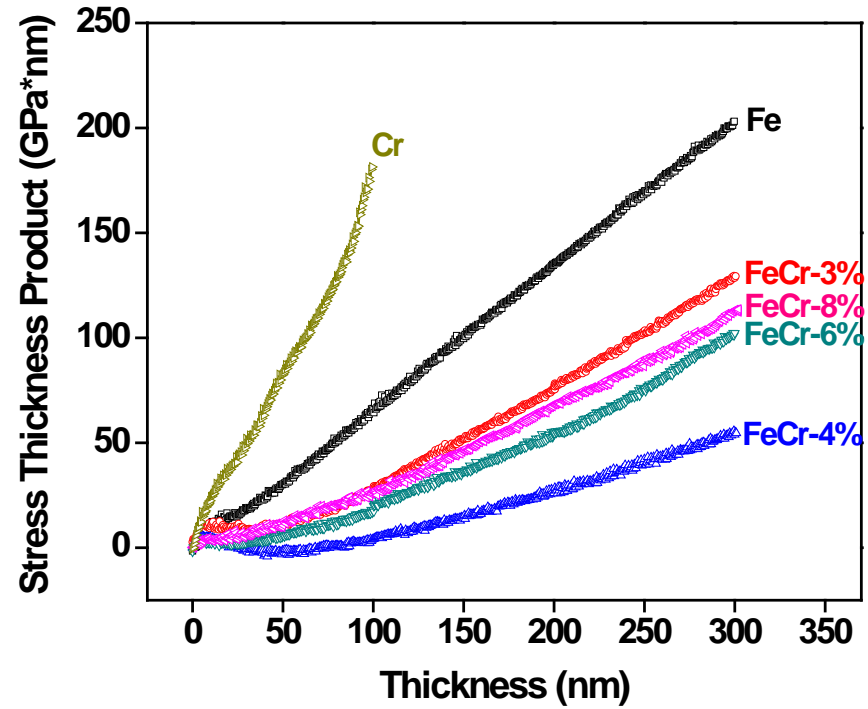


➤ What is the compositional range of this low tensile behavior?

Knowing that the tensile stress can be lowered – let's explore the finer Cr compositional scale of this effect



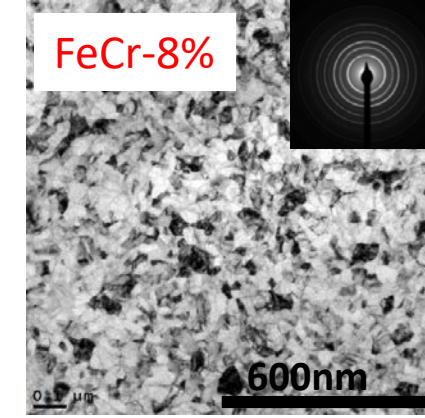
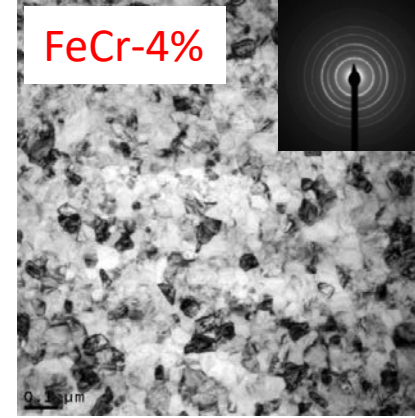
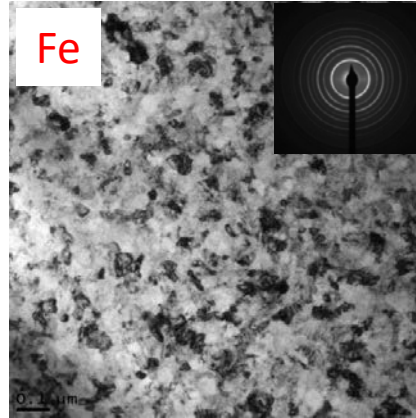
In situ Stress Evolution - Fe(Cr)



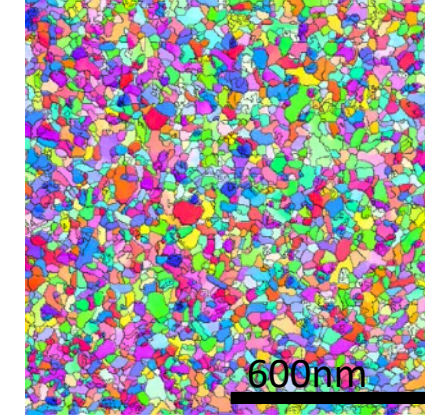
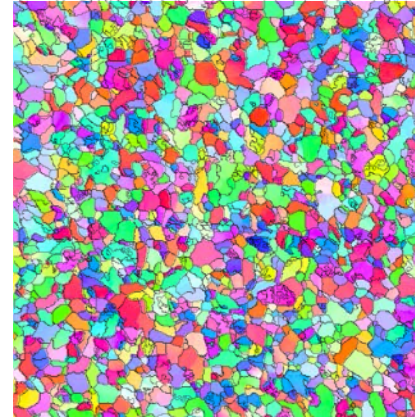
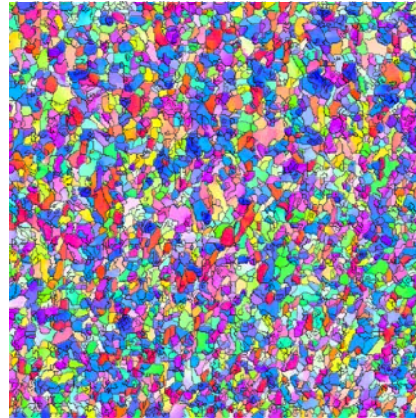
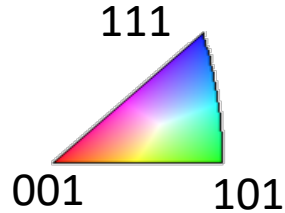
➤ All deposited films show tensile stresses

Grain morphology in the growing plane

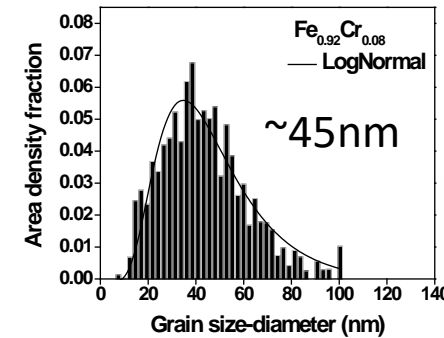
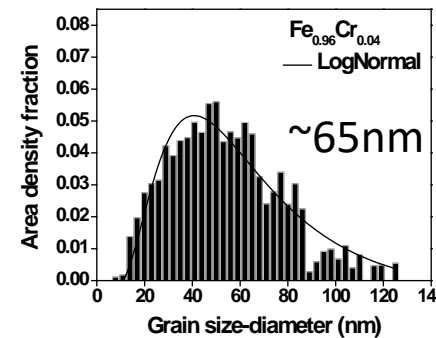
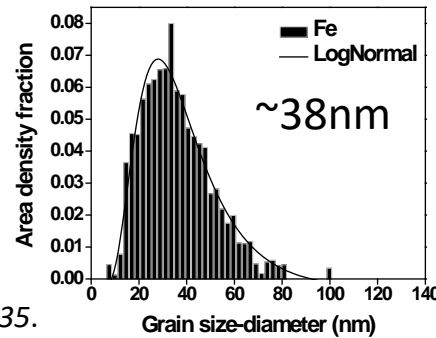
BCC phase



Precession Electron
Diffraction

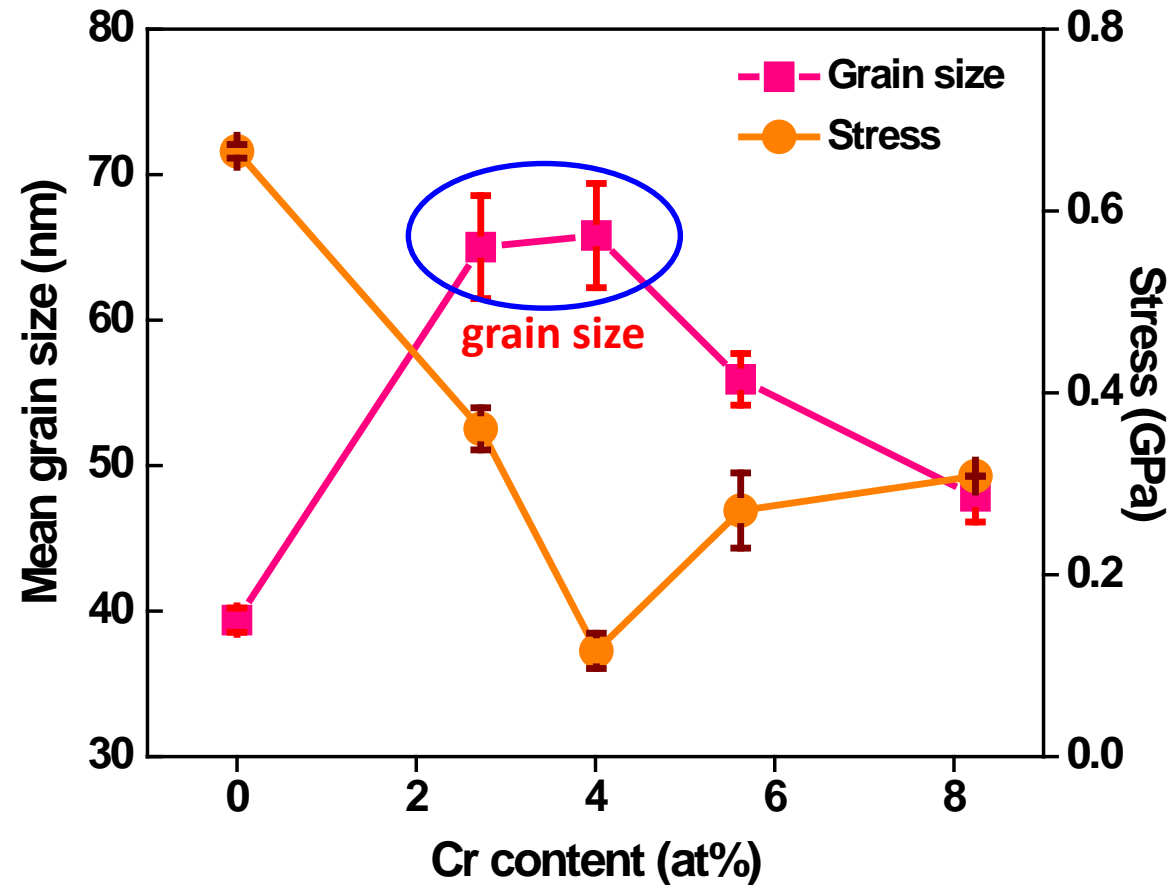


Grain size
distribution



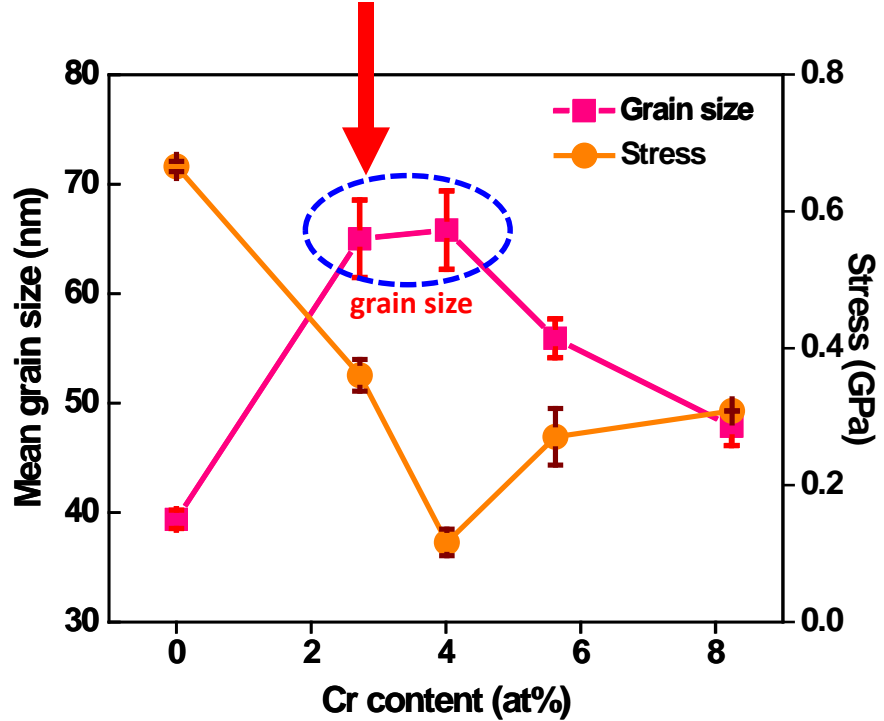
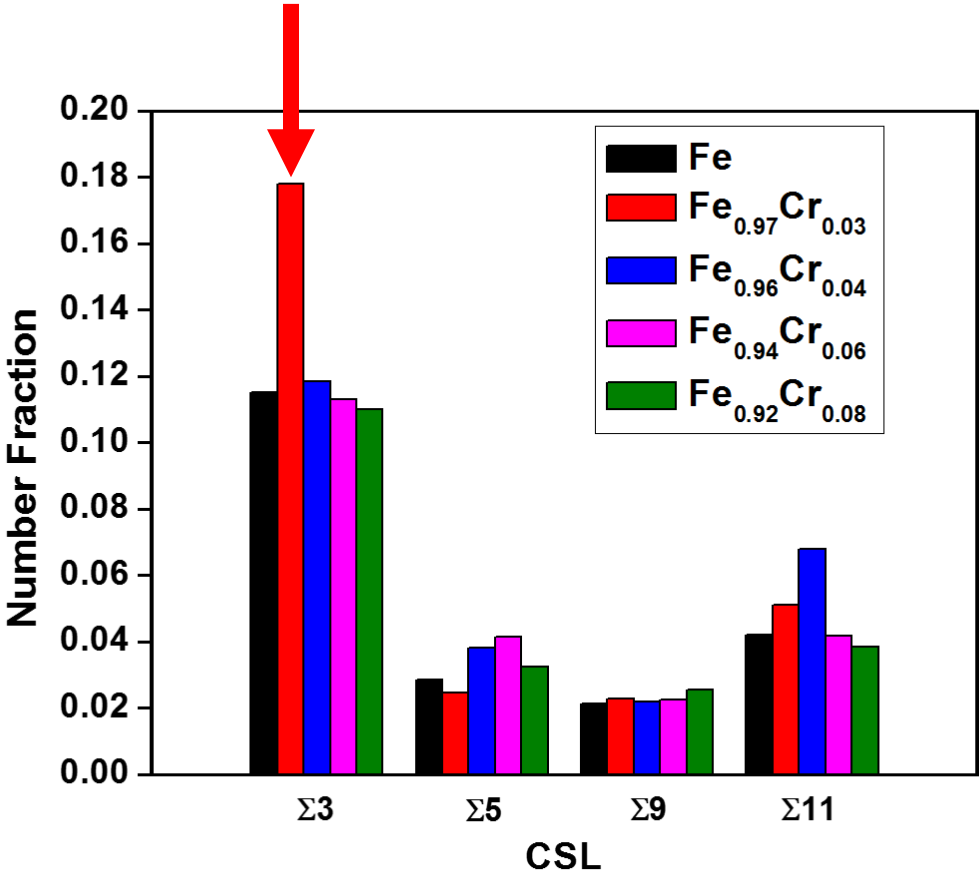
X. Zhou, et al. *Thin Solid Films* **612** (2016) 29-35.

Stress and Grain Size



- In general, for < 4 at.% Cr, tensile stress is reduced by increasing grain size
- In general, as grain size increased (> 4 at. % Cr), the tensile stress increased

Same grain size – Different GB types ($\Sigma 3$)



$$\langle \sigma \rangle = \frac{4(2\gamma_s - \gamma_{gb})}{d}$$

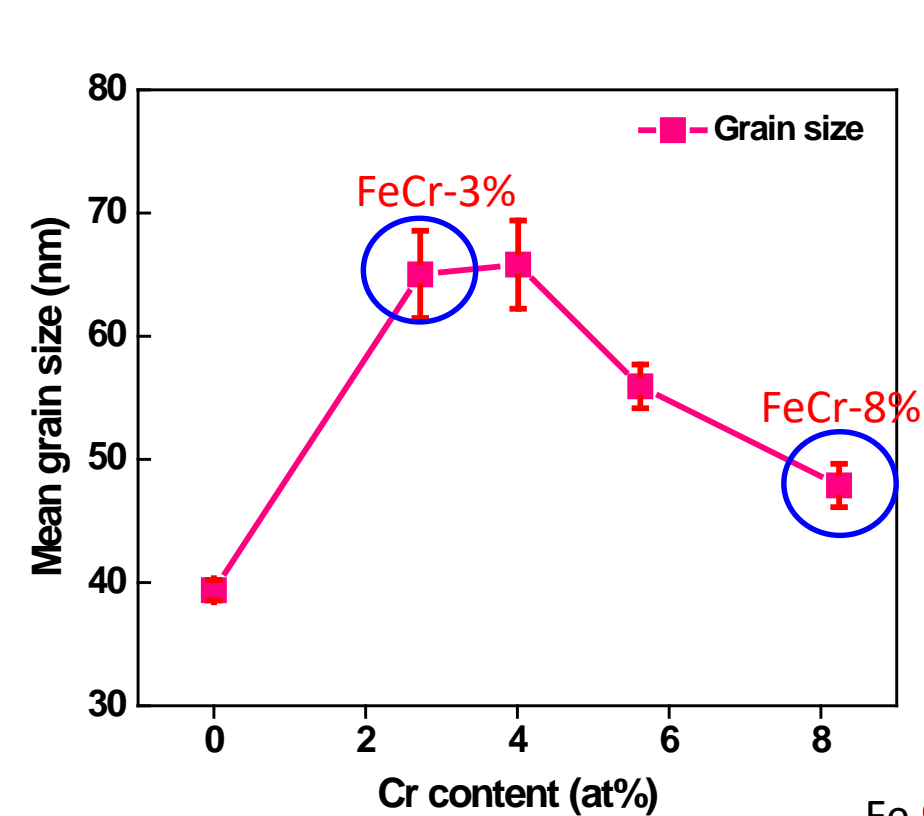
γ_s : Surface energy
 γ_{gb} : Grain boundary energy
 d : Grain size

- $\Sigma 3$ is a low energy GB.
- Low energy GB enabled $\Delta\gamma$ to be larger such that σ is larger for equivalent grain size(d).

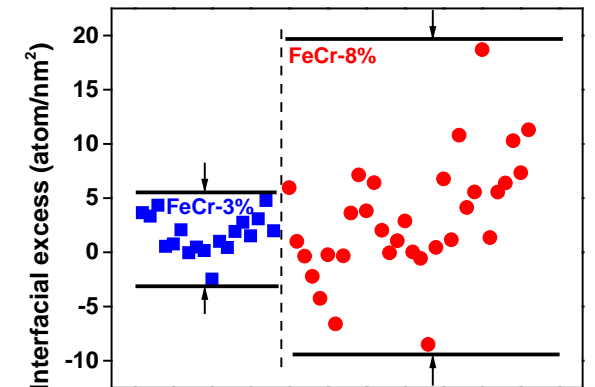
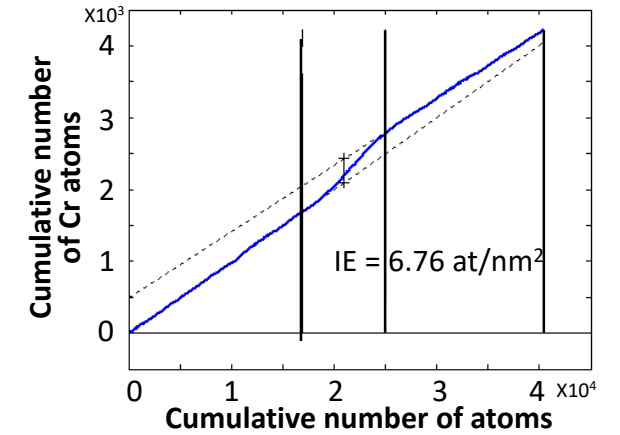
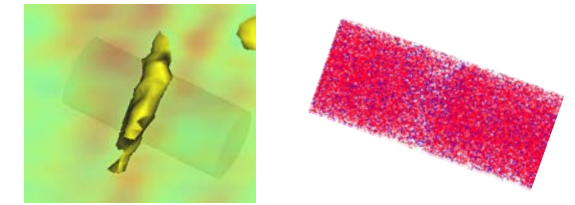
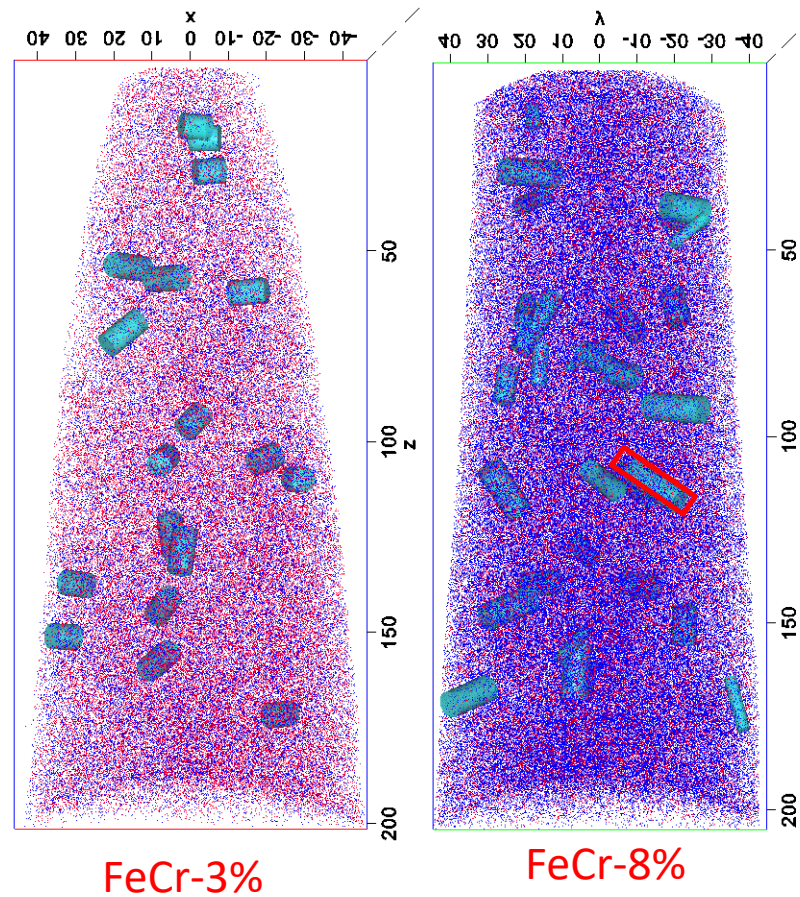
L.B. Freund, E. Chason. *Journal of Applied Physics* **89** (2001) 4866-4872



What about grain boundary composition?

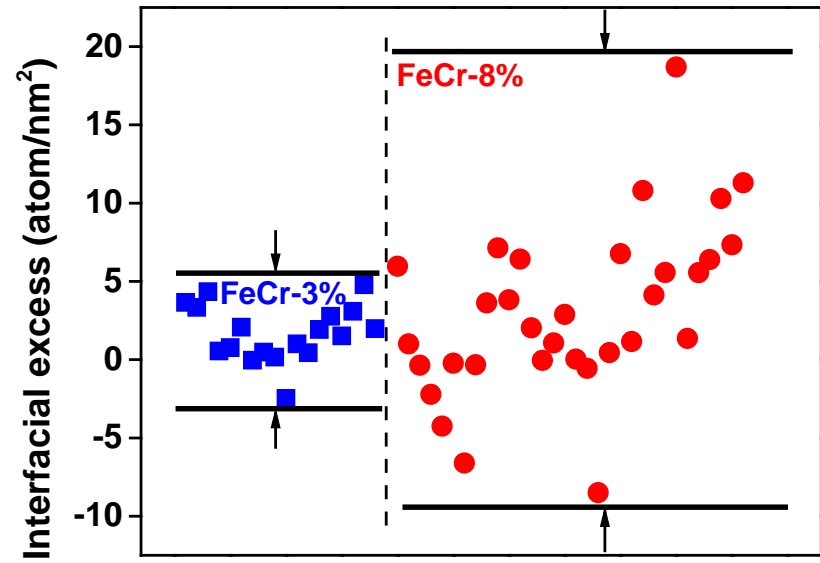
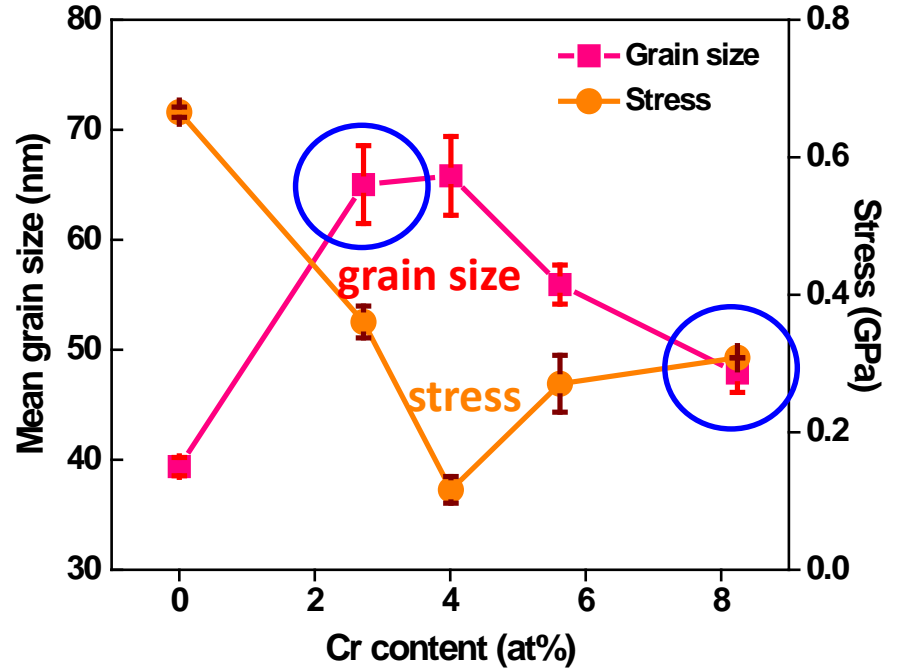
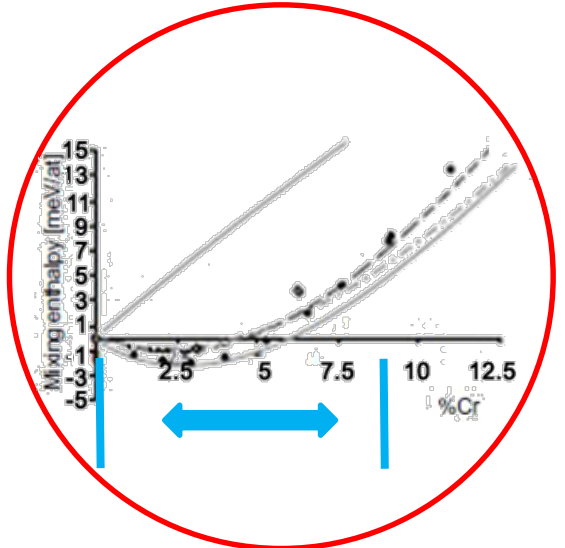


Fe ●
Cr ●



- The Interfacial Excess (IE) values of different GBs are quite different
- The range of IE value of FeCr-8% is larger than FeCr-3%.

Phase separation → grain refinement growth → stress manipulation

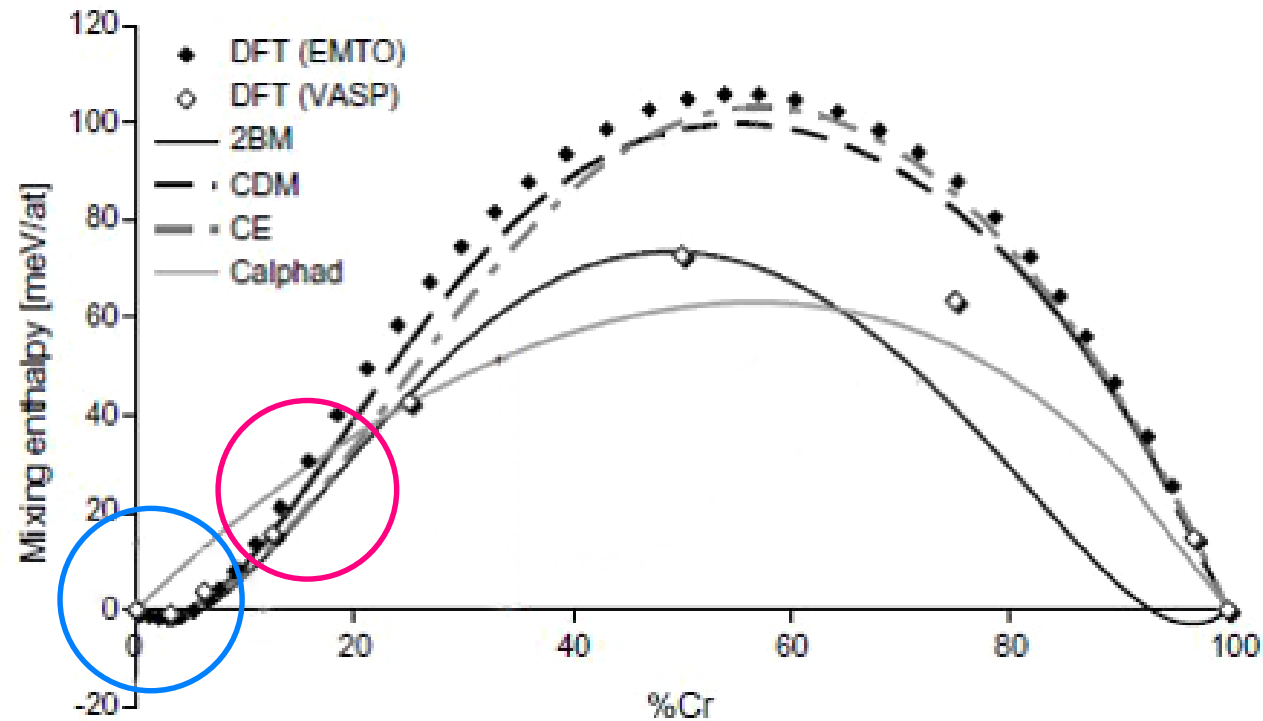


X. Zhou, et al. *Thin Solid Films* **612** (2016) 29-35.



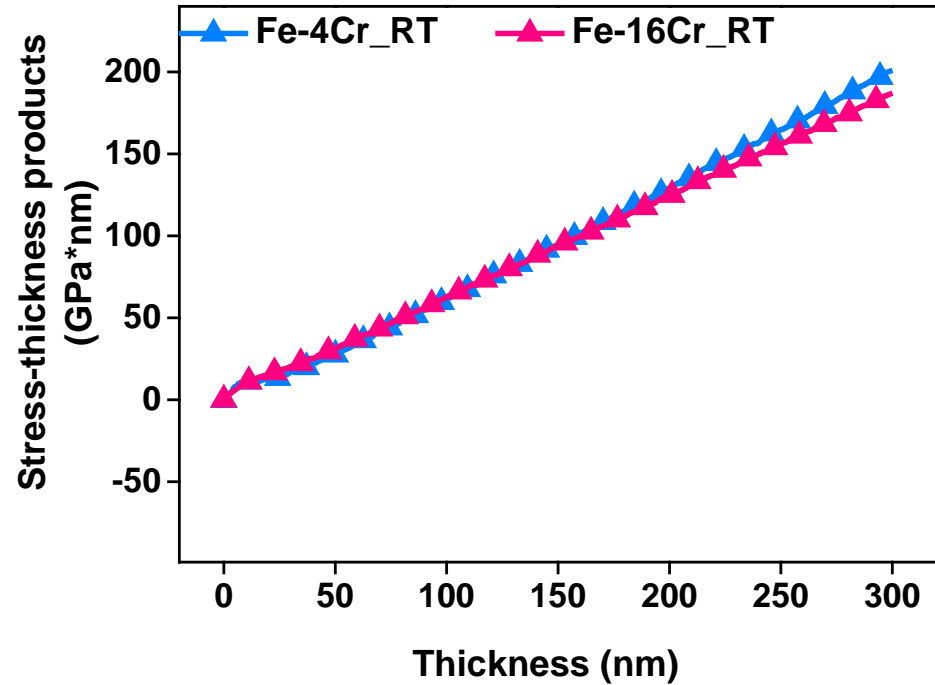


The Choose of Fe-Cr Alloys for *in-situ* heating experiments

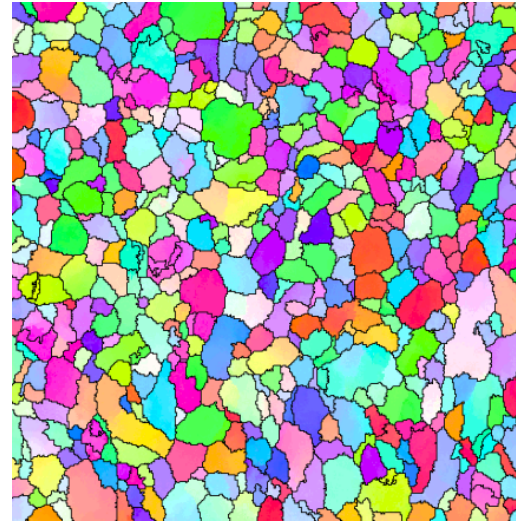


VS.

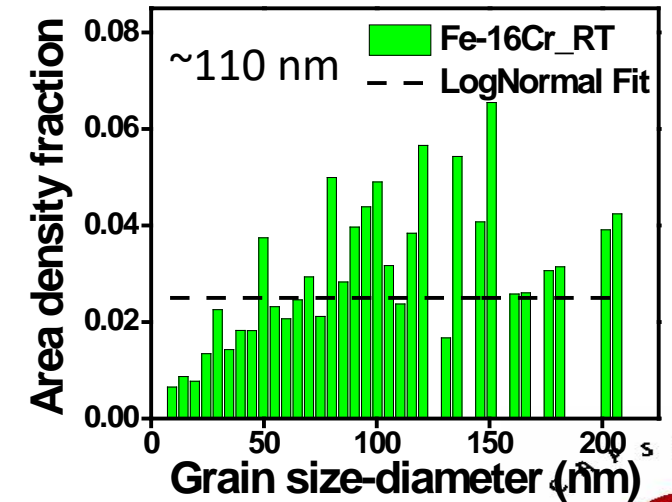
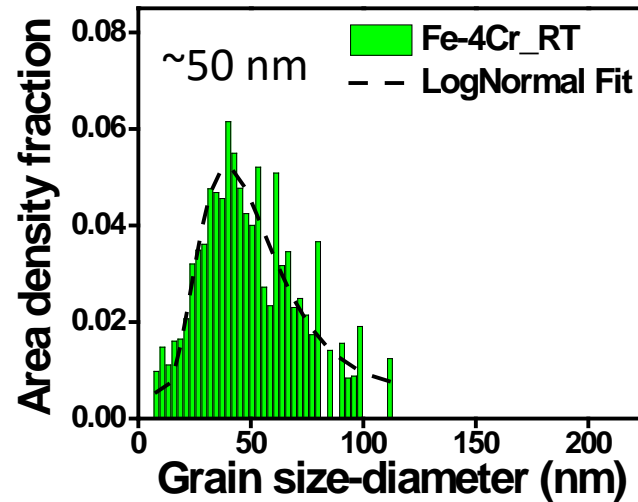
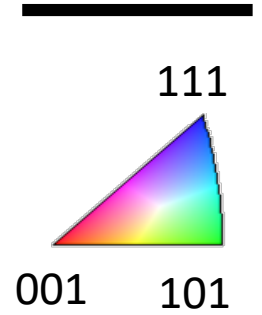
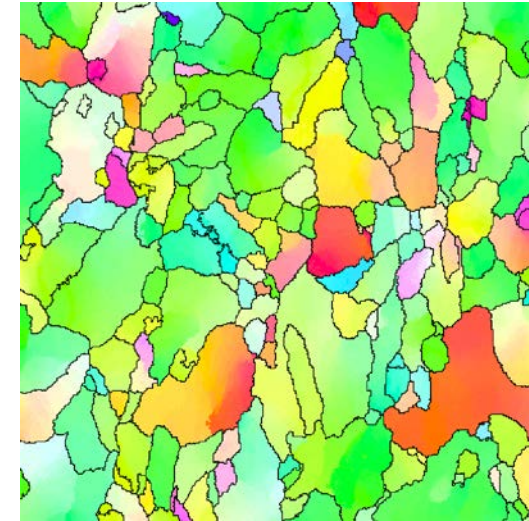
In situ Stress and Grain Size Evolution at RT



Fe-4Cr_RT



Fe-16Cr_RT



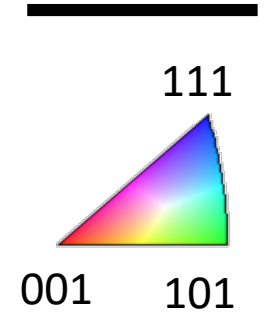
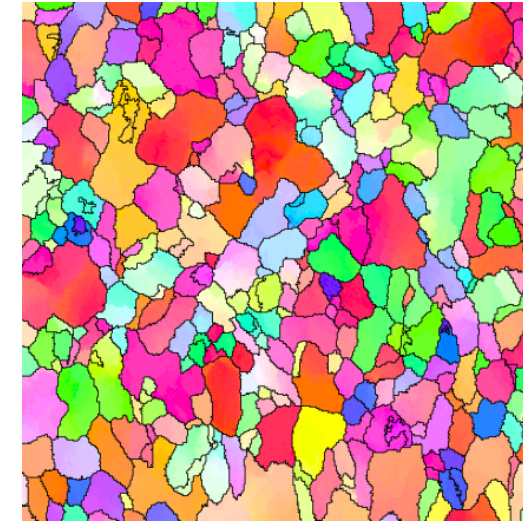
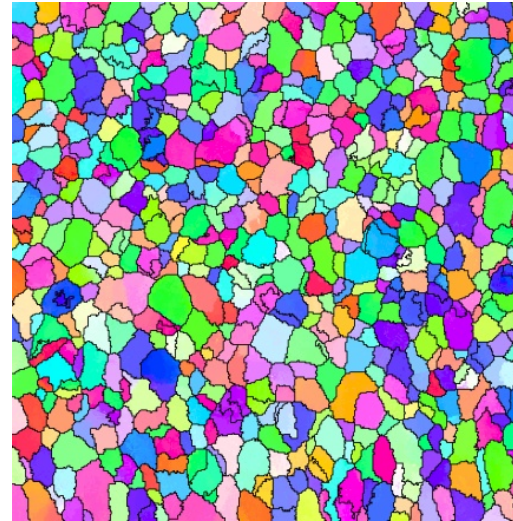
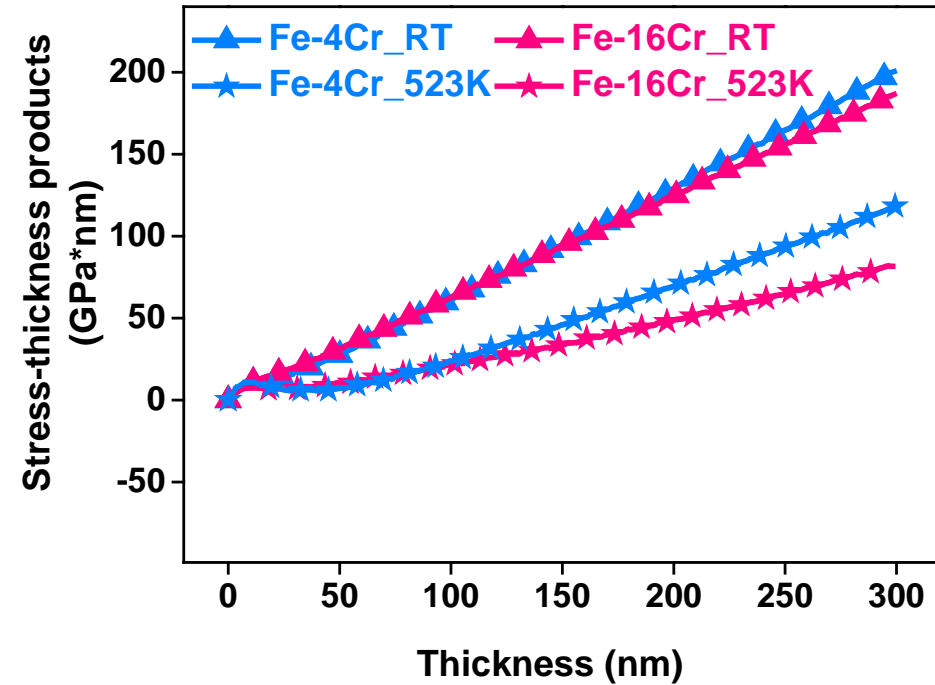
At room temperature:

- Different grain size distributions were noticed;
- Fe-16Cr showed abnormal grain growth.

In situ Stress and Grain Size Evolution at 523K

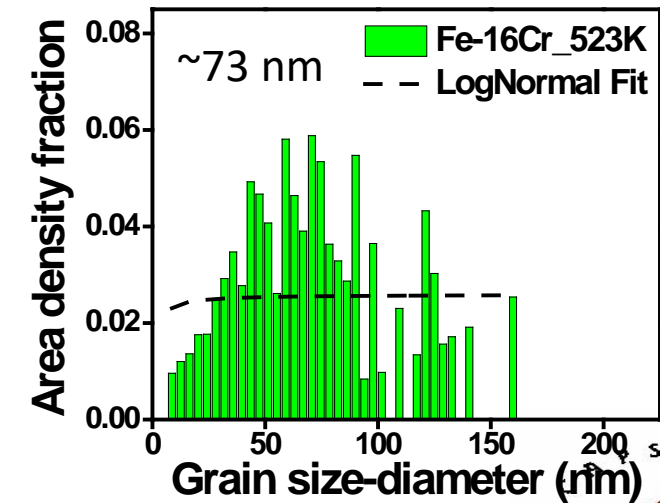
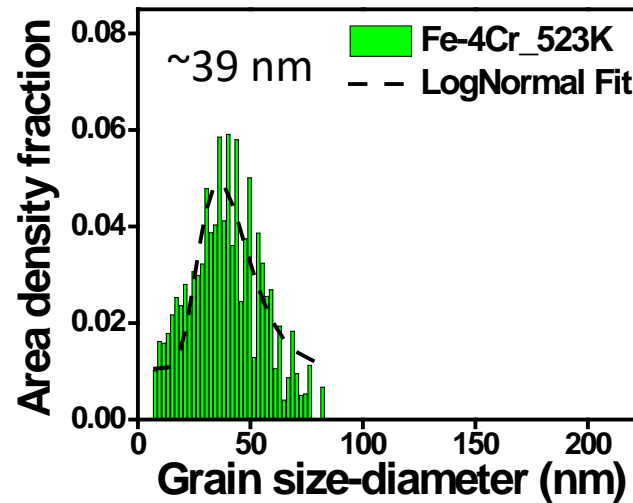
Fe-4Cr_523K

Fe-16Cr_523K



At 523K, for both Fe-4Cr and Fe-16Cr films:

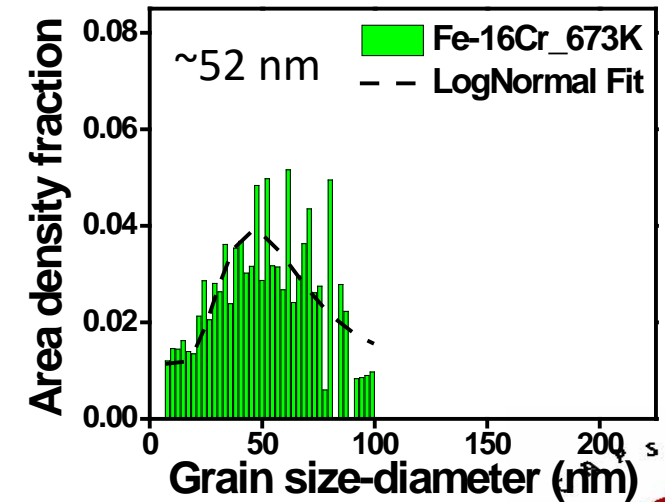
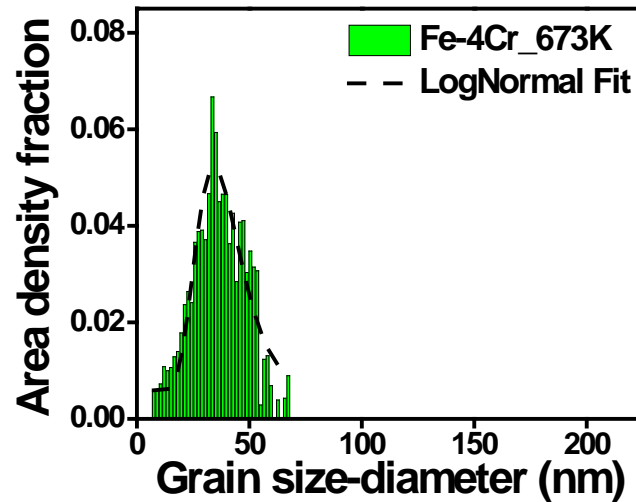
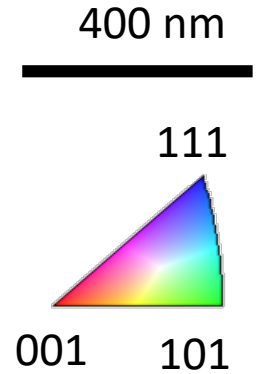
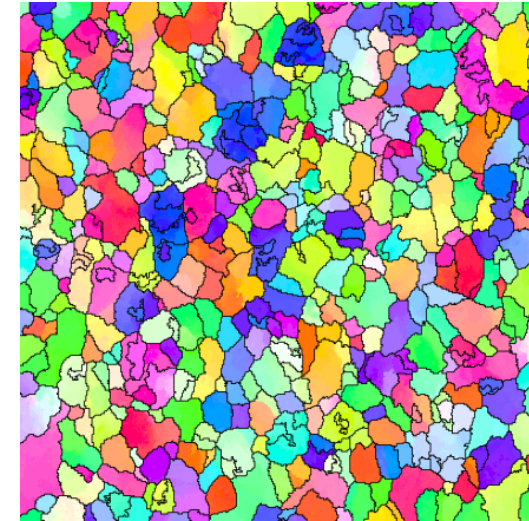
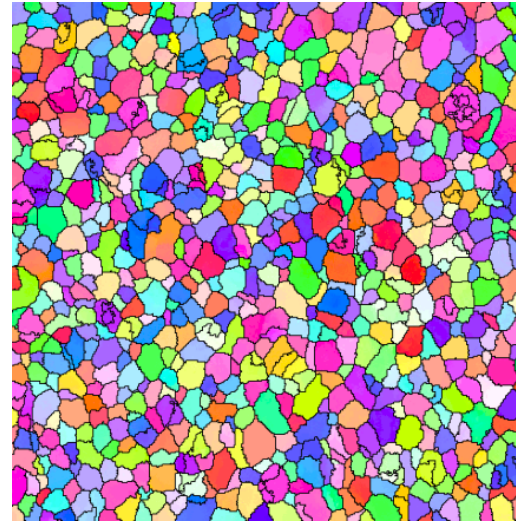
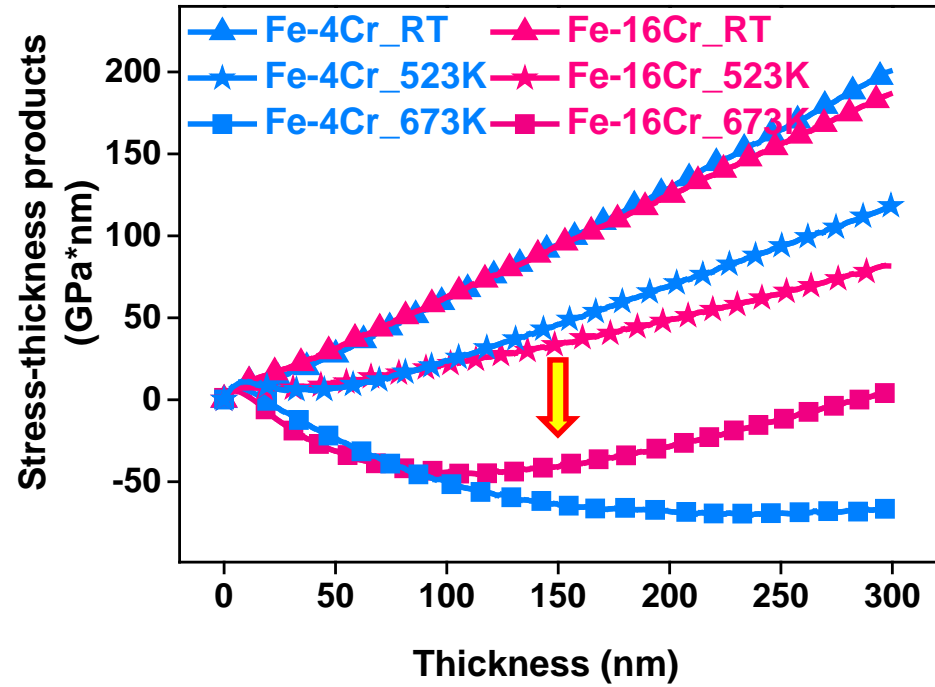
- The tensile stresses were reduced;
- Grain sizes were refined.



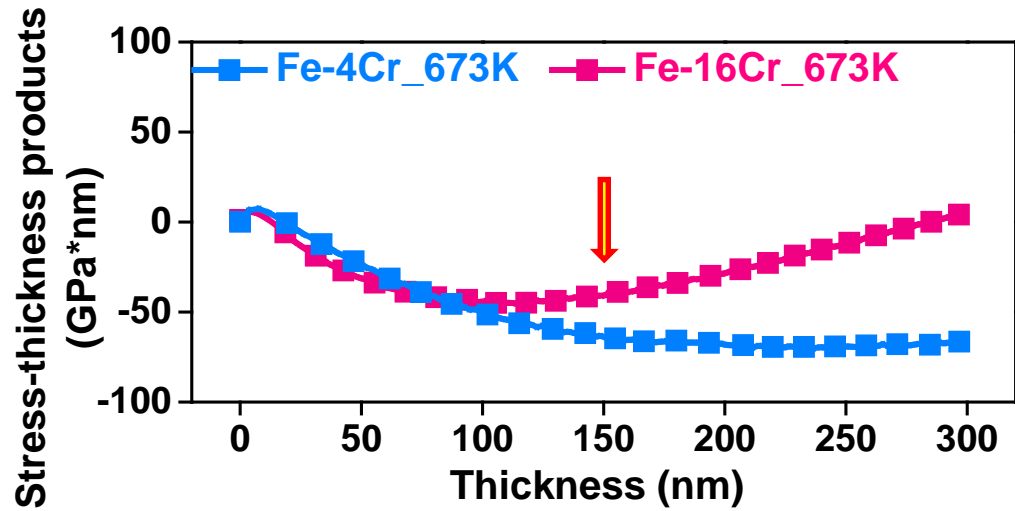
In situ Stress and Grain Size Evolution at 673K

Fe-4Cr_673K

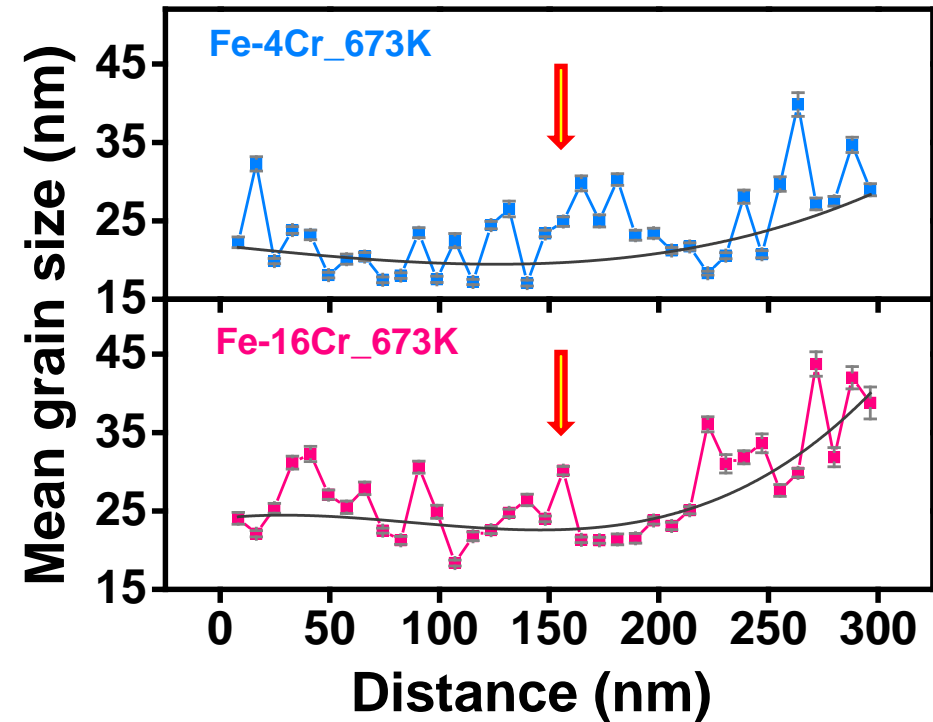
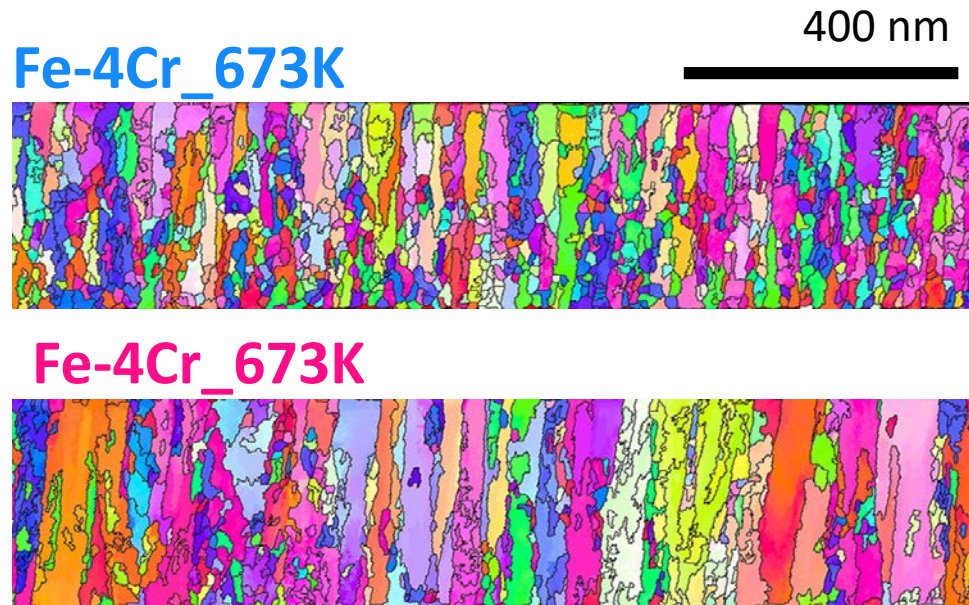
Fe-16Cr_673K



- Turnover points on stress curves were at ~150 nm.

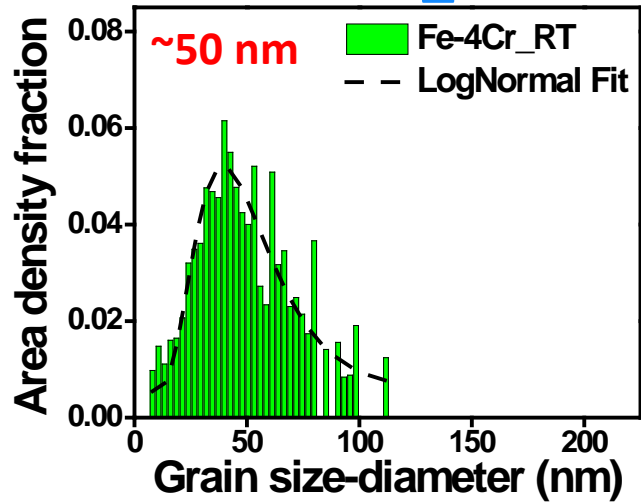


➤ At 673K, the turnover points on stress curves were mainly related to the grains size evolution in the growing direction.

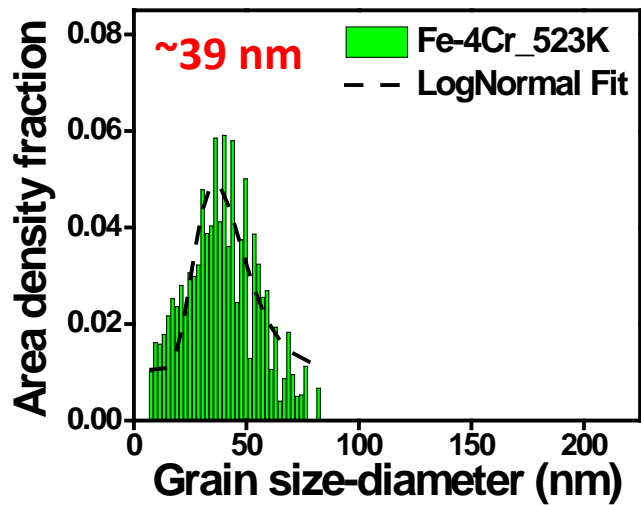


Growing direction
111
001 101

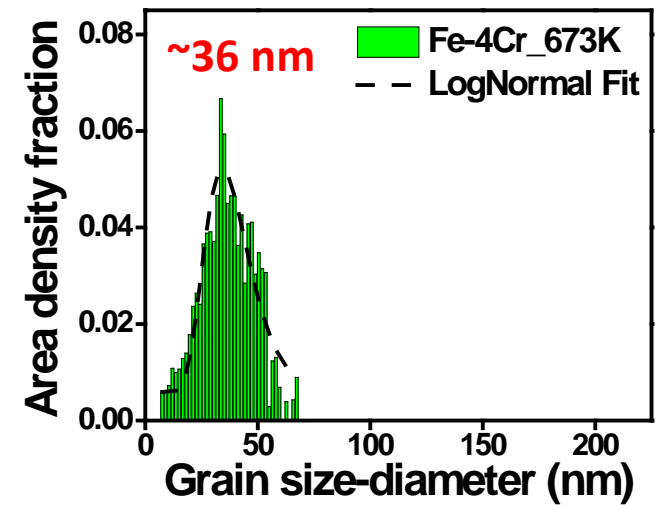
Fe-4Cr_RT



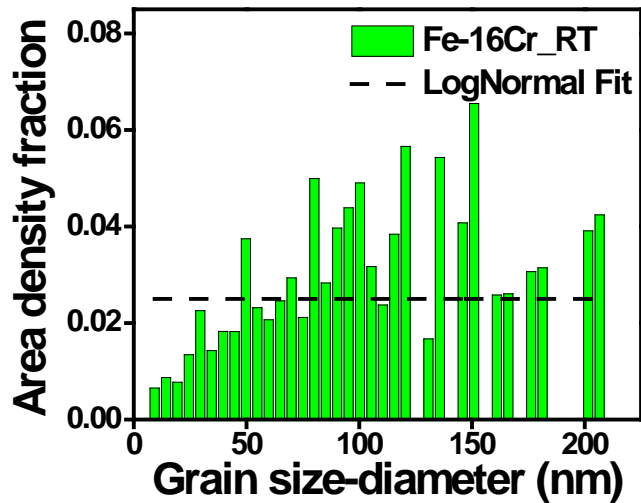
Fe-4Cr_523K



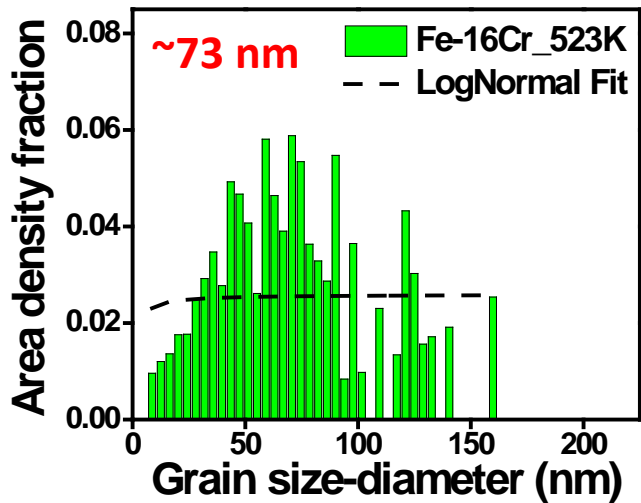
Fe-4Cr_673K



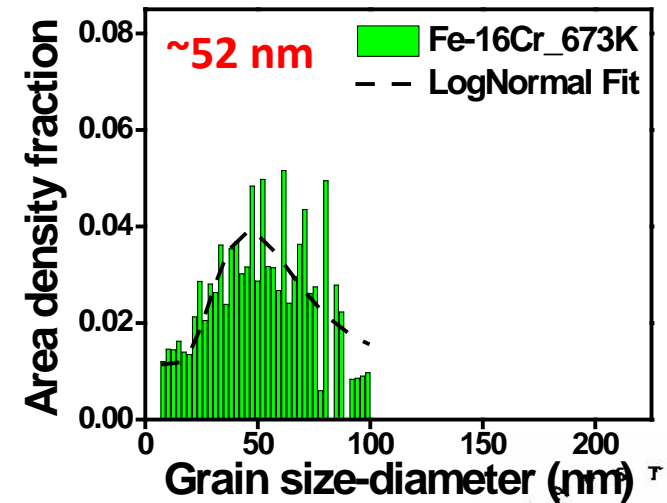
Fe-16Cr_RT



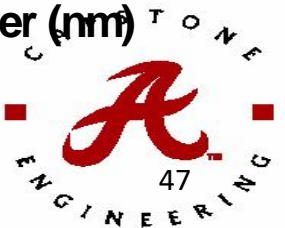
Fe-16Cr_523K



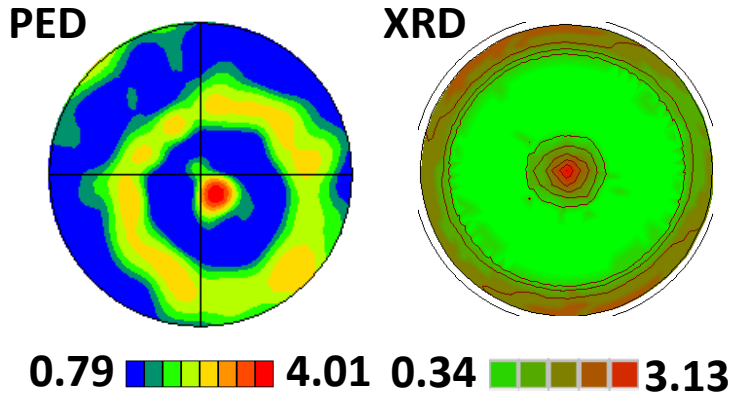
Fe-16Cr_673K



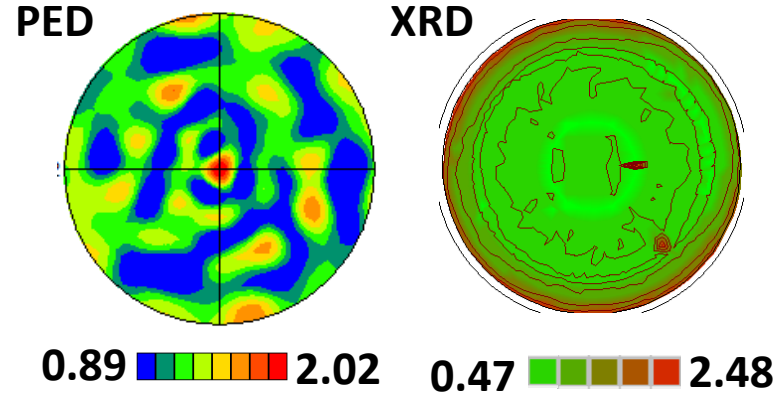
➤ When the temperature was increased, the grain sizes were reduced and the distribution was tightened up. ■



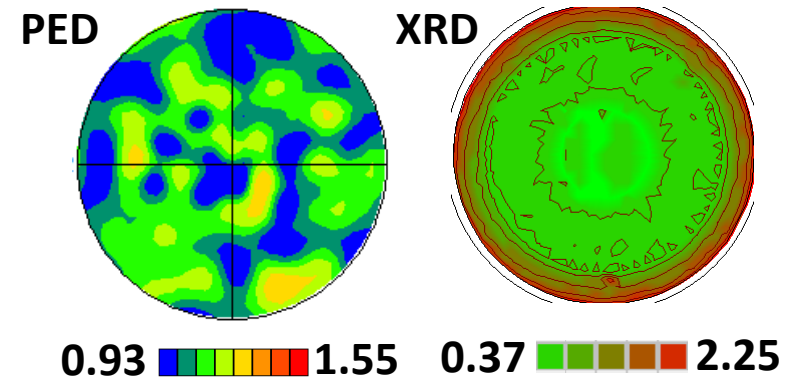
Fe-4Cr_RT



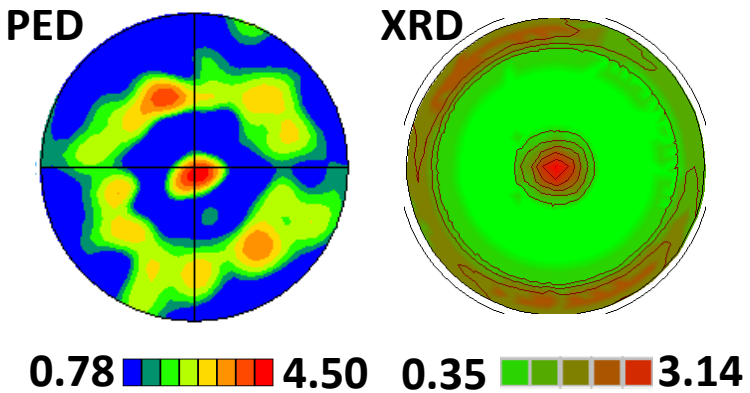
Fe-4Cr_523K



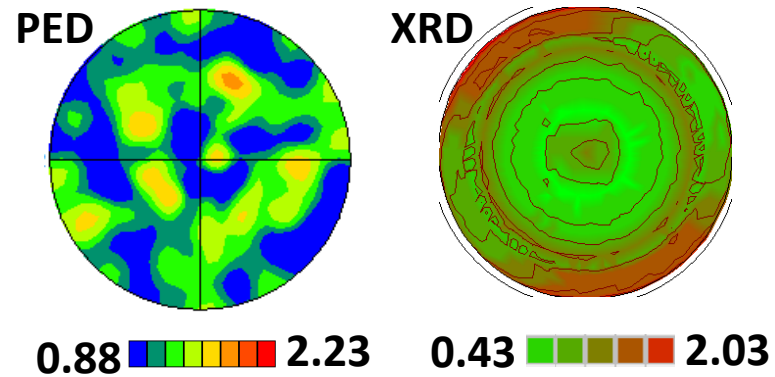
Fe-4Cr_673K



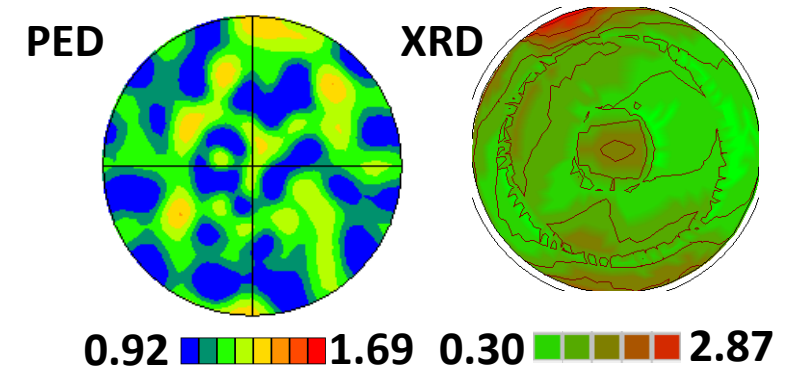
Fe-16Cr_RT



Fe-16Cr_523K



Fe-16Cr_673K



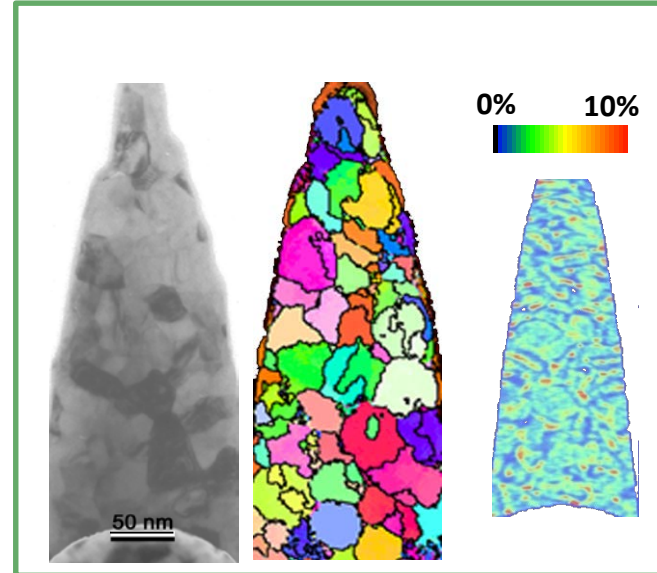
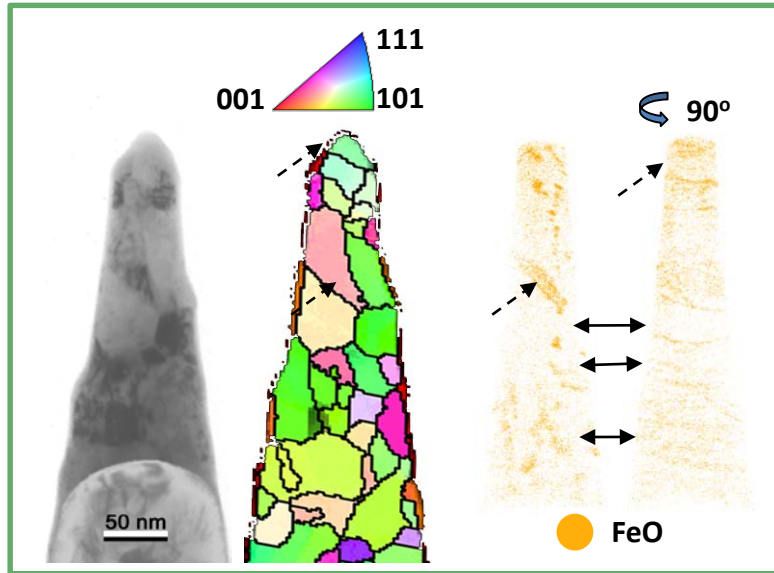
➤ When the temperature was increased, both Fe-4Cr and Fe-16Cr films gradually lost the preferred $\langle 101 \rangle$ texture.

Grain boundary composition

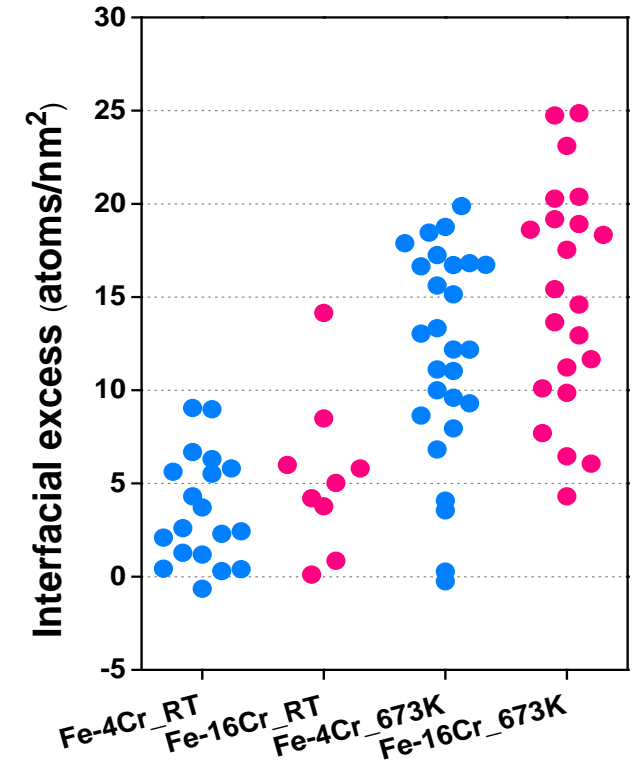
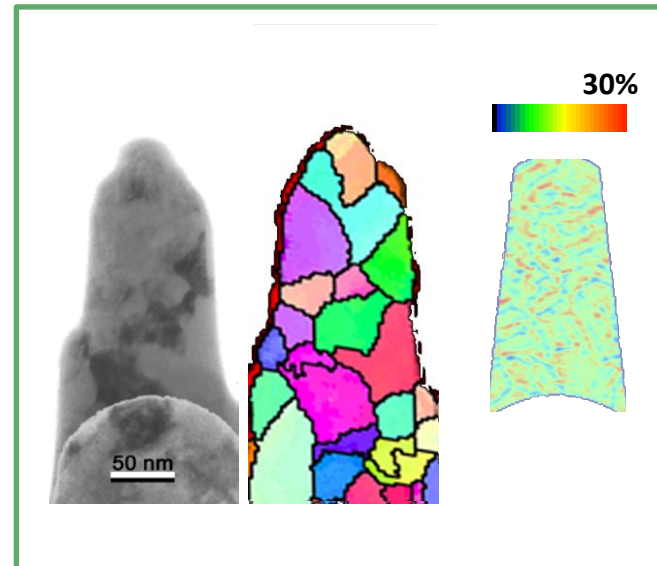
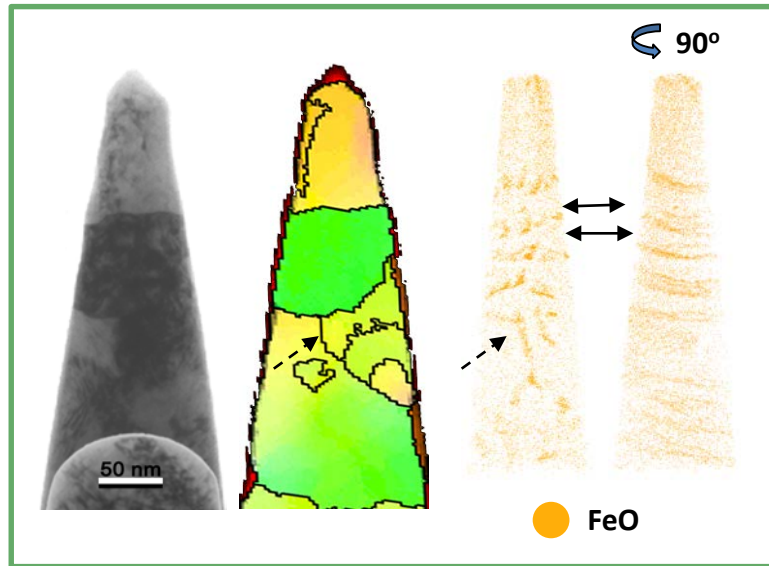
RT

673K

Fe-4Cr

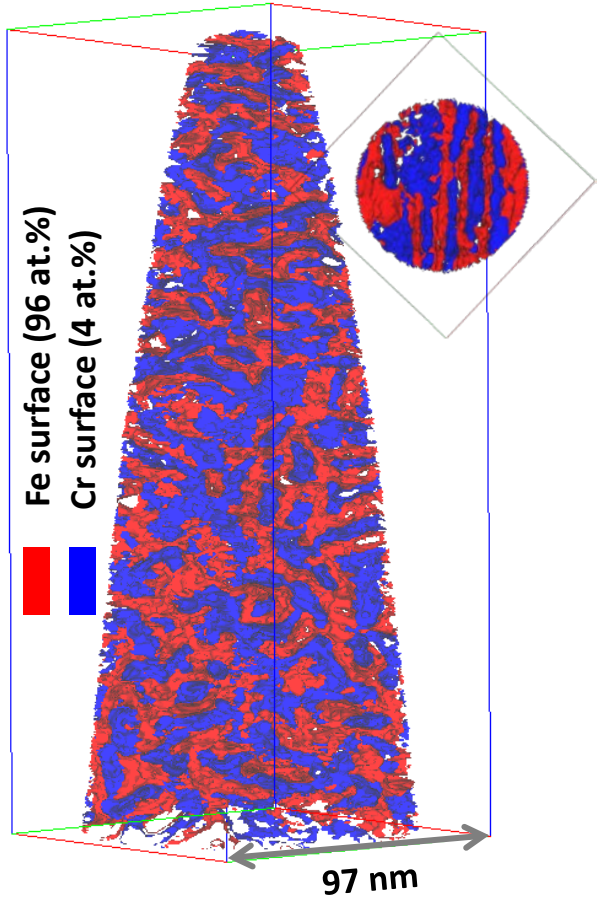


Fe-16Cr



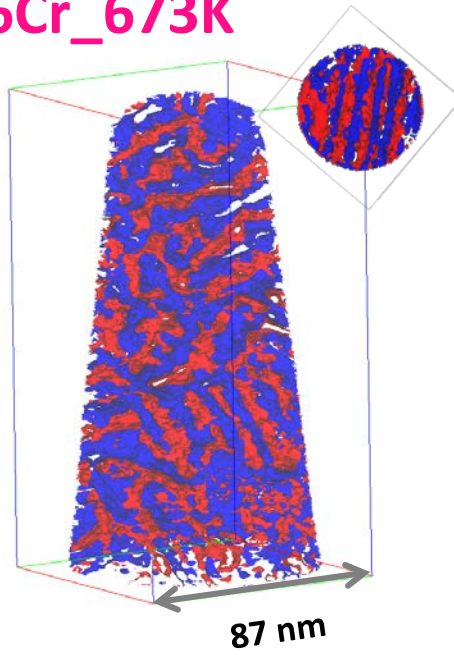
APT analysis

Fe-4Cr_673K

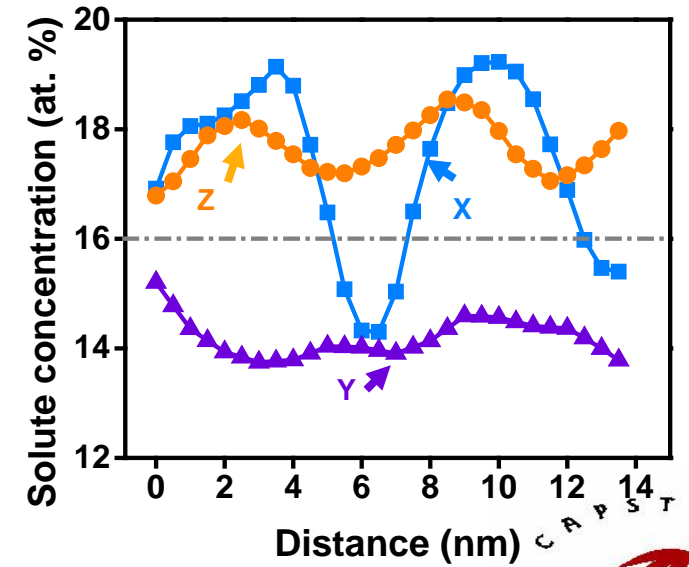
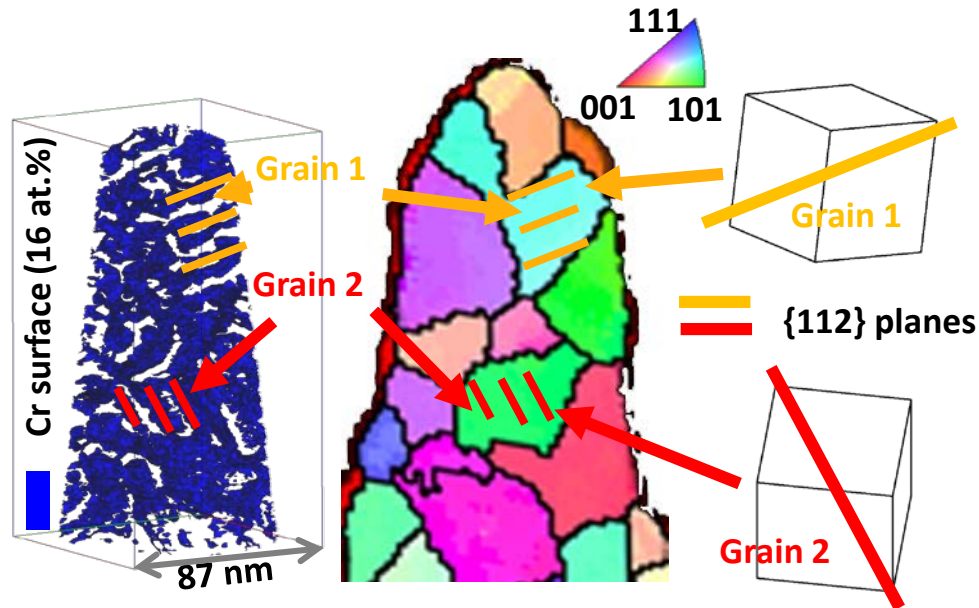
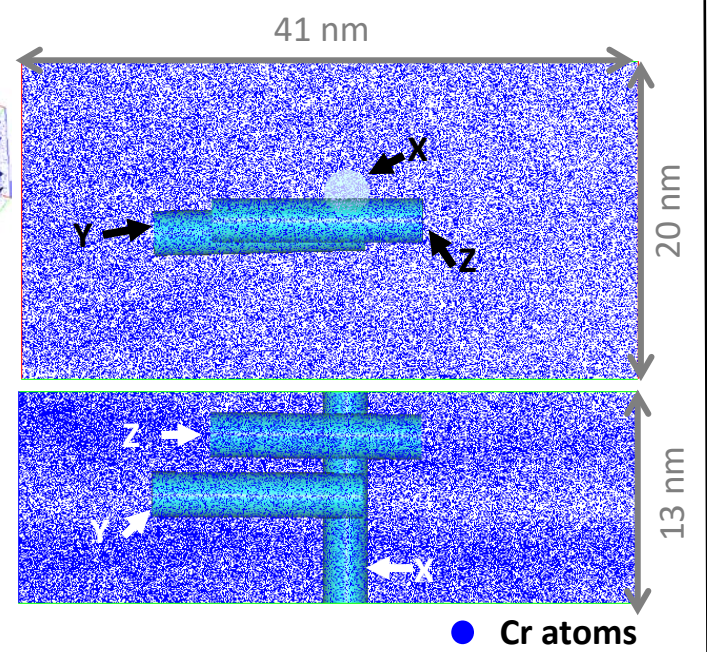
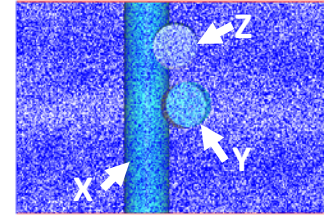


Fe-16Cr_673K

Fe surface (84 at.%)



Cr surface (16 at.%)



➤ Fe-Cr films

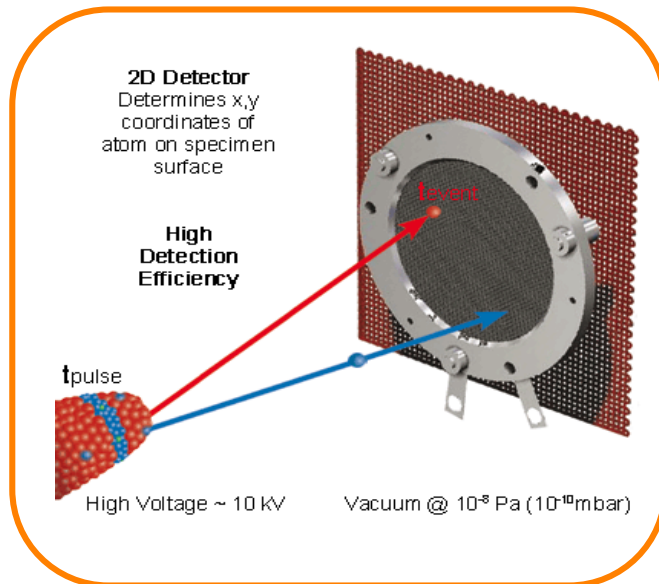
- A higher Cr concentration (≥ 16 at.% Cr), abnormal grain growth was noticed resulting in a relatively low tensile stress.
- The σ -phase Fe-49Cr film appeared to show a small grain size and relatively high tensile stress.
- Upon heating the Fe-4Cr and Fe-16Cr films during deposition, tensile stresses reduced and the grains were refined.



Cross-correlative Microscopy

APT

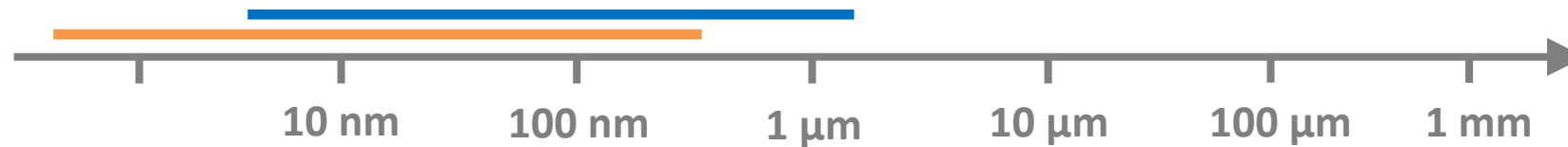
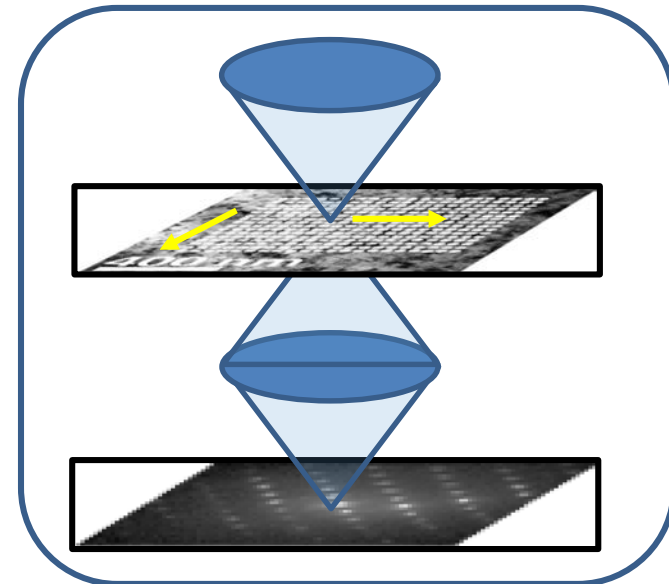
- Chemical evolution
- GB chemistry characterization

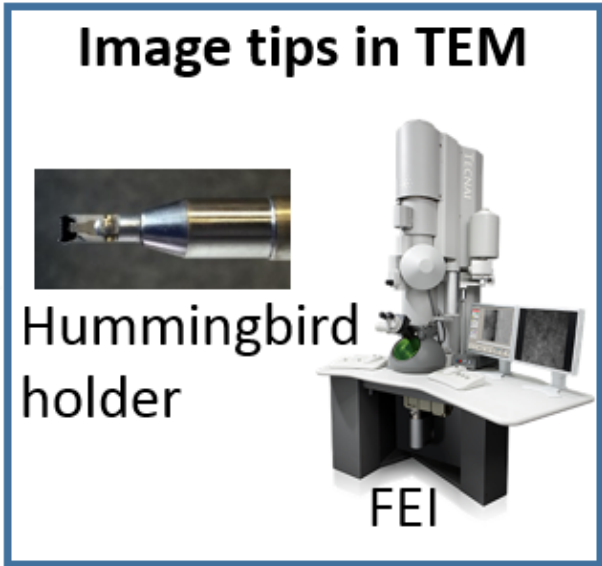
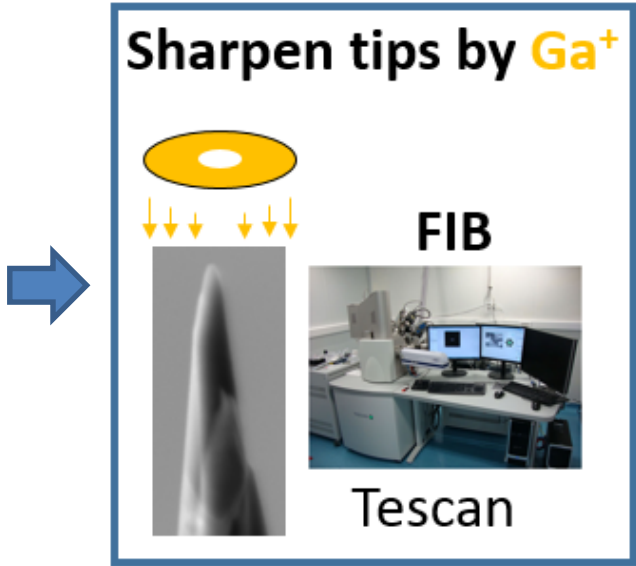
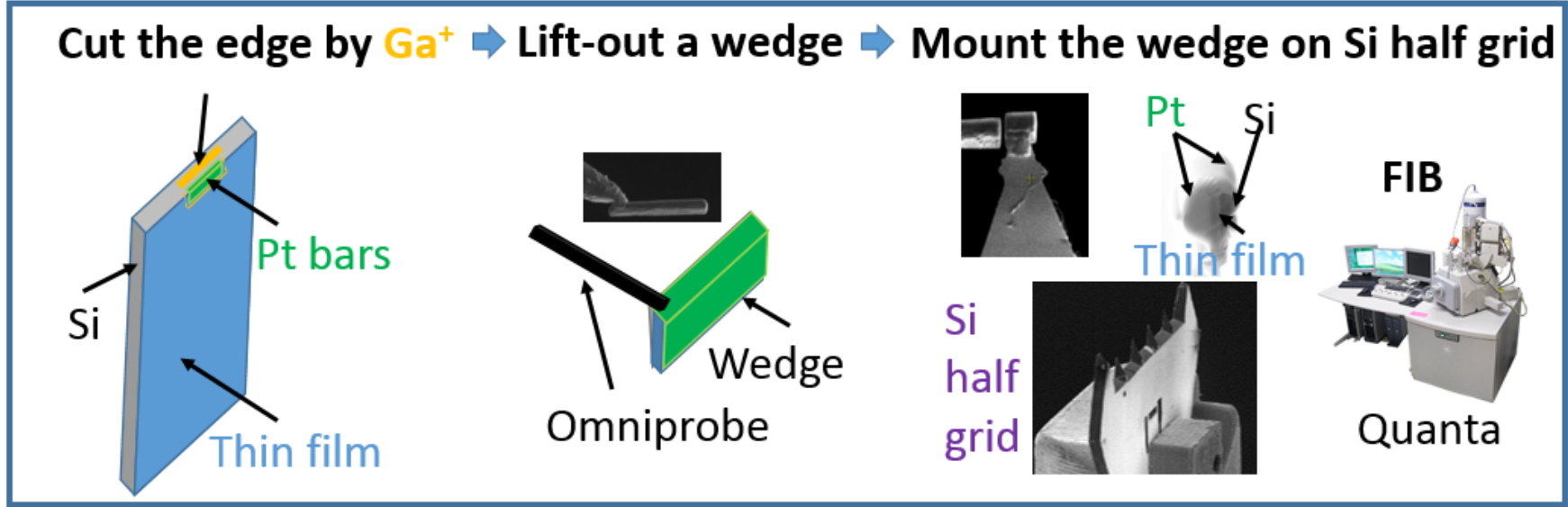


**Grain boundary
segregation**

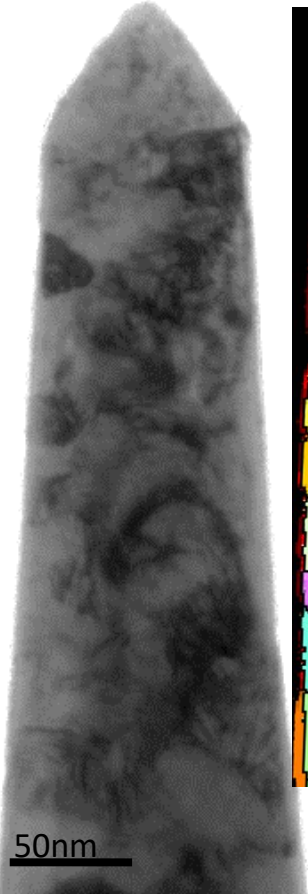
PED

- Microstructural evolution
- GB structural characterization

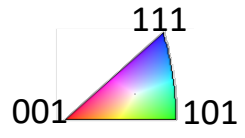
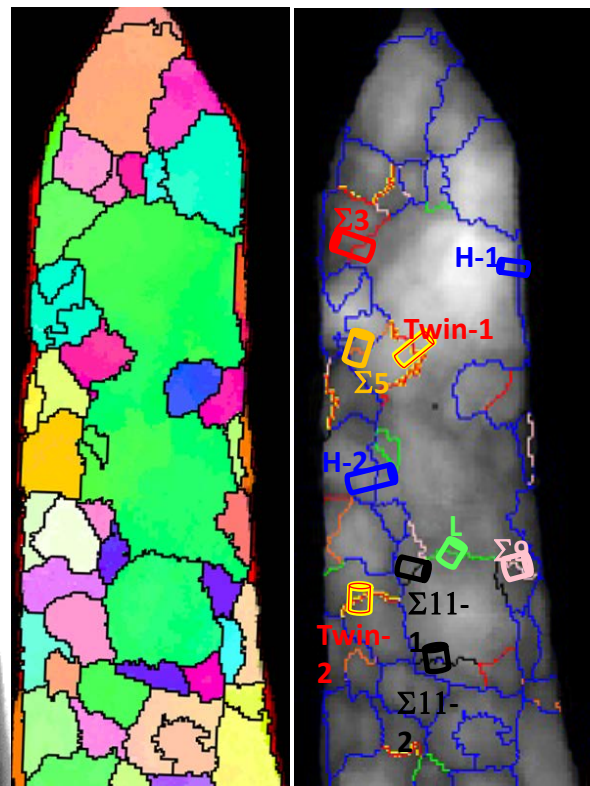




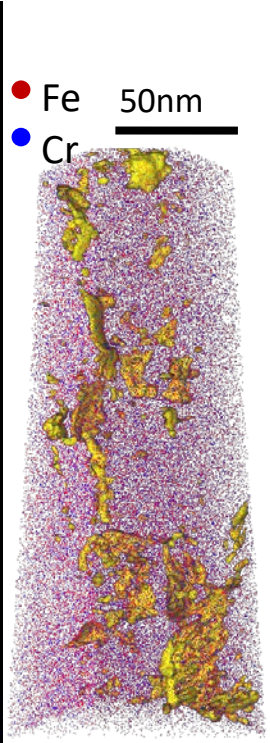
TEM



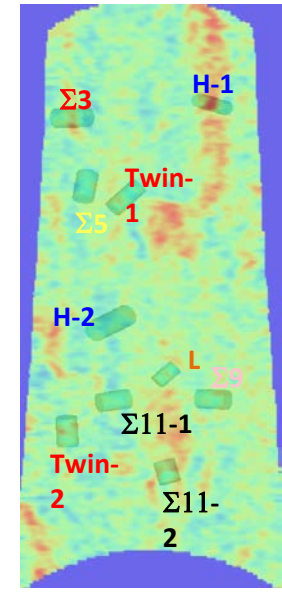
PED



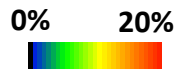
APT



Composition

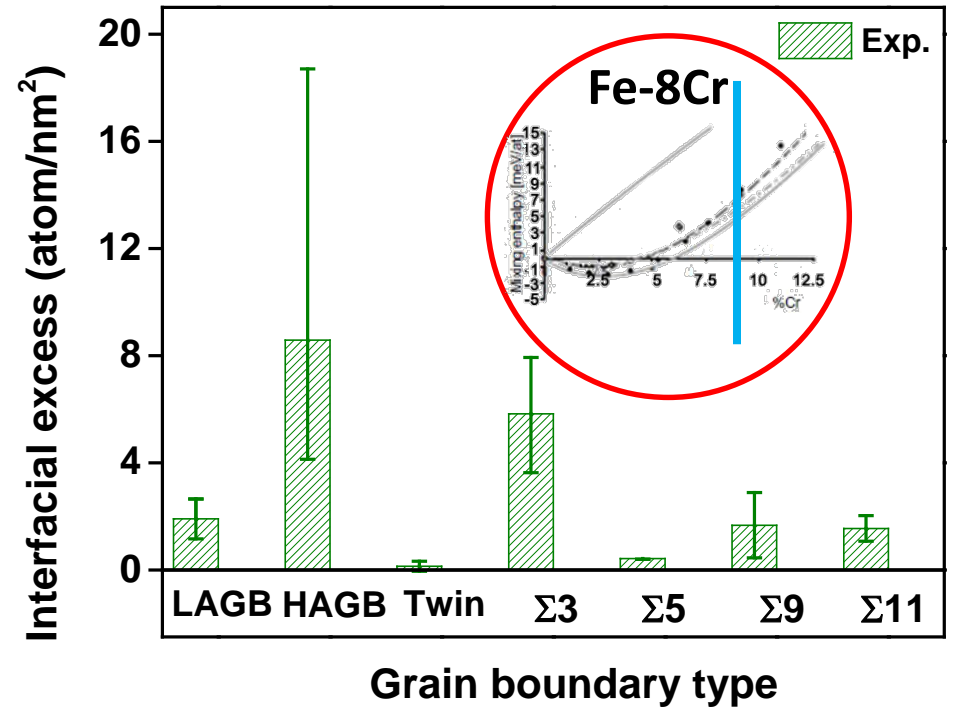


Density Iso-surface



Fe-8Cr

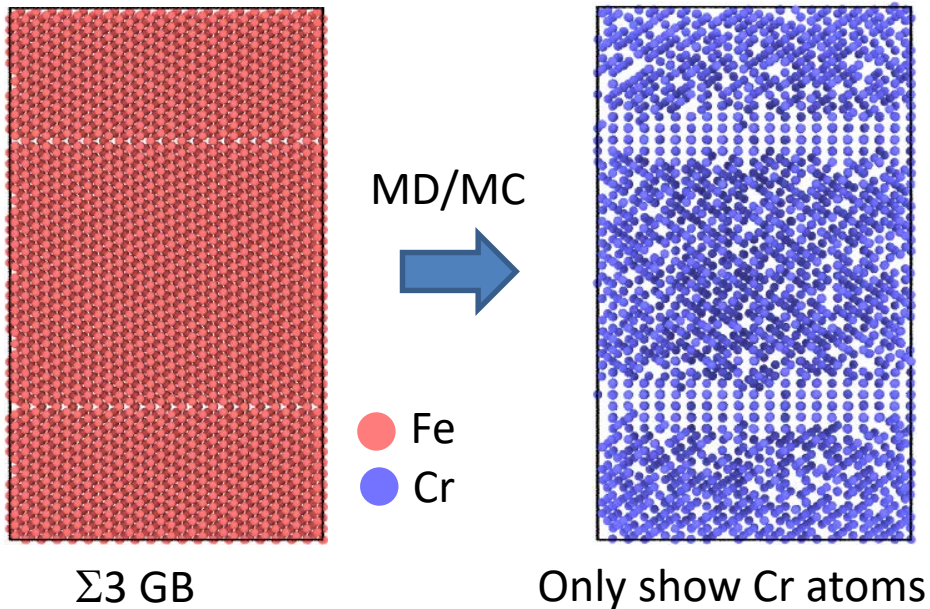
Legends							
GB Types	LAGB	HAGB	Twin	Σ3	Σ5	Σ9	Σ11



- Cr Segregation is strongly related with GB types;
- HAGB appears to have both the largest Cr segregation and biggest range;
- Cr has a weak tendency to segregate into the twin and Σ5 grain boundaries.

Hybrid molecular dynamics/Monte Carlo (MD/MC) simulation

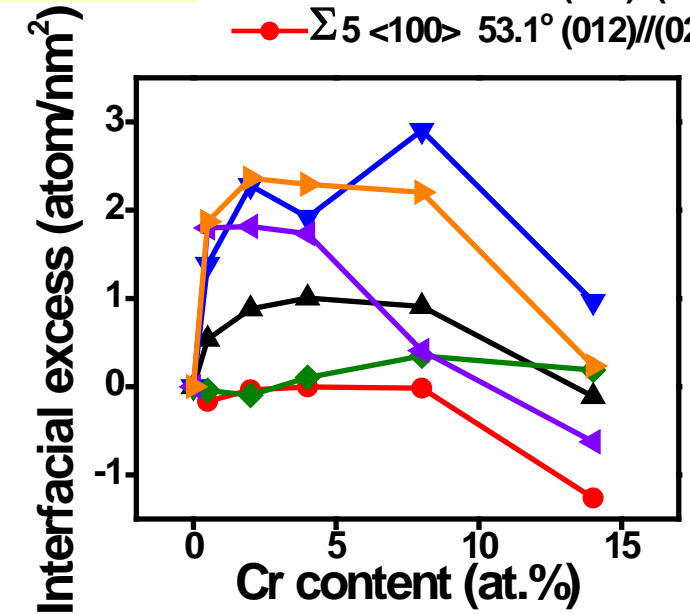
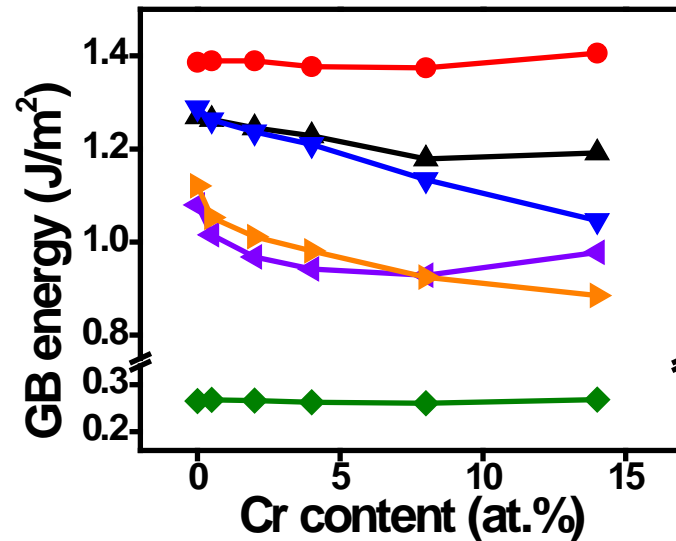
➤ The MD/MC simulation^[1] was conducted in LAMMPS using the Fe-Cr binary concentration dependent embedded atom model potential.



$$E_{GB} = \frac{E_{CSL} - N_{CSL}E_{atom}}{A_{GB}}$$

$$\Gamma E = \frac{N_{excess}}{A_{GB}}$$

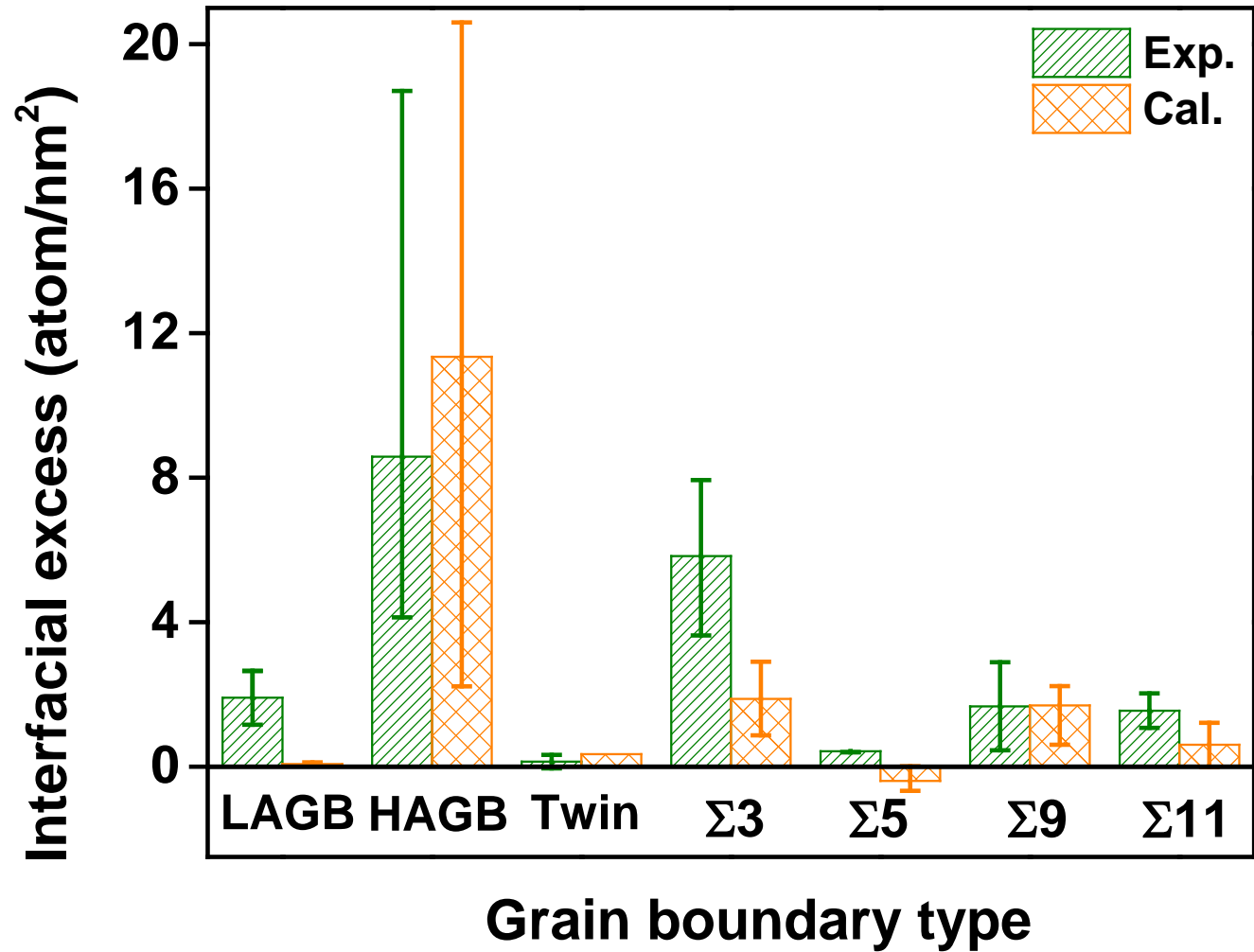
- Σ3 <110> 70.5° (111)//(111)
- ◆— Σ3 <110> 109.5° (2 $\bar{1}\bar{1}$)//(1 $\bar{2}$ 1)
- ▲— Σ9 <110> 38.9° (2 $\bar{2}\bar{1}$)//(2 $\bar{2}$ 1)
- ▶— Σ9 <110> 141.1° (1 $\bar{1}$ 4)//(1 $\bar{1}$ 4)
- ▼— Σ11 <110> 129.5° (1 $\bar{1}$ 3)//(1 $\bar{1}$ 3)
- Σ5 <100> 53.1° (012)//(021)



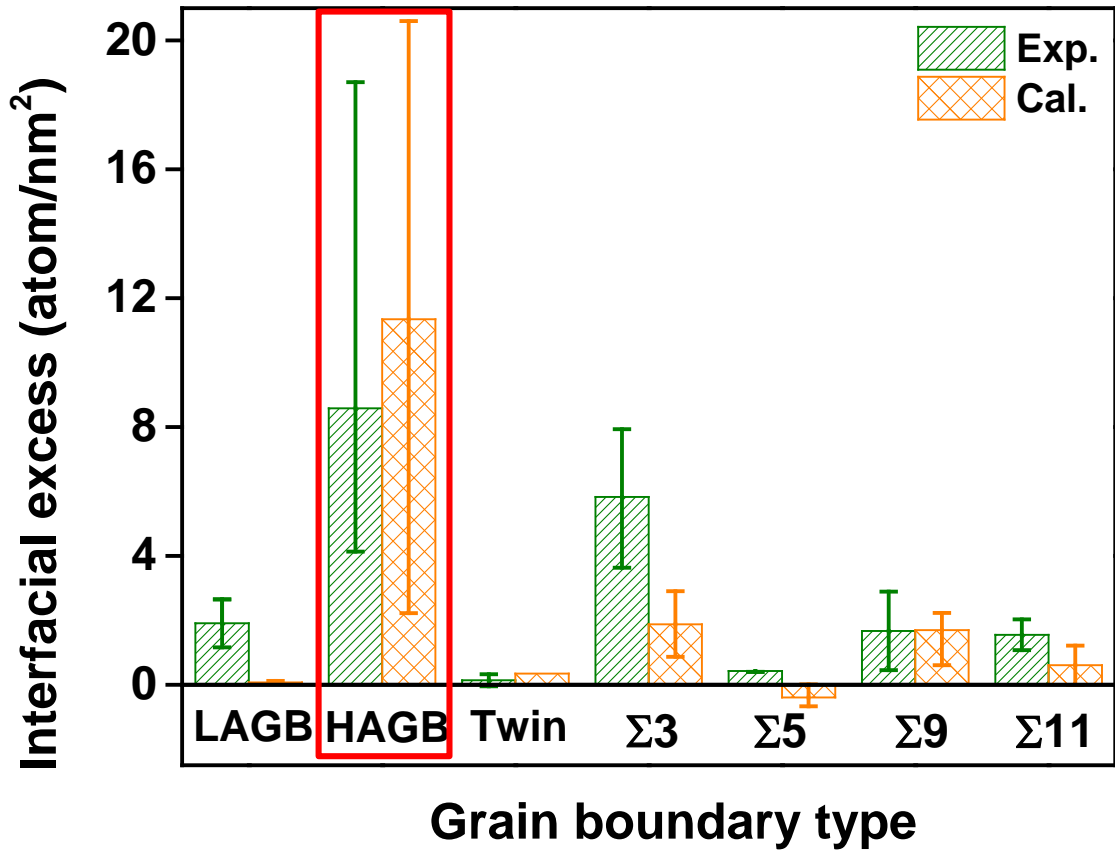
- GB segregation is dependent on GB types and solute content with the highest segregation being around 8 at. % Cr.
- The highest Gibbsian interfacial excess at the incoherent Σ3 followed by Σ9 and Σ11. Negligible segregation to the twin and Σ5 boundaries

[1] Sadigh, B. et al., Physical Review B 85 (2012) p. 184203.

Comparisons between experimental & simulated results



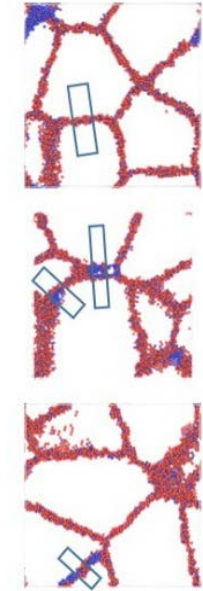
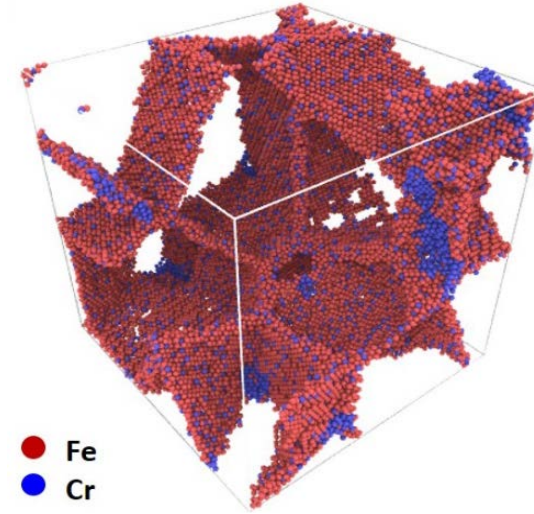
Comparisons between experimental & simulated results



➤ Clusters form at high angle grain boundaries.

Clustering Analysis

Cal. Poly-Crystal

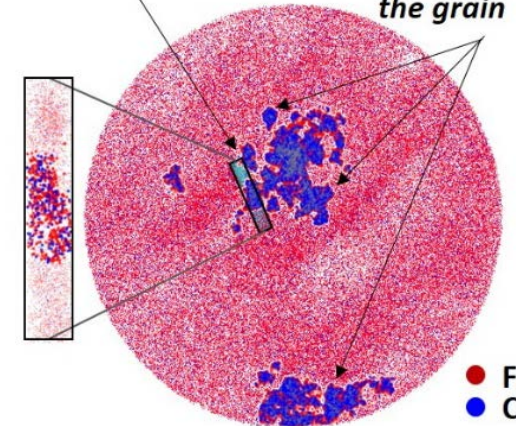


● Fe
● Cr

Exp.

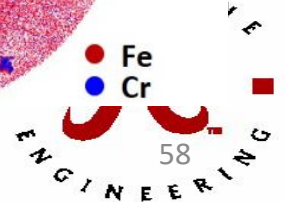
Cluster at HAGB

Clusters inside the grain

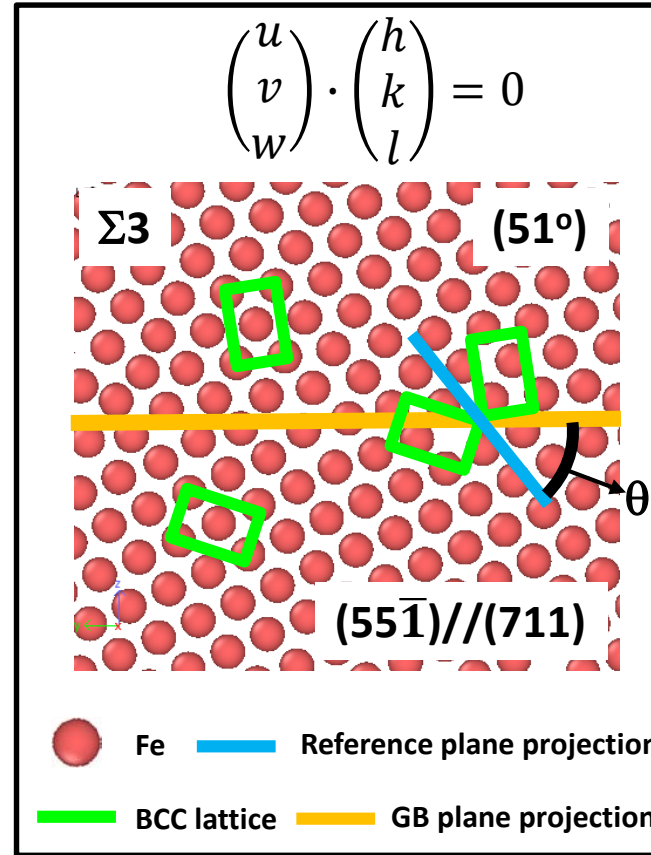
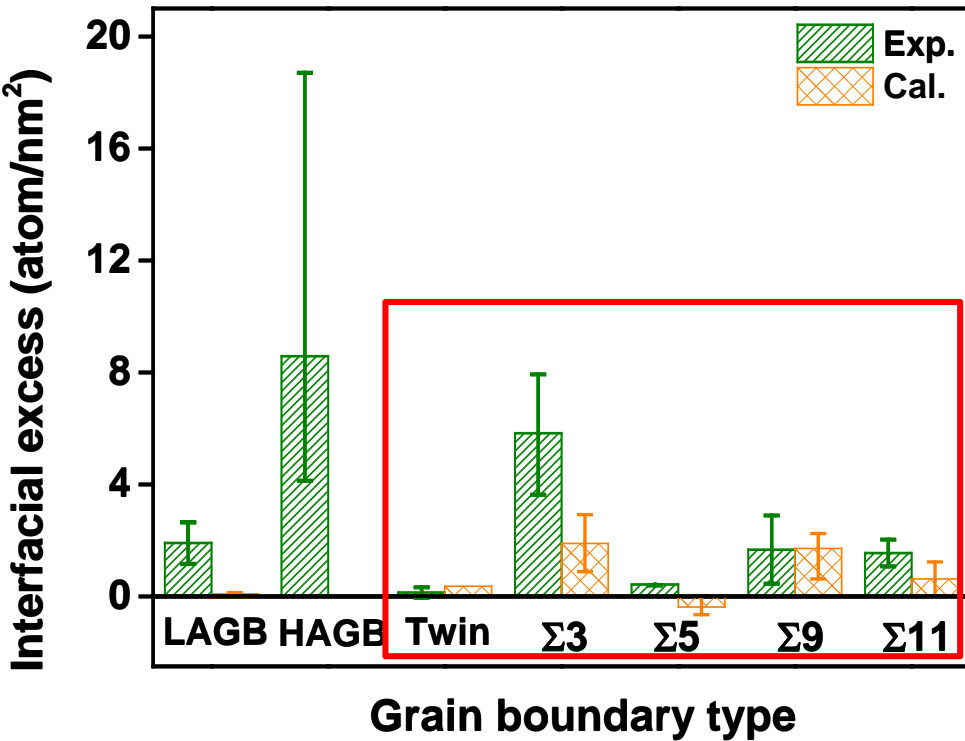


20% Cr iso-surface

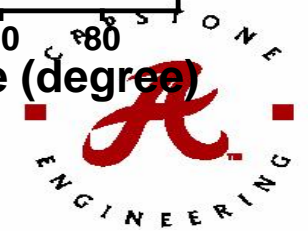
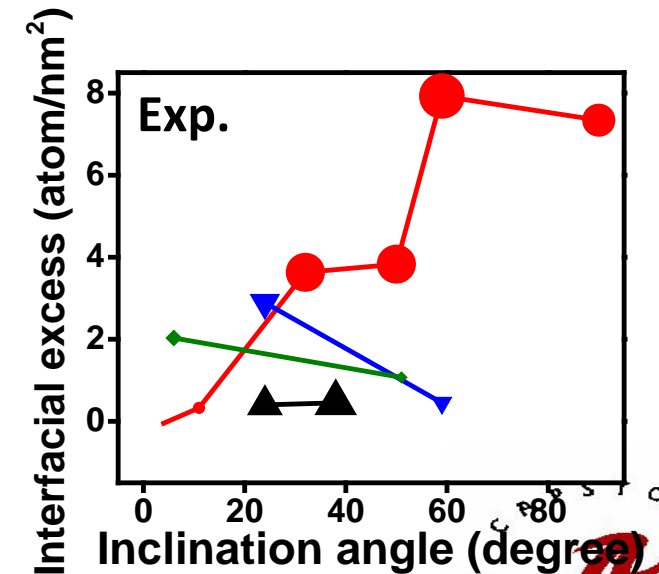
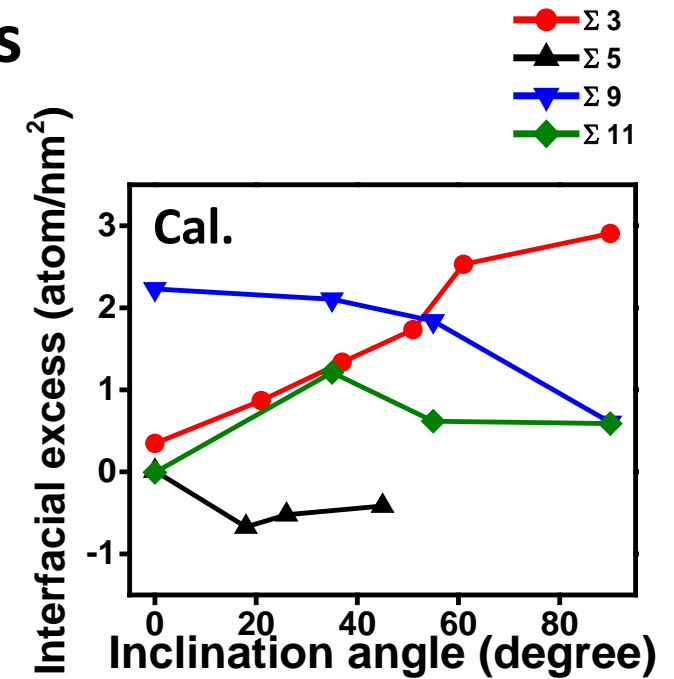
● Fe
● Cr



Comparisons between experimental & simulated results



https://staff.aist.go.jp/h.ogawa/GBstudio/gbs3/GBs_PJ.html



- Experimentally, the segregation values for the same CSL boundary are not always the same.
- MD/MC simulation revealed IE value is also a function of inclination angle.
- Simulated and experimental results matched well especially for Σ3 GB.

- Through cross-corrective PED-APT, high spatial and chemical sensitivity imaging was achieved.
- By quantifying the full character of the boundaries, the specific grain boundary was directly simulated using a hydride Monte Carlo – Molecular Dynamics method. The computational segregation trended well with the experimentally determined values.
- HAGBs had a higher Cr solute concentration. This was contributed to these features being preferred sites for clustering and the eventual initiation sites for Cr precipitation.



➤ Modeling thin film stress revealed

- The generation of tensile stress results from the coalescence of adjacent islands.
- An increase of injection energy of adatoms can change film stress from tensile to compressive.
- The steeper the adjacent face is, the stronger tensile stress can generate.
- The impinging tensile stress is inversely related to grain sizes of islands. But this relationship broke for fine grains.

➤ Compositional effects on stress evolution

- **W-Cr and W-Fe films:** The “zero-stress” films, W-80Cr and W-95Fe, were found. For the W-80Cr film, a laminate phase separating morphology observed in the grains. For the W-95Fe, the solute segregation was not present in the boundaries. Upon heating the ‘zero-stress’ composition films during growth, both W-95Fe and W-80Cr films became compressive with an increase of grain size and a strong segregation behavior observed.
- **Fe-Cr films:** The stresses were mainly controlled by grain size. When the Cr solute concentration is low, ≤ 4 at.% Cr, by adding Cr solute content, the tensile stress decreased due to the grain growth. The grain size refined and the tensile stress increased upon increasing the Cr solute concentration to 8 at.%. A higher Cr concentration (≥ 16 at.% Cr), abnormal grain growth was noticed resulting in a relatively low tensile stress. Upon heating the Fe-4Cr and Fe-16Cr films during deposition, tensile stresses reduced and the grains were refined.
- Through cross-corrective PED-APT, high spatial and chemical sensitivity imaging was achieved.
- The computational segregation trended well with the experimentally determined values.
- HAGBs had a higher Cr solute concentration resulting from their preferred sites for Cr.
- $\Sigma 3$ boundaries are most sensitive to inclination angles changes.



Acknowledgement

Supervisor:

Professor **Gregory B. Thompson**

Committee members:

Professor **Gregory B. Thompson**

Professor **Luke N. Brewer**

Professor **Amber Genau** (UAB)

Professor **Gary Mankey**

Professor **Mark L. Weaver**

Funding support:

Army Research Office, [ARO-W911NF-13-1-0436](#).

All my groupmates.

All my friends and the present audiences.



--Thank you!

